KEK Proceedings 2005-3
June 2005
R

Proceedings of the Third International Workshop on EGS

August 2 - 6, 2004.

KEK, Tsukuba, Japan

Edited by

Y. Namito, H. Hirayama and S. Ban

High Energy Accelerator Research Organization

FOREWARD

The First International Workshop on EGS4 was held at KEK during August 26-29, 1997 and the Second International Workshop on EGS was held at KEK during August 8-12, 2000 to exchange information about EGS itself as well as researches related to EGS internationally. These provided useful information among researchers who use EGS as the tool in various fields.

The third workshop was held at KEK during August 2-6, 2005.

The workshop, sponsored by High Energy Accelerator Research Organization in Japan (KEK), attracted over 100 EGS users from seven nations. Short course on EGS was held on the first and second day of the workshop using test version of EGS5 code.

At the workshop, 42 talks including poster session were presented from low-energy problems to the high-energy ones in the various research fields like the medical physics, radiation detector simulation etc. These proceedings include most of the presentations at this workshop.

Finally, we would like to express our great appreciation to all authors who have prepared manuscript quickly for the publication of this proceedings.

The organizing committee S. Ban (KEK)
A. F. Bielajew (U. Michigan)
H. Hirayama (KEK)
Y. Namito (KEK)
W. R. Nelson (SLAC)

CONTENTS

MODIFIED RANDOM HINGE TRANSPORT MECHANICS AND MULTIPLE SCATTERING STEP-SIZE SELECTION IN EGS5

S. J. Wilderman and A. F. Bielajew
University of Michigan, Ann Arbor, MI, USA

Abstract

The new transport mechanics in EGS5 allows for significantly longer electron transport step sizes and hence shorter computation times than required for identical problems in EGS4. But as with all Monte Carlo electron transport algorithms, certain classes of problems exhibit step-size dependencies even when operating within recommended ranges, sometimes making selection of step-sizes a daunting task for novice users. Further contributing to this problem, because of the decoupling of multiple scattering and continuous energy loss in the dual random hinge transport mechanics of EGS5, there are two independent step sizes in EGS5, one for multiple scattering and one for continuous energy loss, each of which influences speed and accuracy in a different manner. Further, whereas EGS4 used a single value of fractional energy loss (`ESTEPE`) to determine step sizes at all energies, to increase performance by decreasing the amount of effort expended simulating lower energy particles, EGS5 permits the fractional energy loss values which are used to determine both the multiple scattering and continuous energy loss step sizes to vary with energy. This results in requiring the user to specify four fractional energy loss values when optimizing computations for speed. Thus, in order to simplify step-size selection and to mitigate step-size dependencies, a method has been devised to automatically optimize step-size selection based on a single material dependent input related to the size of problem tally region. In this paper we discuss the new transport mechanics in EGS5 and describe the automatic step-size optimization algorithm.

1 Introduction

Because of the very large number of scattering collisions per unit path which electrons undergo as they pass through matter, Monte Carlo simulation of individual electron collisions (sometimes referred to as "analog Monte Carlo electron transport") is computationally feasible only in limited situations. Computationally realistic simulations of electron transport must therefore depart from the physical situation of linear, point-to-point, translation between individual scattering collisions (elastic or inelastic) and instead transport particles through long "multiple-scattering steps," over which thousands of collisions may occur, a technique commonly referred to as the "condensed history" [1] method. If we assume that most electron Monte Carlo simulation algorithms exhibit Larsen convergence[1] [2], then all algorithms exhibit an accuracy/speed trade-off which is driven by solely the length of the multiple scattering step they can take while still remaining faithful to the physical processes which might occur during those long steps. Models describing energy loss, angular deflection, and secondary electron production over long steps are quite well known. Descriptions of the longitudinal and transverse displacement coupled to energy loss and deflection over a long transport step, even in homogeneous media, however, require complete solutions of the transport equation, and so models which are sometimes quite approximate are used. The methods employed in Monte Carlo programs for selecting electron spatial coordinates after transport through multiple-scattering steps have come to be referred to as "transport mechanics." This is illustrated schematically in figure 1.

[1] Larsen noted that electron transport algorithms using multiple-scattering steps ought to converge to the analog result as the number of collisions in the multiple-scattering steps decreases. It must be noted that in general, this is *not* the case.

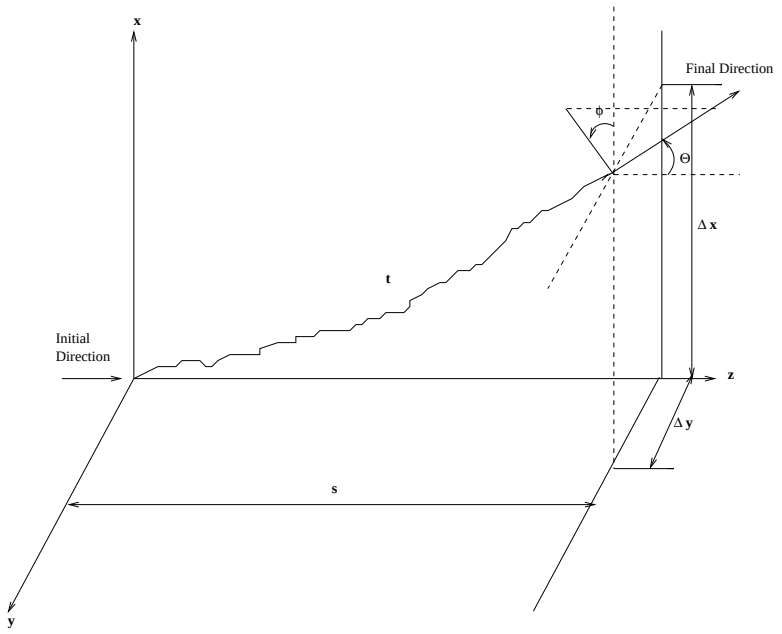

Figure 1: Condensed history/multiple scattering diagram.

As an electron moving in the z direction passes through a semi-infinite region of thickness s, it will have traveled a total distance of t, will have undergone lateral displacements (relative to its initial direction) of Δx and Δy, and will be traveling in a direction specified by Θ and ϕ. That is, relative to it's initial position and direction, the particle's final position is $(\Delta x,\ \Delta y,\ s)$, and the final direction vector given by $(\sin\Theta\ \cos\phi, \sin\Theta\ \sin\phi,\ \cos\Theta)$. The angle Θ can be determined from an appropriate multiple scattering distribution, the angle ϕ is assumed to be uniformly distributed, and the selection of $\Delta x,\ \Delta y$ and s are determined from the transport mechanics of a given simulation algorithm.

The fidelity with which an algorithm's transport mechanics model reproduces true distributions for displacement is almost the only factor driving the speed/accuracy trade-off of the program, and hence a substantial effort was made to improve the transport mechanics model in EGS5 relative to that in EGS4. In this paper, we will describe the motivation and development of the EGS5 transport mechanics model, discuss the parameters used to control the multiple scattering steps sizes in EGS5, and then present a novel approach for automatically determining nearly optimal values of the parameters based on a single, geometry-related parameter.

2 Transport Mechanics in EGS5

In this section we develop the motivation for the novel approach to transport mechanics taken in EGS5. Until the introduction of the PRESTA [3] algorithm, previous versions of EGS corrected for the difference between s and t, but ignored the lateral deflections Δx and Δy. The mechanics of the procedure used to simulate the transport of the electron thus were to translate it in a straight line a distance s along its initial direction and then determine its new direction by sampling the scattering angle Θ from a multiple scattering p.d.f. dependent upon the material, the total distance traveled, t, and the particle energy.

Ignoring lateral deflections introduces significant errors, however, unless restrictions (often quite severe) are placed on the maximum sizes of the electron transport tracklengths t. These restrictions were greatly eased by the introduction of the PRESTA algorithm, which treats Δx and Δy explicitly

during the transport simulation and which also includes a more accurate prescription for relating the straight line transport distance s to the actual pathlength t. It should be noted here that because of the random nature of the particle trajectory, s, Δx, and Δy are actually random variables (dependent upon the scattering angle Θ, In PRESTA, Δx and Δy range between 0 and $t/2$ and s is given by some fraction of t. There are two major drawbacks to the PRESTA formalism, however. First, in situations where an electron is traveling close to a region boundary, translating it lateral distances Δx and Δy perpendicular to its initial direction can sometimes result in moving it across the boundary and into a region with different material properties. Thus PRESTA required computationally expensive interrogation of the problem geometry and sometimes resulted in very small steps when particles were traveling roughly parallel to nearby region boundaries. Second, PRESTA is not adept at modeling backscattering. Electron backscattering in general results from a single, very large angle collision and not as the aggregate effect of a large number of small-angle collisions. It is clear from figure1 that physically, if an electron were to experience a 180 degree collision immediately at $t = 0$, it could potentially travel a distance $s = -t$ in the backward direction. Thus the set of all possible final positions for an electron traveling a pathlength t is a sphere of radius t (this is sometimes referred to as the "transport sphere"). Because it always sets s to be a positive value, the PRESTA formalism tends to overestimate the penetration prior to the large-angle backscatter event, which can lead to significant errors in computations of energy distributions of backscattered electrons, among other quantities.

2.1 Random Hinge Transport Mechanics

In EGS5 a new transport mechanics model, the random hinge, is introduced to address these shortcomings of PRESTA and thus permit very long step-sizes. The random hinge model, first used in PENELOPE [4], derives a large part of its success from being formulated so that the set of all possible termination points is in fact the full transport sphere of radius t. In this methodology, instead of transporting the particle a distance s and then displacing the particle by ΔX and ΔY and updating its direction according to the sampled scattering angles Θ and ϕ, the particle track t is first split randomly into two parts of lengths ξt and $(1-\xi)t$, where ξ is a random number. The electron is transported along its initial direction a distance ξt, at which point (the hinge point) its direction is updated (using Θ and ϕ as the scattering angles) and the particle is then translated in this new direction the remainder of it original tracklength, given by $(1-\xi)t$.

It is clearly seen from the schematic of figure 2 that the case of $\xi = 0$ (*i.e.*, the hinge point falling at the initial position) provides a mechanism to simulate track termination points over the full transport sphere. Formally, the advantages of this method can be demonstrated by examining the moments of the random hinge model. Ignoring energy losses, Kawrakow and Bielajew [5] have shown that this version of the random hinge model yields the correct values of the average straight-line path $\langle s \rangle / t$ and lateral displacement $\langle \Delta x^2 + \Delta y^2 \rangle / t$, and also comes very near to preserving many higher angle spatial moments.

Energy losses, because they result in changes in the single scattering cross section along t, reduce the accuracy of the random hinge. It has been shown by Fernández-Varea *et al.* [6] that when the single elastic scattering cross section is dependent on t, the first moments for axial and lateral displacements in the random hinge model differ from the exact moments in that they effectively evaluate first and second transport cross sections at slightly different distances along t. The transport cross sections (or inverse transport mean free paths), G_ℓ, are given by the Legendre moments of the single scattering cross sections, as in

$$G_\ell(t) = 2\pi \int_{-1}^{1} d\mu \Sigma(\mu; t)[1 - P_\ell(\mu)], \tag{1}$$

where $\Sigma(\mu; t)$ is the spatially dependent macroscopic single elastic scattering cross section and μ is $\cos(\Theta)$. Whereas the correct expressions for $\langle s \rangle / t$ and $\langle \Delta x^2 + \Delta y^2 \rangle / t$ in the energy dependent case

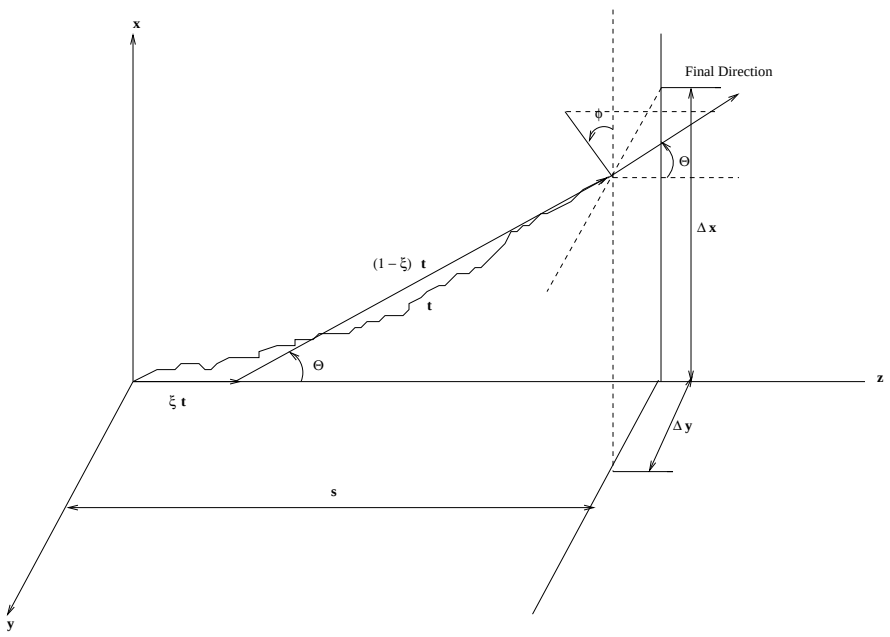

Figure 2: Random hinge transport mechanics.

are

$$\frac{\langle s \rangle}{t} = 1 - \frac{t}{2} G_1(\frac{t}{3}) \tag{2}$$

and

$$\frac{\langle \Delta x^2 + \Delta y^2 \rangle}{t} = \frac{2t}{9} G_2(\frac{t}{4}), \tag{3}$$

the average axial and lateral displacements in the random hinge model are

$$\frac{\langle s \rangle}{t} = 1 - \frac{t}{2} G_1(\frac{t}{2}) \tag{4}$$

and

$$\frac{\langle \Delta x^2 + \Delta y^2 \rangle}{t} = \frac{2t}{9} G_2(\frac{t}{2}) \tag{5}$$

respectively [6]. Since the $G_\ell(t)$'s increase as t increases (and energy decreases), the random hinge model slightly underestimates the average straight-line path s and overestimates the lateral deflections.

2.2 Modified Random Hinge Transport Mechanics

The analysis above suggests a modification to correct the random hinge method which was first employed in the Monte Carlo program DPM [7]. In the original random hinge methodology, energy loss is accounted for by simply evaluating the multiple scattering p.d.f. at the hinge point, which, on average, will occur at $t/2$. In the new methodology, the location of the random hinge is not a randomly selected fraction of the total distance to be traveled, t, but instead it is based on a randomly selected fraction of the integral over t of G_1, the first transport mean free path, commonly referred to as the "scattering power." This integral quantity is commonly called the "scattering strength," and denoted by $K_1(t)$, as in

$$K_1(t) = \int_0^t dt' G_1(t'). \tag{6}$$

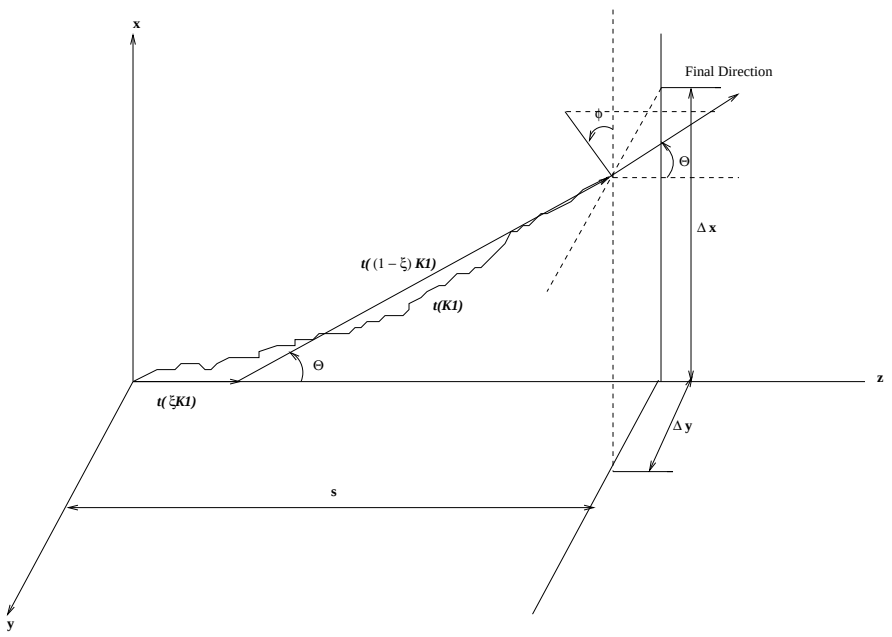

Figure 3: Modified random hinge transport mechanics.

Thus, instead of the hinge consisting of steps ξt and $(1-\xi)t$, it consists of steps of the distances corresponding to the accumulation of scattering strengths $\xi K_1(t)$ and $(1-\xi)K_1(t)$. In this way, the total scattering strength $K_1(t)$ over the step is preserved, and the average location of the hinge will correspond to that location which preserves the first moments of spatial displacements. The modified random hinge transport mechanics of EGS5, illustrated in figure 3, is therefore capable of simulating accurately the average final positions of electrons moving long pathlengths through materials, even when energy loss occurs continuously along the track. The length of an electron step is therefore limited only by the accuracy of the multiple scattering p.d.f., any need to higher order spatial moments (as would be required for some differential tallies), and the accuracy of the method used to compute the integral in Eq.6 along the paths between hinge points.

2.3 Dual Random Hinge Approach

The accuracy with which the integral over the scattering power G_1 is computed over the hinge can be stated more plainly as the accuracy of the computation of the hinge distances in cm given the scattering strength, ξK_1 and $(1-\xi)K_1$. Inverting integrals over pathlength such as Eq.6 is a common process in Monte Carlo electron transport programs, analogous to the computation in EGS4, for example, of the pathlength to be taken given a specified fractional energy loss to occur over the step. In typical Monte Carlo programs this type of calculation is done by some form of the trapezoid rule, which requires that the integrand (stopping power, scattering power, etc) vary no more than linearly through the step.

EGS5 employs a different approach to this problem in an effort to retain as much as possible the very large steps permitted with the multiple scattering hinge as long as average values of K_1 are preserved over the steps. Thus, rather than require small steps to assure accurate integration of G_1 over energy, EGS5 completely decouples energy loss and multiple scattering by employing a second random hinge to described energy loss, relying on the random position of the energy loss hinges to yield the correct energy-averaged computation of K_1. A schematic of the dual random hinge approach is presented in figure 4. Independent energy loss steps $t_E(\Delta E)$ (the distance being determined from some initially specified fractional energy loss) and multiple scattering steps $t_\Theta(K_1)$

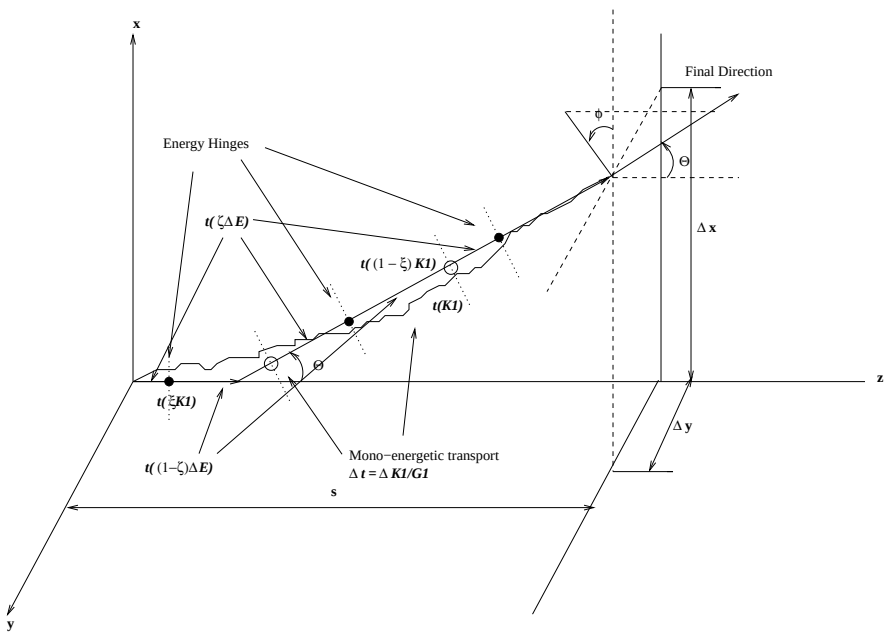

Figure 4: Dual hinge transport mechanics.

(here the distance is determined from an initially specified scattering strength) are simultaneously processed, using random hinges. The lengths of the initial segments are determined by multiplying random numbers ξ_E and ξ_Θ by ΔE and K_1 respectively, as before. A particle is then transported linearly until it reaches a hinge point at either $t_E(\xi_E \Delta E)$ or $t_\Theta(\xi_\Theta K_1)$. When the multiple scattering hinge point is reached, the deflection is modeled assuming that the entire multiple scattering path $t_\Theta(K_1)$ had been traversed, and transport continues. Similarly, the energy of the electron remains unchanged along its track until the energy hinge point $t_E(\xi_E \Delta E)$ is reached, at which time the electron energy is decremented by the *full amount* ΔE prescribed. Subsequent to a reaching a hinge point and undergoing either energy loss or deflection, the electron must then be transported the distance remaining for the given step, $t_E[(1 - \xi_E)\Delta E)$ for energy hinges or $t_\Theta[(1 - \xi_\Theta)K_1$ for multiple scattering hinges. The two hinge mechanisms are completely independent, as several energy hinges may occur before a single multiple scattering is applied, and vice versa.

In evaluating the multiple scattering distribution and sampling for the deflection, all parameters which have an energy dependence are computed using *the most recently updated energy* for the particle. Since energy hinges will occur sometimes before scattering hinges and sometimes after, there is thus an implicit averaging of the electron energies over the full hinge distance. It is in this way that the random energy hinge provides accurate integration of K_1 by, on average, using G_1 at the correct energy. This same methodology is employed when computing the energy loss from the integral of the stopping power: rather than attempt to approximate the average stopping power over the step, EGS5 relies on the random energy hinge to provide the correct average result for the total energy loss.

Note that the quantities that remain fixed over the hinges are ΔE and K_1, and not the distances t_E and t_Θ. Whenever an event occurs in which values of the scattering power or stopping power change, such as an energy hinge, the energy loss and scattering strength remain fixed, and any unused hinge distances t_E and t_Θ must be updated using the new values of the scattering and stopping power. Energy deposition along the track is done using the continuous slowing down approximation (CSDA) model, with updates made whenever a hinge point is reached or any other event occurs.

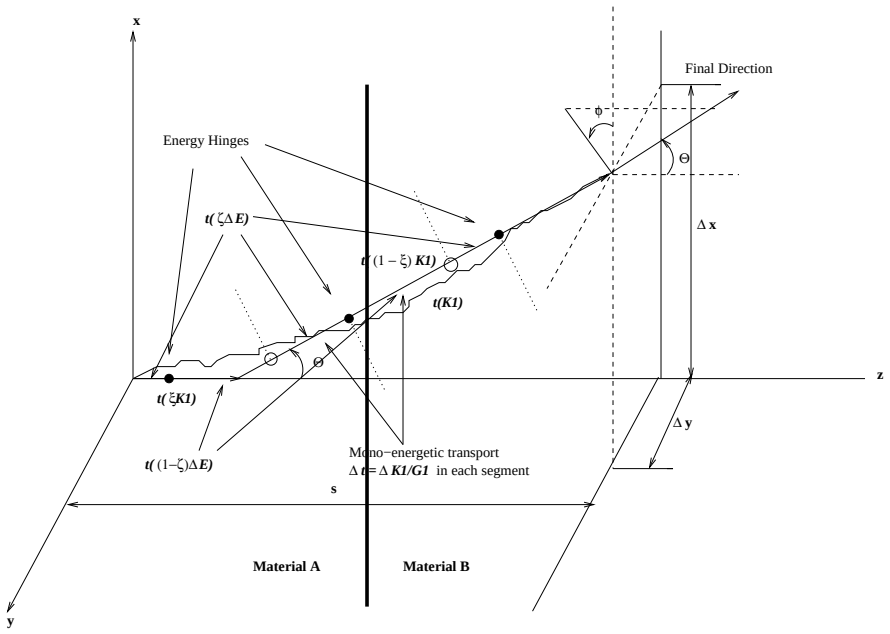

Figure 5: Transport across boundaries.

2.4 Boundary Crossing

One extremely important implication of the use of the modified random hinge for multiple scattering is that it lends itself to a method for seamlessly crossing region boundaries. In all previous versions of EGS, including EGS4 with PRESTA, when a particle boundary was reached multiple elastic scattering was applied and transport started anew in the new region. With the modified random hinge however, multiple scattering occurs only at hinge points. If a boundary is crossed during either the pre-hinge ($\xi K_1(t)$) or post-hinge ($(1-\xi)K_1(t)$) portion of the step, the value of G_1 used in updating the accumulated scattering strength is simply changed to reflect the new value of the scattering power in the new media. Thus it is not necessary to apply multiple scattering at region boundaries, and the expensive re-interrogation of the problem geometry required by PRESTA is completely avoided. Inherent in this is the implication that multiple scattering distributions are equivalent for different materials at a given energy and for pathlengths which correspond to the same scattering strength K_1. This, of course, is not strictly true. It can be shown formally, however, that for a multiple scattering distribution expressed as a sum of Legendre polynomials in Θ,

$$\langle \cos(\Theta) \rangle = \exp(-K_1) \tag{7}$$

so that for small K_1

$$K_1 \simeq \ 1 - \langle \cos(\Theta) \rangle. \tag{8}$$

Thus, in preserving K_1 for cross boundary transport, the EGS5 method also roughly preserves the average cosine of the scattering angle over the boundary.

Inspection of the implementation details reveals that the boundary crossing in EGS5 is analogous to an energy hinge without energy loss. All step-size variables (rates and distances) need to be updated, but otherwise transport to the next event is uninterrupted, as shown in figure 5.

2.5 EGS5 Transport Algorithm

The transport between hard collisions (bremsstrahlung or delta-ray collisions) is superimposed on the decoupled hinge mechanics as an independent, third possible transport process. To retain the

decoupling of geometry from all physics processes, for hard collisions EGS5 holds fixed over all boundary crossing an initially sampled number of mean free paths before the next hard collision, updating the corresponding distance (computed from the new total cross section), when entering a new region. Again, while the random energy hinge preserves the average distance between hard collisions, it does not preserve the exact distribution of collision distances if the hard collision cross section exhibits an energy dependence between the energy hinges. In practice, however, this leads to only small errors in cases where the energy hinge steps are very large and the hard collision mean free path is sharply varying with energy.

Because energy loss, multiple scattering, hard collisions and boundary crossing have been completely decoupled in EGS5, the basic electron transport algorithm can be described simply as the loop until escape or absorption over the most proximal of the following four processes: (For the sake of illustration, it was assumed in table 1 that the particle remained active after collision analysis.)

3 Step-Size Selection Using Fractional Energy Loss

User control of multiple scattering step-sizes in EGS4 is accomplished through the specification of the variable `ESTEPE`, the fractional kinetic energy loss desired over the steps. Because of the complete decoupling of the energy loss and elastic scattering models, there are two separate step-size mechanisms, one based on energy loss and controlling energy hinge steps, and one based on scattering strength and controlling multiple-scattering hinge steps. Of the two, the multiple-scattering step is almost always the more limiting because it is what drives the transport mechanics. As stated earlier, energy hinges are required mostly to provide accurate numerical integration of energy-dependent quantities. Because hard collisions provide *de facto* energy hinges whenever they are encountered, for situations in which these cross sections are large because the PEGS thresholds `AE` and `AP` are small, the numerous hard collisions can provide all of accuracy required in energy integration and energy hinges can be superfluous. Only in cases where hard collisions are small and material cross sections, stopping powers, etc., vary rapidly with energy do small energy hinge steps need to be imposed.

For consistency with EGS4, EGS5 retains `ESTEPE`, as the variable used to specify energy loss hinges. To control multiple scattering step-sizes, it would seem logical for EGS5 to require specification of $\cos\Theta$, because K_1 is very close to $1 - \langle\cos\Theta\rangle$ (see equation 8). Figure 6 shows results from simulations of central axis depth/dose with EGS5 with electron multiple scattering steps set to $\cos\Theta$ of 0.990 and from runs using various values of `ESTEPE` in EGS4. The test problem employed a 30x30x30 cm water phantom broken into 2.5 mm voxels with an incident pencil beam of energy of 10 MeV and an electron cut-off energy of 500 keV. In all cases, 100,000 particles were simulated. The value of $\cos\Theta$ of .990 used in the EGS5 corresponds to roughly a 5% fractional energy loss at 10 MeV, and values of `ESTEPE` of .05, .02, .01, .005 and .002 were used in the EGS4 runs. Simulation time for the EGS5 case was 634 seconds, while the EGS4 runs required 261, 454, 809, 1513, and 3674 seconds, respectively. It is seen that to achieve results comparable to those of EGS5, EGS4 required values of `ESTEPE` of no greater than .005, for which EGS4 it roughly 2.5 times more slowly than EGS5 for this problem.

But we encounter some interesting problems in examining these results. Despite being able to take steps that are 10 times longer than those used in EGS4, EGS5 is only 2.5 times faster. Although there is extra bookkeeping involved in processing the hinge variables[2], it does not account for this large discrepancy. The real problem is that since electron scattering power changes (increases) much more rapidly than stopping power as an electron slows under an MeV or so, fixing K_1 for the entire electron trajectory results in taking very much smaller steps for lower energy electrons

[2]We move particles in distances measured in cm, but we track step-size variables in energy loss and scattering strength, so we are constantly converting between the two. In addition, EGS5 must keep track of both the pre- and post-hinge point values of the step-size variables.

- Energy Hinge
    1. deposit CSDA energy
    2. update remaining N_{hard}, and K_1
    3. change particle energy
    4. update G_1, $\frac{dE}{dx}$, Σ_{hard}
    5. update t_Θ from remaining K_1 and new G_1
    6. update t_{hard} from remaining N_{hard} and new Σ_{hard}
    7. set new energy hinge
- Hard Collision
    1. deposit CSDA energy
    2. update remaining K_1
    3. update particle Energy
    4. perform collision analysis
    5. update G_1, $\frac{dE}{dx}$, Σ_{hard}
    6. update t_Θ from remaining K_1 and new G_1
    7. sample new hard collision mean free paths
    8. set new energy hinge
- Multiple Scattering Hinge
    1. deposit CSDA energy
    2. update remaining N_{hard}, and ΔE
    3. deflect particle
    4. update t_{hard} from remaining N_{hard} and current Σ_{hard}
    5. update t_E from remaining ΔE and current $\frac{dE}{dx}$
    6. set new multiple scattering hinge
- Boundary Crossing
    1. deposit CSDA energy
    2. update remaining N_{hard}, K_1 and ΔE
    3. update G_1, $\frac{dE}{dx}$, Σ_{hard}
    4. update t_Θ from remaining K_1 and new G_1
    5. update t_{hard} from remaining N_{hard} and new Σ_{hard}
    6. update t_E from remaining ΔE and new $\frac{dE}{dx}$
    7. get new distance to boundary

Table 1: Actions at each of the four de-coupled transport processes in EGS5

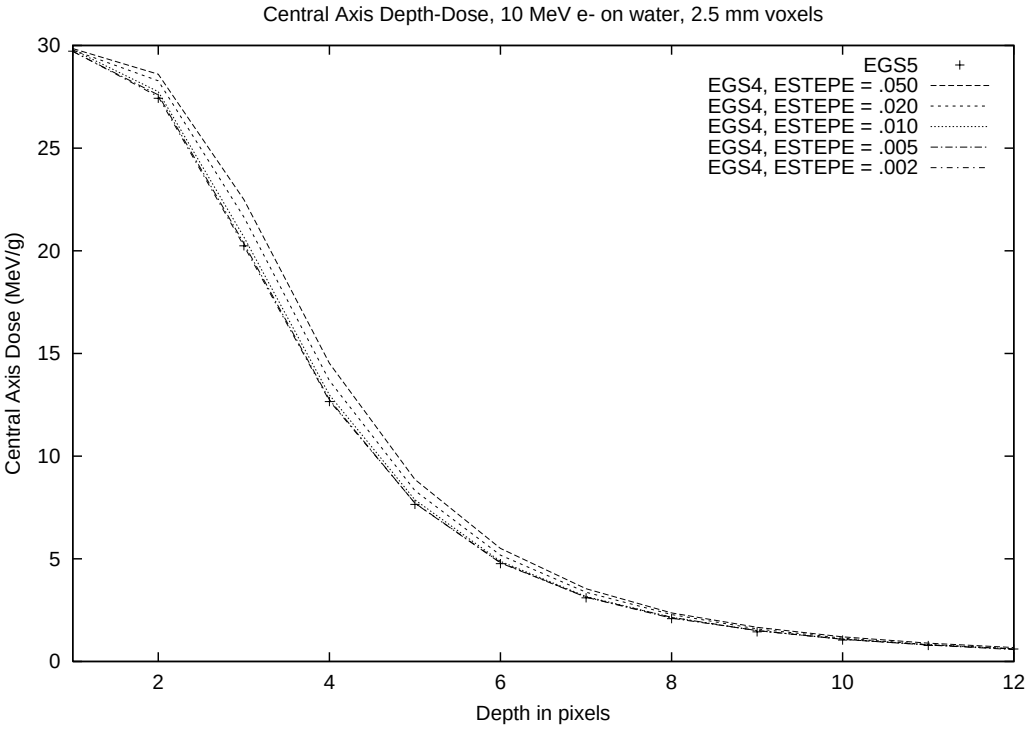

Figure 6: Comparison of EGS5 and EGS4 for 2.5 mm^3 voxel water phantom at 10 MeV.

than the fixed fractional energy loss method using `ESTEPE` of EGS4, given the same step size at the initial (higher) energy. For example, the value of K_1 corresponding to a 2% energy loss for a 10 MeV electron in water corresponds to a 0.3% energy loss at 500 keV. Thus, for small voxel sizes (and the lower energy cutoffs that they require), a step-size control mechanism based on a scattering strength that is constant with energy makes EGS5 take so many small steps at lower energies than EGS4 that it could be slower for certain problems, despite being able to take long steps 10 times as long at high energies. To circumvent this problem, despite still basing multiple scattering steps on scattering strength, EGS5 reverts to specifying the multiple scattering step-size based on a fractional energy loss over the step, which is now called `EFRACH`, to distinguish it from `ESTEPE`, which is still used for energy hinges. `EFRACH` is material dependent and specified in the PEGS input NAMELIST.

One consequence of the work done to assure that EGS5 expends most of its computational effort where it was most important (*i.e.*, at higher energies), was the recognition that additional efficiency might be achieved by allowing the fractional energy loss of the multiple scattering steps to vary over the energy range of the problem. Thus, in addition to `EFRACH`, which is now defined to be the fractional energy loss over a multiple scattering step at the highest problem energy, a second parameter `EFRACL`, corresponding to the fractional energy loss over a multiple scattering step at the lowest problem energy, is used. Like `EFRACH`, `EFRACL` is also material dependent and is specified in the PEGS input NAMELIST, and the fractional energy loss permitting for multiple-scattering steps swings logarithmically over the energy range of the problem.

Because of the dramatic results obtained in permitted multiple scattering step fractional energy losses to vary, a similar method was implemented to permit energy loss hinges to vary, using the parameter `ESTEPE2` to define the fractional loss at the low energies.

The central-axis depth/dose simulation described earlier was then repeated using the four-parameter step size control model of EGS5 on a problem for which EGS4 was actually faster than

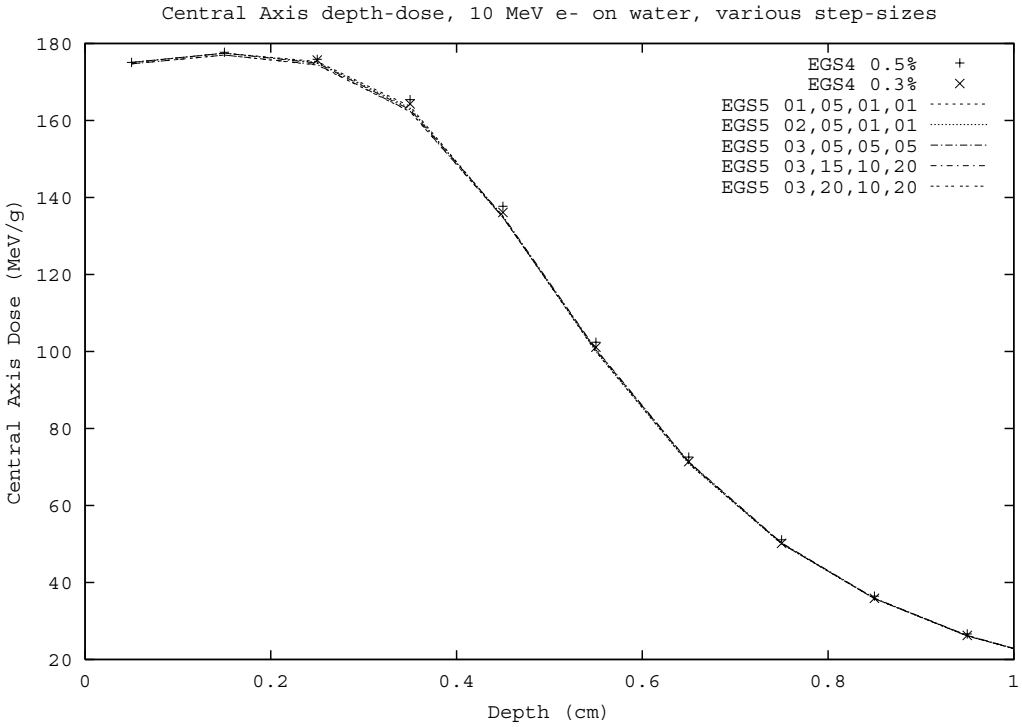

Figure 7: Comparison of EGS5 and EGS4 for 1.0 mm^3 voxel water phantom at 10 MeV.

EGS5 when employing the constant scattering strength model, because of all the extra work EGS5 had been doing at low energies. In this problem, which again uses a 10 MeV pencil beam incident on a water phantom, voxels were reduced to 1 mm and an electron cutoff energy of 200 keV was employed.

We see from figure 7 that EGS5 can again take steps which again are roughly 10 times as long as those require with EGS4 at the initial energy. We also see the relatively small effect that the energy hinge step size has on the computation (because the threshold for secondary particle production is low), and we see how unnecessary it is (for this problem, at least), to take the same size multiple scattering steps (measured in terms of fractional energy loss) needed at high energies at all energies. There is no appreciable differences between computations using 5% and 20% `EFRACL`.

Table 2 can be used to roughly gauge how much various factors (improved transport mechanics, variable `EFRACH`, decoupling of the energy hinge, and variable `ESTEPE`) contribute to the overall gain in efficiency in EGS5 vs. EGS4.

4 Step-Size Specification Using Media Dependent "Characteristic Distances"

Optimal step-size selection (by "optimal" we mean the longest steps and hence the shortest run time which would provide a converged answer for the given desired error limit) is inherently problem-dependent, thus requiring some user input. As illustrated in the two examples from the preceding section, step-size is often a function of the dimension or "granularity" of desired output tally. Central axis dose from a pencil beam is a very fine grain problem, for example, and as the granularity becomes finer (such as by decreasing the voxel sizes), the user step-size must also be selected to be somewhat smaller, for both EGS4 and EGS5.

EFRACH,EFRACL,ESTEPE,ESTEPE2	CPU time for 1M histories
EGS4 with ESTEPE = .003	42160.6
.01,.05,.01,.01	7296.0
.01,.05,.01,.10	4592.3
.01,.05,.10,.10	4073.2
.01,.10,.10,.10	3027.6
.03,.10,.10,.10	2550.8
.03,.15,.10,.10	2261.2
.03,.20,.10,.20	1990.2

Table 2: CPU times for various combinations of EFRACH,EFRACL, ESTEPE,ESTEPE2

Clearly, for any given problem, judicious choices of EFRACH,EFRACL,ESTEPE and ESTEPE2 should result in the largest possible transport throughout the full electron energy range and hence optimize EGS5 for speed. But it is also fairly obvious from the discussion above that only an expert user could appropriately and effectively select these parameters in all situations. Even acknowledging that step-size selection necessarily requires some input from the user because of it is inherently problem-dependent, it is clear that step-size selection based on the four EGS5 parameters EFRACH, EFRACL, ESTEPE, and ESTEPE2 places an undue burden on the user. To address this problem, a method has been devised which will automatically select step-sizes based on a single user input parameter based on the problem geometry.

Development of a method for optimization of step-size selection first requires the adoption of a practical standard for accuracy. From the discussion of the depth/dose example problems in the previous section is it clear there do indeed exist optimal multiple scattering step-sizes for the random hinge mechanics using tally-regions of varying sizes. Since spatial energy deposition profiles are essentially maps of region-dependent electron tracklengths, and because most problem tallies will be correct if the spatial distribution of electron tracklengths is correct[3], the largest value of scattering strength $K_1(E)$ which produces converged results for energy deposition for a given material in a reference geometric element was chosen to be the standard for the EGS5 step-size selection algorithm. Thus, in addition to permitting selection EFRACH and EFRACL to control multiple scattering step-sizes, EGS5 also provides an option by which the user can input a single distance which characterizes the geometric granularity of the problem tallies. This distance is called the "characteristic distance" for the problem, and is set in the user's main program through specifying a value of the variable charD, which is material dependent.

Given an input characteristic distance for a medium, EGS5 then determines energy dependent values of $K_1(E)$ by interpolating data tables of maximum scattering strengths vs. distance for a variety of materials, energies and geometric element sizes. The tables range in energy from roughly 2 keV [4] up to 10 GeV by using values of 2, 3, 5, 8 and 10 in each of the 7 decades spanning the range from 1 keV to 1 GeV. The characteristic geometric distances in the data sets range from the lesser of 10 microns and 10^{-5} times the electron CSDA range up to half of the CSDA range [5]. Because K_1 is the integral over distance of scattering power, which is proportional to ρZ^2 times the integral of the shape of the differential elastic scattering cross section, K_1 should be roughly proportional to $t\rho Z^2$, if t is the distance. Thus interpolation in the material dimension is performed in terms of

[3] See the end of this section for a brief description of special cases in which this is not true.

[4] For high Z materials for which the Bethe stopping power formula is inaccurate at 2 keV, the tables stop at 10 keV.

[5] An additional constraint on the minimum characteristic distance in EGS5 is the smallest pathlength for which the Molière multiple scattering distribution produces viable results. Bethe [8] has suggested that paths which encompass at least 20 elastic scattering collisions are necessary, though EGS4 will compute the distribution using as few as e collisions, which is a numerical limit that simply assures positivity.

Material	Z	ρ	ρZ^2
Li	3	0.534	4.81
H_2O	10	1.000	66.0
C	6	2.260	81.4
Al	13	2.702	456.6
S	16	2.070	529.9
Ti	22	4.540	2197.4
Ge	32	5.360	5488.6
Cu	29	8.933	7512.9
Zr	40	6.400	10240.0
La	57	6.150	19981.4
Ag	47	10.50	23194.5
Gd	64	7.870	32235.5
Hf	72	11.40	59097.6
W	74	19.30	105686.8
Au	79	19.30	120451.3
U	92	18.90	159969.6

Table 3: Reference materials in tables of energy and characteristic distance dependent scattering strength tables.

ρZ^2 rather than Z. For gases, interpolation is done in terms of Z and the values are then scaled in terms of ρ. Positron K_1 values are determined by scaling electron scattering strength by the ratio of the positron and electron scattering power. The list of reference materials is given in table 3. A description of the generation of the data tables of optimal values of K_1 as a function of ρZ^2, E, and t follows.

Perhaps the most severe test of a Monte Carlo program's electron transport mechanics is the "broomstick" problem, in which electrons are normally incident on the planar faces of semi-infinite right-circular cylinders of progressive smaller radii (to isolate the effects of the transport mechanics, hard-collisions are usually ignored in this problem). For cylinders with radii of the CSDA range or greater, all electrons will be fully absorbed in the cylinder (assuming that the energy is so high that backscatter is negligible), meaning that the average track-length was the full CSDA range. In this case, multiple-scattering step-sizes can be pushed to the theoretical limits of the underlying distribution functions will still provide converged results. For cylinders with radii approaching infinitesimal thinness, the average tracklength of an incident electron would given by the single elastic scattering mean-free path, and so only step-sizes which reproduce that value would provide converged results in a Monte Carlo simulation. Clearly, for any given cylinder radius, for any transport mechanics model, if we start at very small step-sizes (we are assuming Larsen convergence) and gradually increase them, we will eventually see encounter divergence in the computed average electron track inside the cylinder as the model will over-estimate the penetration prior to deflection out toward the sides of the "broomstick." This is illustrated in figure 8.

(Note that ignoring hard collisions and using unrestricted stopping powers at the upper end of the energy range in question is physically unrealistic. Computations in this energy range were made nonetheless to fill out the tables with overly-conservative estimates of the appropriate step-size.)

For each material, energy, and distance (broomstick diameter) a series of Monte Carlo simulations were performed, using up to 20 different values of `EFRACH`, covering the range from 30% to 0.05% (except when such steps exceeded the theoretical limits of the Molière distribution). Energy loss hinges were set to 0.5% fractional energy loss, and 50,000 histories were simulated, resulting in relative uncertainties at 2σ of around .4%. Tallies were made of energy deposition, backscatter

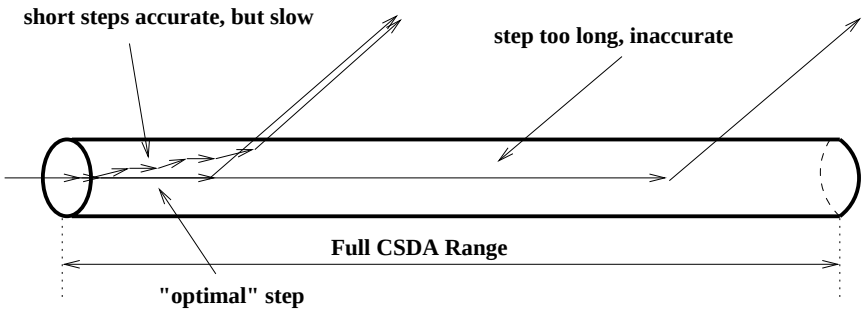

Figure 8: Schematic illustrating the broomstick problem.

and escape from the side of the broomstick. An illustrative plot of the divergence in the results Copper at 5 MeV for several different broomstick thicknesses are shown in figure 9.

Approximately 6000 such plots were generated from over 50,000 simulations to encompass the desired ranges of materials, energies, and distances. The data was then analyzed to determine the initial scattering strength corresponding to the maximum fractional energy loss which showed convergence within the statistical uncertainty of the data, using a least-squares fit to a line with slope zero and intercept given by the converged value at short paths. In order to assure that backscatter was being modeled correctly, the analysis required that results be converged for both energy deposition inside the cylinders and energy escaping the sides. Plot of maximum values of K_1 to assure convergence as a function of broomstick radii for several energies in titanium are shown in figure 10.

The expected nearly linearly relationship between K_1 and t and the appropriate scaling of K_1 with E is clearly evident in the figures. We also see several artifacts of our method. First, we see that our estimation process did not always produce monotonic results, primarily because of noise in the data due to the Monte Carlo statistics (given the large number of runs, some outlier points were to be expected) and because some points were generated outside the applicable range of some of the physics, Traps in the analysis program designed to weed-out data from invalid (too long or too short) step-sizes sometimes resulted in errors for large cylinders, grossly under-determining the maximum scattering strength in some cases. Additionally, the plots exhibit some discrete jumps because of the finite number of possible K_1 values tested in the parameter study. This effect is more clearly evident in figure 11, which presents similar data but in terms of `EFRACH` and fractional range instead of K_1 and t in cm for a variety of elements at 100 MeV. Even though results are presented for 12 elements, only 3 curves are visible in figure 11 because of the finite number of combinations of `EFRACH` and t/R in the runs.

Figure 12 shows the same data presented in figure 11, but in terms of K_1 and t again, which is easier to interpret. We see an additional artifact in this plot, caused by limiting our test runs to a maximum of 30% fractional energy loss. This leads to a plateauing of the plots for high energies. Other data sets show the corresponding artifact caused by numerical limits on the minimum step-size at low energies. Note also from figure 12 that the scaling of K_1 in ρZ^2 rather than Z^2 is evident in the comparison of the plots for silver and lanthanum, which are roughly equivalent in ρZ^2, though obviously not in Z^2.

Despite all of the approximations involved in the definition and determination of convergence, the data exhibits for the most part the linear behavior we expected in ρZ^2, t, and E. Especially for a given element at a given energy, the plots can generally be described as being roughly linear in t, though possibly plateauing at either end. Thus each curve (which represents one energy for a given element) can be wholly defined by the characteristic distances corresponding to the onset (if any) of plateaus, the values of K_1 at those points, and the slope of line between those plateau

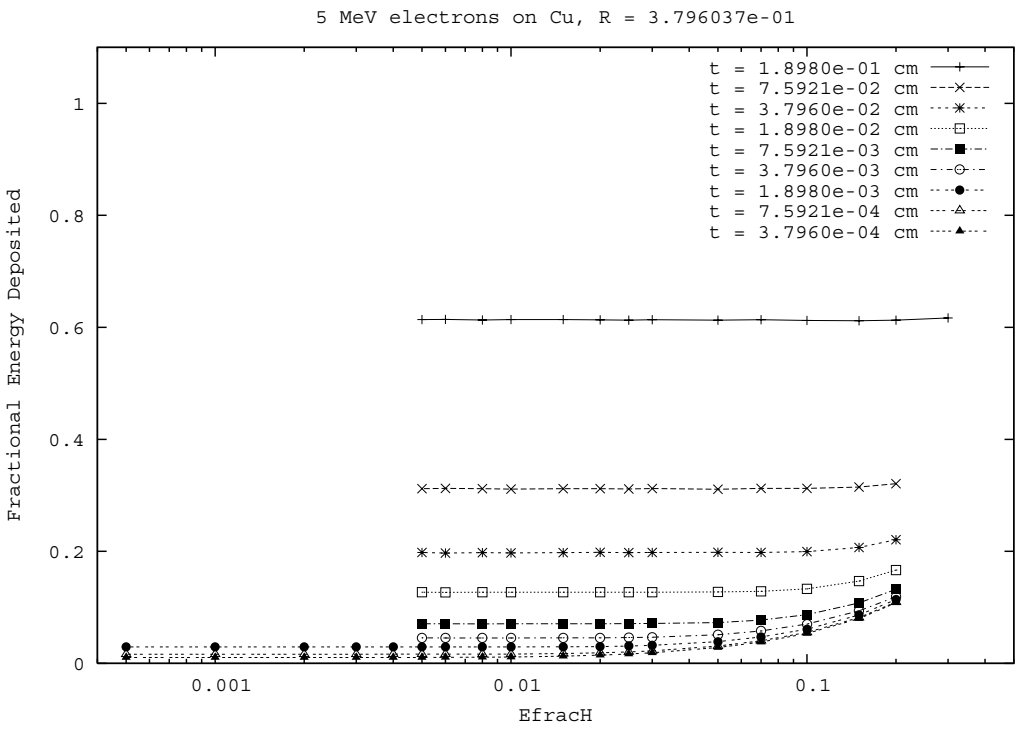

Figure 9: Broomstick energy deposition convergence with step-size in Copper at 5 MeV

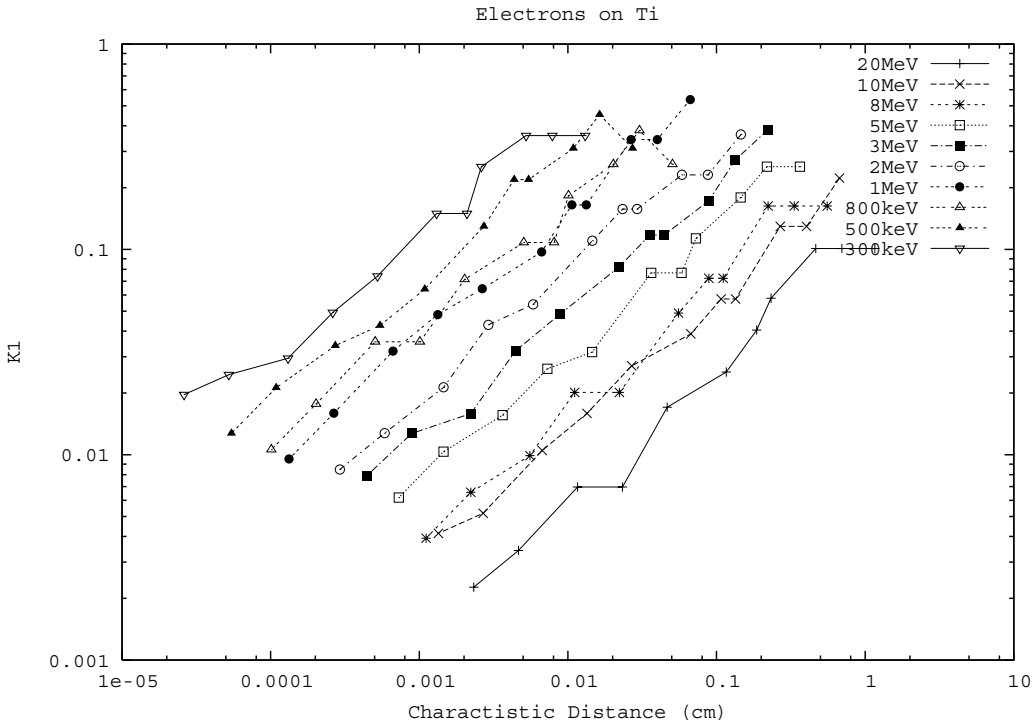

Figure 10: Maximum scattering strength K_1 vs. broomstick diameter in titanium for various energies

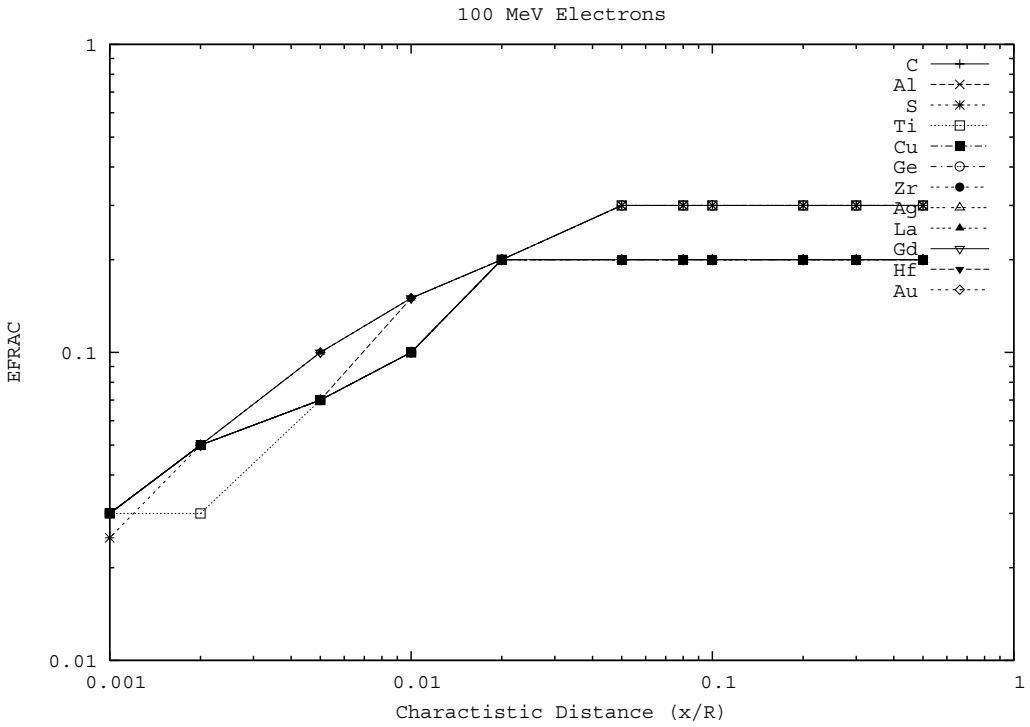

Figure 11: Maximum fractional energy loss `EFRACH` vs. broomstick radius in r/R for various elements at 100 MeV

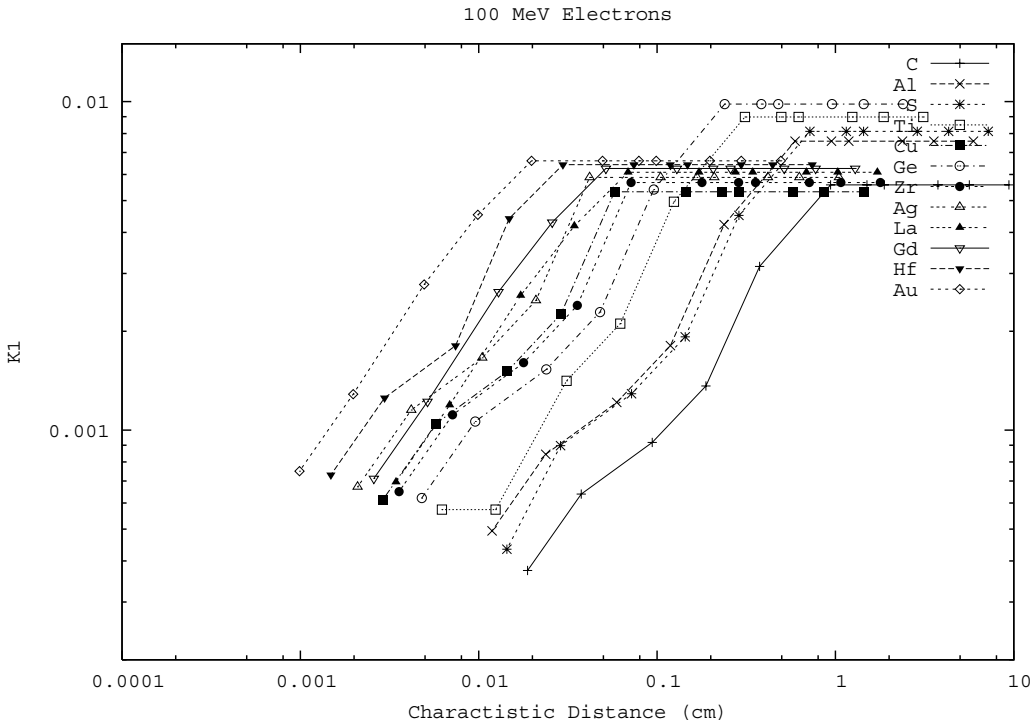

Figure 12: Maximum scattering strength K_1 vs. broomstick diameter for various elements at 100 MeV

Run	E_{dep}	CPU time
`EFRACH, EFRACL` = .05,.05	13.50%	29.34
`charD` = .1395	13.57%	29.63
`charD` w/ ρZ^2 interp.	13.52%	29.01

Table 4: Validation of optimizing K_1 with `charD` interpolation.

points. All of the curves were thus inspected visually and corrected to assure monotonicity and to eliminate the more significant artifacts caused by having a limited set of discrete data points, and eliminate any physically unrealistic trends in K_1 as a function of t or E for the same material. Using these corrected plots, the five parameters defining each line were determined, with a least squares fit applied to calculate the slope. The full set of parameters was compiled into a single data file `K1.dat` provided with the EGS5 distribution.

To verify that the new technique is both accurate and fast, three test cases where run. In the the broomstick problem for silver at 2 MeV and t/R of 10% (t = .1395 cm), the converged value for fractional energy deposition of 13.5% was found to first occur at K_1 = .23635, or 5% fractional energy loss. This problem was then repeated using `EFRACH` and `EFRACL` of 5% to reproduce the original data run. Next, a simulation was performed using the new methodology with `charD` of 0.1395 cm, and finally, to test the interpolation, the computation was repeated with the data for silver removed from the `K1.dat` file. The results shown in table 4 show that the method works well at reproducing accurate results and also maintaining speed-up optimization even with interpolation between materials.

It must be noted that not all classes of problems are guaranteed to be modeled accurately whenever the average tracklength is modeled correctly through given volume regions. In particular, problems using on tallies which have a spatial or directional dependence on secondary particle production which occur prior to the first multiple scattering hinge point can show artifacts not present in EGS4, which always imposes multiple scattering prior to secondary particle production. To counter this problem and still permit EGS5 to take very long steps, a user switch to relate the first multiple scattering hinge step for primary particles to some fraction of the hard collision mean free path.

5 Conclusions

The random hinge transport mechanics of EGS5 has been show to provide a significant improvement over the model of EGS4. In addition to large speed-ups in most general problems, the new method permits EGS5 to simulate accurately some classes of problems, most notably electron backscattering, which EGS4 was know to model imprecisely.

In addition, a new prescription for automatic control of multiple scattering step sizes by relating them to problem geometry dimensions has been devised. This new technique based on providing values of electron tracklengths which are accurate to at least 1% for the given characteristic distance.

Acknowledgments

The authors wish to express special thanks to our colleagues Ralph Nelson and James Liu (from SLAC) and Yoshihito Namito and Hideo Hirayama (from KEK) for, among many other things, identifying challenging test problems and providing extremely helpful suggestions.

References

[1] M. J. Berger. Monte Carlo calculation of the penetration and diffusion of fast charged particles. *Methods in Comput. Phys.*, 1:135 – 215, 1963.

[2] E. W. Larsen. A theoretical derivation of the condensed history algorithm. *Ann. Nucl. Energy*, 19:701 – 714, 1992.

[3] A. F. Bielajew and D. W. O. Rogers. PRESTA: The Parameter Reduced Electron-Step Transport Algorithm for electron Monte Carlo transport. *National Research Council of Canada Report PIRS-0042*, 1986.

[4] J. Baró, J. Sempau, J. M. Fernández-Varea, and F. Salvat. PENELOPE: An algorithm for Monte Carlo simulation of the penetration and energy loss of electrons and positrons in matter . *Nuclear Instruments and Methods*, B100:31 – 46, 1995.

[5] I. Kawrakow and A. F. Bielajew. On the condensed history technique for electron transport. *Nuclear Instruments and Methods*, B142:253 – 280, 1998.

[6] J. M. Fernández-Varea, R. Mayol, J. Baró, and F. Salvat. On the theory and simulation of multiple elastic scattering of electrons. *Nuclear Instruments and Methods*, B73:447 – 473, 1993.

[7] J. Sempau, S. J. Wilderman, and A. F. Bielajew. DPM, a fast, accurate Monte Carlo code optimized for photon and electron radiotherapy treatment planning dose calculations. *Physics in Medicine and Biology*, 45:2263–2291, 2000.

[8] H. A. Bethe. Molière's theory of multiple scattering. *Phys. Rev.*, 89:1256 – 1266, 1953.

NEW PHOTON TRANSPORT PHYSICS IN EGS5

Y. Namito, H. Hirayama
High Energy Accelerator Research Organization (KEK), Oho, Tsukuba 305-0801, Japan

Abstract

We have improved photon transport in egs4 code in various points; 1. Linearly polarized photon scattering, 2. Doppler broadening and binding in Compton scattering, 3. L-X rays, 4. Auger electron, 5. X ray and Auger electron from compound/mixture, 6. K shell electron impact ionization (EII), 7. Use of PHOTX data base, and 8. General treatment of photoelectric cross sections. New photon transport physics in EGS5 also consists of these items. Comparisons of measurements and EGS5 calculation are included. Also, calculations using improved EGS4 code are mentioned.

1 Introduction

Improvement of photon transport in egs4 [1] code has been described in 1st and 2nd international EGS workshop [2, 3]. The items were;

1. Linearly polarized photon scattering: Electric vector of photon is maintained while photon transport calculation. Azimuth angle dependence of photon intensity in Compton and Rayleigh scattering is considered. [4]

2. Doppler broadening and binding in Compton scattering: Doppler broadening of Compton scattered photon energy due to pre-collision motion of electron is treated. [5]

3. L-X rays: Energy dependence of L1-L2-L3 sub shell photoelectric effect cross section is treated. The energy dependent branching ratio of each sub-shell was introduced by fitting from the data provided for limited materials, Ag, Pub and U. [6] Salem's L X-ray emission rate [7] is used. [8, 9]

4. Auger electron: K shell and L shell Auger electron is considered.

5. X ray and Auger electron from compound/mixture: Ratio of photoelectric effect cross sections of each element in compound or mixture is introduced to treat X ray and Auger electron from compound or mixture.

6. K shell electron impact ionization (EII): Five kind of K shell EII cross section is included. [10, 11]

7. Use of PHOTX data base: The principal change is to photoelectric cross section. [12, 13]

After 2nd international EGS workshop, one improvement is introduced;

8. General treatment of photoelectric cross sections: K-, L1-, L2-, L3 and other sub-shell photoelectric cross sections taken from the PHOTX data base are fitted to a quadratic function in a log-log plot and prepared in the form of the BLOCK DATA of EGS4. It becomes possible to calculate the branching ratio of each element inside EGS4 by this improvement and becomes not necessary to use piece-wise linear-fitted data calculated by PEGS4. This means that the general treatment for compounds or mixtures can be applied to the material data calculated defaults PEGS4. [14]

Table 1: Incident photon energy and linear polarization

Energy (keV)	40	30	20
Linear Polarization (P)	0.885	0.877	0.873

Table 2: Samples and their thickness

Sample	C	Cu	Ag	Pb
T (mm)	0.6	2	0.5	0.5

New photon transport physics in EGS5 also consists of these items. Comparisons of measurements and EGS5 calculation are mentioned. Also, calculation using improved EGS4 code are mentioned.

2 Systematic Comparison of Measurement and Calculation

2.1 Photon Beam Incident

We performed a mono-energy photon-scattering experiment at a BL-14C in a 2.5 GeV synchrotron light facility (PF). The experimental arrangement is shown in Fig.1. Photons from a vertical wiggler were used after being monochronized by a Si(1,1,1) double crystal monochrometer. A linearly polarized mono-energy photon beam was scattered by a sample located at point O with its normal vector $(-\frac{1}{2}, -\frac{1}{\sqrt{2}}, \frac{1}{2})$; the scattered photons were detected by two high-purity Ge detectors located at $\theta = 90°$. Incident photon energies and linear polarization are shown in Table 1. Sample and their thickness are shown in Table 2. One Ge detector (Ge_2) was located in the plane of the incident polarization vector($\phi = 0°$), and the other (Ge_1) in the plane perpendicular to it ($\phi = 90°$). Samples were contained in a vacuum chamber, and vacuum pipes were placed between the vacuum chamber and the Ge detectors in order to reduce any scattering due to the air. Collimators of 5.01 mm aperture were placed in front of Ge detectors (C_1, C_2). The distance from the surface of the sample to the collimator was 420 mm. The opening angle of this collimator was 0.33° and the energy spread of a Compton-scattered photon due to this opening angle (without Doppler broadening) was negligibly small, 31eV for incident beam of 40 keV. The incident photon intensity was monitored in a free–air ionization chamber, which was calibrated using a calorimeter [15].

For photon beam incident, calculation result by improved egs4 is compared with measurements, because improved egs4 and egs5 adopt the same physics model for photon transport. And comparison of improved egs4 and egs5 regarding photon incident is performed elsewhere [16].

Two stage EGS4 calculation was performed. In the first stage, photon beam incident on the sample and emergent photons (A) are scored. In the second stage, energy deposition in Ge detector was calculated while using 'A' as a photon source.

Measured and calculated photon spectra are shown in Fig. 2. The spectrum by EGS4 calculation is smeared by Gaussian function of FWHM=0.3 keV to account for the resolution of Ge detector. The shape of Compton scattering, Rayleigh scattering, K-X ray and L-X ray peaks are well reproduced by the EGS4 calculation.

The ratio of measured and calculated peaks are shown in Fig. 3. In the L-X ray comparison, preliminary data of Gd sample and W sample are also shown. $|C/M - 1| \sim 0.03$ for Compton, 0.6 for Rayleigh, 0.05 for K-X and 0.15 for L-X.

Table 3: Geometric average of C/M of K-X ray yields. Gr means the calculation result using Gryziński's cross section.

Target	Al	Ti	Cu	Ag	Au	Av
EGS4	0.0027	0.023	0.053	0.33	0.85	0.061
EGS4+EII(Gr)	0.96	1.12	0.86	0.91	1.07	0.98
EGS5(Gr)	0.96	1.10	0.82	0.96	1.14	1.00

2.2 Electron Beam Incident

We simulated Dick et al's experiment.[17] Dick et al performed a systematic measurement of K-X ray when electron beam of 10, 20, 40, 100, 200, 500, 1500 and 3000 keV hits target(Al, Ti, Cu, Ag and Au) normally. K-X ray yield per incident electron was measured at $\theta = 120°$ and $180°$.

EGS4 calculation with and without the improvement to treat EII were performed. EGS5 calculation with EII is also performed, since different treatment of electron transport in EGS4 and EGS5 may affect the results. As a K-shell EII cross section, Gryziński's relativistic cross section [18] were used. All the comparisons were done in absolute, i.e. no normalization between the measurement and the calculation were done. Following EGS5 parameters were used; EFRACH=0.05, EFRACL=0.2; ESTEPE=0.1, ESTEPE2=0.2, UE=10.511, AE=0.512.

The calculated and measured K-X ray yields are shown in Fig.4. The statistical error in the calculation is within 3% for EGS4+EII and EGS5, 10% and 5% for EGS4 of Al and other targets, respectively. The geometric average of the ratio of the calculated K-X ray yield to the measured one is shown for each target in Table 3. No significant difference was seen between EGS4+EII calculation and EGS5 calculation.

The EGS4 calculation apparently becomes underestimated with decreasing Z of the target. C/M is only 0.0027 for Al, but C/M is 0.85 for Au. The degree of underestimation depends weakly on the electron incident energy and the scoring angle.

For Al, Ti, Cu and Ag sample, dominant contribution of K-X ray is EII. For Au sample, dominant contribution of K-X ray is photoelectric effect of bremsstrahlung photon.

3 Conclusion

Two systematic comparisons of measurements and EGS4 code were performed to verify the validity of the improvement. The first comparison is "20-40 keV synchrotron radiation scattering experiment". Targets are C, Cu, Ag, and Pb. Compton, Rayleigh, K-X, L-X rays are observed using Ge detectors. L-X rays from Gd sample were also measured. The agreement of EGS4 and the measurement was good both in the energy spectral shape and intensity: $|\mathrm{C/M} - 1| \sim 0.03$ for Compton, 0.6 for Rayleigh, 0.05 for K-X and 0.15 for L-X. This indicates the validity of EGS5 code, because photon transport model in EGS5 code and improved EGS4 code is the same.

Systematic comparison of measured and calculated K-X ray yield from various target for electron beam of 0.01 to 3 MeV was performed without any normalization. General agreement between measurement and calculation show the validity of EGS5 code. For Al, Ti, Cu and Ag sample, dominant contribution of K-X ray is EII. For Au sample, dominant contribution of K-X ray is photoelectric effect of bremsstrahlung photon.

References

[1] W. R. Nelson, H. Hirayama, D. W. O. Rogers: SLAC-265 (Stanford University, Stanford, 1985).

[2] Y. Namito, H. Hirayama and S. Ban: "Improvements of Low-Energy Photon Transport in EGS4". In: *Proceedings of the 1st International Workshop on EGS4* Ed. H. Hirayama, Y. Namito and S. Ban, KEK Proc. **97-16**, (1997) pp.32-50.

[3] Y. Namito, H. Hirayama: "Improvements of Low Energy photon Transport for EGS5", In: *Proceedings of the 2nd International Workshop on EGS* Ed. H. Hirayama, Y. Namito and S. Ban, KEK Proc. **2000-20**, (2000) pp.11-22.

[4] Y. Namito, S. Ban and H. Hirayama, Nucl. Instrum. and Meth. A **332**, 277 (1993).

[5] Y. Namito, S. Ban and H. Hirayama, Nucl. Instrum. and Meth. A **349**, 489 (1994).

[6] J. J. Matese and W. R. Johnson, Phys. Rev. **140**, A1 (1965).

[7] S. I. Salem and P. L. Lee, At. Data and Nucl. Data Tables **18**, 233 (1976).

[8] H. Hirayama, Y. Namito and S. Ban, *Implementation of an L-Shell Photoelectron and an L X-ray for Elements into the EGS4 Code* KEK Internal 96-10 (1996).

[9] H. Hirayama and Y. Namito: *General Treatment of Photoelectric Related Phenomena for Compounds and Mixtures in EGS4*, KEK Internal 2000-3.

[10] Y. Namito, H. Hirayama: Nucl. Instrum. and Meth. A **423**, 238 (1999).

[11] Y. Namito, H. Hirayama: *LSCAT: Low-energy Photon-scattering Expansion for the EGS4 Code (Inclusion of Electron Impact Ionization)* KEK Internal 2000-4 (2000).

[12] PHOTX. Photon cross section data base. *Radiation Shielding Information Center Data Package DLC-136/PHOTX, 1995.*

[13] Y. Sakamoto, "Photon cross section data PHOTX for PEGS4 code", In: *Proceedings of the Third EGS4 User's Meeting in Japan"*, KEK Proc. **93-15**, (1993) pp 77-82.

[14] H. Hirayama and Y. Namito, "Implementation of a General Treatment of Photoelectric-Related Phenomena for Compounds or Mixtures in EGS4 (Revised version)", KEK Internal In press (2004).

[15] H. Nakashima et al., Nucl. Instr. Meth. A **310**, 696 (1991).

[16] W. R. Nelson, J. Liu, H. Hirayama, Y. Namito, A. Bielajew, S. Wilderman, "Benchmark calculations for EGS5", In: *Proceedings of the Third International Workshop on EGS*, KEK Proc. To be published.

[17] C. E. Dick, A. C. Lucas, J. M. Motz, R. C. Placious, J. H. Sparrow: J. Appl. Phys **44**, 815 (1973).

[18] M. Gryziński: Phys. Rev. **138**, A 305, A 322, A 336 (1965).

[19] E. Casnati, A. Tartari, C. Baraldi: J. Phys. B **15**, 155 (1982).

[20] E. Casnati, A. Tartari, C. Baraldi: J. Phys. B **16**, 505 (1983).

[21] L. R. M. Morin, J. Phys. Chem. Ref. Data **11**, 1091 (1982).

[22] Ed V. S. Shirley: *Table of Isotopes* 8th edn. (Wiley-Interscience, New York, 1996).

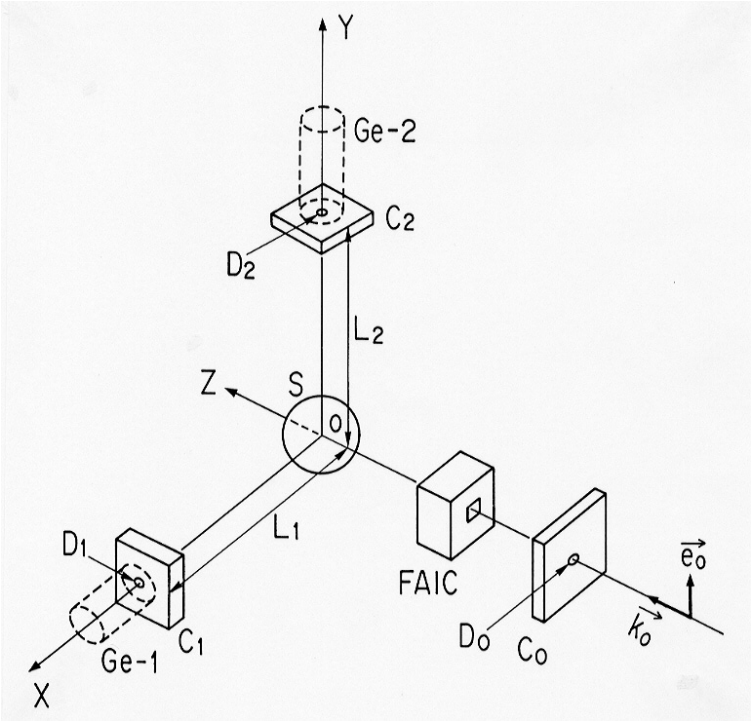

Figure 1: Experiment arrangement. A mono-energetic linearly polarized synchrotron radiation photon beam was scattered by a sample (S); the scattered photons were counted by two high-purity Ge detectors for low-energy photons (Ge_1, Ge_2). The aperture of the C_0 collimator was 2 mm. A free air ion chamber (FAIC) was located in front of the sample to monitor incident photon intensity. The sample was placed at point O; its normal vector is $(-\frac{1}{2}, -\frac{1}{\sqrt{2}}, \frac{1}{2})$. Collimators$(C_1, C_2)$ define the opening angle of Ge detectors. The distance from the surface of the sample to the exit of collimator (L_1) was 420 mm and the aperture of Collimator(D_1) was 5.01 mm.

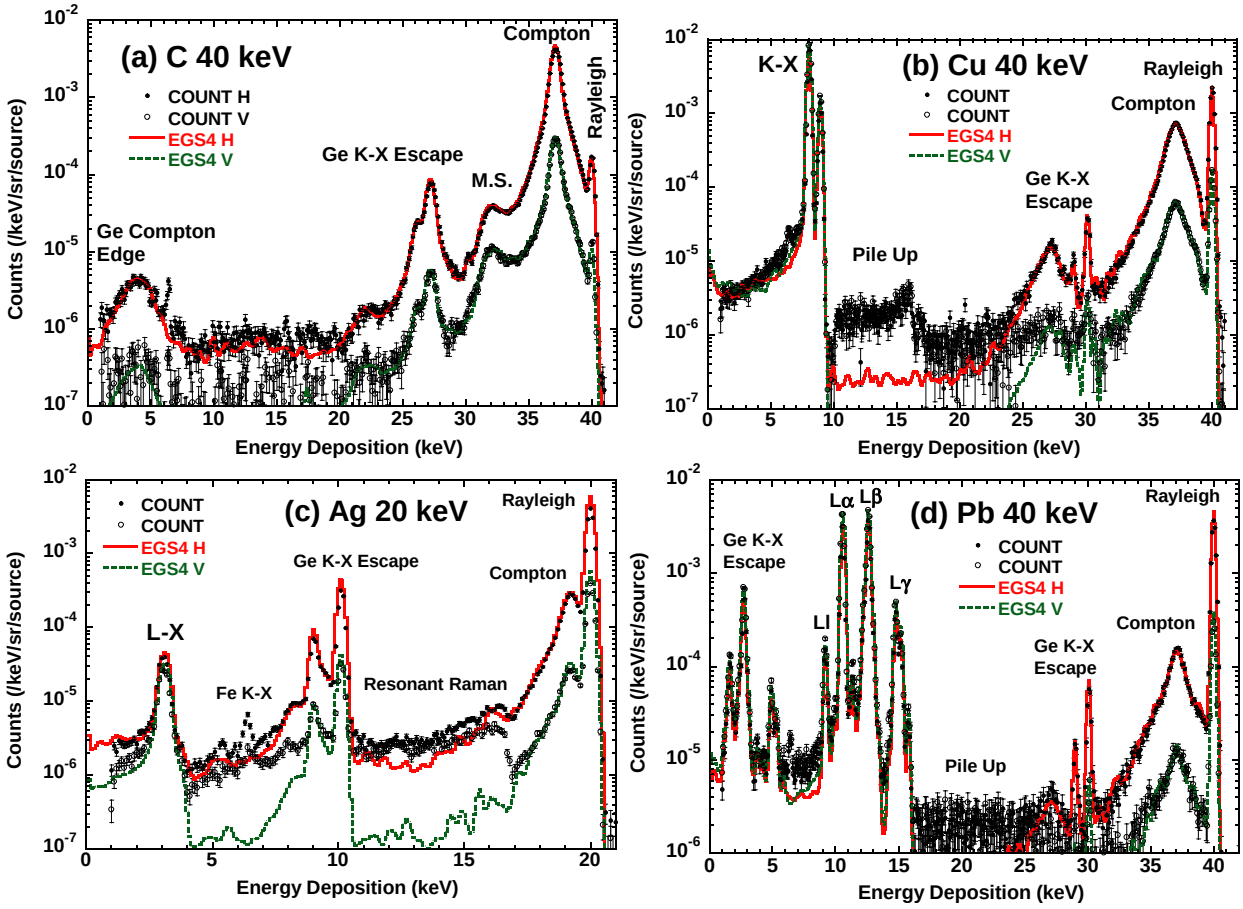

Figure 2: Comparison of the photon spectra. Measurement is shown by filled (horizontal) and open circles (vertical). EGS4 calculations are shown in solid (horizontal) and dashed (vertical). Targets and incident photon energy are, (a) C-40 keV (b) Cu-40 keV (c) Ag-20 keV (d) Pb-40 keV.

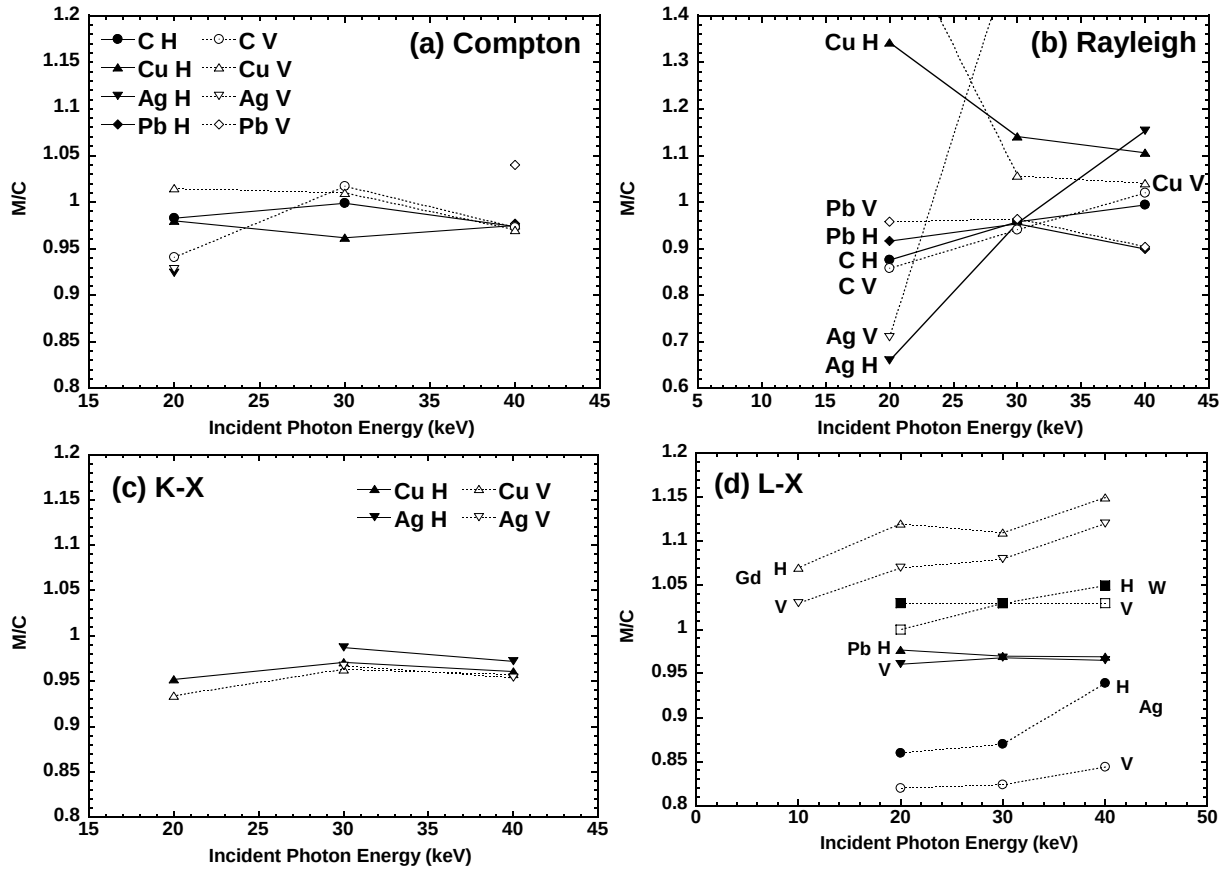

Figure 3: Ratio of measured and calculated intensity of each peak. 'H' and 'V' means horizontal and vertical respectively. (a) Compton scattering (b) Rayleigh scattering (c) K-X ray (d) L-X ray.

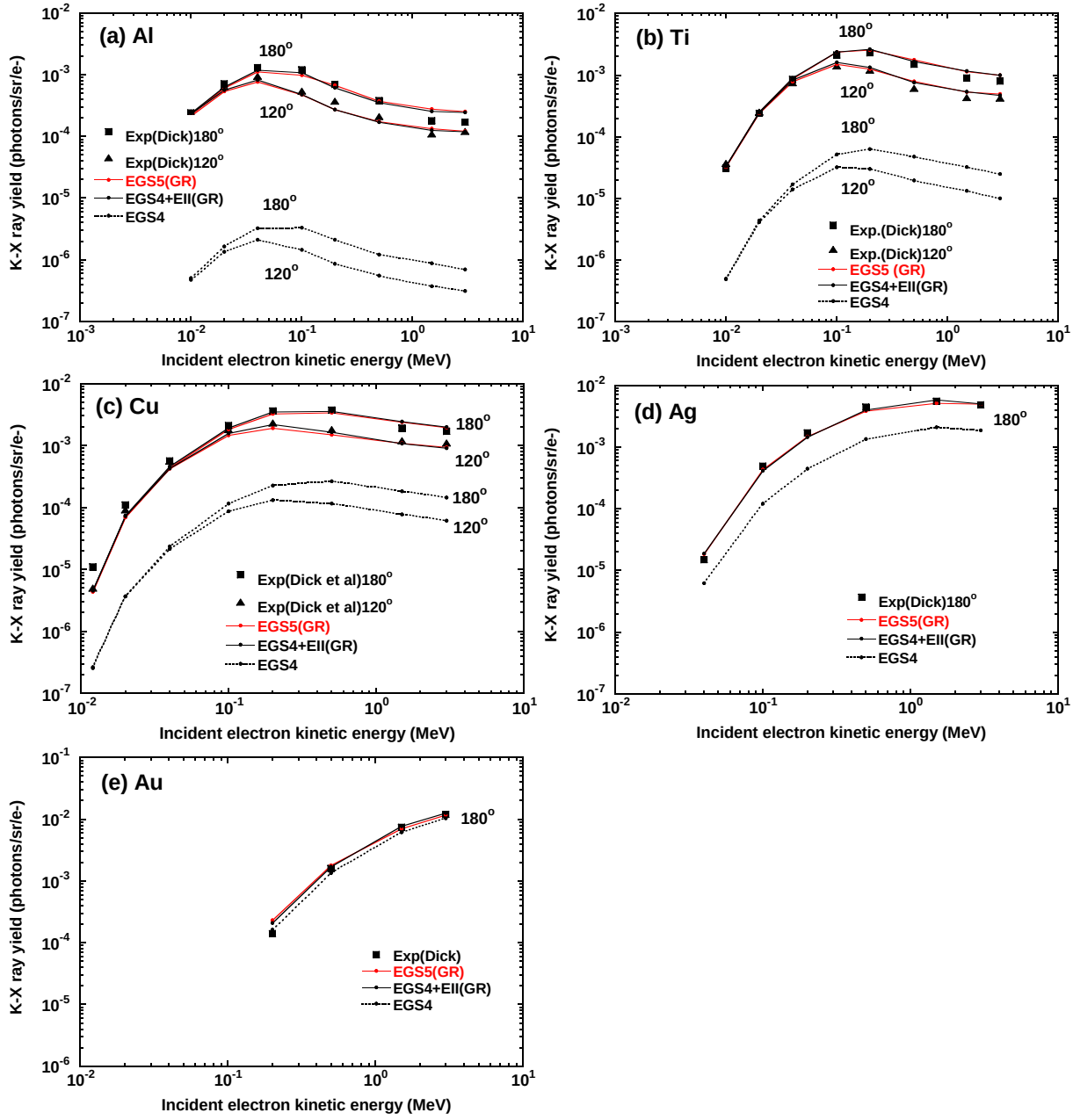

Figure 4: Comparison of the K-X ray yield. The measured values by Dick et al. are indicated by filled boxes ($\theta = 180°$) and filled triangles ($\theta = 120°$); EGS5: EGS5 calculation with EII using Gryziński's cross section, EGS4+EII: EGS4 calculation with EII using Gryziński's cross section, EGS4: EGS4 calculation without EII; (a) Al (b) Ti (c) Cu (d) Ag (e) Au.

SLAC-PUB-10752
(September 24, 2004)

BENCHMARK CALCULATIONS FOR EGS5 *

W. R. Nelson, James C. Liu†
Radiation Protection Department, Stanford Linear Accelerator Center (SLAC),
MS48, P.O. Box 20450, Stanford, CA 94309, USA

Hideo Hirayama, Yoshihito Namito
Radiation Science Center, High Energy Accelerator Research Organization (KEK)
1-1 Oho Tsukuba-shi Ibaraki-ken 305-0801, Japan

Alex Bielajew, Scott Wilderman
Department of Nuclear Engineering and Radiological Sciences, University of Michigan
2355 Bonisteel Blvd., 1906 Cooley Building, Ann Arbor, Michigan, 48109-2104, USA

Abstract

In the past few years, EGS4 has undergone an extensive upgrade to EGS5, in particularly in the areas of low-energy electron physics, low-energy photon physics, PEGS cross section generation, and the coding from Mortran to Fortran programming. Benchmark calculations have been made to assure the accuracy, reliability and high quality of the EGS5 code system. This study reports three benchmark examples that show the successful upgrade from EGS4 to EGS5 based on the excellent agreements among EGS4, EGS5 and measurements. The first benchmark example is the 1969 Crannell Experiment to measure the three-dimensional distribution of energy deposition for 1-GeV electrons shower in water and aluminum tanks. The second example is the 1995 Compton-scattered spectra measurements for 20-40 keV, linearly polarized photon by Namito et. al., in KEK, which was a main part of the low-energy photon expansion work for both EGS4 and EGS5. The third example is the 1986 heterogeneity benchmark experiment by Shortt et. al., who used a monoenergetic 20-MeV electron beam to hit the front face of a water tank containing both air and aluminum cylinders and measured spatial depth dose distribution using a small solid-state detector.

* Invited talk at the "3rd International Workshop on EGS" in KEK, August 4-6, 2004.
† Presenter's e-mail: james@slac.stanford.edu

This work was supported in part by Department of Energy contract DE-AC02-76SF00515.

INTRODUCTION

In the past few years, EGS4 [1] has been upgraded to EGS5 in the following areas: low-energy electron physics[2,3], low-energy photon physics [4,5], the PEGS cross section generation, and the change of coding from Mortran to Fortran language (by Nelson). Therefore, benchmark calculations have been made in various transition phases to assure the accuracy, reliability and high quality of EGS5. This paper reports the three benchmark studies that show the successful upgrade from EGS4 to EGS5, based on the agreements among EGS4, EGS5 and the benchmark measurements. The three benchmark examples, which have been important in testing all versions of EGS4 Code System, are:

1) Shower Experiment, in which 1-GeV electrons hit water and aluminum tanks and three-dimensional distribution of energy deposition were measured [6].
2) Polarization/Doppler Experiment in which 20-40 keV, linearly polarized photons hit carbon and copper targets and the Compton-scattered spectra were measured [7].
3) Heterogeneity Experiment in which 10 and 20 MeV broad electron beam hit the front face of a water tank containing both air and aluminum cylinders. The depth dose distribution and lateral dose distribution at various depths were measured [8].

KEY PARAMETERS IN EGS CALCULATIONS

Table 1 summarizes the input values for the key EGS parameters in the three benchmark examples. The EFRACH, EFRACL, ESTEPE and ESTEPE2 are related to the new EGS5 electron transport mechanics [2]. In the polarization benchmark study [5], which involves the photon physics of polarization, bound Compton scattering, and Doppler broadening, the PEGS inputs for IBOUND / INCOH / ICPROF are 1 / 1 / -3, respectively.

Table 1. Values for the key EGS parameters in benchmark examples.

EGS5 Parameters	**EFRACH / EFRACL**	**ESTEPE / ESTEPE2**
Values	0.05 / 0.20	0.1 / 0.2
Benchmark	**AE / UE**	**AP / UP**
Shower	0.611 / 1000.1	0.001 / 1000
Polarization	0.512 / 0.711	0.001 / 0.200
Heterogeneity	0.711 / 21.0	0.100 / 20.0

BENCHMARK RESULTS

The three benchmark experiments and EGS comparison results, as well as the timing comparison, will be shown in the following sections. In the comparison figures, EGS4.4 is already a Fortran 77 version with PEGS4 cross generation on the fly and with low-energy photon physics included, while EGS5 is a version with the addition of low-energy electron physics.

Shower Experiment

In the Crannell shower experiment [6], a 1-GeV electron beam was incident on 8000 liters of distilled water in a stainless steel tank (140x140x460 cm^3) or an Al block. Measurements of the radial energy deposition (MeV/cm^3/electron) were made at various depths of the targets using a scintillation detector. This is an important benchmark to test shower development. EGS4 has been shown to be in excellent agreement, on an absolute basis, with the measurements [9].

Figure 1 shows the EGS5 user input file (using the format of getRTZ user code) for Shower experiment, which prescribes 2 media, the radii of cylinders, the parallel planes at various depths, the electron beam parameters, number of cases, and various transport and physics switches/values. Note the values of ESTEPE (0.1) and ESTEPE2 (0.2) in the last row.

Figure 2 shows the PEGS input for Shower experiment in EGS5 calculations. It is similar to EGS4, except the addition of EFRACH (0.05) and EFRACL (0.2) values for both media.

Figure 3 compares the depth dose profile in central axis (1-cm-radius) between the experiment, EGS4.4, and EGS5 for the phantom of water (top figure) and Al (bottom figure). The agreement is within the experimental uncertainty. A complete benchmark check of the radial energy deposition profiles has also been made successfully, but the results are not shown here.

Polarization Experiment

Figure 4 shows the set-up for the Polarization/Doppler Experiment [7], which is an important benchmark to test the low-energy photon physics. The 40-keV photons hit an inclined carbon or a copper disc and the scattered photon spectra at 90-degrees (both vertical and horizontal) were measured with High Purity Ge detectors (HPGe) at about 0.4 m. Because the photons from the wiggler are linearly polarized, the scattered photon intensities at vertical and horizontal planes are different and the average of the two spectra is used in the comparison.

Figure 5 shows the EGS5 user input file (using the format of getRTZ user code) for Polarization Experiment. Note that the three switches for polarization, Bound Compton and Doppler broadening effects (ipolarsw, incohrsw and iprofrsw), as well as those important for low-energy photon transport and physics, were activated.

Figure 6 shows the EGS5 PEGS input for Polarization Experiment Note that the three switches for Bound Compton and Doppler broadening effects (IBOUND=1, INCOH=1, ICPROF=-3) were activated.

Figure 7 shows the agreement of the 90^o-scattered Compton spectra for the targets of carbon (top figure) and copper (bottom figure) between the experiment, EGS4.4 and EGS5. Note that the calculated spectra have been broadened by the resolution of the HPGe using a post-processing routine.

Heterogeneity Experiment

Figure 8 shows the set-up for the Heterogeneity Experiment [8], which is one of the most critical benchmark problem in medical physics to test the low-energy electron physics and transport in a Monte Carlo code. The 20-MeV (or 10-MeV) electron broad beam hit the front face of the water phantom, in which a small cylinder disc (air or aluminum) may be inserted at a

distance of 2-mm (or 2-cm) behind the front face. The EGS5 user input files and the PEGS file are similar to those shown for Shower and Polarization Experiments.

Figure 9a shows the agreement of the depth dose curves at central axis for the 3 cases of 20-MeV electron and 2-mm-gap between experiment, EGS4.4 and EGS5. The figure numbers indicated on the figures are those in the original paper [8] so readers can check easily if needed. Figure 9b shows the corresponding radial dose profiles at various depths behind the air disc, while Figure 9c compares the radial dose profiles at various depths behind the Al disc. The discrepancy between measurements and calculations for the dose near the boundary between water and inserted disc was due to the larger spatial bin in the EGS calculations than the detector size.

Similar to Figures 9a, 9b and 9c, Figures 10a, 10b and 10c show the benchmark results for the case of 10-MeV electron at 2-mm gap. Similar to Figure 9a (2-mm-gap), Figures 11 and 12 compares the depth dose curve for the cases of 20-MeV and 10-MeV electron, respectively, at 2-cm gap.

Timing Comparison

The new low-energy electron transport mechanics should make EGS5 run faster than EGS4 [2,3]. Table 2 summarizes the time comparison between EGS4.4 and EGS5 for the three benchmark examples. EGS5 takes less time than EGS4.4, particularly for the Heterogeneity Experiment, in which low-energy electron transport is important (a factor of 5 gain in speed for EGS5 in this case).

Table 2. Time comparison between EGS4.4 and EGS5 for three benchmark experiments.

Shower Experiment (2.5×10^5 cases for EGS4.4 & 10^6 cases for EGS5)			
Phantom	Water		Aluminum
EGS5 / EGS4.4	0.43		0.43
Polarization Experiment (2×10^9 cases)			
Scattering Target	Carbon		Copper
EGS5 / EGS4.4	0.58		0.73
Heterogeneity Experiment (10^5 cases, 20-MeV Beam)			
Inserted Disc with 2-mm-gap	None	Air	Aluminum
EGS5 / EGS4.4	0.16	0.18	0.18
Inserted Disc with 2-cm-gap	None	Air	Aluminum
EGS5 / EGS4.4	0.16	0.18	0.2
Heterogeneity Experiment (10^5 cases, 10-MeV Beam)			
Inserted Disc with 2-mm-gap	None	Air	Aluminum
EGS5 / EGS4.4	0.18	0.19	0.18
Inserted Disc with 2-cm-gap	None	Air	Aluminum
EGS5 / EGS4.4	0.18	0.24	0.20

CONCLUSIONS

EGS4 has undergone an extensive upgrade to EGS5, in the areas of low-energy electron physics and transport, as well as low-energy photon physics. The PEGS cross section can be generated on the fly. And the coding has changed from Mortran to Fortran 77. The EGS5 Code System is now more integrated than EGS4 and it also runs faster. This work, which compares EGS5 with three standard benchmark experiments, has assured the accuracy and high quality of EGS5.

REFERENCES

[1] W. R. Nelson, H. Hirayama and D. W. O. Rogers, "The EGS4 Code System", Stanford Linear Accelerator Center report SLAC-265 (1985).

[2] Alex Bielajew, Scott Wilderman, “New electron transport physics in EGS5”, This Proceedings (2004).

[3] Scott Wilderman and Alex Bielajew, “Optimizing the selection of step-size parameters’, This Proceedings (2004).

[4] Yoshihito Namito and Hideo Hirayama, “New photon transport physics in EGS5”, This Proceedings (2004).

[5] Yoshihito Namito and Hideo Hirayama, “LSCAT: low-energy photon scattering expansion for the EGS code”, KEK Internal report 2000-4 (2000).

[6] C. J. Crannell, H. Crannell, R. R. Whitney and H. D. Zeman, “Electron-induced cascade showers in water and aluminum”, Phys. Rev. 184, p426 (1969).

[7] Namito et. al, “Polarization/Doppler Experiment: 20-40 keV, linearly polarized photons hit carbon and copper targets. Measured Compton-scattered spectra”, KEK Proceedings 97-16, p32 (1997).

[8] Shortt et. al., “Heterogeneity Experiment: 10 and 20 MeV broad electron beam hit the front face of a water tank containing both air and aluminum cylinders. Measured depth dose distribution”, Phys. Med. Biol., Vol. 31, p235, (1986).

[9] W. R. Nelson and T. M. Jenkins, “Solution of the electromagnetic cascade shower problem by analog Monte Carlo methods - EGS”, Chapter 12 in *Computer Techniques in radiation Transport and Dosimetry*, Plenum Press (1980).

```
Crannell water shower experiment
         2                                   nmed (I10)
WATER (CRANNELL)                            media(j,1) (24A1)
AL (INTERFACE)
       0.1          0.1                     ecutin,pcutin (Kinetic) (MeV)
        11            1              12 imax,jmax,kmax (3I10)
       1.0   i=1                            cyrad (cm) (F10.0)
       2.0     =2
       3.0     =3
       4.0     =4
       6.0     =5
       8.0     =6
      12.0     =7
      16.0     =8
      20.0     =9
      24.0     =10
      68.8     =11=imax
       0.0   j=1=jmax                       tpl (degrees) (F10.0)
       0.0   k=1                            zpl (cm)
      20.0     =2
      40.0     =3
      60.0     =4
      80.0     =5
     120.0     =6
     160.0     =7
     200.0     =8
     240.0     =9
     280.0     =10
     320.0     =11
     360.0     =12=kmax
     460.0     =13=kmax+1
  1    11     1     1     1    12     1          0.0 WATER (CRANNELL)
                                                      blank card (required EOF)
       0.0          0.0          0.0     xin,yin,zin (3F10.0)
         1            1            1          iin,jin,kin (3I10)
       0.0          0.0          1.0     uin,vin,win (3F10.0)
   1000000                                 ncases (I10)
    1000.0           -1           0    ekein(mev),iqin,isamp (F10.0,2I10)
    1     1     1     0                  ipeangsw,iedgesw,iraysw,iwatch (4I5)
    0     0     0     0                  ipolarsw,incohrsw,iprofrsw,impacrsw (4I5)
    1     2     0     0                  ibrdst,iprdst,ibrspl,nbrspl (4I5)
   0.10         0.20                    estepe and estepe2 (2F10.0)
```

Figure 1. EGS5 user input (using format of getRTZ user code) for Shower experiment.

```
COMP
&INP NE=2, RHO=1.0, PZ=2,1, IAPRIM=1, EFRACH=0.05, EFRACL=0.20, IRAYL=1,
IBOUND=0, INCOH=0, ICPROF=0, IMPACT=0 /END
WATER (CRANNELL)                    H2O
H    O
ENER
&INP AE=0.611, AP=0.001, UE=1001.0, UP=1000.0 /END
ELEM
&INP RHO=2.65, IRAYL=1, IBOUND=0, INCOH=0, ICPROF=0, IMPACT=0, IAPRIM=1,
EFRACH=0.05, EFRACL=0.20 /END
AL (INTERFACE)                      AL
AL
ENER
&INP AE=0.611, AP=0.001, UE=1001.0, UP=1000.0 /END
```

Figure 2. EGS5 PEGS input for Shower experiment.

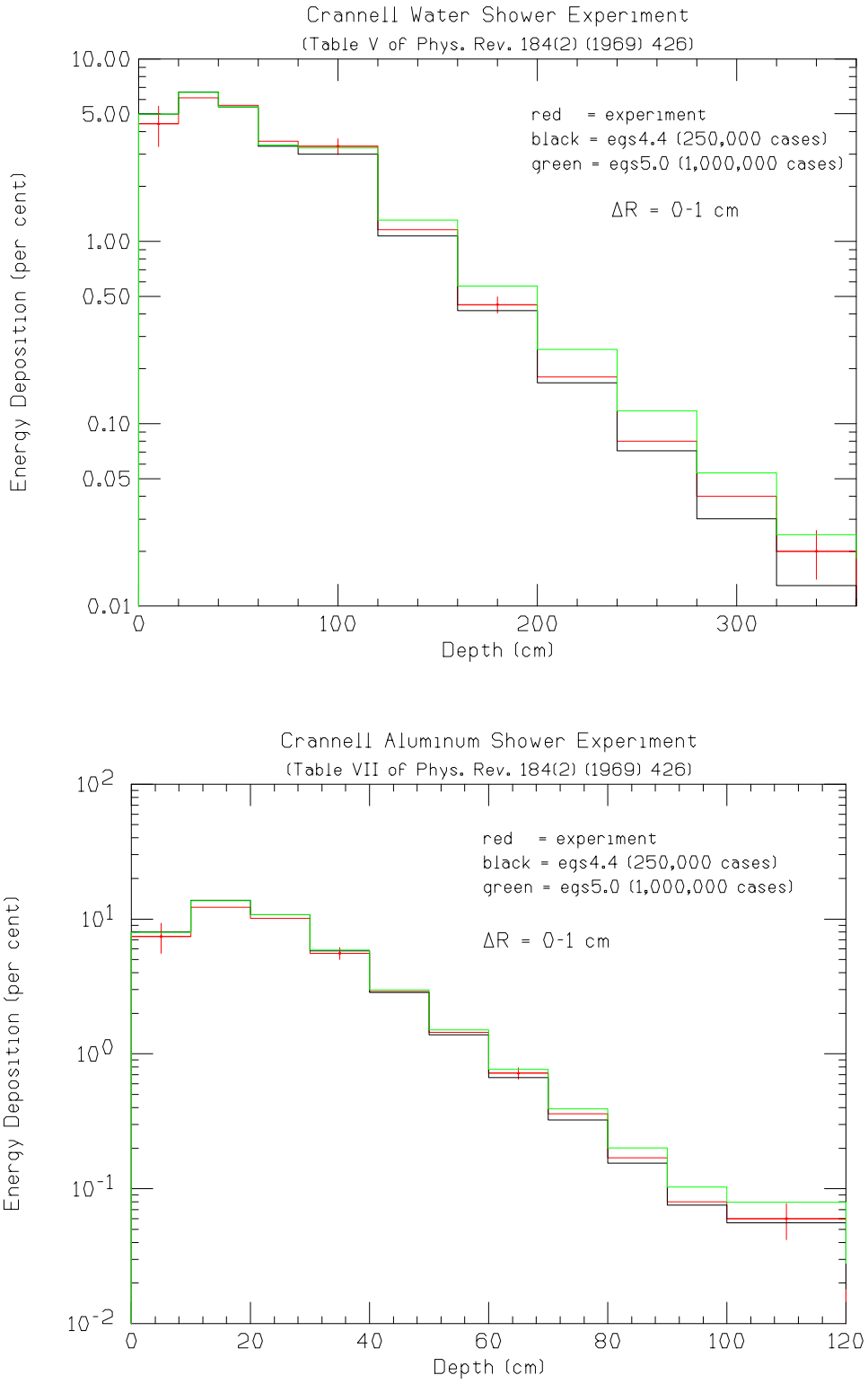

Figure 3. Benchmark results (depth dose profile in central axis, 1-cm-radius) for Shower experiment: water (top) and Al (bottom).

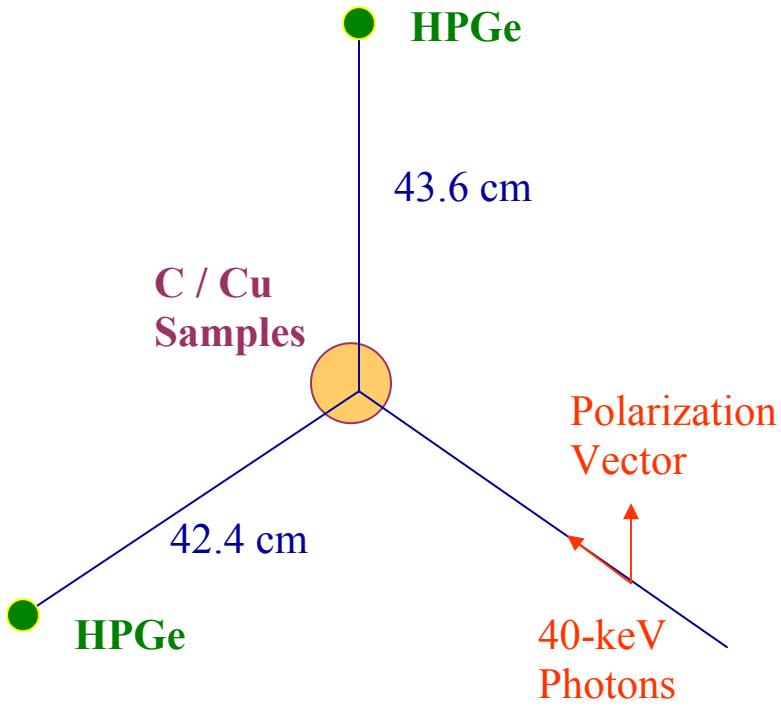

Figure 4. Set-up for Polarization/Doppler Experiement [7].

```
Check of KEK-LSCAT experiment (Fig.4 of KEK-97-16)
                2                                                    nmed (I10)
C-ICPROF3-PHOTX                media(j,1) (24A1)
CU-ICPROF3-PHOTX
             0.5                  0.0                        ecutin,pcutin (Kinetic) (MeV) (2F10.0)
               1                        1                1         imax,jmax,kmax (3I10)
          2.26     i=1=imax                        cyrad (cm) (F10.0)
             0.0     j=1=jmax                        tpl (degrees) (F10.0)
             0.0     k=1=kmax                       zpl (cm)
             0.2     =2=kmax+1                    (actually, the "thickness" of the scatterer)
                 1       1       1       1       1       1       2          0.0 CU-ICPROF3-PHOTX
                                                                                        blank card
(required EOF)
                       0.0             0.0             0.0          xin,yin,zin (3F10.0)
                          1                1                1          iin,jin,kin (3I10)
                       0.0             0.0             1.0          uin,vin,win (3F10.0)
2000000000                                                  ncases (I10)
          0.04007                 0                0         ekein(mev),iqin,isamp (F10.0,2I10)
                 1       1       1       0                        ipeangsw,iedgesw,iraysw,iwatch (4I5)
                 1       1       1       0                        ipolarsw,incohrsw,iprofrsw,impacrsw
(4I5)
                 1       2       0       0                        ibrdst,iprdst,ibrspl,nbrspl (4I5)
                   0.10          0.20                        estepe and estepe2 (2F10.0)
                 100.0                                        sprad (cm) (F10.0) For scoring only
```

Figure 5. EGS5 user input (using format of getRTZ user code) for Polarization Experiment.

```
ELEM
&INP IRAYL=1, IBOUND=1, INCOH=1, ICPROF=-3, IAPRIM=0, EFRACH=0.05,
EFRACL=0.20 /END
C-ICPROF3-PHOTX                        C
C
ENER
&INP AE=0.512, AP=0.001, UE=0.711, UP=0.200 /END
ELEM
&INP IRAYL=1, IBOUND=1, INCOH=1, ICPROF=-3, IAPRIM=0, EFRACH=0.05,
EFRACL=0.20 /END
CU-ICPROF3-PHOTX                       CU
CU
ENER
&INP AE=0.512, AP=0.001, UE=0.711, UP=0.200 /END
```

Figure 6. EGS5 PEGS input for Polarization Experiment.

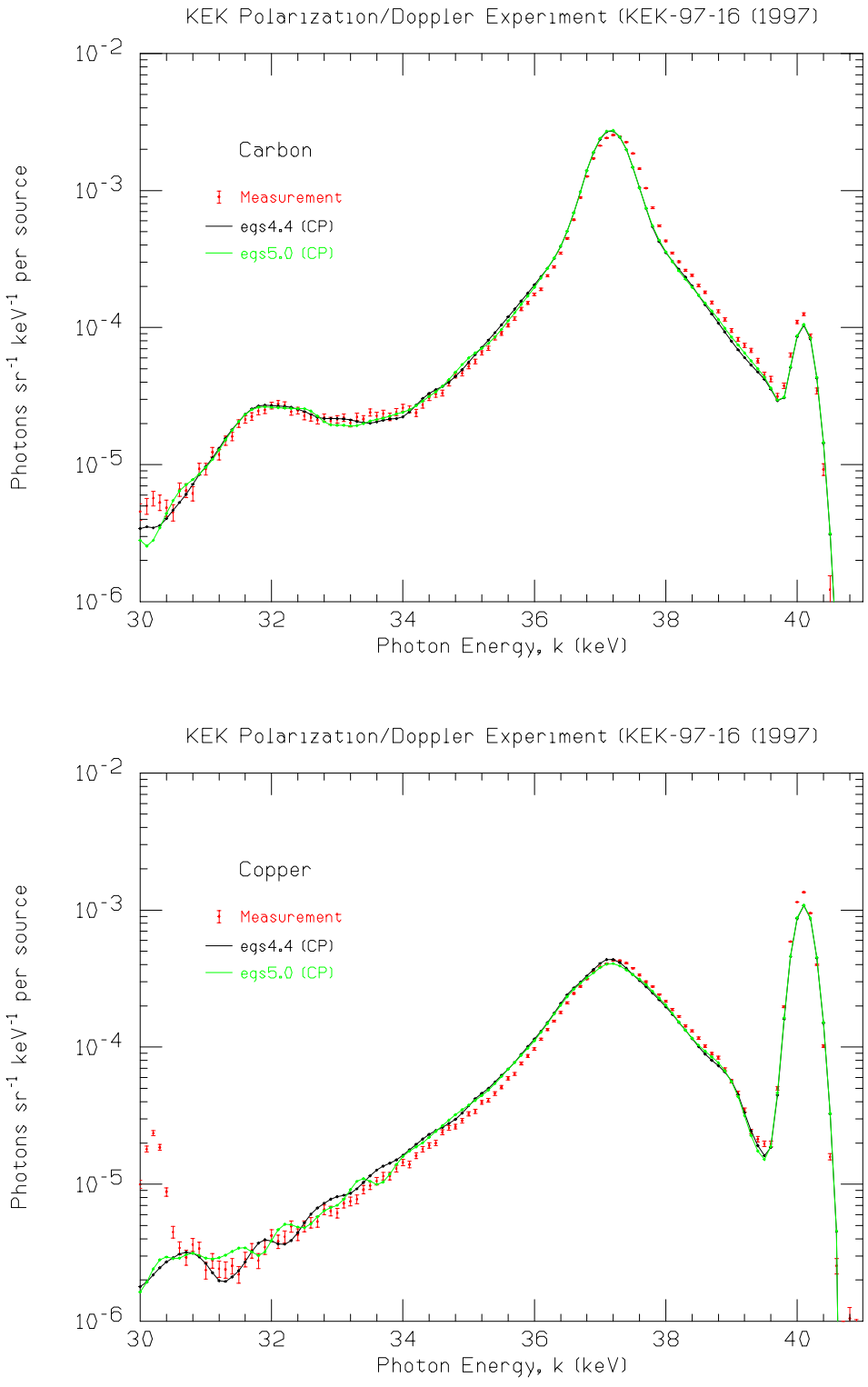

Figure 7. Benchmark results for Polarization Experiment: 90^{o}-scattered Compton spectra for carbon (top) and copper (bottom).

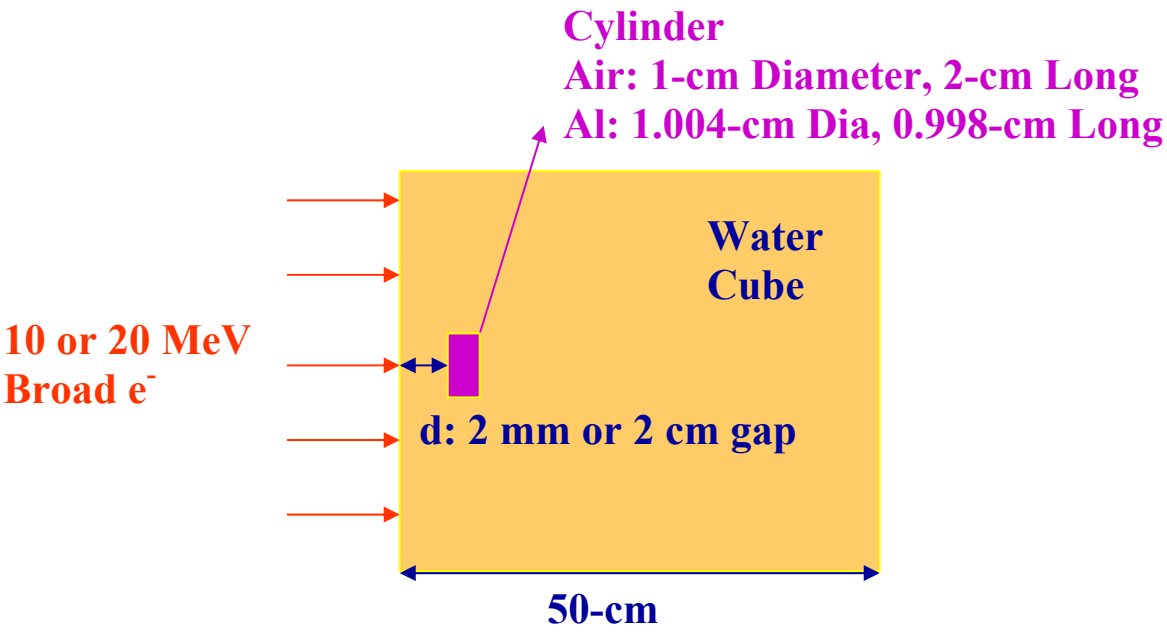

Figure 8. Set-up for HeterogeneityExperiement [8].

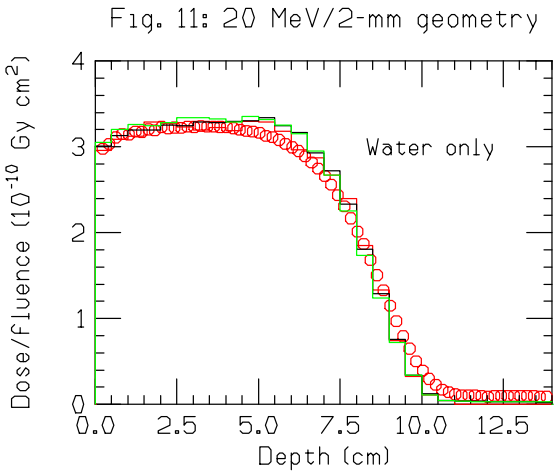

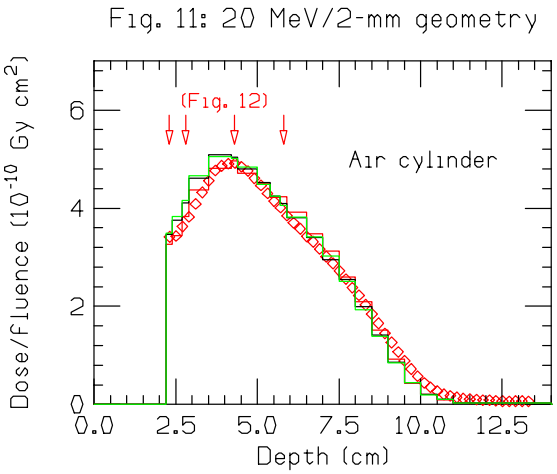

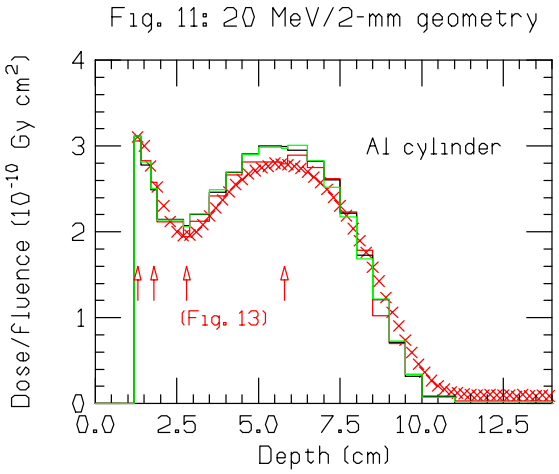

Figure 9a. Benchmark results for Heterogeneity Experiment (20-MeV electron; pure water, and water with air or Al disc at 2-mm gap; depth dose curves at central axis).

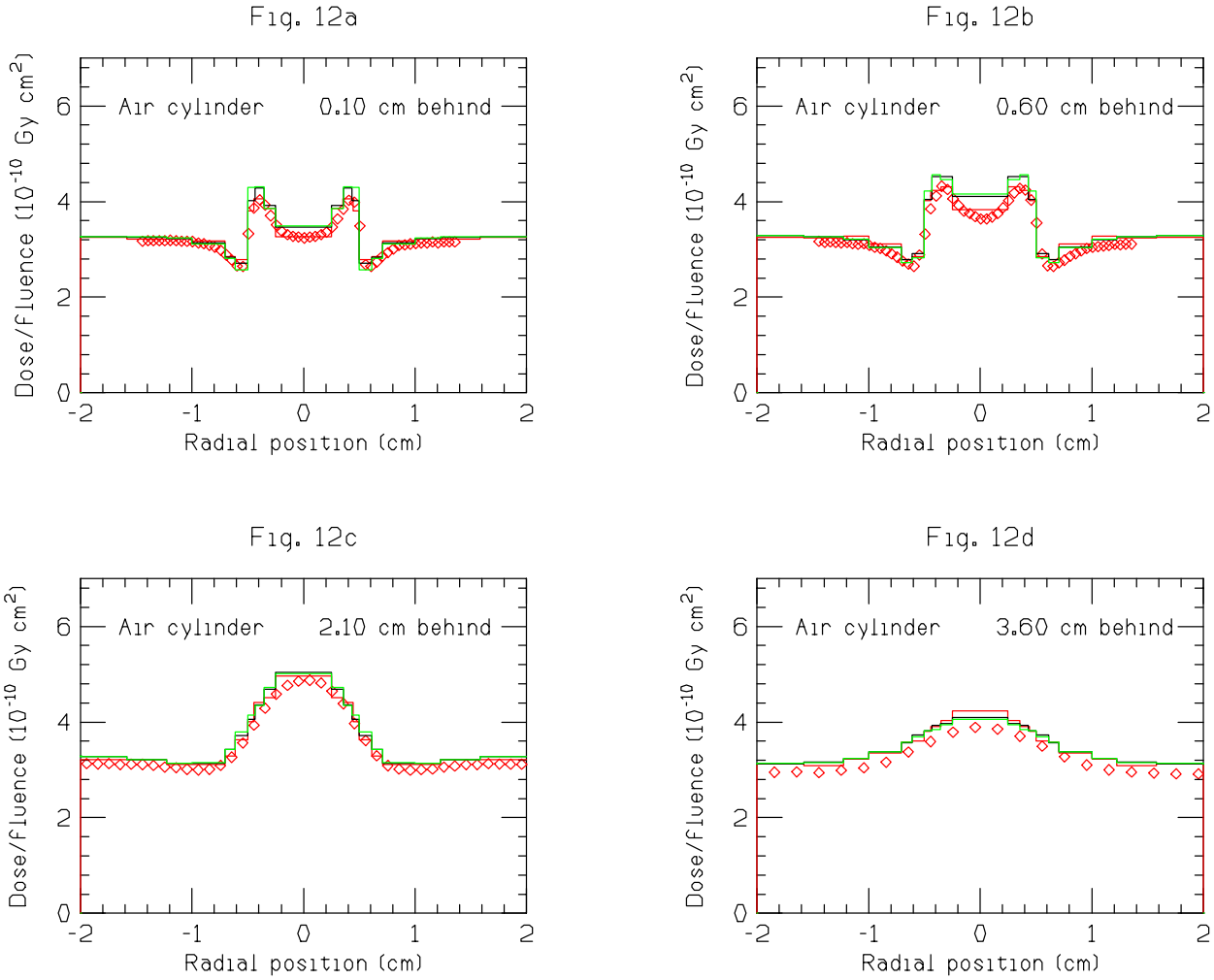

Figure 9b. Benchmark results for Heterogeneity Experiment (20-MeV electron; water with air disc at 2-mm gap; radial dose profiles at various depths behind the air disc).

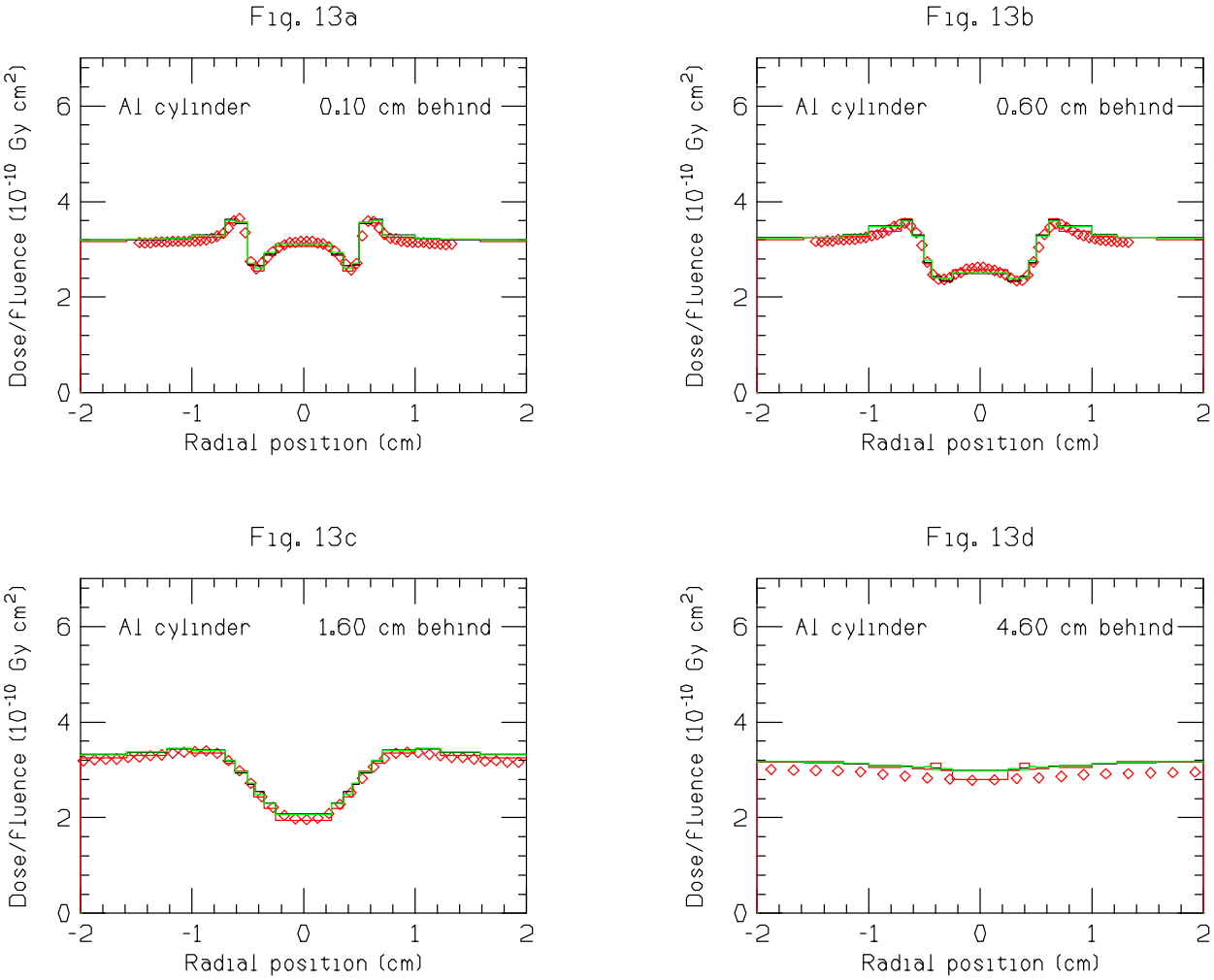

Figure 9c. Benchmark results for Heterogeneity Experiment (20-MeV electron; water with Al disc at 2-mm gap; radial dose profiles at various depths behind the Al disc).

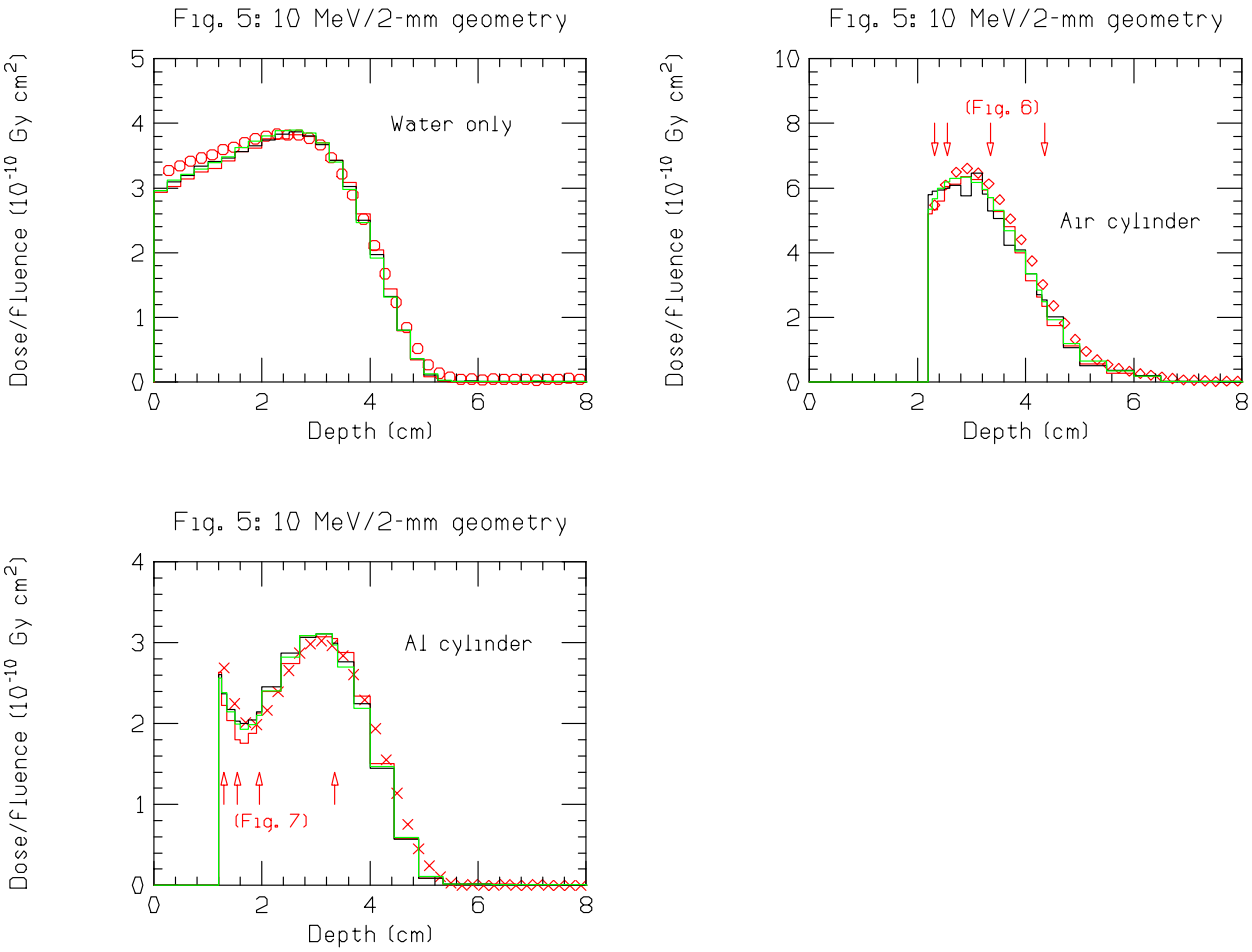

Figure 10a. Benchmark results for Heterogeneity Experiment (10-MeV electron; pure water, and water with air or Al disc at 2-mm gap; depth dose curves at central axis).

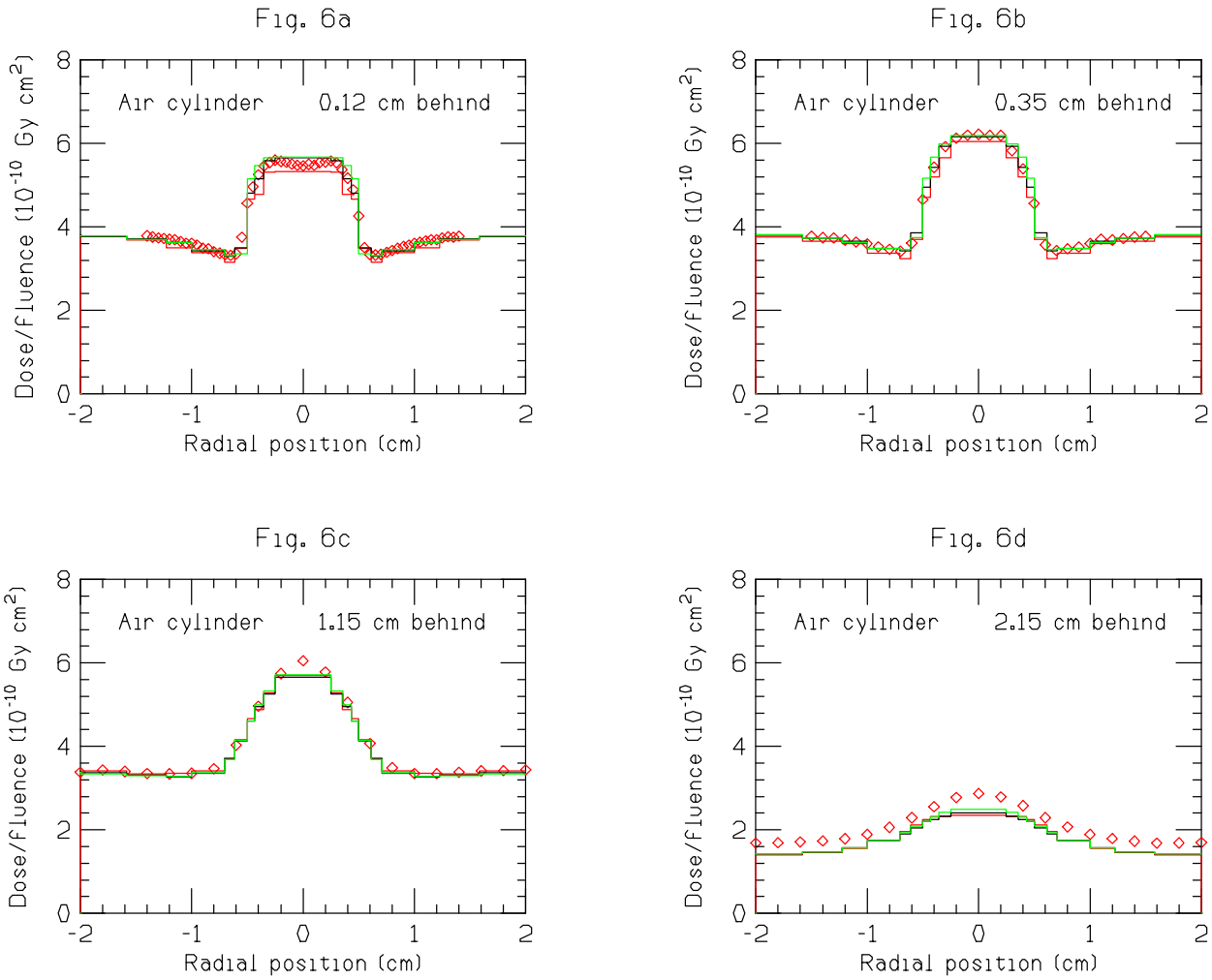

Figure 10b. Benchmark results for Heterogeneity Experiment(10-MeV electron; water with air disc at 2-mm gap; radial dose profiles at various depths behind the air disc).

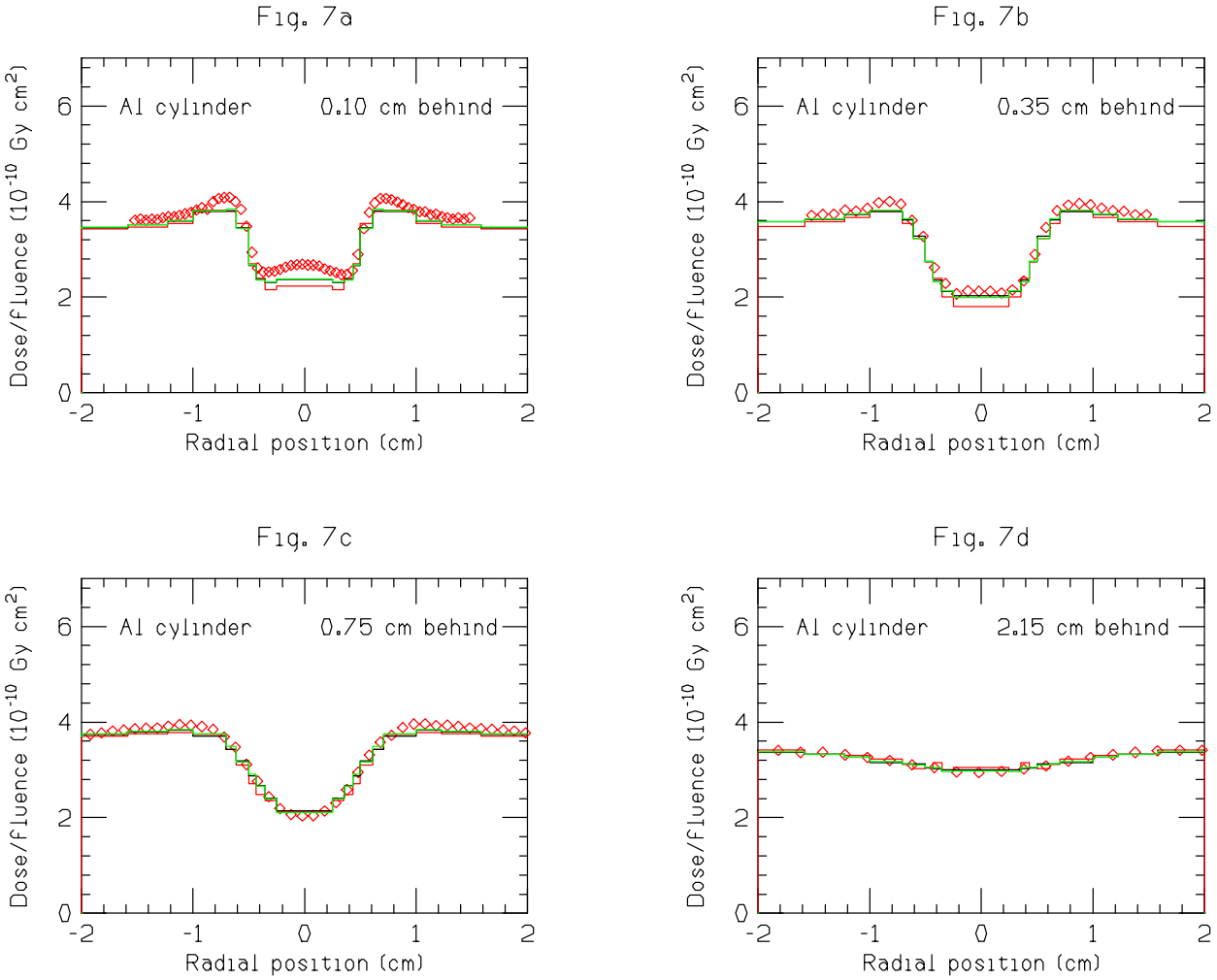

Figure 10c. Benchmark results for Heterogeneity Experiment (10-MeV electron; water with Al disc at 2-mm gap; radial dose profiles at various depths behind the Al disc).

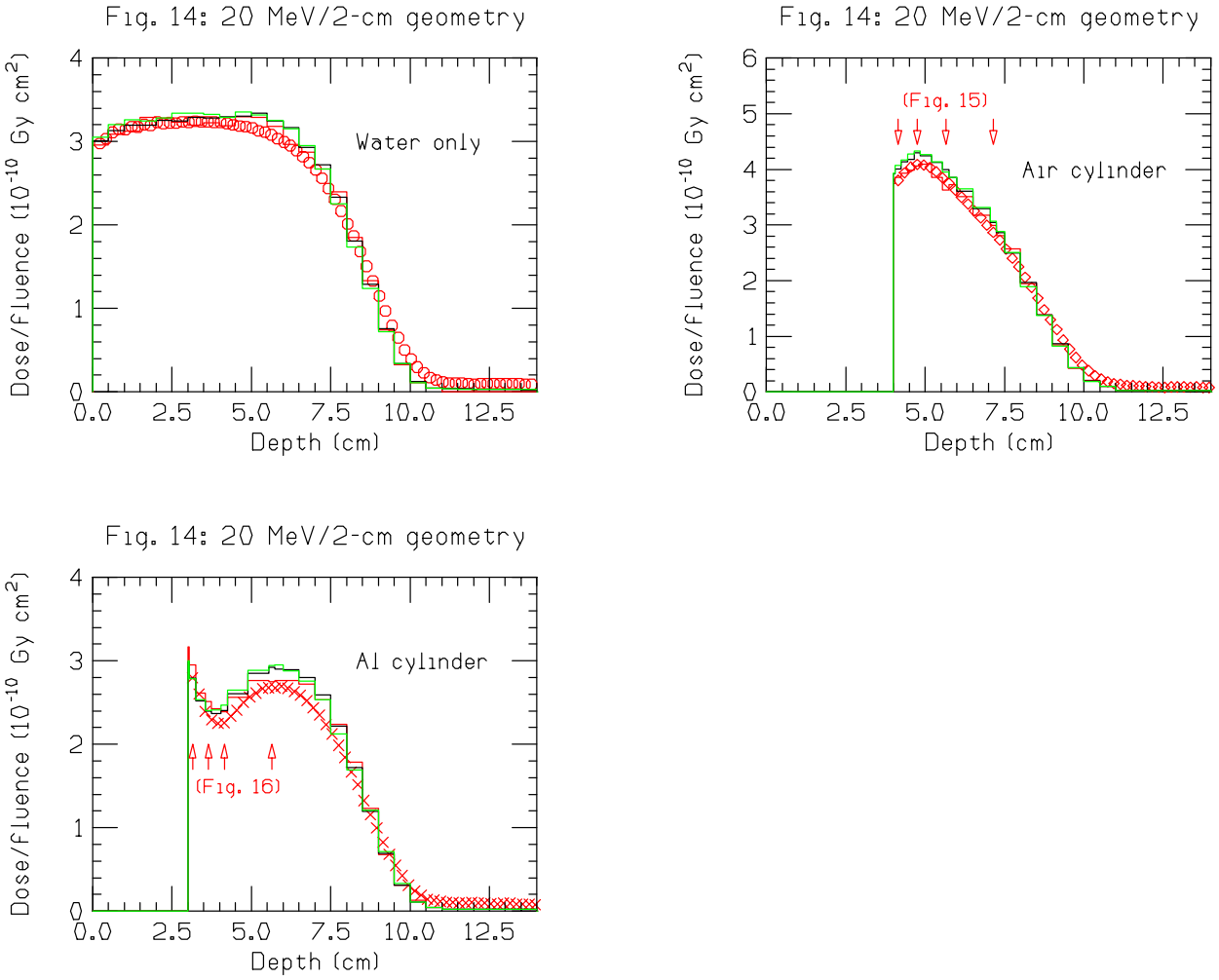

Figure 11. Benchmark results for Heterogeneity Experiment (20-MeV electron; pure water, and water with air or Al disc at 2-cm gap; depth dose curves at central axis).

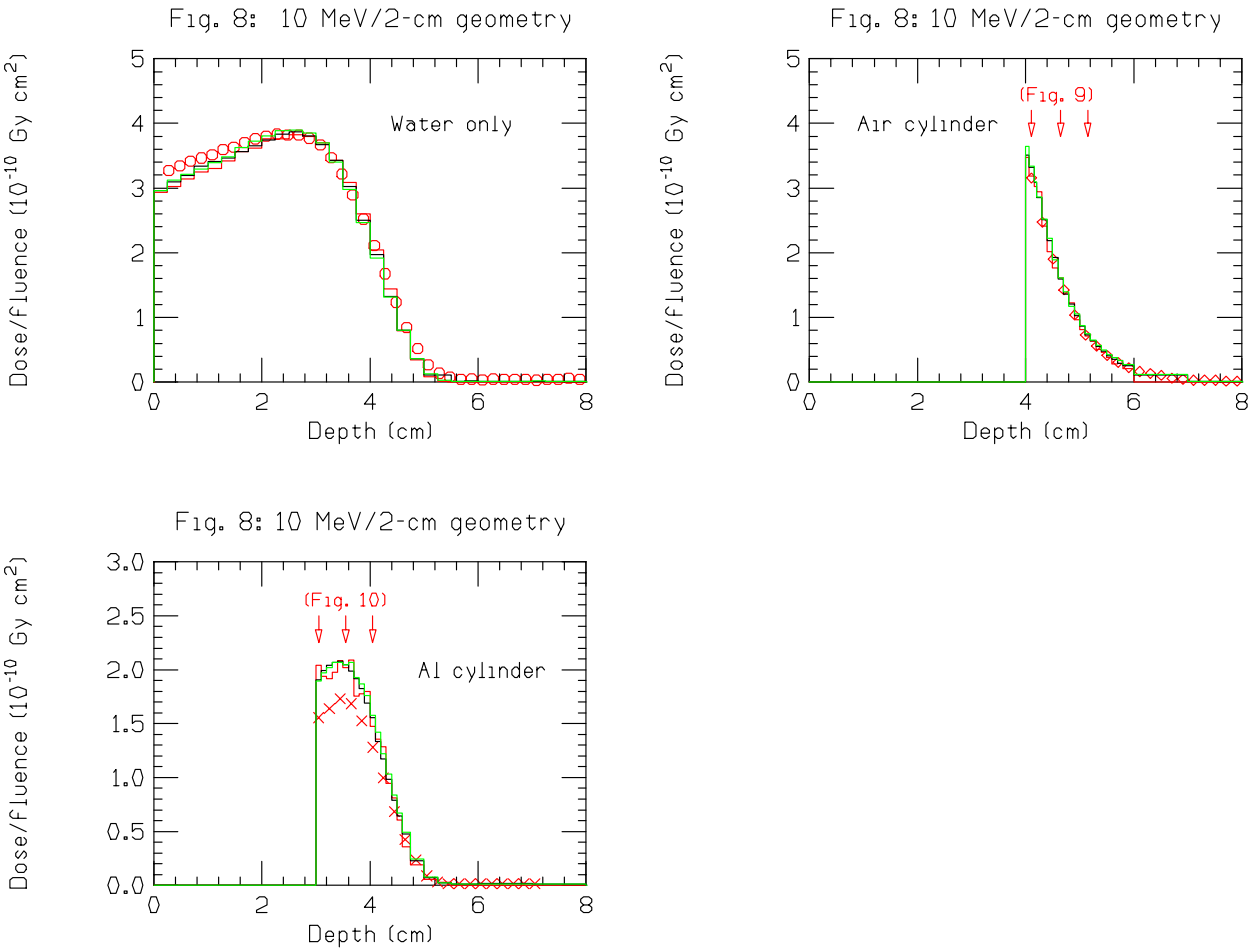

Figure 12. Benchmark results for Heterogeneity Experiment (10-MeV electron; pure water, and water with air or Al disc at 2-cm gap; depth dose curves at central axis).

THE CROSS-SECTION DIVIDING METHOD AND THE SIMULTANEOUS DISTRIBUTION BETWEEN THE DEFLECTION ANGLE AND THE SPATIAL DISPLACEMENT FOR CHARGED PARTICLES PENETRATING THROUGH MATTERS

T. Nakatsuka and K. Okei[†]

Okayama Shoka University, Okayama 700-8601, Japan

[†]*Dept. of Physics, Okayama University, Okayama 700-8530, Japan*

Abstract

Although Molière theory is less accurate than Goudsmit-Saunderson theory due to the small angle approximation, there still remain many superior aspects of Molière theory to the latter. Some problems are yet too difficult to solve through Goudsmit-Saunderson theory itself due to our mathematical insufficiencies and require Molière and other results. Some Molière results are still valuable in solving problems under Goudsmit-Saunderson theory. Some Molière results will be useful in examining accuracy of the results derived through Goudsmit-Saunderson theory. We will look back and look forward again the significance of Molière theory and Molière results.

1 Introduction

We have derived the Molière angular distribution with ionization [1] by using Kamata-Nishimura formulation of the theory [2, 3]. We have investigated the transport mechanism of Molière process with and without ionization, and found the Molière expansion can be well explained by dividing the single-scattering cross-section at an adequate separation angle, where the primary gaussian distribution is generated by the high-frequent moderate scatterings smaller than the separation angle and the subsequent additive correction terms are generated by the low-frequent large-angle scatterings greater than the separation angle [4]. This physical interpretation brought us the highly accurate and the highly efficient sampling sequence of track tracing for charged particle taking account of ionization loss [5, 6].

Although Molière theory [7, 8, 9] is less accurate than Goudsmit-Saunderson theory [10, 11] due to the small angle approximation [12], Molière theory is far rich in mathematical tools and results, compared with the latter. Utilizing these superior aspects of Molière theory, we would like to discuss some problems useful in charged-particles transport even applicable to Goudsmit-Saunderson theory.

2 Improved Molière scattering theory by Kamata-Nishimura formulation to take account ionization loss

The diffusion equation for the Molière angular distribution with ionization is simply described as

$$\frac{\partial \tilde{f}}{\partial t} = -\frac{K^2\zeta^2}{4E^2}\tilde{f}\{1 - \frac{1}{\Omega}\ln\frac{K^2\zeta^2}{4E^2}\} + \varepsilon\frac{\partial \tilde{f}}{\partial E} \tag{1}$$

in Kamata-Nishimura equation, where $\tilde{f}$ denotes the Hankel transforms for the angular distribution. The equation is easily integrated as

$$\tilde{f} \;=\; \frac{1}{2\pi}\exp\{-\frac{\theta_{\rm G}^2\zeta^2}{4}(1 - \frac{1}{\Omega}\ln\frac{\theta_{\rm G}^2\zeta^2}{4\nu t})\}, \tag{2}$$

where

$$\theta_{\rm G}^2 = K^2 t/(E_0 E), \tag{3}$$
$$\nu = e^2 (E/E_0)^{(E_0+E)/(E_0-E)}, \tag{4}$$

and translated to Molière-Bethe solution,

$$\tilde{f} = \frac{1}{2\pi} \exp\{-\frac{\theta_{\rm M}^2 \zeta^2}{4}(1 - \frac{1}{B} \ln \frac{\theta_{\rm M}^2 \zeta^2}{4})\}, \tag{5}$$

so that the angular distribution becomes

$$2\pi f(\vartheta) \;\; = \;\; f^{(0)}(\vartheta) + B^{-1} f^{(1)}(\vartheta) + B^{-2} f^{(2)}(\vartheta) + \cdots, \tag{6}$$

where the expansion parameter B and the scale angle $\theta_{\rm M}$ are determined as

$$B - \ln B = \Omega - \ln \Omega + \ln(\nu t), \tag{7}$$
$$\theta_{\rm M} = \theta_{\rm G} \sqrt{B/\Omega}. \tag{8}$$

Molière angular distributions with and without ionization are compared in Fig. 1.

3 Is Molière theory still valuable in the day of Goudsmit-Saunderson track-tracing ?

There still remain many merits to use Molière theory, such as

- Molière theory is highly efficient, converging within only few terms.
- Molière theory is rich in results of mathematical analysis.
- There still exist many regions to require results solved under the small angle approximation, *e.g.* high energy particle physics, cosmic ray physics, etc..
- It is yet very difficult to solve the problems of multiple Coulomb scattering completely under the solid angle space; *e.g.*
  - only the mean square has been obtained for the transverse distribution,
  - only the restricted few moments have been obtained for the longitudinal distribution,

  through the Lewis theory [13, 14].

and so on.

4 GS-Lewis angular distribution with ionization

Lewis described Goudsmit-Saunderson angular distribution as

$$\begin{aligned} F(\vec{v},t) &= \frac{1}{4\pi} \sum_{l=0}^{\infty} (2l+1) P_l(\cos\theta) \exp\{-\int_0^x dx \int_0^\pi 2\pi N \sigma(\theta)[1 - P_l(\cos\theta)] \sin\theta d\theta\} \\ &\equiv \frac{1}{4\pi} \sum_{l=0}^{\infty} (2l+1) P_l(\cos\theta) \exp\{-\int_0^x \kappa dx\}. \end{aligned} \tag{9}$$

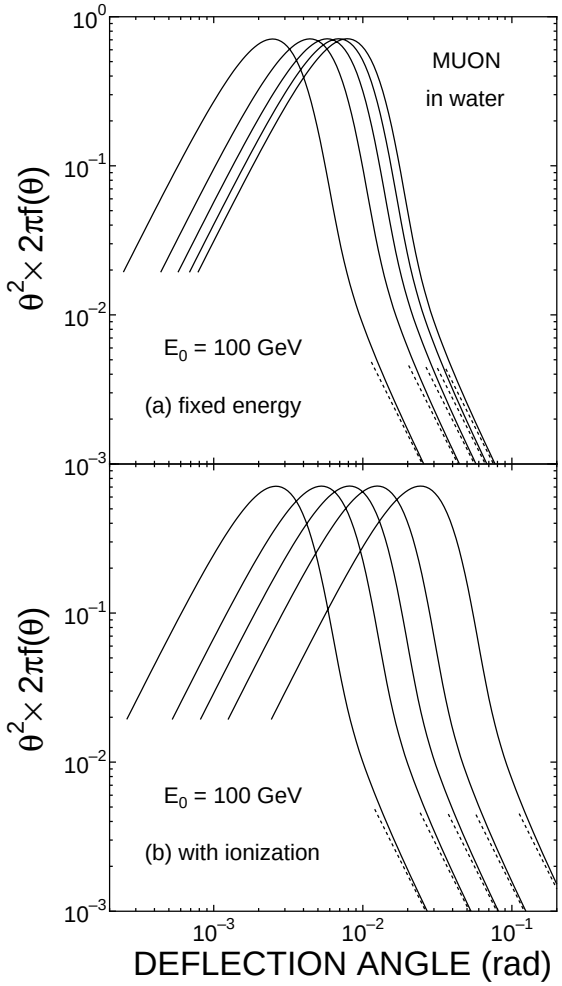

Figure 1: Comparison of expected angular distributions multiplied by θ^2 for muons with and without ionization loss, assuming the rest energy negligible. Solid curves in (b) show the distributions after traverse of thickness at 10, 30, 50, 70, and 90 percent dissipations of the incident energy from left to right, and the curves in (a) show the traditional distributions without ionization loss after traverse of the same thickness. Dot curves denote the asymptotic distributions.

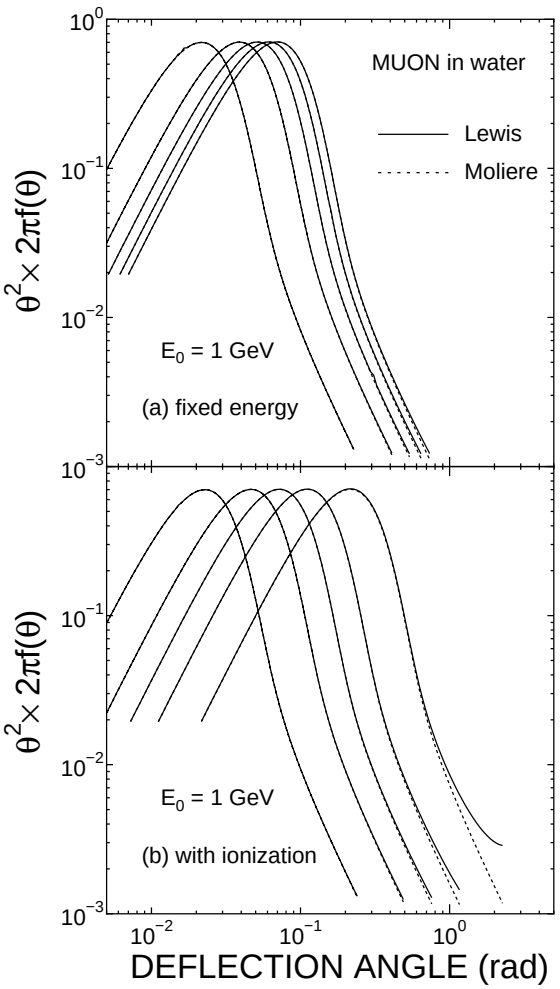

Figure 2: Comparison of expected angular distributions multiplied by θ^2 for muons derived by Lewis theory (solid curves) and by Molière theory (dot curves), assuming the rest energy negligible. Curves in (b) show the distributions after traverse of thickness at 10, 30, 50, 70, and 90 percent dissipations of the incident energy from left to right, and curves in (a) show the distributions without energy loss after traverse of the same thickness.

For the single-scattering cross-section of

$$N\sigma(\theta)2\pi\sin\theta d\theta dx \simeq \frac{K^2}{\pi\Omega E^2}\frac{1}{(1-\cos\theta+\chi_a^2/2)^2}2\pi\sin\theta d\theta dt, \tag{10}$$

we have

$$\begin{aligned} -\int_0^x \kappa dx &= -\int_0^t \frac{2K^2dt}{\Omega E^2}\frac{1}{4}\int_{-1}^1 \frac{1-P_l(\mu)}{(1-\mu+\chi_a^2/2)^2}d\mu \\ &\simeq -\int_0^t \frac{K^2dt}{4\Omega E^2}l(l+1)[\ln\frac{4}{\chi_a^2}+1-2\sum_{m=1}^{l}m^{-1}]. \end{aligned} \tag{11}$$

Assuming the screening angle as

$$\chi_a^2 = \frac{K^2}{E^2}e^{-\Omega+1-2C}, \tag{12}$$

we have

$$\begin{aligned} -\int_0^x \kappa dx &= -\frac{K^2\nu t}{\nu E_0 E}l(l+1)\{1-\frac{1}{\Omega}[\ln\frac{K^2}{\nu E_0 E}-2C+2\sum_{m=1}^{l}m^{1}]\} \\ &= -\frac{\theta_{\rm G}^2}{4}l(l+1)\{1-\frac{1}{\Omega}[\ln\frac{\theta_{\rm G}^2}{4\nu t}-2C+2\sum_{m=1}^{l}m^{-1}]\} \\ &= -\frac{\theta_{\rm M}^2}{4}l(l+1)\{1-\frac{1}{B}[\ln\frac{\theta_{\rm M}^2}{4}-2C+2\sum_{m=1}^{l}m^{-1}]\}, \end{aligned} \tag{13}$$

using B and $\theta_{\rm M}$ of Molière theory.

So we find Lewis angular distribution with ionization is expressed by

$$2\pi F(\vec{v},t) = \sum_{l=0}^{\infty}(l+\frac{1}{2})P_l(\cos\theta)\exp\{-\frac{\theta_{\rm M}^2}{4}l(l+1)\{1-\frac{1}{B}[\ln\frac{\theta_{\rm M}^2}{4}-2C+2\sum_{m=1}^{l}m^{-1}]\}, \tag{14}$$

using the same B and $\theta_{\rm M}$, instead of the Molière-Bethe distribution

$$f_{\rm MB}(\vartheta,t)\vartheta d\vartheta = \theta d\theta\int_0^{\infty}\zeta d\zeta J_0(\theta\zeta)\exp\{-\frac{\theta_{\rm M}^2\zeta^2}{4}(1-\frac{1}{B}\ln\frac{\theta_{\rm M}^2\zeta^2}{4})\} \tag{15}$$

with $\vartheta \equiv \theta/\theta_{\rm M}$. These relations satisfy even if we take account of the rest energy.

5 The cross-section dividing method

5.1 Splitting of the cross-section and the reproduction of Molière series

We split of the cross-section at a separation angle $\chi'_{\rm B}$ of

$$\chi'_{\rm B} \equiv e^{B'/2}\sqrt{e}\chi_{\rm a} \tag{16}$$

into the moderate scattering $\sigma_{\rm M}$ and the large-angle scattering $\sigma_{\rm L}$, as shown in Fig. 3. Then we have the solution

$$\tilde{f} = \frac{1}{2\pi}\exp\{-\frac{\theta_{\rm M}'^2\zeta^2}{4}(1-\frac{1}{B'}[\ln\frac{\theta_{\rm M}'^2\zeta^2}{4}-\ln\tau])\}, \tag{17}$$

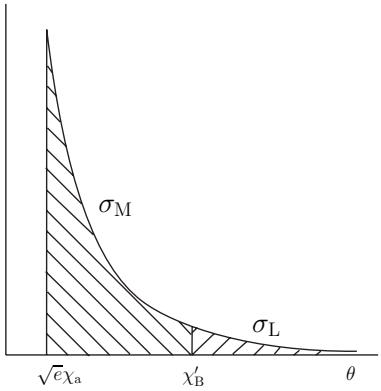

Figure 3: Dividing of the single scattering cross-section σ at $\chi'_{\rm B}$ to the moderate scattering $\sigma_{\rm M}$ and the large-angle scattering $\sigma_{\rm L}$.

where

$$\theta'^2_{\rm M} \equiv \frac{B'}{\Omega}\theta^2_{\rm G} = \frac{B'}{\Omega}\frac{K^2 t}{E_0 E} \qquad \text{and} \qquad \tau \equiv (\theta'^2_{\rm M}/\chi'^2_{\rm B})e^{2-2C}. \tag{18}$$

Using $\vartheta \equiv \theta/\theta'_{\rm M}$, the angular distribution becomes

$$\begin{aligned} 2\pi f(\vartheta) = f^{(0)}(\vartheta) \quad &+ \quad \frac{1}{B'}\{f^{(1)}(\vartheta) + f_1^{(1)}(\vartheta)\ln\tau\} \\ &+ \quad \frac{1}{B'^2}\{f^{(2)}(\vartheta) + f_1^{(2)}(\vartheta)\ln\tau + f_2^{(2)}(\vartheta)(\ln\tau)^2\} + \cdots, \end{aligned} \tag{19}$$

as discussed in *the Tenth EGS4 User's Meeting in Japan* [4]. We remained $\chi'_{\rm B}$ as a free parameter up to now. Only when we put $\ln\tau$ to vanish,

$$\ln\tau = 0 \qquad \text{or} \qquad \chi'^2_{\rm B} = \theta'^2_{\rm M}e^{2-2C}, \tag{20}$$

gives the equation for the expansion parameter B and the scale angle $\theta_{\rm M}$, Eqs. (7) and (8), and defines the Molière splitting angle $\chi_{\rm B}$:

$$\chi_{\rm B} \equiv e^{B/2}\sqrt{e}\chi_{\rm a} = \theta_{\rm M}e^{1-C}. \tag{21}$$

Then we have the Molière expansion of simple series (6). It should be known that the probability p to receive the large-angle scattering in this case is evaluated as

$$p \equiv \frac{N}{A}\int_0^x dx \int_0^\infty \sigma_{\rm L}(\theta)2\pi\theta d\theta = \frac{\nu t}{\Omega}e^{-B+\Omega-2+2C} = \frac{1}{B}e^{2C-2}, \tag{22}$$

so we find the expansion parameter B acts as the probability parameter of large-angle scattering. These facts give us the stochastic interpretation of the Molière expansion, that is the high-frequent moderate scatterings generate the primary gaussian term and the low-frequent large-angle scattering provides the successive correction terms of the central distribution depending on their probabilities within the thickness.

5.2 Single sampling sequence with the cross-section dividing method

The stochastic interpretation of the Molière series described in the preceding subsection bring us a new sampling sequence of the Molière angular distribution, like other authors [15, 16]:

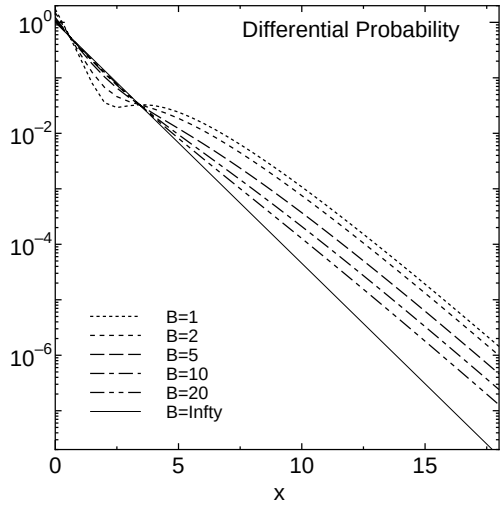

Figure 4: Central distribution produced by the moderate scattering, divided at χ_B. x denotes ϑ^2.

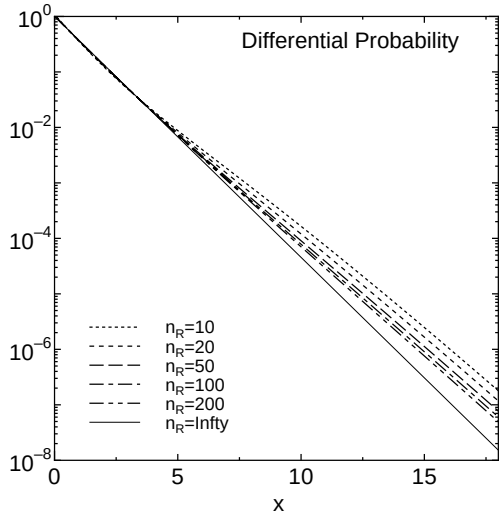

Figure 5: Central distribution produced by the moderate scattering, divided at χ_C. x denotes ϑ^2.

- the first sampling of the central distribution generated by the high-frequent moderate scattering
- the following poisson samplings of the low-frequent large-angle scattering within the penetrating depth and the corrections of the direction angle

5.3 Splitting angle of the cross-section and the results of angular distributions with ionization derived by the cross-section dividing method

We have examined feasibility of the cross-section dividing method by comparing the results with those derived by the detailed Monte Carlo simulation based on the non-divided cross-section [5, 6].

In case we adopt of the Molière splitting angle of χ_B, the small distortions from the gaussian distribution were found in the central distribution generated by the moderate scattering σ_M, as indicated in Fig. 4. The distortion would come from the insufficient traversing thickness for rather wide angular ranges of the moderate scattering expanding from $\sqrt{e}\chi_a$ to χ_B. So we made angular range of the moderate scattering narrower by taking the splitting angle smaller at χ_C, known as the one-scattering angle [12, 17]. Then the central distribution became adequate enough as the central gaussian distribution, as indicated in Fig. 5.

Molière angular distribution with ionization derived by the cross-section dividing method with the splitting angle of χ_C is compared with that derived by the detailed Monte Carlo simulation based on the non-divided cross-section at a traversed thickness corresponding to E-loss of 90%, in Fig. 6.

5.4 Simultaneous distribution between the deflection angle and the lateral displacement

We can obtain the simultaneous distribution between the deflection angle and the lateral displacement $(\vec{\theta}, \vec{r})$ by the cross-section dividing method, where the correlated $\vec{\theta}$ and $\vec{r}$ derived by the central gaussian distribution are corrected by

$$\Delta\vec{\theta} \quad \text{and} \quad \Delta\vec{r} = (t - t')\Delta\vec{\theta} \tag{23}$$

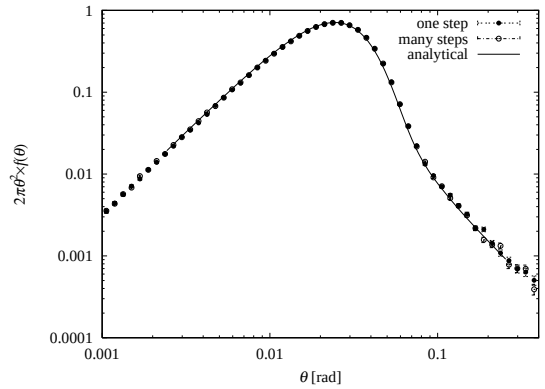

Figure 6: Comparison of Molière angular distribution with ionization derived by the single sequence sampling (filled circle) and that by detailed single-scattering sampling (open circle). Solid curve denotes analytical result.

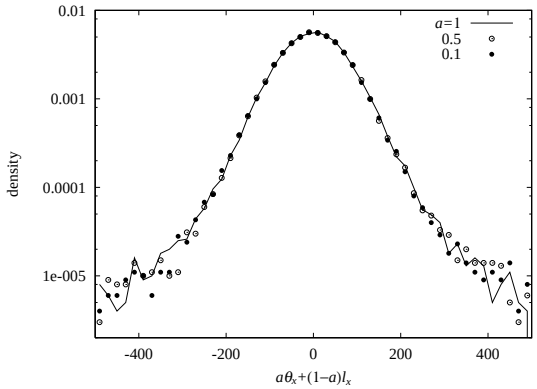

Figure 7: Comparison of the probability densities for linear combination $(E\vec{\theta} + \Delta E \cdot \vec{r}/t)/E_0$ (projected) with different E-loss rates, $a \equiv E/E_0$ of 1 (solid line), 0.5 (open circle), and 0.1 (filled circle) at $t = 1$.

at each large-angle scattering at t', where t denotes the destination thickness. Fig. 7 shows all the linear combinations $(E\vec{\theta}+\Delta E\cdot\vec{r}/t)/E_0$ derived by the cross-section dividing method with different ε agree very well at the common depth t, as predicted by the theory in Appendices.

5.5 The cross-section dividing method for GS-Lewis track-tracing

Track of charged particle will be effectively traced in solid angle space by the cross-section dividing method. Deficits of the Goudsmit-Saunderson theory for insufficient knowledge about the longitudinal distribution [13] will be removed by applying Yang distribution for the simultaneous distribution between the deflection angle and the spatial displacement [18, 19, 20] against tracks before undergoing the large-angle scattering.

Moderate scattering $\sigma_{\rm M}$	Large-angle scattering $\sigma_{\rm L}$
Yang distribution (Gaussian approximation)	Accidental change of direction
Simultaneous distribution between $\Delta\vec{\theta}$ and $\Delta\vec{r}(\Delta x, \Delta y, \Delta z)$	$\Delta\vec{\theta}$

6 Conclusions and discussions

We found Goudsmit-Saunderson angular distribution with ionization is described explicitly by using the same characteristic parameters B and $\theta_{\rm M}$ as for the Molière distribution. Through the cross-section dividing method we derived the method to obtain the simultaneous distribution for charged particles between the deflection angle and the spatial displacement, which is important for natural and smooth track tracing of charged particles in Monte Carlo simulation especially when we take long step sizes. Tracing of charged particles by sampling of primary Yang distribution and subsequent corrections by large-angle scattering is proposed to improve the usual tracings through mere mean spatial displacement predicted by Goudsmit-Saunderson-Lewis theory.

We have found deep understanding of Molière theory is yet very important in investigating the transport mechanism of charged particles penetrating through matters.

Appendix

A Molière distributions for linear combination of the deflection angle $\vec{\theta}$ and the lateral displacement $\vec{r}$

We derive the Molière distribution for a linear combination of the deflection angle $\vec{\theta}$ and the chord-angle $\vec{r}/t$. Let $\vec{p}$ be

$$\vec{p} = a\vec{\theta} + b\vec{r}/t, \tag{24}$$

and $g(\vec{p},t)d\vec{p}$ be its probability density,

$$g(\vec{p},t)d\vec{p} = \frac{d\vec{p}}{a}\iint f(\frac{\vec{p}}{a} - \frac{b\vec{r}}{at}, \vec{r}, t)d\vec{r}. \tag{25}$$

Let $\tilde{g}(\vec{\xi},t)$ be the Fourier transform of g with the Fourier variable $\vec{\xi}$,

$$\tilde{g}(\vec{\xi}) = \frac{1}{2\pi}\iint e^{-i\vec{\xi}\vec{p}}g(\vec{p},t)d\vec{p} = 2\pi\tilde{f}(a\vec{\xi}, b\vec{\xi}/t, t), \tag{26}$$

so that

$$\ln 2\pi\tilde{g} = \int_0^1 \frac{K^2 t\xi^2(a+bu)^2}{4\Omega(E+\varepsilon tu)^2}\ln\frac{K^2\xi^2(a+bu)^2}{4e^{\Omega}(E+\varepsilon tu)^2}du. \tag{27}$$

This definite integral cannot be expressed explicitly within elementary functions in general cases, except for the following cases when we can get both the spatial and the projected distributions from the characteristic parameters B and $\theta_{\rm M}$ described below.

A.1 $b = 0$

This situation with $a = 1$ corresponds to the distribution without taking account of lateral displacements $\vec{r}$, so that it gives the angular distribution under the ionization process described above.

A.2 $\varepsilon = 0$

The situation gives the distribution under the fixed-energy process, for the arbitrary linear combination $a\vec{\theta} + b\vec{r}/t$, as Molière derived for the projected components [21]:

$$\ln 2\pi\tilde{g} \;=\; \frac{K^2 t\xi^2}{4\Omega E^2 b}\{\frac{(a+b)^3 - a^3}{3b}\ln\frac{K^2\xi^2(a+b)^2}{4E^2 e^{\Omega+2/3}} - \frac{a^3}{3b}\ln\frac{a^2}{(a+b)^2}\}, \tag{28}$$

so that we have the same characteristic parameters as Molière:

$$B - \ln B = \Omega - \ln\Omega + \ln t + \frac{2}{3} + \frac{a^3/b}{3a^2+3ab+b^2}\ln\frac{a^2}{(a+b)^2} + \ln\frac{3a^2+3ab+b^2}{3(a+b)^2}, \tag{29}$$

$$\theta_{\rm M}^2 = \frac{3a^2+3ab+b^2}{3}\frac{B}{\Omega}\frac{K^2 t}{E^2}. \tag{30}$$

A.3 $a/E = b/\varepsilon t$

The ratio a to b agrees with E to εt, so that the linear combination becomes

$$\vec{p} = (E\vec{\theta} + \Delta E \cdot \vec{r}/t)/E_0. \tag{31}$$

Then we have the same explicit result

$$\ln 2\pi\tilde{g} = \frac{K^2 t\xi^2}{4\Omega E_0^2} \ln \frac{K^2\xi^2}{4E_0^2 e^{\Omega}}, \tag{32}$$

as under the fixed-energy process. Thus we find the linear combination $(E\vec{\theta} + \Delta E \cdot \vec{r}/t)/E_0$ has the same distribution as the angular distribution at the same traversed thickness derived under the fixed-energy condition of $\varepsilon = 0$.

References

[1] T. Nakatsuka, *"Proceedings of the Second International Workshop on EGS,"* KEK Proceedings 2000-20, 330(2000).

[2] K. Kamata and J. Nishimura, Prog. Theor. Phys. Suppl. **6**, 93(1958).

[3] J. Nishimura, in *Handbuch der Physik, Band 46*, edited by S. Flügge (Springer, Berlin, 1967), Teil **2**, p. 1.

[4] T. Nakatsuka, *"Proceedings of the Tenth EGS4 User's Meeting in Japan,"* KEK Proceedings 2002-18, 1(2002).

[5] T. Nakatsuka and K. Okei, *"Proceedings of the Eleventh EGS4 User's Meeting in Japan,"* KEK Proceedings 2003-15, 1(2003).

[6] K. Okei and T. Nakatsuka, *"Proceedings of the Eleventh EGS4 User's Meeting in Japan,"* KEK Proceedings 2003-15, 9(2003).

[7] G. Molière, Z. Naturforsch. **2a**, 133(1947).

[8] G. Molière, Z. Naturforsch. **3a**, 78(1948).

[9] H.A. Bethe, Phys. Rev. **89**, 1256(1953).

[10] S.A. Goudsmit and J.L. Saunderson, Phys. Rev. **57**, 24(1940).

[11] S.A. Goudsmit and J.L. Saunderson, Phys. Rev. **58**, 36(1940).

[12] W.T. Scott, Rev. Mod. Phys. **35**, 231(1963).

[13] H.W. Lewis, Phys. Rev. **78**, 526(1950).

[14] I. Kawrakow and A.F. Bielajew, Nucl. Inst. and Meth. **B142**, 253(1998).

[15] P. Andreo and A. Brahme, Radiat. Res. **100**, 16(1984).

[16] J.M. Fernandez-Varea, R. Mayol, J. Baro, and F. Salvat, Nucl. Inst. and Meth. **B73**, 447(1973).

[17] B. Rossi, *High Energy Particles* (Prentice-Hall, Englewood Cliffs, NJ, 1952).

[18] C.N. Yang, Phys. Rev. **84**, 599(1951).

[19] T. Nakatsuka, Phys. Rev. **D35**, 210(1987).

[20] T. Nakatsuka, Phys. Rev. **D58**, 056002(1998).

[21] G. Molière, Z. Naturforsch. **10a**, 177(1955).

TRACK TRACING OF CHARGED PARTICLES WITH SIMULTANEOUS DISTRIBUTION BETWEEN THE DEFLECTION ANGLE AND THE SPATIAL DISPLACEMENT

K. Okei[†] and T. Nakatsuka[‡]

[†]*Okayama University, Okayama 700-8530, Japan*

[‡]*Okayama Shoka University, Okayama 700-8601, Japan*

Abstract

A sampling method for multiple Coulomb scattering is presented. The method is constructed by dividing the differential scattering cross section into the moderate and large angle scattering, and exploiting the central limit theorem. That is, the sum of many small angle deflections is simulated by a Gaussian random number and the large angle scattering is directly sampled from the differential scattering cross section. It is found that the appropriate selection of the dividing angle makes the Gaussian approximation of the moderate scattering good while keeping the sampling frequency of large angle scattering low.

If we use the screened Rutherford cross section with the small angle approximation, our method yields the Molière distribution, however, it doesn't require auxiliary numerical tables. Therefore, it can be implemented as simple as, and as fast as Gaussian approximation methods.

The most important feature of our new method is the simultaneous sampling of the deflection angle and the lateral displacement. A correction for taking a constant energy loss per unit length into account is also presented.

1 Introduction

We have been developing a method for sampling multiple Coulomb scattering (see [1, 2] and references therein). The method is constructed by dividing the differential scattering cross section into the moderate scattering and the large angle scattering. Owing to the central limit theorem, the sum of many small angle deflections less than the dividing angle $\chi_{\rm d}$ can be simulated by a Gaussian random number to a good approximation (section 2). On the other hand, the large scattering is rare and directly sampled from the scattering cross section. Our method can yield Molière distribution [3, 4, 5], however, it doesn't require auxiliary numerical tables which are in general used for Molière distribution sampling. Therefore, it can be implemented as simple as, and as fast as Gaussian approximation methods[6, 7].

Since we so far have shown the method for sampling the scattering angle only, in this paper, the method for simultaneous sampling of the angular and lateral deviations with the small angle approximation is presented. A correction for taking a constant energy loss per unit length into account is also presented.

2 The central limit theorem and multiple scattering

If we have N independent random variables X_i $(i = 1, \ldots, N)$, each from a distribution with mean μ_i and variance σ_i^2, the distribution of the sum $S = \sum X_i$ will have a mean $\sum \mu_i$ and variance $\sum \sigma_i^2$. The central limt theorem [8] says that as $N \to \infty$,

$$\left(S - \sum_{i=1}^{N} \mu_i \right) \Bigg/ \sqrt{\sum_{i=1}^{N} \sigma_i^2} \to \mathrm{N}(0, 1). \tag{1}$$

This theorem is very powerful since it does not specify the distribution of X_i except for their means and variances. This means that if we choose the proper dividing angle $\chi_{\rm d}$, the resulting angular distribution from a large number of small angle deflections will be Gaussian no matter what the shape of the differential scattering cross section $f(\chi)$. Following Molière and Bethe [3, 4, 5], we write the screened Rutherford cross section with the small angle approximation as

$$\begin{aligned} f(\chi)\,\mathrm{d}\chi &= 2\chi_c^2\chi\frac{q(\chi)}{\chi^4}\,\mathrm{d}\chi = 2\chi_{cc}^2\frac{t}{E^2}\chi\frac{q(\chi)}{\chi^4}\,\mathrm{d}\chi \qquad (2)\\ q(\chi) &= \frac{\chi^4}{(\chi^2+\chi_a^2)^2}. \end{aligned}$$

The expected total number of scattering n is

$$n = \int_0^\infty f(\chi)\,\mathrm{d}\chi = \frac{\chi_c^2}{\chi_a^2}. \qquad (3)$$

Dividing the cross section at $\chi_{\rm d}$, we have the expected numbers of moderate and large scattering, $n_{\rm M}$ and $n_{\rm L}$,

$$n_{\rm M} = \int_0^{\chi_{\rm d}} f(\chi)\,\mathrm{d}\chi \qquad (4)$$

$$n_{\rm L} = \int_{\chi_{\rm d}}^\infty f(\chi)\,\mathrm{d}\chi \qquad (5)$$

and the variance of anglular deviation due to the moderate scattering,

$$\sigma_\chi^2 = \int_0^{\chi_{\rm d}} \chi^2 f(\chi)\,\mathrm{d}\chi. \qquad (6)$$

The selection of $\chi_{\rm d}$ is crucial since small $\chi_{\rm d}$ makes the Gaussian approximation better but $n_{\rm L}$ larger and vice versa. (Sampling with larger $n_{\rm L}$ requires longer computational time.) The dividing angle should vary with the expected number of deflections, that is, the energy of scattered particle and the thickness of material traversed. Balancing the sampling accuracy and speed, we have selected $\sqrt{\chi_c^2-\chi_a^2}\sim\chi_c$ to be the dividing angle $\chi_{\rm d}$. Then, we have

$$n_{\rm M} = n-1 \qquad (7)$$

$$\sigma_\chi^2 = \chi_c^2\left(\ln n - 1 + \frac{1}{n}\right) \qquad (8)$$

and $n_{\rm L}$ is always unity and the sampling speed would be fast enough. Hence we can focus on the goodness of the Gaussian approximation for the moderate scattering.

One measure of how close to Gaussian a distribution is, is given by the measures of skewness and kurtosis. (For Gaussian, these are zero.) The symmetry of scattering cross section makes the coefficient of skewness be always zero and we use the coefficient of kurtosis γ_2.

The projected distribution of the central part of the screened Rutherford cross section can be written as

$$\begin{aligned} p(\theta_x) &= \frac{\chi_c^2}{\pi}\int_0^{\sqrt{\chi_{\rm d}^2-\theta_x^2}}\frac{1}{\theta_x^2+\theta_y^2+\chi_a^2}\;\mathrm{d}\theta_y\\ &= \frac{\chi_c^2}{\pi}\left[\frac{\sqrt{\chi_{\rm d}^2-\theta_x^2}}{(\theta_x^2+\chi_a^2)(\chi_{\rm d}^2+\chi_a^2)}+\frac{1}{(\theta_x^2+\chi_a^2)^{\frac{3}{2}}}\arctan\left(\sqrt{\frac{\chi_{\rm d}^2-\theta_x^2}{\theta_x^2+\chi_a^2}}\right)\right] \qquad (9) \end{aligned}$$

where θ_x and θ_y are plane angles and $\chi^2=\theta_x^2+\theta_y^2$, $\sigma_{\theta_x}^2=\sigma_{\theta_y}^2=\frac{1}{2}\sigma_\chi^2$. For simplicity, we use $p(\theta_x)$ rather than $f(\chi)$ for examining the Gaussian approximation by calculating γ_2.

Figure 1 shows the coefficient of kurtosis numerically calculated with the cumulant K_4 [8] as a function of the expected total number of deflections $n = n_{\rm M} + n_{\rm L} = n_{\rm M} + 1$ for $\chi_{\rm d} = \sqrt{\chi_c^2 - \chi_a^2}$. It can be seen that $|\gamma_2| < 0.1$ for $n \geq 4$. Since γ_2 for the well known simple Gaussian random number generator which uses 12 uniform random numbers is -0.1, it can be said that the Gaussian approximation for moderate scattering with the dividing angle of $\sqrt{\chi_c^2 - \chi_a^2}$ is good enough for practical purposes. For example, figure 2 shows the moderate scattering distributions for $n = 4$, 20 and 100 ($n_{\rm M}$=3, 19 and 99), obtained from direct Monte Carlo simulations with $p(\theta_x)$. The abscissa and ordinate are scaled so as to compare the results with the standard normal distribution N(0,1). The agreement is very well except for the region where dominated by the large angle deflections in the final multiple scattering distribution.

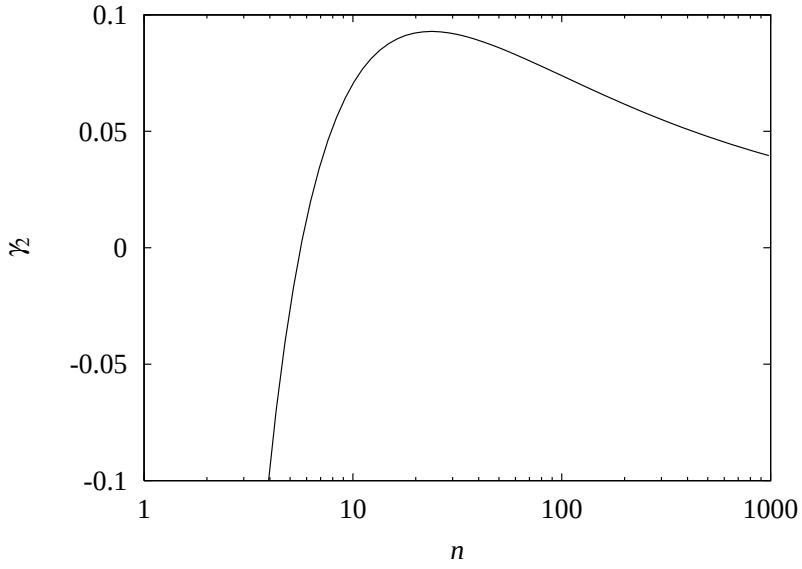

Figure 1: The coefficient of kurtosis γ_2 of the angular distrubution of the moderate scattering as a function of the expected total number of deflections n.

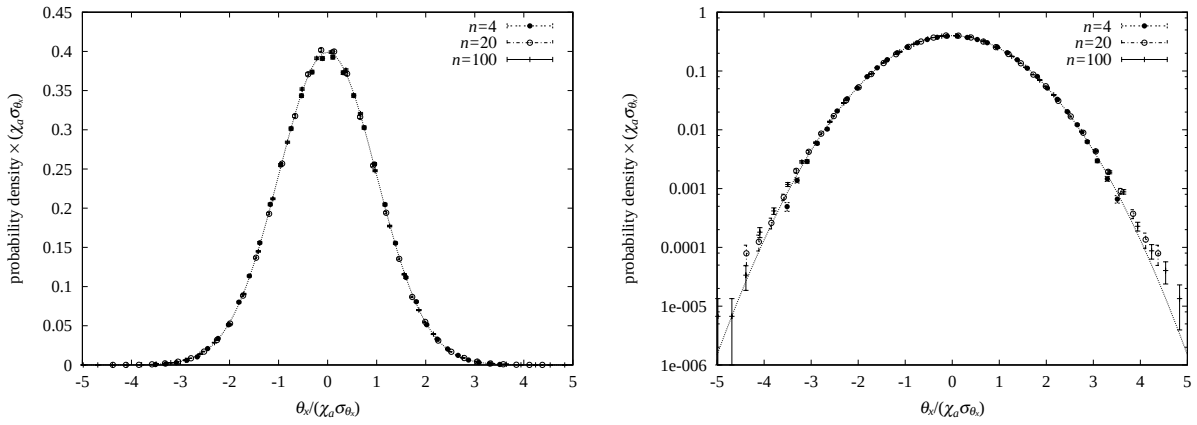

Figure 2: The moderate scattering distributions for $n = 4$, 20 and 100 obtained from direct Monte Carlo simulations. The dotted curve show the standard normal distribution. Left: linear ordinate, Right: logarithmic ordinate.

3 The sampling procedure

3.1 sampling anglular deviation only

Here we describe the procedure for sampling the deflection polar azimuthal angle θ, ϕ due to multiple Coulomb scattering:

1. Calculate χ_c, χ_a and $n = \chi_c^2/\chi_a^2$ (see for example refs. [9, 10]).
2. Using the single scattering cross section, equation (2), that is, according to equation (8), calculate the variance of the central Gaussian distribution.
3. Sample θ and ϕ due to the moderate scattering with Gaussian and uniform random number generators.
4. Sample $n_{\rm L}$ from the Poisson distribution which has the mean value of one.
5. If $n_{\rm L} > 0$, sample the large angle deflections directly from the single scattering cross section.

None of these sampling steps reqires special numerical tables calculated from the Moliére theory. Therefore, a very simple and intuitive implementation is possible.

3.2 simultaneous sampling of anglular and lateral deviations

In a Gaussian approximation of multiple scattering, angular and lateral deviations, θ_x and l_x, can be sampled simultaneously from the probability dinsity

$$P(\theta_x, l_x) = \frac{1}{2\pi\sigma_{\theta_x}\sigma_{l_x}\sqrt{1-\rho^2}} \exp\left[-\frac{1}{2(1-\rho^2)}\left\{\frac{\theta_x^2}{\sigma_{\theta_x}^2} + \frac{{l_x}^2}{\sigma_{l_x}^2} - 2\rho\frac{\theta_x l_x}{\sigma_{\theta_x}\sigma_{l_x}}\right\}\right] \tag{10}$$

where $\sigma_{\theta_x}^2$ and $\sigma_{l_x}^2$ are the variances of θ_x and l_x respectively, and ρ is the correlation coefficient between θ_x and l_x. The conditional probability density of l_x given θ_x is

$$P(l_x|\theta_x) = \frac{1}{\sqrt{2\pi}\sigma_{l_x}\sqrt{1-\rho^2}} \exp\left[-\frac{1}{2\sigma_{l_x}^2(1-\rho^2)}\left\{l_x - \left(\rho\frac{\sigma_{l_x}}{\sigma_{\theta_x}}\theta_x\right)\right\}^2\right] \tag{11}$$

If energy loss during the step is negligible and the step size is t, $\sigma_{l_x}^2 = \sigma_{\theta_x}^2 t/3$ and $\rho = \sqrt{3}/2$ and equation (11) becomes

$$\begin{aligned} P(l_x|\theta_x) &= \frac{1}{\sqrt{2\pi}\sigma_{l_x}/\sqrt{4}} \exp\left\{-\frac{1}{2\sigma_{l_x}^2/4}\left(l_x - \frac{1}{2}\theta_x t\right)^2\right\} \\ &= \frac{1}{\sqrt{2\pi}\sigma_{\theta_x}t/\sqrt{12}} \exp\left\{-\frac{1}{2\sigma_{\theta_x}^2 t^2/12}\left(l_x - \frac{1}{2}\theta_x t\right)^2\right\}. \end{aligned} \tag{12}$$

In usual multiple scattering simulations with the Molièle theory, the lateral displacement in a single step is neglected or aproximated by assuming a deflection point. However, our cross section dividing method makes the simultaneous sampling possible as angular and lateral deviations due to the moderate scattering, $\theta_{x,\rm M}$ and $l_{x,\rm M}$, are sampled from the correlated Gaussian distribution, and the large angle scattering is simulated exactly, that is, not only the deflection angles, the positions where the deflections occurred, $0 < t_1 < t_2 < \cdots < t_{n_{\rm L}} < t_{n_{\rm L}+1} = t$, are also sampled. For example,

under the small angle approximation, θ_x and l_x can be obtained as

$$\theta_x = \theta_{x,\mathrm{M}} + \sum_{i=1}^{n_\mathrm{L}} \theta_{x,\mathrm{L},i} \tag{13}$$

$$\begin{aligned} l_x &= l_{x,\mathrm{M}} + \sum_{i=1}^{n_\mathrm{L}} (t_{i+1} - t_i) \sum_{j=1}^{i} \theta_{x,\mathrm{L},j} \\ &= l_{x,\mathrm{M}} + \sum_{i=1}^{n_\mathrm{L}} (t - t_i)\theta_{x,\mathrm{L},i}, \end{aligned} \tag{14}$$

where $\theta_{x,\mathrm{L},i}$ is the i-th deflection angle due to the large scattering.

Although $t_{i+1} - t_i$ is distributed exponentially, we do not have to take `log` since t_i has unifrom distribution between 0 and t. Hence equation (14) can be rewritten with z_i, a uniform random deviate between 0 and 1, as

$$l_x = l_{x,\mathrm{M}} + t \sum_{i=1}^{n_\mathrm{L}} z_i \theta_{x,\mathrm{L},i}. \tag{15}$$

(Note that the sum does not depend on the order of the values being added.) Therefore, in comparison with a Gaussian approximation method, our method allows us to simulate multiple Coulomb scattering more accurately with little additional computational cost. (The sampling of n_L also can be implemented without taking `log` or `exp` since the mean value is always unity[11].)

3.3 energy loss correction

In this subsection, we describe the correction for the large pathlength case where particle's energy loss cannot be neglected.

When a relativistic charged particle of mass m and energy E_0 traverses material of thickness t and loses its energy at a constant rate of ε, if $E_\mathrm{f} = E_0 - \varepsilon t \gg mc^2$, $\chi_c^2(E)/\chi_a^2(E)$ remains constant and the variances and the correlation coefficient for the moderate scattering can be calculated as

$$\sigma_\theta^2 = \frac{\sigma_0^2}{E_0^2} t \times \frac{1}{a} \tag{16}$$

$$\sigma_l^2 = \frac{\sigma_0^2}{3E_0^2} t^3 \times \frac{3}{(1-a)^3} \left[1 - a^2 + 2a \ln a\right] \tag{17}$$

$$\mathrm{cov}(\theta, l) = \frac{\sigma_0^2}{2E_0^2} t^2 \times \frac{2}{(1-a)^2} \left[a - 1 - \ln a\right] \tag{18}$$

$$\rho = \frac{a - 1 - \ln a}{\sqrt{(1-a)\left(\dfrac{1}{a} - a + 2\ln a\right)}} \tag{19}$$

where $\sigma_0^2 = \chi_{cc}^2(\ln n - 1 + 1/n)$ and $a = E_\mathrm{f}/E_0$. The square root of the variances (the standard deviations) and the correlation coefficient calculated as a function of a are shown in figure 3. It can be seen that σ_θ and σ_l are differently dependent on a and ρ decreases with increasing energy loss (dicreasing a).

For the i-th large scattering occurred at t_i, the dividing angle should be modified as

$$\begin{aligned} \chi_\mathrm{d}(E_i) &= \sqrt{\chi_c^2(E_i) - \chi_a^2(E_i)} \\ &= \frac{E_0}{E_i} \chi_\mathrm{d}(E_0) \end{aligned} \tag{20}$$

where $E_i = E_0 - \varepsilon t_i$.

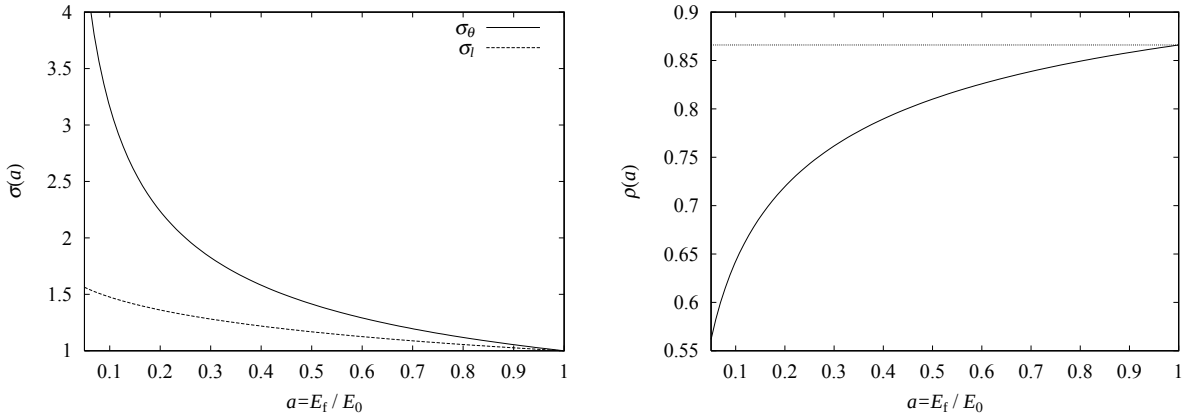

Figure 3: The square root of variances (left) and the correlation coefficient (right) as a function of $a = E_{\rm f}/E_0$ calculated for $\chi_{cc}^2 = 1, E_0 = 1$ and $t = 1$.

4 Results

In this section, multiple scattering distributions obtained from the method described in the previous section are compared with ones obtained from direct Monte Carlo simulations with the screened Rutherford cross section (Rutherford MC) or from the Molière theory. The number of events is 10^6 for every simulation. To generate uniform random numbers, we used Mersenne Twister [12] which has the period $2^{19937} - 1$ and 623-dimensional equidistribution property.

4.1 angular/lateral distribution

Figure 4 shows the multiple scattering angular distribution $f(\vartheta)$ for $n = 10^2$. The open circle, solid histogram and dotted curve show the distributions obtained from our method, Rutherford MC and the Molière theory respectively. Figure 5 shows $\vartheta^2 f(\vartheta)$ for $n = 10^2$ and 10^4 with logarithmic scale. The abscissa is shifted by $\theta_{\rm M} = \chi_c\sqrt{B}$ in units of $\chi_a = 1$. It can be seen that the distributions from the three methods agree very well from the central region to the tail.

Figure 6 and 7 show the projected lateral distributions for $n = 10^2$ and 10^4 respectively. The thick and thin solid curves show the distributions obtained from our method and Rutherford MC respectively. The abscissa and ordinate are scaled so as to compare the results with the standard normal distribution N(0,1) (dotted curve). In the $n = 10^2$ case, the distribution from our method is slightly flatter than the one from Rutherford MC at $l_x \sim 0$ and Gaussian doesn't model the lateral distribution very well.

4.2 simultaneous distribution

The contour plots of the simultaneous distribution of θ_x and l_x for $n = 10^3$ obtained from our method and Rutherford MC are shown in figure 8. Figure 9 shows the conditional probability density of l_x given θ_x for $n = 10^3$. The symbols with error bar and solid histograms show the distributions from our method and Rutherford MC respectively. The variables θ_x and l_x are standardized by $\theta_{\rm M}/\sqrt{2}$ and $\theta_{\rm M}t/\sqrt{6}$ respectively.

Figures 10 and 11 show the same distributions as figures 8 and 9 respectively, but for the $a = 0.1$ (90% energy loss) case. These figures demonstrate that our method works very well even for the case where particles lose significant fraction of their energy.

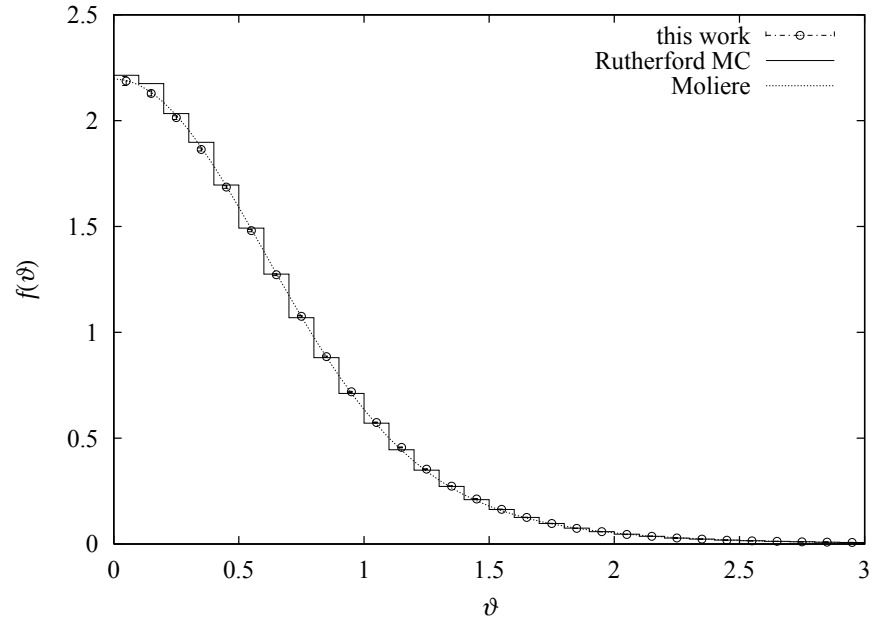

Figure 4: The multiple scattering angular distribution for $n = 10^2$ obtained from our method (open circle), Rutherford MC (solid histogram) and the Molière theory (dotted curve).

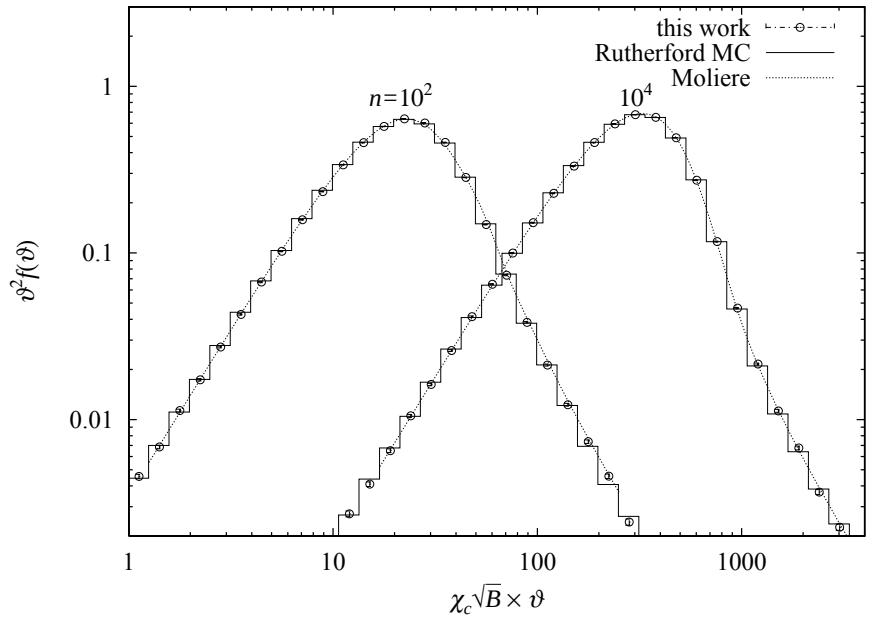

Figure 5: The multiple scattering angular distribution for $n = 10^2$ and 10^4 obtained from our method (open circle), Rutherford MC (solid histogram) and the Molière theory (dotted curve).

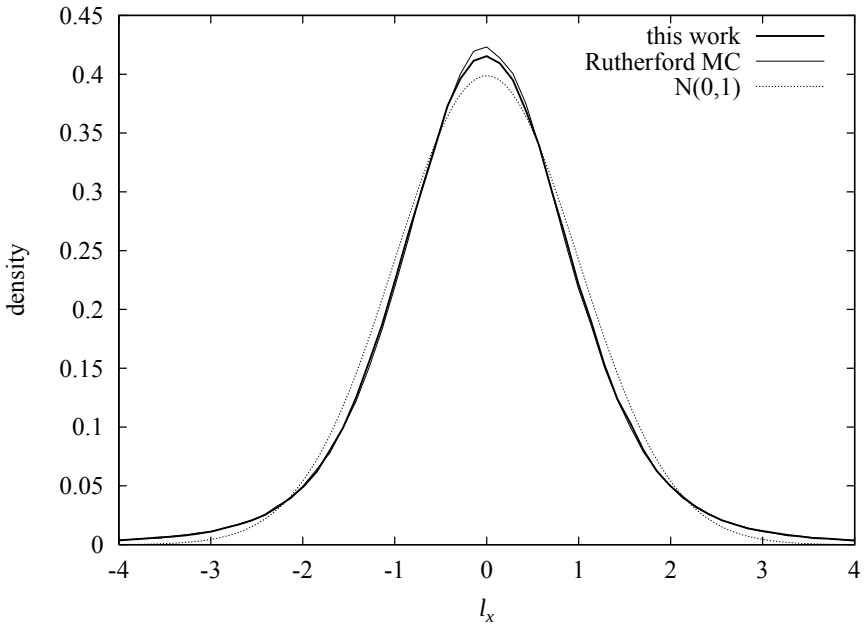

Figure 6: The projected lateral distribution for $n = 10^2$ obtained from our method (thick solid curve) and Rutherford MC (thin solid curve). The dotted curve shows the standard normal distribution N(0,1).

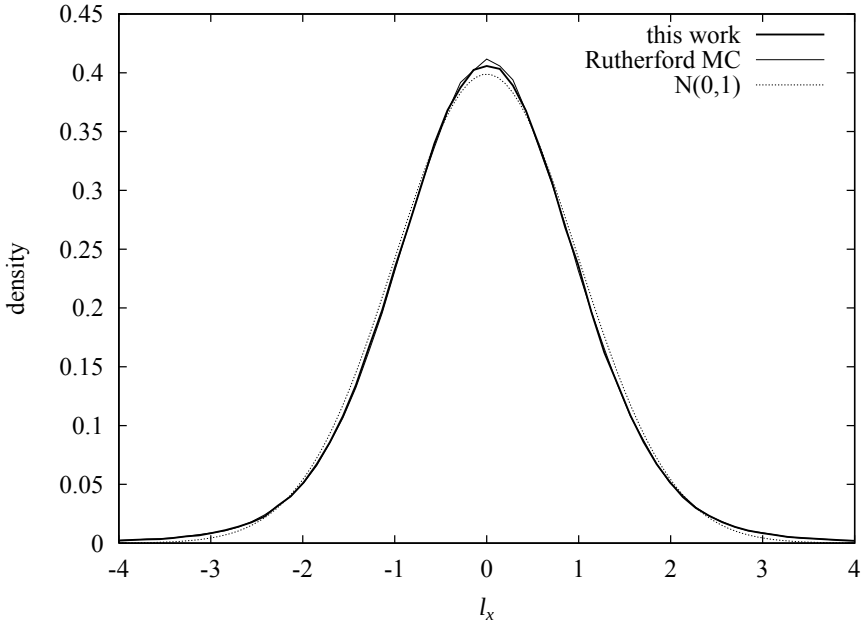

Figure 7: The same distribution as figure 6 but for $n = 10^4$.

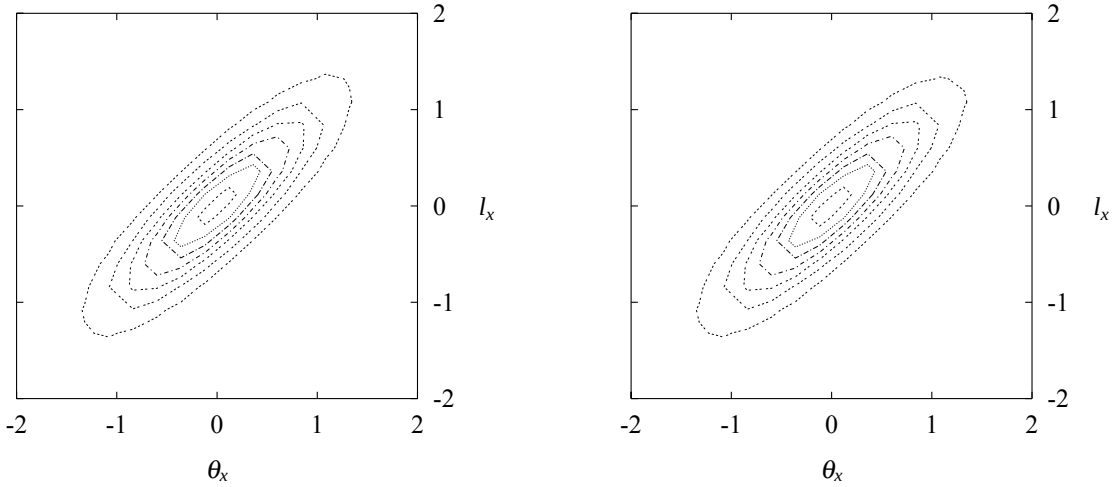

Figure 8: The contour plots of the simultaneous distribution of θ_x and l_x for $n = 10^3$ obtained from our method (left) and Rutherford MC (right).

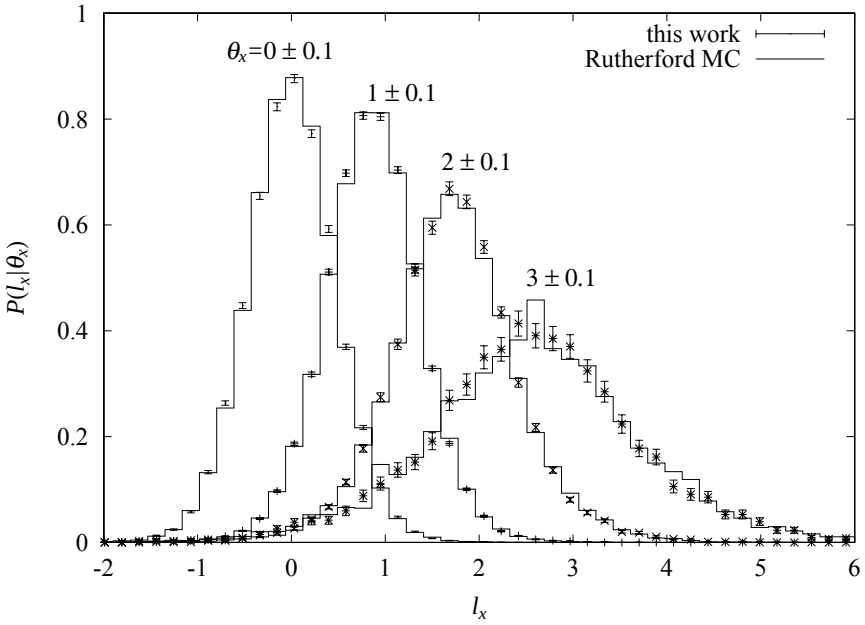

Figure 9: The conditional probability density of l_x given θ_x ($|\theta_x| = 0 \pm 0.1, 1 \pm 0.1, 2 \pm 0.1$ and 3 ± 0.1) for $n = 10^3$ obtained from our method (symbol with error) and Rutherford MC (solid histogram).

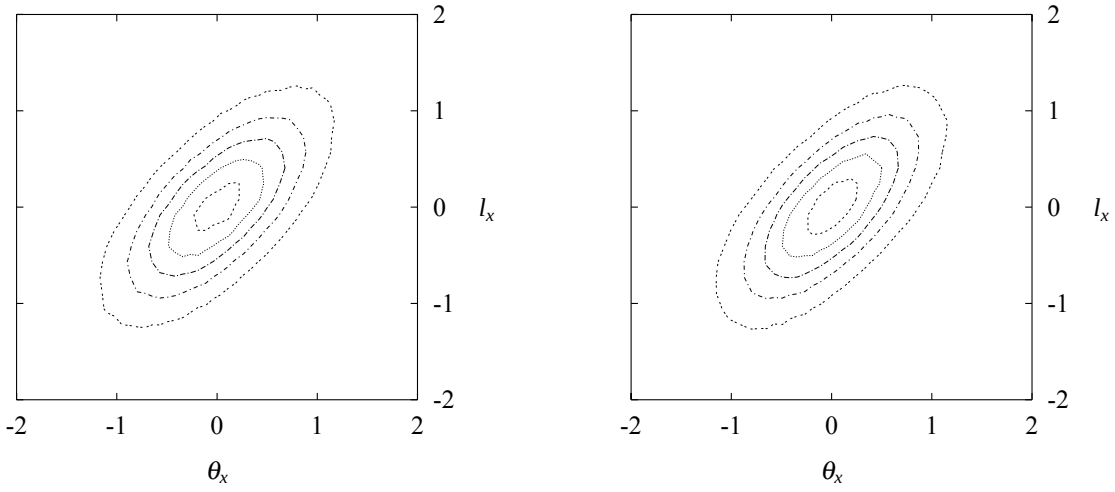

Figure 10: The same plots as figure 8 but for $a = 0.1$.

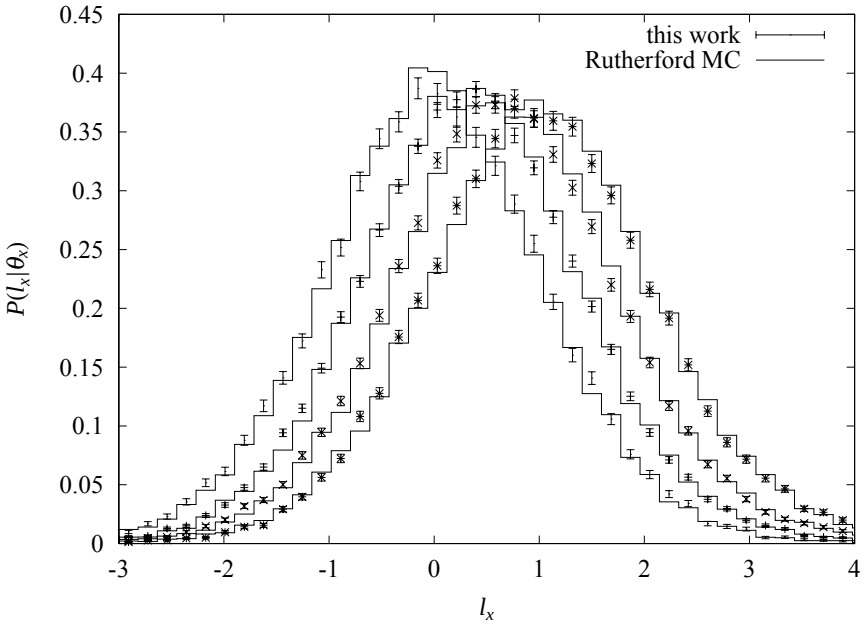

Figure 11: The same plots as figure 9 but for $a = 0.1$.

5 Conclusions

A method for sampling multiple Coulomb scattering is presented. Using the method, we can sample the deflection angle and the lateral displacement simultaneously.

Since our method can be implemented quite simply and intuitively, it would be easily optimized for a particular CPU or application. Furthermore, the method can take account of a constant energy loss process and be used for long step size cases where particles lose significant fraction of their energy. Hence, our method would speed up high energy charged particle transport simulations.

References

[1] T. Nakatsuka and K. Okei, *Proc. 11th EGS4 User's Meeting in Japan*, KEK Proceedings 2003-15, 1 (2004).

[2] K. Okei and T. Nakatsuka, *Proc. 11th EGS4 User's Meeting in Japan*, KEK Proceedings 2003-15, 9 (2004).

[3] G. Molière, Z. Naturforsch. **2a**, 133 (1947).

[4] G. Molière, Z. Naturforsch. **3a**, 78 (1948).

[5] H.A. Bethe, Phys. Rev. **89**, 1256 (1953).

[6] B. Rossi and K. Greisen, *Rev. Mod. Phys.* **13**, 240 (1941).

[7] S. Eidelman et al., *Phys. Lett.* B**592**, 1 (2004).

[8] W.T. Eadie et al., Statistical Methods In Experimental Physics, North-Hollnad Publishing Company (1971).

[9] W.R. Nelson, D.W.O. Rogers and H. Hirayama, The EGS4 Code System, Stanford Linear Accelrator report SLAC-265 (1985).

[10] GEANT Detector Description and Simulation Tool, CERN Program Library Long Writeup, PHYS325 (1993).

[11] W.H. Press et al., *Numerical Recipes in C: The Art of Scientific Computing*, 2nd ed., Cambridge University Press (1992).

[12] M. Matsumoto and T. Nishimura, *ACM Trans. on Modeling and Computer Simulation* **8**, 3 (1998).

A VISUAL USER INTERFACE PROGRAM, EGSWIN, FOR EGS4

Rui Qiu, Junli Li, and Zhen Wu
Department of Physics Engineering, Tsinghua University, Beijing 100084, China
Email: qiuruii@tsinghua.org.cn

Abstract

To overcome the inconvenience and difficulty in using the EGS4 code by novice users, a visual user interface program, called the EGSWIN system, has been developed by the Monte Carlo Research Center of Tsinghua University in China. EGSWIN allows users to run EGS4 for many applications without any user coding. A mixed-language programming technique with Visual C++ and Visual Fortran is used in order to embed both EGS4 and PEGS4 into EGSWIN. The system has the features of visual geometry input, geometry processing, visual definitions of source, scoring and computing parameters, and particle trajectories display. Comparison between the calculated results with EGS4 and EGSWIN, as well as with FLUKA and GEANT, has been made to validate EGSWIN.

1. INTRODUCTION

The EGSWIN system [1] is basically a Windows version of EGS4 [2] combining with some auxiliary functions such as visual geometry input and particle trajectories display. The main goal of EGSWIN is to replace the traditional EGS4 coding requirements for the general main program (MAIN) and the two subroutines HOWFAR and AUSGAB with Visual C++ [3]. This paper introduces the structure, functions, and the implementation approaches of EGSWIN. Benchmark tests and future improvements will also be discussed.

2. STRUCTURE AND FUNCTIONS

2.1 Structure

The structure of the whole EGSWIN system is shown in Figure 1.The user initially inputs all the geometry and material parameters in the Visual Geometry Input module. The information is then stored in an INI type file, which would be imported into the EGSWIN main program (EGS.EXE). As the subroutines of PEGS4 and EGS4 are already converted to Visual Fortran and incorporated into EGSWIN, the main program uses them to calculate and get the results. In the end, particle trajectories

could also be displayed. In addition, users can submit several jobs to different PCs to accelerate the calculation.

2.2 Functions

EGSWIN is an integrated system, it can be divided into three main and modules as follows:

1) Visual Geometry Input Module (SPLIT3.EXE).

This module [4] can be operated independently even though it has been incorporated into the main program (EGS.EXE). Users can input the parameters related to the geometry, define the materials used, and assign medium to each region in a visual interface. This module can process this information and get the definitions of the geometry and material, and then output a file in an INI type, which could be used by the main program.

The basic geometrical bodies include the cube, sphere, cylinder, special hexahedron, and array of cubes and cylinders. The last one is adopted in order to give users convenience when the array of detectors is needed. These bodies are defined by coordinates and dimensions. For example, a sphere could be defined by setting the coordinate of the sphere center and the radius. An image including all kinds of bodies is shown in Figure 2.

The use of OPGL [5] in EGSWIN gives users a colorful 3D display of the geometry during the input process instantaneously. Users could change the viewpoint, the colors of the bodies and background. Furthermore they can zoom out, zoom in, rotate and move the image in different directions. It is quite convenient and explicit.

After the geometry and material are defined, an INI type file can be created automaticly.

2) Program Running Module (the main program).

This module is the kernel of the EGSWIN system. This module processes all the information users input, gets the material cross section data with PEGS4, and simulates the transport of the particles using the subroutines of EGS4.

It includes the following functions:

- To import the geometry information (in an INI type file)
- To show the parameters of the geometry:
  After users import the INI type file into the main program, the information of all the surfaces and regions in the geometry would be automatically shown on the interface, such as the functions of surfaces and the description of material of each region. Figure3 shows an example.
- To set the initial parameters of a source particle:
  The type, energy, direction, position, weight of the particle of the source in an application could be specified. The types of source particles include photon, electron and positron. The energy of particles could be mono or be sampled from a table distribution. The angular distribution could be mono-directional or isotropic. The source could be a point or a surface.
- To define the scorings including surface current, surface flux, and energy

deposition in regions:

The three types of scorings could be given for all 3 different kinds of particles. The first two could also be given in angular bins and energy bins.

- To set calculation parameters:

  The initial random number could be changed if users want to.

  Users could end the running process by limit the total number of particle histories or maximum time.

- To input an INP file and get the material data with PEGS4

  Users need to give an input file used to create material cross section data prior to running an application. The basic format of this file is the same as the input file for PEGS4. However, users could put the information of multiple materials including element, compound and mixture in one input file. The program can automatically separate them, send them to PEGS4, and combine all the created PEMF data together. ????

- To run and show the particle history status in a scroll bar

  Users could know what percentage of particle history has been completed at any moment.

- To show the scoring results:

  The results could be shown on the interface at the end of calculation process and also be saved to a Text type file.

  In addition the function of batch jobs may help users to accelerate the calculation.

A running interface is shown in Figure 4

3) Particle Trajectories Display Module.

This module could be very helpful to check the geometry for the calculation and particle trajectories visually for validating the calculation conditions. It is also useful for understanding the interactions.

Users could choose the particle trajectories, which they are interested in by setting the regions or surfaces and get the 3D display. The main program output the WRL type file with VRML[6], which stores the data of the particle trajectories. Users could open the file to see the 3D geometry and particle trajectories with a software called CosmoPlayer installed in Internet Explorer. The interface is an interactive one in which users could zoom in or out, pan, rotate, and change the viewpoint. The whole geometry may be displayed or switched off. The particle species are distinguished by colors: photons are yellow, electrons are green, and positrons are red. The representation of a given particle species may be switched on or off.

An application of this module is shown in Figure5.

3. BENCHMARK TEST RESULTS

The Crannell water shower experiment has been one of the important benchmarks for testing all versions of the EGS4 Code System [7]. In the Crannell experiment [8], a 1 GeV electron beam was incident on 8000 liters of distilled water in a stainless steel tank (122x122x460 cm^3) and an Aluminum target (61x61x180 cm^3). Radial

energy deposition (MeV/cm^3/electron) measurements were made at various depths of water or Aluminium. EGS4 has been shown to be in excellent agreement, on an absolute basis, with the measurements.

The test geometry for EGSWIN's benchmark was: a single cylinder of Al having a radius of 34.4 cm with a total length of 120 cm broken up into twelve slabs along the z direction. Each has a length of 10 cm except the last is 20 cm. A 1 GeV electron beam was incident on the front face of the target. The longitudinal energy deposition fraction in the radius of 0~1 cm as a function of Al depth was calculated. The comparison of the results obtained with EGS4, EGSWIN, FLUKA, GEANT4 and experiment is shown in Figure6. Figure 7 and Figure 8 show the comparison between EGS4 and EGSWIN in linear scale and log scale, respectively. Different values for ESTEPE in EGSWIN are also used to test the sensitivity of the result to ESTEPE.

The results of EGSWIN and EGS4 agree with each other very well. The statistical errors are so small that they could hardly be shown in the curves except the last two points in Figure 8.

4. DISCUSSIONS AND CONCLUSIONS

In this paper we have described the EGSWIN system, a Windows version of EGS4 developed with Visual C++ and Visual Fortran. The EGSWIN system can produce the same results as the conventional EGS4. EGSWIN could allow users to get the result without any user coding, which could not be achieved with other visual interface systems for EGS4 such as CGVIEW. EGSWIN provides a whole interactive environment for users to input all parameters and get the numeric result as well as the particle tracks display. However, as this EGSWIN is a preliminary version there are some aspects that need to be improved. A simple model is used in which PE-angle sampling, K & L-edge fluorescence, bremsstrahlung and pair production angle sampling are not taken into account. More accurate model, more geometry types and scorings such as track length would be added. Variance reduction techniques also need to be used in order to accelerate the calculation.

References

[1] Yan Shi, "Development of EGSWIN system", postgraduate thesis of Tsinghua University (2001).

[2] W. R. Nelson, H. Hirayama and D. W. O. Rogers, "The EGS4 Code System", Stanford Linear Accelerator Center Report SLAC-265 (1985).

[3] David J. Kruglinski, Scot Wingo, George Shepherd, Inside Visual C++, 5th

Edition (2000).
[4] Hao Dong, “The visual geometry input interface of EGS4”, graduate thesis (2002).
[5] OpenGL Programming Guide. http://fly.srk.fer.hr/~unreal/theredbook
[6] Hartman and J. Wernecke, “The VRML 2.0 Handbook”, Addison Wesley Publishing Company (1996).
[7] W. G. J. Langeveld, James C. Liu, and W. R. Nelson, “The CAD-EGS Project: Using CAD Geometries in EGS4”, (1997).
[8] C. J. Crannell, H. Crannell, R. R. Whitney and H. D. Zeman, “Electron-induced cascade showers in water and aluminum”, Phys. Rev. 184, p426 (1969).

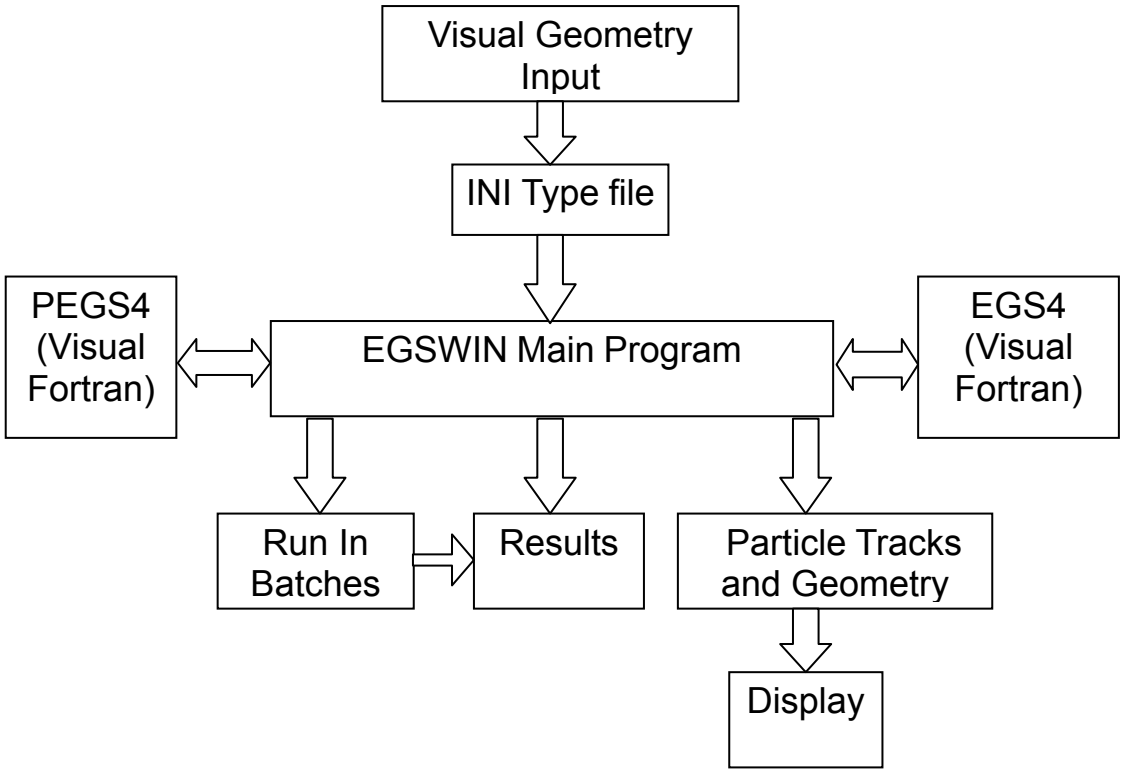

Figure1． The structure of the whole EGSWIN system.

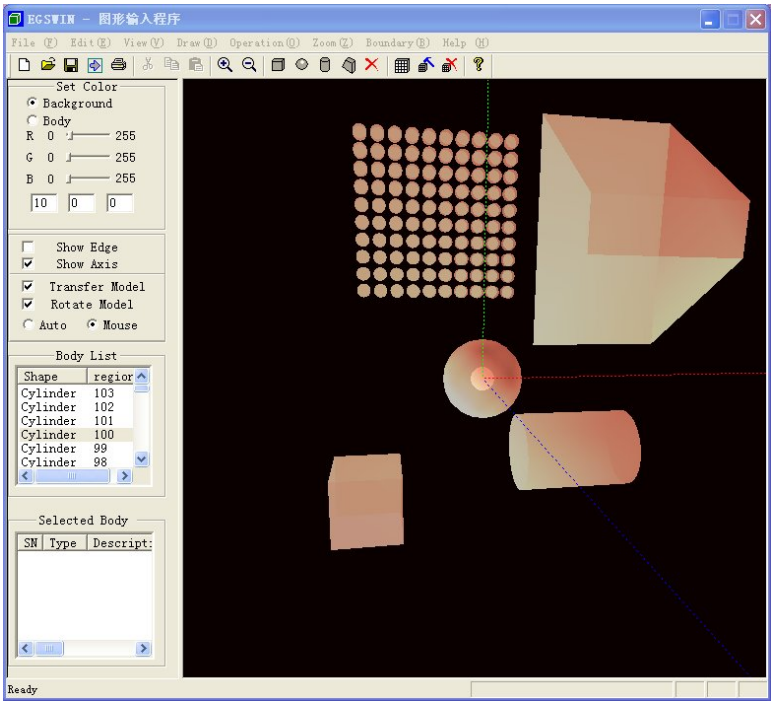

Figure2. Bodies shown in the input interface.

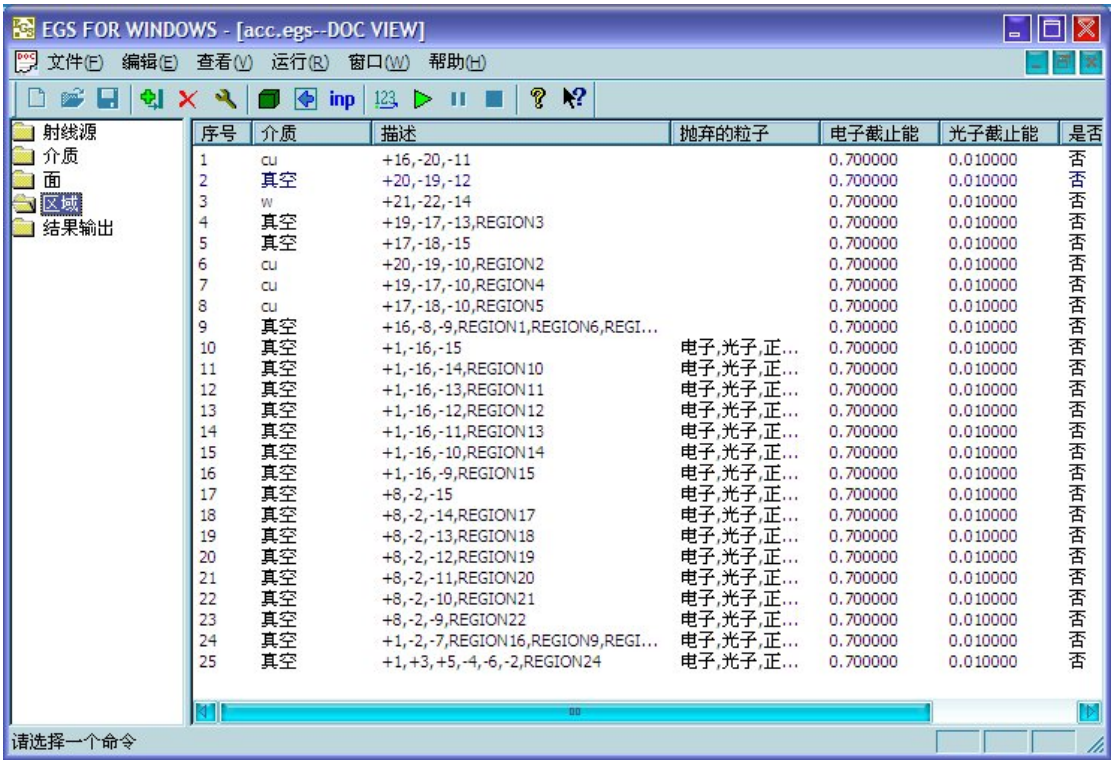

序号	介质	描述	抛弃的粒子	电子截止能	光子截止能	是否
1	cu	+16,-20,-11		0.700000	0.010000	否
2	真空	+20,-19,-12		0.700000	0.010000	否
3	w	+21,-22,-14		0.700000	0.010000	否
4	真空	+19,-17,-13,REGION3		0.700000	0.010000	否
5	真空	+17,-18,-15		0.700000	0.010000	否
6	cu	+20,-19,-10,REGION2		0.700000	0.010000	否
7	cu	+19,-17,-10,REGION4		0.700000	0.010000	否
8	cu	+17,-18,-10,REGION5		0.700000	0.010000	否
9	真空	+16,-8,-9,REGION1,REGION6,REGI...		0.700000	0.010000	否
10	真空	+1,-16,-15	电子,光子,正...	0.700000	0.010000	否
11	真空	+1,-16,-14,REGION10	电子,光子,正...	0.700000	0.010000	否
12	真空	+1,-16,-13,REGION11	电子,光子,正...	0.700000	0.010000	否
13	真空	+1,-16,-12,REGION12	电子,光子,正...	0.700000	0.010000	否
14	真空	+1,-16,-11,REGION13	电子,光子,正...	0.700000	0.010000	否
15	真空	+1,-16,-10,REGION14	电子,光子,正...	0.700000	0.010000	否
16	真空	+1,-16,-9,REGION15	电子,光子,正...	0.700000	0.010000	否
17	真空	+8,-2,-15	电子,光子,正...	0.700000	0.010000	否
18	真空	+8,-2,-14,REGION17	电子,光子,正...	0.700000	0.010000	否
19	真空	+8,-2,-13,REGION18	电子,光子,正...	0.700000	0.010000	否
20	真空	+8,-2,-12,REGION19	电子,光子,正...	0.700000	0.010000	否
21	真空	+8,-2,-11,REGION20	电子,光子,正...	0.700000	0.010000	否
22	真空	+8,-2,-10,REGION21	电子,光子,正...	0.700000	0.010000	否
23	真空	+8,-2,-9,REGION22	电子,光子,正...	0.700000	0.010000	否
24	真空	+1,-2,-7,REGION16,REGION9,REGI...	电子,光子,正...	0.700000	0.010000	否
25	真空	+1,+3,+5,-4,-6,-2,REGION24	电子,光子,正...	0.700000	0.010000	否

Figure 3. Main program interface.

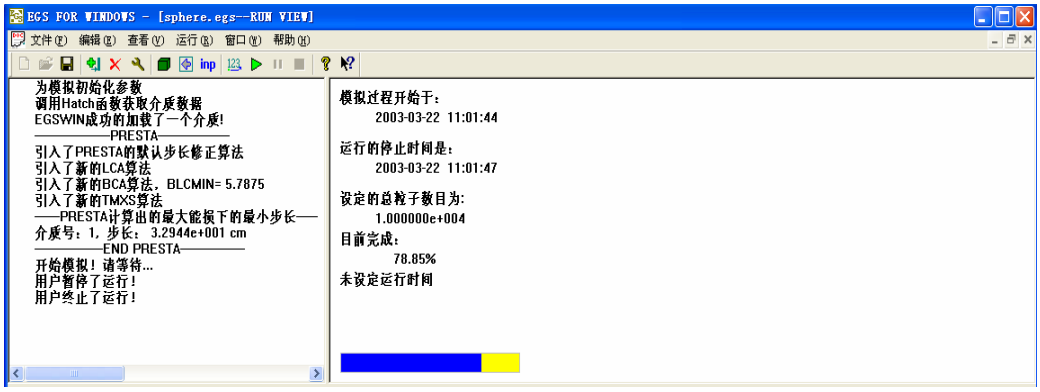

Figure 4. Program running interface.

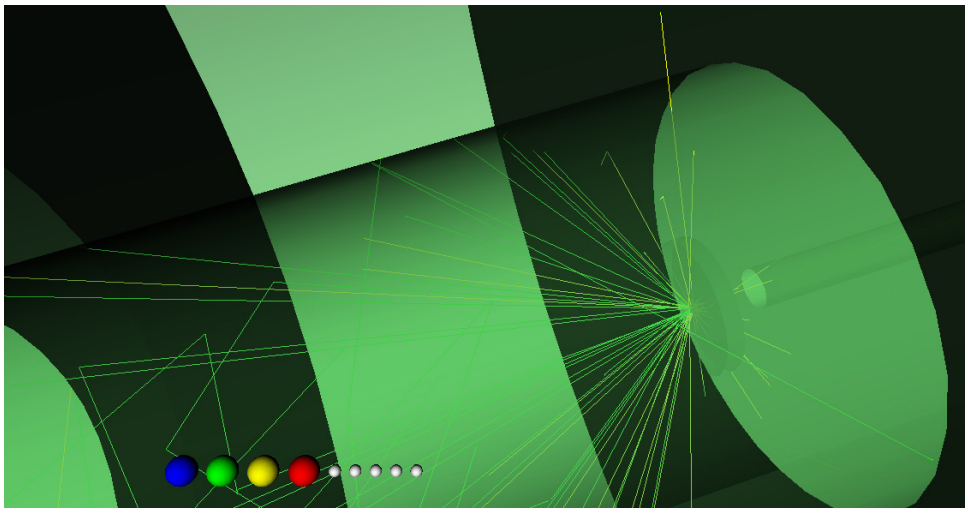

Figure 5. Particle tracks display.

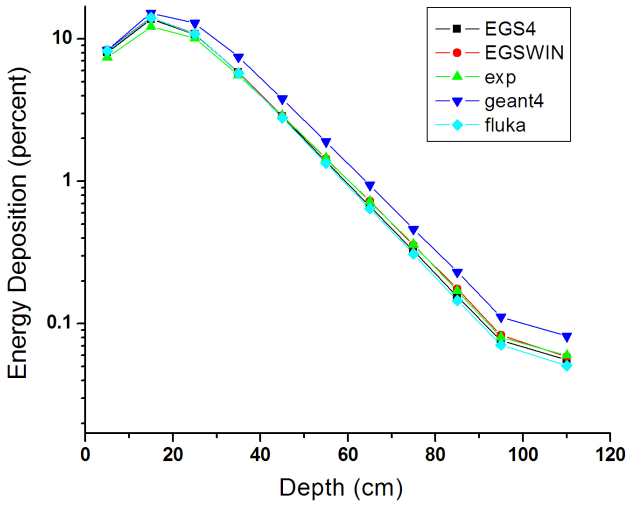

Figure 6. Comparison of depth dose curves calculated with different codes.

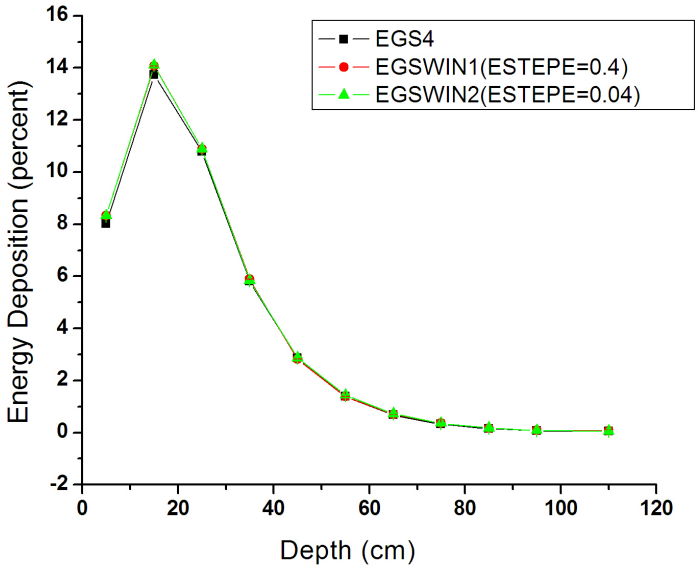

Figure 7. Comparison of EGS4 and EGSWIN with different ESTEPE (Linear scale).

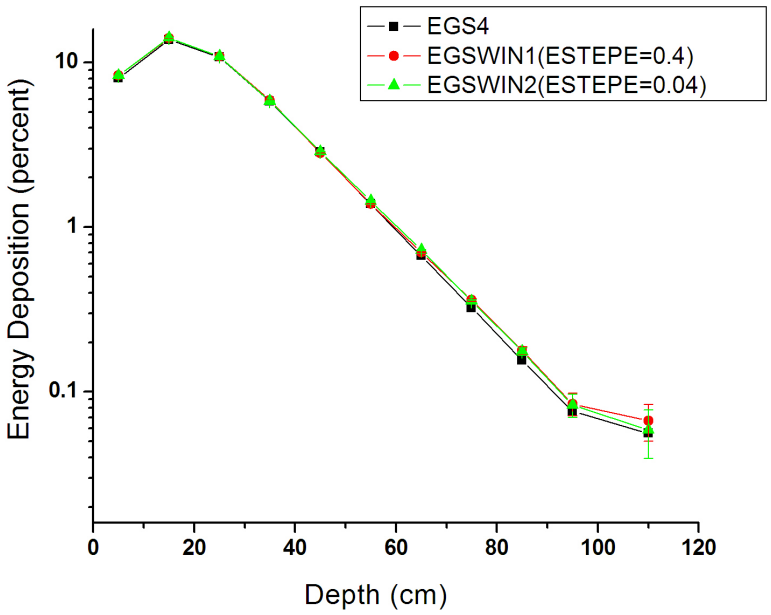

Figure 8 Comparison of EGS4 and EGSWIN with different ESTEPE (Log scale).

INTERFACING EGS4 WITH GEANT4
- AN EXAMPLE OF VIRTUAL MONTE CARLO APPROACH

K. Murakami

High Energy Accelerator Research Organization (KEK), Tsukuba, Ibaraki 305-0801, Japan
e-mail: Koichi.Murakami@kek.jp

Abstract

The idea of Virtual Monte Carlo is that to run different Monte Carlo codes without changing user codes, such as input and output format as well as geometry and detector response. There are several well-known and widely-used simulation packages. However, comparing between different simulation tools often raises controversial issues in geometry description, cut values and so on. In this sense, the approach of Virtual Monte Carlo could be useful to settle down this kind of problems.

Geant4 has rich flexibility and expansibility brought by its Object-Oriented approach, especially in adding physics processes. We can use Geant4 as a framework of Virtual Monte Carlo system and plug-in the part of physics processes of other packages as Geant4 modules. In this paper, we especially focused on interfacing EGS4, which is one of the most well-known simulation packages, with Geant4. Taking advantage of the capability of Geant4 as a framework, we developed a plug-in interface for using EGS4 as a module of Geant4 physics process. By means of this interface, users can make applications on which the two different simulation systems can co-work in an easy and proper way. This is useful and important for making comparisons between EGS4 and Geant4, especially in users' application level. In addition, EGS4 users can share Geant4 powerful resources, such as geometry description, tracking etc.

In this paper, we describe our approach of design and implementation of the interface. And also, through some basic comparison tests, the feasibility and usefulness of Virtual Monte Carlo approach can be shown.

1. Introduction

Geant4 is a toolkit for detector simulation of the passage of particles through matter. It provides a comprehensive set of functionalities for geometry, material, tracking particles, particle interaction, detector response, event, run, visualization and user interfaces [1]. Exploiting an Object-Oriented methodology and C++ programming language, Geant4 enjoys rich flexibility and expansibility as generic simulation system. Particularly in terms of physics process, Geant4 gives clear and definite protocols between particle and process, and tracking and process, so that users can make a choice of models for each process and/or easily implement additional users' own processes. On the other hand, EGS4 is another well-established simulation code [2]. Physics processes implemented in EGS4 are confined to electromagnetic physics of electron and photon. But it is widely used as a standard especially in medical research area.

In general, comparing between different simulation tools often raises controversial issues in geometry description, cut values and so on. In order to minimize these kinds of problems, our attention is focused on interfacing these well-established and commonly-used simulation codes. Taking advantage of the capability of Geant4 as a framework, we developed a plug-in interface for using EGS4 as a module of Geant4 physics process. By means of this interface, users can make applications on which the two different simulation systems can co-work in an easy and proper way. This is useful and important for making comparisons between EGS4 and Geant4 especially in users' application level. In addition, EGS4 users can share Geant4 powerful resources, such as geometry description, tracking etc.

In the following, we describe our design and implementation of the interface, and the results of basic benchmarks are also presented.

2. SYSTEM ANALYSIS AND DESIGN

First of all, our design policy is set. We should care for not to change algorithms and prescriptions which are applied in the EGS4 system in order to get the same output as obtained by using EGS4 itself. According to our policy, we make careful system analysis for each component of EGS4 and decide whether it can be replaced with a corresponding Geant4 component or should be left as it is. Analysis for each functional component is described in the following subsections, and summarized in Table 1.

Table 1
Summary of which package is used in each functional component

Component	Which package?
Control Framework	Geant4
Geometry and Tracking	Geant4
Material	Geant4/EGS4
Cross Section Table	EGS4 (PEGS)
Physics Process	EGS4
Cutoff	EGS4

2.1 Geometry and Tracking

Geometry description model is very different from each other. In Geant4, describing geometry is completely separated from the tracking component in users' implementation level. Geometry model is based on the mother-daughter concept, in which each volume can be described by being placed in its mother volume hierarchically. Functionality of particle transportation is provided in another part of the toolkit. Users can implement their own detector geometries not taking care of matters with tracking particles. In EGS4, on the other hand, geometry description is closely coupled with users' implementation of particle transportation. To implement geometry, users have to calculate the distance between the current location and the closest surface and transport a particle in their own codes. In other words, EGS4 does not provide a generic way of describing geometry and tracking particles. Therefore we can make use of Geant4 functionalities for describing geometry and tracking particles without any care.

2.2 Process and Tracking

The next consideration is focused on how a physics process is invoked in tracking, that is, a way of step size calculation and process selection. In Geant4, each process has its own fate in terms of number of interaction length. Then, a process having minimum fate will be invoked. In EGS4, the next step size is decided based on the total cross section. Then, which process will be applied is chosen at the rate of branching fraction of a process. In principle, these two

treatments function in the same manner. The remaining small difference is fixed in implementation level. Practically, we implement EGS4 physics processes as single Geant4 processes for electron and photon respectively.

Subroutines of physics processes in EGS4 are written in FORTRAN (Mortran in practice). Each of them is reused as it is. This is because the already existing FORTRAN codes are working well and it is more convenient to keep independence from each package for future updates.

2.3 Material and Cross Section Table

In the EGS4 system, defining materials and calculation of cross section tables have to be prepared by PEGS, which is an external program, prior to execution of users' programs. An output file of PEGS is read in an EGS4 program at initialization phase. We make a design decision to share this procedure for defining materials and calculating cross section tables.

Information described as material attributes is slightly different. In Geant4, in most cases, material information has only properties of material itself, such as atomic number, composition, density, etc. In EGS4, additional information associated with process such as cutoff energy, parameters and coefficients of formulas, option flags specific to processes are also given. Therefore, our interface is supposed to manage materials in terms of both Geant4 and EGS4. Besides Geant4 material classes, classes describing materials defined in EGS4 are designed. In addition, a mapping table between Geant4 materials and EGS4 materials is in need to convert a Geant4 material to a corresponding EGS4 material, and vice versa.

2.4 Cutoff

The word "cutoff" is used in two meanings. One is "tracking cut"; particles below the cutoff energy will be discarded. The second meaning is "production cut"; only particles above the cutoff will be generated as secondary particles. In Geant4, only production cut is applied, and particles basically will be transported until they have zero kinetic energy. In EGS4, on the contrary, both cutoffs are applied. A way of setting cutoff values is also different. In Geant4, only one value is set in terms of range, and it is internally converted to energy for each combination of material and particle species. On the other hand, in EGS4, a cutoff parameter is specified for each material. So, we manage cutoff values in material description. According to our policy, care should be taken not to change the cutoff treatment carried out in EGS4. Therefore, we bypass cutoff treatment in Geant4 and set and apply cutoff in the EGS4 style.

3. Implementation

3.1 Material

There are two additional classes presented to describe materials used in EGS4; *EGS2G4PegsMaterial* and *EGS2G4Material*. *EGS2G4PegsMaterial* describes a material defined in a PEGS output file. Its attributes consist of name, index of a material array in the EGS4 common block, density, energy range of cross section tables (*AP, UP, AE, UE*) and some user flags. Its objects will be instantiated from a PEGS output at initialization time. *EGS2G4Matetial*, which is referred by EGS4 processes, represents a practical medium assigned to a volume. It has user parameters, like cutoff (aka *ECUT, PCUT*), density, process switch, etc in addition to a reference to an object of *EGS2G4PegsMaterial*. A correspondence between *EGS2G4Material* and *G4Material* has to be given as a form of a mapping table (*g4-egs4* material map) at initialization. This table is used at tracking time to retrieve an *EGS2G4Material* object corresponding to a *G4Material* one of a current volume.

3.2 Physics Process

Geant4 is designed to allow users to implement new processes in a generic way. All actual process classes inherit from *G4VProcess*, in which definite protocols to invoke interactions from the tracking side are defined. All processes are classified into

the following process types; "AtRest", "AlongStep", "PostStep" and any combinations of these types. Each type of process has two mandatory methods to be implemented. *GetPhysicalInteraction-Length(GPIL)()* limits the step size and calculates when an interaction will occur. *DoIt()* gives actual changes of a particle and creates secondary particles. In EGS4, tracking electrons and photons is handled in the FORTRAN subroutines, *ELECTR* and *PHOTO* respectively. Each actual physics process is called in these subroutines at the rate of its cross section.

Practical implementation is carried out according to the Geant4 scheme. As previously mentioned, single Geant4 processes per electron and photon are implemented; *EGS2G4eProcess* for electron and *EGS2G4gProcess* for photon, inheriting from *G4VProcess*. They are implemented as a "continuous-discrete-at-rest" process and a "discrete" process respectively. The corresponding EGS4 subroutines (*ELECTR* and *PHOTO*) are divided into two parts so as to match with the protocols of Geant4 process. One is a part of calculating *GPIL()*, and the other is to describe actual reaction of processes, i.e. *DoIt()*. The divided parts are written in Mortran codes and wrapped with C++ because it is much easier and safer to handle the original codes.

The list of processes currently covered is summarized in Table 2. At the first target, we start with connecting a plain version of EGS4 package. Some extension components like PRESTA are not included yet. It is noted that the current implementation of multiple scattering is described only by flipping momentum direction. In order to include lateral displacement, which is included in the PRESTA extension, we have to set a safety limit on lateral displacement not to push an electron/positron out to the next volume. This is the next target of our plan.

Table 2
Process list currently covered

Electron processes	Photon processes
multiple scattering	Rayleigh scattering
continuous energy loss	pair production
Bremsstrahlung	photo-electric effect with
Møller scattering	subsequent fluorescence
positron annihilation	Compton scattering
(in-flight / at-rest)	

With regard to cutoff treatment, a particle below cutoff energy will be stopped and killed with depositing its kinetic energy. In case of positron, a positron will be stopped and followed by annihilation to two photons.

3.3 How It Works

In this subsection, how the interface works is described from the tracking view point. We let particles travel in parallel worlds; Geant4 and EGS4 geometries. A Geant4 world is just a geometry constructed in the Geant4 manner, and particles are practically transported in this geometry. On the other hand, an EGS4 world is composed of a single "virtual" volume with no dimensions (huge enough) and a medium dynamically updated at every step. This volume is used only for actual reaction of EGS4 processes. The practical work flow at tracking time is as follows:

1. A Geant4 material of a current volume is converted to a corresponding EGS4 medium through the *g4-egs4* material map.
2. Medium information of the EGS4 volume is updated.
3. Kinematical information in the EGS4 stack is updated from a Geant4 track.
4. An EGS4 process is invoked and recorded to the EGS4 stack.
5. The stack information of EGS4 is evacuated to a change of particle in the Geant4 representation.

3.4 User Interface

What is provided from users' side of view? At first, we provide another user physics list for using EGS4 processes. To use EGS4 processes, any existing Geant4 geometry codes don't have to be modified. As for materials, users have to prepare EGS4 materials by themselves. Practically, users define PEGS materials in a PEGS input file and execute PEGS to generate a cross section file. In addition, users have to give assignments for which PEGS material corresponds to a Geant4 material used in users' geometry. All operations for setting user parameters and flags controlling behavior of EGS4 programs can be performed through Geant4 command line interface. So, users don't have to recompile any programs to modify user parameters and flags.

4. Benchmarks

The development was carried out under Linux system (SUSE Linux 9.1). We used gcc and g77 of version 3.3 and Geant4 of version 6.2. The version of EGS4 used was a version distributed at the KEK site. The first implementation was finished, and we have checked basic functionalities. As for robustness of the system, several million events in a simple geometry were successfully generated without any problems. We also carried out benchmark tests proposed in 3). Fig.1 and Fig.2 show the comparison between EGS4/PRESTA which is presented in 3) and EGS4 on Gean4 with this interface for photon and electron respectively. Good agreements can be seen in these plots despite some small discrepancy. These good agreements demonstrate that our interface is well working. The discrepancy is considered to be due to the difference in describing multiple scattering, because our interface does not include PRESTA yet. For this point, technical study for including PRESTA is planned for more precise simulation. Now, we are ready to make comparisons between Geant4 and EGS4 with this interface on common users' geometries.

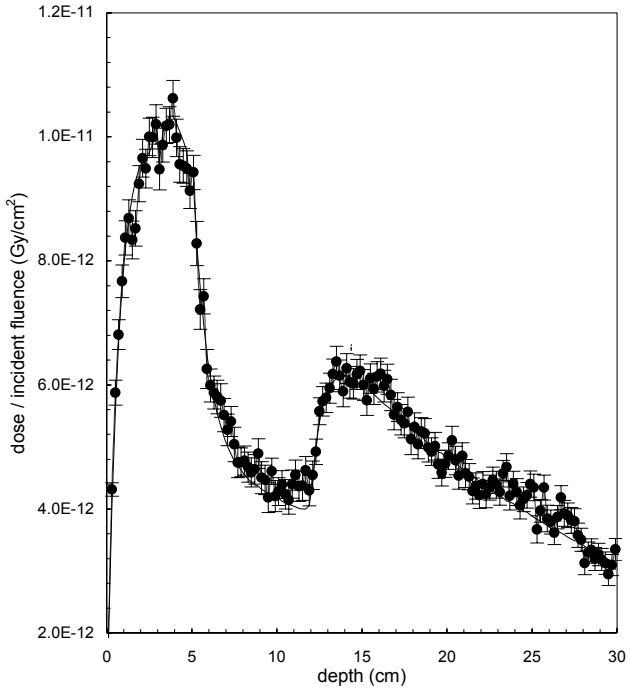

Fig. 1. Comparison of depth-dose curves for the photon case. The geometry is composed of several layers of slab phantoms. From 0 to 3cm is water, 3 to 5 cm is aluminum, 5 to 12 cm is lung material and 12 to 30 cm is water. The photon beam is a uniform 18MV beam from a realistic clinical accelerator as calculated at NRC using BEAM code. The line shows the calculation by EGS4/PRESTA which is presented in 3). The dots with error bars represent the result obtained by EGS4 on Geant4 with this interface.

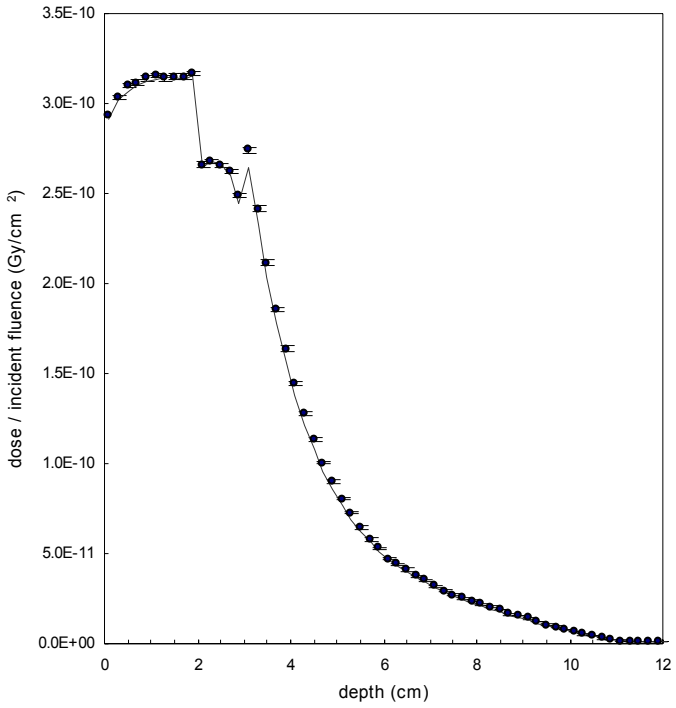

Fig. 2. Comparison of depth-dose curves for the case of 20 MeV mono-energetic electron beam. The composition of the geometry is that from 0 to 2 cm is water, 2 to 3 cm is aluminum, 3 to 6 cm is lung material and 6 to 30 cm is water. The representation of each plot is same as in Fig. 1.

5. Summary

We have successfully developed an interface between EGS4 and Geant4 based on Object-Oriented approach. This work is a proof of flexibility and expansibility of the Geant4 toolkit, and shows a good example of Virtual Monte Carlo approach. This is useful for making comparisons between EGS4 and Geant4 especially in users' application level.

Acknowledgment

This work was achieved in collaboration with K. Amako, T. Sasaki (KEK), M. Asai, T. Koi (SLAC). We wish to thank H. Hirayama and Y. Namito, who are developers of EGS4, for their kind cooperation and useful advice.

References

1) GEANT4 Collaboration, "GEANT4 - a Simulation Toolkit", Nucl. Instr. Meth. A506 250-303pp. (2003), CERN-IT-2002-03, KEK-2002-85, SLAC-PUB-9350, August 2002

2) W.R. Nelson, H. Hirayama and D.W.O. Rogers, "The EGS4 Code System", Stanford Linear Accelerator Center Report SLAC-265, 1985

3) http://www.irs.inms.nrc.ca/inms/irs/papers/iccr00/iccr00.html

LSCAT-GISMO – An Object-Oriented Framework for Particle Simulation

J. Giersch, A. Weidemann
Physikalisches Institut Abt. 4, Friedrich-Alexander-Universität Erlangen-Nürnberg, Erwin-Rommel-Str. 1, 91058 Erlangen, Germany

Abstract

LSCAT-GISMO is an easy-to-use and powerful framework for particle simulation written in C++. It supports the user in setting up his own experimental environment by providing classes for particle sources, geometries, interactions and graphical visualisations. The object-oriented approach and the open design of LSCAT-GISMO makes it flexible and easy to extend. For example classes for hadronic interactions (GHEISHA) as well as electromagnetic interactions (EGS4 and LSCAT) are available. Furthermore it is also possible to extend LSCAT-GISMO fulfilling additional physical needs. We will give a short overview of the physical background of LSCAT-GISMO, present its features and explain the concept by showing the basic class dependencies.

1 Introduction

Computer simulations are a standard tool in modern particle and medical physics. They can be used to design and optimise experiments and to verify the results with theory. The simulation software should therefore be flexible to support the user in realising his own experimental setup and it should provide adequate physics. Due to its object-oriented approach and the use of EGS4 and GHEISHA algorithms LSCAT-GISMO [1] is very well suited for this task.

2 History

LSCAT-GISMO continues a development that started at CERN in 1990, where a discussion about the benefits of an object-oriented particle simulation tool has taken place. In the following years two workshops were held, one at SLAC and one at the University of Florida. These workshops finally led to the first release of GISMO (Graphical Interface for Simulation and Monte Carlo Code with Objects) at SLAC in 1993 [2]. Until 1996 Toby Burnett from University Washington improved GISMO by including CLHEP (C-Library of High Energy Physics) [3] into GISMO and called his version HEP-GISMO [4]. In 1996 our group started two projects in medical physics and used HEP-GISMO for developing simulation tools for nuclear medicine and X-ray imaging. For the need of low energy behaviour we incorporated the LSCAT extension [5] into HEP-GISMO and released a new version of GISMO which we called LSCAT-GISMO.

3 The framework

LSCAT-GISMO is not an executable program but a class library written in C++. It is a framework which supports a programmer in realising particle simulations. For a basic application just five steps are necessary (see fig. 1):

1. Define setup (geometries, materials, fields, etc.)
2. Setup a source and its proporties

3. Choose the interaction algorithm
4. Implement scoring methods for detector objects
5. Start event generation

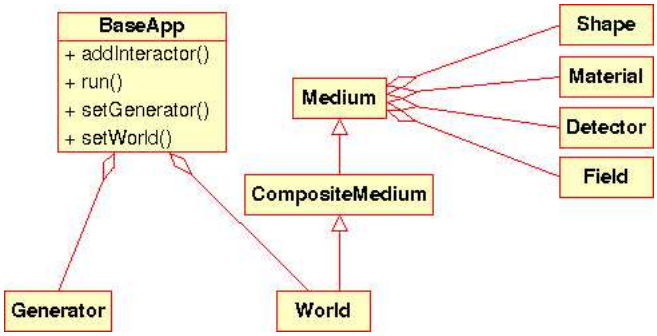

Figure 1: Basic class diagram for applications

LSCAT-GISMO provides a lot of standard geometrical objects like boxes, tubes, cones, etc. By combining these objects also complex geometries can be realised to imitate the real-life experiment. For special shapes the object-oriented concepts of inheritance and derived classes can be used to add additional geometries to LSCAT-GISMO.

The source defines the initial particle of each event. LSCAT-GISMO includes a database of particles with their physical properties. Depending on the source type choosen the position and momentum vector of the individual initial particles can vary. So it is very easy to realise for example an isotropic source or a pencil beam source.

The users hook during the propagation of a particle is the detector property that can be applied to a medium. If an interaction takes place in a medium the associated score method of the detector is called whereas the particle proporties like energy or position are passed. The user must adapt the score method to extract his 'measurement' results. For example the energy deposition in a medium can be calculated and compared to experimental data.

A simple example that demonstrates the usage of LSCAT-GISMO is shown in fig. 2: A gamma ray pencil beam of energy 40 keV hits a germanium detector. The interaction position in z-direction is printed out.

4 Physics

The essential part of a particle simulation are the interaction algorithms. They define the physics covered by the simulation. In LSCAT-GISMO all implementations of interaction algorithms have to be done in classes which are derived from the base class `Interactor`. That means different interactors fulfilling different physical needs can be realised in separate interactor classes. They can be implemented, tested and used independently from each other. In LSCAT-GISMO already three interaction classes exist: `EGSInteractor`, `LSCATInteractor` and `GHEISHAInteractor`.

4.1 EGSInterator

The `EGSInteractor` is a C++ implementation of the standard EGS4 algorithms and describes the interaction of photons, electrons and positrons in matter [6]. It is valid for photon energies between 1 keV and thousands of GeV and includes photo effect, Compton scattering, Rayleigh scattering, pair production and bremsstrahlung. For charged particle the algorithms are valid for

```
#include "gismo/BaseApp.h"
#include "gismo/Box.h"
#include "lscat/LSCATInteractor.h"

class myDetector : public Detector
{
  public :
    myDetector() {}
    void score(MCParticle* currentParticle);
};

void myDetector::score(MCParticle* currentParticle)
{
  // Print out z position for gammas
  if(currentParticle->charge() == 0)
    std::cout << currentParticle->position().z() << std::endl;
}

int main()
{
  BaseApp  myBaseApp;
  World*   myWorld = new World();

  // Use LSCATInteractor
  myBaseApp.addInteractor(new LSCATInteractor("electromagnetic"));

  // Create gamma ray pencil beam of 40 keV at point (0,0,-10) in z-direction
  myBaseApp.setGenerator(new Generator("gamma", Vector(0,0,0.000040), Point(0,0,-10)));

  // Create world consisting of a germanium box detector at origin with detector property
  Medium* myMedium = new Medium((Medium*) 0, new Box(0.5,0.5,0.5), "Ge", new myDetector());
  myWorld->addMedium(myMedium);
  myWorld->setKECutOff(0.0000001);

  // Set world
  myBaseApp.setWorld(myWorld);

  // Trigger one event
  myBaseApp.run(1);
}
```

Figure 2: Example of a `BaseApp` application

kinetic energies between a few tens of keV and a few thousand GeV. It includes Møller interaction for electrons, Bhaba interaction and annihilation for positrons and Coulomb scattering as well as continuous energy loss for both.

4.2 LSCATInterator

The physical model for keV photon transport of EGS4 has been expanded with LSCAT (low-energy photon scattering expansion for the EGS4 code) by Namito and Hirayama [5]. `LSCATInteractor` is a C++ adaption of this package. Using this interactor LSCAT-GISMO takes into account bound Compton scattering, Doppler broadening, linearly polarised photon scattering, fluorescence photons, Auger electrons and electron impact ionisation. Furthermore the improved Bremsstrahlung sampling algorithm of Bielajew [7] has been incorporated.

4.3 GHEISHAInteractor

For the simulation of hadronic interactions `GHEISHAInteractor` is included in LSCAT-GISMO. It is a C++ wrapper for the GHEISHA code which is written in Fortran. Gheisha has been developed by Fesefeldt and is part of GEANT3 [8]. It takes into account elastic scattering, inelastic scattering, nuclear fission with inelastic scattering and neutron capture.

5 Graphical User Interface

Since the implementation of a setup has to be programmed, a graphical visualisation of the result may be useful for verifying and debugging. LSCAT-GISMO offers different output formats, e. g. in a window or in Postscript format. The viewpoint of the scene can be choosen arbitrarily to get a

reasonable 3D representation of the setup. If a particle has been propagated the trajectory of the particle and its daughters can be drawn as well.

In addition to the graphical output LSCAT-GISMO also supports the user in realising applications with a graphical user interface (GUI). Therefore the framework supplies methods e. g. to handle text and graphic windows or to implement menu driven applications. Two examples are shown in fig. 3. On the left hand side a muon has been propagated in liquid argon. The trajectories and the detector response is also drawn. On the right hand side a test setup of a Compton camera for medical imaging is shown where a gamma particle is being Compton scattered in a germanium detector and absorbed in a CdZnTe detector. The menu entry for controlling the detail level of the output is selected. The GUI framework of LSCAT-GISMO can be used on Microsoft Windows and Unix systems.

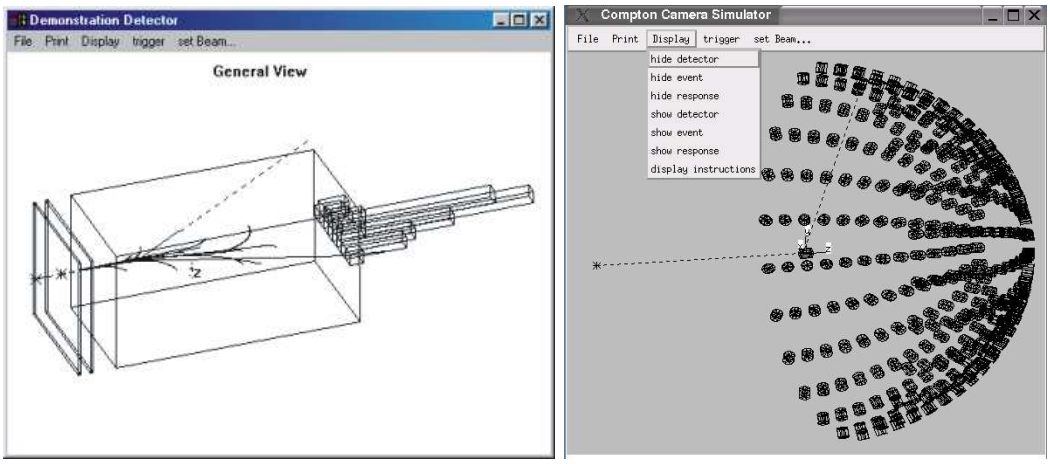

Figure 3: Graphical user interface for Microsoft Windows (left) and Linux (right) systems

6 Applications

LSCAT-GISMO and its predecessors have been successfully used in different applications and demonstrated their versatility. For the Gamma Ray Large Area Space Telescope project (GLAST) for example the interactions of high-energy gamma rays (20 MeV to 300 GeV) with the GLAST detector were simulated to optimise the detector design.

The EDDA experiment investigates the excitation function for elastic proton-proton scattering. For the analysis HEP-GISMO was used and expanded by the MICRES package which leads to a more accurate simulation of hadronic interactions in the mid-energy range. In order to include the MICRES code in HEP-GISMO the concept of derived classes has been used for the interactor and the source.

The Roentgen Simulation ROSI is based on LSCAT-GISMO and is dedicated to X-ray imaging and X-ray tube calculations [9]. It extends LSCAT-GISMO by complex particle sources which are needed to describe the energy spectrum or angular distribution of X-ray tubes. ROSI is capable of parallel computing to accelerate the calculation speed by using the Local Area Multicomputer platform LAM [10]. An information socket enables the user to monitor the simulation progress via internet. The configuration is done by a C++ file. So from the users point of view ROSI can be considerd like a black box where only a few parameters have to be defined to investigate physical problems of X-ray imaging (see Fig. 4).

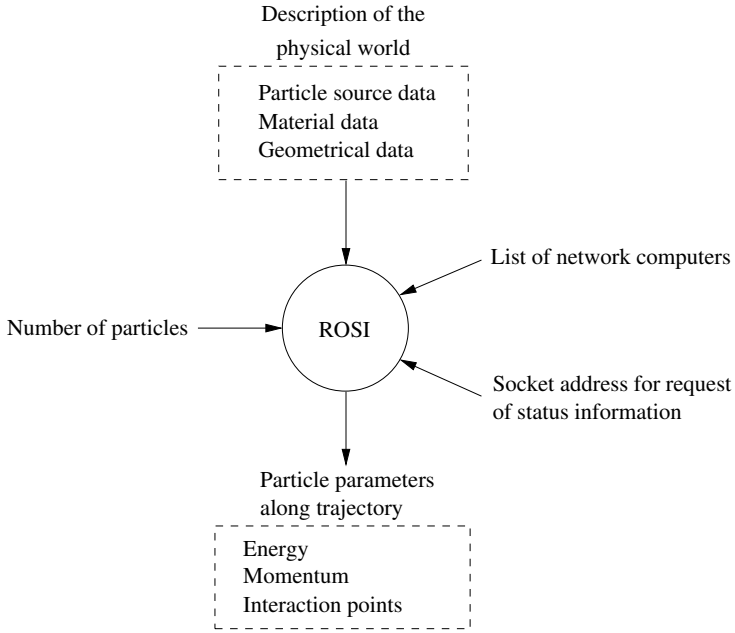

Figure 4: Black box of ROSI

7 Conclusion

LSCAT-GISMO is a framework for particle simulations that has been successfully used in different applications. It supports the user in implementing his setup, propagating particles, visualising the simulated environment and realising applications with a graphical user interface. The interactors included are based on established algorithms of the EGS4, LSCAT and GHEISHA packages. LSCAT-GISMO is written in C++. Due to the object orientated approach it can easily be extended and has an open design for further improvements.

References

[1] www.pi4.physik.uni-erlangen.de/Giersch/LSCAT-GISMO/

[2] W. Atwood, A. Breakstone, D. Britton, T. Burnett, D. Myers, G. Word, *The GISMO Project (C++)*, C++ Report, 5(3):38-43, 1993.

[3] L. Lönnblad. *CLHEP – a Project for Designing a C++ Class Library for High Energy Physics*, Computer Physics Communications, 84:307, 1994.

[4] T. Burnett, C. Chaput, H. Arrighi, J. Norris, D. J. Suson, *Simulating the GLAST Satellite with GISMO*, IEEE Computing in Science & Engineering, July/August 2000, pp. 9-18.

[5] Y. Namito, H. Hirayama. *LSCAT: Low-Energy Photon-Scattering Expansion for the EGS4 Code (Inclusion of Electron Impact Ionization)*, Technical report, Hich Energy Accelerator Research Organization, 1-1 Oho, Tsukuba-shi, Ibaraki-ken, 305-0801, Japan, May 2000.

[6] W. R. Nelson, H. Hirayama, and D. W. O. Rogers, *The EGS4 Code System*, Technical report, Standford Linear Accelerator Center SLAC-265, 1985.

[7] A. F. Bielajew, R. Mohan, C. S. Chui, Ionizing Radiation Standards, Institute for National Measurement Standards, Natinal Research Council of Canada, Ottawa, Canada, K1A 0R6, November 1989, PIRS0203

[8] H. C. Fesefeldt,*GHEISHA program*, Technical Report PITHA 85-02, III, Physikalisches Institut, RWTH Aachen Physikzentrum, 5100 Aachen, Germany, September 1985.

[9] J. Giersch, A. Weidemann, G. Anton, *ROSI - an object-oriented and parallel-computing Monte Carlo simulation for X-ray imaging*, Nuclear Instruments and Methods in Physics Research A 509 (2003), 240-250

[10] G. D. Burns, R. B. Daoud, J. R. Vaigl, *LAM: An Open Cluster Environment for MPI*, Supercomputing Symposium 1994, 1994.

ROSI - A MONTE CARLO SIMULATION FOR X-RAY TUBES

F. Sukowski
Physikalisches Institut IV, Erwin-Rommel-Str. 1, Universität Erlangen-Nürnberg, Germany

Abstract

When developing X-ray tubes, the energy spectrum and the intensity of the X-ray radiation is most important. To calculate X-ray spectra, there are programs which are based on experimental data. These programs are only able to calculate spectra from anode materials which are explicitly provided. Using the object-oriented framework LSCAT-GISMO we have developed ROSI [1], a Monte Carlo simulation which is capable of simulating arbitrary anode materials and even arbitrary tube geometries. ROSI uses the well esablished EGS4 [2]-algorithms with the LSCAT-extension. Comparison with experimental data has been done.

1 Introduction

In the field of X-ray tube development, the main goal is to maximize the dose output of the X-ray radiation while minimizing the heat in the anode due to energy deposition of the electrons. It is also very important to predict the energy spectrum and the angular distribution of the X-rays. With ROSI [1] we provide an X-ray tube simulation tool, which is capable of simulating all these aspects while using arbitrary X-ray filters, anode materials or tube geometries. Therefore no expensive experimental setup is required when studying new tube designs. Furthermore, also X-ray photons can be tracked to simulate X-ray imaging as well.

2 Simulation Setup

Figure 1 shows the simulation setup that was used for the X-ray tube study. First an electron source that emits electrons with kinetic energy E_0 in a certain direction is defined. The origin and direction of the electrons can be randomly varied, so a realistic electron beam can be modeled. The primary electrons hit the anode in the so called "hot spot". The anode is defined as a box inclined by the anode angle θ towards the incident electron direction. All energy losses by electrons in its volume have been recorded. ROSI is capable of simulating the emission of bremsstrahlung and characteristic radiation from the anode which can be detected by an X-ray detector (red circle in Fig. 1) that was defined as a hemisphere around the anode. Furthermore, an additional filtration (green circle in Fig. 1) was applied to model realistic X-ray tubes.

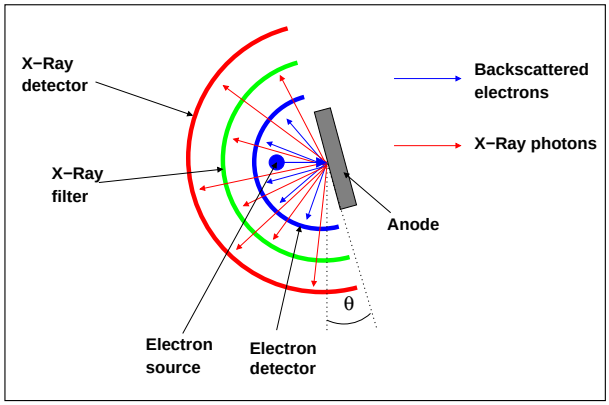

Figure 1: Simulation setup. The primary electrons hit the anode in the "hot spot". From there X-rays and backscattered electrons are emitted and can be detected by the X-ray detector (red) and electron detector (blue). The X-rays are filtered by various materials (green).

In addition to the X-ray radiation, ROSI is capable of simulating backscattered electrons from the anode as well. In order to study the energy and angular distribution of them, an electron

detector (blue circle in Fig. 1) was defined. This electron detectector stops all electrons when they enter its volume and lets all photons pass.

3 X-Ray Generation Process

When electrons propagate into a solid, they are scattered in the Coulomb field of the atoms. While most of the electrons lose kinetic energy to the atoms and heat up the solid, there is a possibility that a bremsstrahlung photon is emitted during this process, since the electrons are accelerated in the coulomb field.

The second mechanism of X-rays production is the collision between either electrons or photons and K- or L-shell electrons of the anode, but this process is only possible, if the kinetic energy of the incident electron is greater than the binding energy of the target electorn of the solid. Electrons from the next shell fill the hole of the inner shell under emission of a photon with energy equal to the binding energy difference between inner and outer shell. These photons have certain energies that are characteristic for the anode material. [3]

3.1 Energy Spectra

For medical applications the X-ray energy spectrum is very important. Therefore it is crucial to verify the correct physical behaviour of the simulation. Figure 2 shows the comparison between measured [4] and simulated energy spectra from a standard diagnostic X-ray tube with a tungsten anode and a total filtration of 2.5 mm Aluminium. The kinetic energy of the primary electrons varies between 60 keV and 150 keV. The plots show energy spectra without detector effects. In the 60 keV spectra there is no characteristic radiation, because the binding energy of K-shell electrons in tungsten is $E_K \approx 70\,\mathrm{keV}$. When going to higher primary energies, the tungsten atoms can be ionized and electrons from the L-shell fill the holes in the K-shell and photons with energy $E_\alpha = 59\,\mathrm{keV}$ are emitted. This effect can be seen in experimental data as well as in the ROSI results (see Fig. 2).

Another type of commonly used X-ray tubes are mammography tubes with molybdenum anodes that have characteristic lines at $E_{\alpha_1} = 17\,\mathrm{keV}$ and $E_{\beta_1} = 19\,\mathrm{keV}$. To cut off photons with higher energies, the radiation is filtered by materials that have ionizing energies slightly above 20 keV, so photons with higher energies are absorbed due to photoelectric effect. Futhermore, the characteristic line is very intense compared to the bremsstrahlung spectrum, which is important in this medical modality.

Figure 3 shows the comparison between experiment [4] and simulation of mammography tube spectra with several filters in addition to the 1 mm beryllium exitation window. The spectra agree very well.

3.2 Detector Effects

In experimental measuring setups, the efficiency of the detector is limited and dependent on photon energy. When photons with energy above the K-shell ionizing energy of the detector material enter the detector volume, there is an additional possibility of photoelectric effect producing fluorescence photons. Fluorescence photons are produced in an arbitrary direction and can leave the detector volume. This mechanism causes the decrease of the effective photon counting rate above K-shell ionizing energies.

In our experiment, the X-ray radiation was measured with a CdTe detector with K-shell ionizing energies of 27 keV (Cd) and 32 keV (Te) and a diagnostic tube (tungsten anode). Figure 4 shows measured and simulated raw spectra (detector effects are now taken into account). The experiment

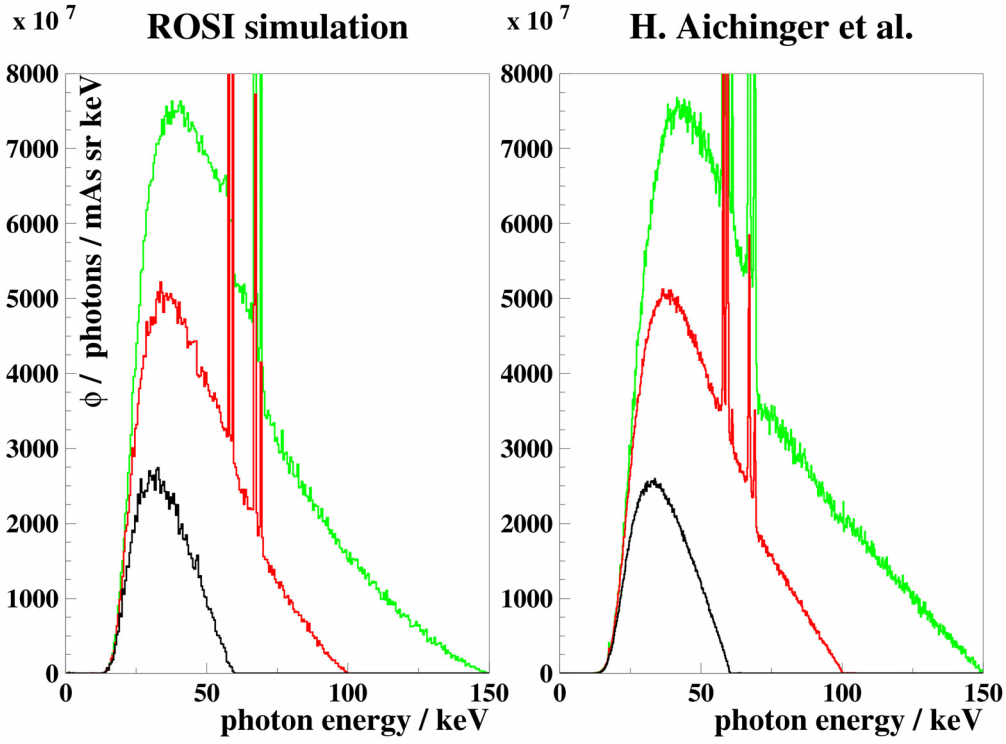

Figure 2: X-ray energy spectra from a diagnostic tube with a tungsten anode and different tube voltages (black: 60 kV, red: 100 kV, green: 150 kV). Left: spectra simulated with ROSI, Right: experimental spectra [4]. These spectra are without detector effects.

was done with the following tube voltages: 40 kV, 60 kV and 80 kV. In both plots the reduced detector efficiency above K-shell ionizing energies can be seen.

3.3 Heel-Effect

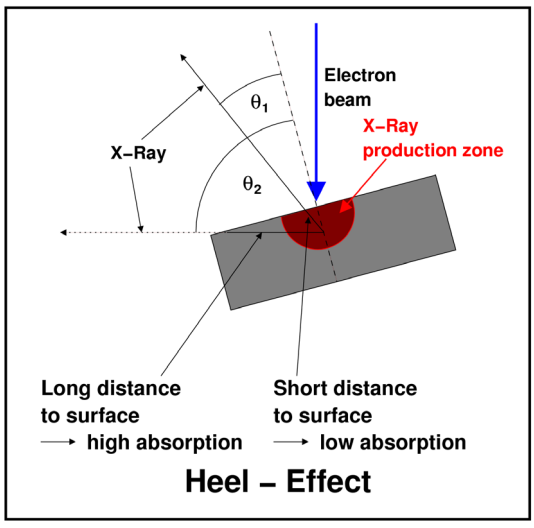

Figure 5: Diagram how the Heel-Effect works. Photons are produces in the red shaded volume. The absorption of the photons in the anode is dependent on the distance from the production point to the surface and therefore on the production angle.

When the incident electrons hit the anode, they are immediately scattered in the Coulomb field of the atoms and propagate in an arbitrary direction already after a few interactions, thus bremsstrahlung is produced nearly isotropically. The photons are produced in a volume slightly below the surface. Photons with direction perpendicular to the surface have a short distance to leave the anode volume with only small absorption while photons with a direction nearly parallel to the surface have a long distance to leave the anode and undergo great absorption as it is shown in Figure 5.

Therefore the radiation intensity is exspected to decrease at flat angles, which is called the Heel-Effect [3]. Figure 6 shows the angle dependency of the simulated X-ray radiation intensity. The simulation was made with a tungsten anode with anode angles of $\theta = 10°$. The origin of the angle in the plot is set to the perpendicular to the electron beam, consequently $\theta = -10°$ means the direction parallel to the surface. Below that angle, there is no intensity, because of the shadow from

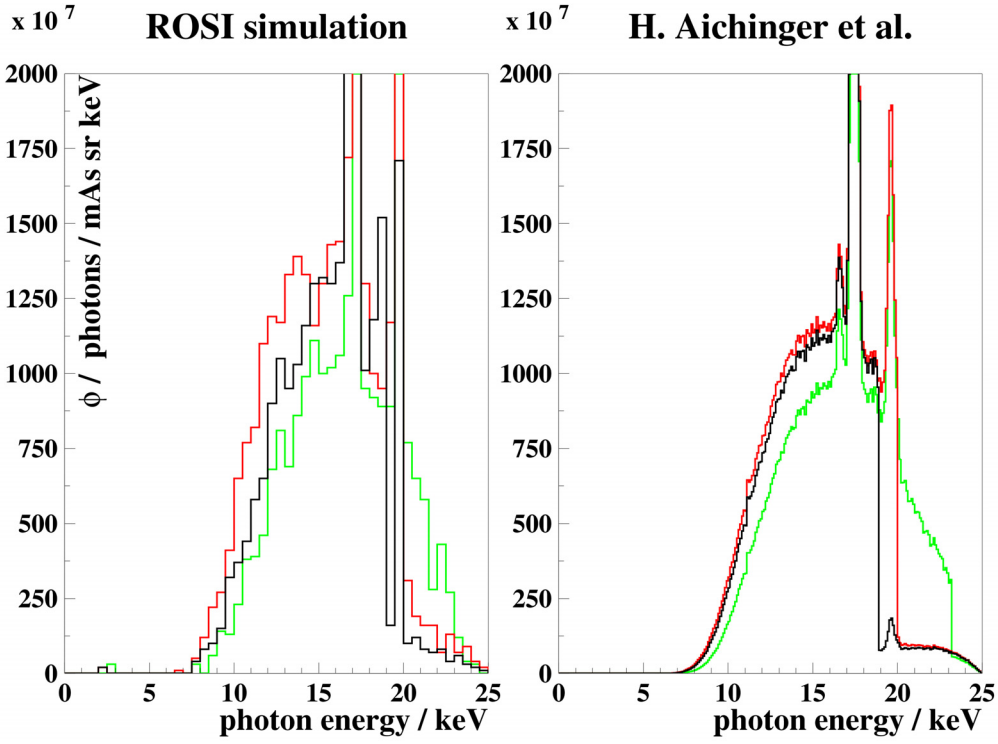

Figure 3: X-ray energy spectra from a mammography tube with a molybdenum anode and different addinional filtration (black: 40 μm Nb, red: 30 μm Mo, green: 25 μm Rh), tube voltage: 25 kV. Left: spectra simulated with ROSI, Right: experimental spectra [4]. The spectra are without detector effects.

the anode. At higher angles, the intensity increases slowly until it becomes nearly constant, where the distance from the photon production point to the anode surface is very weakly dependent on the angle. As the simulation results show this effect can be reproduced with ROSI very well.

4 Energy Deposition in the Anode

Apart from the X-ray radiation, the energy loss of the elctrons in the anode is also a very important aspect when developing X-ray tubes. Since the loss of electron energy to the anode results in heating-up of the anode, especially in the "hot spot", where the electrons hit the anode. The temperature must not exceed the melting point of the anode material, that means the tube current and thus the possible X-ray radiation dose output is limited by the electron energy deposition.

The simulations were made with a tungsten anode at an anode angle of $\theta = 59°$ as it is shown in figure 7.

Figure 8 shows the spacial energy deposition in the anode. The deposited energy was integrated over all anode depths.

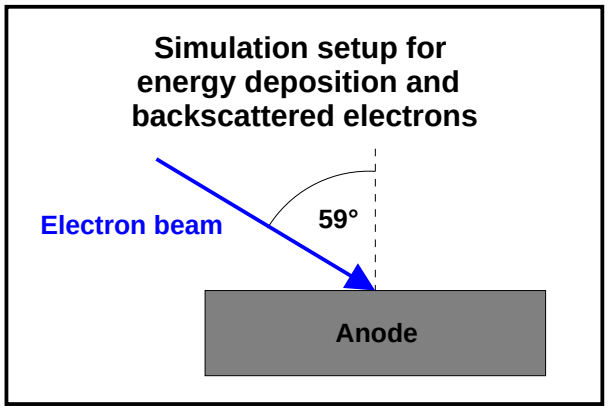

Figure 7: Setup for further simulations. Tungsten was chosen as anode materials, the anode angle was $\theta = 59°$.

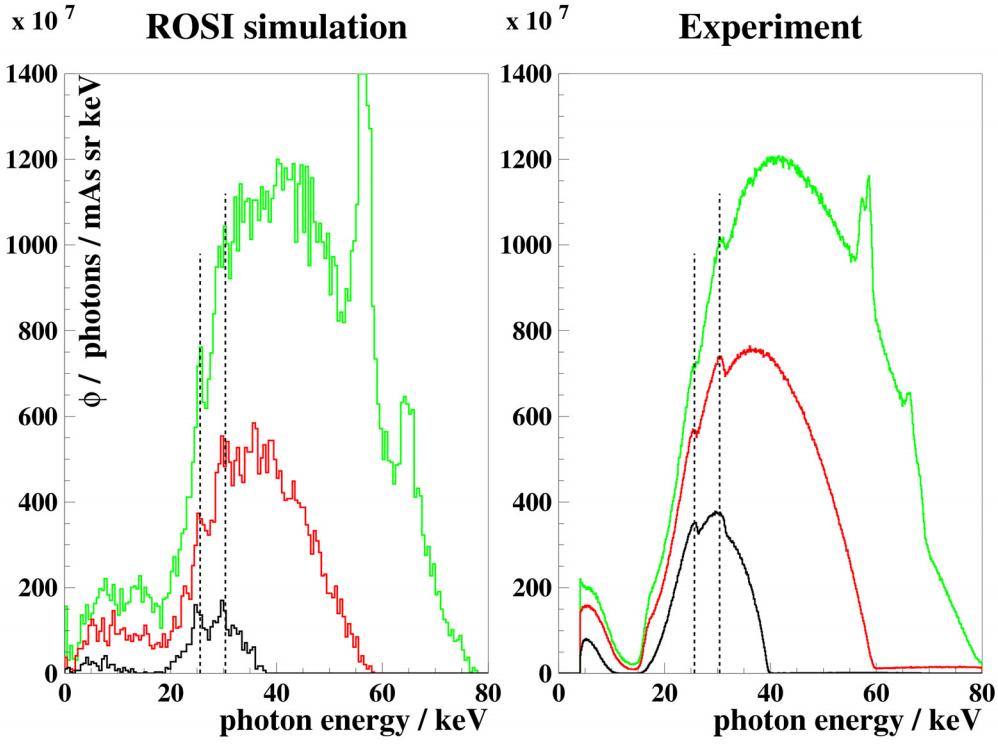

Figure 4: X-ray energy raw spectra from a diagnostic tube with a tungsten anode and different tube voltages (black: 40 kV, red: 60 kV, green: 80 kV). Left: spectra simulated with ROSI, Right: experimental spectra.

The incident electron beam hit the anode from below at the coordinates (0,0). Almost all energy is deposited in a circle about 10 μm in diameter. The energy deposit is shifted slightly in the primary beam direction. The depth of the energy distribution is shown in figure 9. Energy depoisition from electrons occurs only in the first 15 μm from the surface. From that point the gradient of the distribution is getting smaller, since the energy that is deposited comes from photons which can propagate deeper into the anode.

With these data it is possible to calculate heat transportation through the anode with a heat transportation simulation tools. Taking this into account, finally the allowed tube voltage and current can be estimated.

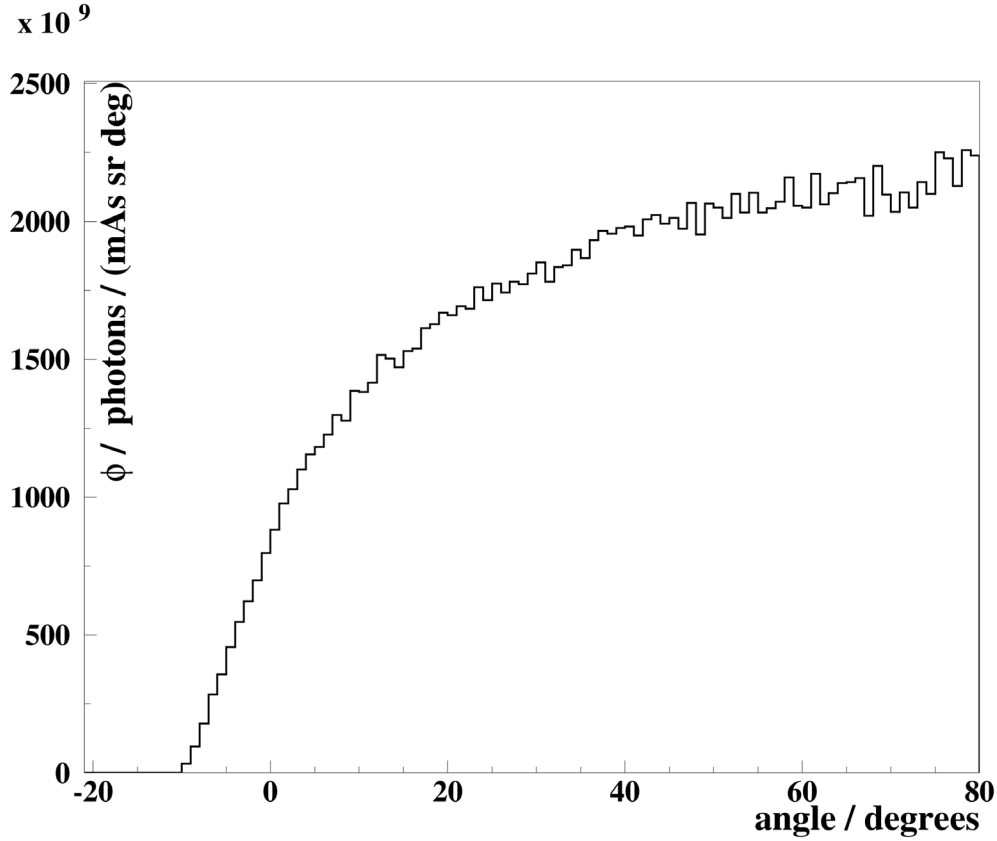

Figure 6: Angular distribution of X-ray radiation. $\theta = -10°$ is parallel to the anode surface, $\theta = 0°$ is perpendicular to the incident electron beam. The intensity increases slowly with the angle until it is nearly constanst where the absorption in the anode is almost not dependent on the angle.

5 Backscattered Electrons

Only about 1 % of the energy of the incident electron beam is used to produce X-ray radiation. $60 - 70\%$ results in heating up of the anode. The missing energy is kinetic energy of electrons that are backscattered from the surface. These are deflected onto other points of impact on the anode due to the electric field and contribute the further heat in the anode. But these electrons are not so critical, because they do not contribute to the heat in the "hot spot". For understanding all physics of X-ray tubes, they are nevertheless an important issue. In this context, we used again the simulation setup from section 4, but now we have recorded the energy and angular distributions of backscattered electrons.

Figure 10 shows the energy spectrum of backscattered electrons from the surface. The primary energy of the electron beam is $E_0 = 120\,\mathrm{keV}$. Most backscattered electrons still have much kinetic energy since they are backscattered near the surface.

A 3-dimensional plot of the angular distribution is shown in figure 11. The number of backscattered electrons were counted by a virtual hemispherical detector above the anode. θ is the polar angle and ϕ is the azimuth angle. $\theta = 0°$ means the top of the hemisphere and $\theta = 90°$ the lower border. The incident electron beam direction was set to $\theta = 59°$ and $\phi = 0°$. As the diagram shows, the backscattered electrons are slightly shifted toward the direction of the incident electron beam. Furthermore, the most electrons are backscattered to low polar angles θ due to the electron Heel-Effect.

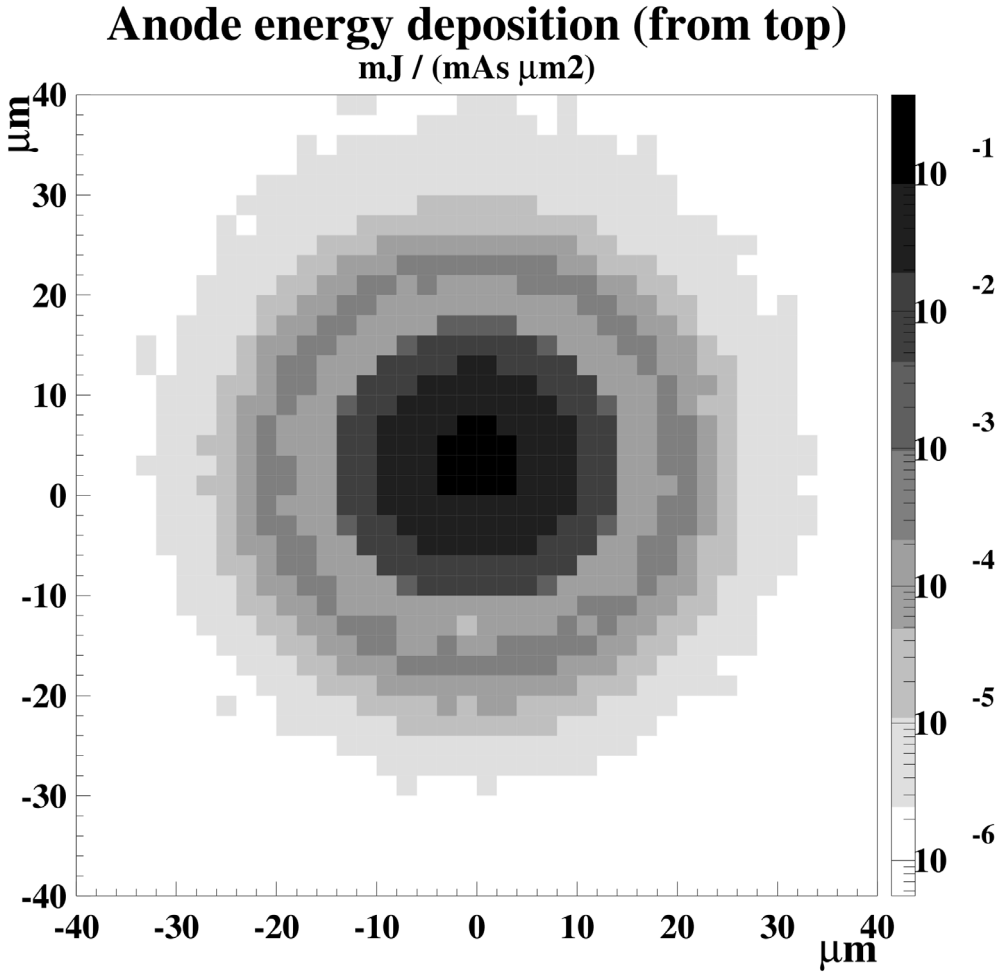

Figure 8: Energy deposition in the anode, top view

6 Conclusion and Outlook

As all results show, ROSI can model the simulated X-ray spectra, the Heel-Effect, the energy deposition in the anode, backscattered electrons and even detector effects. All this is possible using arbitrary anode materials and arbitrary filters. Thus ROSI is a very flexible and versatile simulation tool for X-ray tube design.

In the future, we will also include effects of surface roughness, which will allow the simulation of aging effects of X-ray tubes.

References

[1] J. Giersch et al. (2003), Nuclear Instruments and Methods in Physics Research A 509, 151-156 http://www.pi4.physik.uni-erlangen.de/Giersch/ROSI/

[2] W. R. Nelson, D. W. O. Rogersm, H. Hirayama (1985), *The EGS4 Code System*, Stanford Linear Accelerator Report SLAC-265 (Stanford, CA 94305)

[3] H. Morneburg (1995), Bildgebende Systeme fr die medizinische Diagnostik, SIEMENS

[4] H. Aichinger et al. (2003), Radiation Exposure and Image Quality in X-Ray Diagnostic Radiology, Springer

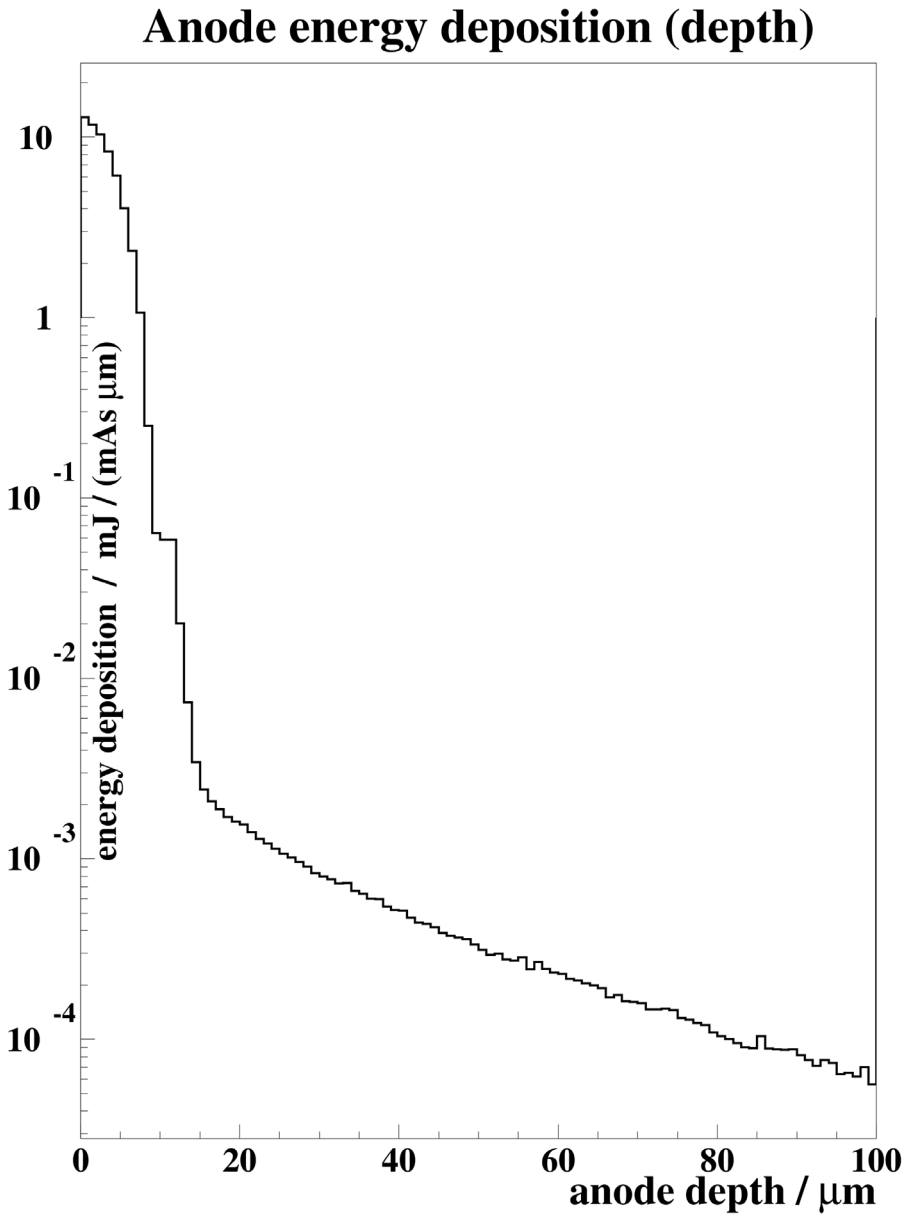

Figure 9: Depth energy deposition in the anode

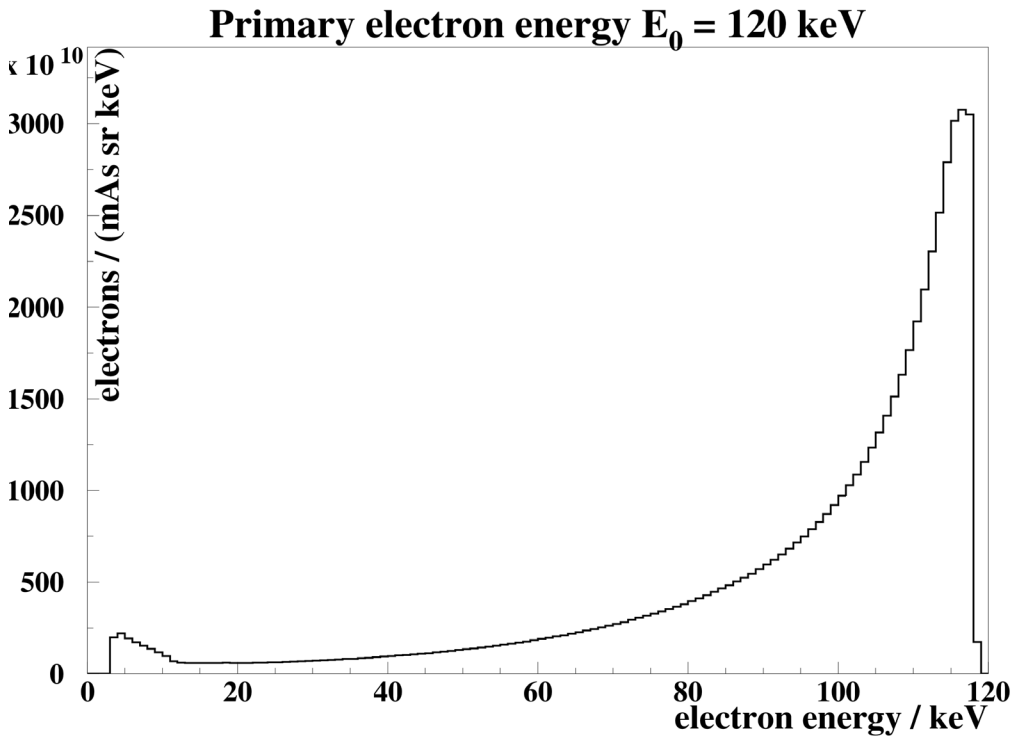

Figure 10: Energy spectrum of backscattered electrons from a tungsten anode and primary energy $E_0 = 120\,\mathrm{keV}$.

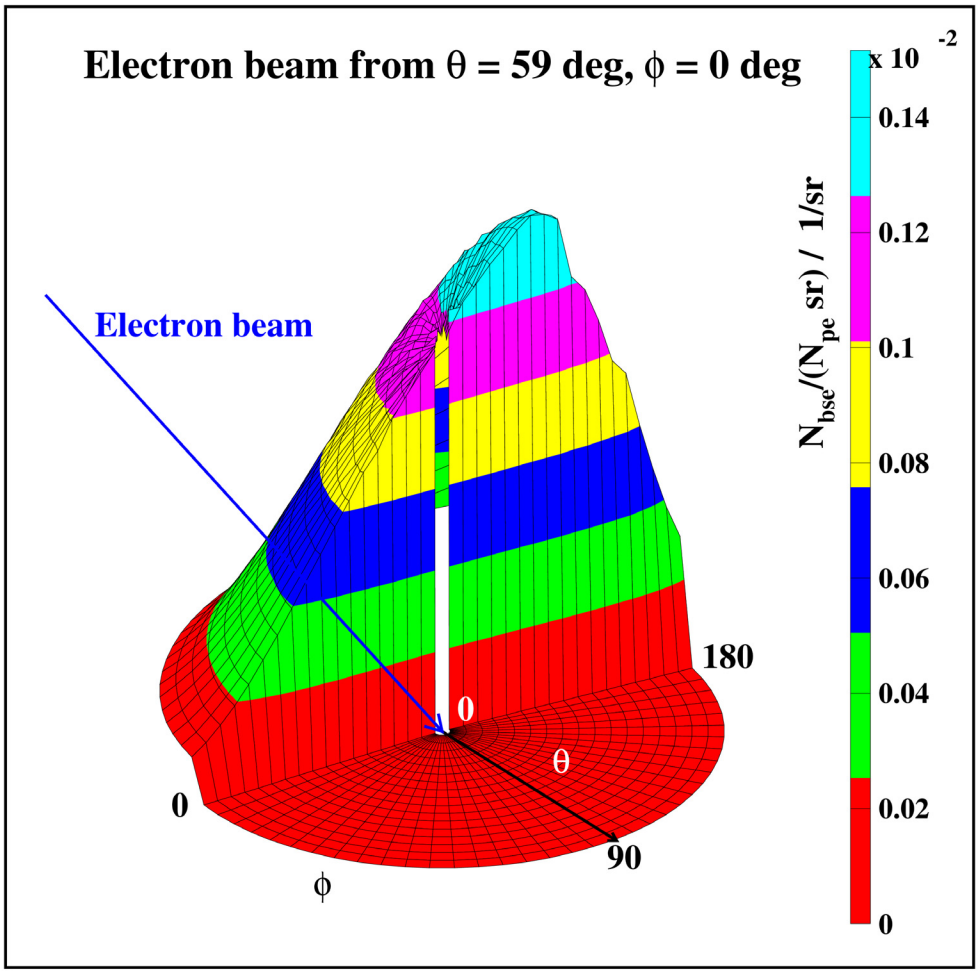

Figure 11: Angular distribution of backscattered electrons from a tungsten anode and primary energy $E_0 = 120\,\mathrm{keV}$. The incident electron beam hits the anode under $\theta = 59°$ and $\phi = 0°$.

EXAMINATION OF THE PROGRAM TO AVOID ROUND-OFF ERROR

Y.Shiota*1, K.Tabushi*2, K.Shimomura*2, S.Kitou*2, T.Kusunoki*1

[1]Department of Radiological Technology, Nagoya University of School Health Science

1 - 1 - 20 Daikou – Minami, Higashi area, Nagoya, Japan

[2]Department of Radiological Technology, Graduate School of Medicine, Nagoya University

e-mail: autumnal-equinox-day@au6.mopera.ne.jp

Abstract

The MACRO programs which express a simple shape such as PLANE, SPHERE, CYLINDER and CONE, are used to the formation of the geometry in EGS4. Each MACRO calculates the important value for the main code to recognize the configured geometry. This calculation process may generate the calculation error due to the effect of a round-off error. SPHERE, CYLINDER and CONE MACRO include the function to avoid the effect, but PLANE MACRO dose not include. The effect of the round-off error is small usually in case of PLANE MACRO, however a slant plane may cause the expansion of the effect. Therefore, we have configured the DELPLANE program with the function to avoid the effect of the round-off error. In this study, we examine the DELPLANE program using the simply geometry with slant plane. As a result, the normal PLANE MACRO generates the round-off error, however DELPLANE program dose not generates one.

1. Introduction

A user can set up the geometry with the several regions by configuring the subroutine HOWFAR in EGS4. This subroutine compares USTEP (step of the transportation) with the distance (TVAL) between the particle position and the boundary of the regions that the particle crosses, and converts USTEP into TVAL when TVAL is less than or equal USTEP. Figure 1 shows the changing transportation distance of the particle due to the subroutine HOWFAR. TVAL is important for this transportation and calculated by the MACRO programs. The MACRO expresses the simple shape such as PLANE, CYLINDER, SPHERE and CONE, and helps a user constructing the geometry.

Using PLANE MACRO, we tried to set up the geometry of the gantry head which is the

radiation aperture of an X-ray generator. In order to set up the gantry head, it needed some slant planes. However, the generation of NEGATIVE-USTEP was increased using this slant planes. NEGATIVE-USTEP indicates calculation errors which are occurred by a round-off error, and the program is stopped by detecting many appearances of NEGATIVE–USTEP.

The effect of the round-off error may occur when a particle is transported to the boundary of the regions. In other words, the new particle position may deviate from the boundary after the transportation (figure 2). Even if the geometry is simple, the round-off error may occur. However generation probability of these errors is low usually. The probability based on slant plane became higher than that based on simple plane such as horizontal or vertical plane.

Other MACROs include the function to avoid the effect of the round-off error, but PLANE MACRO dose not included. Therefore we referenced CYLINDR to configure the program to avoid the effect of the round-off error, and we called this program "DELPLANE" program. In this study, we examine the DELPLANE.

2. Materials and Method

2.1 DELPLANE program

Figure 3 shows the function of DELPLANE program. To avoid the effect of the round-off error, DELPLANE is configured from normal PLANE MACRO by the addition of allowable band, and we called the allowable band " DELBAN " . In addition, if a particle exists in the DELBAN band and crosses the boundary of the regions, TVAL is converted to DELBAN. Flow charts of the normal PLANE MACRO and DELPLANE are shown in figure 4.

2.2 The normal PLANE MACRO and DELPLANE

The geometry was the cube of water which was divided in two regions by a slant plane. The cubic size was $200 \times 200 \times 200$ cm^3 (figure 5). The radiation source was the pencil beam of 5 MeV photon. The distance between the source and the slant plane was 1mm.

1) Confirmation for the normal PLANE MACRO, ①the angles of the slant plane were every 5 degrees from 0 to 45 degrees, ②the directions of the pencil beam were every 5 degrees from 0 to 90 degrees against the slant plane, and ③the number of the history was 10^6 (figure 6).

2) Confirmation for DELPLANE, ①the angles of the slant plane were every 5 degrees from 0 to 45 degrees, ②the pencil beam direction was 0 degree against the slant plane, and ③the number of the history was 10^6.

In addition, ①the angle of the slant plane was 45 degrees, ②the direction of the pencil beam was 0 degree against the slant plane, and ③the number of the history was 10^{10}.

On these situations, the number of the appearance of NEGATIVE-USTEP was counted

without the program stop.

2.3 Comparison of the normal PLANE MACRO with DELPLANE

The slant plane with 0 degree was very simple. The radiation source was isotropic source and the number of the history was 10^7. The distances between the source and the slant plane were 0, 10 and 50 cm. The parameters for comparing the outputs were the number of event, energy deposition, and calculation time. The number of event is equal to the number of time the subroutine AUSGAB was called. The number of event and energy deposition were outputted by the method in EGS4 user code ucnai3. The relative difference between normal MACRO and DELPLANE was used to evaluation of these calculations by the following formula.

$$Ratio_{del/nor} = \frac{X_{del} - X_{nor}}{X_{nor}} \times 100[\%]$$

where X_{del} is value of DELPLANE, X_{nor} is value of normal MACRO.

3. Results and discussions

Table 1-1 shows the number of the appearance of NEGATIVE-USTEP obtained by normal PLANE MACRO, and these data were plotted in figure 7. In case of the 0 degree of the slant plane angle, the effect of the round-off error was negligible because the appearance number was small. However, the effect was large when the slant plane had angles, and the effect was largest when the beam direction was parallel to the plane.

Table 1-2 shows the number of the appearance of NEGATIVE-USTEP obtained by DELPLANE. The normal PLANE MACRO generated many appearances of NEGATIVE-USTEP, but DELPLANE did not generate. In addition, NEGATIVE-USTEP was not generated under the condition that the angle of the slant plane was 45 degrees, the direction of the pencil beam was 0 degree against the slant plane, and the number of the history was 10^{10}. Therefore DELPLANE could avoid the effect of the round-off error.

Tables 2-1 and 2-2 show the relative difference between normal MACRO and the DELPLANE. The maximum relative differences were 1.69×10^{-3} [%] in case of the number of events, and 4.95×10^{-3} [%] in case of the energy depositions. Therefore the changes of output by using the DELPLANE were very small. The calculation time ratio of normal MACRO to DELPLANE was about 1.10, because the DELPLANE was included more IF statement than the normal PLANE MACRO.

4. Conclusions

DELPLANE is available to avoid the effect of the round-off error. Furthermore, the difference between the output by normal PLANE MACRO and that by DELPLANE is very small except for NEGATIVE-USTEP. Therefore DELPLANE program is available for the complicated geometry such as a gantry head.

Acknowledgment

We would like to thank Dr. Namito for valuable suggestions.

References

1) W.R.Nelson, H.Hirayama and D.W.O.Rogers: The EGS4 code system, SLAC Report-265 (1985)

2) H. Hirayama and Y. Namito: Lecture Note of EGS4 Course at KEK (Japanese Part),KEK Internal 99-5 (1999)

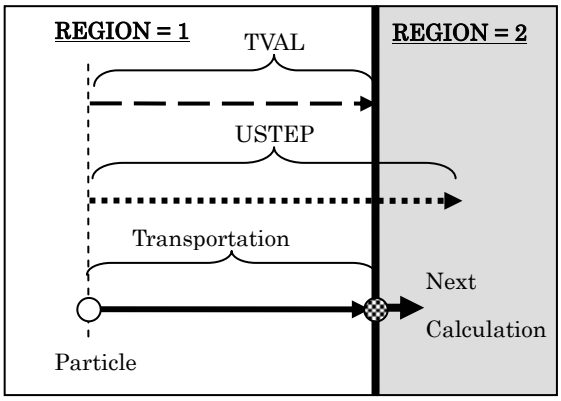

Figure 1 HOWFAR function in case TVAL≦USTEP

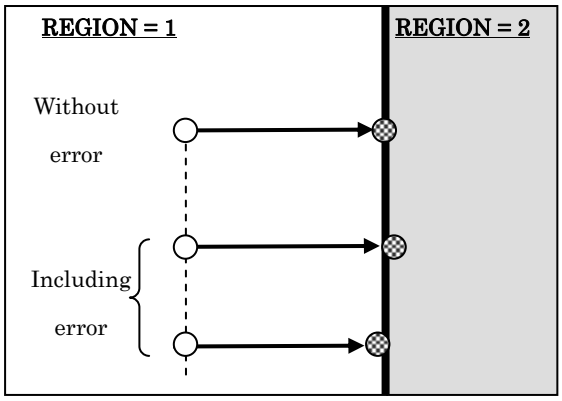

Figure 2 Effect of the round-off error

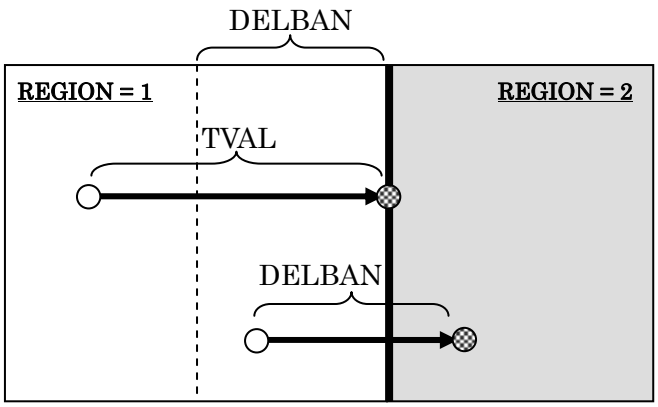

Figure 3 DELPLANE function (see text)

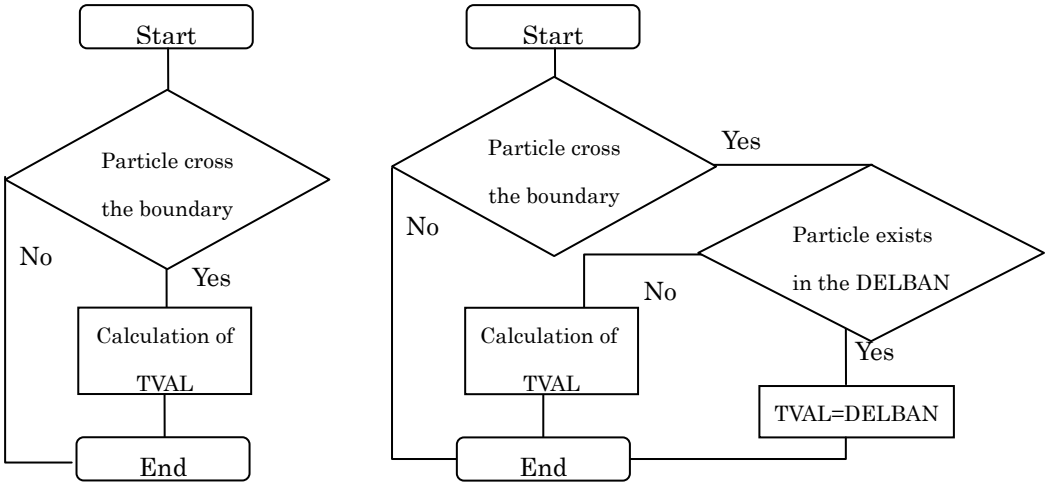

Figure 4　Flow chart

Left side: the normal PLANE MACRO, Right side: DELPLANE

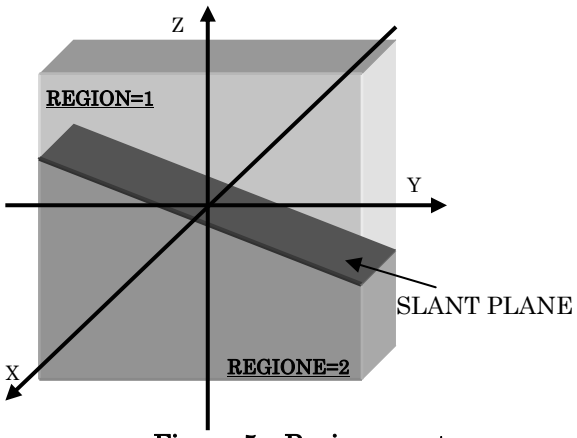

Figure 5　Basic geometry

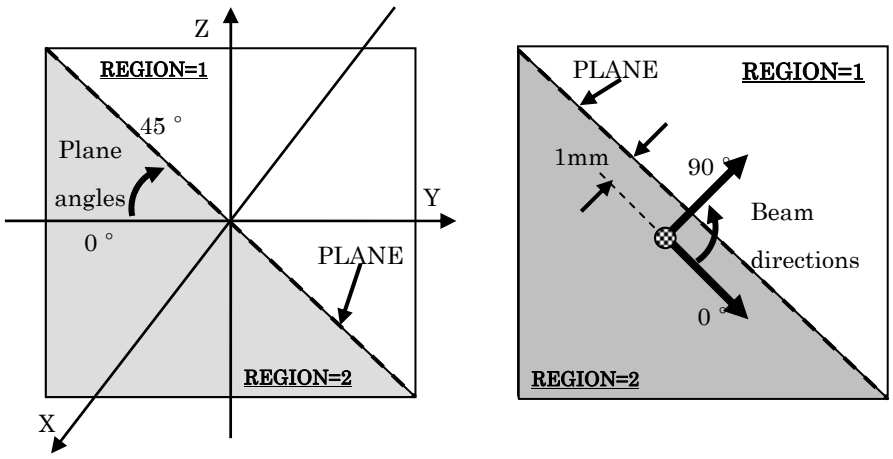

Figure 6　The slant plane angle and beam direction

Table 1-1 The number of NEGATIVE-USTEP using normal MACRO
in case of 10^6 incident particles

PARTICLE DIRECTIONS	PLANE ANGLES									
	0 °	5 °	10 °	15 °	20 °	25 °	30 °	35 °	40 °	45 °
0 °	0	63	153	216	284	326	393	490	499	450
5 °	0	2	6	5	10	12	14	11	16	16
10 °	1	2	0	0	3	5	4	5	4	3
15 °	0	0	1	3	2	3	2	3	1	3
・・・	-	-	-	-	-	-	-	-	-	-
75 °	0	0	0	0	0	0	0	0	0	0
80 °	0	0	0	0	0	0	0	0	0	0
85 °	0	0	0	0	0	0	0	0	0	0
90 °	0	0	0	0	0	0	0	0	0	0

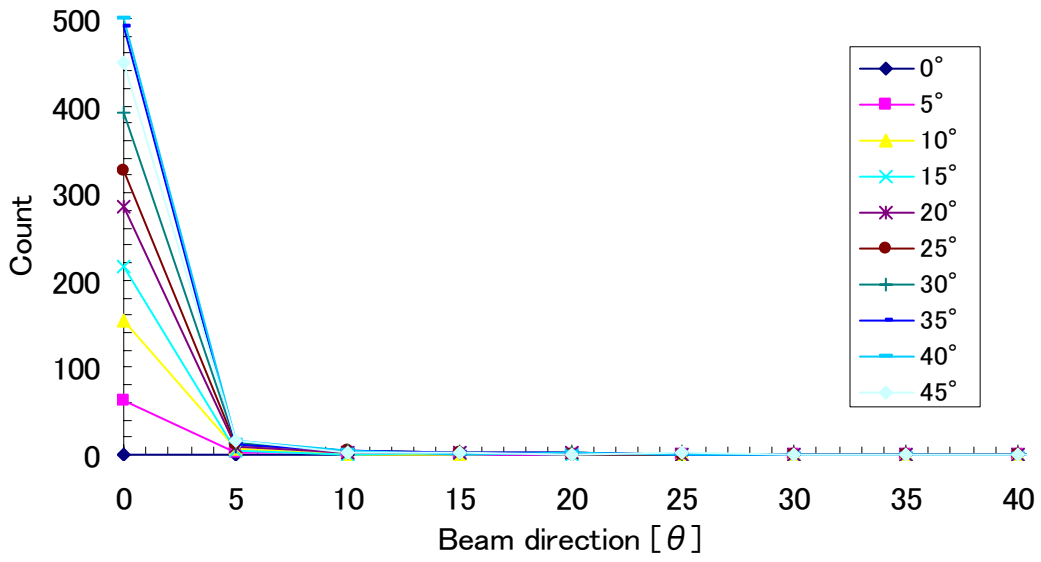

figure 7 The number of NEGATIVE-USTEP by normal MACRO

Table 1-2 The number of NEGATIVE-USTEP using DELPLANE
in case of 10^6 incident particles

PARTICLE DIRECTIONS	PLANE ANGLES									
	0 °	5 °	10 °	15 °	20 °	25 °	30 °	35 °	40 °	45 °
0 °	0	0	0	0	0	0	0	0	0	0

Table 2-1 Relative difference of the number of events*1 in case of 10^7 incident particles

particle	The distances between source and plane		
	0 [cm]	10 [cm]	50 [cm]
electron	1.41E-04 [%]	3.38E-05 [%]	1.08E-04 [%]
photon	3.86E-04 [%]	2.01E-04 [%]	3.40E-05 [%]
positron	1.69E-03 [%]	7.15E-04 [%]	2.28E-04 [%]

*1 The number of events is equal to the number of times the subroutine AUSGAB was called.

Table 2-2 Relative difference of energy deposition in case of 10^7 incident particles

particle	The distances between source and plane		
	0 [cm]	10 [cm]	50 [cm]
electron	3.74E-04 [%]	2.20E-05 [%]	1.49E-04 [%]
photon	4.95E-03 [%]	1.01E-03 [%]	1.26E-03 [%]
positron	1.48E-03 [%]	1.22E-03 [%]	3.48E-04 [%]

RESEARCH FOR DECIDING THE NUMBER AND EACH WIDTH OF BINS OF THE ENERGY SPECTRUM OF THE X-RAYS USED FOR RADIOTHERAPY

S. Kitou*[1], K. Tabushi*[1], K.Shimomura[*1], Y.Shiota[*2], T.Kusunoki[*2]

[*1] *Department of Radiological Technology, Graduate School of Medicine, Nagoya University*
1-1-20 Daikou-Minami, Higashi area, Nagoya city, Japan
e-mail: versaplan@hotmail.com
[*2] *Department of Radiological Technology, Nagoya University of School Health Science*

Abstract

Calculating photon energy spectrum outputted from a liner accelerator needs to consider some matters. Deciding the number of energy bins and the widths of bins are also involved in those.

In this work, we have compared dose distributions in aluminum by monochromatic X-rays and those by X-rays with rectangular spectrum of some widths. So, we have investigated a method to select the number of energy bins and the widths of bins.

To evaluate the level of difference between monochromatic X-rays and X-rays with rectangular spectrum, we introduced the index into each dose distribution by X-rays with rectangular spectrum of the widths. As a result, the optimal width of energy bin was 0.10 MeV in the low energy (1.0 MeV) and that was 4.00 MeV in the high energy (6.0 MeV). However the index needs more assumption to decide more optimal the number of energy bins and the widths of bins.

1. Introduction

With development of radiotherapy, the dose calculating method used for treatment planning system in external radiotherapy has been improved variously, and recently the convolution method and the super position method came to be used. The energy spectra of the X-ray outputted from a linear accelerator are used to these algorithms. Actually, it is very difficult to measure the spectra of the X-rays used in radiotherapy. So, we began to study calculation methods of the energy spectrum outputted from a linear accelerator using EGS4 Monte Carlo code.

Usually transmission data are used for calculating the energy spectrum of the X-rays outputted from a linear accelerator. But, we can also use dose distributions in material by various monochromatic X-rays for calculating the energy spectrum. Consequently, each dose distribution of monochromatic X-rays is individually calculated by EGS4, and the energy spectrum is determined by calculating backward from each dose distribution by monochromatic X-rays.

However, it is very difficult to synthesize the energy spectrum by the large number of monochromatic X-rays because of the complexity of the calculation. Thus, we divide the energy spectra into some rectangles, and we calculate backward the energy spectra from these rectangles. The number of rectangles is expressed as the number of bins.

Generally, it is easy to calculate backward the energy spectrum if the number of bins is small. However, dividing the energy spectrum into a few bins with a constant width may cause changing largely the quality of radiation beam. If the quality of radiation beam is not almost changed by modifying each width of bins, it needs not to be a constant width. Then, the number and each width of bins should be selected under the condition that the quality of radiation beam has not changed. So, in this study, we discussed how to select the number and each width of bins.

2. Materials and Method

2.1 Transmission function

Generally, transmission through a material by X-rays expresses as

$$T(x) = \int_0^{E_{\max}} e^{-\mu(E)\cdot x} \cdot F(E)dE \quad \cdots(1)$$

where, *T(x)* is the transmission function measured with the material of thickness *x*, E_{max} is the maximum photon energy of the spectrum, $\mu(E)$ is linear attenuation coefficient for the energy *E*, and *F(E)* is the fraction of the photons with the energy *E*.

The value measured can be also thought the sum of dose distributions by monochromatic X-rays, it can be expressed as

$$D(x,y,z) = \int_0^{E_{\max}} D(x,y,z,E)\cdot F(E)dE \quad \cdots(2)$$

where, *D(x,y,z)* is the absorbed dose at point *(x,y,z)*, *D(x,y,z,E)* is the absorbed dose at point *(x,y,z)* for the energy *E*. Then, equation (2) can be rewritten as

$$D(x,y,z) = \sum_{k=1}^{n} D(x,y,z,E_k)\cdot F(E_k)\cdot \Delta E_k \quad \cdots(3)$$

where, *n* is the number of bins, *k* is bin number, E_k is the energy of *k* bin, and ΔE_k is the width of *k* bin. When the large number of bins is selected, the calculation of equation (3) becomes troublesome. If the two distributions seem to be nearly equal according to comparison of the dose distributions by the monochromatic X-ray and those by X-ray with the rectangular spectrum, the two spectrums can be assumed equal to each other. Thus the number of bins can be reduced efficiently.

2.2 Assumption of Calculation

The geometry that we can calculate the absorbed dose distribution in aluminum (purity: 100%, density: 2.72g/cm^3) is shown in Figure 1. Incident particle is photon and the energy region was 1.0 to 6.0 MeV. The number of particles was 8.0×10^8 in each simulation. We chose the cut off energy of photon as 20keV, and electron as 50keV. Irradiation field was fan beam with square field (field size: 3×3cm^2 at phantom surface), and source surface distance was 100cm. Calculation voxel size was $1\times1\times1$cm^3, and the number of calculation voxels which were inside irradiation volume was $3\times3\times40$.

2.3 Calculation of absorbed dose distribution

First, the absorbed dose distribution in aluminum by a monochromatic X-ray was calculated. Then, the absorbed dose distributions in aluminum by X-rays with rectangular spectrum, mean energy was

to equal that of the monochromatic X-ray, of various widths (ΔE) were individually calculated. Thus, each absorbed dose distribution by monochromatic X-rays and those by X-rays with ΔE were obtained from 1.0 to 6.0 MeV.

2.4 Evaluation of absorbed dose distribution

The relative differences between each dose distribution by monochromatic X-rays and those by X-rays with ΔE were evaluated at each voxel. The relative difference was expressed as

$$dif_{\Delta E}(x,y,z,E)\ [\%] = \left| \frac{D_{\Delta E}(x,y,z,E) - D_{mono}(x,y,z,E)}{D_{mono}(x,y,z,E)} \right| \times 100\ [\%] \quad \cdots(4)$$

where, $dif_{\Delta E}(x,y,z,E)$ was the relative difference for the energy E at point (x,y,z), $D_{\Delta E(x,y,z,E)}$ was the absolute absorbed dose for the energy E with ΔE at point (x,y,z), $D_{mono(x,y,z,E)}$ was the absolute absorbed dose for the monochromatic energy E at point (x,y,z).

Furthermore, a quantity U_α shown in the following equation was considered as the value which showed the grade of the difference between two dose distributions.

$$U_\alpha\ [\%] = \frac{N_p}{N_{total}} \times 100\ [\%] \quad \cdots(5)$$

U_α was the rate of N_p to N_{total}. N_p was the number of voxels that $dif_{\Delta E}(x,y,z,E)$ was grater than significant value α% (for example, 1.0%, 5.0%, 10.0%, etc…), and N_{total} was the total number of voxels in the irradiation field.

3. Results

The results of each depth dose curve are shown in figures 2 to 4. In every energy region, the difference tended to be large at the deep point. In the higher energy, the difference was hardly observed even if the width of ΔE was very large. In the lower energy, the difference was observed significantly even if the width of ΔE was very small.

Figure 5 shows the relationship between $U_{1.0}$ and ΔE. $U_{1.0}$ is the rate of the number of voxels that $dif_{\Delta E}(x,y,z,E)$ is grater than 1.0%. In every energy region, $U_{1.0}$ raised when the width of ΔE exceeded a certain value. The condition of $U_{1.0}$ =5.0%, was functioning well as the index which showed the stand up part of the grow curve.

Figure 6 shows the relationship between incident photon energy and width of ΔE. Horizontal axis is energy, and vertical axis is the width of ΔE. The index value U_α can be used as a parameter to decide the width of ΔE. In this figure, the maximum widths of ΔE that U_α did not exceed about 1.0 or 5.0 or 10.0 [%] were plotted in each energy region. When large U_α is chosen, the large ΔE is selected. In case $U_{1.0}$ was smaller than or equal 5.0% in 1.0 MeV, the optimal width of ΔE was 0.10 MeV. In case $U_{1.0}$ was smaller than or equal 5.0% in 6.0 MeV, the optimal width of ΔE was 3.50 MeV.

4. Discussion

In this study, we set the lower limits of the width of ΔE to 0.10 MeV. However, in the lower energy region (for example 1.0 MeV), $U_{1.0}$ was large even if the width of ΔE was 0.10 MeV. So, the

results may denotes us the fact that the width of ΔE should be much reduced in the lower energy region. While, in the high energy region, it could be decided only if the width of ΔE was very large. In case of 6.0 MeV, it could not decide that the difference was significant even if the width of ΔE was 4.0 MeV.

These results may be improved using the additional deep point data of the material. Because, the relative difference between those dose distributions will appear at the deeper point.

The energy spectrum can be calculated correctly under the condition that the number and each width of ΔE are selected according to the result in each energy region. In further study, we will put the geometry to the condition of the measurement, and will try this way of the determination of the width of ΔE to be turned into actual utilization.

5. Conclusions

We obtained dose distributions in aluminum by monochromatic X-rays and X-rays with rectangular spectrum of some widths in the region from 1.0 to 6.0 MeV. The number and each width of bins can be decided by comparing the relative difference between dose distributions by the monochromatic X-rays and those by X-rays with rectangular spectrum of widths of ΔE.

6. References

1) Robert G. Waggener and Melissa M. Blough, "X-ray spectra estimation using attenuation measurements from 25kVp to 18MV," Med. Phys. 26(7), 1269-1278 (1999).
2) P.Francois and A. Catala, "Simulation of x-ray spectral reconstruction from transmission data by direct resolution of the numeric system AF=T," Med. Phys. 20(6), 1695-1703 (1993).
3) Radhe Mohan and Chen Chui, "Energy and angular distributions of photons from medical linear accelerators," Med. Phys. 12(5), 592-597 (1985).

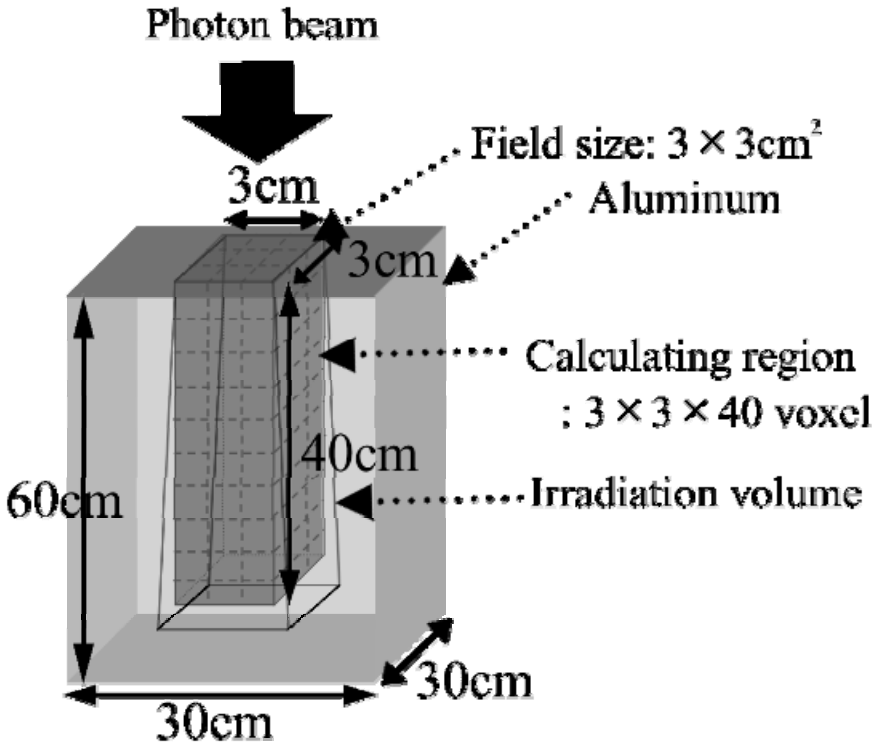

Figure 1: The geometry to calculate dose distribution in aluminum

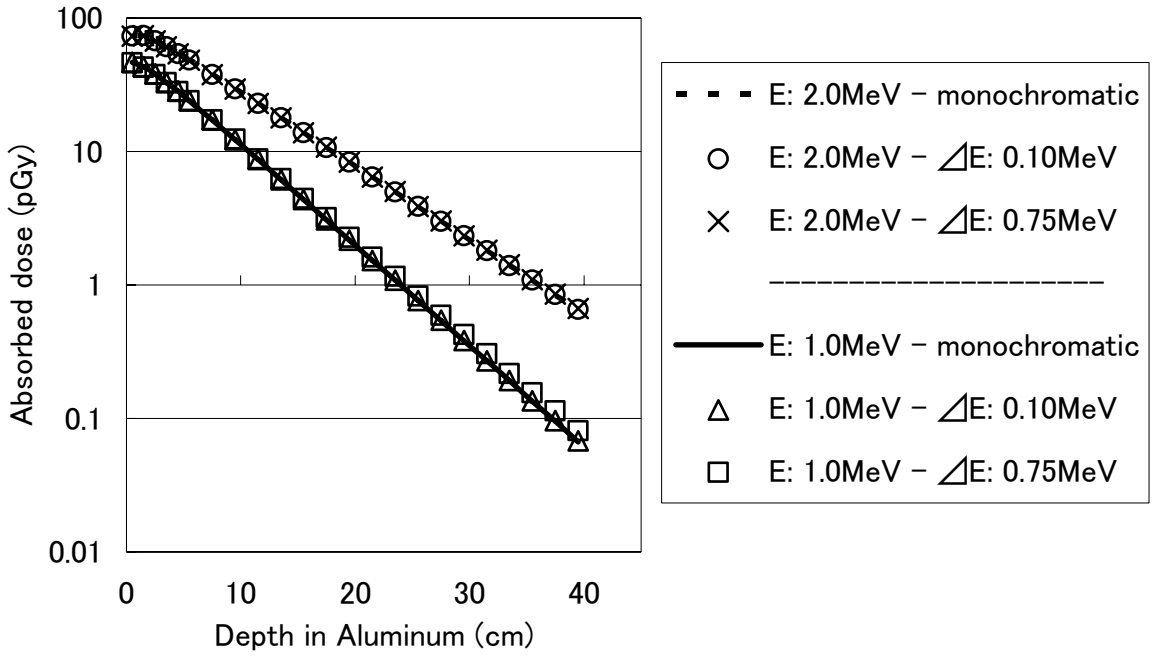

Figure 2: Depth dose curves on beam axis by 1.0 MeV and 2.0 MeV

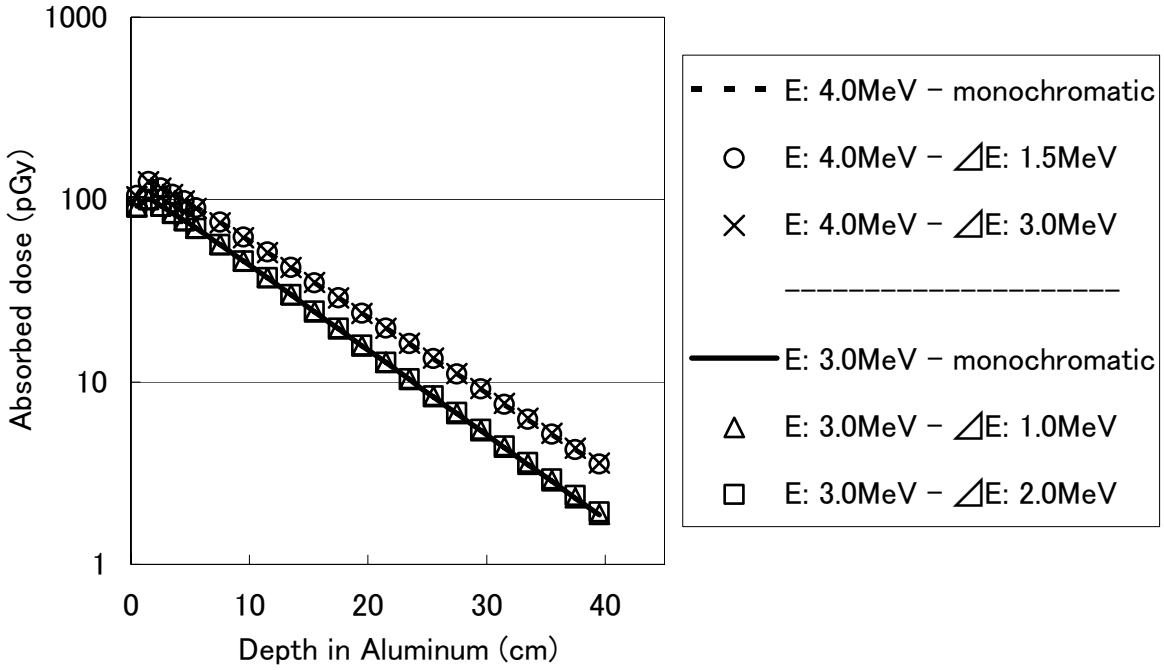

Figure 3: Depth dose curves on beam axis by 3.0 MeV and 4.0 MeV

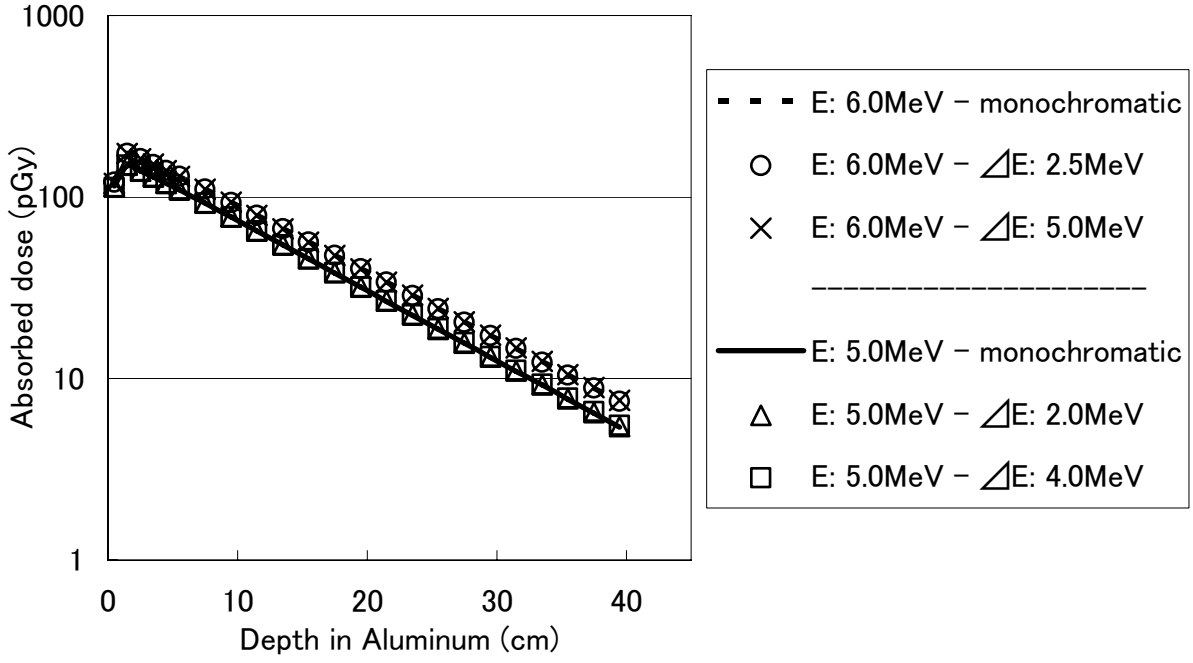

Figure 4: Depth dose curves on beam axis by 5.0 MeV and 6.0 MeV

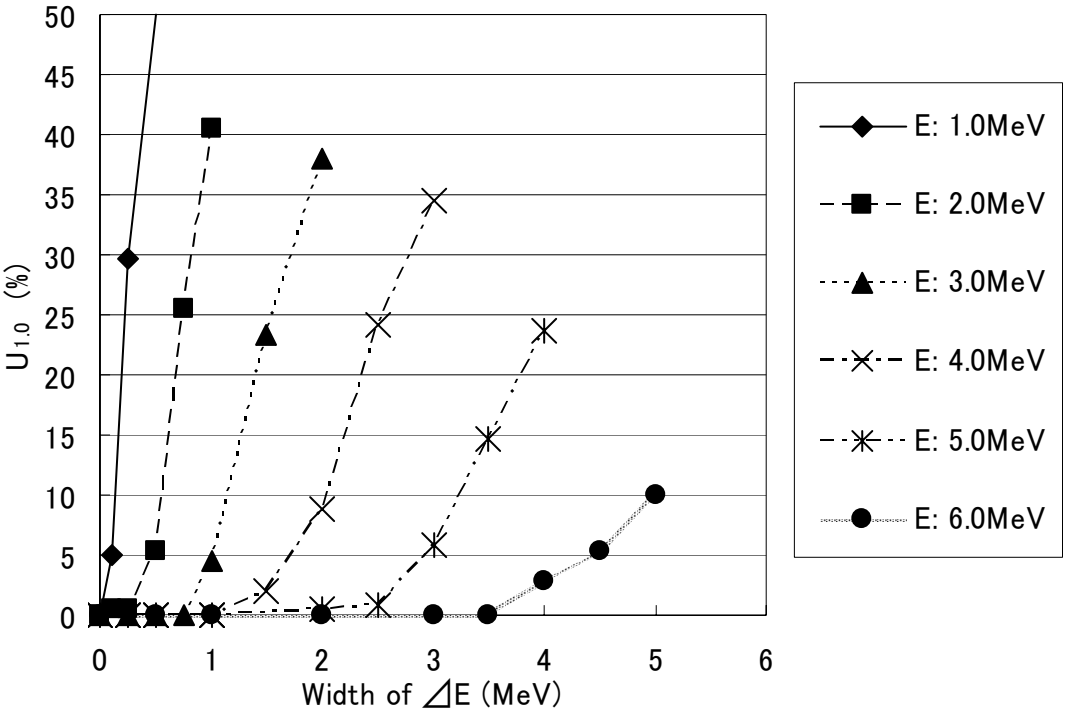

Figure 5: The relationship between width of ΔE and $U_{1.0}$

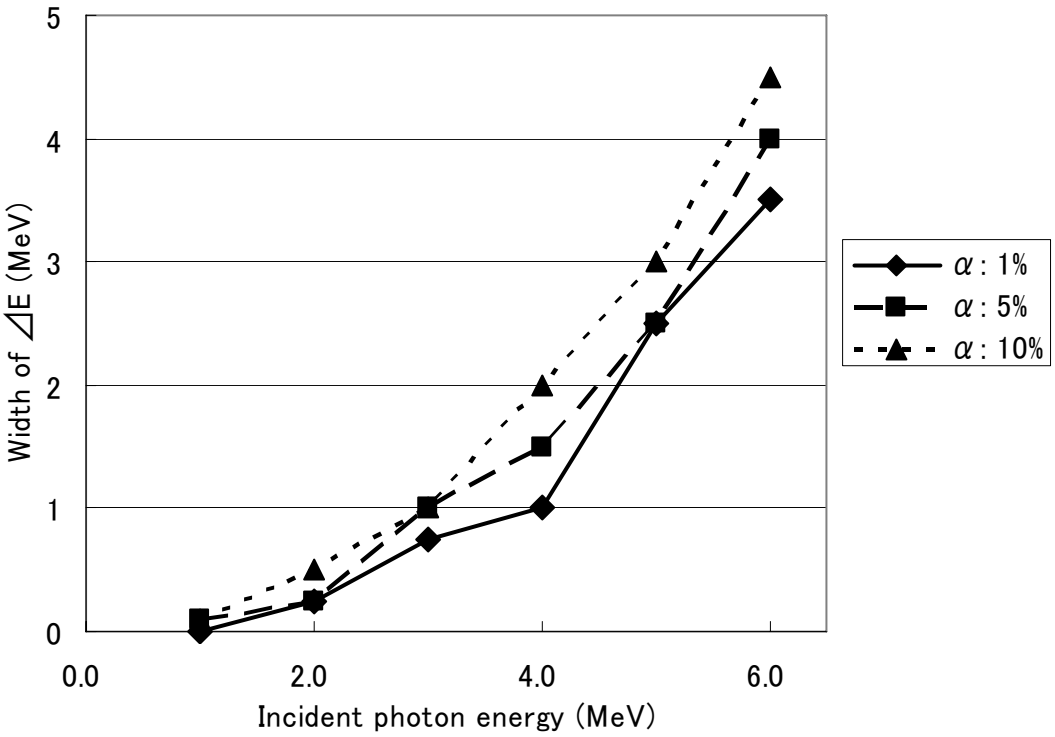

Figure 6: The relationship between incident photon energy and width of ΔE

COMPARISON OF CONVOLUTION METHOD WITH MONTE CARLO SIMULATION BY EGS4

T.Kusunoki[*1)], Y.Obata[*2)], K.Tabushi[*2)], K.Shimomura[*2)], S.Kito[*2)], Y.Shiota[*1)]

[*1)] ***Department of Radiological Technology, Nagoya University School of Health Science, 1-1-20 Daikou Minami, Higashi area, Nagoya, Japan***

[*2)] ***Department of Radiological Technology, Graduate School of Medicine, Nagoya University***

Abstract

A radiation treatment planning system is used for the calculation of three-dimensional dose distribution in a patient. Dose calculation algorithms have been improved to correct the effect of scatter and heterogeneity. Recently, Convolution and superposition methods come to be used in the routine and use terma and kernel to calculate the dose distribution. Terma and kernel are usually calculated by Monte Carlo simulation because those cannot be measured. In this study, we tried to generate terma and kernel with EGS4, and to compare the dose distributions obtained by convolution method and Monte Carlo simulation. As the results, good agreements were obtained when incident photon energies were 4.0MeV and 10.0MeV.

1. Introduction

A radiation treatment planning system is used for the calculation of three-dimensional distribution in a patient. It is important to obtain the proper dose distribution and we must check whether radiation beam irradiates a target correctly or not. Dose calculation algorithms have been improved to correct the effect of scatter and heterogeneity.

The works about convolution method have been already reported by a lot of researchers. The convolution method gives good agreement for the 15MV x-ray dose in electronic disequilibrium situations, such as the buildup region, near beam boundaries, and near low-density heterogeneities (T.R. Mackie, J.W. Scrimger, and J.J. Battista 1985).[1)] In addition, the EGS Monte Carlo code is used to generate energy deposition kernels which describe the energy deposited by charged particles set in motion by primary, first scatter, second scatter, multiple scattered and bremsstrahlung plus annihilation photons (T.R. Mackie, A.F. Bielajew, D.W.O. Rogers, and J.J. Battista 1988)[2)].

On the other hand, terma is used for the calculation of the dose distribution and is defined as total energy released primary photon interaction per unit mass.

We tried to generate terma and kernel with EGS4 and to evaluate the accuracy of convolution method using them.

2. Method

Figure 1 shows the geometry for the calculations by EGS4. The material was water with the volume of 15.5×15.5×15.5cm^3 and calculated voxels were 0.5×0.5×0.5cm^3. Monochromatic parallel beams of 2×10^9 histories with 1.25, 4.0 and 10.0MeV were used in this simulation.

2.1. Generation of Terma

The sum of released energy by interaction of primary photon was stored and terma was obtained by the following conditions.

ECUT: incident energy [MeV]

PCUT: incident energy -10^{-7} [MeV]

2.2. Generation of Kernel

Kernel was generated by utilizing variable LATCH included in EGS4. First, primary photon entering a region was marked a "LATCH=1". Secondary, if primary photon marked by "LATCH=1" interacted with the atom in the region, the released particles were marked by "LATCH=2". Finally, the scattered photon or the charged particles marked by "LATCH=2" were traced until all those particles were deposited. The absorbed dose in each calculated voxel gotten by LATCH was normalized to terma at the depth 2.25cm on the central axis. In addition, both ECUT and PCUT were 10keV.

2.3. Comparison of Convolution Method and Monte Carlo Method

On convolution method, the absorbed dose was calculated by the following convolution integral[3] with terma and kernel obtained with the method 2.1 and 2.2;

$$D(x,y,z)=\iiint T(x',y',z')\cdot K(x-x',y-y',z-z')\times dx'dy'dz' \tag{1}$$

where $D(x,y,z)$ is the absorbed dose at the point (x,y,z), $T(x',y',z')$ is terma at the point (x',y',z'), and $K(x-x',y-y',z-z')$ is kernel at the point (x,y,z) far from the point (x',y',z').

While, we calculated the absorbed dose of water using EGS4 on Monte Carlo method. Both ECUT and PCUT were 10keV.

The absorbed doses between convolution method and Monte Carlo method were compared in this study.

2.4. Sectional modulated photon fluence

The dose distribution by sectionally modulated photon fluence was produced. Figure 2 shows the

modulation of photon fluence. The incident beam was 10.0MeV monochromatic photon and the number of history was 10^9. The irradiation field was $9.5\times9.5cm^2$ and the photon fluence at the left side was two times more than its fluence at the right side. The left side was the area from -4.75cm to 0.25cm for y-axis and the right side was the area from 0.25cm to 4.75cm.

3. Results and discussion

3.1. Generation of Terma and Kernel

Figure 3 shows profile curves of terma and figure 4 shows the shape of kernel with 10.0MeV incident photon by software EGS4win32.

3.2. Comparison of Convolution Method and Monte Carlo Method

Figures 5, 6 and 7 show depth dose curves and horizontal profile curves of 1.25, 4.0, 10.0MeV photons, respectively. Table 1 shows the relative dose difference between convolution method and Monte Carlo method. In depth dose curves, inside of the irradiation field border is 4.5cm far from central axis, and outside of the irradiation field border is 5.0cm far from central axis.

As shown by depth dose curves and horizontal profile curves, the absorbed doses of convolution method tended to be slightly smaller than those of Monte Carlo method. One of the reasons may be the truncation of kernel size. Furthermore, the relative dose difference tended to be smaller as the incident energy was higher. Two reasons can be pointed out. One is a statistical error and the other is a volume size of region. In this study, kernels with the same volume size for each energy were obtained. But, the volume size of region might be too large for 1.25MeV. In the cases of 4.0 and 10.0MeV, the results from convolution method agree well with those of Monte Carlo method.

3.3. Horizontal profile curve for modulating photon fluence

Figure 8 shows the horizontal profile curves by modulated photon fluence with 10.0MeV. The calculated results of convolution method were agreed well with those of Monte Carlo method. This result shows that we may be able to apply for various dose calculations using wedge filter and block filter.

The method with the simple geometry was used for the comparison of the absorbed doses between convolution method and Monte Carlo method. However, we should consider that photon beam used in radiotherapy has continuous energy spectrum and spreads as fan line, and particle and energy fluences on the surface of water are modified due to the geometry of the gantry of the accelerator.

The details of kernel distribution, the effective penetration depth and lateral distance traveled by primary charge particles have been given by Mackie et al. As the future work, we will compare our data with given data by them and examine the dose distribution of more intricate irradiation field.

4. Conclusions

We could get the good agreements between calculated results of convolution method and those of Monte Carlo method in the cases of 4.0 and 10.0MeV.

5. References

1) T.R. Mackie, J.W. Scrimger, and J.J. Battista, “A convolution method of calculating dose for 15-MX x rays” Med Phys. 12,188-196(1985)

2) T.R. Mackie, A.F. Bielajew, D.W.O. Rogers, and J.J. Battista, “Generation of photon energy deposition kernels using the EGS Monte Carlo code” Phys. Med. Biol. 33,1-20(1988)

3) Y. Watanabe, I. Kanamori et al, “Compendium of Radiotherapy science” Iryo-kagaku-sya, Tokyo (2001)

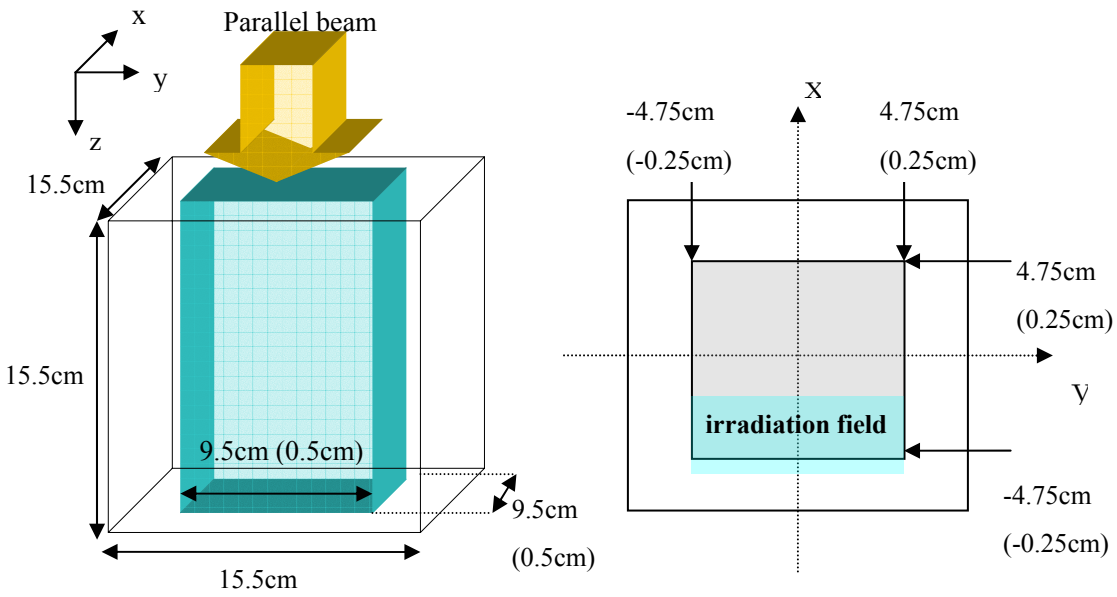

Figure 1 The geometry for calculating absorbed dose by EGS4. When terma and kernel were calculated, the irradiation field was reduce to $0.5 \times 0.5 cm^2$.

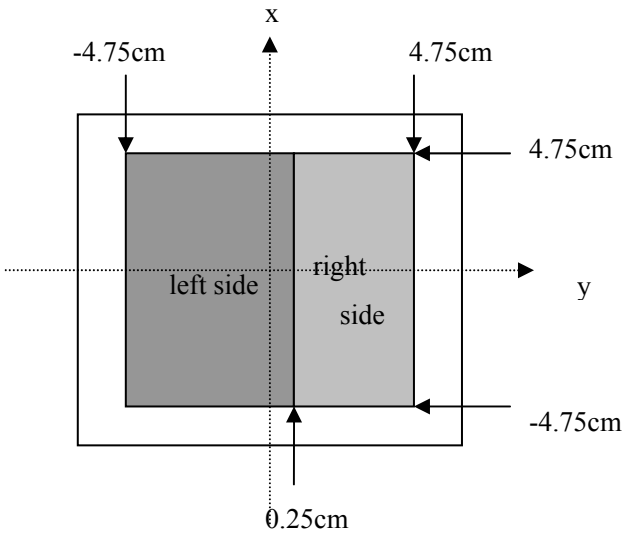

Figure 2 The modulation of photon fluence on the irradiation filed. The irradiation field was 9.5×9.5cm^2 and the photon fluence in the left side was two times more than its fluence in the right side. The left side was the area from -4.75cm to 0.25cm for y-axis and the right side was the area

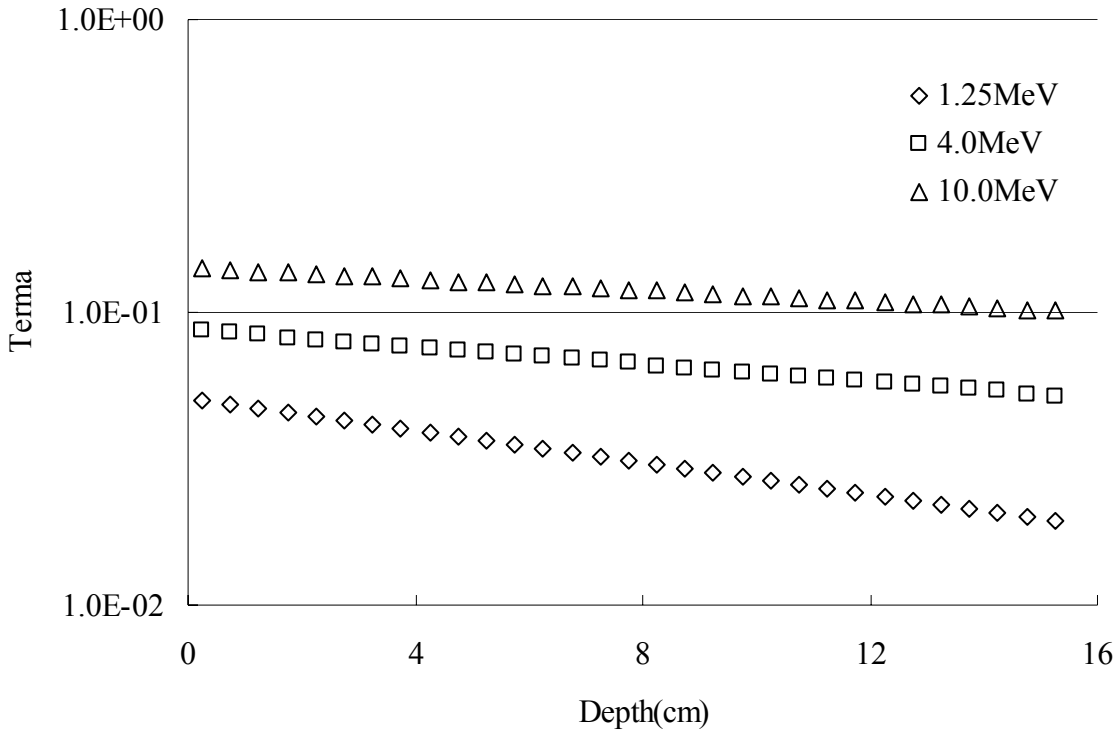

Figure 3 Profile curves of terma

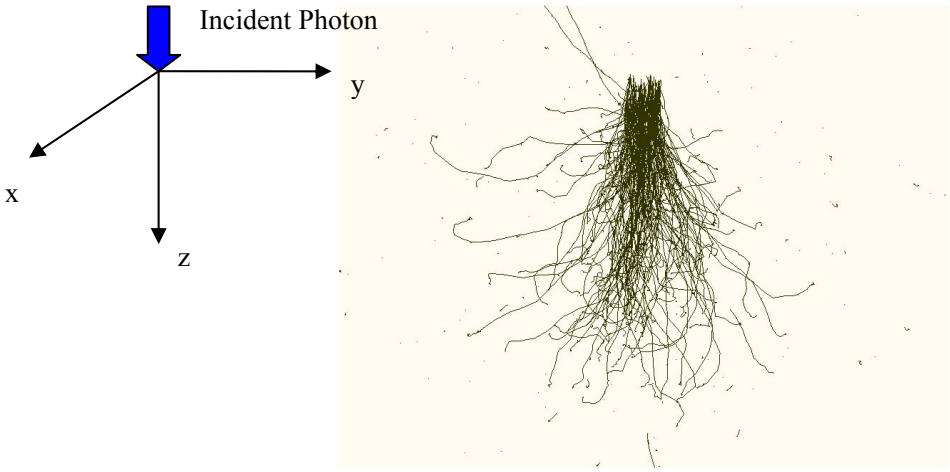

Figure 4 Shape of kernel by photon with 10.0MeV incident energy. Electron and positron are displayed

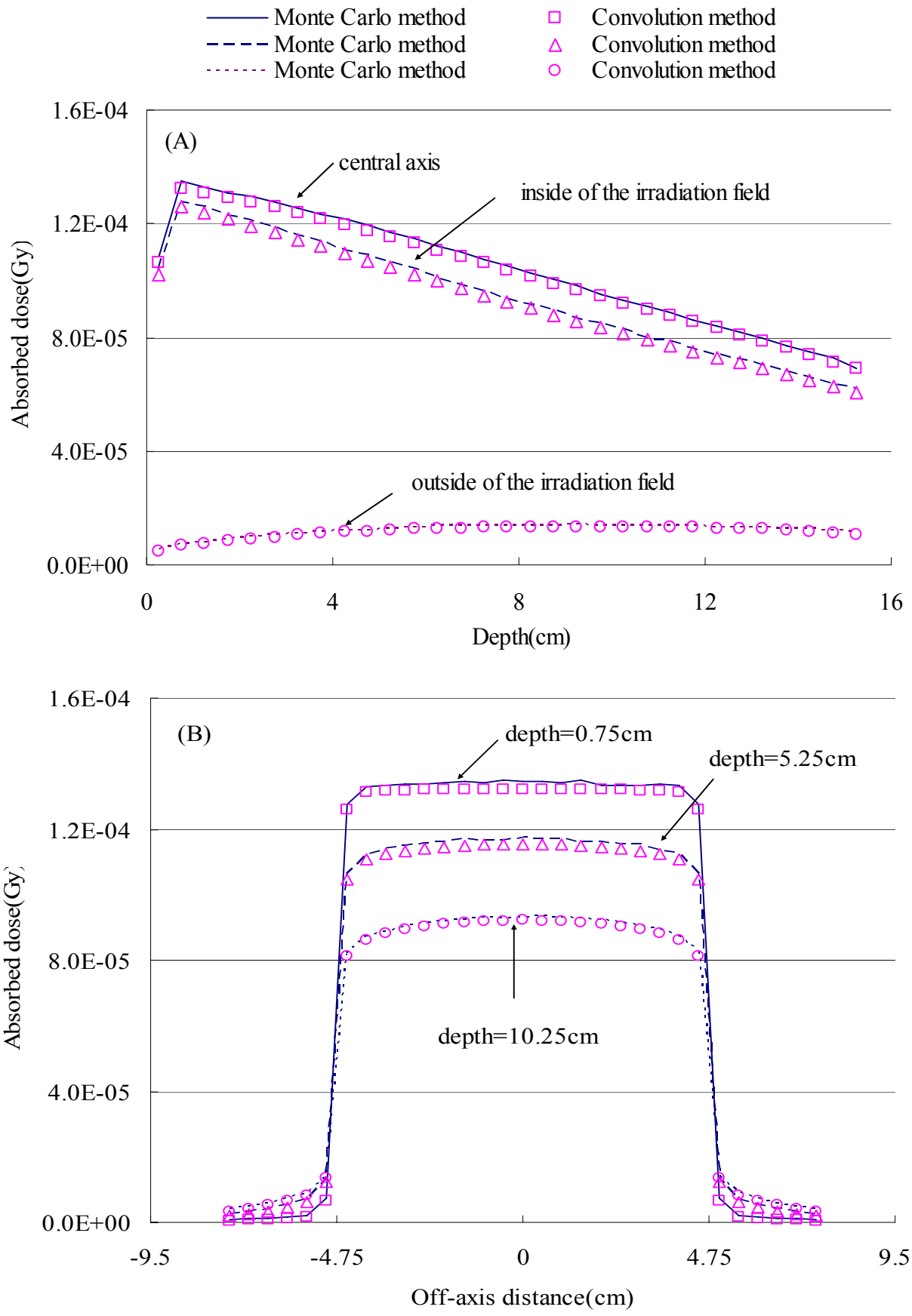

Figure 5 Depth dose curves (A) and horizontal profile curves (B) with 1.25MeV

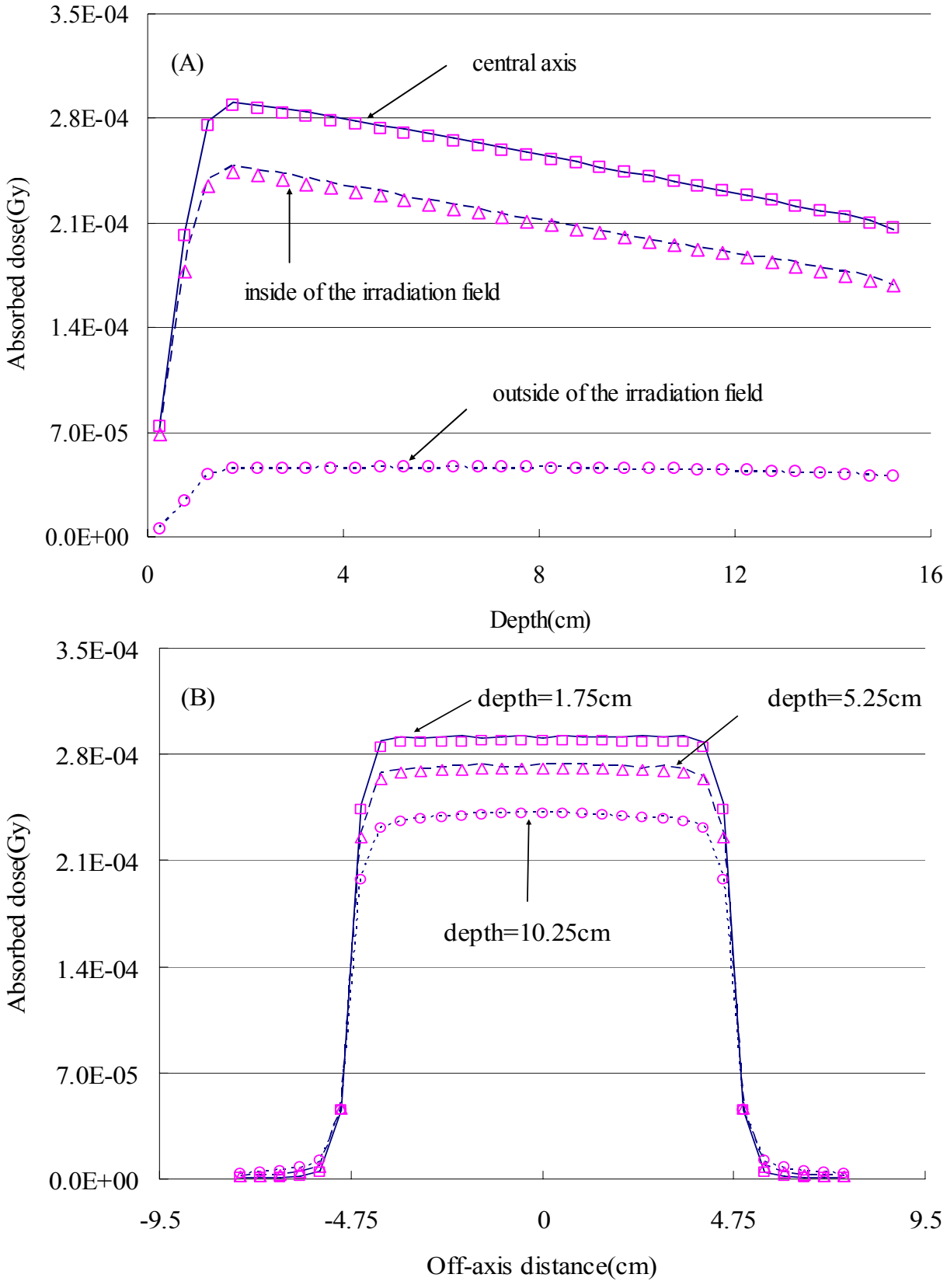

Figure 6 Depth dose curves (A) and horizontal profile curves (B) with 4.0MeV

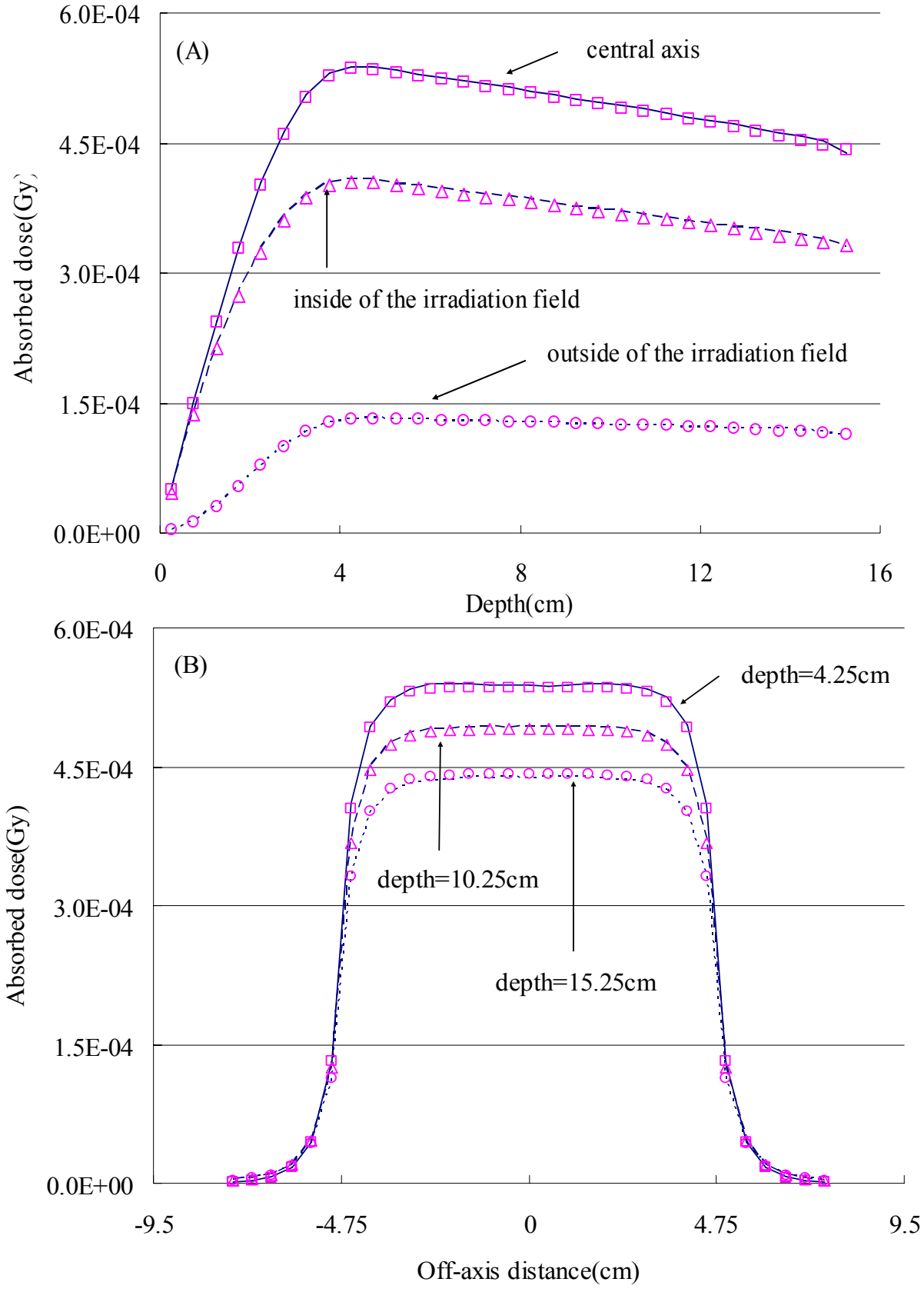

Figure 7 Depth dose curves (A) and horizontal profile curves (B) with 10.0MeV

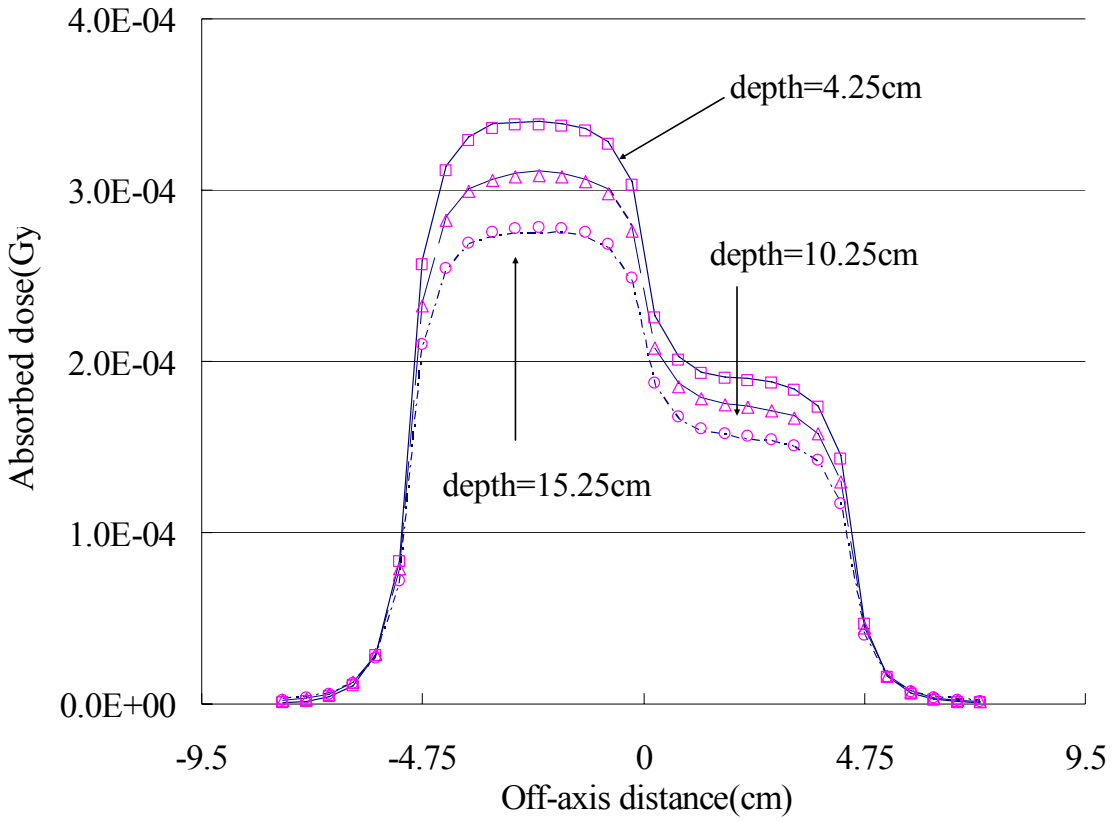

Figure 8 Horizontal profile curves by modulated photon fluence with 10.0MeV

Table 1 Relative dose difference

incident energy[MeV]	central axis	inside of the irradiation field	outside of the irradiation field
1.25	1.26%	1.46%	5.68%
4.0	0.77%	1.26%	1.01%
10.0	0.86%	1.19%	0.93%

$$\text{Relative dose difference}[\%] = \left|\frac{D_M - Dc}{D_M}\right| * 100$$

D_M : Absorbed dose by Monte Carlo method

D_C : Absorbed dose by convolution method

APPLICATION OF EGS4 TO INTENSITY MONITOR DEVELOPMENT FOR SYNCHROTRON RADIATION AT SPring-8

N. Nariyama

[a]*Japan Synchrotron Radiation Research Institute, Beamline Division, Kouto 1-1-1, Sayo, Hyogo 679-5198, Japan*
e-mail:nariyama@spring8.or.jp

Abstract

Synchrotron radiation is a high-intensity x-ray beam. The in-situ absolute intensity measurement is important for various experiments. At SPring-8 of a large-scaled synchrotron radiation facility, we have developed a parallel-plate free-air ionization chamber for photons up to 150 keV from a bending magnet and the uncertainty was confirmed within 3%. At undulator beamlines, a small free-air ionization chamber with 4.2-mm plate separation was developed and the collection efficiency within 3.8% and 1.1% was confirmed for 8 and 10 keV photons up to 4×10^{13} photons/s, respectively. Moreover, parallel-plate ionization chambers of graphite-wall and Al-evaporated-film-wall were developed for the intense beam above 10 keV. A Monte-Carlo code EGS4 was used for these monitor designs by calculating the energy deposition considering linear polarization, and contributed to the estimations of the electron loss.

1. Introduction

SPring-8 is a third-generation synchrotron radiation facility in Japan, which can produce a strong beam intensity and provide high photon energies. For high-energy photons up to 150 keV produced from a bending magnet, a portable parallel-plate free-air ionization chamber has been developed as an absolute intensity monitor with an uncertainty within 3%.[1)] Moreover, for high-intensity photon beams produced from an insertion device undulator, a miniature free-air ionization chamber has been developed.[2)] The linearity was confirmed between 8 and 30 keV and the collection efficiency within 3.8% and 1.1% was confirmed at 8 and 10 keV, respectively. Above 10 keV, a parallel-plate ionization chamber with thin electrodes, gas scintillation detectors and a vacuum chamber were developed and the linearity was confirmed between 15 and 30 keV on the order of 10^{13} photons/sec.

On the designs of these chambers and analysis of the measurements, a Monte Carlo code EGS4 was used. Synchrotron radiation at most of the beamlines in SPring-8 is linearly polarized. In EGS4, dependence of Compton photon and electron emission angle on azimuth is considered.[3)] By adding a routine considering the photoelectron emission angle distribution to the code, the program became satisfactorily available to the simulation of photon and electron transport from synchrotron radiation. In this study, monitor characteristics of the ionization chambers obtained in the experiments using synchrotron radiation are presented with the simulation results of EGS4.

2. Materials and methods

2.1 Chamber design

The sectional view of the ionization chamber for high energy photons is shown in Fig. 1. The length of the guard plate was 130 mm, the width was 260 mm and the plate separation was 85 mm. The size of the collecting electrode was

10 mm by 200 mm. The front and side walls were made of stainless steel and measured 10 and 5 mm in thickness, respectively. The size of the entrance mouth was 10 mm by 150 mm and the exit mouth was 20 mm by 160 mm. The applied voltage resistance ranged up to 10 kV.

For the ionization chamber for high intense photons, the electrode gap was set to 4.2 mm, which was considered to be the minimum distance to avoid the photon scattering. The length of the electrode was 5 mm and the width was 30 mm. The guard electrodes 10 mm long were placed before and behind the collecting electrodes.

Figure 2 shows the cross section of the parallel-plate ionization chamber. The electrodes were circular in 50-mm diameter. The third plate was an electric-field shield. The distance between the electrodes was variable from 1 mm to 10 mm. The electrodes used were 0.15-mm thick graphite and Al evaporated on both sides of polyethylene. The latter electrode thickness was 6 μm: 0.1-μm-thick Al and 5.8-μm-thick polyethylene.

2.2 Simulation method for the monitor to high energy photons

To estimate the electron escape fraction on the design of the ionization chamber for high energy photons, the energy deposition in the air between the collection electrodes was calculated using EGS4 for 40 to 190 keV photons. In the original EGS4 code, the photoelectron is given the same direction of motion as the original photon. In the present simulation, the IPHTER option in the code[4] was used. In addition, when the photons are linearly-polarized, the photoelectrons are emitted more easily in the plane including the electric field vector of the photons. This effect decreases electron loss when electrodes of the ionization chamber are set in the vertical direction, because the electric field vector of the photons is included in the horizontal plane at the bending-magnet beamlines. The angular distribution was sampled based on Sauter's equation.[5]

On the other hand, Compton electrons tend to be strongly scattered vertically to the plane including the electric field vector. The behavior is illustrated in Fig. 3. The polarization degree used for the simulations was 0.9997, which was calculated with a SPECTRA code.[6] The calculations of EGS4 were not highly sensitive to the degree.

In the calculations, to confirm the effect of the beam size, 1- and 5-mm square beams were used for all of the energies, and 10-mm square beams were used below 70 keV. These beam sizes were adjusted to the commonly used beam size. The cutoff energies were 1 and 5 keV for photons and electrons, respectively. For electron loss, the absorbed energies at the plate separations of 8.5 cm and infinity were calculated, and the ratio of these two values was used as the collection efficiency: the difference between the ratio and unity equals the proportion of electron loss. The statistical errors were all below 0.5%.

2.3 Experiments at bending-magnet beamlines

The experiments were carried out at SPring-8 beamlines BL20B2 and BL38B1. The experimental setup is illustrated in Fig. 4. At both beamlines, a monoenergetic photon beam is available through a two-crystal Si monochromator. The constituents were confirmed to be negligible for the first harmonic above 30 keV. The typical beam size used was 10 mm wide by 1 mm high at BL38B1. At BL20B2, the beam sizes of 1 mm by 1 mm to 6 mm by 40 mm were used.

The photon intensity was obtained from the current of the ionization chamber. For comparison, reference monitors were employed and photon intensity was also obtained from the current. One monitor was an ionization chamber with 5-cm plate separation and the other was a Si-PIN photodiode of S1357-04, which had been calibrated with a total absorption calorimeter using synchrotron radiation between 10 and 40 keV.[7]

2.4 Experiments at an undulator beamline

The experiments were carried out at the BL47XU undulator beamline, in which a double-crystal monochromator is cooled with liquid nitrogen. The setup is also shown in Fig. 4. For the reference monitor, the Si-PIN photodiode was used. However, the maximum current is limited to 2 mA, which would be exceeded at the maximum photon intensity. In this

situation, aluminum plates of 0.1- to 2.8-mm thickness were placed between the ionization chamber and the photodiode in order to weaken the intensity to the photodiode. For the parallel-plate ionization chamber, the miniature ionization chamber was used as the reference monitor.

The ratio of the intensity obtained by the ionization chamber and the reference monitor was considered to equal the collection efficiency of the ionization chamber. The photon energies used were 8, 10, 12, 15, 20 and 30 keV. The beam size was about 0.5 mm in height by 1 mm in width. High harmonic components were negligible. Negative voltage up to -5 kV was applied to the ionization chamber and a reverse voltage of –10 V was applied to the photodiode.

3. Results and discussions

3.1 Ionization chamber for high energy synchrotron radiation

The ratio of the measured photon intensity with the ionization chamber to that of the reference monitors is shown in Fig. 5. At the experiments of BL38B1, as expected with the EGS4 calculation, the discrepancies from unity were about 1-1.3% at 30-60 keV, and the ratio decreased to 0.978 at 80-100 keV. At 150 keV, the ratio increased to 0.990, which also agreed with the EGS4 result. At 150 keV, the ionizing current became small and the signal-to-noise ratio drastically increased, especially for the photodiode. The large error bars are due to the weak current, and the errors of the ionization chamber itself are below 1%. Beam-size dependence was not observed between the 1- and 10-mm square beams.

The reason for the collection-efficiency increase at 150 keV is the decreased occurrence of the photoelectric effect that causes electron loss. According to EGS4, the proportion of energy deposition by photoelectrons decreased to only 1% at 150 keV. At 190 keV, even the loss of Compton recoil electrons becomes considerable, and the build-up region is insufficient. Above 190 keV, the efficiency decreased steeply in the calculations.

The collection efficiency was enhanced by about 2% from those without linear polarization except at 190 keV. As explained in section 2.2, this is because the photoelectron is easily emitted in the horizontal direction including the electric field vector, which is parallel to the electrodes. On the other hand, Compton electrons tend to be scattered rather vertically to the plane. The electron does not contribute to the electron loss because of the low energy; nevertheless, above 150 keV, even Compton electrons can reach the electrodes.

After all, the electron loss in Fig. 5 was found to be below 0.5% up to 60 keV, 2.7-3.3% below 150 keV and 1.1% at 150 keV. Up to 100 keV, the decrease is owing to the shortness of the plate separation; on the other hand, above 150 keV the loss is somewhat attributable to the shortness of the buildup region, which is smaller than the electron range.

3.2 Ionization chamber for high intensity synchrotron radiation

Figure 6 shows the saturation characteristics of the ionizing current at 8-30 keV. The photon intensity was converted from the measured current using the collection efficiency described below. The values became almost constant above -2 kV at 8 and 10 keV, and at 15, 20 and 30 keV the only flat region was observed over the voltages; saturation was confirmed on the order of 10^{13} photons/s. As shown in the figure, with decreasing photon energy, both photon intensity and dose rate per incident photon increases, which induces ion recombination more easily. At 8 keV, the photon attenuation was large. The slight scattering on the plateau at 8 keV may also be due to the large photon attenuation.

Figure 7 shows the collection efficiency as a function of photon energy. At 8 and 10 keV, the values became almost unity within 3.8% and 1.1%, respectively, and decreased with increasing photon energy owing to the electron loss: 0.848, 0.690 and 0.517 at 15, 20 and 30 keV, respectively. At 8 keV, the photon attenuation in the air is considered to be a large origin of the difference. The plate distance of 4.2 mm is smaller than the two-fold electron range at 10 keV, that is, 4.8 mm. This range, however, is the maximum value and most of the electrons travel at shorter distances. Moreover, the linear polarization of synchrotron radiation reduces the size of the electron escape fraction. These reasons account for the lack of electron loss observed at 10 keV.

Figure 7 also shows the dependence of the current on the electrode plate position. When the plates were set on the

left and right sides of the beam, the current became smaller compared to the case in which the plates were placed above and below the beam: the ratio is 0.84 at 20 keV and 0.78 at 30 keV. This is owing to the linear polarization. When the plates are placed on the left and right sides, some high-energy electrons reach the plates without becoming sufficiently ionized, which results in the decrease of the measurement current. The reproducibility of the collection efficiency was confirmed at the same beamline, while the values will depend on the beam size.

Increasing the gap was expected to extend the applicable range of this type of chamber to a higher energy level than 10 keV. The electron loss fraction was calculated at various gap widths using EGS4. The energy deposition in the chamber was calculated for the infinite plate separation, while the minimum plate separation at which the energy deposition equaled the value at the infinite separation was also determined. As a result, values of 26, 14 and 8 mm were obtained as the gaps required to prevent electron loss at 30, 20 and 15 keV, respectively.

3.3 Parallel-plate ionization chamber for high intensity synchrotron radiation

Saturation of the graphite wall chamber is shown in Fig. 8. To 15, 20 and 30 keV photons, saturation was obtained at ±400 V, 300 V and 200 V, respectively. On the other hand, the chamber did not show the linearity at the positive or negative voltage. This was attributed to Compton current.[8)] When the average values were obtained from those at positive and negative voltages, linearity was obtained as shown in Fig. 9. The plate separation was 1 mm.

Influence of Compton current becomes smaller for thinner electrodes and lower photon energies. Figure 10 shows the linearity of the Al-evaporated wall chamber at 1- and 2-mm plate separations. Between 10 and 20 keV, linearity was observed at 1-mm plate separation. While nonlinearity appeared at 30 keV, the degree decreased at 2-mm plate separation. At 3- or 4-mm separation, linearity will be attained even to 30 keV photons.

Energy deposition between the plates was calculated with EGS4 and the current converted from the values were compared with the experimental values. The result is shown in Fig. 11, in which disagreement was obtained. The degree, however, was lower for thinner electrodes and lower photon energies, which was attributable to Compton current.

4. Conclusions

EGS4 simulations considering linear polarization contributed to the designs of the ionization chambers for measuring the absolute photon intensity of synchrotron radiation at SPring-8. For high energy photons from bending magnet and photons between 8 and 10 keV from an undulator, the absolute intensity monitors have become available. Above 10 keV for an undulator, an Al-evaporated-wall parallel-plate ionization chamber will be calibrated at each energy level.

References

1) N. Nariyama, N. Kishi and S. Ohnishi: Development of a portable free-air ionization chamber as an absolute intensity monitor for high-energy synchrotron radiation up to 150 keV, Nucl. Instru. Meth. **A524**, 324-331 (2004).

2) N. Nariyama: Characteristics of a miniature parallel-plate free-air ionization chamber for measuring the intensity of synchrotron radiation from an undulator, Rev. Sci. Instru. **75,** 2860-2862 (2004).

3) Y. Namito, S. Ban and H. Hirayama: Implementation of linearly-polarized photon scattering into the EGS4 code, Nucl. Instr. and Meth. **A332,** 277 (1993).

4) A.F. Bielajew and D.W.O. Rogers: Photoelectron angular distribution in the EGS4 code system, PIRS-0058 (1986).

5) C.M. Davisson and R.D. Evans: Gamma-ray absorption coefficients, Rev. Mod. Phys. **24**, 79-107 (1952).

6) T. Tanaka and H. Kitamura: SPECTRA: a synchrotron radiation calculation code, J. Synchrotron Rad. **8**, 1221-1228 (2001).

7) S. Ban, H. Hirayama, Y. Namito, S. Tanaka, H. Nakashima, Y. Nakane and N. Nariyama: Calibration of silicon PIN

photodiode for measuring intensity of 7-40 keV photons, J. Nucl. Sci. Tech. **31**, 163-168 (1994).

8) F.H. Attix, Introduction to radiological physics and radiation dosimetry, John Wiley & Sons, Inc. (1986).

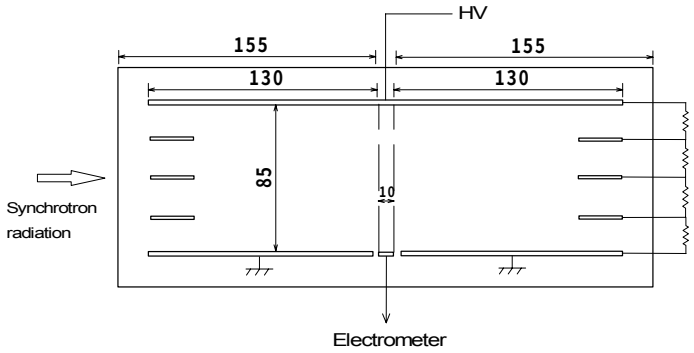

Fig. 1 Cross section of the ionization chamber for high energy photons (unit: mm)

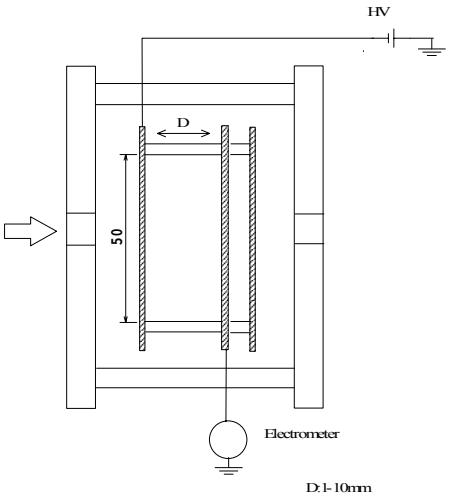

Fig. 2 Cross section of the parallel-plate ionization chamber for high intensity photons (unit: mm)

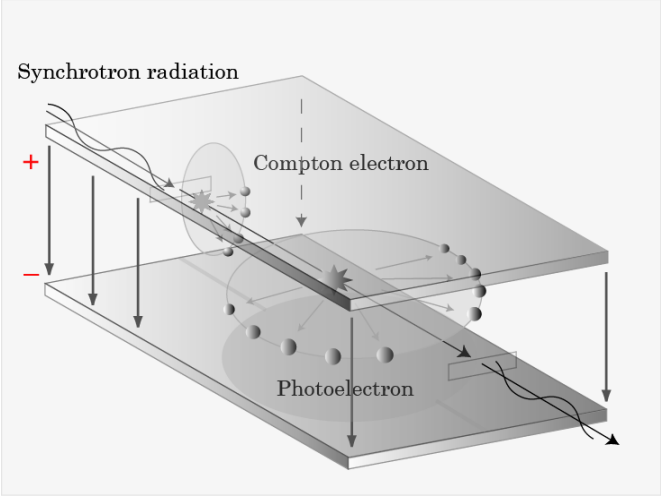

Fig. 3 A schematic of the electron motion produced in the air of the monitor. Photoelectrons have almost the same energy as the incident photons and some are emitted at large angle with respect to the beam axis. Linear polarization, however, makes the emission more in the horizontal plane. By contrast, Compton electrons have much lower energy while emitted in the vertical plane.

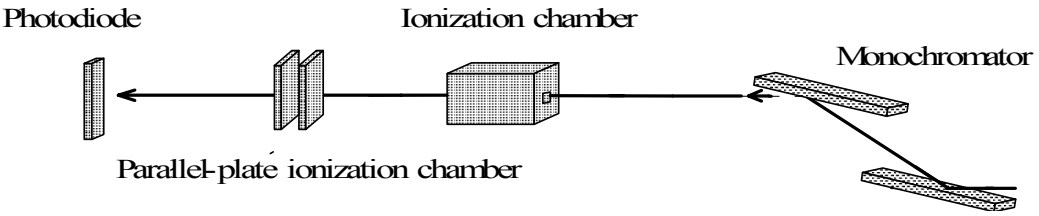

Fig. 4 Experimental setup

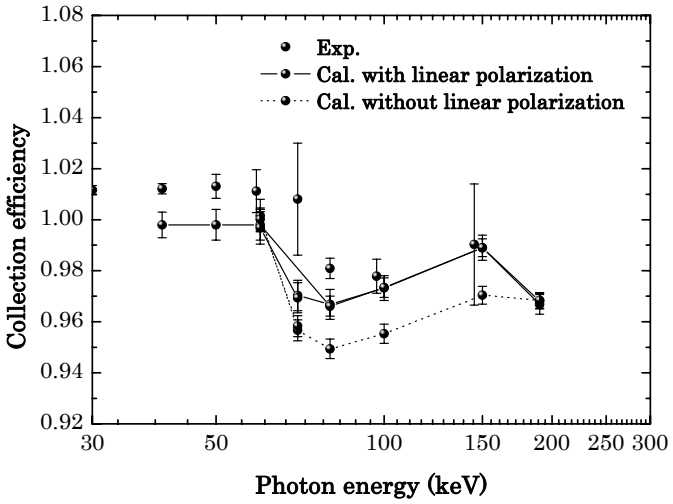

Fig.5 Collection efficiency measured and calculated considering linear polarization. The both values almost agreed: the decrease between 80 and 150 keV is owing to the electron loss. Without linear polarization, the collection efficiency became clearly smaller between 70 and 150 keV.

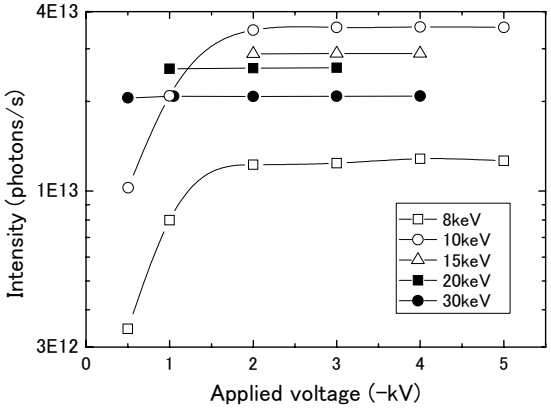

Fig.6 Saturation characteristics at 8-30 keV. A Si-PIN photodiode was used as the reference dosimeter. Aluminum plates were placed before the photodiode to decrease the photon intensity because the intensity was too strong for the dosimeter.

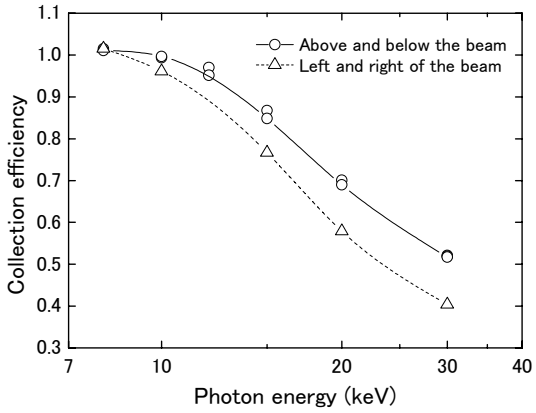

Fig. 7 Collection efficiency measured between 8 and 30 keV. The electrodes were set above and below the beam, and on the left and right sides of the beam, respectively. The difference of the collection efficiencies shows the effect of linear polarization.

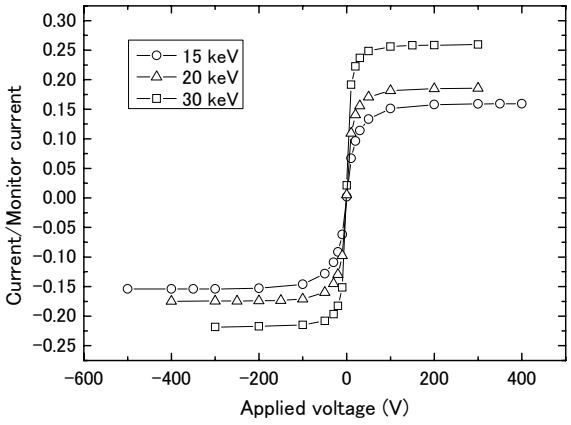

Fig. 8 Saturation characteristics of the graphite wall chamber with 1-mm separation

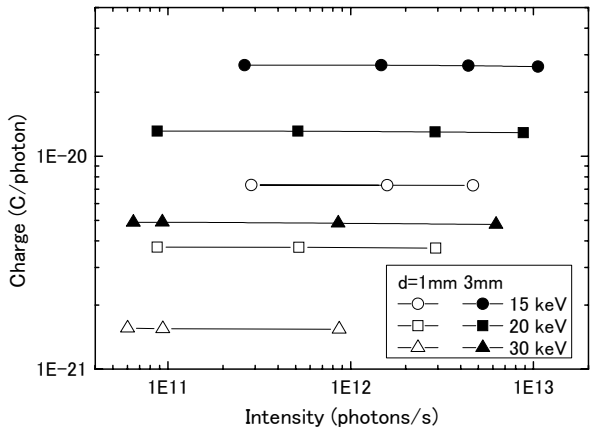

Fig. 9 Linearity of the graphite wall chamber at 1- and 3-mm plate separation

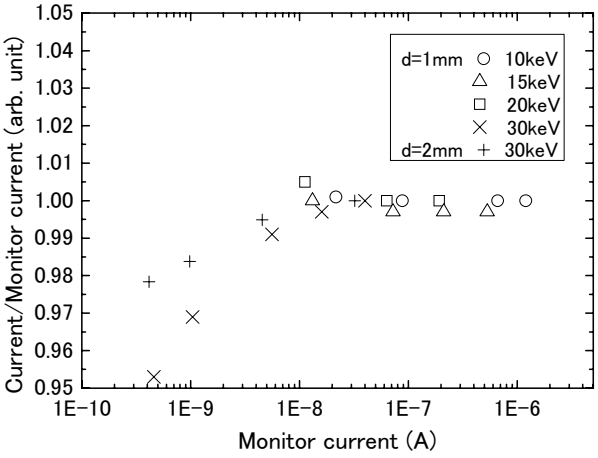

Fig. 10 Linearity of the Al-evaporated wall chamber at 1- and 2-mm plate separations

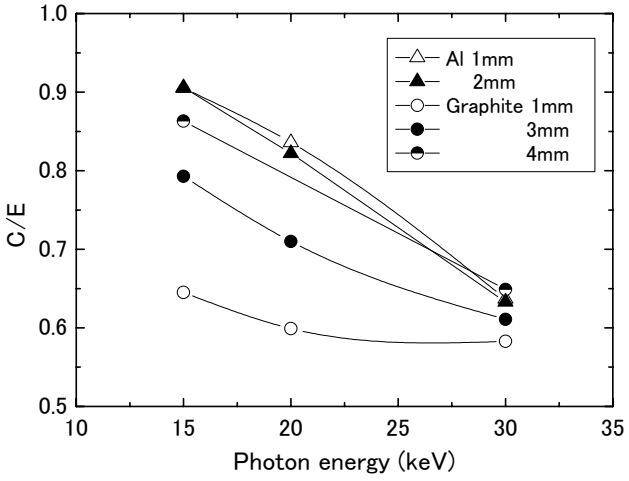

Fig. 11 Comparison of the current obtained from the calculated energy deposition and measured current for the graphite and Al-evaporated wall between 1- and 4-mm plate separation

INVESTIGATION OF FEASIBILITY AND UNFOLDING METHOD OF A MEASURED SPECTRUM USING EGS4 CODE

Gwang Ho Yoo[a], Kook Jin Chun[b], Suck Ho Hah[b], Hyun Moon Kim[b]

[a]Department of Computer Engineering, Daebul University,
Young-Arm Kun, Chonnam, Korea

[b]Ionizing Radiation Group, Division of Materials Evaluation and Chemistry,
Korea Research Institute of Standards and Science
P. O. Box 102, Yusong, Taejon, Korea

ABSTRACT

A feasibility of the simulation method with EGS4 code was investigated by comparing the energy spectra measured using a high purity Ge detector with the calculated ones. A collimator consisting of lead disks with 3mm diameter holes was used to reduce the scattered photons from the surrounding material entering the detector. The measured spectra with the collimator were then compared with the theoretical calculations using EGS4 code. The comparisons showed excellent agreements for the two radioisotopes with negligible difference in the shapes of the absorption energy spectra. And the measured spectrum obtained with a source to detector distance 60cm for ^{60}Co source was unfolded. To unfold the measured spectrum, pulse height distributions of the high purity Ge detector were first calculated using EGS4 code and the calculated spectrum was normalized to the measured one at the peak of incident beam energy. The strengths of the main peaks in the unfolded spectrum appeared to be stronger than the ones in the measured spectrum about 5 times. In the unfolded spectrum, about 36% of the total events were caused by the scattered photons from the surrounding materials.

1. INTRODUCTION

Since the photon beams radiated from the source are uncharged particles, the detection is only possible by the creations of photoelectrons to transfer all or part of their energies to the electrons in the material. Because the mean free paths of the electron and positron in the detector is very small, typically order of μm, all the charged particles produced in the detector can be assumed to transfer all the energies to the detector, and contribute to the absorption energy spectra. The surrounding materials also contribute to the absorption energy spectra. [Fig.1]

Even though the incident photons have the unique energy, the energies absorbed by detecting photons in the detector are not equal, but spread through the whole energy regions from zero up to the maximum

energy of incident photons.[1,2,3,4,5] As a result, no matter how good detector we might use, the measured energy spectrum may be much different from the real one and it appears to be very hard to determine right values of the physical constants in order to measure the air kerma rate for gamma- and X-rays. This dilemma can be solved for the exact investigations of the radiation-related materials through theoretical approach using a computer simulation in which all the characteristics of the detecting materials and measurement system are considered.[6]

One of the most powerful theoretical tools currently being used worldwide is a simulation using EGS4 (Electron Gamma Shower version 4) code.[7] Using this code, we can calculate energy spectra deposited to the material in the detector for the incident photon and electron beam with kinetic energies ranging from a few keV to hundreds of GeV. The energy deposit spectra thus calculated at many different values of energies can then be compared with the experimentally measured spectra by using an interpolation in order to simulate the real spectra, which is called unfolding of the measured spectra. In the previous experiment to measure the energy spectra radiating from the ^{60}Co and ^{137}Cs,[8] the calculated energy spectra with an assumption that the incident photons entered a detector directly from the source showed noticeable disagreement with the measured ones. In this experiment, to investigate the feasibility of the simulation method using EGS4 code, the energy spectra were measured with a collimator to avoid the scattered photons from the surrounding walls and detecting equipment entering the detector. A couple of measured spectra were then compared with the theoretical calculations to investigate the feasibility of the computer simulations using EGS4 code. The radiation sources used for this feasibility are ^{60}Co and ^{137}Cs. We measured the energy spectra with a high-count rate HPGe (high purity Ge) detector. The spectrum measured in the open space with SDD(Source to Detector Distance) of 60cm for the ^{60}Co source was unfolded to find a real spectrum that arrived at the front surface of a detector. The procedures and results of unfolding of the measured spectrum are presented in this paper.

2. EXPERIMENTAL SETUP AND DATA ACQUISION

The collimator was designed to reduce the contribution of the scattered beam from the surrounding walls and detecting equipments. It consists of a cylindrical pipe of 8cm diameter with 5mm thickness and a number of lead disks in the pipe. The schematic diagram of the collimator is given in Fig.2. Each lead disk is 8cm in diameter and 1cm thick and has a hole of 3mm diameter at the center so that only primary beam from the source and some secondary beam scattered at the lead disks are allowed to arrive at the detector. The acrylic spacers are placed in between the lead disks and were used to vary SDD. Ge crystal is a cylindrical shape of 4.98cm in diameter and 4.73cm in length. The HPGe detector is a high-count rate detector that can accept more than 10,000 photons per second and has a high resolution, about 1.85keV FWHM (full width half maximum) for 1,332keV gamma ray of ^{60}Co and 628eV for 5.9keV of ^{55}Fe. For feasibility check of simulation, two radiation sources were used and a number of the lead disks. The SDDs used to investigate the feasibility were 9cm for ^{60}Co and 30cm for ^{137}Cs.[Fig.3] and the spectrum

obtained with SDD=60cm for the ^{60}Co source in open space was unfolded. The dead time of the detector has been maintained below 15% during the measurement. Measurement time intervals have been determined by keeping total count of the measured events to be more than one million. The measuring time was about 6,000sec during the experiment.

3. INVESTIGATION OF FEASIBILITY OF SIMULATION METHOD USING EGS4 CODE

To investigate the feasibility of a simulation method, energy absorption pulse height distribution of the HPGe detector for incident photon was first calculated using EGS4 code by putting all the information about the radiation sources, detecting units and surrounding conditions of the measuring system into the calculation. The kinetic energies and relative weight of the incident photons for each source were input in the program. The energy spectra passing through the collimator were measured by HPGe detector and compared with the calculated ones, which are again normalized to the measured one at the main peaks of the incident beam energy.

In the calculations, the cutoff energies for the photon, electron and positron were set to be 10keV. All the particles with kinetic energies lower than the cutoff energy were assumed to transfer all their kinetic energies to the media and converted to electrical signal. The direction of the photon was chosen randomly so that the photons hit the surface of a detector uniformly in radial direction. No two particles were assumed to follow the same trajectory. To obtain a good statistical result, three million incident photons at each energy step with 200 batches, and 1keV bin have been used. The corresponding spectra measured using HPGe detector with a collimator are compared with the calculated ones that are normalized to the measured spectra at the main peaks of incident beam energies. [Fig.3].

In a calculated spectrum for the ^{60}Co source at SDD = 9cm, the photons of 1,173keV and 1,332keV with a weight of 0.9986 and 0.9998 were used as incident particles. The result is shown in Fig.3(a) with an experimental spectrum. The sharp peaks around 75keV and 85keV are contributed by the characteristic X-rays of the lead disks and the lead blocks that surround the collimator. The calculated spectrum is normalized to the measured one at the 1,332keV peak. The Gaussian distributions rather than a single energy value at each bin are adopted in the calculation to fit the calculated peak to the experimental one. The comparison gives an excellent agreement in the shape between the simulated one and measured one. The total strength of a calculated spectrum is about 98.7% of the experimentally measured strength. This means that 98.7% of the detected photons are the primary photons emitted from the source or the photons scattered at the collimator, and the other 1.3% of the detected particles is assumed contributed by the photons scattered at the wall of a detecting room or experimental table. As was expected, no other particles except the photons of 1,173keV and 1,332keV from the source and the photons scattered by the collimator entered the detector significantly.

Fig.3(b) shows the energy spectra for ^{137}Cs source at SDD=30cm. The peaks at 662keV and 32keV

are from the ^{137}Cs source with the relative weight of 0.85 and 0.13 respectively. The result of theoretical calculation with the input of 85% of 662keV photons and 13% of 32keV photons has been normalized to the 662keV peak of the measured spectrum. The comparison shows also good agreement with slight discrepancies at 75 and 85keV peaks. The reason for the difference seems mainly due to the imperfect duplication of the real experimental conditions. Because we used a collimator with small holes of 3mm diameter, a slight mismatch with the real experimental conditions seemed to cause the noticeable difference in producing the characteristic X-rays of the lead.

In both cases using a collimator preventing the scattered beam from the surrounding materials to enter the detector, the simulations with EGS4 code showed very good agreements to the experimental measurements in the shapes of the spectra. This suggests that the simulations with EGS4 code can be applied in prediction of radiation detection and in further research of radiation detection.

4. UNFOLDING PROCEDURE OF THE MEASURED SPECTRUM

To unfold the measured spectrum, the pulse height distributions were calculated for the incident photons entering the detector in radial direction with the kinetic energies from 20keV up to 1,400keV in 10keV step. Then a simulated energy spectrum of photons entering the detector with any incident energy between 20keV and 1,400keV can be obtained from these data files. For example, if the incident photons have the kinetic energy of 1,332keV, the simulated energy absorption spectrum can be obtained using the previously calculated spectra of 1,330keV and 1,340keV at the same SDD with a weight of 0.8 and 0.2. With the same way, any spectrum for arbitrary incident energy can be obtained using interpolation. The spectrum is then normalized to the measured one at the peak of the highest energy $E_{\max}$=1,332keV to find a ratio, $r = \frac{S_{\text{measured}}(E_{\max})}{S_{\text{calculated}}(E_{\max})}$, where $S_{\text{measured}}(E_{\max})$ is the measured strength with the absorbed energy of $E_{\max}$ = 1,332keV and $S_{\text{calculated}}(E_{\max})$ is the calculated one with $E_{\max}$. The ratio r should be multiplied to the strength of each energy bin of the theoretically calculated spectrum, starting from the highest energy $E_{\max}$ to the lowest energy 1keV. The spectrum calculated and adjusted in this way represents the strength contributed by the incident photons of 1,332keV, and thus the strength of this spectrum should be subtracted from the measured one. The newly obtained measured spectrum is then the contribution of the photons that enter the detector with energies less than 1,332keV and the unfolded strength at energy $E_{\max}$ can be obtained from the following equation, $S_{\text{unfolded}}(E_{\max}) = \frac{1}{eff(E_{\max})} r \cdot S_{\text{calculated}}(E_{\max})$, where $eff(E_{\max})$ is a detector efficiency to absorb full energy of the incident photon with energy $E_{\max}$. $S_{\text{unfolded}}(E_{\max})$ is the real strength of the photons that arrive at the surface of the detector with the energy $E_{\max}$=1,332keV. Once it's done, the next step is to lower down the energy of the incident photons by 1keV, and obtain the simulated spectrum for the incident photons of $E_{\max}$=1,331keV from the data files and normalize this spectrum to the remaining one at the energy of 1,331keV peak to get the next highest one. By repeating

the same process until the energy of the incident photons becomes 20keV, which is considered to be the minimum energy that could contribute to the measured spectrum, the unfolding of the measured spectrum can be achieved. This process should be repeated in a descending order, from the highest energy down to the lowest energy.

The energy spectra measured with SDD=60cm for the ^{60}Co in the open space is unfolded with this method and is given in Fig.4. In the measured spectra for the radiations emitted from the ^{60}Co source in the open source with SDD=60cm, the strength of the two peaks of 1,173keV and 1,332keV to the whole strength is about 12.83%. However, in the unfolded spectrum, the ratio of the two peaks is 63.7%. This means that 63.7% of the whole measured strength is originated from the photons which have 1,173keV or 1,332keV. The rest 36.3% is assumed to be the contribution by the scattered photons from the surrounding materials. The relative strengths of the 1,173keV peak to the 1,332keV peak in the measured spectra are about 1.15, whereas they are almost 1.0 in the unfolded spectra. This suggests that almost equal number of the photons with energies of 1,173keV and 1,332keV entered the detector as was expected.

5. SUMMARY AND DISCUSSION

To check the validity of the program, we measured the energy spectra from ^{60}Co and ^{137}Cs sources using the newly homemade simple collimator that prevents the beam scattered from the surrounding materials to arrive at the detector. Also, we made the pure theoretical calculation in the condition simulating the experimental one as much as possible and they were compared with the measured ones. The calculated energy spectra showed an excellent agreement with the measured ones for each radioactive source with small but acceptable discrepancy, which may be contributed by radiation beam from the surrounding materials that were not considered in the calculation. This suggests that the simulations with EGS4 code can be used in prediction of radiation detection and in further research of radiation detection.

To unfold the measured spectrum, the pulse height distributions were first calculated using EGS4 code for the detection of the incident photons entering the detector from a source. The strengths of the main peaks in the unfolded spectra appeared to be about 5 times stronger than the ones in the measured spectrum. The relative strengths of the 1,173keV peak to the 1,332keV peak in the measured spectrum are about 1.14, whereas they are almost 1.0 in the unfolded spectra. This means that almost equal number of the photons with energies of 1,173keV and 1,332keV entered the detector as was expected, and suggests that the unfolding is very reliable.

6. REFERENCES

[1] Glenn F. Knoll, “Radiation detection and measurement”, John Wiley and Sons (1989)

[2] F. H. Attix, “Introduction to radiological Physics and radiation dosimetry”, John Wiley and Sons (1986)

[3] National Institute of Standards and Technology, Criteria for the Operation of Federally-Owned Secondary Calibration Laboratories (Ionizing Radiation), NIST SP 812 (1991)

[4] A. R. S. Marsh and T. T. Williams, 50 kv Primary Standard Exposure: Design of Free-Air Chamber, NPL Reports RS (Ext) 54 (1982)

[5] M. Boutillon, "Volume recombination parameter in ionization chambers, Phys. Med. Biol. 43 pp, 2061-2072 (1998)

[6] Stephen M. Seltzer, NIM, 188 133-151 (1981)

[7] W. R. Nelson, Hideo Hirayama and D. Rogers, EGS4 and PEGS4 CODE, Stanford University (1985)

[8] K.J. Chun, S.H. Ha, H.M. Kim and G. H. Yoo, The First Asian and Oceanic Congress for Radiation Protection-1, PS-7-33(1-10) (2002)

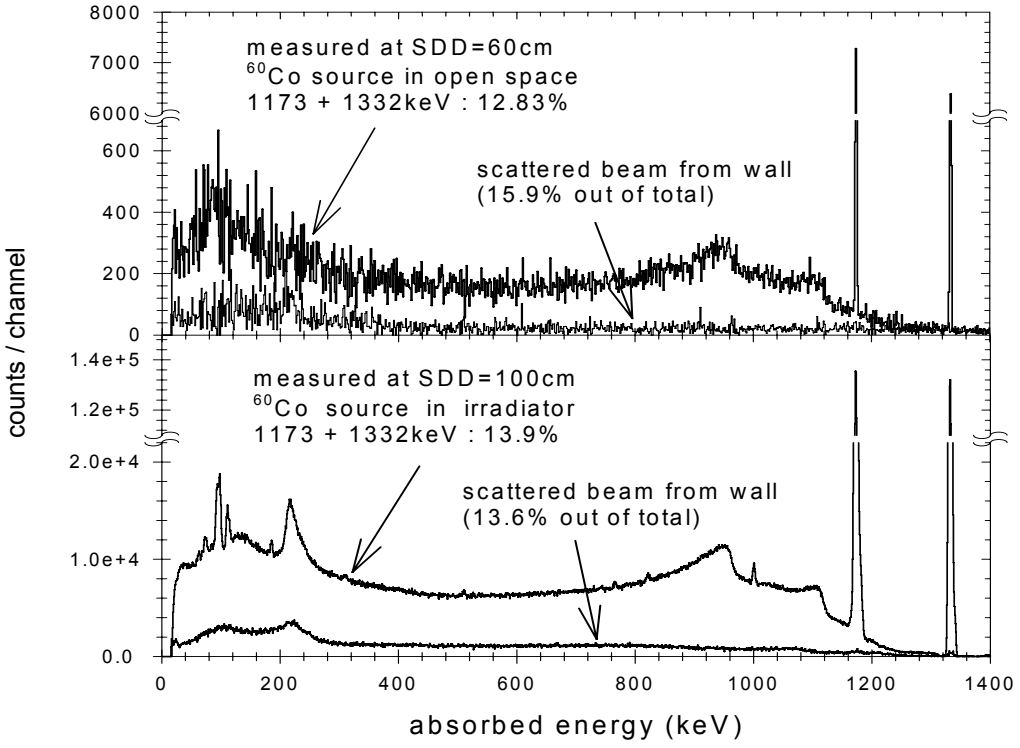

Figure.1 Graphs of measured energy spectra for the ^{60}Co sources with SDD=60cm and 100cm. The plots in the bottom in each graph are obtained by blocking the primary beam to enter the detector directly from the source using a 3cm thick lead disk.

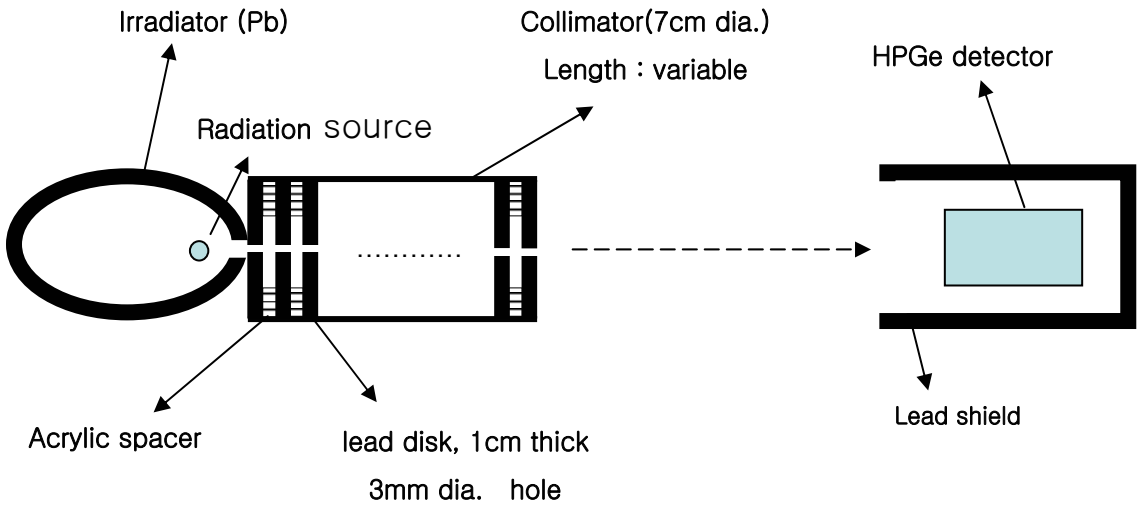

Figure.2 Schematic diagram of the measuring system to reduce the contribution of the scattered photons from the surrounding materials

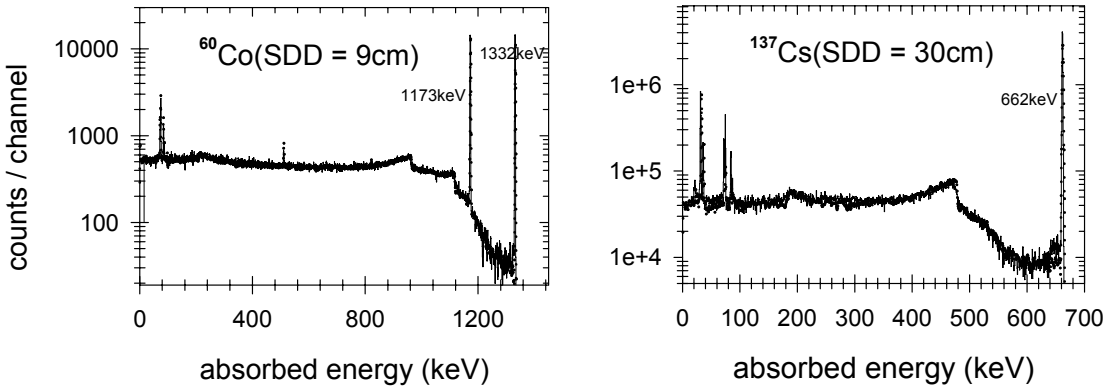

Figure.3 Graphs of measured energy spectra with a collimator versus theoretically calculated ones at SDD=9cm for the ^{60}**Co** and 30cm for the ^{137}Cs in the open space

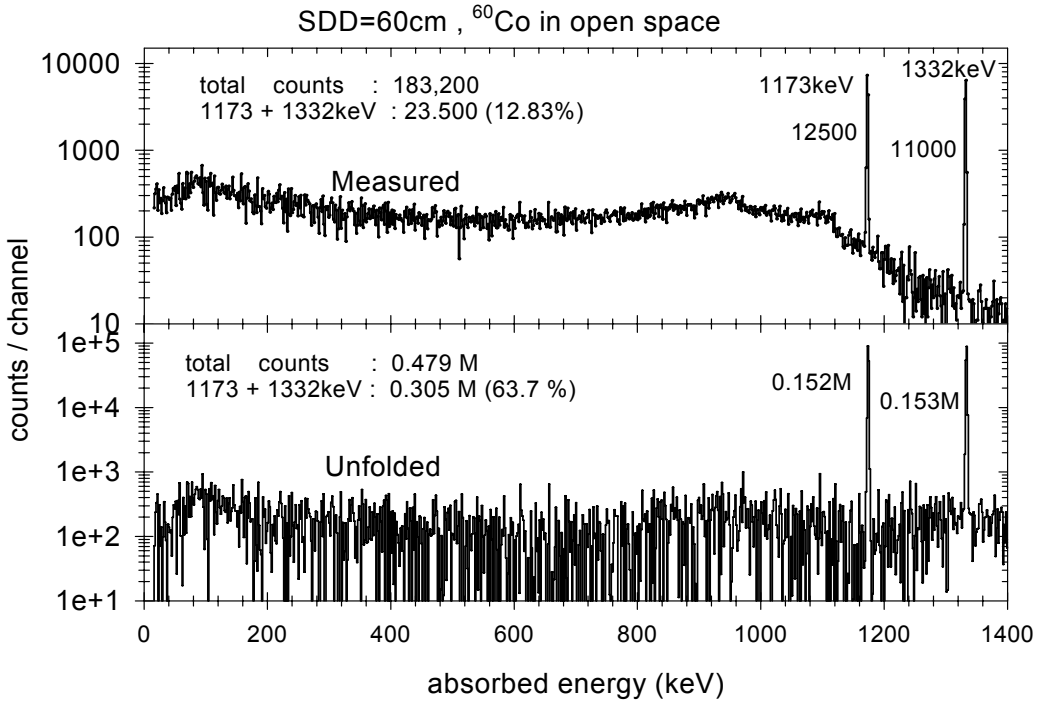

Figure.4 Graphs of the measured, and unfolded spectra for the ^{60}Co source. The numbers of percentage represent the relative ratio of the peak strength to the total strength.

VERIFICATION FOR THE DISAGREEMENT BETWEEN EFFECTIVE POINT AND GEOMETRICAL CENTER OF THIMBLE IONIZATION CHAMBER

K. Shimomura, K. Tabushi

Department of Radiological Technology, Graduate School of Medicine, Nagoya University

j040210m@mbox.nagoya-u.ac.jp

Abstract

In radiotherapy, it is certainly necessary to grasp the quantity and the distribution of the radiation administered to the human body. To measure these correctly, the standard measurement method of the absorbed dose of water is recommended by AAPM[1)], IAEA[2)] and JSPM[3)]. The standard method also recommends that absolute measurements should be performed using the thimble ionization chamber (TIC). The absorbed dose of water measured by TIC should be corrected for diverse effects. There is the definition of measurement point for TIC based on these effects. Because TIC is cylindrical form and has finite volume, the measurement point differs from the geometrical center of TIC. In the standard definitions, the point is called the effective point and recommended that its location is a shift equal to 0.6 times of the inner radius of TIC from the geometrical center. In this work, we examined the accuracy of the definitions of the effective point for TIC by simulation with EGS4.

1. Introduction

The quantity and the distribution of the radiation dose administered to the human body should be correctly measured in radiotherapy. But it is very difficult to achieve these because the absorbed dose in the body can not be directly measured. Therefore, the absorbed dose in the body is replaced with that of water. The water absorbed dose is generally measured by *Thimble Ionization Chamber* (TIC). To measure the water absorbed dose correctly, the standard methods are recommended by AAPM[1)], IAEA[2)] and JSPM[3)]. The measurement of the water absorbed dose using TIC is carried out according to these standard definitions.

To make secondary electric equilibrium easily and measure the water absorbed dose based on Bragg-Gray cavity theory, TIC had been modified by replacing the air slab with an air equivalent material. The geometry of TIC consists of the cylindrical ionization cavity as shown in figure1. The ionization cavity has finite radius. It causes that the measurement point is shifted from the geometrical center of TIC. Therefore, the measurement point of TIC is defined as the effective point, which is related to the radius of

the ionization cavity and the attenuation of radiation etc. In this study, to verify the accuracy of these standard methods for high energy photon beam, we evaluated the effective point of these methods with the simulation of TIC using EGS4.

2. Material and Method

2.1 The effective measurement point recommended by standard methods of AAPM, IAEA and JAMP

In the case of high energy photon beam, the effective measurement points recommended by standard methods of AAPM[1)], IAEA[2)] and JSPM[3, 4)] are decided as the location reduced 0.6 times of the inner radius of the ionization cavity from the geometrical center in inverse direction of radiation beam as shown in figure2.

2.2 Comparison method

1) The profile curves of the absorbed doses.

The profile curves were obtained under the simulation condition as shown in figure3. The point source was used for the simulation and the energies of incident particle were 1.17 and 1.33 MeV (Co-60), the source-surface distance (SSD) was 80cm, the irradiation field size was 5.0×5.0 cm^2, the incident beam was cone beam and the phantom was tough water with the composition as shown in table1. Tough water is a kind of water equivalent material, in this work; the absorbed dose of tough water was regarded as that of water. The phantom size was $30 \times 30 \times 30$ cm^3. The numbers of the incident particle are 2×10^9 and 2×10^{10} to calculate the absorbed dose of air in TIC and that of water, respectively.

The profile curve of the air absorbed dose using TIC was obtained by moving the location of TIC in the direction of radiation beam on the center axis of the phantom. TIC used for this simulation was the type of JARP (Ouyougiken, Japan). The geometry and the composition of this TIC are shown in figure1 and table1, respectively. While, the profile curve of the water absorbed dose was obtained on the center axis of phantom. The size of regions is $1.0 \times 1.0 \times 1.0$ mm^3.

2) Comparison of the effective measurement point of the standard methods and that of the simulation.

Each profile curve obtained by the simulation was normalized at each peak of depth dose. Furthermore those were compared (figure4). Then the profile curve of the air absorbed dose was shifted to the location reduced by the distance between the effective measurement point and the geometrical center of TIC in the direction of radiation beam. Because r_{cyl} is 3.0mm, in the case of TIC used this work, the displacement is 1.8mm $=0.6 \times r_{cyl}$ according to the standard methods. In addition, the profile curve of the air absorbed dose was shifted to the location reduced by the distance between both peaks of depth doses of

profile curves.

3. Results and Discussion

Figure4 shows the comparison of the relative dose profile curve of air with TIC and that of water without TIC on the center axis of phantom. The difference between both peak points was 2.5mm.
Figures5-1,-2 show that two profile curves, which are shifted equal to $0.6\times r_{cyl}$ (1.8mm) and the distance (2.5mm) between both peak points, are compared with the dose profile curve of water measured without TIC. The profile curve with the movement of 2.5mm is good agreement with that of water more than that of $0.6\times r_{cyl}$. However, this result is obtained using the simple simulation, so we will compare the results of other energy.

4. Reference

1) P.R. Almond, P.J. Biggs, AAPM TG-51: Protocol for clinical reference Dosimetry of high energy photon and electron beams,"*Med.Phys.***26**, 1847-1870 (1990).
2) IAEA: The use of plane-parallel ionization chambers in high-energy electron and photon beams. An Internal Code of Practice for Dosimetry, TRS 381 IAEA Vienna 1997.
3) JSMP: Standard Dosimetry of Absorbed Dose for External Radiotherapy, Tsusho-Sangyo Kenkyu-sha, Tokyo (2003).

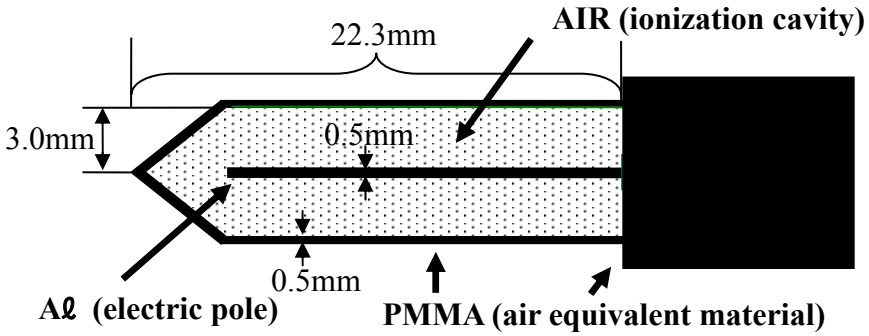

Figure1 The geometry of thimble ionization chamber

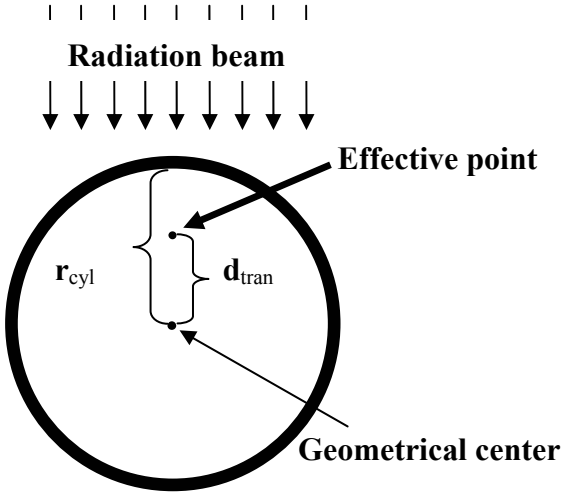

Figure2 The location of effective point

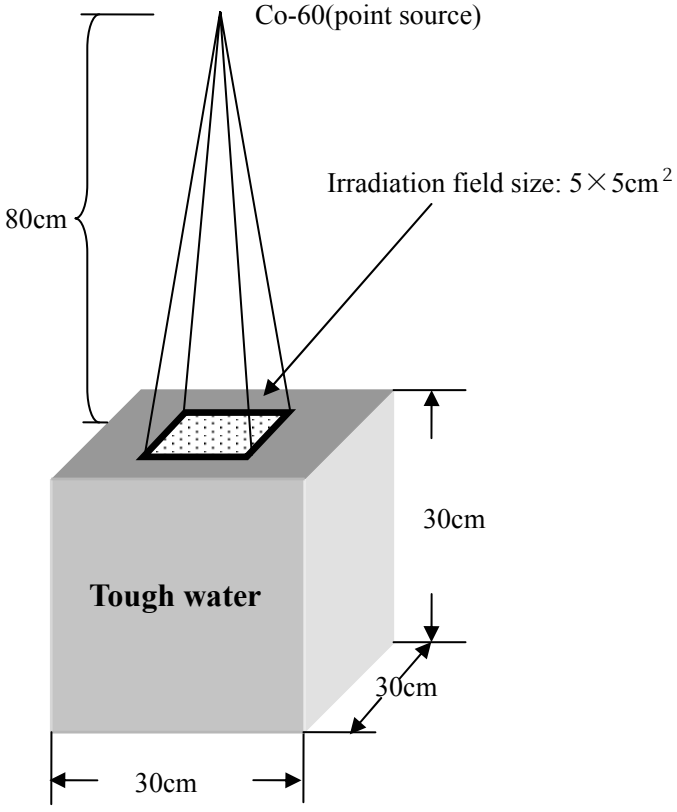

Figure3 The geometrical arrangements of simulation

Table 1 Material data and details for PEGS4.

		ELEMENT	WR(%)	RHO(g/cm3)	PCUT(MeV)	ECUT(MeV)
Chamber						
cavity	Air			1.205E-03	0.01	0.521
		N	75.575			
		O	23.143			
		Ar	1.282			
wall	PMMA			1.19	0.01	0.521
		H	8.05			
		C	59.98			
		O	31.96			
electric pole	Aluminum			****	0.01	0.521
		Al	100.0			
Phantom						
	Tough water			1.017	0.01	0.521
		H	8.21			
		C	66.33			
		N	2.21			
		O	20.65			
		Cl	0.40			
		Ca	2.20			
				*WR(%): weight rate		

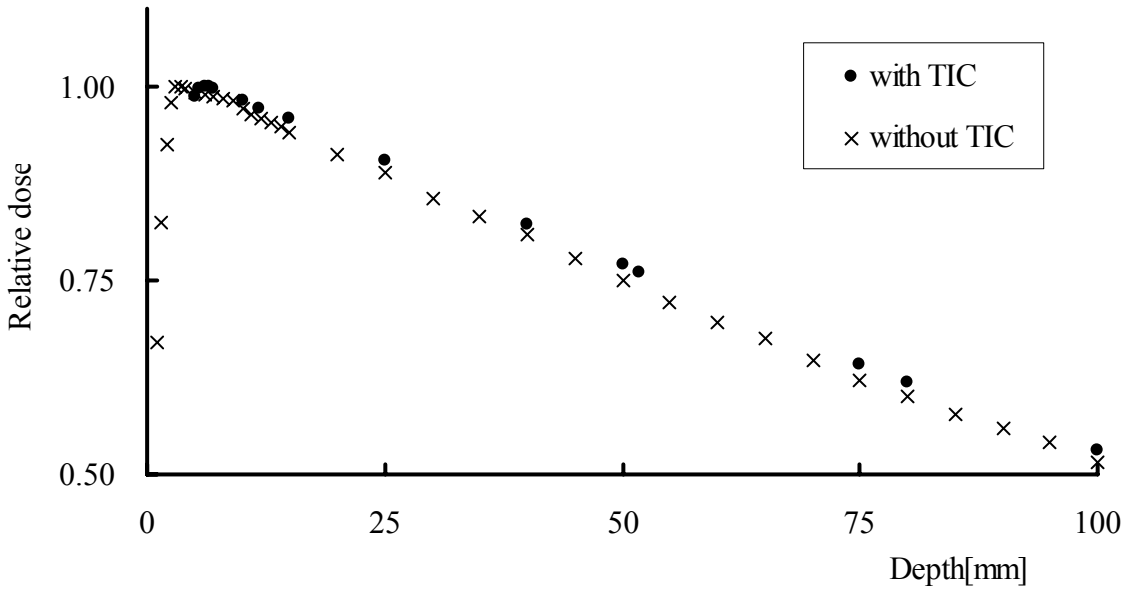

Figure4 Comparison of relative dose profile curves of obtained in air with TIC and that of water without TIC

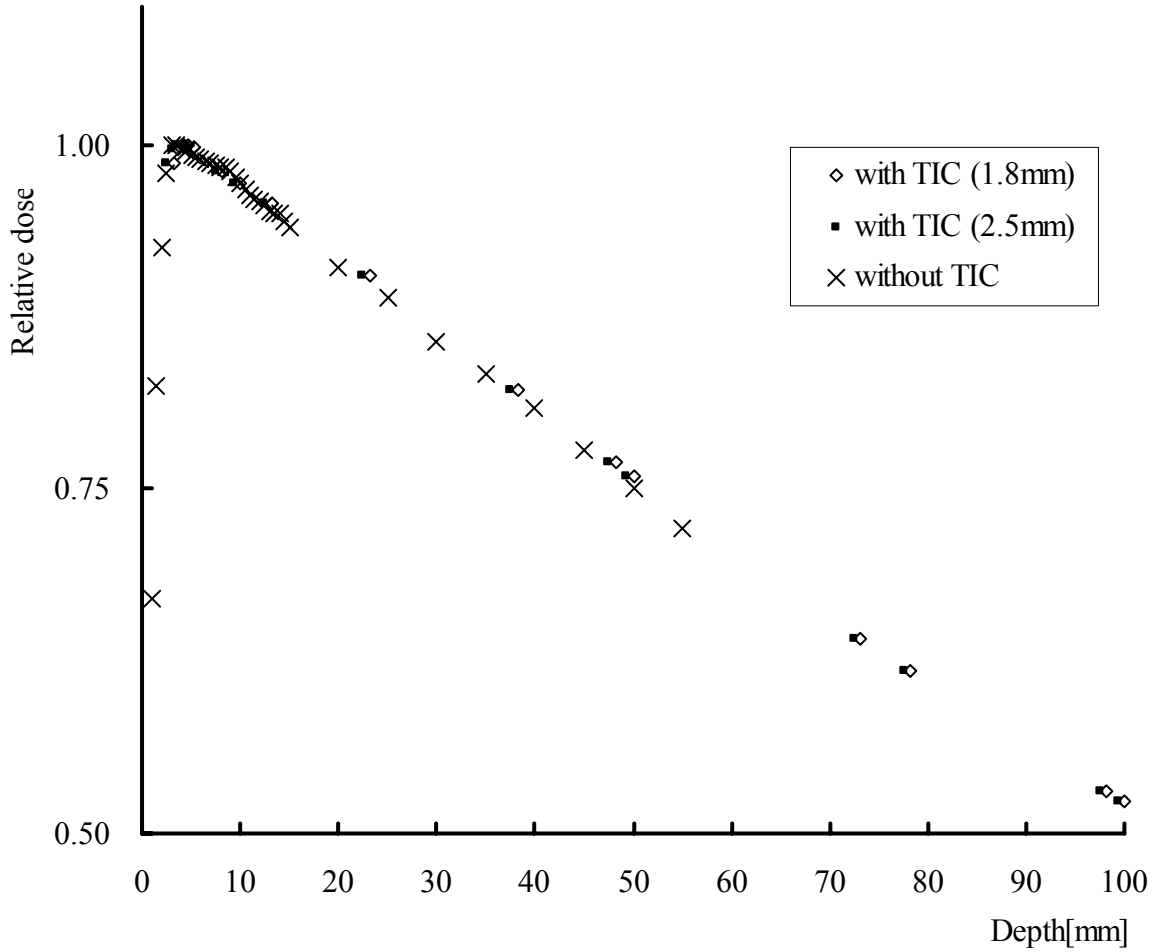

Figure5-1 Comparison of relative dose profile curves obtained in air with TIC(shited 1.8mm and 2.5mm) and that of water without TIC

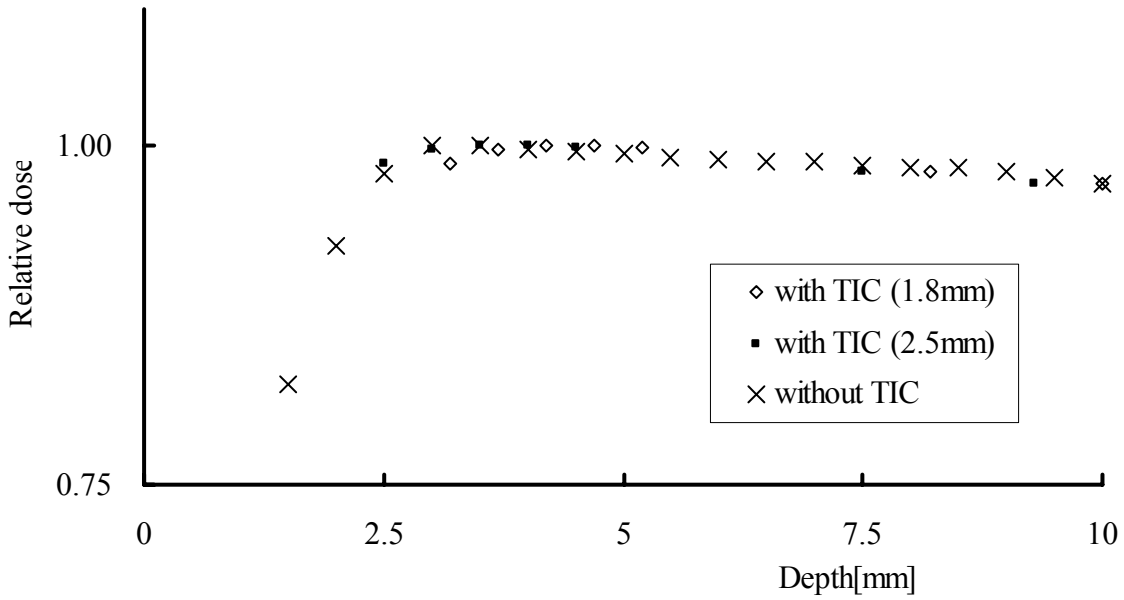

Figure5-2 Comparison of relative dose profile curves obtained in air with TIC(shited 1.8mm and 2.5mm) and that of water without TIC

OUTLINE OF THE DOSE CALCULATION SYSTEM IMAGINE FOR RADIOTHERAPY

K. Saito[a,h], E. Kunieda[b,h], Y. Narita[c,h], H. Kimura[a,h], M. Hirai[h], H. M. Deloar[h], K. Kaneko[d,h], M. Ozaki[e,h], T. Fujisaki[f,h], A. Myojoyama[g,h] and H. Saitoh[g,h]

[a]Center for Promotion of Computational Science and Engineering, Japan Atomic Energy Research Institute , Kyoto, 619-0215, Japan

[b]Department of Radiobiology, Keio University, Tokyo,160-8582, Japan

[c]Division of Radiation Therapy Physics, Chiba Cancer Center, Chiba, 260-8680, Japan

[d]CMS Japan, Tokyo, 102-0093, Japan

[e]CT Group, Toshiba Medical System Corporation, Tokyo, 113-8456, Japan

[f]Department of Radiological Sciences, Ibaraki Prefectural University of Health Sciences, Ibaraki,300-0394 Japan

[g]Department of Radiological Sciences, Tokyo Metropolitan University of Health Sciences, Tokyo, 116-8551, Japan

[h]CREST, Japan Science and Technology Agency (JST), 332-0012, Saitama

Abstract

The dose calculation system IMAGINE is under development for supporting X-ray radiotherapy by rapidly providing the accurate dose distribution in a patient body utilizing precise models of the patient body and accelerator assembly incorporated with Monte Carlo calculations. The system will be used for the quality assurance of the current radiotherapy widely carried out at present, and further for promoting the prevalence of advanced therapy. The system is scheduled to be completed in 2007 after the five-year project.

1. Introduction

The main cause of death in Japan is cancer. Tough radiotherapy has been considered to be an advantageous therapy method, the contribution of radiotherapy to the whole cancer treatments in Japan is less than one half of that in USA[1)]. The main reason for the relatively low usage of radiotherapy is often attributed to the extreme shortage of medical staffs able to properly estimate the doses in radiotherapy. While, it has been pointed out that under some specific conditions the commercial treatment planning systems used for dose evaluation may not give sufficiently accurate doses [2)]. ICRP recommends that the overall error of dose evaluation for radiotherapy should be within 5%[3)]. Considering these situations, a system supporting radiotherapy on the basis of reliable dose evaluation is expected to contribute to the improvement of the quality assurance of radiotherapy. In this paper, the outline of the system IMAGINE for supporting photon therapy by providing accurate doses is described.

2. Outline of the System

The project for developing the system started in 2002 and is scheduled to continue for five years being funded by JST. The system utilizes a sophisticated human model constructed from CT images and Monte Carlo calculations with the EGS4 code[4]. The system is planned to work on the ITBL (Information Technology Based Laboratory) computer consisting of 512 CPUs located at the Kankai Establishment, JAERI. Figure 1 gives the schematic design of the system. The data on CT images and treatment plan are transferred from a hospital to the dose calculation center; a voxel phantom is constructed immediately and the dose distribution in the patient body for the treatment is calculated in a short time; then, the calculated dose distribution is sent back to the hospital. The purposes of the system are: to provide benchmarks for the quality assurance and safety control of current radiotherapy; and to contribute to the promotion of the usage of advanced therapy.

In this system a voxel phantom - the numerical human model where organs and tissues are defined as sets of small cuboid units called voxels - will be automatically constructed from CT data of a patient. In this project, a procedure will be developed to rapidly construct the voxel phantom that has the least information needed for dose calculation with an accuracy of a few percent. The basic technique for constructing voxel phantoms has been cultivated through research on dose evaluation for radiation protection[5].

Radiation transport calculation is performed in two different ways. First, the particle fluence entering a patient body is calculated modeling the accelerator assembly (target, collimators, filters etc.) precisely. The EGS4 user code BEAMnrc[6] developed at National Research Council Canada (NRCC) is used for this simulation. Second, the dose distribution in a patient body is calculated using the voxel phantom described above. A prototype of the dose calculation code for radiotherapy incorporated with voxel phantoms has been already developed as a EGS4 user code[7]. Basically, we try to avoid as much as possible the usage of the approximations which might lead to degradation of dose accuracy. While, it is an essential requirement to reduce computational time significantly in order to obtain the dose distribution within a reasonably short time. Super parallel computing on the ITBL computers will be fully utilized to fasten the computational time.

The IMAGINE system is planned to apply to the advanced radiotherapy of intensity modulated radiation therapy (IMRT)[8] and CT radiotherapy (CTRTx) [9] besides common photon therapy. Since the both radiotherapy needs sophisticated dose calculation, the IMAGINE system is expected to be quite effective. The IMAGINE system specified for CTRTx is going to be developed in this year at the same time that the treatment system is completed.

The system will be completed in 2007. However, to make the system practically useful, the discussion concerning the administrative framework of the system operation is also very important as well as the technical investigation. We would appreciate receiving comments widely from doctors, medical staffs engaged in radiotherapy, and anyone interested in the system.

Acknowledgment

We would like to express our thanks for all the people supporting this project directly and indirectly. Without their help, the project never succeeds.

References

1) M. Hiraoka: Hoshasen Chiryo no Genjo to Shorai Tembo, Gensiryoku Choki Keikai Sakutei Kaigi Shiryo (1999).

2) R. Sakai,et al., Dose Distribution of stereotactic Irradiation for thorax, KEK Proceedings 2000-20, p.100-106 (2000)

3) ICRU: Prescribing, Recording and Reporting Photon Beam Therapy, ICRU Report 50 (1984).

4) W. R. Nelson, H. Hirayama, D.W.O. Rogers: The EGS4 code system, SLAC Report SLAC-265 (1985).

5) K. Saito et al.: The construction of a computed tomographic phantom for a Japanese male adult and the dose calculation system. Radiation and Environmental Boiphysics, 40, 69-76 (2001).

6) D.W.O. Rogers et al.: BEAMnrc user manual, NRCC Report PIRS-0509(A) revG (2002).

7) J. Funabiki,et al.: An EGS4 Monte Carlo user code for radiation therapy planning, KEK Proceedings 2001-22, p.80-86 (2001).

8) Intensity Modulated Radiation Therapy Collaboration Working Group: Intensity-Modulated Radiotherapy, Int. J. Radiation Oncology Biol. Phys. **51**, 880-914(2001).J. H. Rose, et al.: First radiotherapy of human metastatic brain tumors delivered by a computerized tomography scanner (CTRx), Int. J. Radiation Oncology Biol. Phys. **45,** 1127-1132 (1999).

9) H. M. Hossain, et al.: Monte Carlo Simulations for Stereotactic Radiotherapy System with Kilo Voltage X-ray energy, 3th International EGS4 workshop (2004).

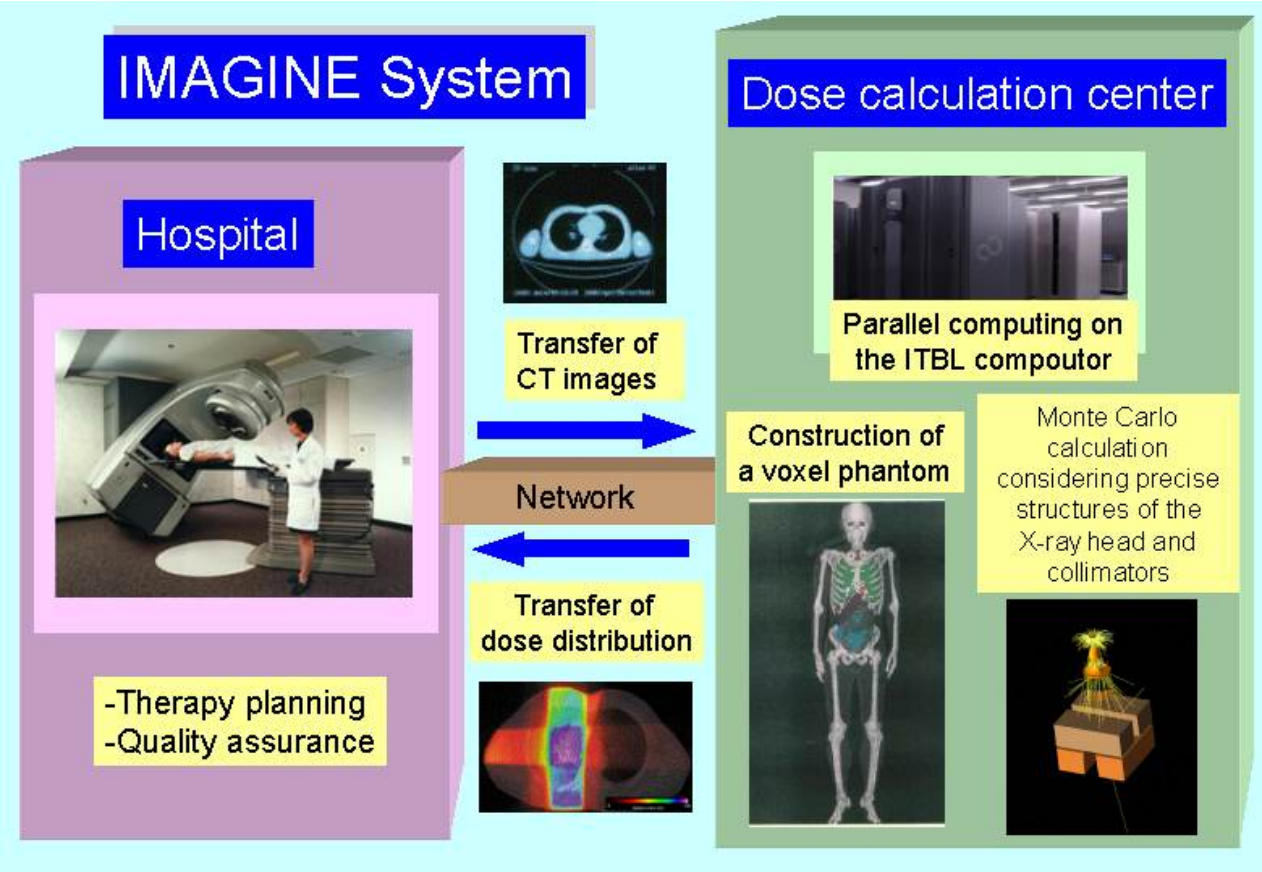

Figure 1 Schematic design of the IMAGINE system.

DEVELOPMENT OF EGS4 USER CODES FOR IMAGINE

S. Takagi[a], J. Funabiki[a], Y. Oyatsu[a], O. Sato[a], K. Saito[b,d], H. Kimura[b,d], M. Hirai[d], H. Saitoh[c,d] and A. Myojoyama[c,d]

[a]Mitsubishi Research Institute, Inc., Tokyo, 100-8141, Japan
[b]Japan Atomic Energy Research Institute, Ibaraki, 319-1195, Japan
[c]Department of Radiological Sciences, Tokyo Metropolitan University of Health Sciences Tokyo, 116-8551, Japan
[d]CREST, Japan Science and Technology Agency (JST), 332-0012, Saitama
e-mail: takagi@mri.co.jp

Abstract

EGS4 user codes were developed to calculate dose distributions in a patient body for the IMAGINE project intending to supports radiation therapy remotely. The codes were designed to provide accurate dose distributions for any postulated therapy cases using with sophisticated patient models and avoiding approximations leading to uncertainties. These user codes will be tuned up to show best performance with parallel computers. They will be implanted in IMAGINE system and connected with other modules, such as the radiation source data base, the human body modeling system, the user interface launching dose calculations and obtaining the results remotely, and commercial treatment planning systems such as FOCUS™ within two or three years.

1. Introduction

The purpose of the IMAGINE system[1)] is the improvement of the quality assurance of radiotherapy being widely performed. For the purpose, the calculated dose distributions with the IMAGINE system are to be reference values which are calculated with the least assumptions. This is the reason why we adopted Monte Carlo method with EGS4 code[2)] as a solver of dose distribution in a human body.

The body of a patient is modeled by voxels of which minimum size is 1mm cubic. The required statistical uncertainty of dose in each voxel is below a few %. A huge number of histories are required to achieve the statistical accuracy in such small voxels, and it will spend a lot of computing time, typically few tens of days with a recent fastest processor. The IMAGINE must return calculated dose distributions to remote users before they begin treatment, thus the computing time allowed will be within a day or hopefully much shorter. It requires to apply some techniques for speed up or acceleration of EGS4 user codes used in the IMAGINE. For the acceleration, the computing time spent in each part of EGS4 was analyzed, and parameters such as energy cut off of each kind of particle are determined. Parallel computing technique was applied for speed up by using the ITBL computer consisting of 512 CPUs located at the Kansai Establishment, JAERI.

In this paper, the software configurations of the IMAGINE system and the developed EGS4 user codes are described first. Then, effects of the parallelization are shown for a prototype user code with a human voxel phantom developed at JAERI. Finally, the test results are shown for the user codes and IMAGINE system with CT data of a rabbit for CTRTx, a tomotherapy system using medium-energy X rays as radiation source.

2. Software configuration of IMAGINE and EGS4 user codes

2.1 Software configuration of IMAGINE

Figure 1 shows the software configuration of the IMAGINE system. The IMAGINE will support any medical facilities using LINAC, and the users are supposed to use commercial radiation treatment planning systems such as FOCUS™, XiO™ etc. These commercial systems will be appropriated for the user interface of IMAGINE to be used by many users without additional experiences. Treatment planning servers are placed at user sites (i.e. hospitals), and convert data from CT machines and treatment planning systems into data used in the IMAGINE system. These data will be sent to the dose calculation center that has fast parallel computers. The dose distributions in patients are calculated with the dose calculation engine installed in the parallel computers.

Figure 2 shows the constituents of the dose calculation engine. Two EGS4 user codes are installed in the dose calculation engine to calculate dose distribution in the body of a patient. UCDSE was developed for electron linear accelerators (LINAC) which are commonly used for radiotherapy. UCCTRTx is for a new radiotherapy system called CTRTx which is under development for stereotactic radiotherapy (SRT) of lung tumors with medium-energy (few-hundred keV) X rays produced by a X-ray tube. Both user codes are based on the prototype version called UCRTP which was developed to calculate the dose distribution in a human body using the voxel phantom developed in JAERI[3]. UCRTP was parallelized with MPI and installed on the ITBL computer. This prototype code was used for the investigation on the effect of the parallelization.

UCDSE can calculate the dose distribution in the patient body considering the change of multi-leaf collimator (MLC) shapes for intensity modulated radiation therapy (IMRT) or 3D conformal radiation therapy. UCCTRTx was tuned to accelerate the calculations for medium-energy photons. Both user codes have the interface for the human body modeling system which creates a voxel model of a patient from CT data. UCDSE is now in development and UCCTRTx has been developed and is in test with rabbit phantom data.

The collimator calculation module is used to simulate photon fluence entering the patient body according to the data on energy, position, and angular distributions of photons at a plane above the MLC stored in the photon source database. The photon distributions in the database are previously calculated using BEAMnrc[4] user code originally developed at NRCC and modified for this system. The correct photon distributions will be obtained based on the procedure called commissioning of LINAC, in which accelerator parameters are adopted to reproduce the measured dose distributions in water phantoms.

2.2 Detail of UCCTRTx user code

UCCTRTx was tuned up to simulate transport of medium- and low-energy electrons and photons efficiently. This code treats the voxel geometry based on CT data, and the minimum voxel size available is about 1mm. The data of material ID and the weight density have been given to each voxel. The weight density is based on CT value, and the following material data are treated in the code.

- Lung
- Adipose
- Muscle
- Bone
- Bone Marrow

The cross sections of above five materials are prepared by PEGS4 previously. The weight density of each voxel used in EGS4 is corrected by the CT value. There are two assumptions or methods to convert CT values to weight densities of above materials.

Method 1: The ratio of the weight density by the CT value (*DMAS_CT*) and the standard density of the material (*DENSIT*) is set to the variable RHOF in EGS4, using with $SET-RHOF macro.

$$RHOF = DMAS\_CT / DENSIT$$

Method 2: The voxel is divided into the void region and the material region by the volume corresponding to

the ratio of the weight density by the CT value (*DMAS_CT*) and the standard density of the material (*DENSIT*).

$$a / (a+b) = DMAS\_CT / DENSIT$$

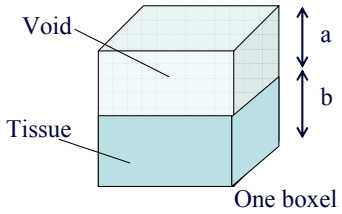

Difference of calculated dose distributions due to the assumptions were significant for low energy photons, and the results using a rabbit phantom are described below.

3. Test Results

3.1 Parallelization

Figure 3 shows the speed up results of the parallelization of UCRTP. In this figure, the speed-up factors are shown as a function of the number of processors. The results of the following two irradiation conditions are shown: (a) 6MV X-ray single port and (b) 6MV X-ray rotation. The total number of histories of each case is 2.56×10^6, and the voxel size is 2x2x2 mm^3. The calculated dose distributions did not depend on the number of used PE (Processor Element) , because UCRTP utlizes the parallelized random number generator called SPRNG[6] and is parallelized for each "batch" loops. The batch is grouped histories which has the same history number. The measured elapsed time ("total" in Figure 3) are divided into three components, CPU time in the batch loop (“batch loop”), the inter-processor communication (“comm.”), and the time to process input and output data (“I/O”). The time in the batch loop is the maximum of CPU time spent in the processors for calculations. The time for “I/O” is a rest part of subtracting "batch loop + comm." from "total".

There are no significant differences in the computing time and the performance between the single port irradiation and the rotation irradiation. The acceleration of the calculation was almost in inverse proportion to the number of PEs, and 63 times or more speed up were obtained with 64-PEs for "batch loop". The time for the inter-processor communication and I/O increases along with the number of PEs used. In the case of 64 PEs, the required time for the communication and the I/O were 20 and 83 seconds respectively, and they were comparable to the time for batch loop, 172 seconds. It is necessary to decrease the processing time for I/O and communications for more efficient parallel calculations with a larger number of processors. The improvements will be performed for the practical version of user codes.

3.2 Test of UCCTRTx with Rabbit CT data

UCCTRTx was tested with actual CT data of a rabbit. Figure 5 shows the CT image of the rabbit. The dose distribution was calculated with the rabbit model created from the CT data which consist of eleven slices with 512×512 pixels sized at 0.158mm square. The voltage of an X-ray tube was 120kV. Figure 4 shows the X-ray energy spectrum from the X-ray tube[5]. The rabbit was rotationally irradiated around the axis of the body. The iso-center of the irradiation was set to the center at the slice of CT data, and the extension of the beam was assumed to be 1 cm from the iso-center. The number of histories was 10000 histories × 100 batches.

Figure 6 compares the dose distributions calculated with the two assumptions of the weight density. The difference due to the weight density assumptions was about 10% at the highest dose point. Assumption 2 is considered to be valid if the tissues are constructed from void and dense material, such as lungs or bones. These assumptions must be carefully applied according to the anatomical knowledge of human organs and tissues for low-energy irradiations.

The relation of electron cut-off energy to computational times spent in each part of simulations were investigated for CTRTx. Table 1 shows the difference of computing time according to the electron cut-off energy and there was no

significant difference of computing time. The lower electron energy cut off can be used in UCCTRTx. Further, it was found that most of computing time is spent in the HOWFAR routine. Table 2 shows the numbers to call the HOWFAR routine. In most cases, the HOWFAR routine was called for the photon transport calculation. Therefore, further speed up can be expected by changing the transport calculation algorithm of the photon of EGS4, using a method to reduce the number of region judgments such as the Coleman's method[7,8].

4. Conclusions

The two EGS4 user codes for the IMAGINE system have been developed, and one of them was tested in the condition similar to actual usages with parallel computers. We found that the speed up of calculations were nearly proportional to the number of processes. For the low-energy photon irradiation, the effect of increasing electron cut-off energy on the speed up was not large. Regional judgments for the photons took place frequently in the calculation, and it required a lot of processing time.

The user codes are going to operate on parallel computers, such as the ITBL computer. We will try to examine the possibility of speed up by the Coleman's method which can reduce the frequency of the region judgment. It is necessary to verify the calculation result by the comparison with the measurement data, carefully considering the conditions that the experiments meet. We also plan to develop the software to properly simulate direct and scattered photons from multi-leaf collimators without spending much time.

All developed user codes will be tuned up to show best performance with parallel computers. They will be implanted in the IMAGINE system and connected with other modules, such as the radiation source data base, the human body modeling system, the user interface launching dose calculations and obtaining the results remotely, and commercial treatment planning systems such as FOCUS™ within two or three years.

References

1) K. Saito, in the Proceedings of the Third International EGS4 Workshop(2004)

2) W. R. Nelson, H. Hirayama, D. W. O. Rogers: The EGS4 code system, SLAC Report SLAC-265 (1985).

3) K. Saito, A. Wittmann, S. Koga, Y. Ida, T. Kamei, J. Funabiki and M. Zankl, Construction of a Computed Tomographic Phantom for a Japanese Male Adult and Dose Calculation System, *Radiat. Environ. Biophys*. 40, 69-76 (2001).

4) D.W.O. Rogers, B. Walters and I. Kawrakow, *BEAMnrc User's Manual*, NRCC Report PIRS-0509 (2004).

5) D. Hossain, private communication.

6) http://sprng.cs.fsu.edu/

7) R.Kramer, Determination of Conversion Factors Between Tissue Doses and Relevant Radiation Quantities for External X and Gamma Radiation, GSF-Report-S-556, 1979.

8) W.A.Coleman, Mathematicla Verification of a Certain Monte Carlo Sampling Technique and Applications of the Technique to Radiation Transport Problems, NSE, 32, 1968.

Table 1　Difference of computing time according to the electron cutoff energy.

electron cutoff energy	10 keV	1 MeV
computing time [sec]		
total	359	338
in HOWFAR	156	147
in AUSGAB	69	68
in SOURCE routine	3.7	3.7

Table 2: Number of calculation steps

No.	Material	Number of steps (include voxel boundary crossing)		
		Photon	Electron	Total
2	Lungs	10,354,554 *(98.9%)*	119,950 *(1.1%)*	10,474,504 (5.3%)
3	Fat	29,391,103 *(97.3%)*	801,577 *(2.7%)*	30,192,680 (15.3%)
4	Muscle	55,678,635 *(95.0%)*	2,955,314 *(5.0%)*	58,633,949 (29.8%)
5	Marrow	704,934 *(96.6%)*	24,584 *(3.4%)*	729,518 (0.4%)
6	Bone	2,508,443 *(57.9%)*	1,821,628 *(42.1%)*	4,330,071 (2.2%)
7	Air(vacuum)	92,540,033 *(99.99%)*	12,738 *(0.01%)*	92,552,771 (47.0%)

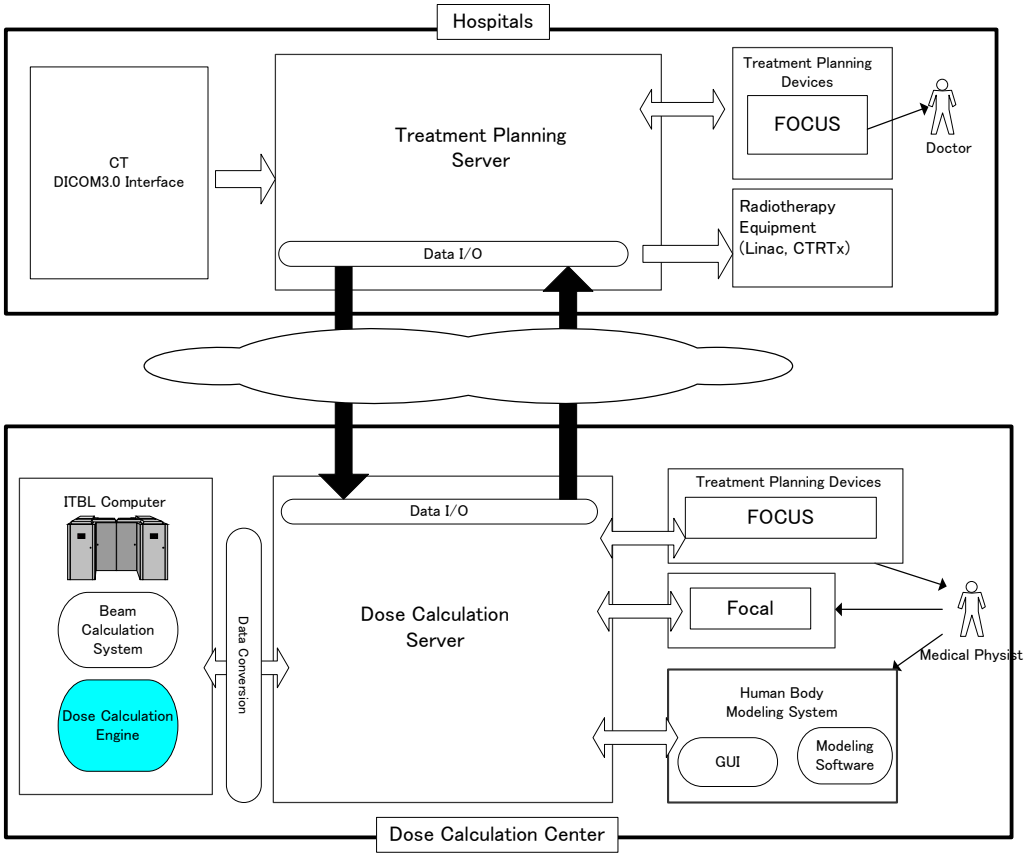

Figure 1: Overview of IMAGINE Software

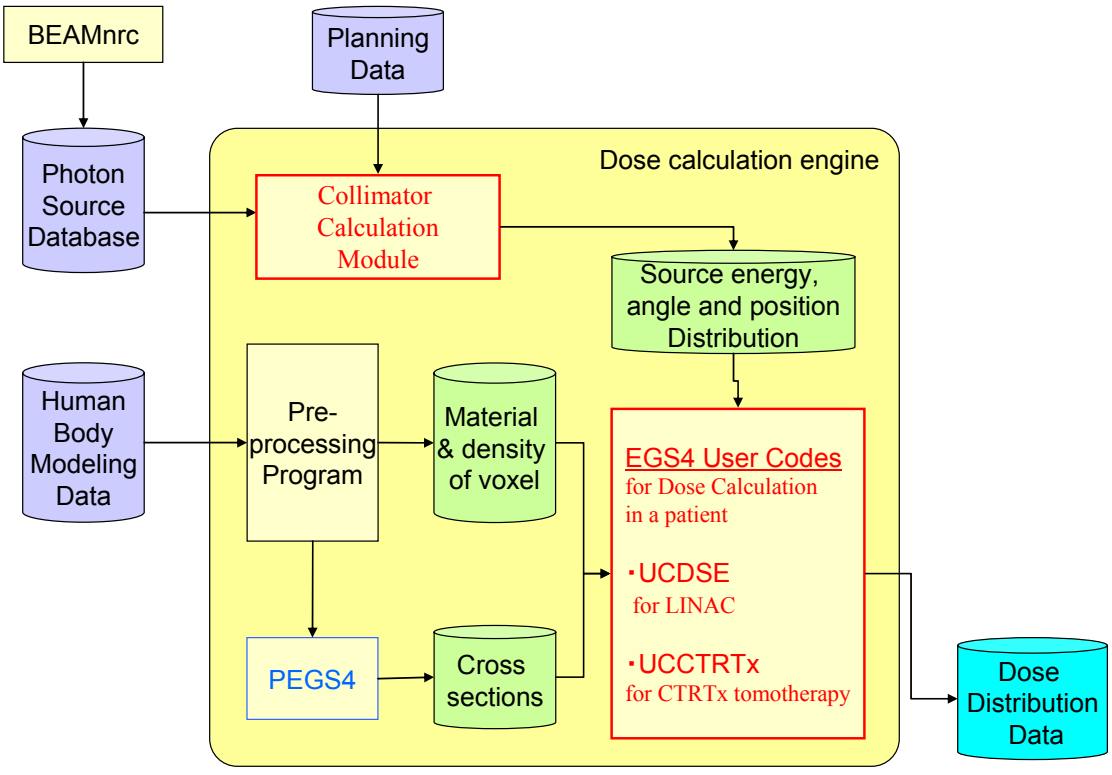

Figure 2: Flow of the Dose Calculation Engine

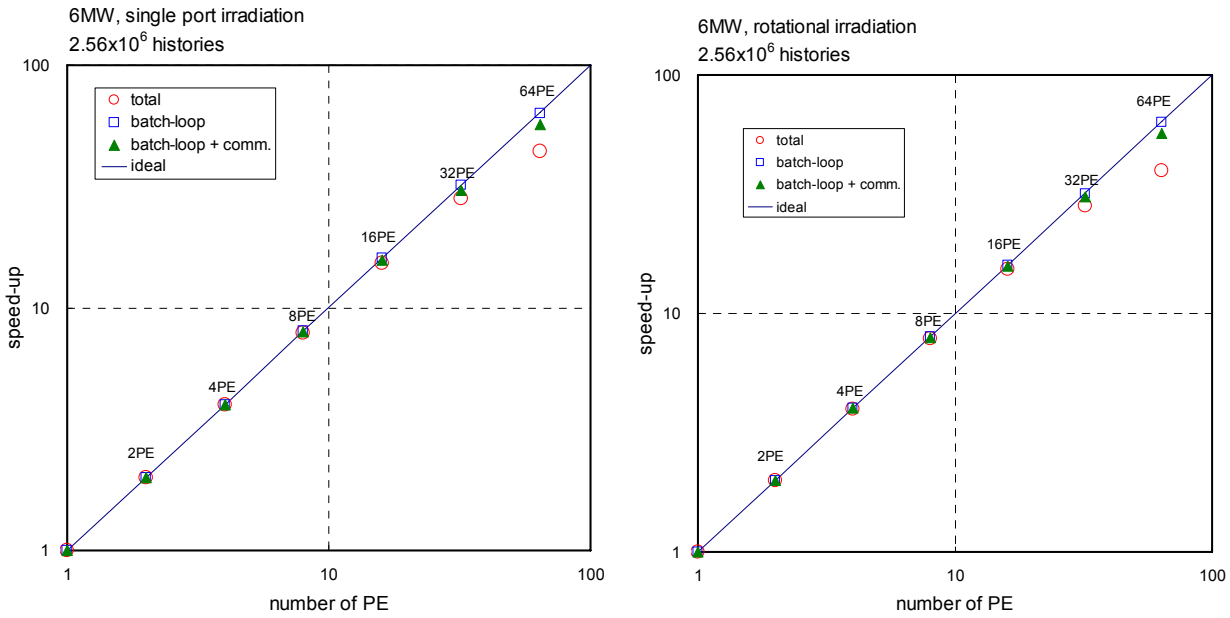

(a) 6MV single port (b) 6MV rotation

Figure 3: Parallelization Results by the two different irradiation conditions

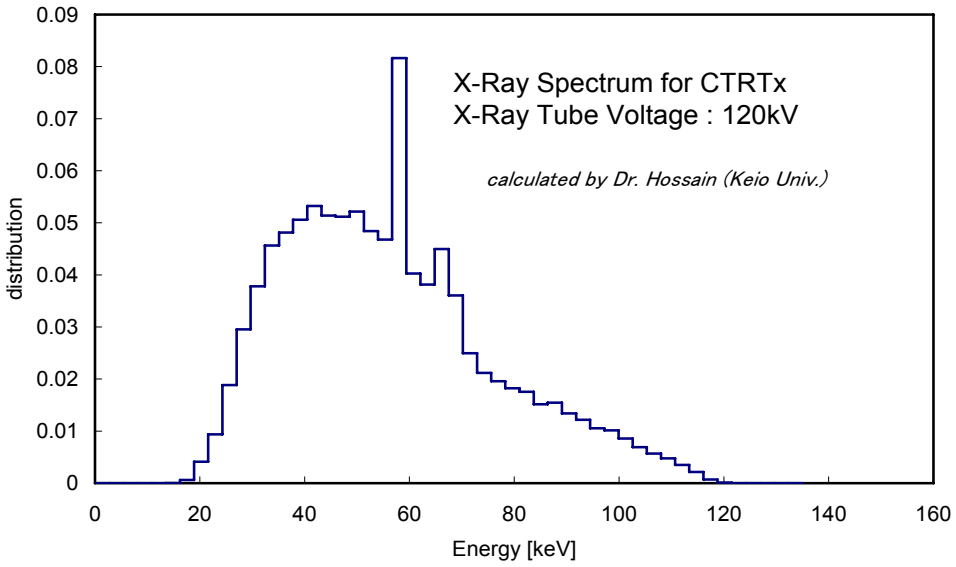

Figure 4: X-ray spectrum from the 120kV X-Ray Tube for CTRTx

Figure 5: CT image of the rabbit drawn by a treatment planning system.

Colored lines were used for markings and not used to create the model for dose calculations.

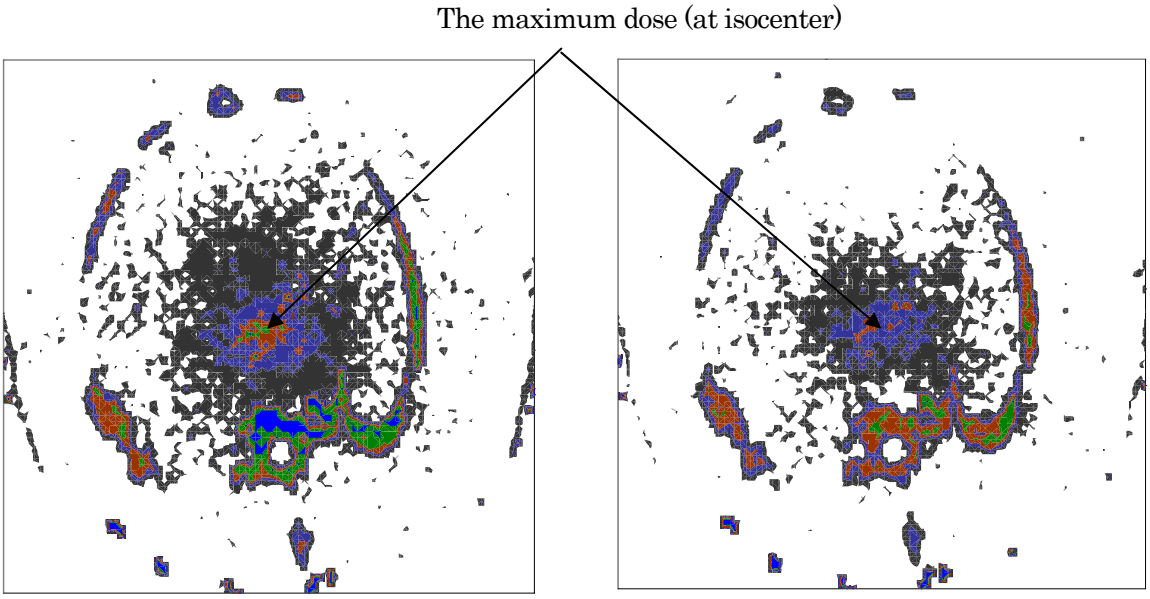

(a) Method 1 (b) Method 2

Figure 6: Dose distribution of the rabbit voxel model by the two methods for the weight density correction.

The maximum dose with method 1 was 10% higher than those with method 2.

Optimal Parameters for Energy Spectral Calculations of Mega Voltage Photon Beam Using Monte Carlo Simulations

Atsushi Myojoyama[1,5)], Hidetoshi Saitoh[1,5)], Tatsuya Fujisaki[2,5)], Yuichiro Narita[3,5)], Kimiaki Saito[4,5)]

1) Tokyo Metropolitan University of Health Sciences, Tokyo, Japan
2) Ibaraki Prefectural University of Health Sciences, Ibaraki, Japan
3) Chiba Cancer Center, Chiba, Japan
4) Japan Atomic Energy Research Institute, Ibaraki, Japan
5) JST, CREST, Tokyo, Japan

Abstract

For the Convolution, Superposition and Monte Carlo methods, energy spectrum data is an essential parameter. Especially, by using Monte Carlo method, if the adequate properties of electrons are set, complex energy spectrum data can be calculated by simple input. However, adjustment of the property of electrons incident on the target of linear accelerator is time-consuming procedure. To cover the difference of many accelerators, it is important how we obtain accurate energy spectrum by simple methods. Especially, the total accuracy of dose calculation depends on the agreement of measured and calculated percentage depth dose (PDD) and off-axis ratio (OAR). Thus, a simple method for the determination of the simulation parameters was considered. To reduce the adjustment procedure, we selected values of important three parameters, which were the mean energy of the input electron beam, the energy distribution of the input electron beam and the radial distribution of the electron beam. The mean energy of the incident electron beam was determined by two equations and compared. The three parameters were applied to the properties of incident electrons, and PDDs and /or OARs were calculated. Then they were compared to the measured those. The calculated PDDs by adjusting only mean energy of the input electron beam could not be matched to the measured PDDs at small fields, such as the field size of 3x3 cm. On the other hand, by adjusting selected two parameters, calculated PDDs could be matched to the measured PDDs for a wide range of field size. And the radial distribution of the electron beam influenced OARs.

1 Introduction

The present radiotherapy needs high accuracy. For accurate radiotherapy, more accurate dose distributions are required. Convolution, Superposition and Monte Carlo are well known as accurate dose distribution calculation methods. For the Convolution, Superposition and Monte Carlo methods, energy spectrum data is an essential parameter. Especially, by using Monte Carlo method, if the adequate properties of electrons are set, complex energy spectrum data can be calculated by simple input. However, adjustment of the property of electrons incident on the target of linear accelerator is time-consuming procedure. To cover the difference of many accelerators, it is important how we obtain accurate energy spectrum by simple methods. Especially, the total accuracy of dose calculation depends on the agreement of measured and calculated percentage depth dose (PDD) and off-axis ratio (OAR). The first advantage of the Monte Carlo method is that the accurate energy spectrum data can be calculated by a simple energy spectrum input. The second advantage is that the energy spectrum can be generated not only in the central part of beam, but also simultaneously in regions away from it.

Fig. 1 describes a diagram of accelerator head and the variations of the energy spectrum. When accelerated electrons enter the target, bremsstrahlungs are generated in the target. The photon energy spectrum distribution varies due to target material and thickness. The photons pass and/or interact with the primary collimator and flattening filter. From flattening filter, scattered photon, secondary electron and positron are added to the beam. Finally, at beam collimating jaw and multi leaf collimator, scattered photon and electron are added to treatment beam. Thus, spectrum of treatment beam is complicated.

In order to calculate the energy spectrum with Monte Carlo method, it is necessary to reproduce the actual accelerator faithfully on computers. Generally, it is known that PDD of within 1% of error is gener-

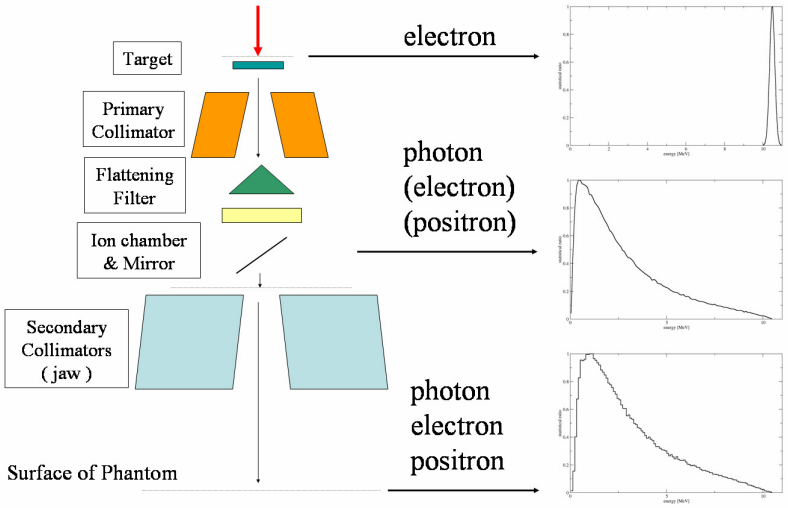

Fig. 1 The diagram of an accelerator head and the variation of the energy spectrum at each position

able when an accelerator is designed accurately. However, there are slight differences in the realistic accelerators that currently installed in hospitals etc., and the trials of a lot of frequencies are needed to reduce those differences. On the other hand, those differences appear in OAR notably. Therefore, strictly fitting calculated OARs to measured OARs leads to the calculation of the accurate energy spectra of realistic accelerators.

In this study, optimal parameters for accurate energy spectrum calculation were introduced. These parameters were very sensitive to Monte Carlo calculations to generate accurate energy spectrum. The calculated data that had applied several parameters were compared to measured PDD and OAR. Then, by analyzing the difference between calculated and measured data, optimal parameters were determined. The study to obtain the accurate in-air off-axis factors for average accelerators was described by D. S. Bagheri and D. W. O. Rogers [1]. In this study, the important three parameters for energy spectrum calculations were selected from the parameters that described in [1].

2 Material and Methods

In the Monte Carlo for dose calculations in water including accelerator head simulations, the important simulation parameters to obtain an accurate dose distributions are almost the behaviour of the electrons which incident to the target.

It is an iterative process to determine a consistent set of simulation parameters (i.e. electron beam energy and radial distribution of the incident beam). First, the simulation was run by starting with the manufacturer's specifications or suggestions for these parameters. If this didn't lead to a strict match of the PDD or OAR values, one then adjusted the incident electron mean energy and the energy distribution of the incident electron beam to match the calculated PDD to measured PDD. Once this was matched, the radius of the incident radial distribution was varied to get a match with the OAR. If a match cannot be achieved, it was necessary to re-adjust the mean energy somewhat to achieve agreement with the OAR. Once this agreement was satisfactory, it was essential to verify that the PDD was still matched adequately since the incident mean energy had been changed.

This section describes how the PDD and OAR values were calculated and compared with measurements.

2.1 Monte Carlo Parameters for PDD Calculations

According to the reference [1], both PDD and OAR were very sensitive especially to the three parameters; the mean energy of the electron beam, the energy distribution of the electron beam and the radial intensity distribution of the electron beam. Fig. 2 shows the relations of those three parameters at the surface of the target. In Fig.2 (1) is the mean energy of the incident electron beam. This is a mean of kinetic energy of the electrons immediately before the incidence in the target. Fig.2 (2) is the energy distribution of the electron beam. This shows the extension of the kinetic energy of the electron immediately before the target. Fig. 2 (3) is the radial distribution

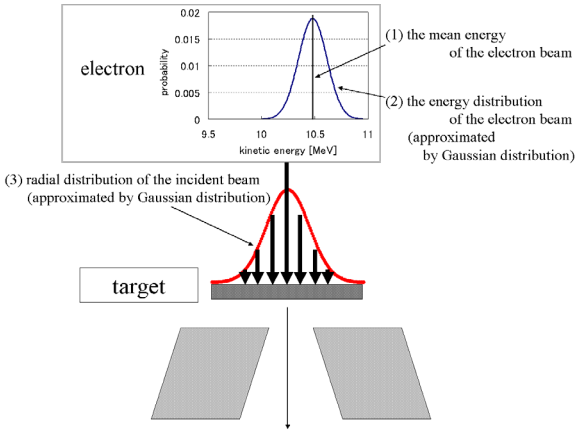

Fig. 2 The relation of the three parameters for the electron which incident to the target. (1) The mean energy of the electron beam, (2) the energy distribution of the electron beam and (3) the radial distribution of the incident beam

of the incident beam. This parameter shows the probability that an incidence electron extends from center of the target to radial. The probability of the point of an electron incident to the target was approximated Gaussian model.

To start Monte Carlo simulations, at first, the determination of the mean energy of the electron beam was required. Then, the following three kinetic energies of electrons were tested. The first was the nominal kinetic energy that was manufacturer's specification. The second was the kinetic energy that was calculated by LaRiviere's equation [2]. This equation is shown as follows,

$$E = 10^{(D_{10}-46.78)/26.09} \quad (1)$$

where E is the mean kinetic energy of electron and D_{10} is the PDD value of 10×10 cm^2 field size and the 10 cm depth from water surface. Because our measured data were PDDs, it was possible to apply this equation easily. The third was the kinetic energy that was calculated by the equation as follows,

$$E = 0.01391\times10^{0.039164\times D_{10}} \quad (2)$$

where E and D_{10} are the same to the above mentioned. This equation is proposed by Hiraoka [3].

Next, the energy distribution of the electron beam was considered. In general, the electron energy spectrum isn't symmetrical distribution for realistic accelerators. However, we used the model that approximated simply by the Gaussian distributions in this study.

2.2 Monte Carlo Parameters for OAR Calculations

The above-mentioned two parameters were changed and OAR was calculated by using the parameters that matched to the measurements most among obtained PDDs. In the calculation of OAR, the third parameter, the radial distribution of the incident beam was introduced.

In this study, this parameter was approximated by Gaussian distribution model. The FWHM was varied from no distribution to 4 mm. Then the output OARs were compared with measured OAR.

2.3 Calculation Tools for Accelerator Head Simulations

In this study, BEAMnrc code system was used for energy spectrum calculation of accelerators [1] [4]. The BEAMnrc code system is a general purpose EGS user-code for the simulation of radiotherapy beams, especially those from linear accelerators. The code has been widely used to simulate electron, positron and photon beams. The advantage of BEAMnrc code system is that all dimensions and materials of the linear accelerator, as well as the incident electron beam energy and spatial intensity distribution can be specified independently and did not need to be derived from dose measurement. The BEAMnrc code is able to output the description of particles, it is called "phase-space file". The Phase-space file contains data relating to particle position, direction, charge, etc. for every particle crossing a scoring plane. Phase-space file can be output for each scoring plane in an accelerator, and can be used as an input of BEAMnrc code.

In this study, the two phase-space data were produced in the accelerator that constructed strictly on the computer. One was at the front of secondary collimators (phase-space1), and the other was just before the phantom surface (phase-space2). The phase-space1 was calculated by field size of 40×40 cm^2 to cut the influences of back scatter from the secondary collimators. By using this method, if the incident electron parameters didn't change, the same phase-space1 could be used in different field sizes. Then, the phase-space2 was calculated by using the phase-space1 as the input data. From the obtained phase-space2, the energy spectrum could be generated by using BEAMDP sub code [5].

2.4 Calculation Tools for Dose Distribution Simulations

To calculate dose distributions in water, DOSXYZnrc code was applied [6]. DOSXYZnrc is an EGSnrc-based Monte Carlo simulation code for

calculating dose distributions in a rectilinear voxel phantom and is based directly on the DOSXYZ code developed for the EGS4 code system [5]. This code is able to simulate the 3D dose distribution in phantom by input of simple particle data, energy spectrum data and phase-space data. By using this code, the water phantom of the size of 40×40 ×35 cm^3 (x, y, z:depth) was constructed in the computer. The inside of water phantom was divided by voxel size of 2×2 ×2 mm^3 at all region. The PDD and OAR were obtained by editing the output value by using the statdose sub code in DOSXYZnrc code [6].

In this study, no variance reduction technique was used because we aimed to recognize the slight differences of output PDDs or OARs by changing the three parameters. And, to our regret, we had not understood enough the influence given to the output value when these were used. Thus, to obtain better than 1% uncertainty, more enough histories of the input particles were needed than the needs of standard calculations.

2.5 Matching PDD and OAR

The calculated PDD and OAR should be compared strictly with the measured those. In this study, to evaluate the error margin equally by the comparison between a small value and a big value, the relative error was applied. The relative error (*RE*) was defined as,

$$RE = \frac{Val_c - Val_m}{Val_m} \quad (3)$$

where Val_c was calculated value and Val_m was measured value. All the results of the calculation were compared by this equation.

The measured PDD and OAR were the values that were detected by ion chamber. So these were the values that averaged the range of the detector's diameter. Therefore, calculated values were required to average by the diameter of the detectors. These differences were shown notably at the penumbra of OAR. In our case, averaging the range of 4 mm or 6 mm was required.

2.6 Computational Conditions

These codes were running on a cluster system. This cluster system was consisted of 12 PCs that each computer was mounted two CPUs with Symmetric Multiple Processor (SMP) and Hyper Threading (HT) technology was enabled. By using HT technology, two threads or tasks could be executed at the same time. Thus, theoretically, 48 parallel processing were available. Nevertheless, in this study, because the decrease at the processing speed was observed in 48 parallels, then 36 parallels were permitted. Each cluster was operated by Generic NQS for batch system.

2.7 Simulation Conditions

Two types of accelerators were simulated. The first accelerator had the nominal kinetic energy of 6 MeV, and the second had nominal kinetic energy of 10 MeV. Both of these accelerator heads were constructed strictly in the computer.

In the 6 MV accelerator simulations, only PDD was calculated. The water phantom was used by both measured and calculated PDD. The source-surface distance (SSD) was 100 cm. At first, the PDD of 10×10 cm^2 field size was calculated. In this study, the three mean kinetic energies of incident electrons were decided to 6.0 MeV of nominal energy, 6.1 MeV that was derived by Eq. (1) and 6.2 MeV that was derived by Eq. (2). Each PDD was calculated by 300 million histories. These conditions were described in Table 1. Each calculated PDD was compared to measured

Table 1 Simulation conditions (6 MV X-ray)

	measurement	simulations
material	water	water
SSD	100 cm	100 cm
field size	3×3, 10×10, 20×20 cm^2	
electron-beam mean energy	6 MeV (nominal)	6.0, 6.1, 6.2 MeV
history	----------	300 millions
accelerator	Mitsubishi EXL-15DP 6MV X-ray	
compared data	PDD	

Table 2 Simulation conditions (10 MV X-ray)

	measurement	simulations
material	water	water
SSD	100 cm	100 cm
field size	4×4, 10×10, 20×20 cm^2	
Kinetic enegy of electrons	10 MeV (nominal)	10.48 MeV
history	----------	2 billions
accelerator	Varian Clinac EX21 10MV X-ray	
compared data	PDD and OAR	

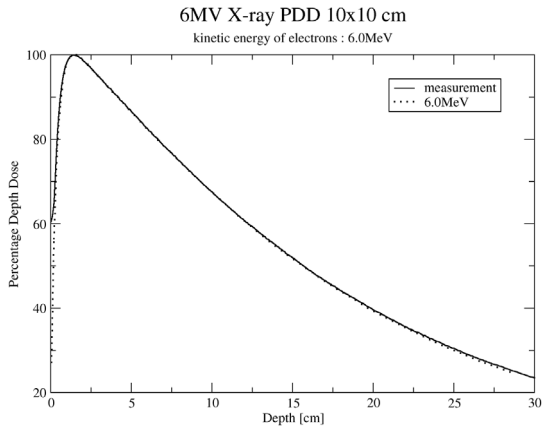

Fig. 4 The calculated PDD that was introduced by 6.0 MeV incident electrons

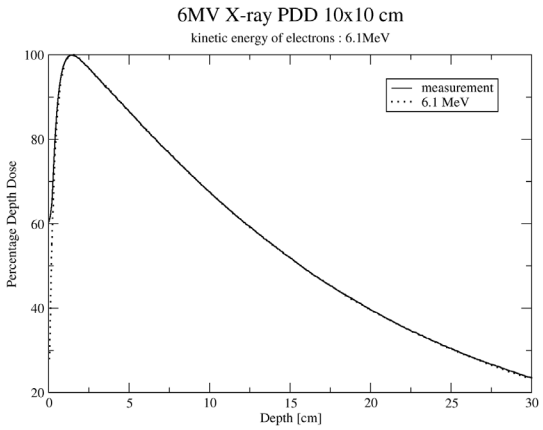

Fig. 5 The calculated PDD that was introduced by 6.1 MeV incident electrons

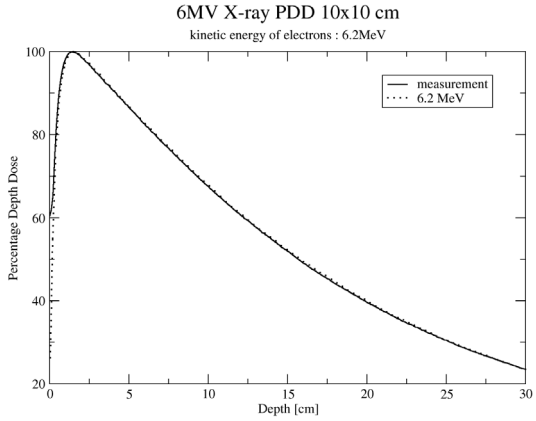

Fig. 6 The calculated PDD that was introduced by 6.2 MeV incident electrons

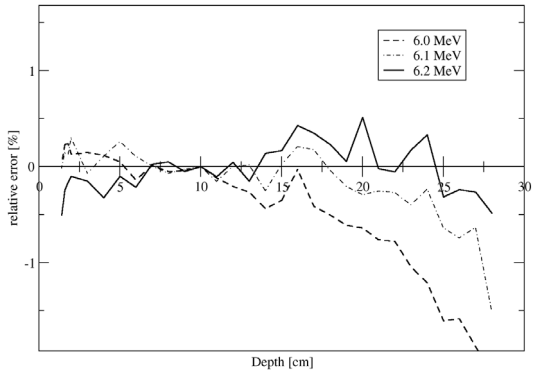

Fig. 7 The relative errors of PDDs of three mean kinetic energies

PDD. The PDD of 3×3 cm^2 and the PDD of 20×20 cm^2 were simulated by using the parameters of deriving the most corresponding calculated PDD of 10×10 cm^2 to the measured PDD of 10×10 cm^2. Next, the PDD of each field size were simulated in using the input electron with the energy distribution of FWHM of 3 % in the mean electron energy.

In the 10 MV accelerator simulations, PDD and OAR were calculated. The process to obtain the optimal parameters for PDD calculation was same as the case of the 6 MV accelerator simulations. The condition of the 10 MV accelerator simulations was described in Table 2. In this study, because the same mean energy was derived by Eq. (1) and Eq. (2), the mean energy of the electron beam was decided to 10.48 MeV. And each OAR was simulated by 2 billion histories. After the optimal values of two parameters were decided, the parameter of the radial distributions of the incident beam was added to the OAR simulations. The OARs were calculated in the case of no distributions, FWHM of 0.15 cm and FWHM of 0.4 cm. If the optimal value of this parameter was decided, The three parameters were applied to the OAR calculations of the two different field sizes that were 4×4 cm^2 and 20×20 cm^2. Those results were compared with the measured OARs of each 2.5, 7.5, 12.5, 17.5, 22.5 and 27.5 cm depth.

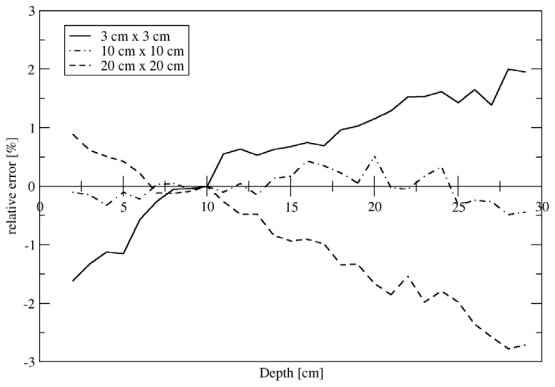

Fig. 8 The relative errors of the PDDs of the different field sizes (non energy distribution)

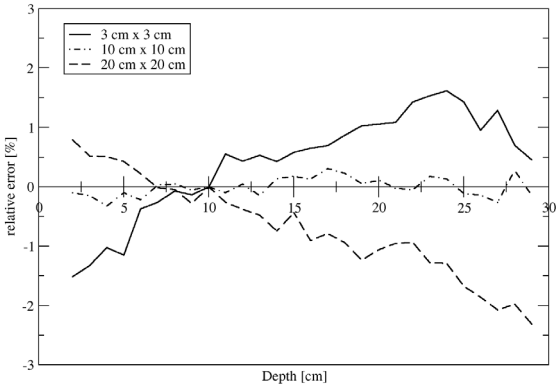

Fig. 9 The relative errors of the PDDs of the different field sizes (FWHM of 3% of energy distribution)

3 Results and Considerations

3.1 Results of the 6 MV Accelerator

Fig. 4 to Fig. 6 showed the variation of the calculated PDDs by the difference of the mean energy of electrons. From these figures, it was almost impossible to recognize the difference with measured PDD. Then, the relative error of each calculated PDD was shown in Fig 7. According to Fig. 7, specifically, the 6.2 MeV PDD was confirmed that the relative errors were the smallest and the all of the relative errors were within 1%. Thus, from this in the following calculation, the mean energy of the electrons was assumed to be 6.2 MeV. The relative errors with the measurement PDD of calculated PDD by the change in the field sizes were shown in Fig. 8. Fig. 8 showed that the relative error of the PDD of 3×3 cm^2 , the PDD of 10×10 cm^2 and 20×20 cm^2. In Fig. 8, the relative error increased by two field sizes except the PDD of 10×10 cm^2 and those exceeds 1%. Then, the relative error of PDD that had been obtained by the calculation that applied the second important parameter, the energy distribution of the electron beam, was examined for the same field size.

In Fig. 9, though the relative error reached a small value overall, the relative error still exceeded 1% at the deep of the water phantom. The energy distribution of 7 % FWHM was also tested. Then the relative errors decreased. However, the degree of decrease was smaller than in the case of 3%. As these results, it was suggested that there was a difference in a fundamental part. Therefore, in this accelerator simulation, OAR simulation didn't execute. Though, by adding the energy distribution, the relative error decreased overall. At the point of this, the energy distribution of the electron energy was an effective parameter.

3.2 Results of the 10 MV Accelerator

The calculated PDD of 4×4 cm^2, 10×10 cm^2 and 20×20 cm^2 were compared to the measured them. These results were shown in Fig.10. In the simulation of this accelerator, the calculated PDD in all the field sizes matched to measurement PDD very well. In addition, the statistical uncertainty of all the areas in the phantom was all much smaller than 1% according to the simulation by an enough history. The energy distribution of the electron beam was determined to 3% by three trial of the head simulation.

Next, by using decided parameters, the OARs were simulated. Fig. 11 showed that the calculated OAR of 10×10 cm^2 at the depth of 2.5 cm was compared to the measured OAR. In the OAR simulation, third parameter, the radial distribution of the incident beam was examined. In the case of no distribution, dose at the central axis was relatively decreased. In the case of FWHM of 0.15 cm, almost the same dose at the central axis and at the near the penumbra, and this FWHM was the best value to match with the measured OAR. In the case of FWHM of 0.4 cm, dose at the central axis relatively increased. Then, the calculated OAR of 20×20 cm^2 and 4×4 cm^2 were compared to the measured OARs. These were shown in Fig. 12 and Fig. 13. Both OARs were well agreed with the measured OARs. On the other hand, because the measured OAR was slight asymmetrical with respect to the central axis, there were the regions that the relative error wasn't within 1%.

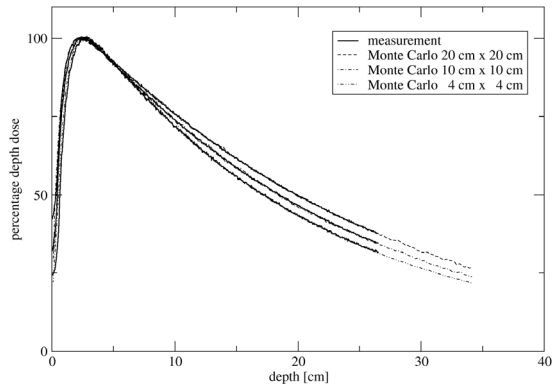

Fig. 10 Comparison between the calculated and measured PDDs

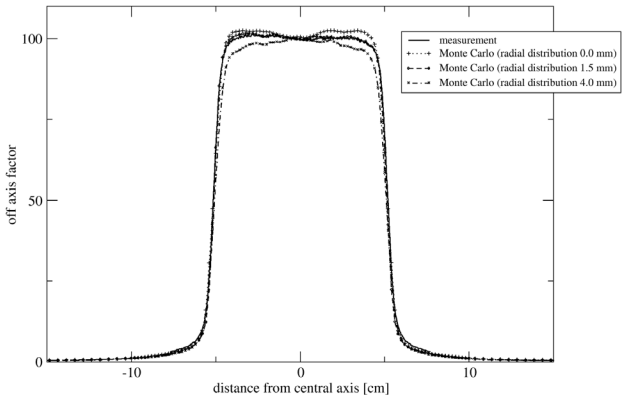

Fig. 11 Comparison between 10×10 cm^2 measured and calculated OARs with the radial intensity distributions

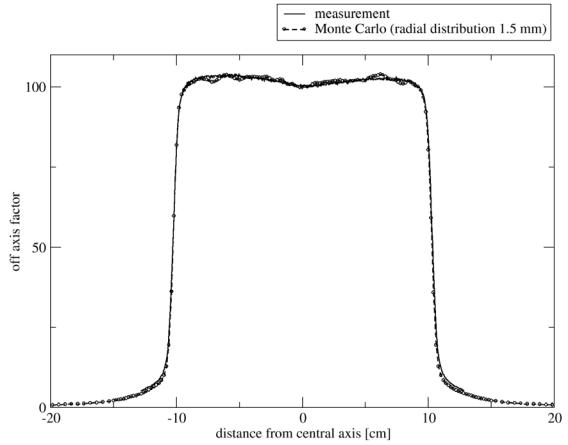

Fig. 12 Comparison between 20×20 cm^2 measured and calculated OARs

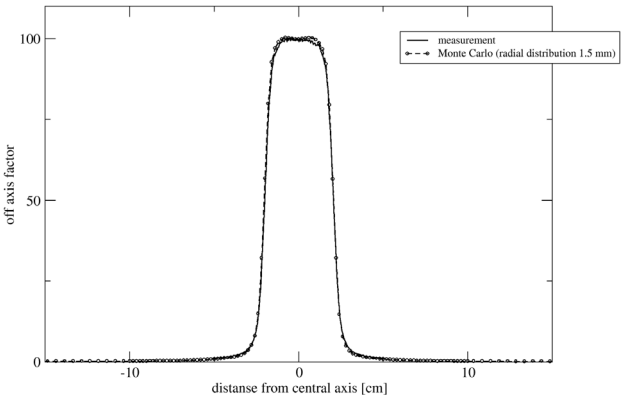

Fig. 13 Comparison between 4×4 cm^2 measured and calculated OARs

4 Conclusions

The purpose of our study was to reduce the parameters for adjustment of the property of electrons incident on the target and to obtain highly accurate energy spectrum by simple method. In this paper, we paid attention to the three Monte Carlo parameters; the mean energy, energy distribution and the radial distribution of the incident beam. Both of PDD and OAR were very sensitive to the mean energy of the electron beam and the energy distribution of the electron beam. The radial distribution of the incident beam notably influenced OAR properties.

5 Literature

[1] D.S.Bagheri and D.W.O.Rogers: Sensitivity of megavoltage photon beam Monte Carlo simulations to electron beam and other parameters : Med Phys.,Mar, 29(3), pp.379-390, 2002

[2] LaRiviere PD: The quality of high-energy X-ray beams : Brit. J. Rad., 62, 473-481, 1989

[3] Takeshi Hiraoka: Appendix 14, Stanard Dosimetry of Absorbed Dose in External Beam Radiotherapy, edited by Japan Scociety of Medical Physics : pp.170-171, Tsusho-Sangyo Kenkyu-Sha, Tokyo, 2002

[4] D.W.O. Rogers, C.-M.Ma B.Walters et al.: : BEAMnrc Users Manual : NRCC Report PIRS-509(A)revF, 2001

[5] C.-M.Ma, D.W.O. Rogers: BEAMDP Users Manual: NRCC Report PIRS-509(C), 1999

[6] D.W.O. Rogers, C.-M.Ma B.Walters et al.: : DOSXYZnrc Users Manual : NRCC Report PIRS-509B(revF), 2001

SOFT TISSUES IN THE PATIENT DIGITIZATION FOR THE MONTE CARLO RADIOTHERAPY TREATMENT PLANNING

Masaaki Hirai[a,b], Jun Funabiki[c], Shunji Takagi[c], Hidetoshi Saitoh[b,d] and Kimiaki Saito[a,b]

[a]Center for Promotion of Computational Science and Engineering, Japan Atomic Energy Research Institute, Tokai-mura, Ibaraki, 319-1195, Japan
[b]CREST, Japan Science and Technology Agency, Kawaguchi, Saitama, 332-0012, Japan
[c]Research Center for Safety Science, Mitsubishi Research Institute, Chiyoda-ku, Tokyo, 100-8141, Japan
[d] Department of Radiological Sciences, Tokyo Metropolitan University of Health Sciences, Arakawa-ku, Tokyo, 116-8551, Japan
e-mail: m_hirai@riskest.tokai.jaeri.go.jp

Abstract

A preliminary study about the advantage of the multiple composition patient model to the traditional single composition model for the dose distribution calculation in the radiotherapy treatment planning was performed. We have developed a prototype dose calculation code UCRTP with based upon EGS4. We also employed two CT-based anthropomorphic voxel phantoms. The organs and tissues in the phantoms were categorized into six groups, skeleton, lungs, skin, muscle and other organs, adipose tissues and the target, and we calculated the X-ray irradiation simulation with replacing the materials corresponding to lungs, skin, muscle and other organs and adipose tissues. Comparing D_{mean} among the composition models, the deviation between the most detailed model (ICRU lung, ICRU skin, ICRU adipose tissue and ICRU skeletal muscle) and the most simple model (liquid water) was up to 1.2 % for the X-ray tube spectrum, and up to 0.5 % for linac X-ray spectrum. Though these deviations themselves were quite small, it is necessary to study further to conclude the advantage of the multiple composition model because the other aspects like the dose uniformity were out of the scope at present.

1. Introduction

In the external radiotherapy, calculation of accurate dose distribution in a patient body is essential to achieve the tumor control and to avoid the complications of the healthy tissues and organs. However, performing these calculations with good accuracy takes much computing time so that most of clinically implemented treatment planning systems utilize simple and analytical algorithms which do not thoroughly account for the electron non-equilibrium due to the tissue inhomogeneities in a patient body, or the ratio of the partial cross sections of photon-electron reaction.

In recent years, the drastic advancement of the computing power and parallel computing techniques enables us to perform the Monte Carlo radiation transport calculation, which can provide the result of best accuracy, for obtaining the dose distribution in a patient body. At present, they begin to be utilized for the

quality assurance of the linac and beam delivery systems, and are considered as very promising. In near future, the further advancement of the computing technology may enable us to utilize the radiation transport codes for the routine treatment planning widely.

IMAGINE (IT-Based Medical Aiding Gear for Instantaneous Numeration of Energy deposition distribution) project has been started in autumn, 2002[1]. The aim of this project is to develop an accurate and high-speed Monte-Carlo dose distribution calculation system employing large scale parallel computing technique (100 ~ 1000 CPU) in order to provide a reference dose calculation tool to the medical physicists, or someone who is responsible for the quality assurance of the treatment planning system in remote hospitals.

Because the IMAGINE is intended to provide doses with the best accuracy for any irradiation condition, we need to select sufficiently detailed models and parameters. The whole system of the external radiotherapy can be considered as three individual parts: the beam model, the models of beam modification devices and the patient model. The former two parts have been well studied because they are useful to the quality assurance of the treatment devices. The studies about the patient model is, on the other hand, still rarely performed because the quality assurance of the treatment planning system was not considered as important until the modern beam delivery technique, like 3D-CRT (conformal radiotherapy) or IMRT (intensity modulating radiotherapy) was widely employed. In addition, the new technology of CT radiotherapy system, which irradiates tube X-ray from the multiple arcs to the target, is under developing by Keio University and Toshiba, in parallel with IMAGINE system. Due to the low energy of the tube X-ray, the effects of the tissue compositions are more important in the CT radiotherapy than those in the linac radiotherapy.

The patient modeling can be basically understood as a 2D or 3D image filter converting X-ray CT images or the images of other modalities into the geometrical input data to the radiation transport calculation. In the traditional patient model, each voxel (volume element) has a single parameter, electron density, and all the materials were supposed as water-equivalent. However, the branching ratio of photon-electron interaction processes in the materials varies depending on the elemental compositions of the materials. Some of Monte Carlo dose calculation codes employ the patient model that consist of a weight density map and an elemental composition map and a similar patient model will be employed to our IMAGINE system also. However, the advantage of multiple composition models was not discussed quantitatively.

In recent years, the advancement of medical image processing technique related to the computer aided diagnosis enabled us to create more detailed patient model automatically or semi-automatically so that the correlation between the degree of detail in the patient model and the dose calculation accuracy was be studied. We surveyed the advantage of the multiple soft tissue compositions model to the dose calculation accuracy, focused on the target dose and soft tissues substitution.

2. Materials and Method

2.1 Voxel Phantoms

Voxel phantoms, the computer phantoms which consists of a number of small rectilinear voxels (volume elements) of an identical shape, have been developed and widely used for the radiation protection dosimetry and the basic study of medical imaging. In this study, we have employed two voxel phantoms originally planned to be used in the radiation protection studies: The phantom of Japanese male adult 'otoko' (170 cm height, 65 kg weight) and the Japanese female adult phantom 'onago' (162 cm height, 57 kg weight, a slice was shown in Figure 1) developed by JAERI in collaboration with GSF [2,3]. These are based upon the whole-body X-ray CT images. Each slice of the CT images included 512 x 512 pixels with dimensions of 0.98 x 0.98 mm^2 and a slice thickness of 10 mm. The voxels in phantoms were the same shape as the CT pixels so that the voxel volume was around 9.5 mm^3.

These phantoms are described by the format developed in GSF. In this format, each phantom consists of two text files. One is for describing region index number (ID) that represents the tissues or organs the voxel belongs to. The other is for describing the CT value only for the skeletal voxels. All the skeletal voxels are supposed to be a mixture of cortical bone and bone marrow, with its ratio determined by the interpolation of CT-value. These voxel phantoms have no density information in themselves, which is supplied by external files. Thus every region except the skeleton has uniform density distribution in the voxel phantoms. Note that this is not a naïve extension of traditional patient model which has density information in every non-air voxels. In order to save the computer memory, the run length compression is applied to the region ID map and the CT map. As a result, the file sizes were reduced to around 5 to 8 megabytes for each file, while that of 2-byte-per-pixel base CT images are 90 megabytes in total.

We modified the original phantoms in two points for this research. First, we removed both arms, because the original phantoms have arms along the body trunk while in the radiotherapy the arms are often raised in order to avoid the unnecessary exposure. Second, several target regions were added to the original voxel phantoms. Nine targets, one on the brain, two on the lung, one on the liver for both 'otoko' and 'onago', and one as the prostate of 'otoko' (whole-organ irradiation was often performed for prostate cancer) were created, while only five of them were presented in this paper. All the targets except the prostate were 2 cm in diameter and thickness, while the prostate tumor was 3 cm in diameter and thickness.

2.2 Calculation Code and Computers

The prototype dose calculation code for radiotherapy UCRTP[4] was developed as a user code of EGS4[5]. UCRTP was derived from UCPIXEL[6], the dose calculation code for radiation protection. UCRTP can be executed on the parallel environment by utilizing MPICH parallel processing library[7] and SPRNG 2.0 random number generation library[8]. The primary aim of UCRTP was the survey of the dose calculation accuracy and the estimation of the network load so that no variance reduction technique was employed.

In this study, three X-ray energy spectra, 120 kV (tube), 6 MV and 24 MV (linac) were taken into calculations. The spectra of 6 MV and 24 MV were from the calculation of Mohan *et al*[9] and the 120 kV spectrum was according to the measurement of the CT radiotherapy system. In this study, we used the 360-degree-rotating coplanar (the beam axis is perpendicular to the body axis) cone-beam. The source was 100cm apart from the isocenter (same as target center) and the field diameter was same to those of targets. No multileaf collimator, modulator or other beam modification devices were modeled.

As geometrical inputs, UCRTP needs three kinds of information: the voxel phantom described in GSF format, the material data created by PEGS preprocessor and the table of the correspondences between region ID in the voxel phantom and the materials described in PEGS files. Every skeletal voxel was reconstructed to a cortical bone voxel and a bone marrow voxel of fractional volumes. UCRTP can output the organ doses and three-dimensional dose distribution. Only D_{mean}, the volume average of the absorbed dose in the target volume was considered in this study because the irradiation conditions here do not deliver the uniform dose distribution in the target volume.

For all the calculation describing here, we have used the Beowulf-type cluster-computer consisting of nine 3.0 GHz Pentium4 PCs. Every node has 1 GB memory and is connected via one Gigabit network and one 100Base network with each other. SuSE Linux 7.3 was used as their operating systems. For building the executable, we used Intel FORTRAN Compiler ver.7.1 because of the strictness of warning message during the compilation, and the speed advantage of the executable.

2.3 Material Data and Tissue Substitution Method

We categorized all the regions in the voxel phantoms into six groups except the air in the inner cavity:

skeleton, muscle (including most organs), skin, lungs, adipose tissue, and targets. The female breast and all the contents in the GI-tract and urinary bladder were categorized as adipose tissue. Four soft tissue groups, muscle, skin, lung and adipose tissue were to be substituted by other materials in this study so that the material of the skeleton, inner air and target groups were kept unchanged.

The elemental compositions and weight densities of the human body tissues and substitution materials were based upon ICRU report 46[10] and ICRP publication 89[11]. Most of the material data were utilized literally, while the "bone marrow" was assumed to be the half-and-half mixture of the red bone marrow and yellow bone marrow. Also the "average tissue" was the average over that of male and female ones. We used "adult #2" composition and density in ICRU Report 46 for the adipose tissue, and "muscle-skeletal" for the muscle and target compositions.

The seven composition models we have calculated were summarized in Table 1. The model A (muscle, skin, lungs, adipose tissue) was the most detailed model so that it was treated as a reference model. The next three, model B, C, and D were the simplified models of the model A, which supposed the compositions of lungs and/or skin as identical as the muscle. Therefore the model D and the model E (water-ethanol) was two-composition model. The model E were studied because it is comparably similar to the conventional water-only model and the elemental composition of ethanol is quite similar to that of the adipose tissue, while its weight density is much smaller. We also studied the two one-composition models, the model F (average tissue only) and the model G (water only). In order to keep the weight density of the target volume unchanged, the composition of the target region was muscle for all the composition models.

As the method of substituting materials, we employed "CT-invariant" weight density adjustment. First we supposed the patient model A (reference model) as the true physical existence. In order to create the patient model of other composition model, we adjust the density of substitutes with keeping its CT value unchanged. Because of difficulty in calculating CT value for continuous energy X-ray, we assumed that the linear attenuation coefficient for 50 keV monoenergetic X-ray as the *ideal* CT value. This assumption can be expressed as,

$$\mu_{\text{Original}} = \alpha \times \mu_{\text{Substitution}},$$

where μ_{Original} and $\mu_{\text{Substitution}}$ denote the linear attenuation coefficient of the tissue material to be substituted and the substitution material for 50 keV X-ray, and α is the adjustment factor. Breaking the linear attenuation coefficients into the mass attenuation coefficient and the weight density and we obtain the conversion formula,

$$\alpha \times \rho_{\text{Substitution}} = \rho_{\text{Original}} \times \left[\left(\frac{\mu}{\rho}\right)_{\text{Original}} \Big/ \left(\frac{\mu}{\rho}\right)_{\text{Substitution}} \right],$$

where $\rho_{\text{Substitution}}$ and $\left(\frac{\mu}{\rho}\right)_{\text{Substitution}}$ denote the weight density and the mass attenuation coefficient of the substitution, and ρ_{Original} and $\left(\frac{\mu}{\rho}\right)_{\text{Original}}$ denote those of the tissue material to be substituted. The linear attenuation coefficients were calculated by X-COM developed by NIST[11].

In this conversion scheme, for example, in the case the liquid water ($\rho_{\text{Substitution}}$ = 1.000 g/cm^3) replacing the muscle (ρ_{Original} = 1.050 g/cm^3), α becomes 1.0477 so that the substitution material is a water but has slightly high density. Similarly in the case the liquid water replacing adipose tissue adipose tissue (ρ_{Original} = 0.950 g/cm^3), the substitution becomes a water which density is 0.8897 g/cm^3. Hereafter we denote the substituting

materials as “104.77 % water”, “88.97 % water”, and so on.

3. Results and Discussions

The five figures of the positions we calculated were shown on Figure 2. Though we have calculated four other positions (three for lung position and one for liver position), they displayed similar results as those we present in this paper. The target dose differences when compositions of soft tissues were changed were summarized in Figure 3. All the results were normalized as the results of the model A to unity. The error bars in the figure indicates statistical errors. The number of histories were 160 millions for each calculation, which corresponds to around 0.04 % target dose errors.

When skin or lungs were substituted by the muscle (model B,C), the target dose deviation up to 0.2% was observed for all the target positions. For the case where the both skin and lungs were substituted by the muscle (model D), the deviation was up to 0.3%.

The one-composition models (model F,G) showed 0.5-1.2 % deviations for 120 kV calculations in the some target positions. For the 6 MV and 24 MV calculations, the maximum deviation was 0.5 %. The deviations of one-composition models were larger in the liver and the prostate positions so that there may be the correlation between the body fat ratio and the dose deviations for one-composition model. The average tissue model (model F) shows larger deviations than the water-only model (model G) in the liver position, while the model G shows larger than the model F. Therefore it can be concluded that utilizing the average tissue as a soft tissue substitution causes no accuracy gain, and the liquid water is still one of the best substitution material for soft tissue.

The water-ethanol model (model E) showed less than 0.2 % deviations for most positions, so that this model can give us better accuracy than water-only model (model G).

We should note that the phantom and the target position dependences of the dose deviations were quite large, which can be seen in the results of the ‘otoko’ head and ‘onago’ head, so that the more studies about the different targets in the different phantoms may be necessary to discuss about the advantage of the multi-composition model more quantitatively.

Though this study was preliminary, it seems to be almost clear that the discriminating skin and lungs from the muscle-like tissue causes small accuracy gain, so that the segmentation of skin and lungs from the muscle-like tissues will be considered only from the viewpoint of estimating complications and/or the step length optimization. Discriminating adipose tissue from the soft tissue will showed finite accuracy gains in many cases. The deviations were around 0.5 % for linac radiotherapy, which is still quite small so that it can be justified to utilize the water-only model.

However, honestly speaking, D_{mean} was easy to obtain but not an only parameter to evaluate the advantage of the multiple composition models. The advantage should be evaluated more precisely by performing the dose-volume analyses of the target itself and neighbor organs at risk, which will be done by our group collaboration.

4. Conclusions

We studied the relation between the tissue substitution and target dose for tube and linac X-ray using the prototype dose calculation code and the voxel phantoms.

For the tube X-ray radiotherapy, the target dose errors caused by one-composition model were estimated around 0.5 % for head and lung positions, and 1.2 % for liver and prostate positions. If we employed two-composition soft-tissue model for tube X-ray, the tumor dose error was reduced to 0.3 %. Most calculations

for the models for 6 MV linac X-ray and some of 24 MV linac X-ray calculations showed 0.5 % dose deviations for one-composition model. To mention about the one-composition model, changing the tissue substitution from water to more realistic materials provided no advantage. Separating skin and/or lungs from the muscle like tissues gain the tumor dose accuracy 0.3 % at most.

Though the dose errors estimated in this study were not large in general, further studies on the relation between the dose calculation accuracy and the tissue composition are preferred. Because the advantage of the IMRT is the ability to avoid the complications on the healthy neighbor tissues and organs with irradiating the prescription dose for whole target volume, dose-volume analysis of the target dose and the doses of the organs at risk are necessary.

Acknowledgement

The IMAGINE project was funded by JST (Japan Science and Technology Agency) as a part of "The Innovation of Simulation Technology and Construction of Foundations for its Practical Use." We especially thank to all the project members, especially Prof. Etsurou Kunieda from Keio University Hospital, Mr. Kentaro Kaneko from CMS Japan, Mr. Osamu Ozaki and Mr. Keiji Yamamoto from Mitsubishi Space Software, Dr. Atusi Myojoyama from Tokyo Metropolitan University of Health Science, for giving me the many helps and opportunities of the useful discussion. We also thank to the member of Department of Health Physics and Center for Promotion of Computational Science and Engineering, Japan Atomic Energy Research Institute, which are my (M.Hirai) host institute.

References

1) Saito K, Kunieda E, Narita Y, Deloar H M, Kimura H, Hirai M, Fujisaki T, Myojoyama A and Saitoh H 2003 Development of the Accurate Dose Calculation System IMAGINE for remotely aiding radiotherapy *KEK Proceedings 2003-15 (the Eleventh EGS4 Users' Meeting in Japan)* 81-87
2) Saito K, Wittmann A, Koga S, Ida Y, Kamei T, Funabiki J, Zankl M 2001 *Radiat. Environ. Biophys.* **40** 69-76
3) Petoussi-Henss N, Zankl M, Fill U and Regulla D 2002 The GSF family of voxel phantoms *Phys. Med. Biol.* **47** 89-106
4) Funabiki J, Saitoh H, Sato O, Takagi S, Saito K 2001 An EGS4 Monte Carlo User Code for Radiation Therapy Planning *KEK Proceedings 2001-22 (Ninth ESG4 Users' Meeting in Japan)* 80-86
5) Nelson W R, Hirayama H, Rogers D W O 1985 The EGS4 code system *SLAC-265*
6) Funabiki J, Terabe M, Zankl M, Koga S and Saito K 2000 An EGS4 User Code with Voxel Geometry and a Voxel Phantom Generation System KEK *Proceedings 2000-20 (Second International Workshop on EGS, 8-12, August, 2000 Tsukuba, Japan)* 48-55
7) Gropp W, Lusk E, Doss N and Skjellum A 1996a A high-performance, portable implementation of the MPI message passing interface standard *Parallel Computing* **22** 789-828; Gropp W D and Lusk E 1996b User's Guide for MPICH, a Portable Implementation of MPI *ANL-96/6*
8) Mascagni M, Ceperley D and Srinivasan A 1998 Sprng: A scalable library for pseudorandom number generation *Proceedings of the Third International Conference on Monte Carlo and Quasi-Monte Carlo Methods in Scientific Computing* (http://sprng.cs.fsu.edu/)
9) Mohan M, Chui C, Lidofaky L 1985 Energy and angular distributions of photons from medical linear accelerators *Med. Phys.* **12** 592-597
10) International Commission on Radiation Units and Measurements 1992 Photon, Electron, Proton and Neutron Interaction Data for Body Tissues *ICRU Report 46* (Bethesda, MD:ICRU)

11) International Commission on Radiological Protection 2001 Basic Anatomical and Physiological Data for Use in Radiological Protection: Reference Values *ICRP Publication 89* (Oxford: Pergamon)
12) Berger M J, Hubbell J H, Seltzer S M, Coursey J S and Zucker D S 1987 XCOM: Photon Cross Sections Database, NIST Standard Reference Database 8 (XGAM) *NBSIR* 87-3597 (http://physics.nist.gov/PhysRefData/Xcom/Text/XCOM.html)

Table 1 The sets of soft-tissue substitution model we have calculated. The first four were for the substitution of muscle-like tissues. The first one was the reference. The latter three were for whole soft-tissue substitution. "average tissue" and "water" were called as the one-composition model.

Name of Model		Name of Category			
Signature	Detail	Muscle/Organ	Skin	Lung	Adipose
A	muscle/skin/lung -adipose	100 % muscle	100 % skin	100 % lung	100 % Adipose
B	muscle/lung -adipose	100 % muscle	102.16% muscle	100 % lung	100 % Adipose
C	muscle/skin-adipose	100 % muscle	100 % skin	24.85 % muscle	100 % Adipose
D	muscle-adipose	100 % muscle	102.16% muscle	24.85 % muscle	100 % Adipose
E	water-ethanol	104.77 % water	107.03 % water	26.03 % water	118.00 % ethanol
F	average tissue	104.49 % average	106.75 % average	25.97 % average	88.73 % average
G	water	104.77 % water	107.03 % water	26.03 % water	88.97 % water

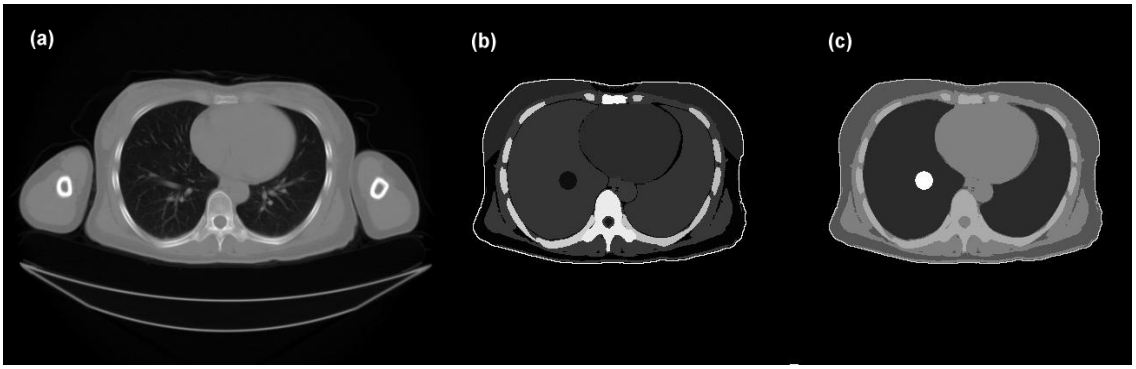

Figure 1 An example of the anthropomorphic voxel phantom. Here showed a slice in the chest of Japanese female phantom "onago". (a) The base X-ray CT image used in the phantom production, (b) the region index number map and (c) the map that the material ID was assigned are shown. The bright circle in the material ID map (dark circle in the region ID map) was the target. Note that we have used armless phantom.

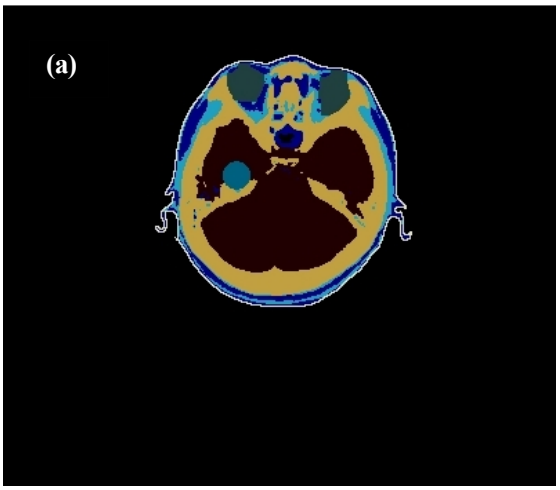

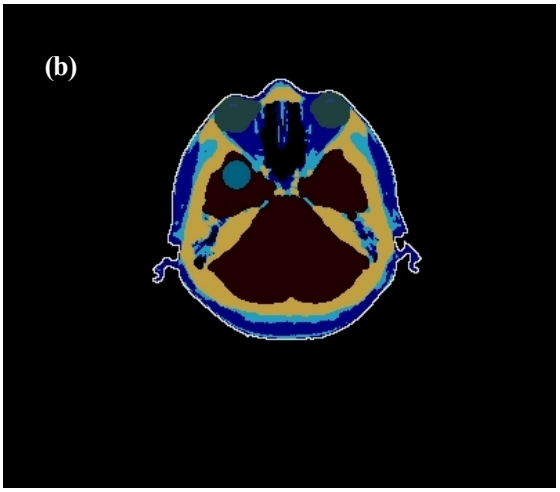

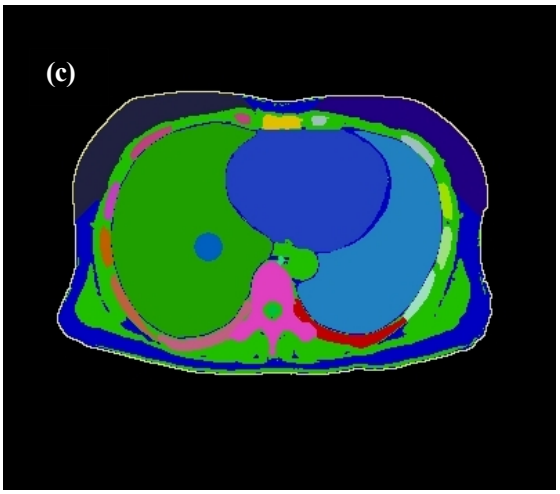

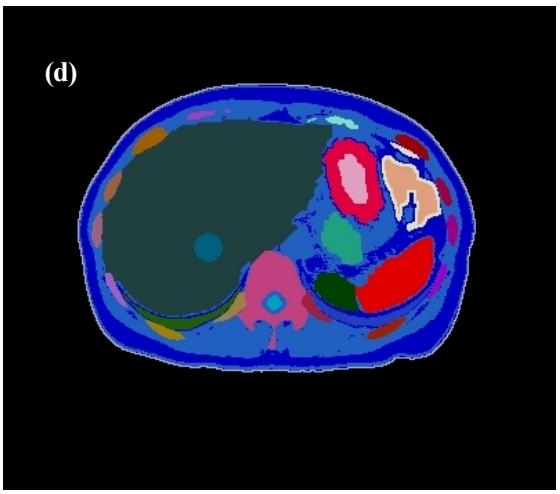

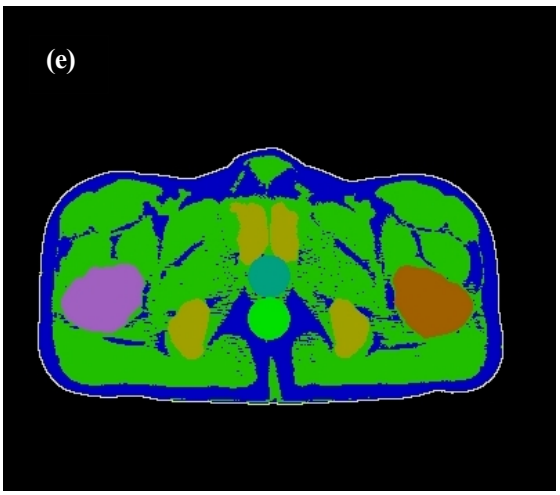

Figure 2 Target created in the voxel phantoms. (a) 'Onago' (female phantom) head (b) 'Otoko' (male) head, (c) 'Onago' lung, (d) 'Onago liver', (e) 'Otoko' prostate. In the figure (e), Two circles are shown: one is prostate, and another is rectum.

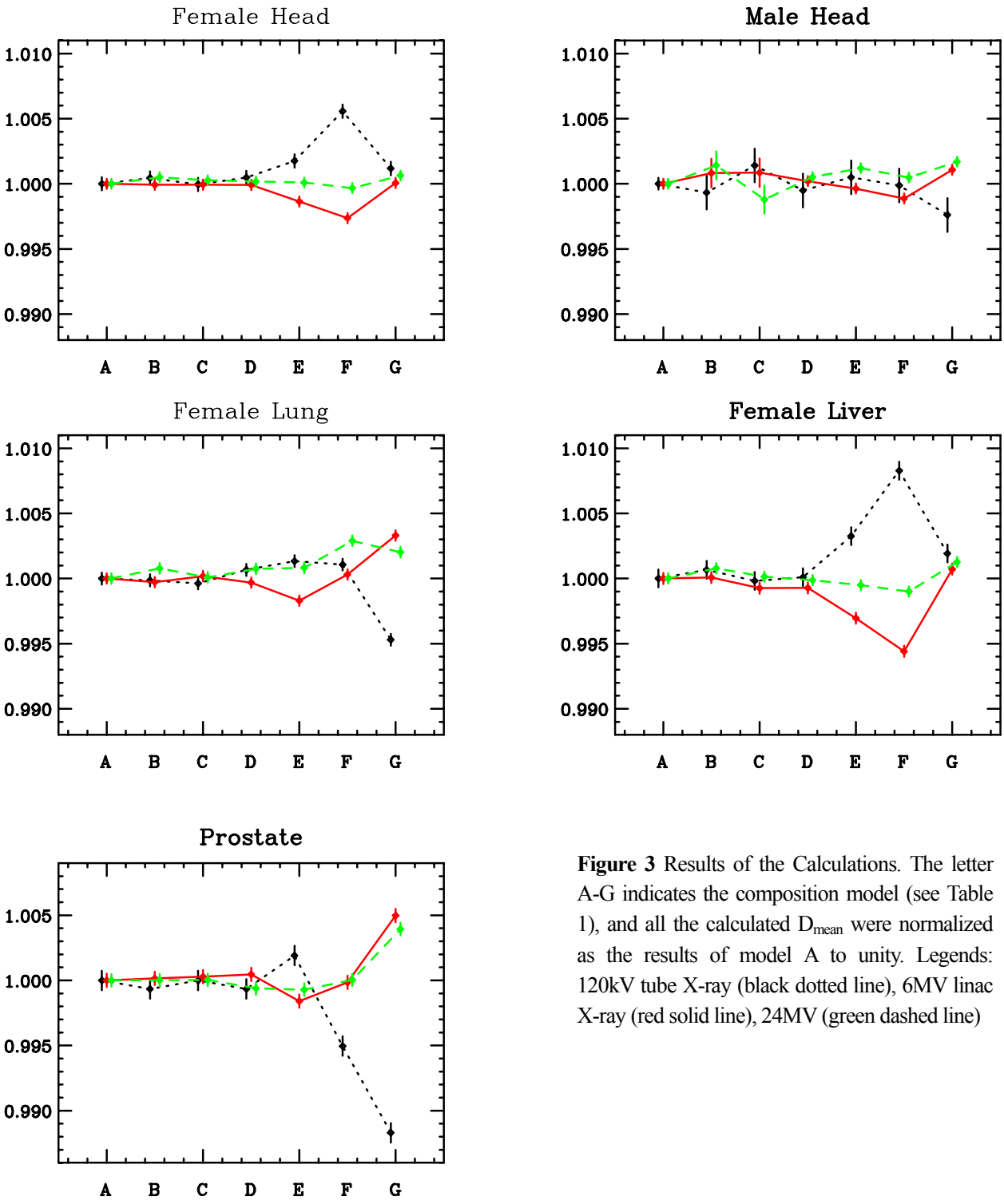

Figure 3 Results of the Calculations. The letter A-G indicates the composition model (see Table 1), and all the calculated D_{mean} were normalized as the results of model A to unity. Legends: 120kV tube X-ray (black dotted line), 6MV linac X-ray (red solid line), 24MV (green dashed line)

MONTE CARLO SIMULATIONS FOR STEREOTACTIC RARIOTHERAPY SYSTEM WITH VARIOUS KILO-VOLTAGE X-RAY ENERGY

HM Deloar[1,2]), E Kunieda[1]), T Kawase1), H Saitoh[3]), M Ozaki[4]), T Fujisaki[5]), A. Myojoyama[3]), K. Saito[6]), S Takagi[7]), O. Sato[7]), and Atsushi Kubo[1])

1) Department of Radiology, Keio University, Tokyo, Japan
2) CREST, Japan Science and Technology Agency, Tokyo, Japan
3) Department of Radiological Sciences, Tokyo Metropolitan University of Health Sciences, Tokyo, Japan
4) CT Systems Division, TOSHIBA MEDICAL SYSTEMS CORPORATION, Japan
5) Department of Radiological Sciences, Ibaraki Prefectural University of Health Sciences, Ibaraki, Japan
6) Center for Promotion of Computational Science and Engineering, Japan Atomic Energy Research Institute
7) Safety Engineering and Technology Department, Mitsubishi Research Institute, INC, Japan

Abstract

Stereotactic Radiotherapy (SRT) of lung tumors with a narrow and precise medium energy x-ray beam where the homogeneous high dose area will be confined within the tumors are desirable. A conventional x-ray CT with medium energy x-ray has been modified to develop a radiotherapy system for lung SRT. A cylindrical collimator (0.3 cm ϕ) made of tungsten was introduced to collimate the X-ray beam. The system was simulated with BEAMnrc(EGS4) Monte Carlo code and various x-ray energy spectra were generated to investigate the dose distributions with our kilo-voltage SRT system. Experiments were performed to acquire the energy spectra of 100, 120 and 135 kVp (kilo-voltage peak) from CT measurements and those results were compared with the spectra obtained from Monte Carlo simulations. Verifications of percentage of dose depth (PDD) for 120 and 147.5 kVp were investigated in a water phantom with experiments and Monte Carlo simulations. Finally dose distributions of 120, 135, 147.5, 200, 250, 300, 350, 400, 500 kVp spectra were investigated with lung phantom and human lung. The Percentage of Depth Dose (PDD) in the water phantom calculated from the experimental and simulated spectra of 120 and 147.5 kVp show good agreement with each other. The PDD of 147.5 and 120 kVp spectra at 9 cm depth was approximately 10% and 9%, respectively. Dose distributions around the lung tumor in the phantom and human for all x-ray energies were almost uniform but in the case of the human lung absorptions of dose at ribs for the energy lower than 135kVp was more than 35% and those absorptions for the energy spectra of 147.5 kVp and above was less than 30%. This absorption gradually decreases with increasing x-ray energies. Uniform dose distributions in the lung region of human and thorax phantom demonstrated the possibility of SRT system with medium energy X-ray. A detail performance of this system as a kilo-voltage conformal radiotherapy is under investigations.

1. Introduction

Orthovoltage radiotherapy units with kilo-voltage x-ray energy usually used to treat superficial lesion near to the skin and dosimetries of kilo-voltage with x-ray beam have been described in the literature [1, 2] with protocols [3 4] considering its growing interest for radiotherapy and radiobiology. Although the point of interest of kilo-voltage therapy is to treat the superficial lesion often near the body surface, treatment of tumor at a large depth [3 4] is not been well investigated in these few decades. With the kilo voltage x-ray energy, 140 kVp (kilo-voltage peak), a conventional computed tomography (CT) scanner has been used as a therapy machine [5] by adding a collimator to produce rectangular or square radiation filed. This machine was used as an arc therapy to treat brain tumors on animal [6] and human [7] with the infusion of x-ray contrast materials (CM), to enhance radiation doses.

For stereotactic irradiation (STI) of a lung tumor in terms of higher uniformity in the target volume, Saitoh et al [8] recommended the lower, rather than higher energy, with multiple converging arcs or multiple static port irradiations. In a Monte Carlo simulation with arc therapy, it has been shown that dose uniformity in a small lung tumor (2cm ϕ) for low energy photon (250kVp) is much higher than the high energy photon(>4MV) (personal communications) and the penumbra effect is vice versa. To treat lung tumor we are developing a kilo voltage radiotherapy system with the conventional CT. The concept is very similar to the system described by Iwamoto et al. [5] but our system will have a micro-multileaf collimator (μMLC) to control the beam size and the system will capable to do non-coplanar multiple arc therapy (gantry rotation =0 ~ 360 degree and tilting rotation = 30 -150 degree). But in before hand, the possibility to treat lung tumors with our kilo-voltage radiotherapy system, Monte Carlo simulations with various energies were performed in water phantom, thorax phantom and human lung. A prototype collimator was used in this study. As we have the flexibility to change the x-ray energies, the percentages of depth doses (PDD) in a water phantom were verified for the x-ray energies of 100, 120, 147.5, 200, 250, 300, 400 and 500 kVp to investigate the dependency of PDD on kilo-voltage energies.

2. Material and methods

This study consists of two parts: (1) modeling of x-ray tube for energy spectra and (2) verifications of dose distributions in various medium. In both cases BEAMnrc Monte Carlo (MC) simulation [10] was used.

To obtain energy spectra, the x-ray tube of the CT canner (Toshiba Aquilion TSX-101A) used in our study was simulated with the BEAMnrc MC code [10]. The target in the x-ray tube was composed of tungsten and rhenium and inclination of the target towards the electron beam was 7^{o}. A collimator made of tungsten was designed to open in such a way that it can give 2cm × 2cm beam at 50 cm source to surface distance (SSD). Source to collimator distance was 25cm and an Al filter of 3mm thickness was used. To obtain the energy spectra to be used for dosimetry calculations, a phase space [10] file below the collimator was modeled. The energy spectra of 100, 120, 147.5, 200, 250, 300, 400 and 500kVp were extracted from the phase space file by using beamdp

graphical user interface [10]. The global electron and photon cut off energy used in the simulation was 0.05 and 0.001 MeV, respectively and 100 million electron events were used in all cases. To validate the simulated energy spectra, the CT machine was operated at 100, 120 and 135 kVp with 400mA current and energy spectra of 100, 120 and 135 kVp were measured and compared with the corresponding simulated spectra.

Energy spectra obtained from experiments and simulations were used to calculate the PDD's and isodose in a water phantom with the xyz_gui MC simulations [10]. The dimension of the water phantom was 20cm × 20cm × 20cm. The beam size at a SSD of 50cm was 2cm × 2cm. Using the same phantom geometry and beam configurations, the isodose curves due to irradiation of Co^{60} source were plotted and compared with the isodose curves obtained from kVp spectra. In all cases, point source from the front with rectangular collimation was considered [10]. The calculated PDD for experimental and simulated energy spectra of 100, 120 and 135 kVp were compared with each other. To reconfirm the PDD results, the x-ray beam from CT operated at 120 and 147 kVp with 400mA were irradiated to hard-water phantom with normal incidence and PDD were measured with the tissue air ratio (TAR) method. Those PDD's were compared with the calculated PDD from simulated spectra. A pinpoint ionization chamber (IC) was used in the experiment. As the PDD's strongly depends on the energy spectra, variations of PDD's with their corresponding energy spectra were compared with each other. Explicit dependency of PDD's on energy for the phantom depths of 5, 7.5, 10 and 12.5 cm were also compared with each other. Finally a comparison of dose distributions was done for 200kVp and Co^{60} source in a thorax phantom. Multiple non-coplanar arcs were applied to irradiate the target volume situated in the thorax phantom.

3. Results

Experimental and simulated x-ray energy spectra of 100, 120 and 135 kVp were compared with each other. A comparison of energy spectra for 120 and 135 kVp in experiment and simulation are shown in figure 1. In spectral distribution, each energy bin was normalized with their corresponding area under the curve (AUC) and in all cases the simulated energy spectra shows good agreement with the experimental spectra except near to the lower energy of the peak. Other energy spectra for 147.5, 200, 250, 300, 400 and 500 kVp were also simulated.

A comparison of experimental PDD with TMR method was done with the PDD's calculated from the simulated energy spectra of 120 and 147.5 kVp (not shown). The experimental PDD obtained from the TMR method showed good agreement with those PDD calculated from the energy spectra. Comparisons of PDD, calculated from various (kVp) energy spectra are shown in figure 2. All data were well fitted with an exponential fit. Variations of PDD with x-ray energy can be seen in figure 3. The PDD data of 5, 7.5, 10 and 12.5 cm phantom depths were plotted in figure 3 with respect of the energy. All the data were fitted with a polynomial function. With increasing energy of the x-ray photons PDD is also increased but this increment is not linear to the x-ray energy.

In figure 4, the isodose curves in a water phantom due to irradiation of 147.5, 200, 300 and 400kVp spectra were plotted and compared with the isodose curves irradiated with the Co^{60} source. With increasing the x-ray

energy, the percentage of dose also increased but that increments of doses are not comparable with the dose of Co^{60} source. For 200kVp spectra the dose at 10cm depth is 10% but for Co^{60} source that dose is around 40%. Irradiation to a lung tumor in a thorax phantom has shown in figure 5. Usually in Co^{60} therapy multiple non-coplanar arcs doesn't considered, but for the comparison of our system we applied the same technique to Co^{60} also.

4. Discussion

In this study we have investigated several kilo voltage x-ray energies to explore the possibility to treat lung tumors with Monte Carlo simulations. The BEAMnrc Monte Carlo code [10] is based on EGS4 [11] is a nice tool to simulate radiotherapy beam with LINAC system, which includes lot of build in modules including x-ray tubes. In the latest version of the BEAM code the low energy photon treatments [12] are included, therefore BEAM code enable us to simulate the x-ray tube accurately. The phase space files below the collimator were considered and energy spectra of the beam were extracted from the phase space files. Some discrepancies between the experimental spectra and simulated spectra in figure 1 were observed, it was because the semiconductor detector used to measure the experimental energy spectra was not modeled in the simulations

From figure 2 and 4 it can be seen that, for all energies 70% to 100% doses are deposited within the 2 cm depth of the phantom and with increasing energy the PDD also increased. Variations of doses with energy for the phantom depth of 5, 7.5, 10 and 12.5 cm can be seen in figure 4. For 200kVp the PDD's for the mentioned depths are 33%, 18%, 11% and 6%, respectively. Those PDD's for 147.5kVp are 29%, 15%, 8% and 5%, respectively. At present our system can give highest 147.5kVp energy but it is possible to extend the energy up to 200kVp in future, therefore, 147.5 and 200kVp were considered in all possible studies. In figure 4 it can be clearly seen that with increasing energy the PDD are increased but the increment is not linear with the energy. Usually photo electric effect with low energy x-ray is sensitive to the high density materials like bone and with increasing energy this effect decreases.

This study enables us to give some idea to use kilo-voltage energies to treat lung tumors. Usually mega-voltage x-rays with higher energy is preferred for the therapy because that have less attenuation in the tissue than those with lower energy, and therefore a higher dose in the deep target is obtained. Another reason is that mega-voltage beams allow a reduced skin dose, and therefore less skin damage than lower energy beams because of the build-up effect of mega-voltage x-rays. However, with the development of 3DCRT, as the target is irradiated with the beam from multiple arcs, the skin dose is reduced. In figure 5, it can be seen that with 200kVp the target can be irradiated uniformly.

Conclusions

We are investigating a stereiotactic converging radiotherapy system with kilo voltage x-ray energy by using a CT scanner which will produce narrow x-ray beams with a μMLC collimator. Practical investigation of system with micro multi leaf collimator is going on. But in beforehand the dosimetry property of the system with a

prototype collimator for various kVp x-ray energies we have investigated with BEAMnrc MC code. The main disadvantage to treat the lung tumor with the low energy x-ray is the ribs bone where dose enhancement is relatively higher due to the photo electrons in the calcium of the bone. This can be minimized with increasing the x-ray energy.

References

[1] Ma C M, Li X A, Seuntjens J P. Study of dosimetry consistency for kilovoltage x-ray beams Med Phy 25 2376-84 (1998).

[2] Nahum A E and Knight R T. Consistent formalism for kilovoltage x-ray dosimetry Proceedings of the IAEA International Symposium on Measurement Assurance in Dosimetry IAEA, Vienna , IAEA-SM-330/24 451-459, (1994).

[3] Ma C M, Coffey C W, DeWerd L A, Liu C, Nath R, Seltzer S M. AAPM protocol for 40-300 kV x-ray beam dosimetry in radiotherapy and radiobiology Med Phy 28 868-93, (2001).

[4] Yoo S, Grimm D, Zhu R, Jursinic P, Lopez F, Rownd J, Gillin M. Clinical implementation of AAPM TG61 protocol for kilovoltage x-ray beam dosimetry Med Phys 29 2269-73, (2002).

[5] Iwamoto K S, Norman A, Kagan A R, Wollin M, Olch A, Bellotti J, Ingram M, Skillen R G. The CT scanner as a therapy machine Radiother Oncol 19 337-43, (1990).

[6] Iwamoto K S, Norman A, Freshwater D B, Ingram M, Skillen R G. Diagnosis and treatment of spontaneous canine brain tumors with a CT scanner 26 76-78, (1993).

[7] Rose J H, Norman A, Ingram M, Aoki C, Solberg T, Mesa A. First radiotherapy of human metastatic brain tumors delivered by a computerized tomography scanner (CTRx) Int J Radiat Oncol Biol Phys 45 1127-32, (1999).

[8] Saitoh H, Fujisaki T, Sakai R, Kunieda E. Dose distribution of narrow beam irradiation for small lung tumor. Int J Radiat Oncol Biol Phys 53 1380-7, (2002).

[9] Saitoh H . Department of Radiological Sciences, Tokyo Metropolitan University of Health Sciences, Tokyo, Japan.

[10] Rogers D W O, Faddegon B A, Ding G X, Ma C M, Wei J, and Mackie T R. BEAM: A Monte Carlo code to simulate radiotherapy treatment units Med Phys 22 503-524, (1995).

[11] W. R. Nelson, H. Hirayama, and D. W. O. Rogers. The EGS4 Code System, Report SLAC-265, Stanford Linear Accelerator Center, Stanford, California, (1985).

[12] Y. Namito, H. Hirayama, and S. Ban. Improvements of low-energy photon transport in EGS4, Radiation Phys. Chem. 53, 283 – 294, (1998).

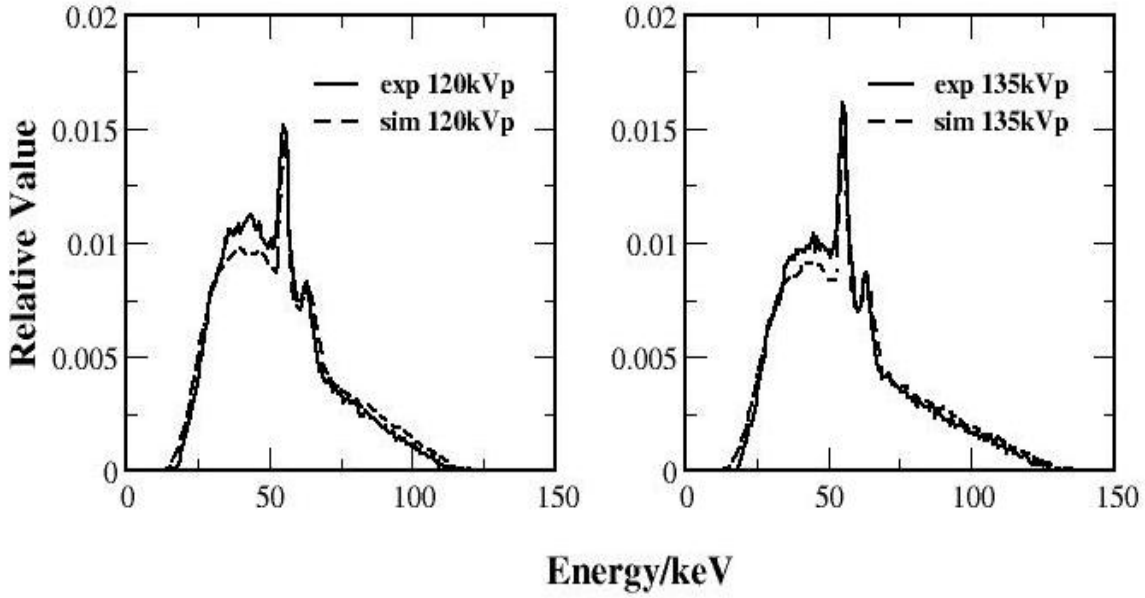

Figure1: Comparison of experimental and simulated energy spectra for 120 and 135 kVp x-ray. All the data were normalized with their corresponding area under the curve (AUC).

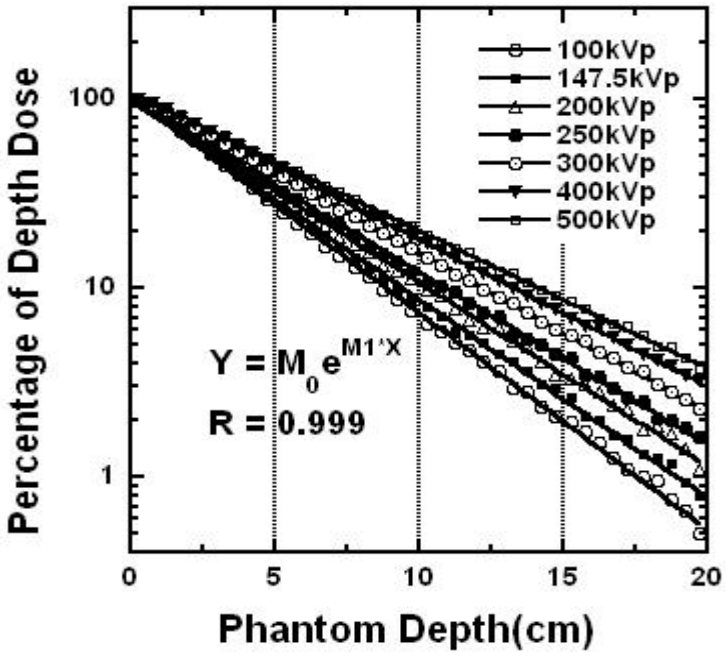

Figure2: Logarithmic plots of simulated PDD's for various kVp x-ray spectra (100, 147.5, 200, 250, 300, 400, and 500 kVp). Maximum water phantom depth used was 20cm with SSD 50cm.

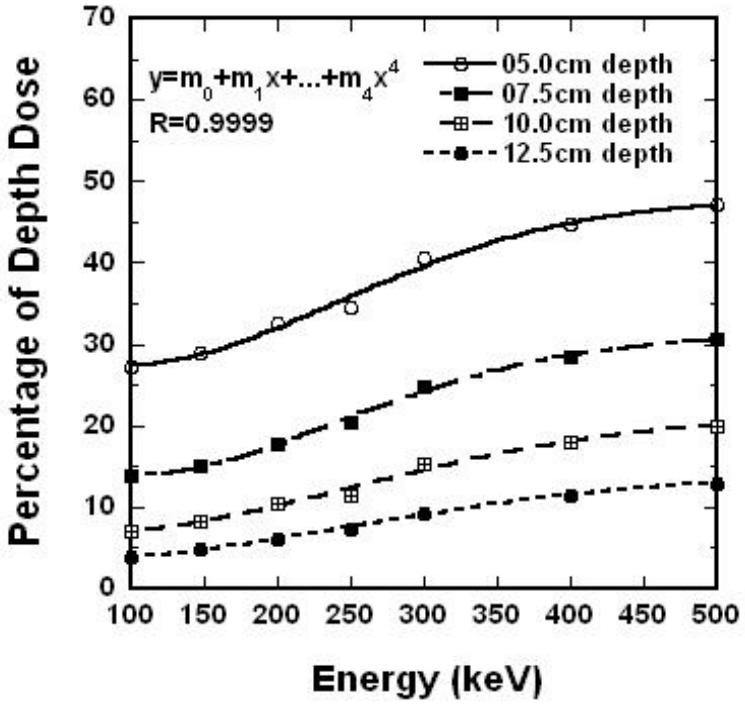

Figure3: Variations of PDD's with kilo-voltage energy at the phantom depths of 5, 7.5, 10 and 12.5 cm.

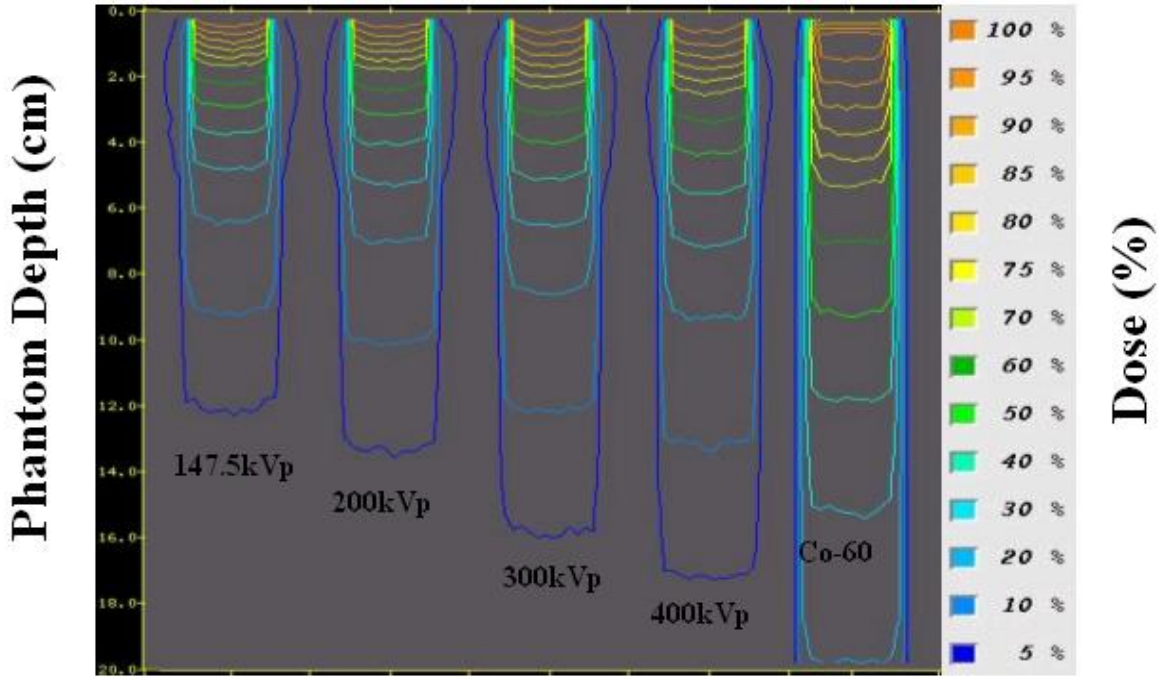

Figure4: Several kVp isodose curves in a water phantom with the isodose curves of Co-60. Left side scale indicates phantom depth and right side color scale indicates percentage of dose. In all cases 50cm SSD was considered to calculate doses in the water phantom.

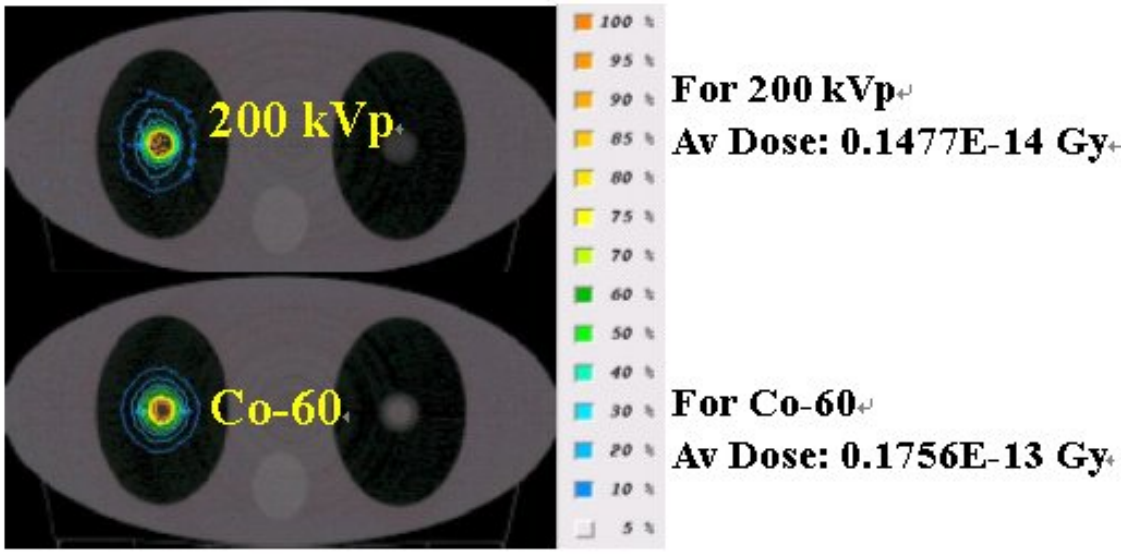

Figure5. Irradiation to the target in a lung phantom with 200kVp x-ray (top) and with 1.33MeV photon from Co-60 (bottom). Irradiated volume size (2cm) appeared in figure. In both cases seven non-coplanar arcs irradiation were considered in this study.

MONTE CARLO SIMULATIONS OF DOSE DISTRIBUTIONS FOR 4 AND 10 MV PHOTON BEAMS FROM A VARIAN CLINAC 2100C ACCELERATOR

Fujio Araki

Department of Radiological Technology, Kumamoto University School of Health Sciences, Kumamoto 862-0976, JAPAN

E-mail: f_araki@hs.kumamoto-u.ac.jp

Abstract

This study shows detailed characteristics of dose distributions for realistic incident photon beams. It provides more comprehensive information for radiotherapy photon beams including incident photons as well as contaminating electrons and positrons in a radiation beam for different field sizes and beam energies. The EGSnrc Monte Carlo code, BEAMnrc has been used to simulate 4 and 10 MV photon beams from a Varian Clinac 2100C accelerator. A simulated realistic beam is stored in a phase space files, which contains details of each particle's complete history including where it has been and where it has interacted. The phase space files are used to calculate depth-dose components from different particles and surface dose and contribution from different particles to surface dose across the filed. The accuracy of a simulated beam is validated by the excellent agreement between the Monte Carlo calculated and measured dose distributions except for 10 MV at the 40×40 cm^2 field in the buildup region. At 4 MV, the incident charged particles contribute 6% to 26% of maximum dose at the surface when the field size increases from 10×10 to 40×40 cm^2. Similarly, their contributions at 10 MV are up to 7% and 23% of maximum dose at the surface for 10×10 cm^2 and 40×40 cm^2 fields, respectively.

Key word: Monte Carlo simulations, linear accelerators, contaminant particles, dose calculations

1. Introduction

The BEAM code[1)] is a general purpose Monte Carlo user code for the simulation of radiotherapy beams, especially those from linear accelerators. It has been benchmarked against measurements for electron and photon beams from various accelerators.[1)-6)] Recently, Ding[6)] had calculated energy spectra, angular spread, fluence profiles and dose distributions of 6 and 18 MV photon beams from a Varian 2100EX accelerator using the EGS4 Monte Carlo code, BEAM. The results are also included detailed information for contaminant charged particles (electrons and positrons) and primary photon beams in the photon beams. It is difficult to analyze experimentally such components of the photon beams incident on a phantom surface because of various limitations in the clinical environment and detectors. One of the major advantages of the Monte Carlo technique is that it allows detailed information about each particle's history to be known. Therefore, Monte Carlo simulation can be used to obtain the information that cannot be measured experimentally.

The purpose of this study is to show detailed characteristics of dose distributions for realistic incident photon beams. It provides more comprehensive information for radiotherapy photon beams including incident photons as well as contaminating electrons and positrons in a radiation beam for different field sizes and beam energies.

2. Methods and materials

2.1. Monte Carlo simulations

The EGSnrc[7)] user code BEAMnrc[8)] was used to simulate 4 and 10 MV radiotherapy photon beams emerging from a Varian Clinac 2100C accelerator (Varian Oncology Systems, Palo Alto, CA). The geometry and the materials used in the simulation reflect a realistic construction of the linear accelerator. The component modules for the Varian Clinac machine 2100C consist of the following: target, primary collimator, exit window, flattening filter, monitor chamber, mirror, secondary jaws and protection window. A diagram of the machine head operated in the photon mode is illustrated in Fig. 1. The front face of a water phantom is placed at 100 cm SSD (source-to-surface distance) from the upstream surface of the target.

The position, energy, angle, charge and weight of scored particles were scored in a phase space files. The variable LACH[1)] was used to record each particle's complete

history of where a particle has been or where a particle has interacted in the beam simulation. The phase space plane was designed at the surface of the water phantom. The stored phase space files were used repeatedly as input to the EGSnrc user code DOSXYZnrc[9] to calculate the dose distributions in the water phantom.

The CPU used for the simulation was a Pentium IV with 3.2 GHz processors. For 4 MV beams, a total of 7.5×10^8 and 4×10^7 electron histories were simulated for the 10×10 cm^2 and 40 x 40 cm^2 fields, respectively. While at 10 MV, a total of 2.5×10^8 and 1×10^7 electron histories were simulated for 10×10 cm^2 and 40×40 cm^2 fields, respectively.

The parameters for simulating 4 and 10 MV photon beams were: AE=ECUT=0.7 MeV, AP=PCUT=0.1 MeV, no photon interaction forcing and no Rayleigh scattering. A variance reduction technique[1] was used to increase the simulation speed. The parameters used with the electron range rejection[1] were ESAVE=0.7 MeV in the target and ESAVE=1.0 MeV in other component modules for 4 MV. While at 10 MV, they were ESAVE=1.0 MeV in the target and ESAVE=2.0 MeV in other component modules. The variance reduction technique called selective bremsstrahlung splitting (SBS)[8] was also used and the parameters were: N_{min}=10, N_{max}=100. Russian roulette of secondary electron is not employed.

Both the distribution of the energy and the radial intensity of the electron beam incident on the target were adjusted to produced the best match between Monte Carlo calculated and measured dose distributions of the largest field size for a given beam energy. For 4 MV beams, the final incident electron mean energy and energy spread were 4.2 MeV and a Gaussian with a FWHM (full-width half-maximum) of 3%, respectively. The electron radial intensity distribution was also taken as Gaussian with the FWHM of 1.2 mm. While at 10 MV, final incident electron mean energy and energy spread were 10.3 MeV and the FWHM of 3%, respectively, and the radial intensity distribution was the FWHM of 1.5 mm.

It is worth mentioning that dose profiles of large fields were very sensitive to the width of the radial intensity distribution of incident electrons. While the central axis depth-dose curves strongly depend on the incident electron mean energy but show a weak sensitivity to the electron energy spread.[4]

2.2. Measurements

All measurements were performed using a water phantom (Dynascan, Computer Medical Systems Inc). Depth-ionization curves and ionization profiles were made using a PTW-31002 ionization chamber. The active scanning dimensions of the water phantom are 50 cm × 50 cm × 43 cm. The scanning system has a position accuracy of ≤ 0.5 mm and a reproducibility of ≤ 0.25 mm for scanning. The PTW-31002 cylindrical chamber has an inner diameter of 5.5 mm and a length of 6.5 mm (0.125 cm^3 active volume). The measurement point for the ion chamber is taken to be the center of the chamber cavity. Measured depth-ionization curves were sifted by $0.6r_{cav}$ (where $0.6r_{cav}$ is the radius of the chamber cavity) upstream of the center of the chamber, consist with the AAPM TG-51 protocol[10] or IAEA code of practice.[11] A reference chamber, which is mounted on the accelerator head, is used to correct beam output variations during scanning.

2.3. Stopping-power ratio calculations

Spencer-Attix water-to-air stopping-power ratios were calculated using EGSnrc code SPRRZnrc[12] for 4 and 10 MV photon beams. Calculated stopping-power ratios are presented in Fig. 2 as a function of depth for 10 × 10 cm^2 and 40 × 40 cm^2 fields. The phase space files created with the BEAMnrc code were used as input to the SPRRZnrc code. The variation of the stopping-power ratios with depth is 0.4% at 4 MV and 0.7% at 10 MV from surface to 40 cm depth in water. The variation is field size dependent as well as contaminant charge particles. Measured depth ionizations were converted to depth-dose by accounting for the water-to-air stopping power ratios.

3. Results and discussion

3.1. Depth-dose curves

Comparisons of depth-dose curves are shown in Figs. 3(a)-(d) for a 10 × 10 cm^2 and 40 × 40 cm^2 fields at 4 and 10 MV, respectively. The Monte Carlo calculation also breaks the depth-dose curve into various components. The dose contribution from incident photons is referred to as photons. Photons, which have not interacted with any part of the accelerator except at the target, are referred to as primary photons. The contribution from incident contaminant electrons is referred to as electrons. The

contribution from incident contaminant positrons is referred to as positrons.

All measured depth-dose curves were derived from the measured depth-ionization curves by accounting for Spencer-Attix water-to-air stopping power ratios calculated in Sec. 2.3. Each measured depth-dose curve was normalized at the depth of maximum dose at beam central axis. The Monte Carlo calculated depth-dose curve was scaled so that it had the same value at a 10 cm depth as that of the corresponding measured data. All profiles data were normalized and scaled in the same manner.

The Monte Carlo calculated depth-dose curves are in good agreement with measured data except for 10 MV at the 40 × 40 cm^2 field in the build-up region. It can be seen that the charged particle contamination contributes significantly to the surface dose and the build-up region. At 4 MV the contaminant electrons contribute 5.8% and 26.0% of the maximum dose at the surface for 10 × 10 cm^2 and 40 × 40 cm^2 fields as shown in Figs. 3(a) and 3(b), respectively. The surface dose is calculated as the average dose between 0 and 0.25 cm depth in the water phantom. Beyond d_{max} (=1 cm) their contributions are negligible. While at 10 MV, the surface dose from the contaminant electrons contributions contribute 6.7% and 21.4% of the maximum dose for 10 × 10 cm^2 and 40 × 40 cm^2 fields as shown in Figs. 3(c) and 3(d), respectively. Their contributions are <1% beyond d_{max} (=2.5 cm). The contribution from the contaminant positrons is only 1.4% of the maximum dose at the surface for the 40 × 40 cm^2 field as shown in Fig. 3(d). The dose contributions from the contaminant electrons and positrons to the surface dose calculated in this work were compared to Ding's data[2] for 6 and 18 MV in Table 1. The calculated dose is the average dose between 0 and 0.25 cm depth in water. It can be seen that the increase of the surface dose with the increase of the field size is mainly due to the increase of the contaminant electrons. The positron contamination contributes insignificantly for photon energies below 10 MV.

The dose discrepancies between Monte Carlo calculations and measurements in the build-up region as shown in Fig. 3(d) agree with Ding's results[6] for 18 MV at a 40 × 40 cm^2 field. Ding *et al*[13),14)] have investigated possible causes to resolve the dose discrepancies in the build-up region. However, the true cause of the discrepancy is still unknown.

3.2. Dose profiles

Figures 4(a) and 4(b) present Monte Carlo calculated surface dose and contribution from different particles to surface dose across the fields for 10×10 cm^2 and 40×40 cm^2 fields at 4 and 10 MV, respectively. It is seen that the contaminant charged particles play a significant role in making the surface dose flat across the field, particularly at 10 MV.

Figures 5(a) and 5(b) show the comparisons between measured and the Monte Carlo calculated dose profiles and contributions from primary photons for the 40×40 cm^2 field at 4 and 10 MV, respectively. The profiles are at depths of d_{max}, 5, 10, 20 and 30 cm. The calculated dose profiles match the measurements at all depths. It is seen that the dose profiles from all particles and from primary photons have a very similar shape beyond the depth where contaminant charged particles can reach.

4. Conclusions

The Monte Carlo calculated and measured dose distributions in the water phantom are in good agreement in all cases except for 10 MV at the 40×40 cm^2 field in the dose build-up region. The unsolved discrepancy may indicate the limitation in the EGS modeling as well as the limitation of measurements at the build-up region in the high-energy photon beams. In any case the real cause of the discrepancy needs further investigation.

At 4 MV, the incident charged particles contribute 6% to 26% of maximum dose at the surface when the field size increases from 10×10 to 40×40 cm^2. Similarly, their contributions at 10 MV are up to 7% and 23% of the maximum dose at the surface for 10×10 cm^2 and 40×40 cm^2 fields, respectively.

Acknowledgements

We would like to thank Varian Oncology Systems for providing detailed treatment head designs to simulate a Varian Clinac 2100C accelerator.

References

1) Rogers D W, Faddegon B A, Ding G X, Ma C M, We J and Mackie T R, BEAM: a Monte Carlo code to simulate radiotherapy treatment units, *Med. Phys.* 22, 503-24,

1995

2) Ding G X and Rogers D W, Energy spectra, angular spread, and dose distributions of electron beams from various accelerators used in radiotherapy, *National Research Council of Canada*, *Report* No PIRS-0439, 1995

3) Sheikh-Bagheri D, Rogers D W, Ross C K and Seuntjens J P, Comparison of measured Monte Carlo calculated dose distributions from the NRC linac. *Med. Phys*. 27, 2256-66, 2000

4) Sheikh-Bagheri D and Rogers D W, Sensitive of megavoltage photon beam Monte Carlo simulations to electron beam and other parameters, Med. Phys. 29, 379-90, 2002

5) Sheikh-Bagheri D and Rogers D W, Monte Carlo calculation of nine megavoltage photon beam spectra using the BEAM code, *Med. Phys*. 29, 391-402, 2002

6) Ding G X, Energy spectra, angular spread, fluence profiles and dose distributions of 6 and 18 MV photon beams: results if Monte Carlo simulations for Varian 2100EX accelerator, *Phys. Med. Biol.* 47, 1025-46, 2002

7) Kawrakow I, Accurate condensed history Monte Carlo simulation of electron transport: II. Application to ion chamber response simulations, *Med. Phys*. 27, 499-513, 2000

8) Rogers D W, Ma C, Ding G X, Walters B R, Sheikh-Bagheri D and Zhang G G, BEAMnrc users manual, *National Research Council of Canada Report* PIRS-509(a)revF, 2001

9) Ma C, Rogers D W and Walters B R, DOSXYZnrc users manual, *National Research Council of Canada Report* PIRS-509b(revF), 2001

10) Almond P R, Biggs P J, Coursey B M, Hanson W F, Huq M S, Nath R and Rogers D W, AAPM's TG-51 protocol for clinical reference dosimetry of high-energy photon and electron beams, Med. Phys. 26, 1847-70, 1999

11) Andreo P, Burns D T, Hohlfeld K, Huq M S, Kanai T, Laitano F, Smyth V G and V ynckier S, Absorbed dose determination in external beam radiotherapy: an international code of practice for dosimetry based on standards for absorbed dose to water, *Volume 398 of Technical Report Series* (IAEA, Vienna: International Atomic Energy Agency), 2000

12) Rogers D W, Kawrakow I, Seuntjens J P and Walters B R, NRC user codes for

EGSnrc, *National Research Council of Canada Report* PIRS-702(revA), 2002

13) Ding G X, Dose discrepancies between Monte Carlo calculations and measurements in the build-up region for a high-energy photon beam, Med. Phys. 29, 2459-63, 2002

14) Ding G X, Duzenli C and Kalach N I, Are neutrons responsible for the dose discrepancies between Monte Carlo calculations and measurements in the build-up region for a high-energy photon beams?, Phys. Med. Biolo. 47, 3251-61, 2002

Table 1. Monte Carlo calculated dose contributions from contaminant electrons and positrons to surface dose. The calculated dose is the average dose between 0 and 0.25 cm depth in water. The data for 6 and 18 MV photon beams are obtained from Ding (Reference 6).

Unit: % for maximum dose

Photon energy	Electron		Positron	
(MV)	10 × 10	40 × 40	10 × 10	40 × 40
4	5.8	26.0		
6	7	21		
10	6.7	21.4	0.5	1.4
18	9	24	2	5

Data for 6 and 18 MV are from Ding (Reference 6).

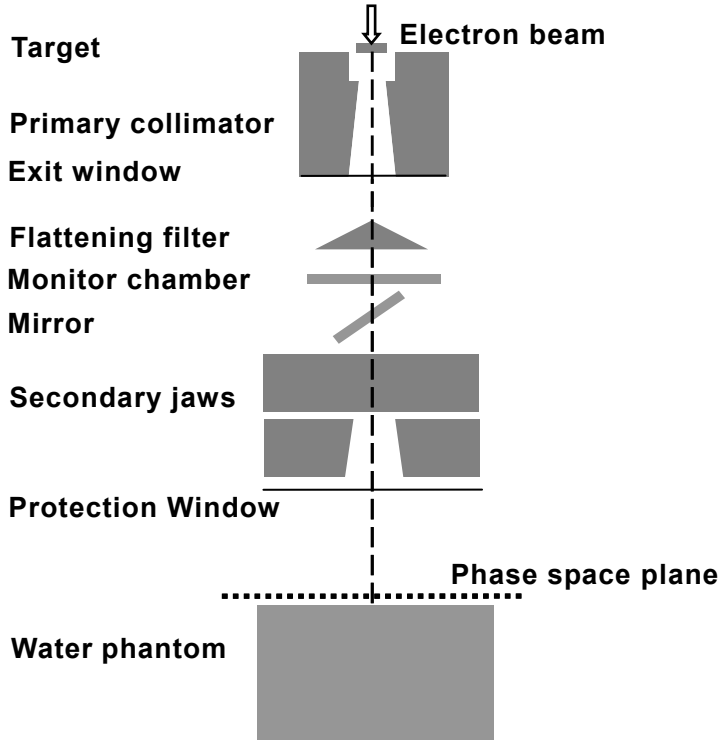

Figure 1. Illustration of the treatment head and the component modules used in the BEAMnrc simulation for a Varian Clinac machine operated in photon mode. The phase space scoring plane is taken at the surface of a water phantom.

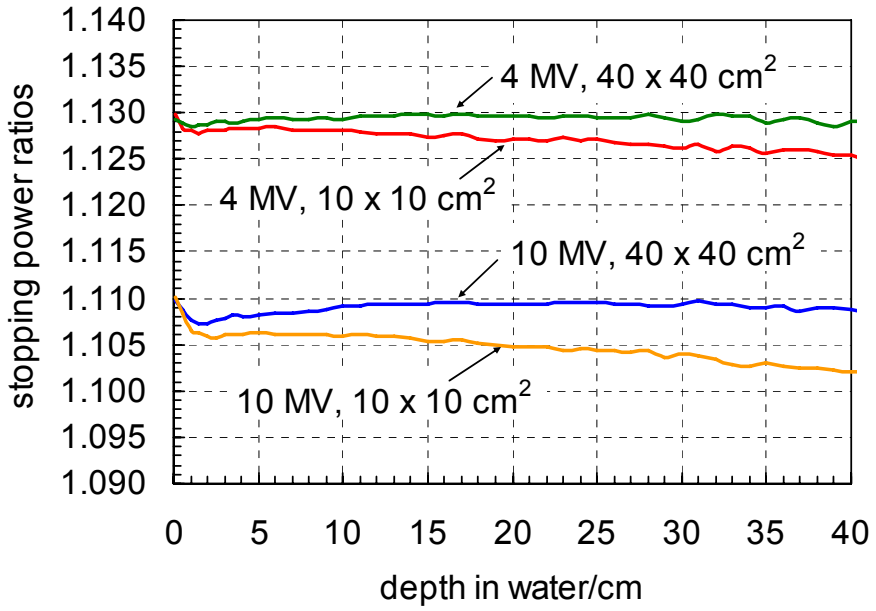

Figure 2. Calculated Spencer-Attix water-to-air stopping ratios as a function of depth for realistic photon beam from a Varian Clinac 2100C accelerator calculated using EGSnrc/SPRRZnrc. The SSD is 100 cm for the incident beams.

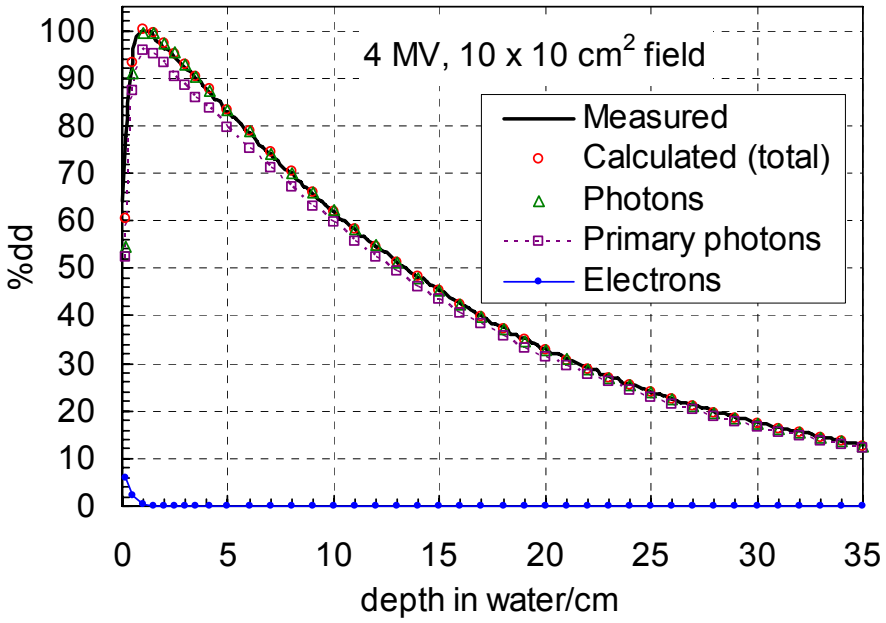

Figure 3(a). Comparison of measured and Monte Carlo calculated central axis depth-dose curves along with dose distributions from incident photons, primary photons and electrons for a 10 × 10 cm^2 field at a 4 MV photon beam from a Varian Clinac 2100C accelerator (SSD=100 cm).

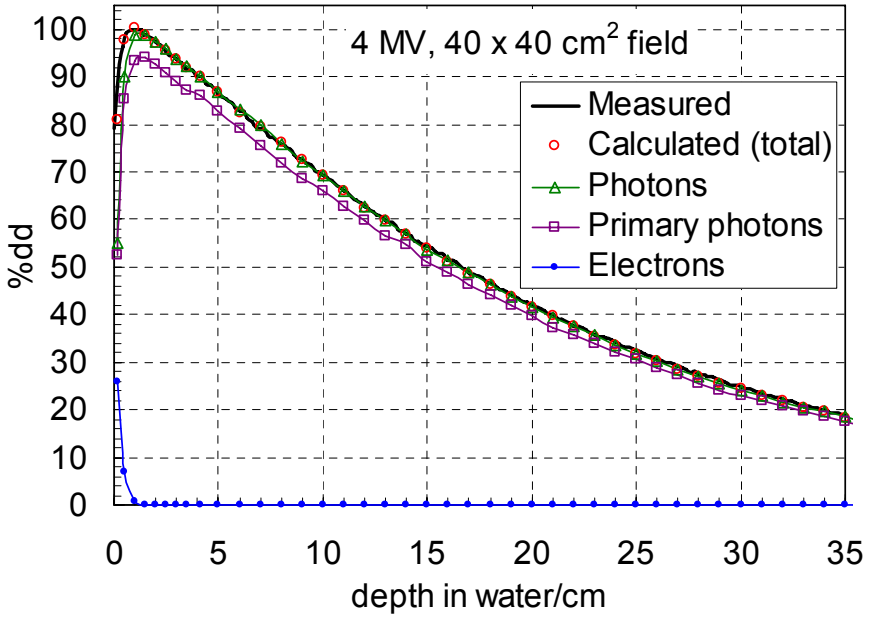

Figure 3(b). Comparison of measured and Monte Carlo calculated central axis depth-dose curves along with dose distributions from incident photons, primary photons and electrons for a 40 × 40 cm^2 field at 4 MV (SSD=100 cm).

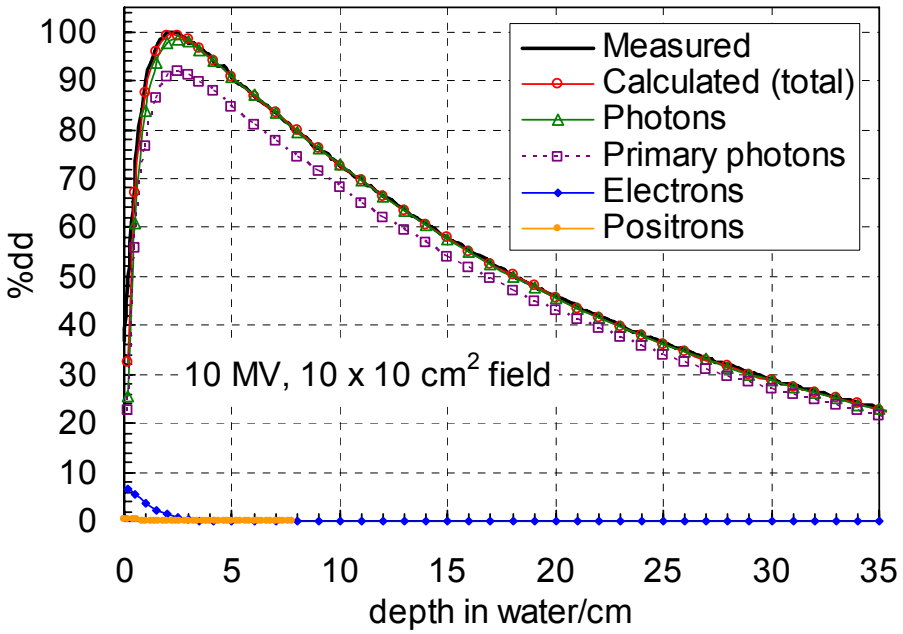

Figure 3(c). Comparison of measured and Monte Carlo calculated central axis depth-dose curves along with dose distributions from incident photons, primary photons, electrons and positrons for a 40 × 40 cm^2 field at 10 MV (SSD=100 cm).

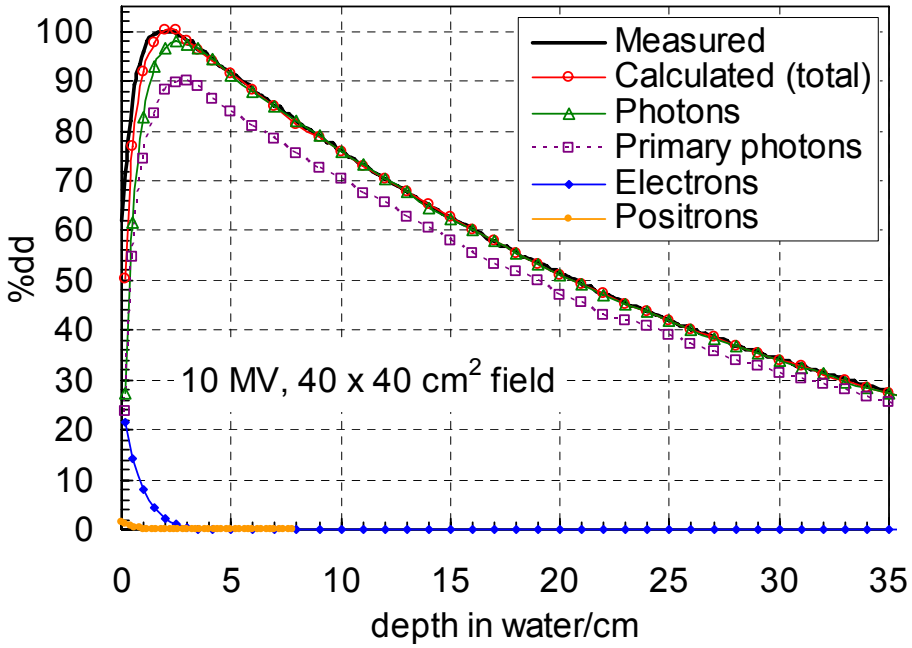

Figure 3(d). Comparison of measured and Monte Carlo calculated central axis depth-dose curves along with dose distributions from incident photons, primary photons, electrons and positrons for a 40 × 40 cm^2 field at 10 MV (SSD=100 cm).

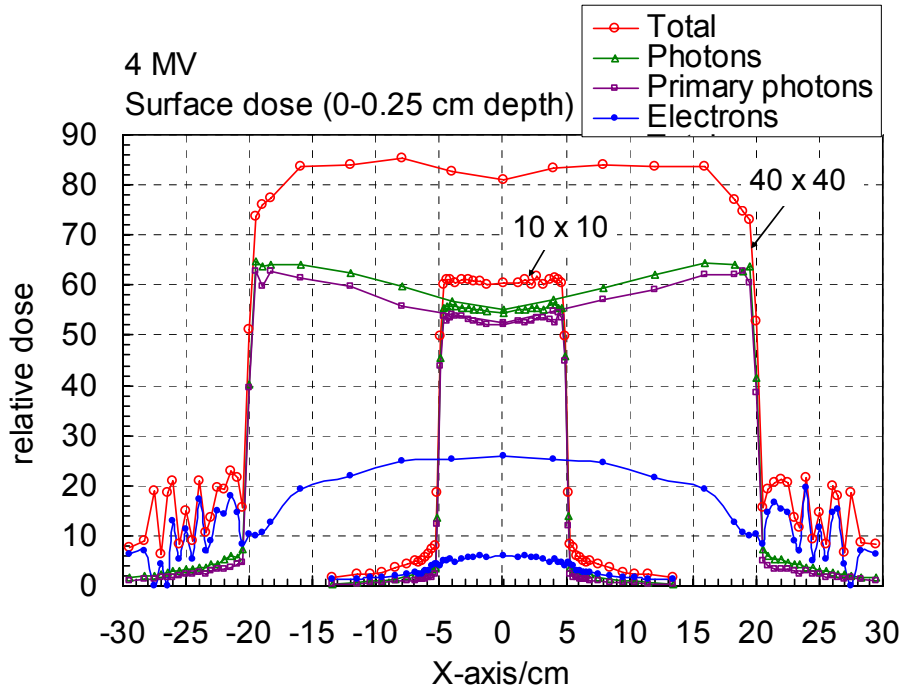

Figure 4(a). Monte Carlo calculated surface dose and contribution from different particles to surface dose across the fields for 10×10 cm^2 and 40×40 cm^2 fields at 4 MV. The calculated dose is the average dose between 0 and 0.25 cm depth in water.

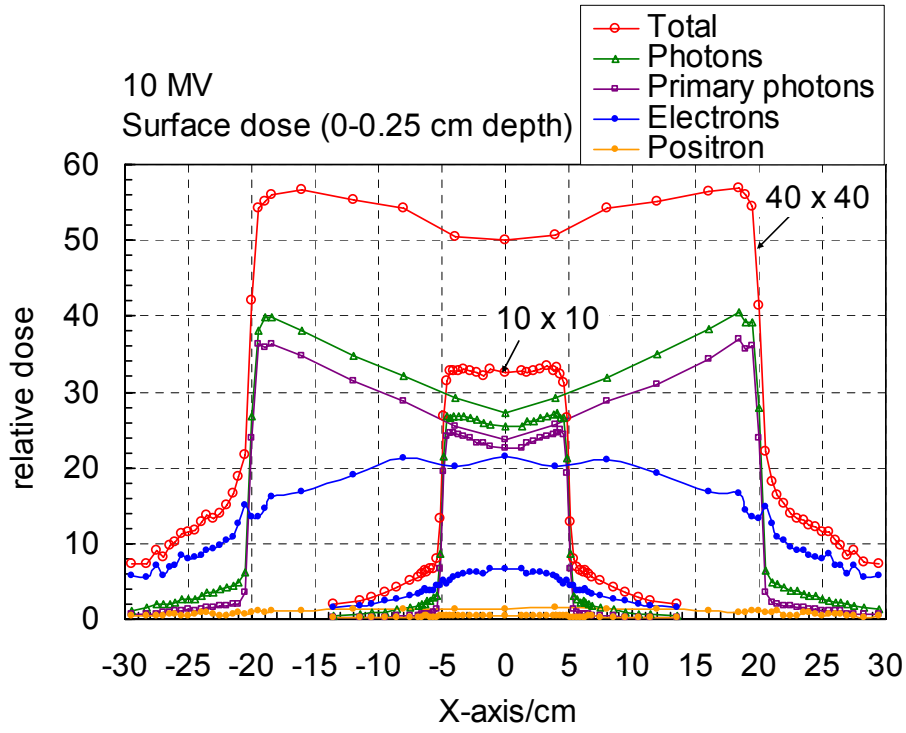

Figure 4(b). Monte Carlo calculated surface dose and contribution from different particles to surface dose across the fields for 10×10 cm^2 and 40×40 cm^2 fields at 10 MV. The calculated dose is the average dose between 0 and 0.25 cm depth in water.

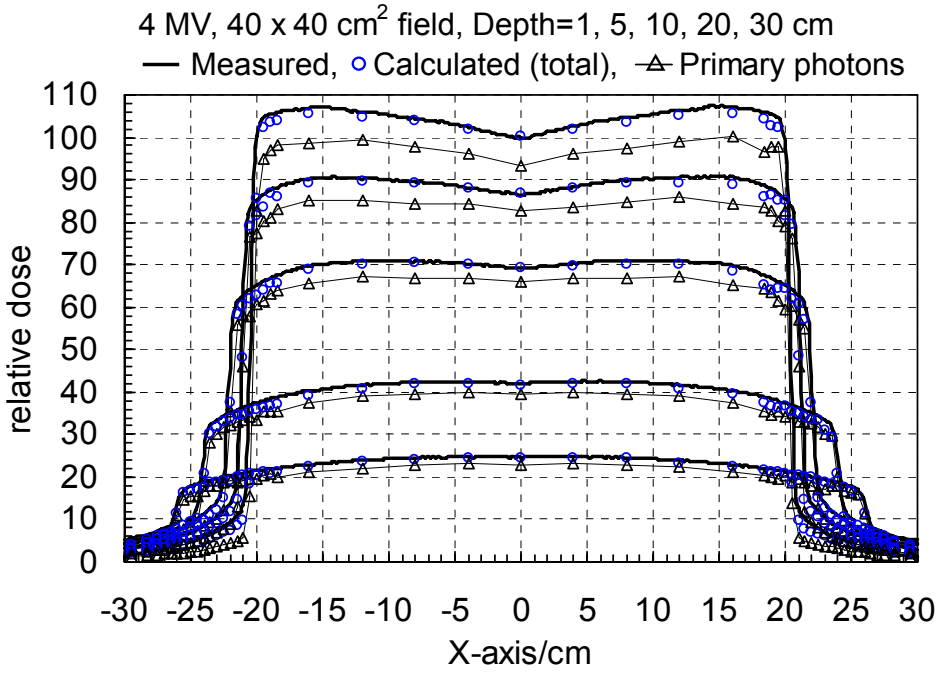

Figure 5(a). Comparison of measured and Monte Carlo calculated dose profiles and contributions from primary photons for a 40 × 40 cm^2 field at 4 MV, SSD=100 cm. The profiles are at depths of 1, 5, 10, 20 and 30 cm.

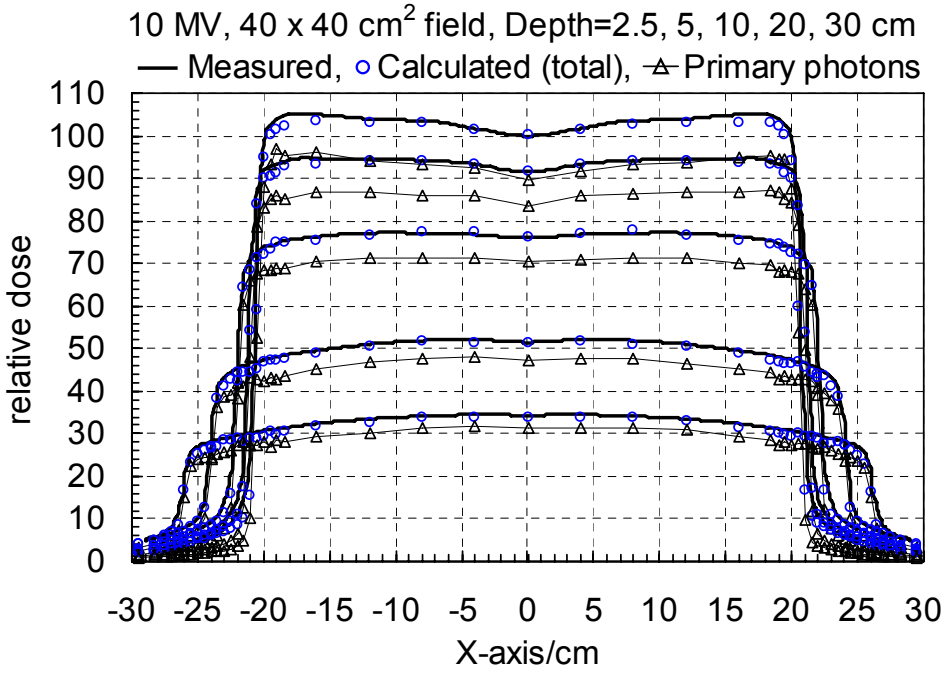

Figure 5(b). Comparison of measured and Monte Carlo calculated dose profiles and contributions from primary photons for a 40 × 40 cm^2 field at 10 MV, SSD=100 cm. The profiles are at depths of 2.5, 5, 10, 20 and 30 cm.

MONTE CARLO CALCULATION OF IN-AIR OUTOUT FACTORS

Pang-I Wang[1], Ren-Dih Sheu[2], Ching-Jung Lo[3], Chen-Shou Chui [4], Uei-Tyng Lin[2], Wei-Li Chen[1]

1. National Yang-Ming University, Taipei, TW

2. National Radiation Standard Laboratory, Institute of Nuclear Energy Research, Tao-Yuan, TW

3. Chang Gung Memorial Hospital, Tao-Yuan, TW

4. Memorial Sloan-Kettering Cancer Center, New York, NY

Abstract

Monte Carlo techniques have been widely used in different areas of medical physics. For example, in radiation therapy, Monte Carlo calculation provides a method to simulate dosimetry. Although computationally intensive and time consuming, Monte Carlo simulation is still an ideal tool for this purpose. In this work, we used Monte Carlo simulations to study the in-air output factors of a clinical photon beam produced by a treatment machine. The variation of in-air output factor with field shape and size is an important problem in radiation therapy and has been studied extensively in the past. 1~4 For intensity modulated radiation therapy (IMRT), this problem is even more pronounced as each field is composed of many irregularly shaped small fields. We will describe the simulation of the treatment machine, present the results and compare them with measured data, and discuss the limitations of the current method.

I. Introduction:

In external beam radiation therapy, the in-air output factor discussed today which also called head scatter factor is one of the parameter of field size. Three major contributors of scatter radiation to the in-air output of a medical linear accelerator are flattening filter, wedge, and collimators. In addition, the variation of in-air output factor is caused by the backscatter of radiation into the monitor ionization chamber. Conventionally, the in-air output factor is expressed as

$$S_c = D_{x\times y} \big/ D_{10\times 10} \qquad (1)$$

Where Dx×y is the dose in air on the central axis at reference plane, and x×y is the collimator setting. 5 The in-air output factor is often calculated from a finite set of measured data, usually based on a series of square fields. However, these methods do not work well for other field configurations. For example, they cannot accurately account for the well-known problem of collimator exchange effect, which can cause errors as great as 1~3%. One way to improve the accuracy is to gather extensive measured in-air output data of different field configurations. This obviously requires a lot of efforts. Besides, it still does not work well in general for irregularly shaped fields. The objective of this study was to utilize a Monte Carlo technique to simulate linear accelerators and to evaluate the scatter radiation from the construction materials of linear accelerator. This method can accurately calculate in-air output factors of varied field configurations with correction for the monitor backscatter.

II. Materials and Methods

A. Experimental methods

In this study, in-air output factors can be divided into two parts, one is the effect of backscatter radiation which results from the monitor chamber in the head of linear accelerator, and the other arise from the construction materials of the linear accelerator. All measurements were made with a PTW 23323 chamber (collection volume 0.1 cc). In order to restrict small measuring volume and reach the state of electron equilibrium, a 1 mm brass build-up cap was placed around the ion chamber. All measured data were collected from a Varian 21EX with a 6 MV photon beam.

Clinically, when we want to create a constructed irradiated field, two pairs of movable collimators are used. However, there is one monitor ion chamber in the head of the accelerator to control the output monitor unit. But this monitor ion chamber has a shortcoming, that the chamber cannot distinguish whether the radiation coming from source or collimators. As long as monitor chamber's reading value reaches to the establishing value, the accelerator will stop radiation output immediately. Thus we know that, when the backscatter is detected by the monitor ion chamber, the actual output dosage of the machine will be lower than what we expect. Due to this reason, it will reduce the scatter factors which we actually measure. In order to separate this effect of monitor backscatter, one series of measurements was made in a telescopic setting as shown in Figure 1.6~7 The chamber was placed at 150 cm surrounded by a lead shield. A 7.5-cm thick lead plate was placed below the machine head to absorb the scattered radiation from the head. A small center hole was drilled in the middle of the plate to allow the primary radiation to go through. These measurements were made for a series of rectangular fields with one set of the jaws fixed at 40 cm while the other set of jaws varied from 5 cm to 40 cm.

The in-air output factors were measured at the isocenter for the same series of square and rectangular fields. These measurements include the effect of backscatter from the collimating jaws into the monitor chamber. The second part of experiments is to measure head scatter value. Ion chamber was placed at the erect way and source-to-detector distance is 100 cm (Figure 2). Three series of the following results were then collected separately: (a) square fields from 5×5 to 40×40 cm2; (b) symmetric rectangular fields with 40 cm X-jaw setting and Y-jaw settings from 5 to 40 cm; (c) symmetric rectangular fields with Y-jaw fixed at 40 cm and X-jaw varied from 5 to 40 cm.

B. Monte Carlo simulation

Monte Carlo techniques have become popular in different areas of medical physics due to the stochastic nature of radiation emission, transport and detection processes. The Monte Carlo program EGS4 and the user code OMEGA/BEAM were used to simulate the 6 MV photon beam from a Varian 21EX.8 The component modules we have built for the linear accelerator consist of the following: x-ray target (SLABS), primary collimator (CONS3R), Be vacuum window (FLATFILT), flattening filter (FLATFILT), monitor chamber (SLABS), mirror (MIRROR), movable collimator (XYJAWS), clearance (SLABS), and the phantom (CHAMBER). Scoring region was set as a cylindrical water phantom with radius 3 cm and height 1.5 cm. A generic version of the machine head structure is illustrated in Figure 3. The source part of the accelerator was assumed to be a Gaussian distribution, and its FWHM is 0.15 cm, electron beam energy is 6.2 MeV. Each simulation used monoenergetic electrons incident on the target. Due to limit of calculation time, we have adopted some Variance reduction techniques, such as selective bremsstrahlung splitting, geometry splitting and raising energy cutoff settings. The cutoff energies for electron and photon transport were 2 MeV and 2 MeV, respectively. The bremsstrahlung photons generated by electrons below the cutoff energy were ignored. Each particle is followed until its energy falls below the cutoff energy or it escapes from the system. Energy deposited

in the phantom (chamber) was collected for a series of square and rectangular field sizes as defined by the movable jaws.

III. Results and discussion:

As the irradiated field size increases, the in-air output factor also raises. This variation of output factor with the field geometry is attributed to two factors. The primary reason is due to the radiation scattered from the components in the accelerator head. The secondary reason is due to the backscattered radiation into the monitor ionization chamber. Our current implementation of the Monte Carlo method simulated the head scatter very accurately. However, it did not simulate the backscattering into the monitor chamber. Thus, for fair comparison, our Monte Carlo results were compared to the measured data with the monitor backscatter effect removed. Under these conditions, the calculated data agreed with the measured values to less than 1% for symmetric square field sizes from 5 cm to 40 cm showed in Figure 4. The average difference is 0.54%. For rectangular fields with a set of the jaws fixed at 40 cm and the other set of jaws varying from 5 cm to 40 cm, the average difference between measured and calculated output factors was within 1%. Figure 5 shows the results that lower jaws fixed at 40 cm and changing upper jaws sizes. We can observe that the minimum and maximum differences between the calculated and measured data are all less than 1%, and about 0.36% for average difference. As shown in Figure 6, the average difference of upper jaws fixed at 40 cm is about 0.33%.

IV. Conclusion:

While calculating using the Monte Carlo technique, we tried to maintain every group's variance less than 1%. The results of these three groups showed a good agreement between calculation and measurement. From the results, we can not only double check the results, but also can evaluate the accuracy of measured results with revised monitor backscatter effect. The measured data in this study can be used for future work where monitor backscatter effect has to be considered.

Nowadays, Monte Carlo methods are used to simulate only the head scatter factors of rectangular and square field. In future work the simulation can be extended to simulate the head scatter factors of irregular fields. In addition, we can also use Monte Carlo simulation to analyze the source and contribution of the head scatter, and thus evaluate the influence of monitor backscatter.

Acknowledgments:

The author appreciates Dr. Chen-Shou Chui and Ching-Jung Lo for their helpful discussions and assistance. The author is also grateful to communicate on Monte Carlo techniques with Ren-Dih Sheu and Uei-Tyng Lin.

Reference:

1. Timothy C.Z. & Bengt E.B. Head scatter off-axis for megavoltage x rays. Medical Physics 30 (4), 533-543 (2003).
2. Timothy C.Z., Bengt E.B., Ying X. & Yang C.J. Modeling the output ratio in air for megavoltage photon beams. Medical Physics 28 (6), 925-937 (2001).
3. Anders A. Collimator scatter in photon therapy beams. Medical Physics 22 (3), 267-278 (1995).

4. Helen H.L., Rock T.M. & Edwin C.M. A dual source phton beam model used in convolution/superposition dose calculations for clinical megavoltage x-ray beams. Medcial Physics 24 (12), 1960-1974 (1997).
5. Attix F.H. Introduction to radiological physics and radiation dosimetry. A Wiley-Interscience publication, United States (1986).
6. Hideo K. Telescopic measurements of backscattered radiation from secondary collimator jaws to a beam monitor chamber using a pair of slits. Medical Physics 16 (2), 295-298 (1989).
7. Helen H.L., Rockwell T.M. & Edwin C.M. Modeling photon output caused by backscattered radiation into the monitor chamber from collimator jaws using a Monte Carlo technique. Medical Physics 27 (4), 737-744 (2000).
8. Ren-Dih S., Bor-Jing C., Chung-Kung L.. INER-2418 REPORT: The Monte Carlo simulation of LINAC - Varian 21EX 6X photon mode. Institute of Nuclear Energy Research, R.O.C.(2003)

Fig. 1. Setup for monitor chamber backscatter measurement.

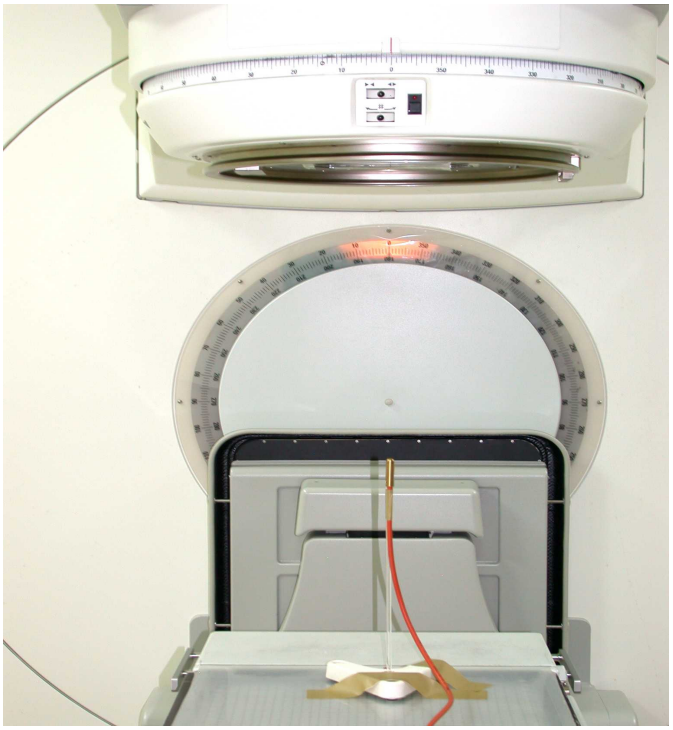

Fig.2. The setup method of in-air output factors measurement.

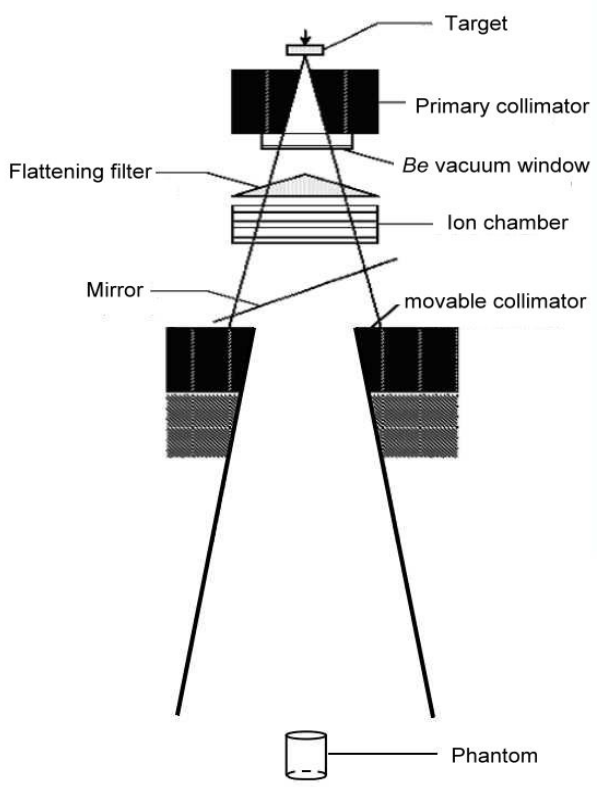

Fig. 3. Schematic drawing of the component modules of a linear accelerator used in the Monte Carlo simulation.

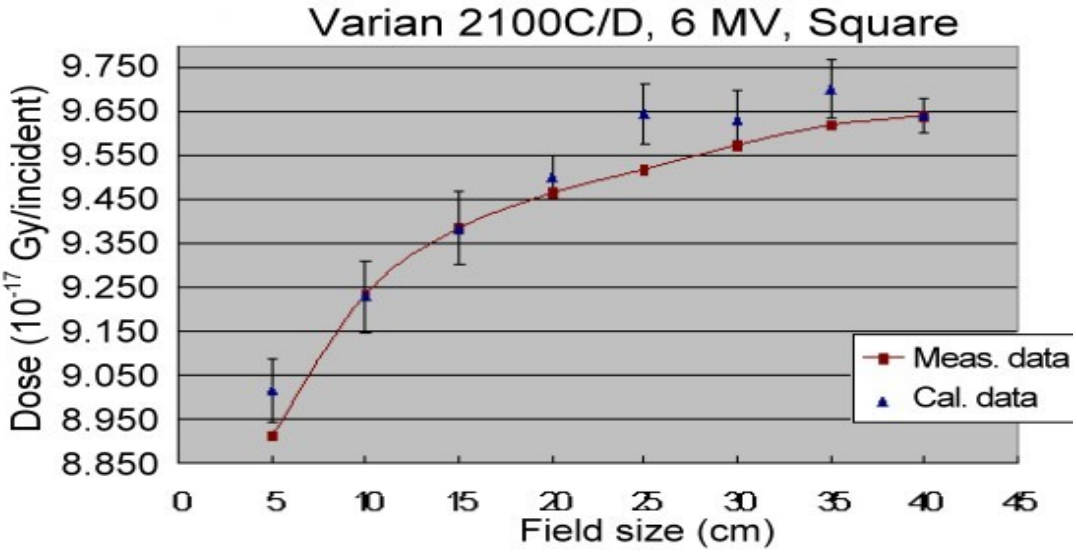

Fig.4. The comparison between the calculated and measured in-air output factors for 6 MV. For a set of fields: symmetric square fields with field sizes form 5 cm to 40 cm.

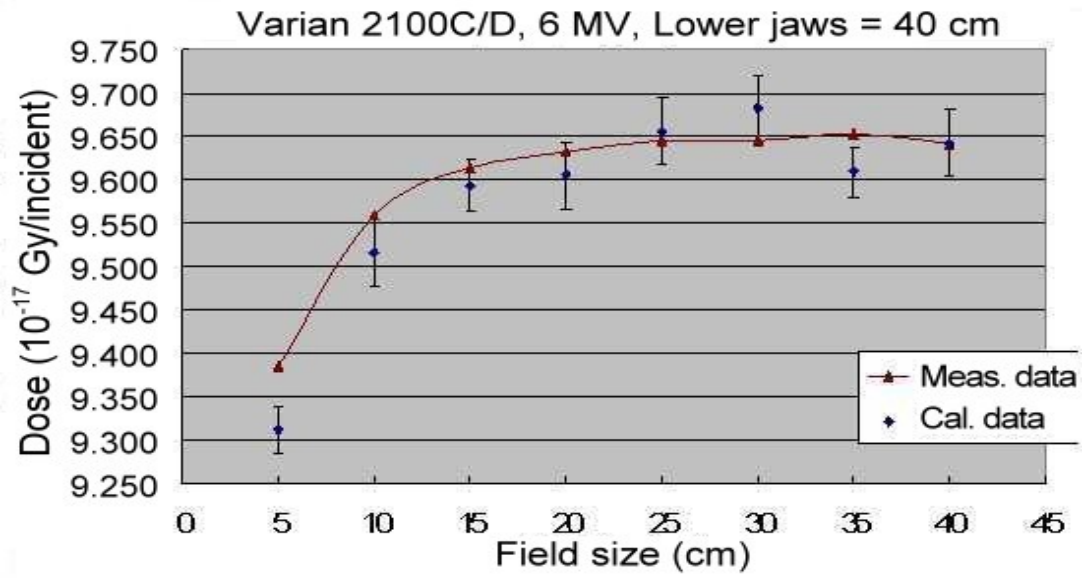

Fig.5. In-air output factors for 6 MV photon beam as a function of the lower jaws moving from 5 cm to 40 cm with the upper jaw pairs completely opened.

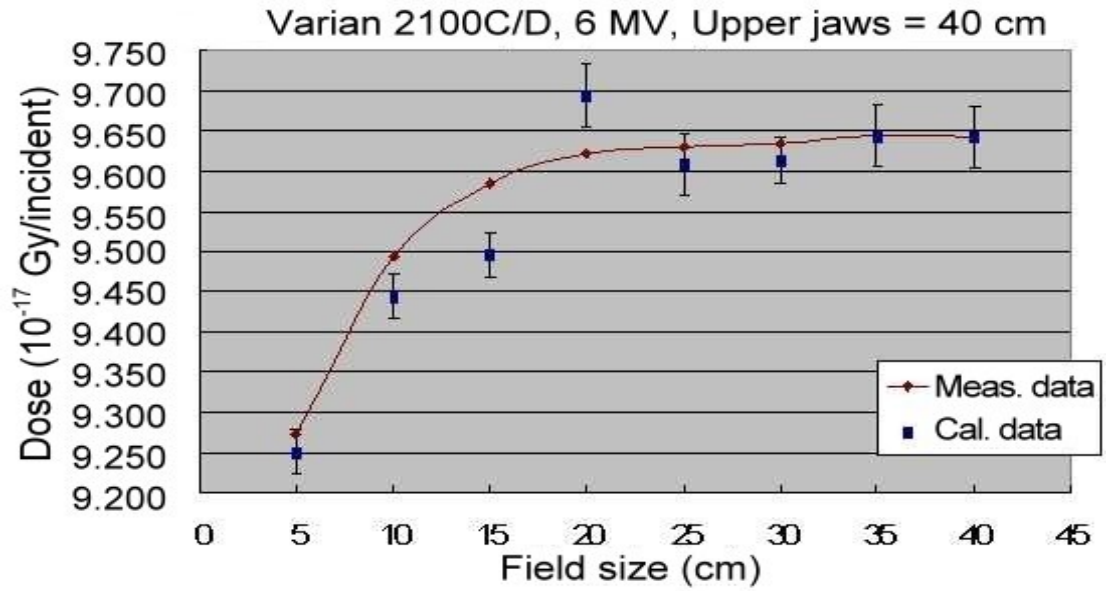

Fig.6. In-air output factors for 6 MV photon beam as a function of the upper jaws moving from 5 cm to 40 cm with the lower jaw pairs completely opened.

MONTE CARLO CALCULATIONS AND GafChromic FILM MEASUREMENTS FOR LEKSELL GAMMA KNIFE UNIT

Hsiu-Wen Lee[1], Ren-Dih Sheu[2], Uei-Tyng Lin[2], Wei-Li Chen[1]

1. Institute of Radiological Science, National Yang-Ming University, Taipei, TW
2. National Radiation Standard Laboratory, Institute of Nuclear Energy Research, Tao-Yuan, TW

Abstract

The Leksell Gamma Knife is a standard radiosurgical tool for treating brain lesions by directing beams of gamma radiation to a specific region. The diameter of the gamma beams is confined by collimator systems and the available collimator sizes are 4, 8, 14 and 18 mm. The reduction in dose rate for each collimator helmet is called the output factor. Experimental determination of output factors is difficult due to the extremely narrow beams by which the dose is determined. In the present work, the Monte Carlo technique and GafChromic films were employed to verify the dose distribution and the output factor of Gamma Knife (type B) radiosurgery. The output factors measured with GafChromic film and the results of our Monte Carlo trials were within uncertainty range and showed consistency with the value provided by the manufacturer of Leksell Gamma knife, Elekta. Moreover, good agreement in dose profiles along x, y, and z axes for all collimator helmets were summed up over all 201 sources.

1. Introduction

The Leksell Gamma Knife is a radiosurgical instrument used to treat deep-seated intracranial tissues. The benign or malignant tumors, which are inaccessible or unsuitable for conventional invasive surgery. The Gamma Knife delivers a single dose of ionizing radiation exiting from 201 ^{60}Co sources. Each individual beam is mechanically focused on the target and the precision at the target. It makes the Gamma Knife ideal for treating critically located structures. Different beam diameters, 4, 8, 14 and 18 mm, can be varied by the exchange of collimator helmets [1]. This allows lesions of different size and shape to be treated. A steep dose gradient creates a region with sharply circumscribed boundaries, providing precise eradication of the target while sparing surrounding tissues by strictly respecting the boundaries of the target.

The reduction in dose rate for each collimator helmet is called the output factor. It is a way of relating the absorbed dose at a point in a given field at a certain depth to the absorbed dose of the reference field at the same point. The output factors for small field sizes show strong field size dependence, with a rapidly decreasing output factors as diameter of the field decreases. Experimental determination of output factors is difficult due to

the extremely narrow beams by which the dose is determined [2-4]. In this work, the Monte Carlo technique and GafChromic films were employed to verify the dose distribution and the output factor of Gamma Knife radiosurgery.

2. Material and Methods

2.1 Gafchromic film dosimetry

The type of the film employed in this experiment was GafChromic MD-55 were produced by Nuclear Associates, which has a measurement range of 3-100 Gy. The film is colorless and transparent before being exposed to ionizing radiation. The sensitive layer changes from colorless to blue by dye polymerization without processing, until exposure to radiation. The darkness of the blue color depends on the absorbed dose and can be measured with a laser reader. The reader for GafChromic film was manufactured by Kodak, and was comprised of a He-Ne laser light-sensor density scanner LS-50. The image resolution of the LS-50 laser reader was 12 bit, and the spatial resolution was set to 0.2 mm.The LS-50 laser light-density scanner system was calibrated before each GafChromic film reading [5-6]. All output factors from the Gamma-Knife fields are measured with a spherical polystyrene head phantom made of two hemi-spheres, having a diameter of 16 cm. Two 1cm thick film holder plates are manufactured from the same polystyrene (Figure 1). The plates snugly fit into the cutout made in the center of the spherical phantom. All 201 gamma beams passed through the opening of the collimators to the target point. The diameters of the radiation beams at the focus were confined by the size of collimators which were 4, 8, 14 and 18 mm. Figure 2 shows the Spherical phantom was mounted at the unit center point position with in the 18 mm collimator helmet [7].

2.2 Monte Carlo simulation

The Monte Carlo modeling of particle transport problems in medical radiation physics offers significant advantages over other techniques. Experiments can be performed without having to set up the physical situation. Actual results are obtained with no perturbation introduced [8-9]. The Monte Carlo program EGS4 and the user code OMEGA/BEAM is a general purpose Monte Carlo code to simulate the radiation beams from radiotherapy units including high-energy electron and photon beams, ^{60}Co beams and orthovoltage units. It concludes two parts: the BEAM code and the DOSXYYZ. BEAM code produces the phase-space output of the beam include the position, energy, direction, charge and history tag for each particle at any specified plane in the model. The model is built up from a series of individual component modules (CMs).The DOSXYZ is an EGS4 based Monte Carlo simulation code for calculating dose distributions in a rectilinear voxel phantom. Density and material in every voxel may vary. A variety of beams may be incident on the phantom, including full phase-space files from BEAM [10].

A spherical water phantom of 160 mm in diameter was used to simulate the patient's head. Each source was modeled by a cylinder of 1 mm in diameter and 20 mm in length. The ^{60}Co sources were arranged in a

sector of a hemispherical surface with a radius of about 400 mm. All 201 gamma beams passed through the opening of the collimators to the target point. The diameters of the radiation beams at the focus were confined by the size of collimators which were 4, 8, 14 and 18 mm. A single isocenter was delivered at the centre (unit centre point: x =100 mm, y =100 mm, z =100 mm) of the simulated water phantom using different size of collimator helmets (Figure 2). Scoring bins with dimensions 1 × 1 ×1 mm were defined along the x-, y- and z-axes for each collimator helmets. Histories of 10^8 simulations were performed and all history runs were divided into 10 batches for calculation of statistics and were large enough to give a standard error of less than 5% at the dose maximum region of the isodose curves. The primary photon spectrum of ^{60}Co was contained two peaks, viz. 1.173, 1.333 MeV. The global photon cutoff energy (PCUT) was set as 0.01MeV and the global electron cutoff energy (ECUT) was set as 0.7MeV.

Figure 3 shows the design chart of a single beam channel in Gamma knife unit and the model that built up from a series of individual component modules based on the design chart [11].

The CT phantom option of DOSXYZ allows calculation of dose distributions in phantoms that are derived from CT data sets. The process by which CT phantoms are created by ctcreate are outlined here and described in detail in the following sections [10]:

1. Read in the format of the CT data.
2. Read in the CT header parameters (binary or ASCII).
3. Read in the binary CT data.
4. Choose a subset of the CT data set (if desired).
5. Resample the CT data to correspond to volume elements that dose will be scored in.
6. Convert the CT data to materials and densities for each voxel.
7. Transfer the data to a disk file to be input to DOSXYZ.

Figure 4 is the default ramp for converting CT values to material and density in ctcreate. If the CT number is below the first material's upper bound then the lower CT number used for the interpolation is zero. Voxels that are read with CT numbers of less than zero will cause the program to print a message. Those voxels with CT numbers above the last material's upper CT number bound will have the density set to the maximum density for this last material and execution will continue [10].

Figure 5 shows the result that input the experimental spherical phantom CT data and use ctcreate program to create.

3. Results and conclusions

Table 1 summarized the GafChromic film measurement data and the results of our Monte Carlo simulation. The superposition of all 201 beams then produces approximately spherical shaped dose distributions, with the 50% isodose curve dimensions in x and y directions of 6,11,19 and 24 mm, respectively, at the isocenter. Table 2 shows the output factor measured with GafChromic film and the results of our Monte Carlo simulation. And both were within uncertainty range and showed consistency with the value provided by the manufacturer of

Leksell Gamma knife, Elekta [12]. Moreover, good agreement in dose profiles along x, y, and z axes for all collimator helmets were summed up over all 201 sources. On the other side, the change in dose distributions can also be predicted by simulation at the interface area. The application of EGS4 Monte Carlo technique is important, because the accurate measurement results may not be obtained easily. It should be included as a part of quality assurance program for the Gamma Knife radiosurgery.

References:

1) Leksell Gamma Unit, "User's Manual" Elekta, 1987

2) Mack A, Scheib SG, Major J, Gianolini S, Pazmandi G, Feist H, Czempiel H, Kreiner HJ. "Precision dosimetry for narrow photon beams used in radiosurgery-determination of Gamma Knife output factors." Med Phys. 2002 Sep;29(9):2080-9

3) Johns, H.E., and Cunningham, J.R., "The physics of radiology " 4th edition, Charles C Thomas, Springfield, IL. 1983

4) Attix, F.H., "Introduction to radiological physics and radiation dosimetry", Wiley, New York, 1986

5) A. Piermattei, R. Miceli, L. Azario, A. Fidanzio, S. delle Canne, C. De Angelis, S. Onori, M. Pacilio, E. Petetti, L. Raffaele, and M. G. Sabini, "Radiochromic film dosimetry of a low energy proton beam", Med Phys. 2000 Jul;27(7):1655-60.

6) A. Niroomand-Rad, C.R. Blackwell, B.M. Coursey, K.P. Gall, J.M. Galvin, W.L. McLaughlin, A.S. Meigooni, R. Nath, J.E. Rodgers, C.G. Soares "Radiochromic film dosimetry:Recommendations of AAPM Radiation Therapy Committee Task Groupe 55,"Med. Phys. 1998 Nov;25(11):2093-115

7) Cheung YC, Yu KN, Ho RT, Yu CP. "Stereotactic dose planning system used in Leksell Gamma Knife model-B: EGS4 Monte Carlo versus GafChromic films MD-55." Appl Radiat Isot. 2000 Sep; 53(3):427-30.

8) Richard L. Morin. "Monte Carlo simulation in the radiological sciences", CRC Press, Inc. Florida. 1988

9) Carter, L. L. and E. D. Cashwell, "Particle-Transport Simulation with the Monte Carlo Method ", ERDA Critical Review Series, National Technical Information Service, TID-26607,1975 Introduction to Mathematical Modeling, Leksell Gamma Plan User

10) D.W.O Rogers, C.M.Ma,G .X. Ding, and B. Walters. “BEAM users Manual.” NRC Report PIRS 509a, 1995

11) Manual, Elekta

12) Elekta 1998 New 4-mm helmet output factor Leksell Gamma Knife Public Bulletin

Figure 1. A spherical homogenous polystyrene phantom with a diameter of 16 cm

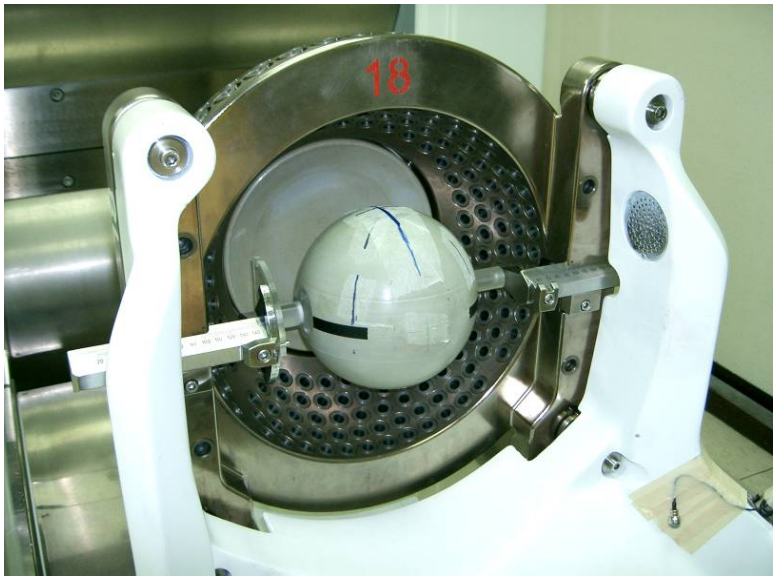

Figure 2. Spherical phantom was mounted at the unit center point position (x=y=z=100 mm) with in the 18mm collimator helmet.

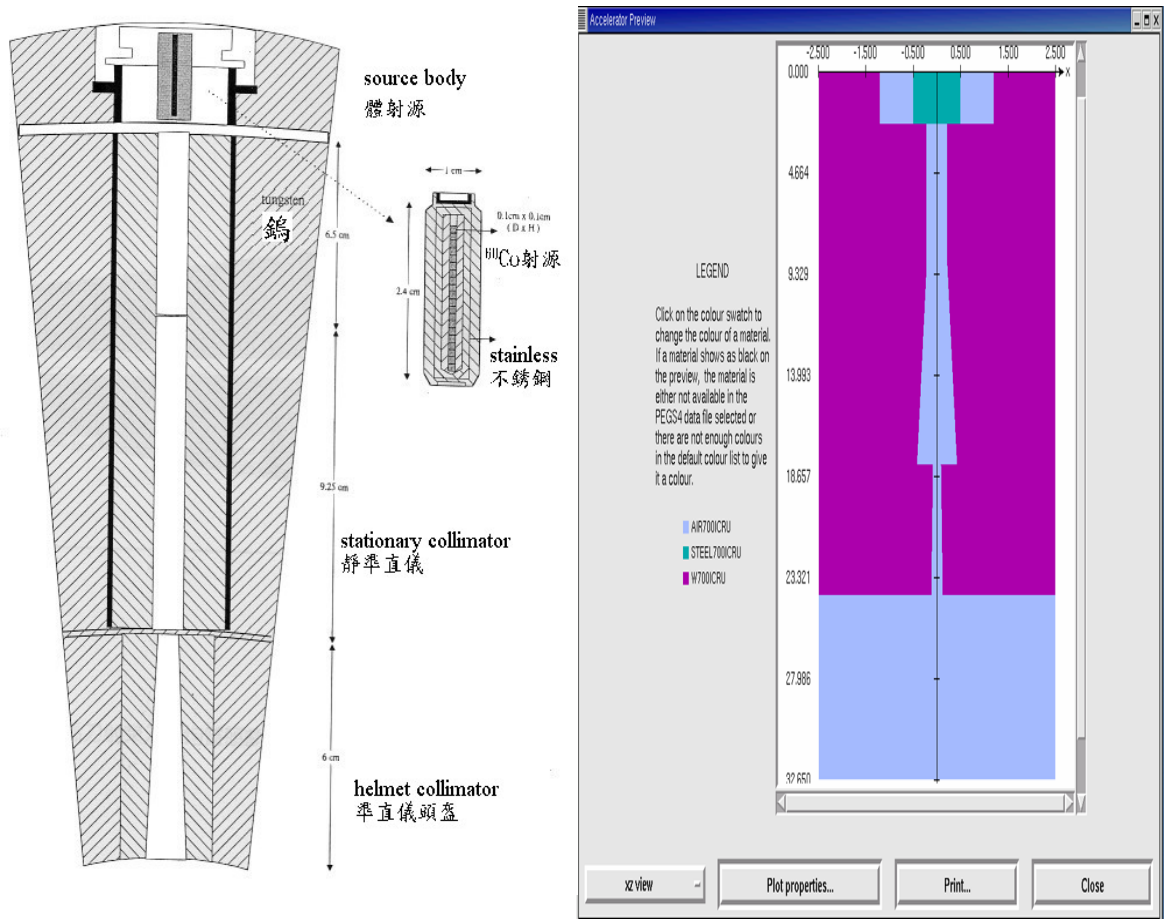

Figure 3. The design chart of Gamma knife unit a single beam channel and the model that built up from a series of individual component modules.

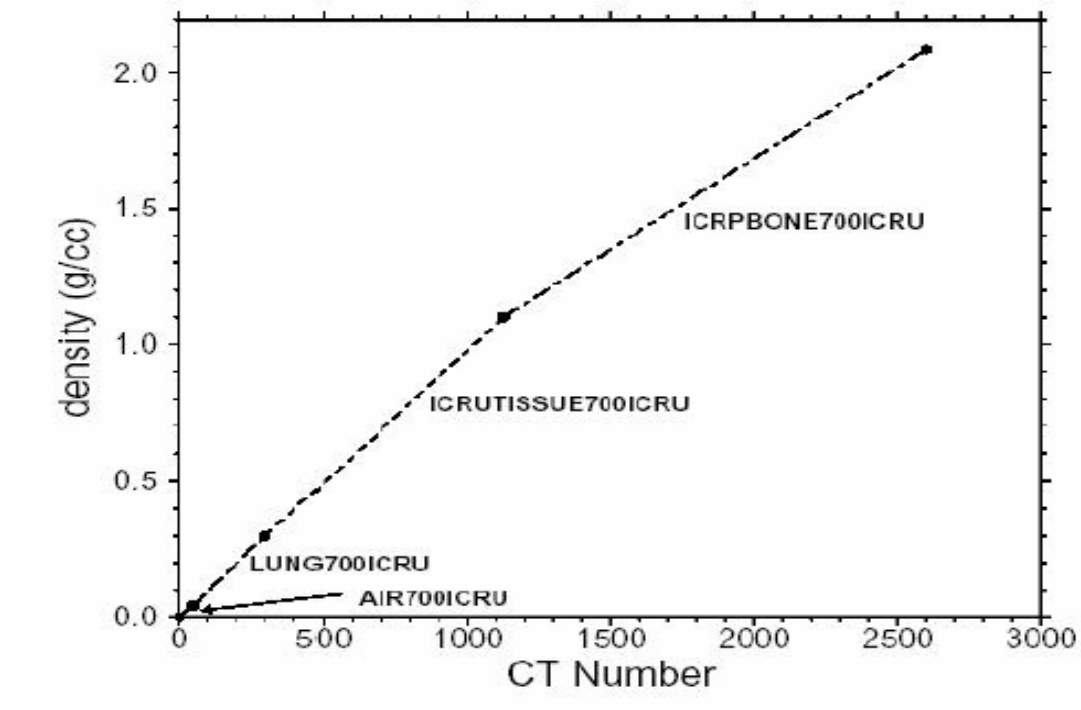

Figure 4. The default ramp for converting CT values to material and density in ctcreate program [10].

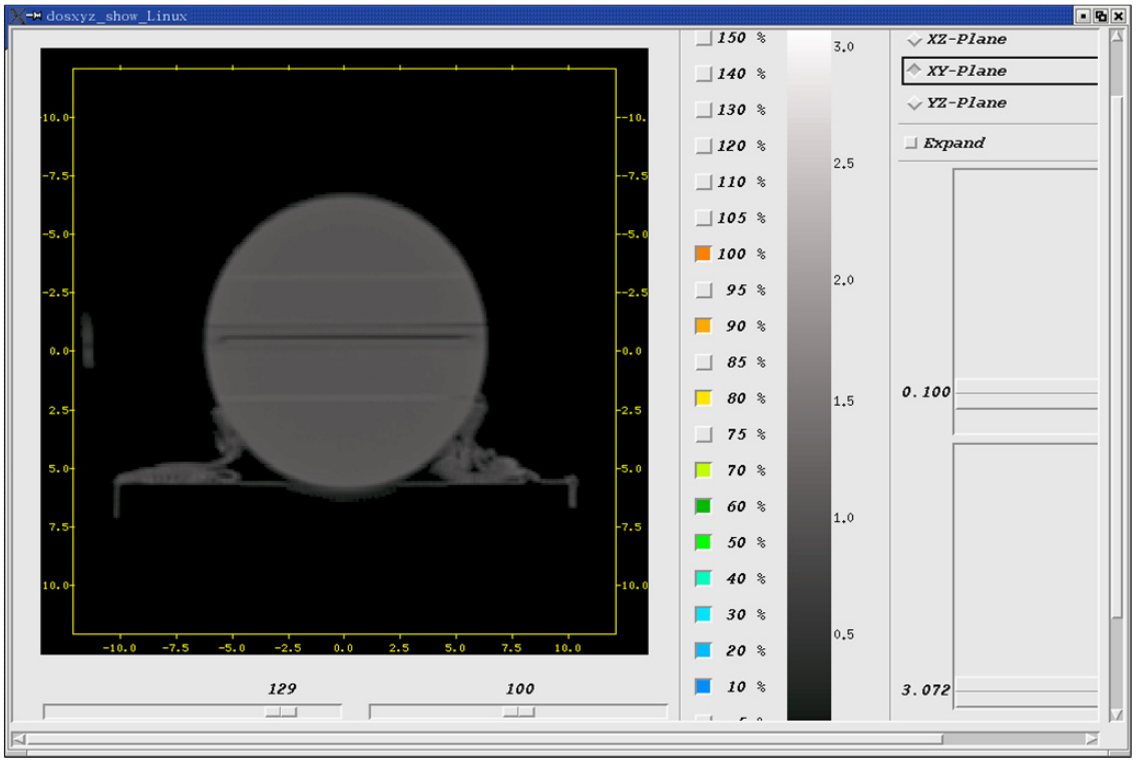

Figure 5. This image shows the result that input the spherical phantom CT data and use ctcreate program to simulate.

Table 1. The results of superposition of all 201 beams then produces approximately spherical shaped dose distributions, with the 50% isodose curve dimensions in X and Y directions. A comparison of GafChromic film measurement data, the results of our Monte Carlo simulation and Ref. 2.

size	Gafchromic film	Monte Carlo	Ref[2]
4mm	6.1±1mm	5.95mm	6mm
8mm	12.1±1mm	11.08mm	11mm
14mm	18.4±1mm	17.91mm	18mm
18mm	25.1±1mm	23.73mm	24mm

Table 2. The output factors (OPT) measured with GafChromic film and the results of our Monte Carlo simulation. Both were within uncertainty range and showed consistency with the value provided by the manufacturer of Leksell Gamma knife, Elekta [12].

size	OPF(MD-55)±1SD	OPF(Monte Carlo)	Elekta
4mm	0.843 ± 0.0270	0.860 ± 0.0129	0.870
8mm	0.954 ± 0.0161	0.954 ± 0.0143	0.956
14mm	0.982 ± 0.0145	0.985 ± 0.0147	0.984
18mm	1.000 ± 0.0065	1.000 ± 0.015	1.000

EGS PARTICLE TRAJECTORY AND GEOMETRY DISPLAY PROGRAM –CGVIEW Ver 1.2 -

A. Takamura[a],T. Sugita[a],Y. Namito[b] and H. Hirayama[b]

[a]Science System Laboratory, Sumiyoshi, Tomobe, Ibaraki, 309-17, Japan

[b]High Energy Accelerator Research Organization (KEK), Tsukuba, Ibaraki 305-0801, Japan

1. Introduction

In a calculation using the EGS code[1)], it is important and convenient to check geometry for calculation and particle trajectory visually for validating the of calculation conditions. Also, a graphical interface is useful for understanding the interactions. For these purposes, EGS particle trajectory and geometry(ex, PRESTA-CG [2)]) 3D-display program CGVIEW Ver 1.1 is made.[3)]

CGVIEW Ver 1.2 is added to a new function. The function can be used to check the geometry. Also, CGVIEW running on Linux is made.

2. Environment

Hardware : PC/AT-Compatible machine

OS : Windows98 or later or Linux(with X-Window System)

3. Outline of functions

3.1 Functions for the geometry display

1) The following 4 kinds of geometry data are displayed:
   - Spheres of co-center.
   - Cylinders of co-center line.
   - 3-dimensional slabs.
   - CG (combinatory geometry)
2) Method of display (default is plane)
   - Plane display
   - Wire-frame display
3) Level of display

   The following 3 levels can be specified for displaying the geometry:
   - Body …Display of each body can be turned ON/OFF with a specified color.
   - Zone …Display of each zone can be turned ON/OFF with a specified color.
   - Material …Display of each material can be turned ON/OFF with a specified color.
4) Hide a part of the geometry

By specifying a virtual box, it is possible to hide a part of the geometry that overlaps with the virtual box. Specify the minimum and maximum of x-, y- and z-directions of a virtual box. If some of them are left blank, the minimum and maximum values are automatically set from the data being displayed.

5) Area of the display

The area of the display is automatically set using input data.

6) Axis for the display

The axis for the display can be selected from the following 4 sets. A right-hand system of coordinates is adopted:

- Z-Y … Z-axis plus in right direction, Y-axis plus for upper direction (default).
- Y-Z … Y-axis plus in right direction, Z-axis plus in upper direction.
- X-Z … X-axis plus in right direction, Z-axis plus in upper direction.
- X-Y … X-axis plus in right-direction, Y-axis plus in upper direction.

7) Specification of the background color

It is possible to select the background color (default color is black).

8) Specification of the character color

It is possible to select the character color (default color is white). Characters are used in the axis, title, memo etc.

9) Correction option in specifying zones

Zone may not be properly displayed due to a numerical problem of the computer. This tends to happen when subtraction of the body is performed. To correct this, the size of the subtracting body is made bigger. The amount of correction is calculated from the following items and equation:

- Correction factor … A correction is specified as ratio to the original length (default = 1E-6).
- Correction value … Specify a correction value directly (default=0.005cm).

Corrected length = original length + original length * correction factor + correction value

3.2 Function regarding particle trajectory display

1) The following 3 kinds of particles are displayed:

- Photon (gamma,x)
- Electron (e^-)
- Positron (e^+)

2) The following items can be specified:

- History region

By inputting the upper and lower boundaries of the history, the area of history to be displayed is specified. If not specified, the minimum and maximum history numbers are automatically

used. Also, by specifying the number of the last history, that number of the last part of the history is displayed.

- Line color

  Specify for each kind of particle.

  Photon - Yellow (Default)

  Electron - Red

  Positron - Blue

- Line type

  Select line type from the following 4 types for each particle: The default value is the solid line for all particles.

  [Solid, Chain, Dot-chain, Double dot chain]

- Line width … Possible to select the line width for each particle. The default is 1.
- Turn ON/OFF … Displaying each kind of particle can be turned ON/OFF.
- Energy region

  By specifying the energy region for each kind of particle, it is possible to turn off displaying particles whose energies are outside of the specified energy region. If not specified, 0 and 1E+15 are specified as the lower and upper boundary, respectively.

3) Particle weight

It is possible to modify the line width using WEIGHT information of each particle. The width of each particle is set as the line width for each kind of particle * WEIGHT. If the WEGHT value is not written in the input data, 1 is specified for all points.

4) LATCH

It is possible to control the turning ON/OFF display by using a flag for each history. Also, turning ON/OFF latch function can be specified.

3.3 Function using mouse

The following 3 functions are related to mouse operation:

1) Zoom in/out

Move mouse while pushing the right button of the mouse. Zoom in and out by moving the mouse downward and upward, respectively.

2) Parallel movement

Move the mouse while pushing both the right button and the left button, or the central button of the mouse.

3) Rotation

Move the mouse while pushing the left button of the mouse.

3.4 Peripheral functions

1) Functions on the displaying axis
   - Turning ON/OFF of axis
   - Unit of scale … Unit of scale for the axis (default is cm).
   - Interval of scale … Interval of the scale line (default value = 1).
   - Scale length … Length of the scale line for the axis (default value = 0.25).
   - Arrow size … Arrow size at the top of the axis (default value = 1)
   - Character size … Character size for a scale label (default value = 1)
   - Character space … Character space for a scale label (default value = 5)
2) Functions on displaying a title box
   It is possible to add a title box in a displayed figure. The user inputs the contents of the title box. The position of title box can be changed using the mouse. (Multi-line input is allowed for the title box.)
3) Functions on displaying the memo box
   It is possible to add a memo box in a displayed figure. The user inputs the contents of the memo box. The position of a memo box can be changed using the mouse. (Multi-line input is allowed for the memo box.)
4) Functions on displaying a legend
   It is possible to add a legend of particles in a displayed figure. The contents of the legend are:
   - Region of history being displayed
   - Line type and color for each particle
5) Functions on the printing figure
   It is possible to print a figure displayed on the screen.
6) Functions on saving a figure
   It is possible to save a figure displayed on the screen in a bit map file.
7) Open a DOS window
   It is possible to open a DOS window from the main window of cgview.
8) Read a file in again
   It is possible to read in the current data file. Specification of file name is not necessary. After an EGS calculation is finished, the data file can be read in again to see the calculated result. Using this function a semi-interactive use of EGS and cgview is possible.
9) Initialization of a specification
   It is possible to clear the specifications for the display and use default values.

3.5 Function to create geometry data

CGVIEW can be used to help create geometry data for an EGS calculation. Only CG data are

supported for this function. Input geometry data of the EGS code to CGVIEW, and check them in a 3-dimensional figure on the screen. Also, it is possible to save created data. This data can be used as a CG input file in an EGS calculation.

3.6 Function to check geometry data

CGVIEW can be used to help check geometry data for an EGS calculation. Input start position and direction region for particle. CGVIEW checks a geometry data at middle point of boundaries.

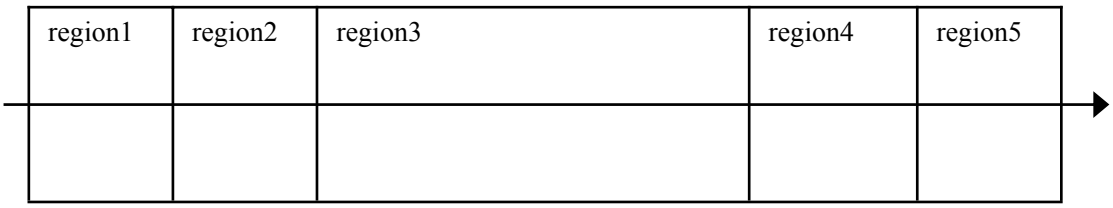

Checked errors are

- overlap region

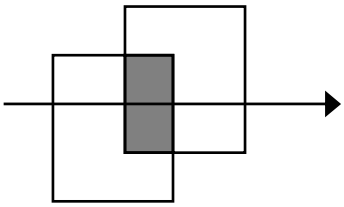

- no define region

- outside region's material number is not 0

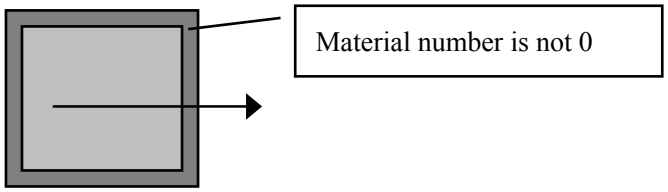

4. Relationship between EGS and CGVIEW

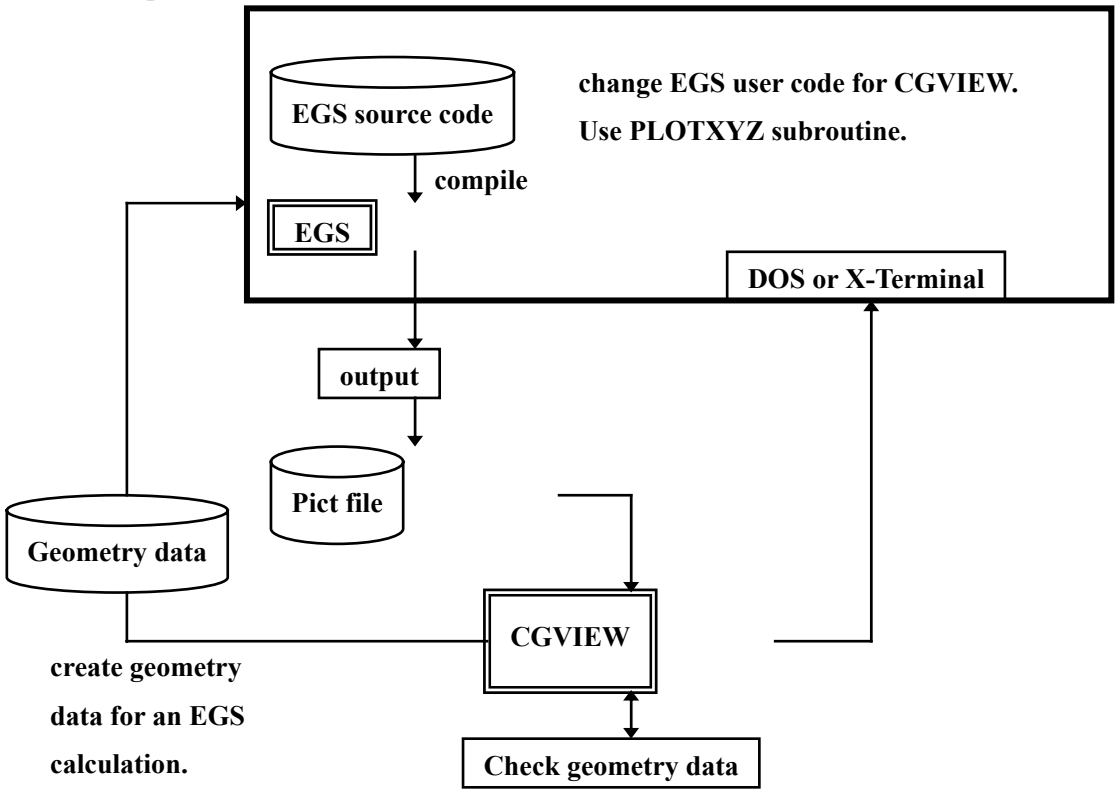

5. Example of display

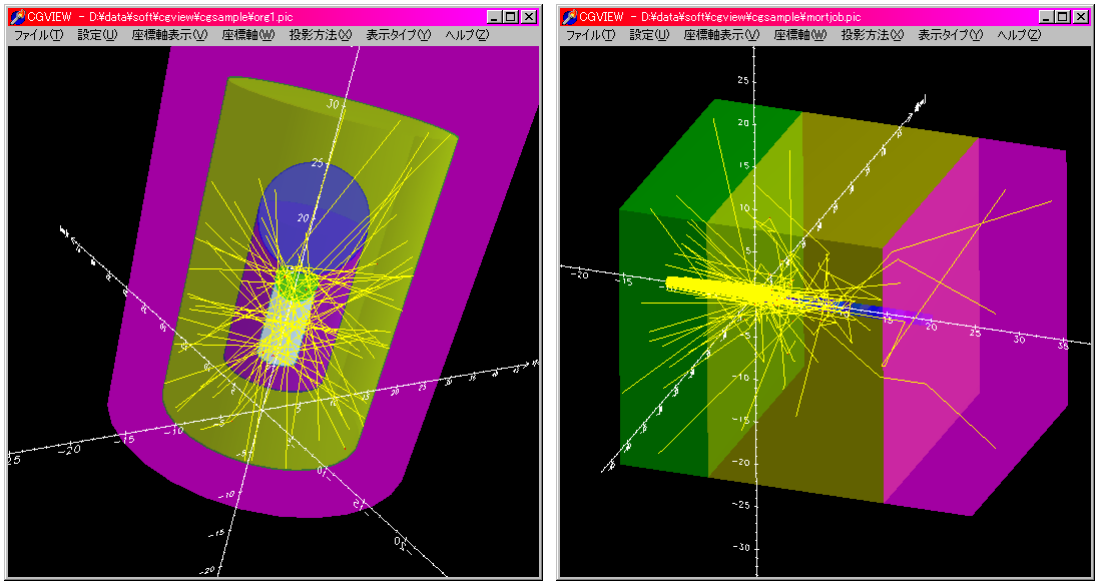

References

[1] W.R.Nelson, H.Hirayama, and D.W.O.Rogers, SLAC-265,SLAC(1985)

[2] T.Torii et al, JNC TN1410 2002-001

[3] Y.Namito, H.Hirayama, A.Takamura and T.Sugita, KEK Proceedings 2003-15

DEVELOPMENT AND VALIDATION OF A MONTE CARLO DOSIMETRIC QUALITY ASSURANCE SYSTEM FOR DYNAMIC INTENSITY-MODULATED RADIOTHERAPY

T. Yamamoto[1], Y. Miyabe[1], S. Yano[2], T. Teshima[1], T. Mizowaki[3], Y. Nagata[3], and M. Hiraoka[3]

[1]Department of Medical Physics & Engineering,
Osaka University Graduate School of Medicine, Osaka 565-0871, Japan
[2]Clinical Radiology Service, Kyoto University Hospital, Kyoto 606-8507, Japan
[3]Department of Therapeutic Radiology and Oncology,
Kyoto University Graduate School of Medicine, Kyoto 606-8507, Japan
e-mail: tyama@sahs.med.osaka-u.ac.jp

Abstract

Intensity-modulated radiotherapy (IMRT) is one of the advanced radiotherapy techniques which can deliver high doses to tumor and spare surrounding normal tissues, however, the commercial treatment planning systems cannot predict the accurate dose in the intensity modulated fields. The main purpose of this study is to develop a Monte Carlo (MC) dose calculation system for routine dosimetric quality assurance (QA) of dynamic IMRT. The Varian Clinac 2300C/D linear accelerator equipped with the 80-leaf Mark II MLC was modeled using the EGS4 MC code for a 6 MV photon beam. The MLC was modeled fully incorporating its specific design. The MC models of treatment head and MLC was validated by the measurements. A user-friendly graphical user interface (GUI) application was developed to construct a CT-based patient model and enable the dose calculation under the identical conditions with the commercial system. In the treatment head model, the MC calculated results agreed with the measurements to within 2% for depth doses, whereas there were large differences for dose profiles. The MLC dosimetric effects were well reproduced by MC, however, there were large discrepancies up to 8% between MC and film measurement. In this study, an MC dosimetric QA system for dynamic IMRT was developed, although its accuracy must be improved. This system can be a powerful QA tool to provide the benchmark data for routine verification of the results from the IMRT commercial system.

1. Introduction

Intensity-modulated radiotherapy (IMRT) [1] has been widely used in the treatment of cancers in the sites such as prostate [2,3], head and neck [4,5], and breast [6]. IMRT is based on the mathematically optimized non-uniform complex intensity distributions, which can be generated by a computer-controlled multileaf collimator (MLC). It is difficult to determine the accurate dose in the intensity modulated fields mainly because of two reasons. First, a precise dose calculation algorithm is required in the variable intensity situation of IMRT. An IMRT beam is comprised of a number of discrete beam elements called beamlets, which correspond to a portion of the travel of a MLC leaf. IMRT Collaborative Working Group [7] has reported that the 1 x 1 cm^2 field, typical size of the area of a beamlet, showed severe perturbation in the central axis 4 MV x-ray depth doses. The necessity of the dose calculation algorithm, which can accurately predict the electronic disequilibrium effects, has been pointed out. Secondly, the designs of MLCs have specific dosimetric characteristics affecting the resultant dose distribution, i.e. inter-leaf leakage, intra-leaf transmission

[8,9], tongue-and-groove underdosage effect [10], and rounded leaf tip transmission [11]. Precise consideration of these designs is required to predict the dose distribution incorporating these effects.

The Monte Carlo (MC) simulation is the only option for achieving accurate IMRT dose computations with completely considering the above issues. Some commercial treatment planning systems use superposition [12] or MC algorithms, however, commonly used approaches are still convolution [13,14] or pencil beam methods [15]. The pencil beam algorithm is not able to predict the electronic disequilibrium effect. Although the convolution and/or superposition methods can account for that effect, the MC approach is more accurate to compute the multiple scattered photon dose near the surface of a patient and scattered electrons in higher atomic number materials [16].

The main purpose of this study is to develop an MC dose calculation system for routine dosimetric quality assurance (QA) of dynamic IMRT. The linear accelerator treatment head equipped with the MLC was modeled using the EGS4 [17] MC code, and it was then validated by the measurements. A user-friendly graphical user interface (GUI) application was also developed to easily construct a CT-based patient model and enable the dose calculation under the identical conditions with the commercial system.

2. Materials and Methods

2.1 MC modeling of the linear accelerator treatment head with the MLC

We have developed the MC models of the treatment head of the Varian Clinac 2300C/D (Varian Medical Systems, Palo Alto, CA) linear accelerator equipped with the Varian 80-leaf Marl II MLC for a 6 MV photon beam. Figure 1 shows schematic drawings of the Mark II MLC. The EGS4 MC code with the PRESTA algorithm [18] was used in this study. To model the treatment head with the MLC, they were divided into the field-independent part (i.e. from target to mirror) and the field-dependent part (i.e. jaws and MLC). The electron beam incident on the target was modeled as follows: the distributions of the energy and the radial intensity were assumed as Gaussian shape and the electron beam was incident to the target perpendicularly with no divergence. The Gaussian parameters of the electron beam, i.e., the mean energy, the FWHM of the intensity distribution, and that of the energy distribution, were assumed to be 5.7 MeV, 0.20 cm, and 3%, respectively. Specific design of the Varian Mark II MLC was accurately modeled in great detail fully considering the inter-leaf minute air gap, the tongue-and-grove design, the rounded leaf tip and the leaf alignment parallel to the beam divergence. When simulating dynamic motion of the MLC leaves, the leaf sequence file generated by an IMRT treatment planning system (Varian Eclipse) was used. The cut-off energies for transport calculation of electron (ECUT) and photon (PCUT) in all calculations of this study were set to 700 keV and 10 keV, respectively.

2.2 Validation of the MC models of the treatment head and the MLC

To validate the treatment head model, the central axis depth dose curves and the lateral dose profiles were calculated for a 6 MV photon beam with field size of 10 x 10 cm^2 in the water phantom placed at 100 cm source-to-surface distance (SSD). The dose profiles were calculated at the calibration depth of 5 cm. Corresponding measurements were performed using the Farmer type ion chamber (610-JARP, Applied Engineering Inc., Tokyo, Japan).

The static tests for validation of the MLC model were implemented for investigation of the following effects: inter-leaf leakage, intra-leaf transmission, and tongue-and-groove effect. These effects are strongly affected by geometry of the MLC model. Dose profiles were simulated and measured with films using the particular MLC leaf test pattern for each effect. Figure 2 shows the MLC leaf settings in the beam's eye view for investigation of above MLC dosimetric effects. The dynamic test to investigate the case incorporating the dynamic leaf motion was also implemented using a clinical leaf sequence file for a prostate cancer patient. Kodak X-Omat V films (Eastman Kodak Co., Rochester, NY) were used in each measurement. The solid water phantom (Gammex RMI, Middleton, WI) was employed for calibration and subsequent experiments. Optical density data of the films were obtained at 96 dpi using the DD-System (R-TECH Inc., Tokyo, Japan).

2.3 Development of a GUI application

A GUI application was developed in C++ Builder (Borland Software Corp., Scotts Valley, CA) and runs under the Windows XP (Microsoft, Inc., Redmond, WA) operating system, to enable users to easily develop the CT-based patient models, implement in-patient dose computations, and compare the results from MC and Eclipse. The data sets of CT, Structure, Plan, and Dose established in treatment planning process were exported in Digital Imaging and Communications in Medicine (DICOM) format and then read into the GUI. The MC dose calculations could be implemented under the identical conditions with Eclipse. In the CT-based patient model, the CT numbers were converted to materials and mass densities based on the recommendations in the ICRU Report 44 [19]. Materials were divided into six types, i.e., soft tissue, adipose, breast, marrow, bone, and air.

3. Results

3.1 Linear accelerator treatment head model

Figure 3(a) shows a comparison of the MC calculated and measured central axis depth dose curves normalized to the dose at d_{max} for 6 MV photon beam with field size of 10 x 10 cm^2 in the water phantom. The discrepancies were overall within 2% at all points beyond d_{max}. Figure 3(b) represents a comparison of the calculated and measured lateral dose profiles normalized to the central axis dose at the depth of 5 cm. There were large differences between the MC and the measurement, especially in the penumbral regions.

3.2 MLC model

3-2-1. MLC leaf transmission

Figure 4 shows the MC calculated and measured dose profiles of inter-leaf leakage and intra-leaf transmission at x= -2.5 cm for the field setting of Figure 2(a). The doses were expressed as percentages of 10 x 10 cm^2 open field central axis dose at the depth of 5 cm. The peaks and the valleys of the profile due to the leakage and transmission were clearly reproduced by MC. However, there were slight dose differences about 0.5% at the peaks, about 0.1% at the valleys, and about 0.5% in the penumbral regions. Average transmission showed a good agreement with the values of 1.47% of the MC and 1.51% of the measurement. The peak positions of the MC profile were almost equally spaced by 1 cm and agreed well to the measurement.

3-2-2. Tongue-and-groove effect

Figure 5 shows the dose profiles of the MC and the measurement for the complementary field depicted in Figure 2(b). All data were normalized to the 10 x 10 cm^2 open field central axis dose at the depth of 5 cm. The underdosages were explicitly predicted by MC and the discrepancies relative to the measurement were about 8%. The positions of the underdosage valleys were completely reproduced and showed good agreements with the measurement. In the penumbral region, the measurement showed lower doses than the MC and the differences were about 2%.

3-2-3. Dynamic intensity-modulated field

Figure 6 represents a result of film dosimetry of the intensity-modulated dynamic test pattern. Figure 7 shows the comparisons of calculated and measured lateral dose distributions in that field. Although the relatively large discrepancies up to 7% were found between them, the intensity modulation was successfully predicted by MC. In all y positions, the MC results indicated a slight underestimation of the field size.

3.3 GUI application

Figure 8 shows an overview of the GUI application. On this form, the users can easily develop the patient models from the CT data sets exported from Eclipse. And they can then implement in-patient MC dose calculations under the identical conditions with the treatment plan, and compare the results from MC and Eclipse qualitatively by dose distribution curves, and quantitatively by dose-volume histograms (DVHs).

4. Discussion

In this study, an EGS4 MC dose calculation system was developed for dynamic IMRT with the Varian linear accelerator equipped with the 80-leaf MLC. The MC models of the treatment head and the MLC were validated by the measurement data sets. In the treatment head model, there were large discrepancies between MC and measurement in the results of in-phantom depth doses and dose profiles. The parameters of the incident electron beam were set to 5.7 MeV (the mean energy), 0.20 cm (the FWHM of the intensity distribution), and 3% (the FWHM of the energy distribution) in this study. An iterative tuning process is required to determine a consistent set of parameters, and it is currently in progress for both of 6 and 15 MV photon beams with several field sizes. The MLC dosimetric effects (i.e. total leaf transmission and tongue-and-groove effect) were well reproduced, and the dynamic simulation could predict the intensity modulation. However, there were dose discrepancies between the results of MC and measurement. It will be investigated in detail after tuning the incident electron beam parameters.

The necessity to accurately consider the MLC design in the IMRT dose calculation was stated by some investigators. Palmans *et al*. [20] have compared the two component modules (CMs) of the BEAM/EGS4, i.e. MLC (focused flat leaf tip surface) and MLCQ (curved shape of rounded leaf tip), and indicated that the default MLC model of the BEAM (CM MLC) can lead to differences of up to 15% in the penumbral regions. Van de Walle *et al*. [21] compared two simulations with the CM MLCQ (exclusive of inter-leaf air gap) and MLCE (inclusive of inter-leaf air gap). Their results showed that the total MLC transmission and the tongue-and-groove effect could be reproduced with MLCE, however, MLCQ was not able to predict those effects at all. The MLC design was fully modeled in our study, and leaf transmission and tongue-and-groove effect were successfully reproduced. The rounded leaf tip model will also be validated in future.

The MC dose calculation system built in this study will be further developed into the dosimetric QA system. This system can allow the routine verification of the calculated results from the commercial treatment planning system. The MC data can be used as a benchmark in order to quantitatively detect the area where the commercial system fail to calculate the accurate dose due to electron disequilibrium, tissue heterogeneities, multiple scatters and/or MLC dosimetric effects. Although this system can be a powerful QA tool, the MC calculation requires long CPU time in order to decrease the statistical uncertainties and it is required to be reduced. The approach to accelerate the MC calculation by parallelization is now in progress.

5. Conclusions

An EGS4 MC dose calculation system for dynamic IMRT was developed. MLC dosimetric effects were then successfully reproduced well for both of the static and the dynamic test patterns. Discrepancies between the MC and the measurement will be investigated after tuning the parameters of the incident electron beam. This system will be developed into the QA system for the routine verification of the commercial treatment planning system for dynamic IMRT.

Acknowledgments

This study was based on the Monte Carlo Project agreement with Varian Medical Systems, Inc. This proceeding had been reviewed and permitted by Varian. We acknowledge Chudo Kazusa of Varian ME Medical Systems, K.K. for providing the accurate specifications of Clinac 2300C/D and Mark II MLC. This study was supported by grants from Japan Society for the Promotion of Science (Grant-in-Aid for Scientific Research No. 16390338) and Ministry of Health, Labour and Welfare (Grant-in-Aid for Cancer Research No. 14-6).

References

1) S. Webb, Intensity Modulated Radiation Therapy (Institute of Physics Publishing, Bristol, UK, 2001).
2) C. C. Ling, C. Burman, C. S. Chui, G. J. Kutcher, S. A. Leibel, T. LoSasso, R. Mohan, T. Bortfeld, L. Reinstein, S. Spirou, X. H. Wang, Q. Wu, M. Zelefsky, and Z. Fuks, "Conformal radiation treatment of prostate cancer using inversely-planned intensity-modulated photon beams produced with dynamic multileaf collimation," Int. J. Radiat. Oncol., Biol., Phys. **35**, 721-730 (1996).
3) C. Burman, C. S. Chui, G. J. Kutcher, S. Leibel, M. Zelefsky, T. LoSasso, S. Spirou, Q. Wu, J. Yang, J. Stein, R. Mohan, Z. Fuks, and C. C. Ling, "Planning, delivery, and quality assurance of intensity-modulated radiotherapy using dynamic multileaf collimator: A strategy for large-scale implementation for the treatment of carcinoma of the prostate," Int. J. Radiat. Oncol., Biol., Phys. **39**, 863-873 (1997).
4) A. L. Boyer, P. Geis, W. Grant, and M. Carol, "Modulated beam conformal therapy for head and neck tumors," Int. J. Radiat. Oncol., Biol., Phys. **39**, 227-236 (1997).
5) K. Sultanem, H. K. Shu, P. Xia, C. Akazawa, J. M. Quivey, L. J. Verhey, and K. K. Fu, "Three-dimensional intensity-modulated radiotherapy in the treatment of nasopharyngeal carcinoma: The University of California-San Francisco experience," Int. J. Radiat. Oncol., Biol., Phys. **48**, 711-722 (2000).
6) L. Hong, M. Hunt, C. Chui, S. Spirou, H. Forster, H. Lee, Y. Yahalom, G. J. Kutcher, and B. McCormick, "Intensity-modulated tangential beam irradiation of the intact breast," Int. J. Radiat. Oncol., Biol., Phys. **44,** 1155-1164 (1999).
7) Intensity Modulated Radiation Therapy Collaborative Working Group, "Intensity- modulated radiotherapy: Current status and issues of interest," Int. J. Radiat. Oncol., Biol., Phys.**51**, 880-914 (2001).
8) T. LoSasso, C. S. Chui, and C. C. Ling, "Physical and dosimetric aspects of a multileaf collimation system used in the dynamic mode for implementing intensity modulated radiotherapy," Med. Phys. **25**, 1919-1927 (1998).
9) M. R. Arnfield, J. V. Siebers, J. O. Kim, Q. Wu, P. J. Keall, and R. Mohan, "A method for determining multileaf collimator transmission and scatter for dynamic intensity modulated radiotherapy," Med. Phys. **27**, 2231-2241 (2000).
10) J. R. Sykes and P. C. Williams, "An experimental investigation of the tongue and groove effect for the Philips multileaf collimator," Phys. Med. Biol. **43**, 3157-3165 (1998).
11) A. L. Boyer and S. Li, "Geometric analysis of light-field position of a multileaf collimator with curved ends," Med. Phys. **24**, 757–762 (1997).
12) A. Ahnesjö, "Collapsed cone convolution of radiant energy for photon dose calculation in heterogeneous media," Med. Phys. **16**, 577–592 (1989).
13) T. R. Mackie, J. W. Scrimger, and J. J. Battista, "A convolution method of calculating dose for 15 MV x-rays," Med. Phys. **12**, 188-196 (1985).
14) A. Boyer and E. Mok, "A photon dose distribution model employing convolution methods," Med. Phys. **12**, 169-177 (1985).
15) J. D. Bourland and E. L. Chaney, "A finite-size pencil beam model for photon dose calculations in three dimensions," Med. Phys. **21**, 1031-1041 (1994).
16) M. K. Woo, J. R. Cunningham, and J. J. Jerioranski, "Extending the concept of primary and scatter separation to the condition of electronic disequilibrium," Med. Phys. **17**, 588-595 (1990).
17) R. Nelson, H. Hirayama, and D. W. O. Rogers, The EGS4 Code System, SLAC-265 (Stanford Linear Accelerator Center, Stanford, CA, 1985).
18) A. F. Bielajew A F and D. W. O. Rogers, "PRESTA: The parameter reduced electron-step transport algorithm for electron Monte Carlo transport," Nucl. Instrum. Methods B. **18**, 165-181 (1987).
19) ICRU Report No. 44, "Tissue substitutes in Radiation dosimetry and measurements," International Commission on Radiation Units and Measurements, Washington D.C. (1989).
20) H. Palmans, F. Verhaegen, F. M. Buffa, and C. Mubata, Considerations for modeling MLCs with Monte Carlo techniques, in *Proceedings of the XIIIth International Conference on the Use of Computers in Radiation Therapy*,

edited by W. Schlegel and T. Bortfeld (Springer-Verlag, Heidelberg, Germany, 2000), pp. 458-460.
21) J. Van de Walle, C. Martens, N. Reynaert, H. Palmans, M. Coghe, W. De Neve, C. De Wagter, and H. Thierens, "Monte Carlo model of the Elekta SL*i*plus accelerator: validation of a new MLC component module in BEAM for a 6 MV beam," Phys. Med. Biol. **48**, 371-385 (2003).

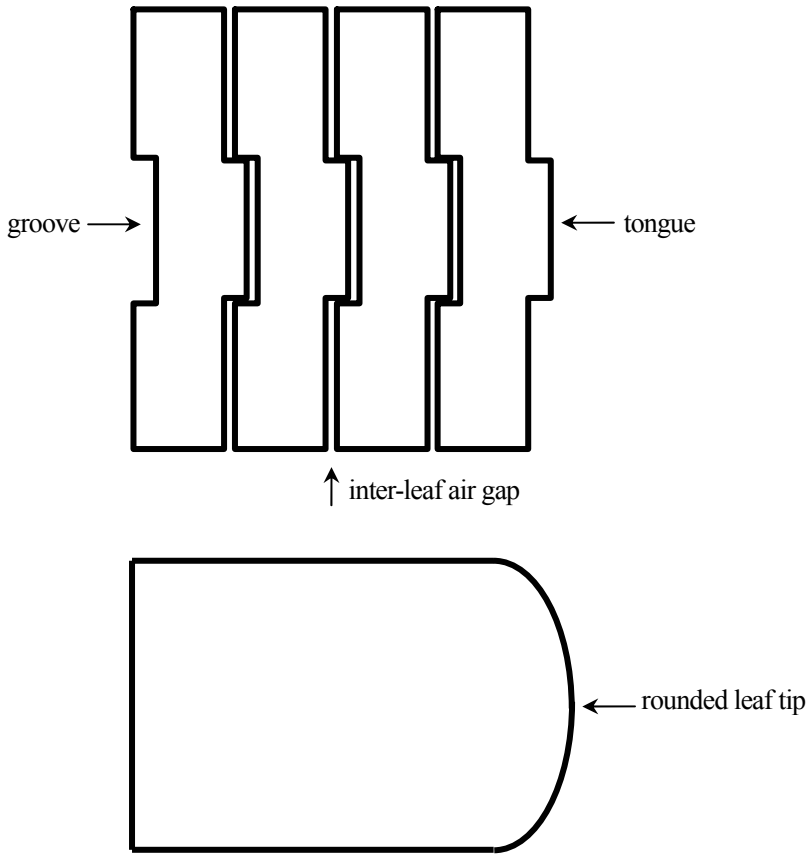

Figure 1. Schematic drawings of Varian 80-leaf Mark II MLC.

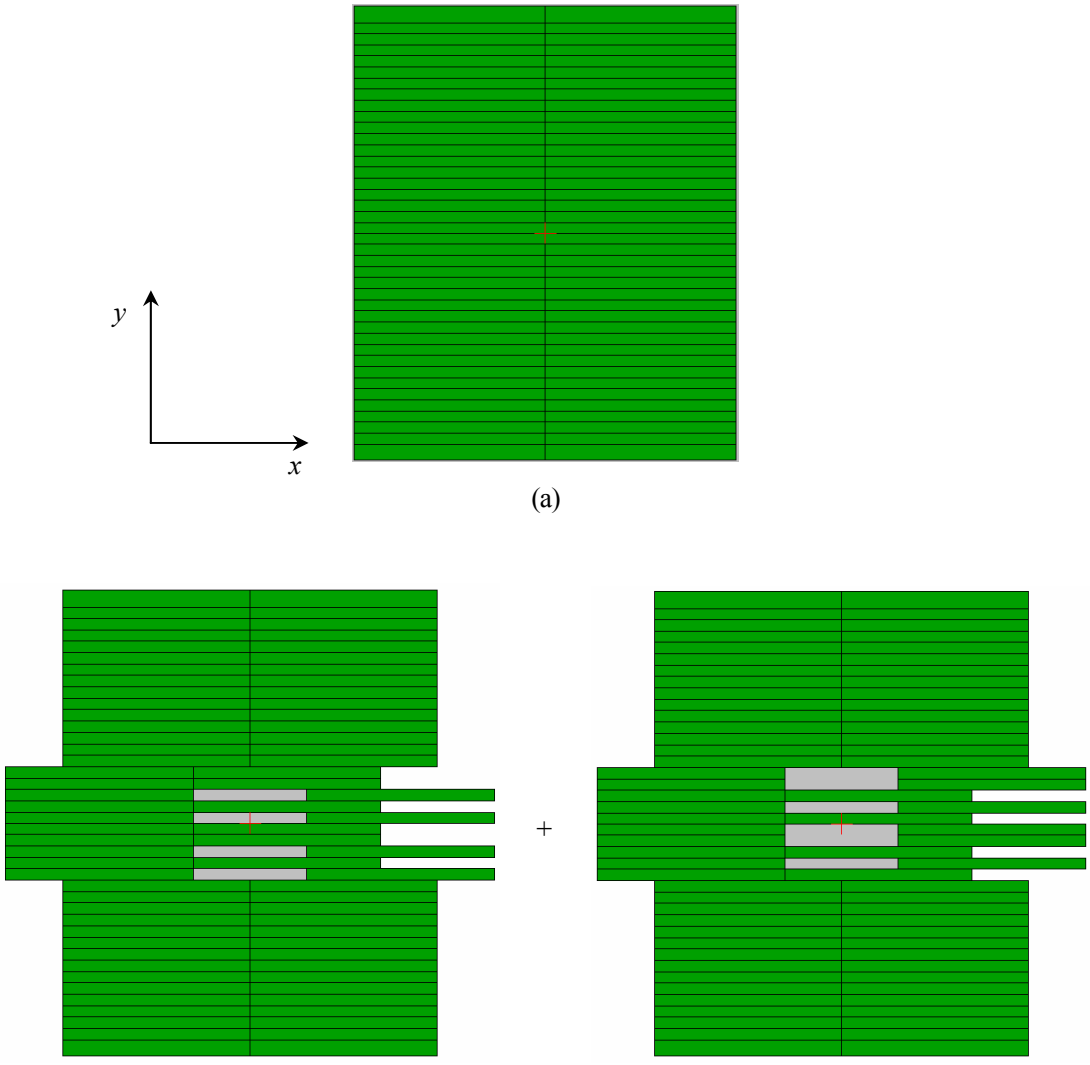

Figure 2. MLC leaf settings in the beam's eye view: (a) for inter-leaf leakage and intra-leaf transmission (b) for tongue-and-groove underdosage effect.

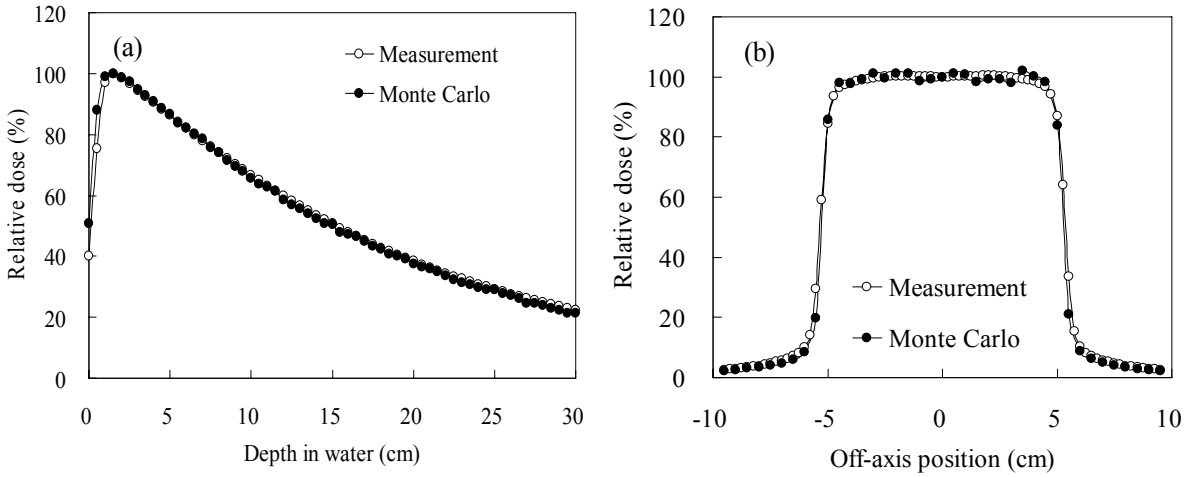

Figure 3. Comparisons of the results of MC and measurement: (a) depth doses and (b) lateral dose profiles in the water phantom for a 6 MV photon beam with the field size of 10 x 10 cm^2.

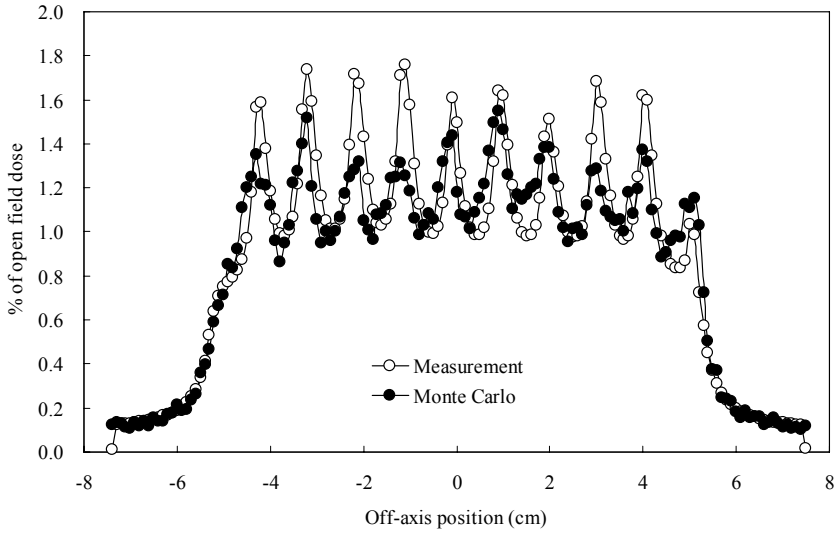

Figure 4. Dose profiles in *y*-direction at *x* = -2.5 cm of the fields with the MLC leaf setting depicted in Figure 2(a).

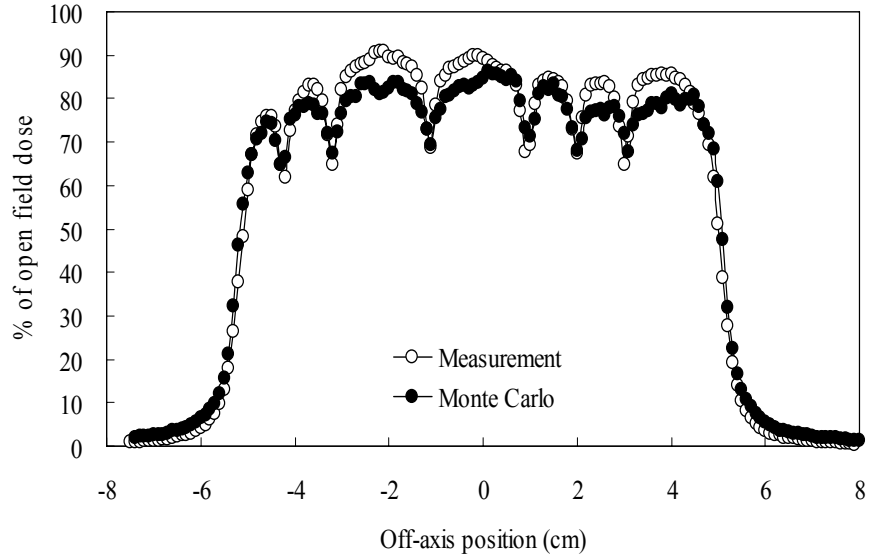

Figure 5. Dose profiles in *y*-direction at *x* = -2.5 cm of the fields with the MLC leaf setting depicted in Figure 2(b).

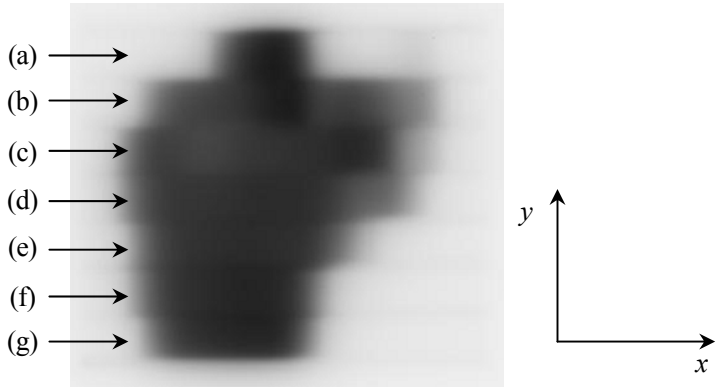

Figure 6. Film dosimetry of the intensity-modulated dynamic test pattern. Arrows represent the directions to obtain the lateral dose profiles and each alphabet corresponds to that in Figure 7.

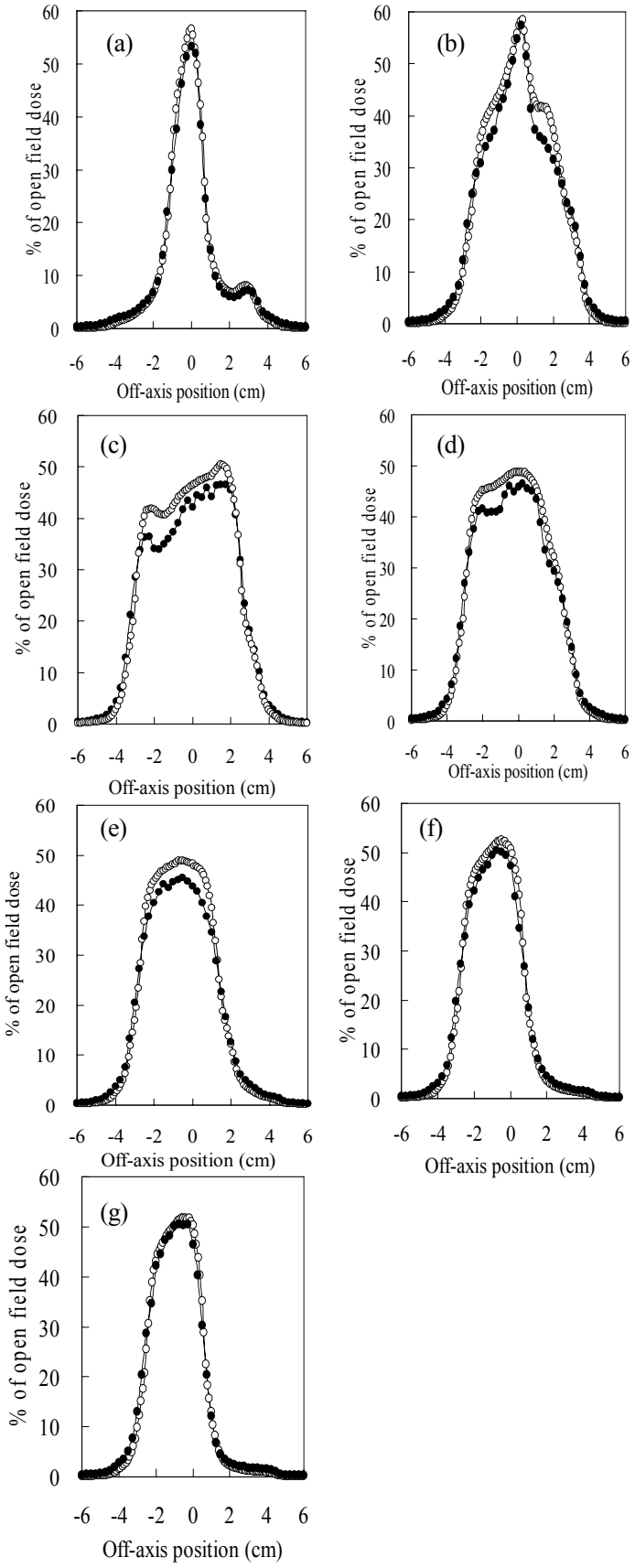

Figure 7. Dose profiles in *x*-direction of the intensity-modulated dynamic test pattern.

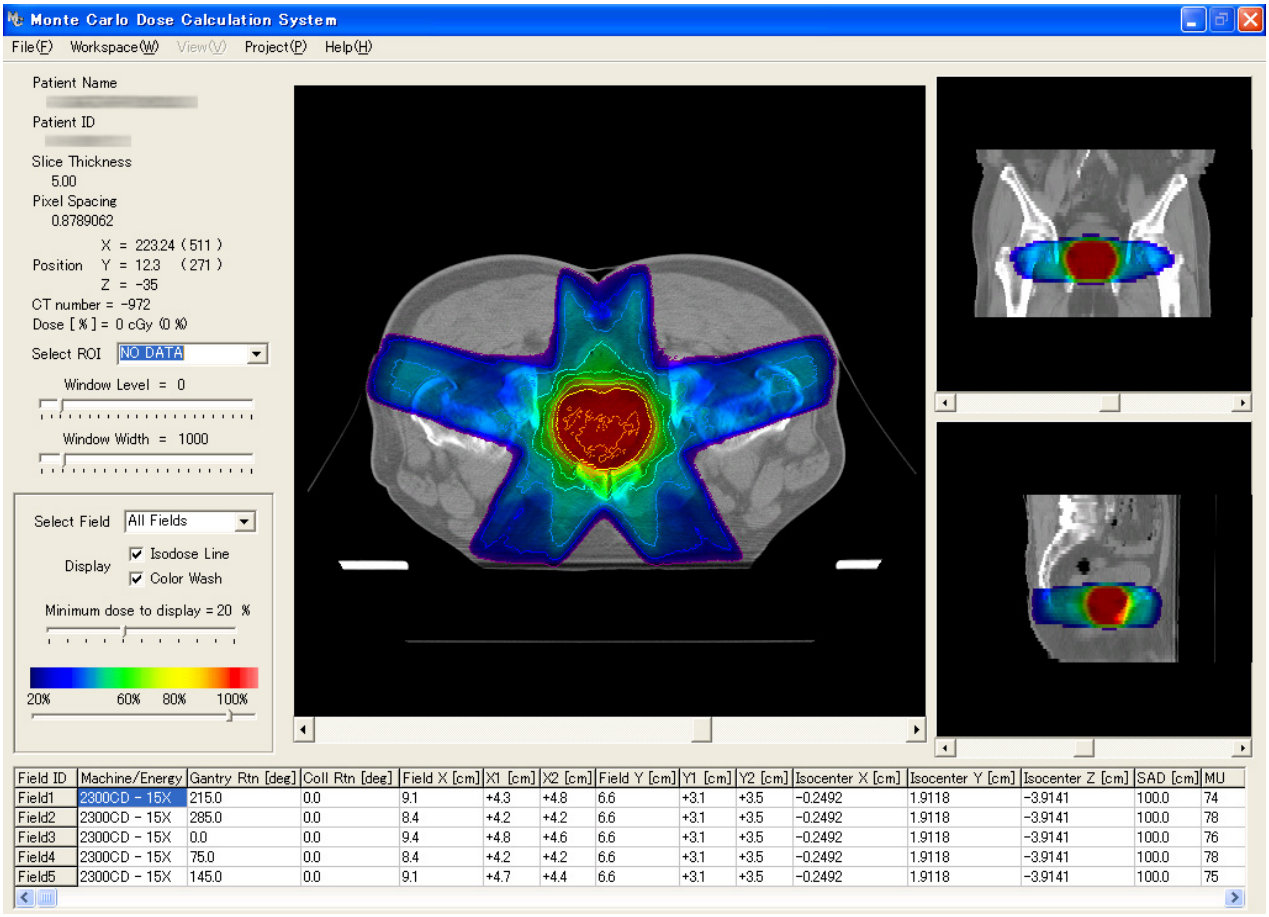

Figure 8. An overview of the GUI application.

COMPARISON WITH A 4 MEV X-RAY DOSE AND MONTE CARLO SIMULATION USING A HUMAN BODY PHANTOM

A.Chadani[1] , K.Koshida[2] , K.Minami[3] , K.Ejiri[3] , M,Shimo[3] , Y.Hibino[4], K.Egami[4] , S.Arakawa[4] , H.Nakagawa[1] , C.Kawabata[1] and M.Hayakawa[1]

[a1]Division of Health Science, Graduate School of Medical Science, Kanazawa University
[2]Department of Radiological Technology, School of Health Sciences, Faculty of Medicine, Kanazawa University
[3]Faculty of Radiologial Technology, school of Health Sciences, Fujita Health University
[4]Department of Radiological Technology, Fujita Health University

Abstract

It is not easy to evaluate the accuracy of a human body model in a dose simulation. For this reason, a mathematical phantom (voxel phantom) of a human body phantom is used as a model that can be compared with the measurement. The difference between the simulation and the measurement was examined.

A female human body phantom (made in the Phantom Laboratory company: Alderson RAND Phantom RAN-100 Type) was used. The Monte Carlo calculation code was used the Electron Gamma Shower Version 4 (EGS4). The depth doses in a RANDO phantom were measured using a radiophoto-luminescence glass dosimeter and thermo-luminescence dosimeter. Exposure conditions were performed using 4 MeV X-rays and Antero-posterio geometry.

The difference between the calculation values and the measurements was about 10%. It is considered that is the values are different between the structure material and the domain setup of the RAND and voxel phantoms.

1. Introduction

In recent years, the simulation technology using the mathematics phantom has also developed with development of a computer. The Monte Carlo simulation using the mathematics phantom (voxel phantom) of a human body model can choose form and composition freely, and can know the details of the dose in a human body. But it is not easy to evaluate the accuracy of a human body model in a dose simulation. Thus, a mathematical phantom of a human body phantom is used as a model, to allow comparison with the measurements. The mathematical phantom was constructed from the CT data of the female human body phantom which can measure the internal dose. The Monte Carlo simulation is performed using this mathematics phantom, and the absorbed dose in the phantom is computed. The internal dose distribution obtained by the simulation was compared with the measurement using the rand phantom, and the differences between the simulation and the measurement were examined.

2. Materials and Method

2.1 Materials

A female human body phantom (made in the Phantom Laboratory company: Alderson RAND Phantom RAN-100 Type) was used. The height of 163cm, the weight of 54kg, 35 slice numbers, and the number of the holes which insert an element (hole grid) are 868 pieces. The voxel phantom consisted of an air (cavity part), natural human bone, and soft tissue , lungs, and acrylics. Figure 1 shows the female human body phantom. The Monte Carlo calculation code was used the Electron Gamma Shower Version 4 (EGS4). The substance data of tissue substitutes used by EGS4 referred to ICRU Report 44[1)].The depth doses in a RANDO phantom were measured using a radiophoto-luminescence

glass dosimeter[2]. Exposure conditions were performed using 4 MeV X-rays by Linear Accelerator[3] and Antero-posterio geometry.

2.2 4MV X-rays energy spectrum by the simulation

4MV X-rays energy spectrum was calculated using the approximation formula of Schiff[4]. The obtained photon energy spectrum[5] was taken as the spectrum after being filtered with the flattening filter (stainless steel) with an average thickness of 7.7 mm. Figure 2 shows the sectional view of a linear accelerator showing the generating process of X-rays. Figure 3 shows 4MV X-rays energy spectrum by the simulation.

2.3 The conditions of EGS4 simulation and measurement

In measurement, the radiophoto-luminescence glass dosimeters were inserted into the human body phantom. 4 MV X-rays were irradiated with the Linear Accelerator, and the depth doses were measured. Table 1 shows the conditions of EGS4 simulation and measurement. The obtained doses were standardized by the calculation value and measurement value at the standard point of the first cervical vertebrae. It was based on the first cervical vertebrae because the measurement value was stable.

3. Results

3.1 The statistical accuracy of the simulation and measurement

The statistical accuracy of the simulation had a coefficient of variation (CV) of <2% (number of histories, 1 billion×20 times). The statistical accuracy of the measurement using a radiophoto-luminescence glass dosimeter had a coefficient of variation becomes a maximum of 15% and less than a minimum of 1%, and is an average of 5.03%.

3.2 Comparison with the calculation value by EGS4 and measurement value

Some results are reported. In measurement, it measured at least 3 times or more, and computed as an average. Figure 4 shows the result of the head and processes xiphoideus level. The calculation values over the actual measurement of the head differed by about 3%. Especially large differences were accepted near the irradiation field center of the chest, and the maximum was about 12%.

4. Discussion

The disagreement between the calculation and actual measurement value in the chest was thought to be due to problems in the X-ray energy spectrum used in the simulation. Figure 5 shows Percentage Depth Dose (PDD) of the 4MV X-ray spectrum by the calculation value and measurement value. PDD of the X-ray spectrum (the approximation formula of Schiff) had a difference of about 13% as compared to PDD of measurement. This was because the flattening filter of the special cone form used in the process of X-ray generation was calculated for an average thickness of 7.7 mm.

5. Conclusions

To evaluate the construction accuracy of the mathematical phantom for the Monte Carlo simulations by the human body phantom, it is necessary to increase the accuracy, such as the reproducibility and the coefficient of variation (CV). Therefore, after confirming these conditions in a simple form, it is necessary to apply to a human body phantom.

References

1) ICRU: Tissue Substitutes in Radiation Dosimetry and Measurement, ICRU Report 44 (1989).

2) Hidenori Sakai and Hidetarou Yoshimura: Jpn. Film Badge News, No.315, 1-5, 2003

3) A Chaves, C Alves, M Fragoso and etc. : EGS4 and MCNP4b MN Simulation of a Siemens KD2 Accelerator in 6 MV Photon Mode, Laboratorio de Instrumentacao e Fisica Experimental de Particulas/01-01 January 2001

4) Schiff LI : Energy-angle distribution of thin target bremsstrahlung. Phys. Rev., Vol.82(2), 1951.

5) Hideki Kato: The Monte Carlo simulation with a personal computer. Jpn. J. Radio. Technol. Vol.55(2), 1999.

Table 1. The conditions of EGS4 simulation and measurement

	EGS4 simulation	**Measurement by the Radiophotoluminescent glass dosimeter**
Field size	**120 × 60 cm^2**	**112 × 112 cm^2**
Source-phantom distance	**300 cm**	**300 cm**
Incident particle	**Photon Continuation spectrum**	**Photon bremsstrahlung**
Irradiation conditions	**10^9 Number of histories**	**1.0 Gy Air absorbed dose in 300cm**
Handling of acquisition data	**Computed as an absorbed dose (Gy) of one photon.**	**The obtained measurement value (Gy) is rectified by the proofreading constant.**

Fig 1.　Female human body phantom（RANDO Phantom）

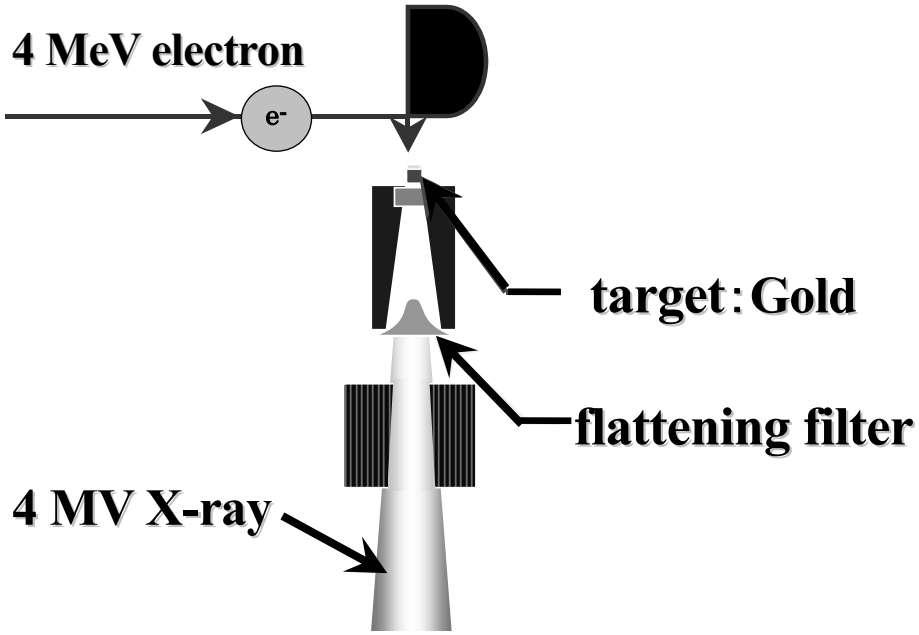

Fig 2.　The sectional view of a linear accelerator

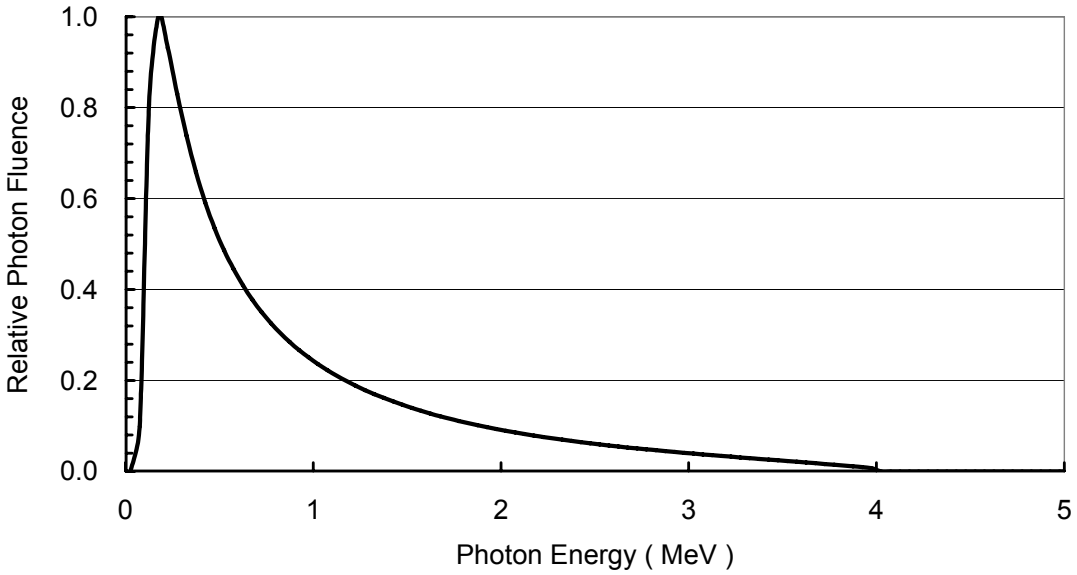

Fig 3. 4MV X-ray spectrum by the simulation

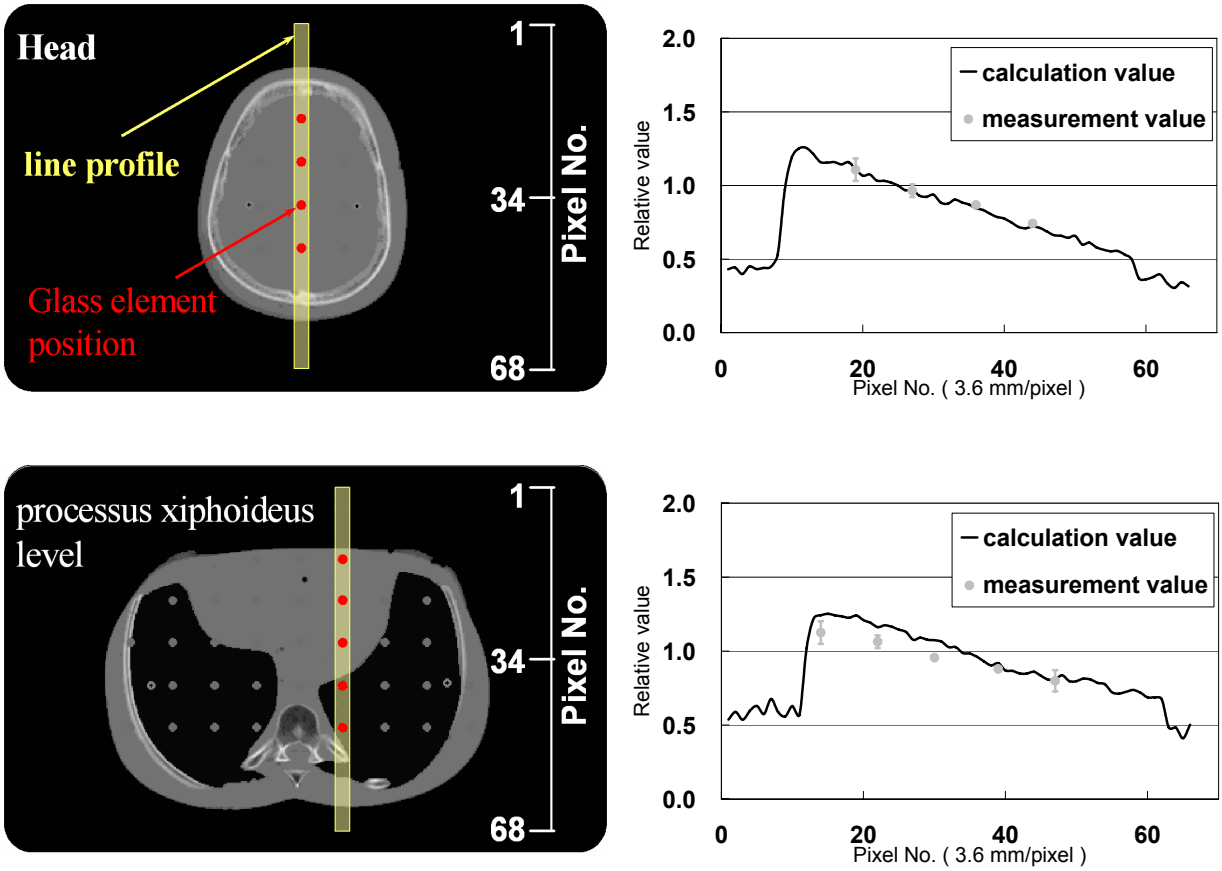

Fig 4. Comparison with the calculation value by EGS4 and measurement value.

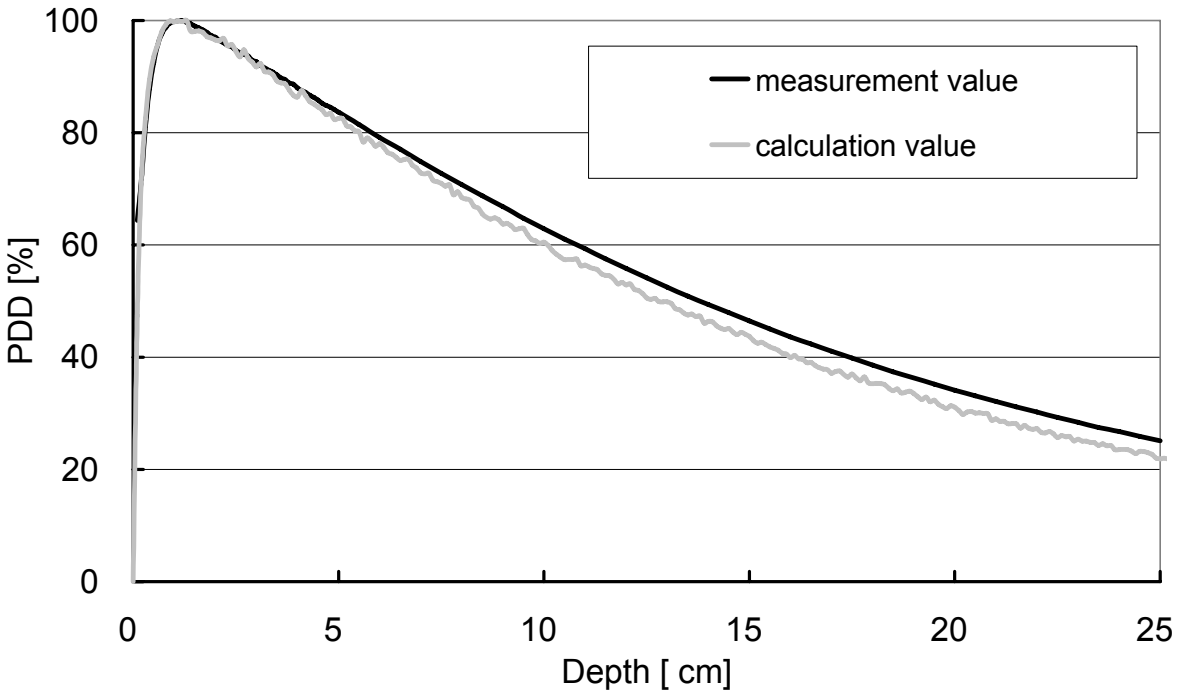

Fig 5. PDD (Percentage Depth Dose) of the 4MV X-ray spectrum by the calculation value and measurement value.

MONTE CARLO SIMULATION FOR ELECTRON-LOSS AND PHOTON-SCATTERING CORRECTIONS FOR PARALLEL-PLATE FREE-AIR CHAMBERS

T.Kurosawa, N.Takata, Y.Koyama

National Metrology Institute of Japan, National Institute of Advanced Industrial Science and Technology, Ibaraki, 305-8568, Japan

e-mail: tadahiro-kurosawa@aist.go.jp

Abstract

The parallel-plate free-air ionization chambers are used for X-rays air-kerma rate standards at National Metrology Institute of Japan (NMIJ), National Institute of Advanced Industrial Science and Technology (AIST). The electron loss and scattering correction factors are needed for the evaluation of air-kerma rate from measured current. The electron loss correction factor (K_e) is a correction of the charge loss by giving energy to the electrode part without a high-speed electron stopping in the air area where the charges are collected. The scattering correction factor (K_{sc}) is for a correction of extra charges produced by scattered photon generated after an incidence photon is interactive. The electron-loss and photon-scattering correction factor for 3 different size parallel-plate free-air chambers are estimated by the EGS4 code. One is used as primary standards for absolute measurements of air kerma in beams of medium-energy X-rays and two are of low-energy X-rays. These correction factors are calculated for mono-energetic photons. It is obtained that electron-loss and photon-scattering correction factors depend on the chamber size, and especially, the photon-scattering correction value changes greatly depending on the size. The K_e and K_{sc} value for medium- and low-energy X-ray fields at AIST are estimated by averaging the energy deposition contributions over the X-ray spectrum. The overall uncertainty of the electron loss or scattering correction factor is evaluated to be 0.14%.

1. Introduction

The parallel-plate free-air ionization chambers are used for X-rays air-kerma rate standards at National Metrology Institute of Japan (NMIJ), National Institute of Advanced Industrial Science and Technology (AIST). The air-kerma rate for free-air chambers measurement is estimated from measured current by using following equation,

$$X = \frac{i}{v\rho_0} \cdot \frac{273.15+T}{273.15} \cdot \frac{1013.25}{P} \cdot \frac{W}{e} \cdot \frac{1}{(1-g)} \cdot K \quad (1)$$

where, i is measured current (C/s), v is correcting volume (cm^3), ρ_0 is air density (kg/cm^3) at reference condition(273.15 K, 1013.25 hPa), T and P are air temperature (K) and pressure(hPa) in the free-air chamber, W/e is W value (J/C), g is bremsslung correction value and K is multiplied value of several correction factors. K include following correction factors, a) air attenuation between reference point to the center of correcting volume, b) recombination loss, c) electron loss, d) scattering, e) electric field distortion, f) humidity of the air, and etc. The correction value of a), b), e) can be estimated by measurements for each free-air chambers, and the value of f) is suggested by ICRU [1] report. The electron loss correction factor (K_e), c), is a correction of the charge loss by giving energy to the electrode part without a high-speed electron stopping in the air area where the charges are collected. The scattering correction factor (K_{sc}), d), is for a correction of extra charges produced by scattered photon generated after an incidence photon is interactive. The correction factors of c) and d) depends on a geometry of a free-air chamber and are very difficult to estimate by experiments, so Monte Carlo calculations are applied for the estimation of these values[2, 3]. In this study, these correction factors for one medium x-ray chamber and two low energy x-ray chambers are evaluated by Monte Carlo simulations, and the effective value of these correction factor for standard X-ray fields developed by AIST are estimated.

2. Calculation of K_e and K_{sc} for mono-energy photons

The K_e and K_{sc} are calculated by using EGS4-KEK [4] improve code for mono-energetic photon with energies from 10keV to 300keV for medium energy x-ray free-air chamber and 4keV to 50keV for low energy ones. ECUT and PCUT are set to 1keV. For estimation of the effect of X-ray fluorescence from Ar in air, the two calculations are done with and without fluorescence from Ar for large low energy x-ray chamber. Figure 1 shows the simulation arrangement, and Table 1 is the values of geometry parameters for each chambers.

The K_e and K_{sc} are evaluated by following equations,

$$K_e = \frac{\sum E_{ap}}{\sum E_{ap} + E_{as}} \quad (2)$$

$$K_{sc} = \frac{\sum E_{ap} + E_{bp}}{\sum E_{ap}} \quad (3)$$

Where E_{ap} is the energy deposited from electrons generated by primary photons in region A, E_{as} is the energy deposited from electrons generated by scattered photons in region A and E_{bp} is the energy deposited by primary photons in region B.

3. Results

3.1 Results for mono-energy photons

Figure 2 shows the K_e values and Figure 3 shows the K_{sc} values for each free-air chambers. There is a peak around 150keV for K_e of medium energy x-ray free-air chamber that is caused by the photo-electron interaction. As the kinetic energy of electrons by the photo-electron interaction increase with incident photon energy, electron loss events increase. But the cross section of the photo-electron decrease with photon energy, correction factor becomes smaller above 150keV. The increase of K_e with photon energy above 230keV is assumed that the effect of Compton scattering electron, because the kinetic energy of electrons by Compton scattering increase with incident photon energy. The K_e for large free-air chamber of low energy x-ray becomes 1.0 except 50keV, but for small chamber, correction factor becomes more than 1.0 above 40keV and it becomes more than 1.01 for 50keV. The photo-electron interaction becomes dominant in this energy region.

The K_{sc} value for medium and low energy x-ray chambers becomes similar tendency that the correction value becomes small as the photon energy lowers. As figure 3 shows, these influence is due to X-ray fluorescence from Ar in air. The K_{sc} depends on the chamber size and corrected value becomes larger for large chamber.

3.2 Results for medium-energy and low-energy x-ray qualities

The K_e and K_{sc} value for medium- and low-energy X-ray fields at AIST are estimated by averaging the energy deposition contributions over the X-ray spectrum:

$$K_i = \int K_i(E)(\mu(E)/\rho)E\phi(E)dE \Big/ \int (\mu(E)/\rho)E\phi(E)dE \qquad (4)$$

where $\varphi(E)$ is the photon energy spectrum, $\mu(E)/\rho$ is the mass energy absorption coefficient of air, and $K_i(E)$ is the correction factor of K_e or K_{sc} for mono-energy photon. From this equation it can be concluded that the correction factors for a X-ray quality can be calculated by weighting the corresponding correction factors for mono-energetic photons with the air kerma spectrum. The spectra of the medium- and low-energy X-rays are also estimated by Monte Carlo calculations.

The results of the combination of the correction factors for mono-energetic photons and the calculated spectra are shown in Table 2, 3, 4, 5 and 6. The characteristics of the X-ray fields is expressed by Q.I. (Quality Index) value estimated by the following equation,

$$Q.I. = \frac{E_{eff}}{E_V} \qquad (5)$$

where E_{eff} is the effective energy of X-ray field estimated by half value layer (HVL), and E_V is the tube voltage.

There is no table of electron loss correction factor for large free-air chamber for low-energy X-rays because all value of that become 1.0000.

3.3 Uncertainties in the calculated correction factors

The statistical uncertainties in the results of the Monte Carlo calculations were smaller than 0.02%, and the uncertainties introduced by weighting the mono-energetic correction factors with the calculated X-ray spectra were estimated to be less

than 0.1%. Other contributions may contain the uncertainties of the theoretical modeling and cross section data of photon and electron interactions. It is very difficult to estimate quantitative analysis of those uncertainties. From the agreement of the EGS4 calculations with experimental data in the previous paper [], the relative uncertainty of Monte Carlo calculations may be estimated to be less than 0.1%. Thus, the overall uncertainty of the electron loss or scattering correction factor is evaluated to be 0.14%.

4. Conclusion

The electron loss and scattering correction factor for x-ray free-air chamber are evaluated by EGS4 Monte Carlo simulation. From the results, it is confirmed that K_e and K_{sc} value depend on the chamber size, and especially, the K_{sc} value changes greatly depending on the size.

As the correction value largeness means an increase in the uncertainty for the absolute measurements of air-kerma rate, it is need for accurate measurements to select proper size chamber with estimation of K_e value against measured photon energy.

[1] "Average Energy Required To Produce An Ion Pair", ICRU REPORT 31, May 1979

[2] D.T. Burns "Consistent set of calculated values for electron-loss and photo-scattering corrections for parallel-plate free-air chambers", CCRI(I) 99-4, 1999

[3] T.W.M. Grimbergen, E van Dijk and W de Vries, "Correction factors for the NMi free-air ionization chamber for medium-energy x-rays calculated with the Monte Carlo method", Phys. Med. Biol., 43 (1998) 3207-3224

[4] W.R. Nelson, H. Hirayama and D.W.O. Rogers, "The EGS4 Code system", Stanford Linear Accelerator Report SLAC 265 (1985)

[5] Y. Namito and H. Hirayama, "Implementation of the electron impact ionization into the EGS4 code", Nucl. Instrum. and Meth., A423 (1999)238-246

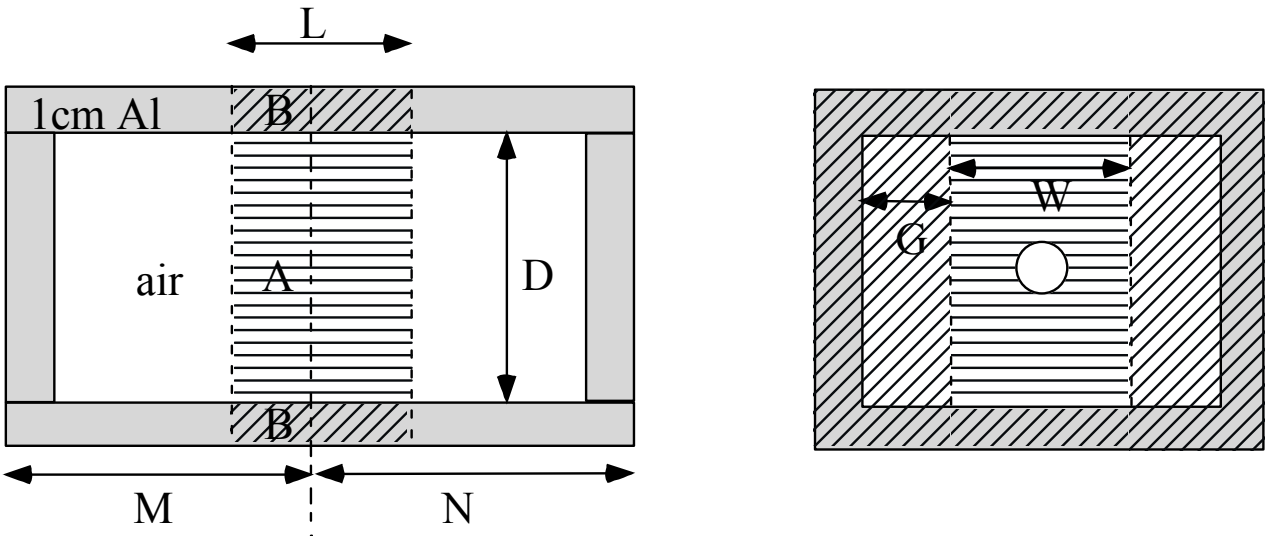

Figure 1 The Free-air chamber geometry for calculations of Ke and Ksc. The horizontal line region is A and the slant line region is B.

Table 1. Dimension of free-air chambers

Chamber	Attenuation length M (cm)	Collector length L (cm)	Attenuation length N (cm)	Electrode separation D (cm)	Electrode width W (cm)	Air gap G (cm)
Medium	37.2	10.0	20	24.0	23.0	5
Low-large	6.5	2.0	6.5	9.2	8.0	2.0
Low-small	5.5	2.0	5.5	8.2	6.0	2.0

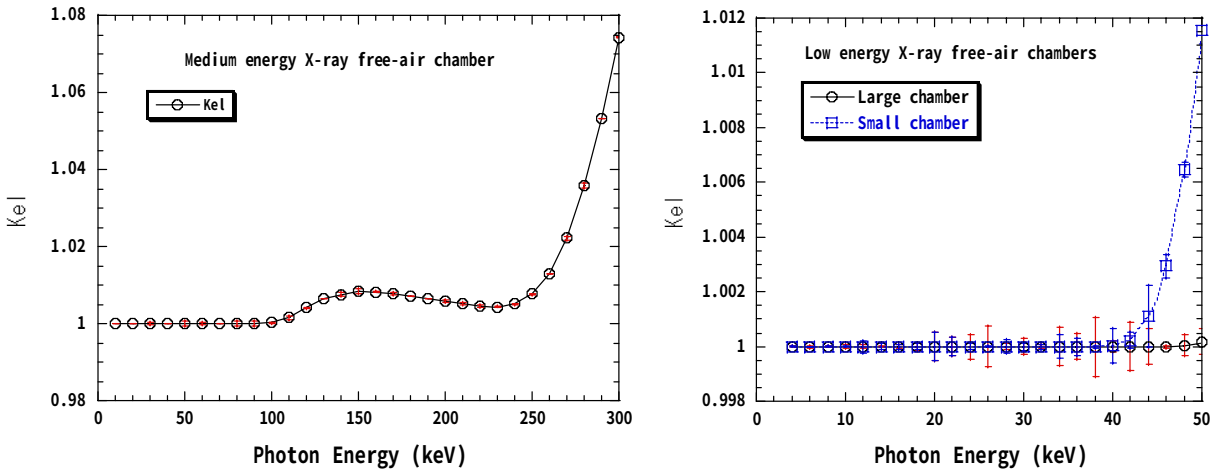

Figure 2 Calculated electron loss correction factor for medium (left) and low energy (right) X-ray free-air chambers

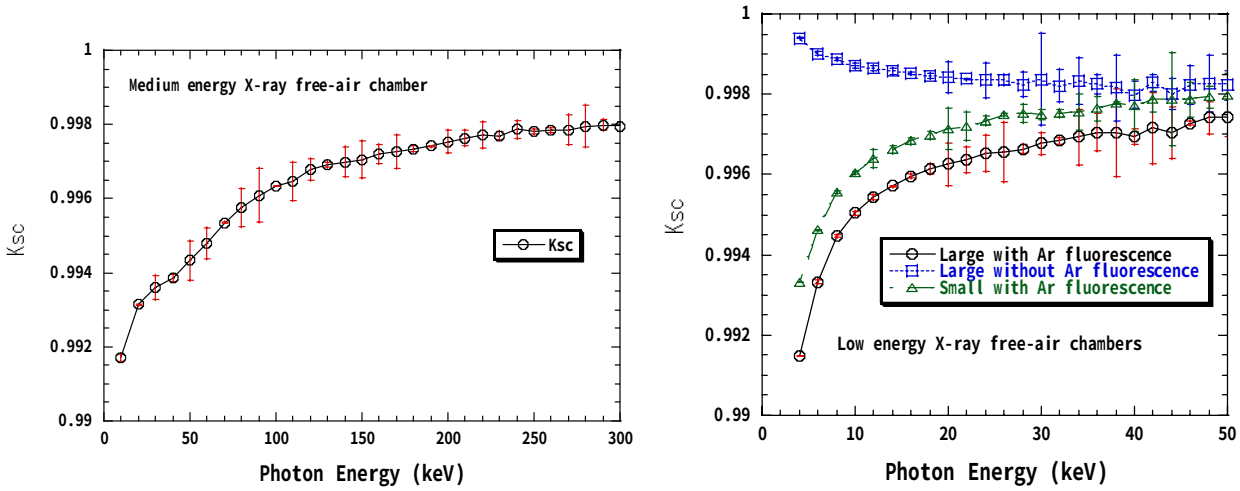

Figure 3. Caluclated photon scattering correction factor for medium (left) and low energy (right) X-ray free-air chambers

Table.2 The scattering correction factor for medium-energy X-ray free-air chamber

Tube voltage (kV)	Q.I.				
	0.4	0.5	0.6	0.7	0.8
40	0.9928	0.9931	0.9933	0.9935	0.9937
50	0.9931	0.9934	0.9936	0.9938	0.9939
60	0.9933	0.9936	0.9938	0.9940	0.9943
75	0.9936	0.9939	0.9942	0.9945	0.9949
100	0.9942	0.9945	0.9949	0.9953	0.9957
125	0.9945	0.9950	0.9955	0.9960	0.9963
150	0.9949	0.9955	0.9960	0.9964	0.9967
175	0.9953	0.9959	0.9964	0.9967	0.9971
200	0.9957	0.9962	0.9967	0.9970	0.9972
225	0.9960	0.9965	0.9969	0.9972	0.9974
250	0.9962	0.9967	0.9971	0.9973	0.9975

Table 3. The electron loss correction factor for medium-energy X-ray free-air chamber

Tube voltage (kV)	Q.I.				
	0.4	0.5	0.6	0.7	0.8
40	1.0000	1.0000	1.0000	1.0000	1.0000
50	1.0000	1.0000	1.0000	1.0000	1.0000
60	1.0000	1.0000	1.0000	1.0000	1.0000
75	1.0000	1.0000	1.0000	1.0000	1.0000
100	1.0000	1.0000	1.0000	1.0000	1.0000
125	1.0001	1.0001	1.0003	1.0005	1.0011
150	1.0005	1.0008	1.0015	1.0025	1.0042
175	1.0011	1.0019	1.0030	1.0047	1.0070
200	1.0018	1.0030	1.0044	1.0061	1.0073
225	1.0025	1.0037	1.0052	1.0065	1.0067
250	1.0030	1.0043	1.0057	1.0064	1.0059

Table 4. The scattering correction factor for low-energy X-ray free-air chamber(large)

Tube voltage (kV)	Q.I.					
	0.4	0.5	0.6	0.7	0.8	0.9
50	0.9963	0.9965	0.9968	0.9969	-	-
40	0.9960	0.9962	0.9965	0.9967	0.9968	-
30	0.9957	0.9959	0.9961	0.9963	0.9965	0.9966
20	-	0.9953	0.9956	0.9958	0.9959	0.9961
15	-	-	0.9950	0.9953	0.9955	0.9957
10	-	-	-	-	0.9947	0.9949

Table 5. The scattering correction factor for low-energy X-ray free-air chamber(small)

Tube voltage (kV)	Q.I.					
	0.4	0.5	0.6	0.7	0.8	0.9
50	0.9971	0.9973	0.9975	0.9977	-	-
40	0.9969	0.9971	0.9973	0.9974	0.9976	-
30	0.9966	0.9968	0.9970	0.9972	0.9973	0.9975
20	-	0.9963	0.9965	0.9967	0.9968	0.9970
15	-	-	0.9960	0.9963	0.9965	0.9966
10	-	-	-	-	0.9957	0.9959

Table 6. The electron loss correction factor for low-energy X-ray free-air chamber(small)

Tube voltage (kV)	Q.I.					
	0.4	0.5	0.6	0.7	0.8	0.9
50	1.0001	1.0001	1.0002	1.0005	-	-
40	1.0000	1.0000	1.0000	1.0000	1.0000	-
30	1.0000	1.0000	1.0000	1.0000	1.0000	1.0000
20	-	1.0000	1.0000	1.0000	1.0000	1.0000
15	-	-	1.0000	1.0000	1.0000	1.0000
10	-	-	-	-	1.0000	1.0000

Q_β MEASUREMENTS USING A TOTAL-ABSORPTION-TYPE HPGe DETECTOR WITH SIMULATED RESPONSE FUNCTIONS BY EGS4

H. Hayashi[1], I. Miyazaki[1], M. Shibata[2], K. Kawade[1], Y. Kojima[3], and A. Taniguchi[4]

[1]*Graduate School of Engineering, Nagoya University, Nagoya 464-8603, Japan*
[2]*Radioisotope Research Center, Nagoya University, Nagoya 464-8602, Japan*
[3]*Graduate School of Engineering, Hiroshima University, Higashi-Hiroshima 739-8527, Japan*
[4]*Research Reactor Institute, Kyoto University, Kumatori 590-0494, Japan*

Abstract

We tested an ability to deduce Q_β-values of a total-absorption-type HPGe detector. To analyze the spectra, the response functions are necessary. It is difficult to measure response functions for electrons experimentally. Then, the EGS4-code is available to simulate the response functions. It was found that the simulated response functions needed modification to reproduce the experimental spectra well. The endpoint energies are deduced using the folding method. Correction factors to deduce Q_β-values are estimated to be 164±10 and 164±20 keV in an energy range of 1-5 MeV and 5-9 MeV, respectively.

1. Introduction

The Q_β-values are fundamental physical quantities, and they are related to the mass predictions and the nuclear structures. One of the precise methods for Q_β measurements is the β-γ coincidence method [1-3]. Small HPGe detectors that have thin beryllium entrance windows (0.05-0.38 mm in thickness) can deduce Q_β-values within accuracy of about 2 keV, in a case of having good response functions for monoenergetic electrons and good statistics [1]. This method strongly depends on information of the decay schemes. For low-yield nuclides, it is difficult to construct the decay schemes.

A concept of a total absorption detector is to absorb all radiation from the radioactive nuclei. Then, endpoint energies of the β-decay to the ground state and β-decays to the excited states, which have subsequent γ-rays, show the Q_β-values. It has a possibility to deduce Q_β-values without the knowledge of the decay schemes. A total absorption detector which consists of large twin BGO detector (2×120 mm in diameter×100 mm in thickness) has developed by M. Shibata *et al.* The detector can measure Q_β-values with accuracy about 100 keV [4-6].

To achieve more precise Q_β measurements, we are developing a total-absorption-type HPGe detector. The response functions for γ-rays and electrons are needed to analyze the spectra. In this paper, we describe the properties of our detector and analyzing procedure using the EGS4-code.

2. The total-absorption-type HPGe detector

Figure 1 shows our detector. It consists of an HPGe detector (85 mm in diameter×89 mm in length) and a surrounding BGO scintillation detector (170 mm in diameter×25 mm in thickness×150 mm in length). The central HPGe detector has a through-hole (15 mm in diameter) in the center. The thickness of an entrance aluminum window of the hole is 0.4 mm. Radioactive sources can be put into the hole and large solid angle is achieved ($\Omega \approx 98\%$). The BGO detector is used to detect scattered photons, which are not absorbed by the HPGe detector. From geometrical restrictions of the HPGe detector, the BGO detector can not cover with the HPGe detector completely.

Figure 2 shows the simulated spectrum of the total-absorption-type HPGe detector, in the case of a radioisotope which has a simple decay scheme like inset in Fig. 2. Three problems are found; (1) The endpoint energy becomes smaller than Q_β-values, because of energy losses, (2) The β-ray spectra are distorted, caused by electron scatterings in aluminum window, (3) The Compton scattered photons distorted the spectrum.

Singles spectra and coincidence spectra were measured with the detector. The effect of the Compton scattering were removed by subtracting the coincidence spectra from the singles ones. The folding method was adopted to deduce the endpoint energies. The response functions for monoenergetic electrons were calculated by EGS4-code. The energy losses of electrons were calculated from endpoint energies and evaluated Q_β-values. The details of analysis were described in the following sections.

3. Measurement and Analysis

3.1 Measurement

Radioactive sources that have well-evaluated Q_β-values and strong β-feedings to the ground states were measured. At the Kyoto University Reactor (KUR), nine radioisotopes (^{142}Pr, ^{90}Y, ^{139}Ba, ^{27}Mg, ^{42}K, ^{56}Mn, ^{52}V, ^{72}Ga, ^{38}Cl) were prepared by (n,γ) reactions using the pneumatic tube facility, and three radioisotopes (^{140}Cs, ^{142}Cs, ^{92}Rb) were prepared by ^{235}U(n,f) reactions using the on-line isotope separator (ISOL) facility.

3.2 Subtraction of distorted spectra for Compton scattered photons

The singles spectra with the HPGe detector include distorted spectra originated from Compton scattered photons. If a BGO detector can detect the scattered photons completely, the effects of Compton scattered photons can be removed by subtracting coincidence spectra from singles ones. In the present geometrical condition as described in chapter 2, the observed coincidence spectra need to be corrected for detection efficiency. The detection efficiency was deduced using the EGS4-code. The simulated singles spectrum and the coincidence one for γ-ray are shown in Fig. 3. The Compton continuum is removed by subtracting the coincidence spectrum corrected for coincidence efficiency from the singles one. In the subtracted spectrum, only full energy peak is obtained. A typical result for ^{42}K decay is shown in Fig. 4.

3.3 Response functions for monoenergetic electrons

The singles spectra corrected for Compton scatterings were also distorted by scatterings for electrons. To fold the spectra, response functions for monoenergetic electrons are needed. From the geometrical restrictions (see chapter 2), it is difficult to measure the response functions experimentally. We simulated the response functions using EGS4-code for an energy range of 1-9 MeV. Then, the response functions were simplified by dividing into 3 parts using functions (Fig. 5). As shown in Fig. 6, a folded spectrum (open circles) calculated by the original response functions is in agreement with experimental one in an energy range of 300 keV below the endpoint energy. We consider that the inconsistency in low energy region (in Fig. 6) is caused by discrepancies between the simulated response functions and the realistic ones.

To test the simulated response function for the electron, a response function for internal conversion electron (^{137m}Ba, 624 keV) was measured using a planar-type HPGe detector (36 mm in diameter $\times$13 mm in thickness). Figure 7 shows the comparison between experimental response functions and simulated ones. In the simulated spectra, a peak form is in agreement with the experimental one, but relative intensity of the scattering part is smaller than the experimental one.

It is considered that the similar discrepancies exist in the simulated response functions for the total-absorption-type HPGe detector. By changing the ratios of three components as shown in Fig. 8, we obtained the folded spectra which agreed with experimental ones in an energy range of more than 1000 keV below endpoint energies (closed circles in Fig. 6).

3.4 Endpoint deduction using the folding method

From total absorption spectra, endpoint energies were deduced using the folding method. A folded spectrum (S_{folded}) for assumed endpoint energy (W) can be calculated as

$$S_{folded}(W) = \sum R(E) \times F(E, W), \quad (1)$$

where R(E) is a response function for electron of an incident energy E, and F is a theoretical β-ray spectrum. The folded spectrum was compared with experimental one in a fitting range. The endpoint energy was deduced from the folded spectrum which had a minimum χ^2-value. By changing the fitting regions between 300 and 1000 keV below a spectrum endpoint, uncertainty was evaluated.

4. Results

The endpoint energies of measured nuclides were deduced as mentioned above. Owing to energy losses for an aluminum window of an HPGe detector, the endpoint energies were smaller than Q_β-values. By taking the differences between endpoint energies and evaluated Q_β-values [7], the correction factors were evaluated to be 164±10 keV below 5 MeV and 164±20 keV above 5 MeV (Fig. 9). The factors also include the influences of changing the response functions.

5. Summary and future plans

We tested performance of the total-absorption-type HPGe detector to deduce the Q_β-values. EGS4-code was used to correct the distortions caused by Compton scattered photons and scatterings for electrons. We measure radioisotopes, which have well-evaluated Q_β-values in an energy range of 2-8 MeV, and the Correction factors to deduce Q_β-values were estimated. It is considered that our detector can deduce Q_β-values with accuracy about 10 and 20 keV in an energy range of 1-5 MeV and 5-9 MeV, respectively.

In the present case we chose β-sources, which have strong β-feedings to the ground states. For the nuclei far from the β-stability, it is necessary to check the reliabilities of analysis by measuring some nuclei which have various types of decay schemes. We will measure Q_β-values of neutron-rich rare-earth isotopes using the on-line isotope separator.

References

[1] Y. Kojima, M. Shibata, H. Uno, K. Kawade, A. Taniguchi, Y. Kawase, K. Shizuma, Nucl. Instrum. Method. **A 458**, (2001) 656-669.

[2] M. Groβ, P. Jürgens, U. Keyser, S. Kluge, M. Mehrtens, S. Müller, F. Münnich, J. Wulff, H.R. Faust, Nucl. Instrum. Method. **A311**, (1992) 512.

[3] R.C. Greenwood, M.H. Putnam, Nucl. Instrum. Method. **A337**, (1993) 106.

[4] M. Shibata, Y. Kojima, H. Uno, K. Kawade, A. Taniguchi, Y. Kawase, S. Ichikawa, F.Maekawa, Y. Ikeda, Nucl. Instrum. Method. **A459**, (2001) 581.

[5] M. Shibata, T. Shindo, A. Taniguchi, Y. Kojima, K. Kawade, S. Ichikawa, Y. Kawase, J. Phys. Soci. Jpn. **71**, (2002) 1401.

[6] F. Maekawa, M. Wada, Y. Ikeda, Nucl. Instrum. Method. **A450**, (2000) 467.

[7] G. Audi, A.H. Wapstra, C. Thibault, Nucl. Phys. **A729**, (2003) 337.

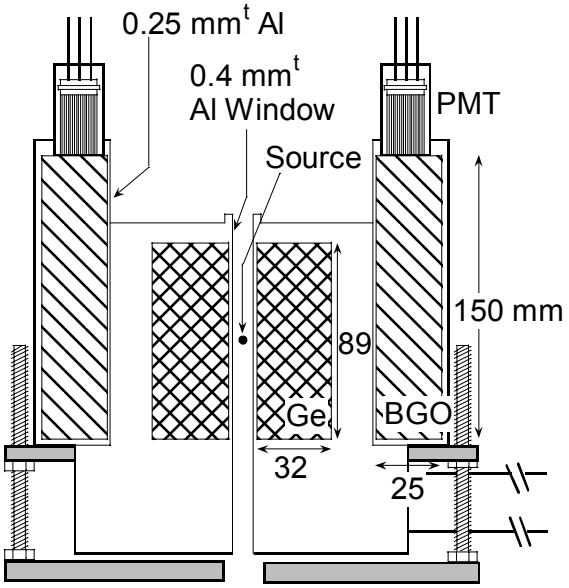

Fig. 1. Schematic cross-sectional view of a total-absorption-type HPGe detector.

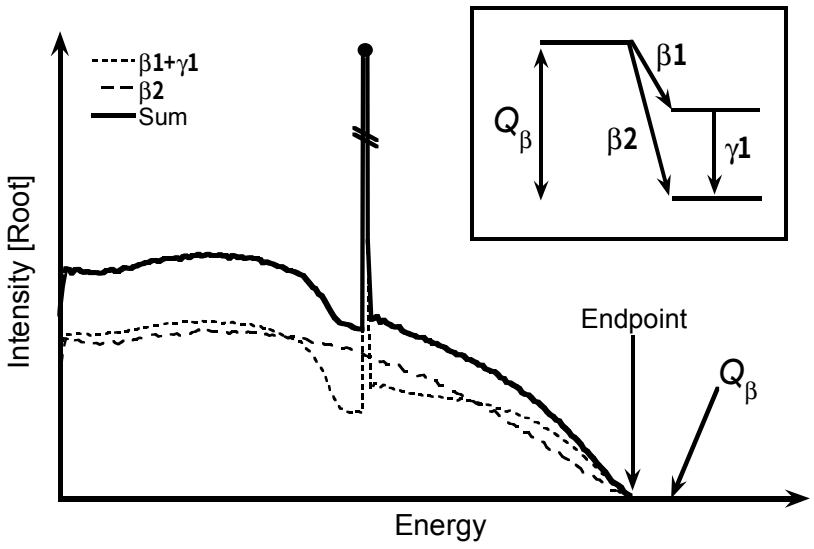

Fig. 2. Simulated singles spectrum with the HPGe detector, in the case of measuring the nucleus, which has decay scheme like inset. Beta-ray spectra are distorted originated from the aluminum window, and the endpoint energy become smaller than the Q_β-value. Compton scattered photons are also distorted the singles spectrum.

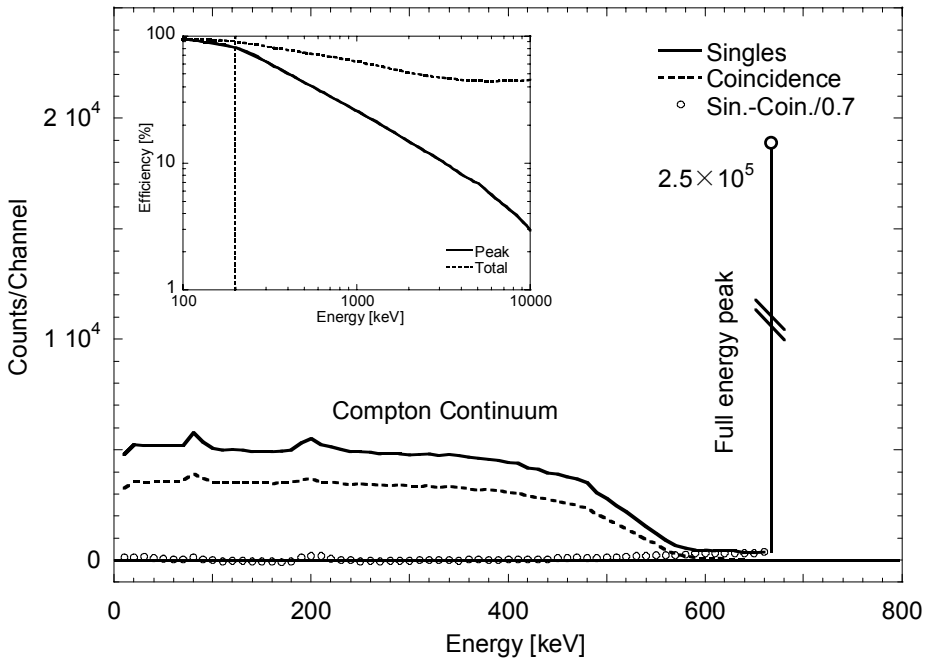

Fig. 3. Simulated response functions for 662 keV γ-ray. The Compton continuum is removed by subtracting the coincidence spectrum multiplied a factor from the singles one. The factor of 1/0.7 is correction of detection efficiency for scattered photons.

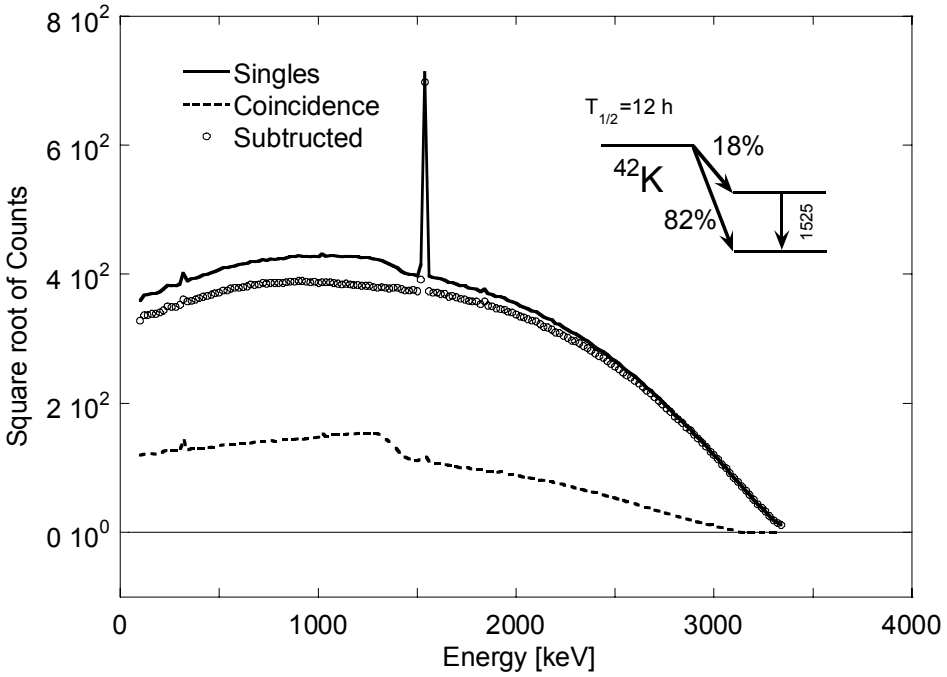

Fig. 4. Measured spectra for ^{42}K decay.

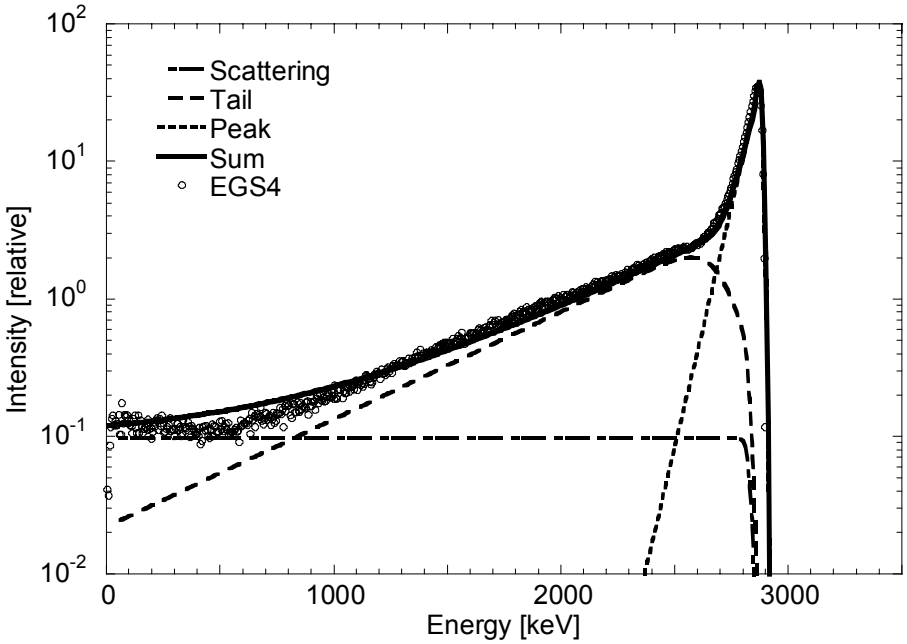

Fig. 5. Simulated response function for monoenergetic electron of 3 MeV in the singles mode. It is constructed of 3 parts.

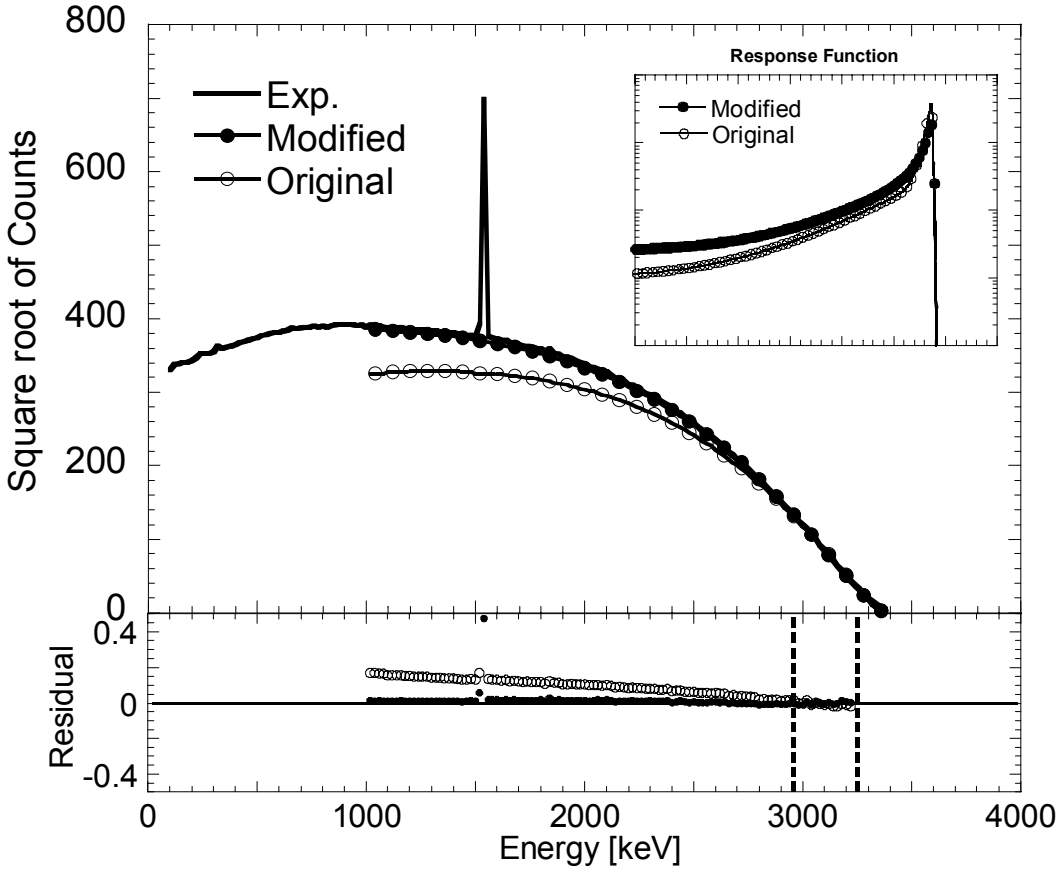

Fig. 6. Comparisons of experimental total absorption spectrum for ^{42}K with folded spectra. The folded spectrum using modified response functions well agreed with experimental one in a range of 1000 keV below end point energy.

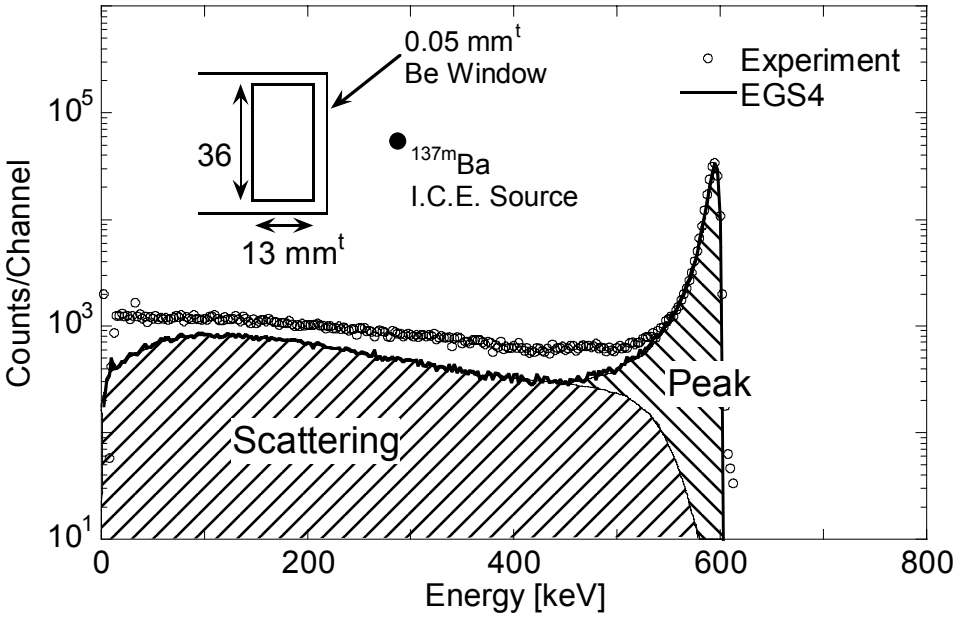

Fig. 7. Comparisons between experimental response function and simulated one, using the LEPS detector. The simulated spectrum is normalized by peak counts.

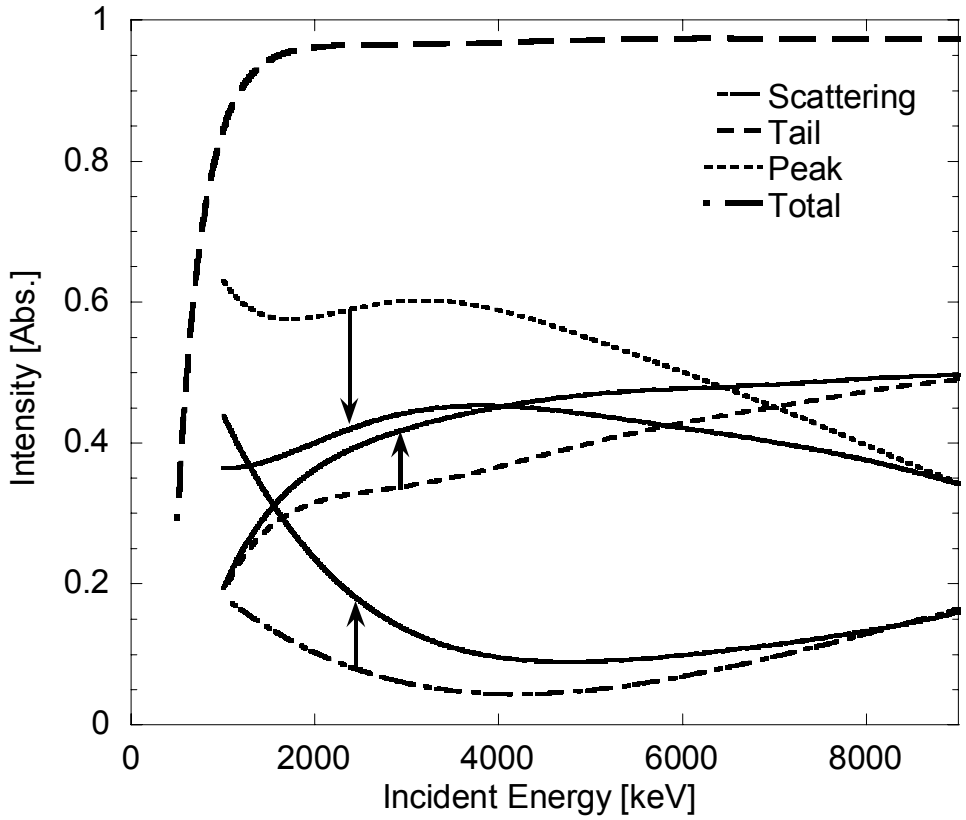

Fig. 8. Energy dependences of intensities of each component for electron response functions. The solid line shows ratios for modified response functions.

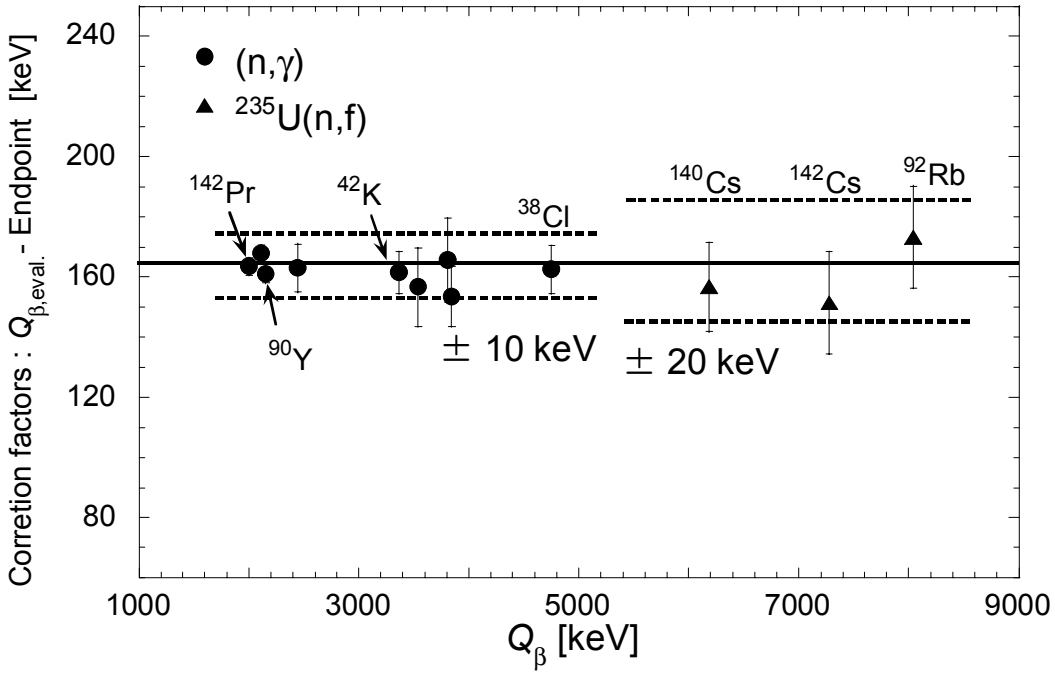

Fig. 9. Comparisons between evaluated Q_β-values and endpoint energies.

MONTE CARLO CALCULATIONS OF FREE-AIR IONIZATION CHAMBER CORRECTION FACTORS FOR ELECTRON LOSS AND PHOTON SCATTER AT INER

Uei-Tyng Lin, Ren-Dih Sheu, and Wen-Song Hwang

National Radiation Standard Laboratory, Institute of Nuclear Energy Research, Taiwan, R.O.C.

Abstract

The Monte Carlo method was used to evaluate two self-made cylindrical free-air ionization chambers correction factors for electron loss and scattered photons, corresponding to the medium- and low-energy x-ray ranges. For the medium-energy chamber, the calculated results were in close agreement with current values of the National Radiation Standard Laboratory. For the low-energy chamber, the results showed that the electron loss and scattered photons using measured BIPM spectra were extremely close to those obtained using simple x-ray unit geometry calculated spectra.

1. Introduction

The free-air ionization chambers are widely used by standards laboratories as primary standards for absolute measurement of air kerma in beams of low- and medium-energy x-rays. Generally, there are two types of free-air ionization chamber used in standard ionization laboratories: the plane-parallel type and the cylindrical type [1-3]. In Taiwan, based on the original design by F. H. Attix [4], two improved cylindrical type free-air ionization chambers, one medium-energy and one low-energy, were constructed at the National Radiation Standard Laboratory (NRSL) of the Institute of Nuclear Energy Research (INER, Taiwan).

These two free-air ionization chambers have different physical dimensions; therefore the correction factors for electron loss (K_e) and scattered photons (K_{sc}) have to be evaluated separately. In this study, the cylindrical free-air chambers geometry model were simplified, and the Monte Carlo code LSCAT (low-energy photon-scattering expansion for the EGS4 code) [5] was used to calculate the values of K_e and K_{sc} for mono-energetic photons with energies ranged from 2 keV to 300 keV. Further,

these results were weighted by photon spectra to obtain the values of $\overline{K}_e$ and $\overline{K}_{sc}$ for each chamber.

The calculated values of $\overline{K}_e$ and $\overline{K}_{sc}$ for the medium-energy chamber at the NRSL x-ray unit spectra were compared with NRSL current values [6], and the energy spectra weighting values were also compared with the values calculated using the x-ray unit effective energies. For the Monte Carlo calculations of the low-energy chamber, energy spectra weighting values of $\overline{K}_e$ and $\overline{K}_{sc}$ for measured BIPM spectra [7] were compared with the energy spectra calculated using NRSL simple x-ray unit geometry.

2. Material and Methods

2.1. Simplified model for free-air chambers

The cylindrical free-air chambers geometry model is simplified and as shown in Figure 1. The geometry model used in the simulation mostly consists of 3 cylinders: a fixed central cylinder (L_a cm in length) and two movable cylinders at the front and back ends (each of L_b cm in length). Except the length of the 3 cylinders described above, the configuration of the cylindrical free-air chamber is mainly characterized by the following 5 parameters, namely the incident photon beam radius r_{iap} cm, the attenuation length A cm, the cylinder incident aperture radius r_{cap} cm, the cylinder radius r_{cy} cm, and all cylinders enclosed sides thickness T cm (each of aluminum). The materials used in the front and back movable cylinders were aluminum and plastic for the medium- and low-energy free-air ion chamber respectively, and the central cylinder material was aluminum. The main structural data of the simplified chambers are given in Table 1. The shaded regions in Figure 1 indicate the scoring regions, in which the energy deposition is counted.

2.2. LSCAT code and calculation of mono-energetic K_e and K_{sc} values

The Monte Carlo calculations were performed by using the LSCAT code with the PRESTA electron transport algorithm. The transport parameters were set as PCUT=1 keV and ECUT=512 keV, and we created a user code to allow the energy deposition due to that primary electrons and their progeny can be separated from the total energy deposition. Our analysis follows the method recommended by D. T. Burns [8], a “primary” electron is the one generated in the first interaction of an

incident photon and the energy deposition arising from such an electron and its progeny is referred to as primary energy. For a given incident photon energy E, the $P_{tot}(E)$ was set to be the total primary energy deposited in the scoring regions and $P_{col}(E)$ be the primary energy deposited in the collecting region. Then $K_e(E)$ is calculated as

$K_e(E) = P_{tot}(E) / P_{col}(E)$.

Similarly, the $S_{col}(E)$ was the scattered energy deposited in the collecting region. Then

$K_{sc}(E) = P_{col}(E) / [\, P_{col}(E) + S_{col}(E)]$

For the medium-energy chamber, calculations were made in 10 keV steps from 10 keV to 300 keV, with 10^8 histories at each energy. For the low-energy chamber, calculations were made from 2 keV to 50 keV in steps of 2 keV, also with 10^8 histories each. Statistical uncertainties were estimated for each energy range by sub-dividing the histories into twenty batches. The statistical uncertainty of all values for mono-energetic Ke and Ksc were not more than 0.01 % (one standard deviation).

2.3 Energy spectra weighting calculations of $\overline{K}_e$ and $\overline{K}_{sc}$

In our analysis, for a photon fluence spectrum $\Phi(E)$, the energy spectra weighting calculations of $\overline{K}_e$ and $\overline{K}_{sc}$ are evaluated as

$$\overline{K}_e = \frac{\int_{E_{\min}}^{E_{\max}} K_e(E) \cdot \left(\frac{\mu_{tr}}{\rho}\right)_{air} \cdot E \cdot \frac{d\phi}{dE} dE}{\int_{E_{\min}}^{E_{\max}} \left(\frac{\mu_{tr}}{\rho}\right)_{air} \cdot E \cdot \frac{d\phi}{dE} dE}$$

and

$$\overline{K}_{sc} = \frac{\int_{E_{\min}}^{E_{\max}} K_{sc}(E) \cdot \left(\frac{\mu_{tr}}{\rho}\right)_{air} \cdot E \cdot \frac{d\phi}{dE} dE}{\int_{E_{\min}}^{E_{\max}} \left(\frac{\mu_{tr}}{\rho}\right)_{air} \cdot E \cdot \frac{d\phi}{dE} dE}.$$

For the medium-energy free-air ionization chamber, the spectra were calculated by using the Monte Carlo code OMEGA/BEAM [9-10] with NRSL simple x-ray unit geometry (Figure 2); for the low-energy free-air ionization chamber, the spectra were those using the measured photon fluence spectra for the BIPM reference

qualities [7], and some of the energy spectra were calculated using the Monte Carlo code OMEGA/BEAM with NRSL simple x-ray unit geometry for comparison.

3. Results and Discussion

3.1. Results for medium-energy x-ray qualities

3.1.1. Mono-energetic values of K_e and K_{sc}

The mono-energetic results for K_e for NRSL's medium-energy chamber are shown in Figure 3, where the uncertainty bars represent one statistical uncertainty. Where K_e is equal to unity for photon energies below 110 keV, because no secondary electrons hitting the electrode are detected. The peak value at around 160 keV is due to photoelectrons, although the photoelectron energy escapes is larger when the photon energy is increased. Noteworthy in the energy range between 170 keV and 250 keV are that the photoelectric cross-section is rapidly decreasing and the competition of these two effects which reduce the electron loss. Above 250 keV, Compton effect increases rapidly, therefore a larger fraction of the Compton electrons energy escapes the collecting volume.

The mono-energetic results of K_{sc} for NRSL's medium-energy chamber are shown in Figure 4. At the higher energies, almost all interactions are Compton interactions. This means that the relative contribution of scattered photons is equal to the probability that a Compton-scattered photon has a second Compton interaction before leaving the air volume of the chamber. The increase at lower energies arises from the rapidly increasing cross-section for the production of photoelectrons by Compton-scattered photons. This phenomenon was discussed in detail by T. W. M. Grimbergen et.al. [11] and D. T. Burns [8]. Maybe it is that the higher value obtained at 10 keV is an artifact of the calculations, but this has no significant effect on the energy spectra weighting values of $\overline{K}_{sc}$ because there is little measured fluence at this energy.

3.1.2. Values of $\overline{K}_e$ and $\overline{K}_{sc}$ at the reference spectra

The calculated values of $\overline{K}_e$ and $\overline{K}_{sc}$ for the medium-energy chamber at the x-ray unit effective energies were compared with the current values applied in NRSL. The calculated values of $\overline{K}_e$ and $\overline{K}_{sc}$ for the medium-energy chamber at the NRSL x-

ray unit spectra were compared with NRSL's current values first, and the energy spectra weighting values were also compared with the values calculated using the x-ray unit effective energies. The results for $\overline{K}_e$ and $\overline{K}_{sc}$ of NRSL's medium-energy chamber are shown in Table 2. When using x-ray unit effective energies, the maximum difference between the calculated values and NRSL current values of $\overline{K}_e$ was 0.11 % (at radiation quality 250 kV) and for $\overline{K}_{sc}$ was 0.22 % (at radiation quality 100 kV). When using energy spectra weighting, the maximum difference between the calculated values and the NRSL's current values for $\overline{K}_e$ was 0.07 % (at radiation quality 180 kV) and for $\overline{K}_{sc}$ was 0.22 % (at radiation quality 100 kV). And the maximum calculation difference between using energy spectra weighting and using x-ray unit effective energies for $\overline{K}_e$ was 0.13 % (at radiation quality 250 kV) and for $\overline{K}_{sc}$ 0.04 % (at radiation quality 135 kV). As shown in Table 2, the maximum difference for $\overline{K}_e \times \overline{K}_{sc}$ was 0.22 % as the determined with energy spectra weighting and NRSL current values at radiation quality 100 kV.

3.2. Results for low-energy x-ray qualities

3.2.1. Mono-energetic values of K_e and K_{sc}

The mono-energetic results of K_e for NRSL's low-energy chamber are shown in Figure 5, where the uncertainty bars represent one statistical uncertainty. For photon energies below 48 keV, no secondary electrons hitting the electrode are detected and the rise due to photoelectrons reaching the chamber walls begins photon energy above 50 keV.

The mono-energetic results of K_{sc} for NRSL's low-energy chamber are shown in Figure 6, and they show the similar trend as medium-energy x-ray calculations. The higher value obtained at 2 keV is also an artifact of the calculations, and it has no significant effect on the energy spectra weighting values of $\overline{K}_{sc}$ because there is little measured fluence at this energy.

3.2.2. Values of $\overline{K}_e$ and $\overline{K}_{sc}$ at the reference spectra

For the Monte Carlo calculations of the low-energy chamber, energy spectra weighting values of $\overline{K}_e$ and $\overline{K}_{sc}$ for measured BIPM spectra were compared with the

energy spectra calculated using NRSL simple x-ray unit geometry. The results of $\overline{K}_e$ and $\overline{K}_{sc}$ for NRSL's low-energy chamber are shown in Table 3. The results showed that $\overline{K}_e$ and $\overline{K}_{sc}$ by using measured BIPM spectra were extremely close to those obtained using simple x-ray unit geometry calculated spectra and the maximum difference of $\overline{K}_e \times \overline{K}_{sc}$ was 0.02 %.

4. Conclusions

The values of $\overline{K}_e$ and $\overline{K}_{sc}$ calculated by using the Monte Carlo method with energy spectra were established at the NRSL of the INER. For the medium-energy chamber, the agreement between the correction factors determined in this study and NRSL current values is better than 0.22 %. For the low-energy chamber, the correction factors derived by using measured spectra were extremely close to those obtained using simple x-ray unit geometry calculated spectra and the difference is less than 0.02 %.

References

1. National and International Standardization of Radiation Dosimetry, Proc. Ser. STI/PUB/471, Vols. 1 and 2, Vienna, International Atomic Energy Agency, 1978.
2. H. O. Wychoff , F. H. Attix, Design of free-air ionization chambers, Nat. Bur. Stand. Handbook, 1969, No. 64, 1-16.
3. R. Thoraeus, H. O. Wychoff, Calibration of the portable Swedish free-air chamber equipment at the U.S. National Bureau of Standards, Acta Radiol., 1956, 46, 741-746.
4. F. H. Attix, Electronic Equilibrium in Free-air Chambers and a Proposed New Chamber Design, NRL Report 5646, Washington, D.C., U.S. Naval Research Laboratory, 1961, 15 p.Y. Namito, H. Hirayama, LSCAT: Low-energy photon-scattering expansion for the EGS4 code (inclusion of electron impact ionization), 2000, KEK Internal 2000-4, high Energy Accelerator Research Organization.
5. W. L. Chen, S. H. Su, L. L. Su, and W. S. Hwang, Improved free-air ionization chamber for the measurement of x-rays, Metrologia, 1999, 36, 19-24.

6. T.W.M. Grimbergen, E. V. Dijk, and M. Boutillon, Photon fluence spectra of the BIPM reference qualities for low energy x-rays, 1997, CCEMRI(I)/97-31 (BIPM).

7. D.T. Burns, Consistent set of calculated values for electron-loss and photon-scatter corrections for parallel-plane free-air chambers, 1999, CCRI(I)/99-4 (BIPM).

8. D. W. O. Rogers, C. M. Ma, G. X. Ding, and B. Walters, BEAM Users Manual, NRC Repoer PIRS 509a, 1995.

9. J. A. Treurniet, D. W. O. Rogers, BEAM, DOSXYZ and BEAMDP GUI User;s Manual, NRC Report PIRS 0623(rev A), 1999.

10. T. W. M. Grimbergen, E. van Dijk, and W de Vries, Correction factors for the Nmi free-air ionization chamber for medium-energy x-rays calculated with the Monte Carlo method, Phys. Med. Biol., 1998, 43, 3207-3224.

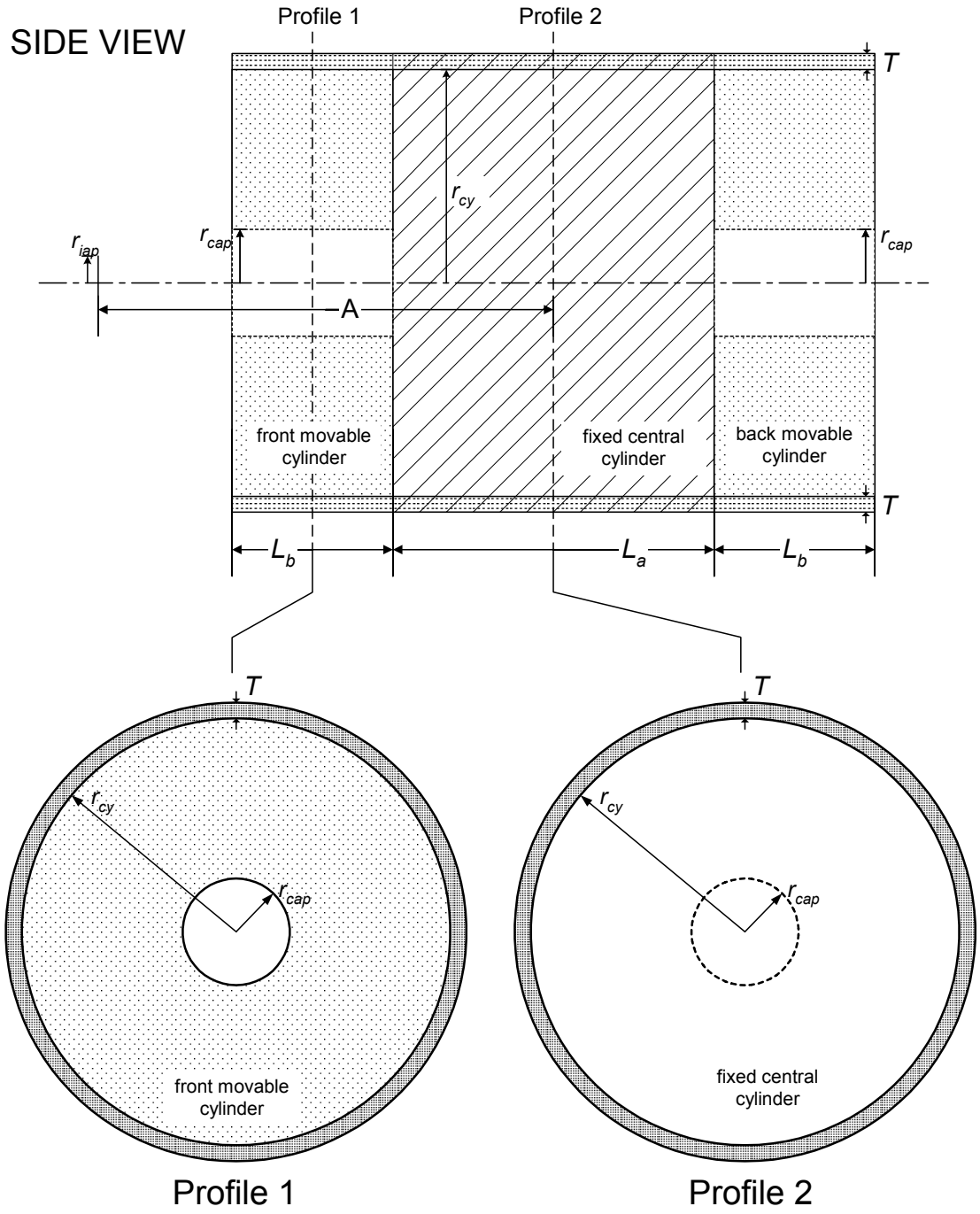

Figure 1. The simplified geometry of the NRSL cylindrical free-air chamber used in the Monte Carlo simulations. The shaded region represents the energy-scoring region.

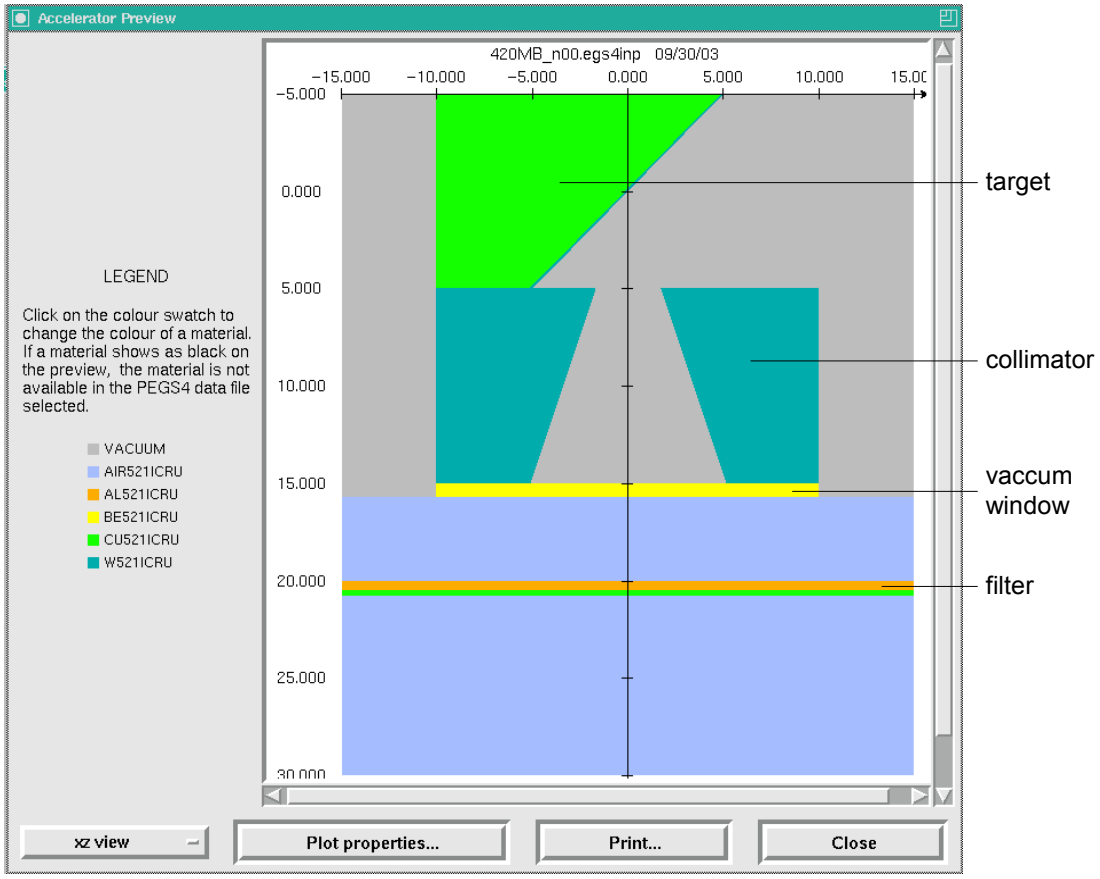

Figure 2. The simple geometry configuration of NRSL x-ray unit

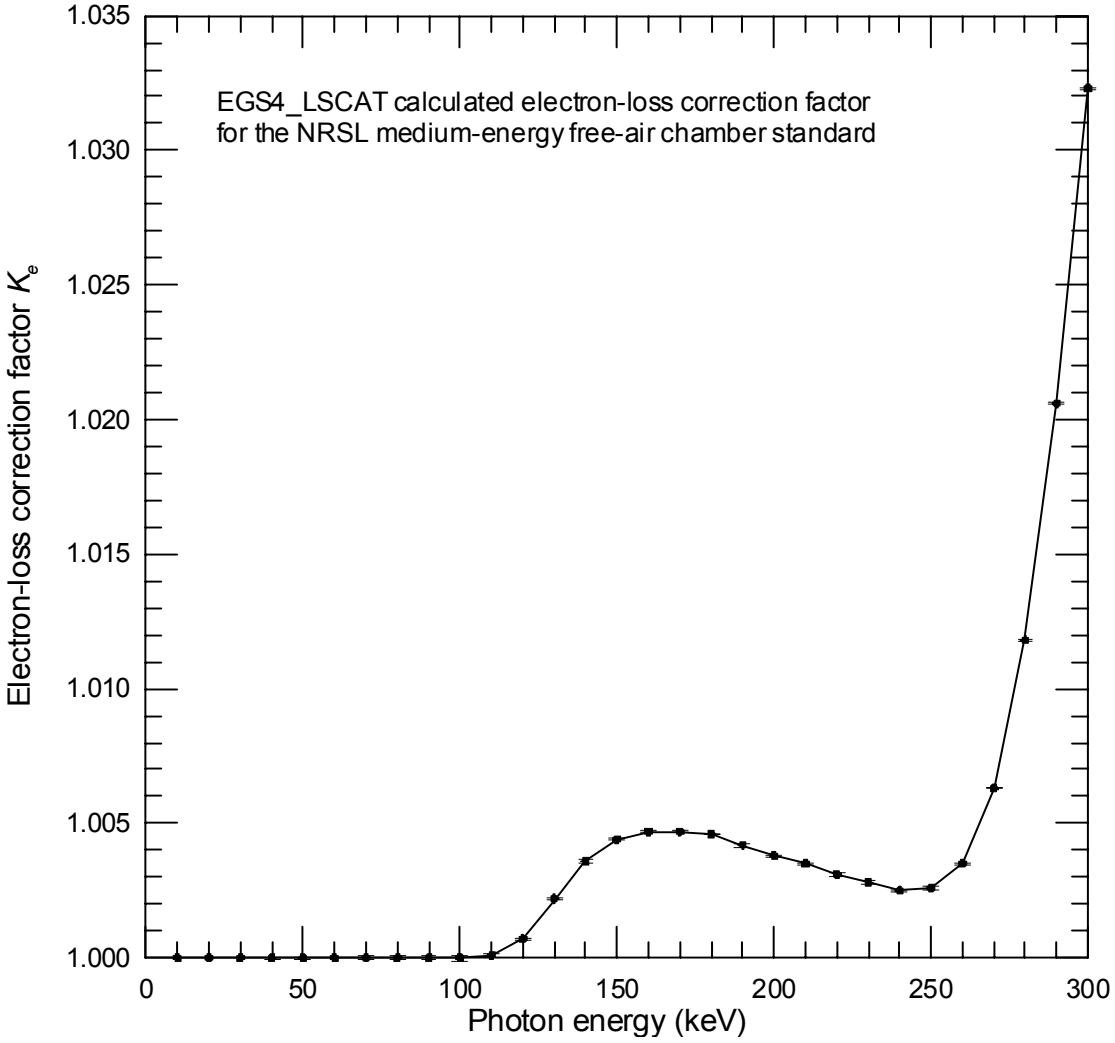

Figure 3. Mono-energetic values of K_e for the NRSL medium-energy free-air chamber

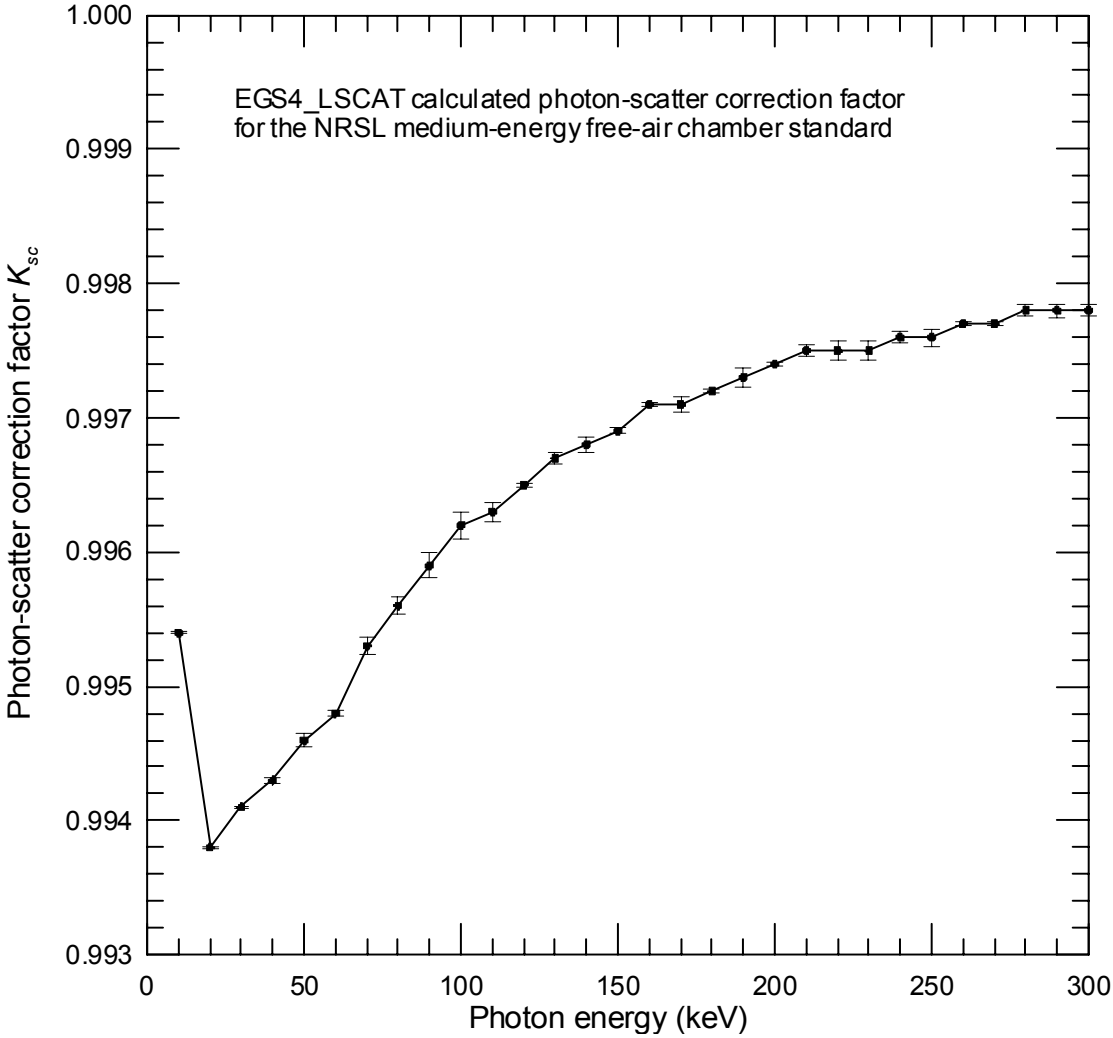

Figure 4. Mono-energetic values of K_{sc} for the NRSL medium-energy free-air chamber

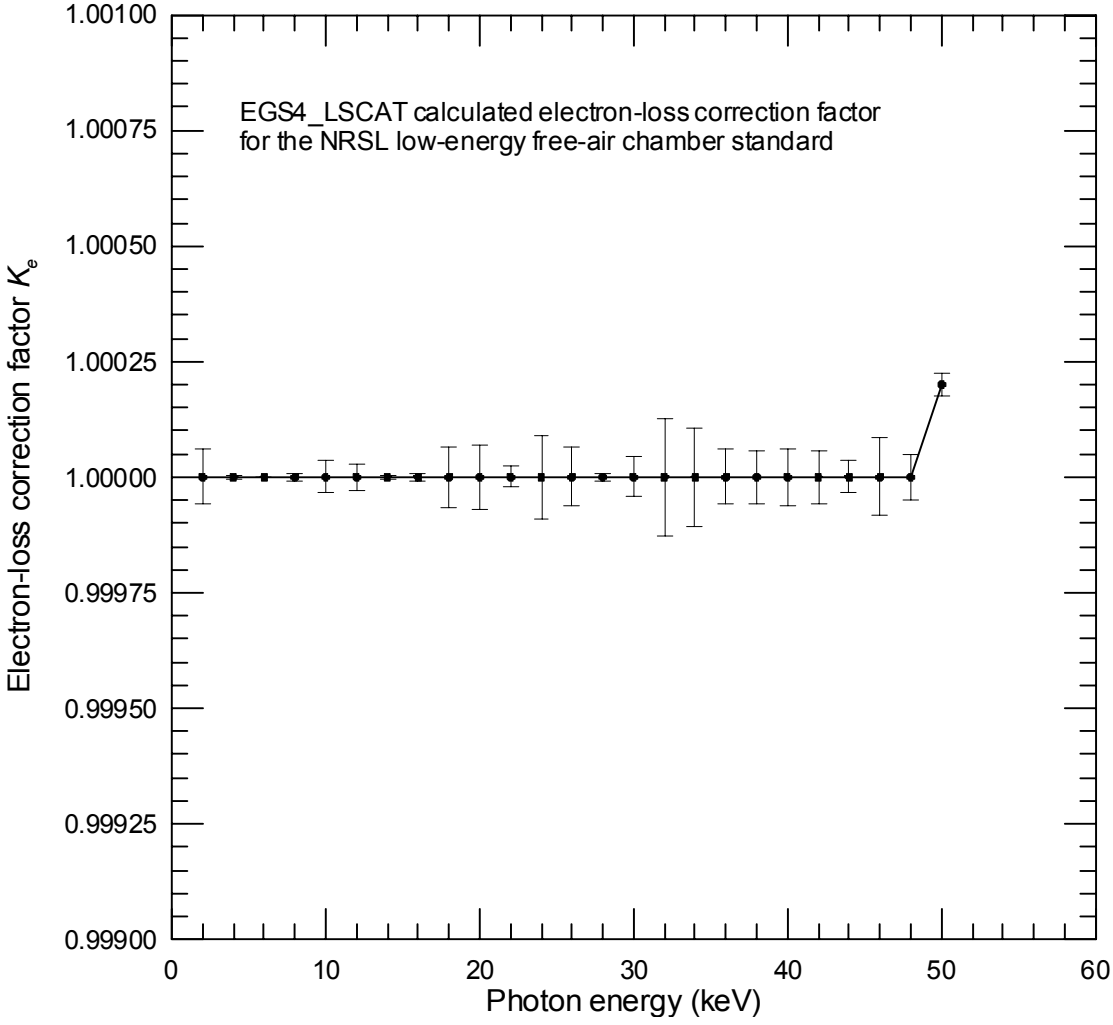

Figure 5. Mono-energetic values of K_e for the NRSL low-energy free-air chamber

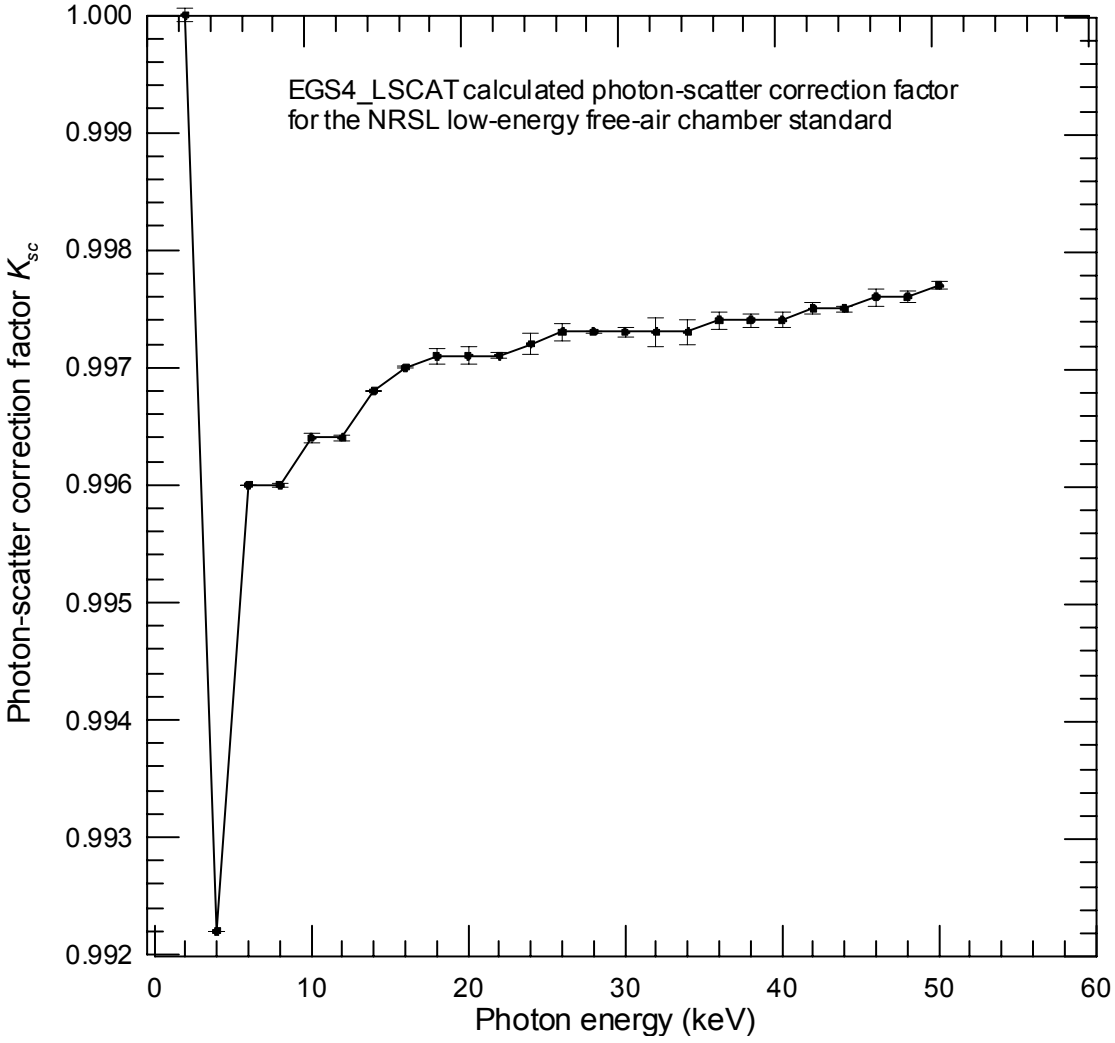

Figure 6. Mono-energetic values of K_{sc} for the NRSL low-energy free-air chamber

Table 1. The main structural data of the NRSL free-air chambers

Chamber Type	Medium-Energy	Low-Energy
Fixed central cylinder length L_a (cm)	30	7
Two movable cylinders length L_b (cm)	15	3.5
Incident photon beam radius r_{iap} (cm)	0.5	0.2
Cylinder incident aperture radius r_{cap} (cm)	1.75	0.5
Attenuation length A (cm)	43.87	15.513
Cylinder radius r_{cy} (cm)	15	4
Cylinders enclosed sides thickness T (cm)	0.25	0.3

Table 2. The comparisons of $\overline{K}_e$ and $\overline{K}_{sc}$ for NRSL medium-energy chamber

NRSL Current Values (D)				
X-ray unit voltage (kV)	100	135	180	250
Effective Energy (keV)	35	55	80	125
$\overline{K}_e$	1.0000	1.0000	1.0000	1.0025
$\overline{K}_{sc}$	0.9921	0.9945	0.9951	0.9953
$D = \overline{K}_e \times \overline{K}_{sc}$	0.9921	0.9945	0.9951	0.9978
EGS_LSCAT with effective energy (G_e)				
X-ray unit voltage (kV)	100	135	180	250
Effective Energy (keV)	35	55	80	125
$\overline{K}_e$	1.0000	1.0000	1.0000	1.0014
$\overline{K}_{sc}$	0.9943	0.9947	0.9956	0.9966
$G_e = \overline{K}_e \times \overline{K}_{sc}$	0.9943	0.9943	0.9956	0.9980
EGS_LSCAT with spectrum weighting (G_s)				
X-ray unit voltage (kV)	100	135	180	250
$\overline{K}_e$	1.0000	1.0000	1.0007	1.0027
$\overline{K}_{sc}$	0.9943	0.9951	0.9957	0.9968
$G_s = \overline{K}_e \times \overline{K}_{sc}$	0.9943	0.9951	0.9964	0.9995
Comparison				
X-ray unit voltage (kV)	100	135	180	250
G_e/D	1.0022	0.9998	1.0005	1.0002
G_s/D	1.0022	1.0006	1.0013	1.0017
G_s/G_e	1.0000	1.0008	1.0008	1.0015

Table 3. The comparison of $\overline{K}_e$ and $\overline{K}_{sc}$ for NRSL low-energy chamber

Measured photon fluence spectra for the BIPM reference qualities (D)			
X-ray unit voltage (kV)	30	50a	50b
$\overline{K}_e$	1.0000	1.0000	1.0000
$\overline{K}_{sc}$	0.9968	0.9974	0.9973
$D = \overline{K}_e \times \overline{K}_{sc}$	0.9968	0.9974	0.9973
Energy spectra calculated using the Monte Carlo code OMEGA/BEAM with NRSL simple x-ray unit geometry			
X-ray unit voltage (kV)	30	50a	50b
$\overline{K}_e$	1.0000	1.0000	1.0000
$\overline{K}_{sc}$	0.9968	0.9973	0.9971
$G = \overline{K}_e \times \overline{K}_{sc}$	0.9968	0.9973	0.9971
Comparison			
X-ray unit voltage (kV)	30	50a	50b
G / D	1.0000	0.9999	0.9998

DEVELOPMENT OF EGS-BESED 3D BRAIN SPECT SIMULATOR (3DBSS)

Takashi Yokoi [a], Takeyuki Hashimoto [b], Hiroyuki Shinohara [c]

[a]Bioimaging Laboratory, Inc.,Kyoto, Japan
[b]Department of Information Processing, Yokohama Soei College, Yokohama, Japan
[c]Department of Radiological Sciences, Tokyo Metropolitan University of Health Sciences Tokyo, Japan
e-mail:tyokoi@bioimaging-lab.com

Abstract

We developed the EGS-based Monte Carlo simulation system to generate 3D brain SPECT data. This system, called 3DBSS (3D Brain SPECT Simulator), can generate various radioactivity patterns for human brain images measured by SPECT. We generated three types of radioactivity patterns for the cerebral blood flow pattern (CBF), striatum (putamen and nucleus) image pattern (STR) and the skull bone image pattern (SKL) using the Zubal digital brain phantom. These patterns are simulated as images of Tc-99m ECD (or Tc-99m HMPAO), Tc-99m TRODAT-1, and Tc-99m MDP, respectively. Monte Carlo simulations were performed using ultra-high resolution (UHR), high resolution (HR) and general all purpose (GAP) collimator. The spatial resolutions for UHR, HR and GAP collimator were estimated as 6.6, 8.5 and 12.5 mm FWHM, respectively, using a point source. Scatter fraction (= number of scatter photons/number of primary photons) was almost independent of the collimator resolution, whereas it depended on the radioactivity pattern. The scatter fractions for the STR were slightly higher (36.8% for UHR, 36.8% for HR, and 36.9% for GAP) than those for the CBF (34.5% for UHR, 34.6% for HR, and 34.6% for GAP), whereas those for the SKL were considerably lower (23.8% for UHR, 23.6% for HR, and 23.7% for GAP) than the others. The 3DBSS system is powerful tool to simulate human brain SPECT images with various radioactivity patterns.

1. Introduction

In recent years, Monte Carlo simulation is used increasingly to solve various problems in the field of medical engineering [1-6]. Monte Carlo experiments have been used in a large number of SPECT (single photon emission computed tomography) studies such as an optimization of imaging system design [7], a development of correction method [8, 9] for improvement of image quantitation (scatter correction, attenuation correction and partial volume correction), and an evaluation of iterative reconstruction algorithms [10-12]. SPECT can obtain various types of physiological images according to characteristics of administrated tracer; for example cerebral blood flow, neuroreceptor/neurotransmitter, cardiac perfusion and bone metabolism. Such radioactivity distributions are very different for each tracer; consequently the photon interaction in the target organ depends on the tracer.

We develop 3D brain SPECT simulator (3DBSS) based on EGS4 (Electron Gamma Shower version 4) [13,14] and digital brain phantom. This system can define the radioactivity distribution for various tracers. It can generate SPECT projection data including physical processes of photon attenuation, Compton scatter and blurring due to collimator and detector response. We applied this system to investigate the influence of Compton scatter with three radioactivity patterns.

2. Simulation system

2.1 Digital brain phantom and Monte Carlo simulation code

Radioactivity distribution and material distribution are defined by a voxel-based representation using Zubal digital brain phantom [15], which has a matrix size of 256 x 256 x 128 (voxel size: 1.1 x 1.1 x 1.4 mm). Each brain segment of the Zubal phantom is assigned by an 8-bit value, as shown in Fig.1. The radioactivity distribution and material distribution are defined for each brain segment via the graphical user interface (GUI), as described later in section 2.3. A component of the brain tissue is assumed to be equivalent to water (mass density, ρ=1.00 g/cm^3). On the other hand, the skull bone (ρ=1.40 g/cm^3) consist of six elements from H, C, N, O, P, and Ca. The photon interaction cross sections for the brain tissue and skull bone are calculated by the PEGS program in advance.

Monte Carlo code is based on EGS4 (KEK version) [14] with the user code for SPECT system by Narita et al. [8, 16]. We modified the Narita's code to add the effect of intrinsic spatial resolution of the detector. Moreover, we rewrote this user code such that the detector parameters can be variable.

2.2 Detector and acquisition parameters

Detector is assumed to be a gamma camera-type detector with a NaI(Tl) scintillator and parallel hole collimator. The detector size is defined simply by a product of the acquisition matrix and the pixel size. Possible maximum frame (or angle) is 452 for a 128 x 128 matrix and 113 for a 256 x 256 matrix. System sensitivity and spatial resolution can be changed by the collimator geometry (the length and the hole diameter). In this system, penetration and scatter of γ-ray at the collimator septa are not considered at all. In addition, it is assumed that γ-ray does not incident from outside of field of view (FOV). The intrinsic spatial resolution and the energy resolution of the detector are modeled by a Gaussian response function with variable FWHM. Energy window can be used up to maximally three channels with arbitrary central energy (keV) and width (%). Detected events are stored separately for the primary (scatter-free) photons and the scattered photons into computer memory according to the detected position, angle and photon energy. The energy spectrum can be acquired with 1keV bins including multiple-order Compton scattered photons.

2.3 Program

Figure 2 illustrates diagram of the 3DBSS system. The activity distribution and material distribution are defined for each brain segment via the graphical user interface (GUI) by Excel + VB Macro. The radioactivity is given by a loop count per voxel which is iteration number through the 'SHOWER' subroutine. "Voxel phantom generator" interprets the distribution definition table to generate voxel phantoms (voxel size: 2.5 x 2.5 x 2.5 mm) for the radioactivity and material distributions using the Zubal phantom; subsequently the generated voxel phantoms are converted into text files ("distribution text files"). The acquisition parameters are also entered on the GUI ("acquisition parameter file"). When the simulation program starts, it reads the "distribution text files", "acquisition parameter file" and the "material file"; and photons (140keV for Tc-99m) are then generated. Finally, the simulation program output the projection data for each projection angle and each energy window. Energy spectrum is also obtained. The μ-map is generated with substituting the theoretical values of the linear attenuation coefficient for each material at the photon energy (140keV).

3. Methods

3.1 Monte Carlo experiment

Monte Carlo simulation was performed using three radioactivity distributions: 1) cerebral blood flow image pattern (CBF), 2) striatum (putamen and caudate) image pattern (STR) and 3) skull bone image pattern (SKL). The CBF pattern is simulated as image of Tc-99m ECD (or Tc-99m HMPAO). The radioactivity ratio of gray and white matter was assumed to be 4:1. The STR pattern is simulated as image of Tc-99m TRODAT-1. The radioactivity ratio of stratum and background was 8:1. The SKL pattern is simulated as image of Tc-99m MDP. The images of three activity distributions

and attenuation coefficient map (μ-map) are shown in Fig. 3.

SPECT projection data were simulated using three kinds of collimator: ultra high-resolution type (UHR), high-resolution type (HR), and general all purpose type (GAP). The collimator geometries and the acquisition parameters used in this simulation are summarized in Table 1. In addition, we measured point spread function (PSF) to estimate spatial resolution using each collimator and Tc-99m point source (voxel size: 0.1 x 0.1 x 0.1 mm). The spatial resolution was calculated as FWHM of the PSF. The acquisition matrix was a 1024 x 1024 (pixel size: 0.5 x 0.5 mm) and the source-to-detector distance was 13 cm. Other parameters were the same with the brain phantom experiment.

3.2 Image reconstruction

The projection data were reconstructed by the ordered subset-expectation maximization (OSEM) algorithm [17] (subset size = 20, iteration=3) as the following equation:

$$\lambda_j^{k+1} = \frac{\lambda_j^k}{\sum_{i \in S_l} C_{ij}} \sum_{i \in S_l} \frac{C_{ij} y_i}{\sum_j C_{ij} \lambda_j^k + s_{c\,i}}, \quad (1)$$

where λ_j^k is the reconstructed image at pixel j with k-th iteration, C_{ij} is the detection probability that gives the fraction of photons from pixel j to projection bin i, and S_l is the l-th subset of the measured (simulated) projection data y_i. One iteration is defined as when all subsets have been visited once. Attenuation correction (AC) was incorporated into the OSEM algorithm using the μ-map. Scatter component ($s_{c\,i}$) was estimated by triple energy window (TEW) method [18] and the sub-window data. Butterworth filter (f_c=0.20 cycles/pixel, order=8) was used as a prefilter to reduce for statistical noise. The simulations and data analyses were performed on a PC (Pentium-4, 2.8 GHz, 512 MB).

4. Results and discussion

The spatial resolution for the UHR, HR and GAP collimator was estimated as 6.6, 8.5 and 12.5 mm FWHM, respectively. Figure 4 shows the projection data of total photons (primary +scatter), scattered photons and sub-window photons for the CBF, STR and SKL pattern using the HR collimator. Figure 5 shows the energy spectrum for each radioactivity patterns when using the HR collimator. Table 2 summarizes the scatter fraction (= the number of the scattered photons/the number of primary photons in the main window) for each activity pattern and each collimator. The scatter fraction was almost independent of collimator resolution, whereas it depended on the activity pattern. The values of scatter fraction for the STR were slightly higher (36.8% for UHR, 36.8% for HR, and 36.9% for GAP) than those for the CBF (34.5% for UHR, 34.6% for HR, and 34.6% for GAP), whereas those for the SKL were considerably lower (23.8% for UHR, 23.6% for HR, and 23.7% for GAP) than the others. Figure 6 shows the reconstructed images for the CBF, STR and SKL patterns using each collimator. With the UHR collimator, small brain structures could be observed for the CBF and STR images. On the other hand, the GAP collimator could not resolve the brain structures completely. But SKL images were not influenced by collimator resolution.

5. Conclusion

We developed the EGS-based 3D brain SPECT simulator (3DBSS) to generate SPECT projection data using digital brain phantom. This system involves physical processes of attenuation, Compton scatter and blurring due to the collimator and detector response. This simulation system revealed that the scatter fraction does not depend on the collimator resolution, whereas it depended on the activity pattern. The 3DBSS system is powerful tool to simulate human brain SPECT images with various radioactivity patterns.

References

1) Y. Namito, H. Hirayama: EGS4 calculation in diagnostic energy region. Nippon Hoshasen Gijutsu Gakkai Zasshi **60**, 43-48 (2004) (in Japanese).
2) Y. Narita, M. Shidahara, T. Nakamura, et al.: Simulation of Compton scatter in 3-dimensional PET. Proceedings of the First International Workshop on EGS. KEK Proceedings **97-16**, 174-180 (1996).
3) M. Shidahara, Y. Narita, T. Nakamura, et al.: A preliminary study of Compton scattering correction in 3D-PET study based on the unfolding method. Proceedings of the First International Workshop on EGS. KEK Proceedings **97-16**, 181-187 (1996).
4) L-E. Adam, J. S. Karp: Optimization of PET scanner geometry. Proceedings of the Second International Workshop on EGS. KEK Proceedings **2000-20**, 92-99 (2000).
5) H. Zaidi: Relevance of accurate Monte Carlo modeling in nuclear medical imaging. Med Phys **26**, 574-608 (1999).
6) I. Buvat, I. Castiglioni: Monte Carlo simulations in SPET and PET. Q J Nucl Med **46**, 48-61 (2002).
7) J. Bradshaw, C. Burnham, J. Correia: Application of Monte Carlo methods to the design of SPECT detector systems. IEEE Trans Nucl Sci **32**, 753–757 (1985).
8) Y. Narita, S. Eberl, H. Iida, et al.: Monte Carlo and experimental evaluation of accuracy and noise properties of two scatter correction methods for SPECT. Phys Med Biol **41**, 2481-2496 (1996).
9) K. Ogawa, T. Ono, H. Shinohara, et al.: Comparison of scatter and attenuation correction methods in single photon emission CT: simulation study. Jpn J Nucl Med [Kaku Igaku] **37**, 131-142 (2003) (in Japanese).
10) T. Yokoi, H. Shinohara, T. Hashimoto, et al.: Implementation and performance evaluation of iterative reconstruction algorithms in SPECT: a simulation study using EGS4. Proceedings of the Second International Workshop on EGS. KEK Proceedings **2000-20**, 224-234 (2000).
11) T. Yokoi, H. Shinohara, A. Takaki: Improvement of signal-to-noise ratio using iterative reconstruction in a ^{99m}Tc-ECD split-dose injection protocol. Eur J Nucl Med Mol Imaging **30**, 1125-1133 (2003).
12) D. Pareto, A. Cot, J. Pavia, et al.: Iterative reconstruction with correction of the spatially variant fan-beam collimator response in neurotransmission SPET imaging. Eur J Nucl Med Mol Imaging **30**, 1322-1329 (2003).
13) W. R. Nelson, H. Hirayama, D. W. T. Rogers: The EGS4 code system. Stanford Linear Accelerator Center Report SLAC-265 (1985).
14) Y. Namito, H. Hirayama, S. Ban: Improvement of low-energy photon transport in EGS4. Proceedings of the First International Workshop on EGS. KEK Proceedings **97-16**, 32-50 (1997).
15) I. G. Zubal, C. R. Harrell, E. O. Smith, et al.: Computerized three-dimensional segmented human anatomy. Med Phys **21**, 299-302 (1994).
16) H. Iida, Y. Narita, S. Eberl: Simulation of Compton scatter in single photon-emission computed-tomography. Fifth EGS4 User's Meeting in Japan. KEK Proceedings **95-9**, 33-46 (1995).
17) H. M. Hudson, R. S. Larkin: Accelerated image reconstruction using ordered subsets of projection data. IEEE Trans Med Imaging **13**, 601-609 (1994).
18) T. Ichihara, K. Ogawa, N. Motomura, et al.: Compton scatter compensation using the triple-energy window method for single- and dual-isotope SPECT. J Nucl Med. **34**, 2216-2221 (1993).

Fig1. Digital brain phantom by Zubal et al. [15]

Table 1. Simulation parameters

Acquisition matrix size	128 x 128
Pixel size	2.50 x 2.50 mm
Projection view	120 views over 360 degree
Rotation radius	13 cm
Collimator geometry	
Ultra high resolution (UHR)	1.0 mmϕ x 40 mm
High resolution (HR)	1.2 mmϕ x 36 mm
General all purpose (GAP)	1.4 mmϕ x 28 mm
Scintillator material and thickness	NaI(Tl), 9.5mm
Energy windows	
Main window	141 keV ± 10% (127-155keV)
Sub window	120 keV ± 5% (119-125keV)
Energy resolution	8% FWHM
Intrinsic spatial resolution	2.2 mm FWHM

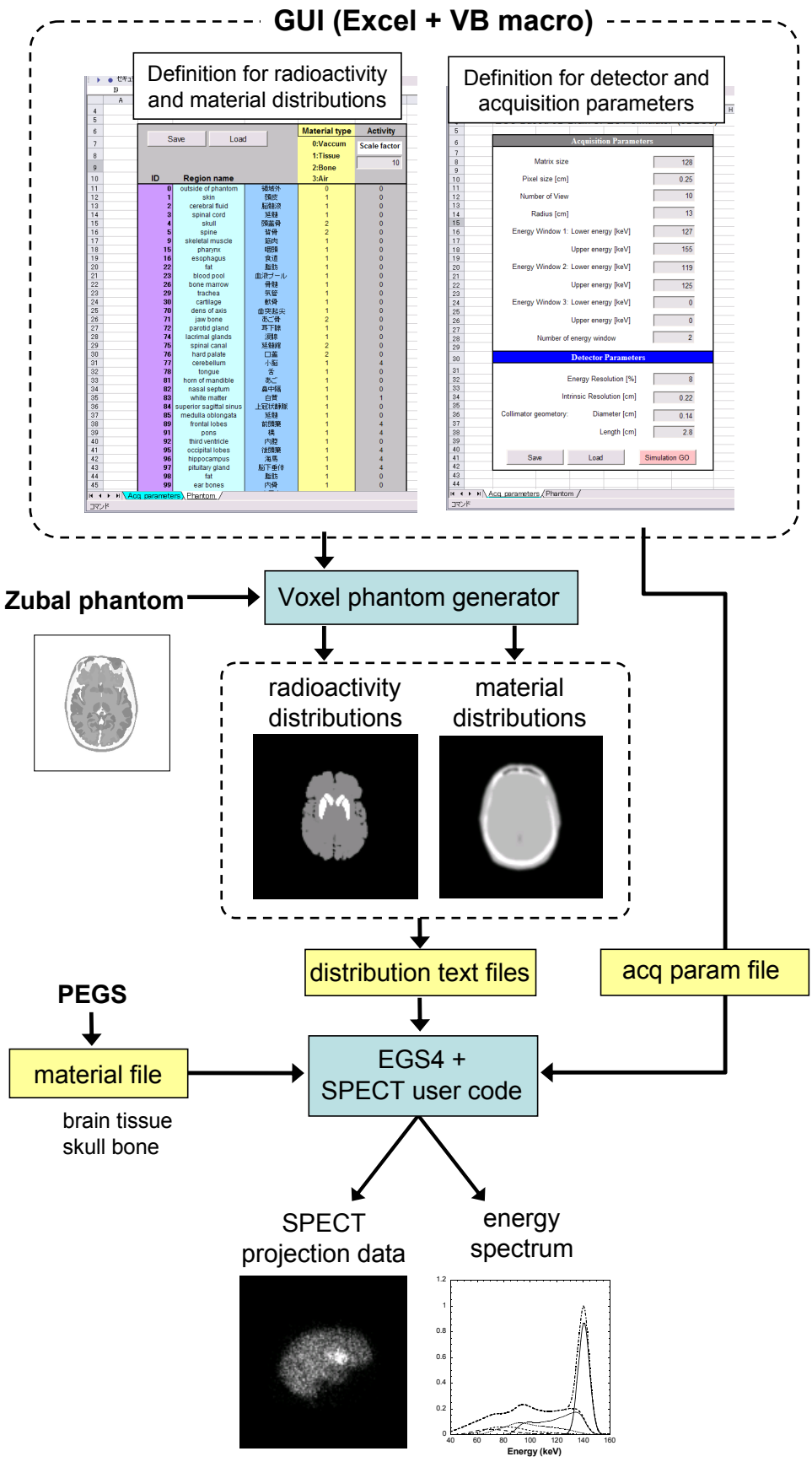

Fig 2 Diagram of the 3D brain SPECT simulator (3DBSS) system

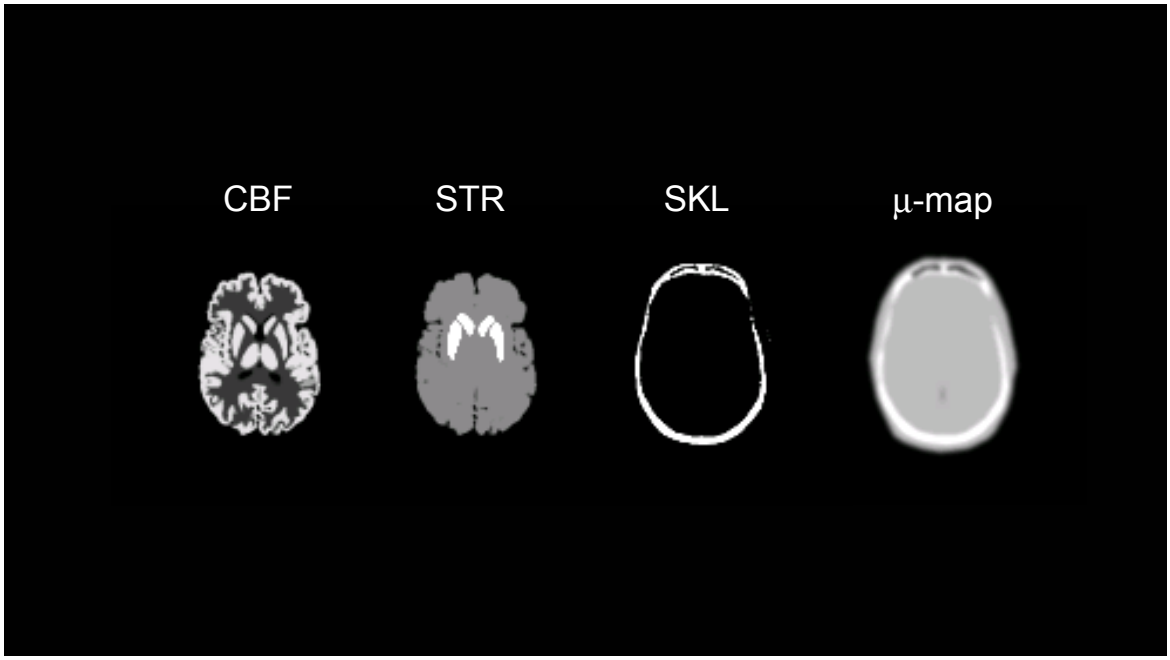

Fig 3 Voxel-based radioactivity distributions for cerebral blood flow (CBF), striatum (STR) and skull bone (SKL) patterns, which are simulated as images of Tc-99m ECD, Tc-99m TRODAT-1, and Tc-99m MDP, respectively. Attenuation coefficient map (μ-map) is also shown.

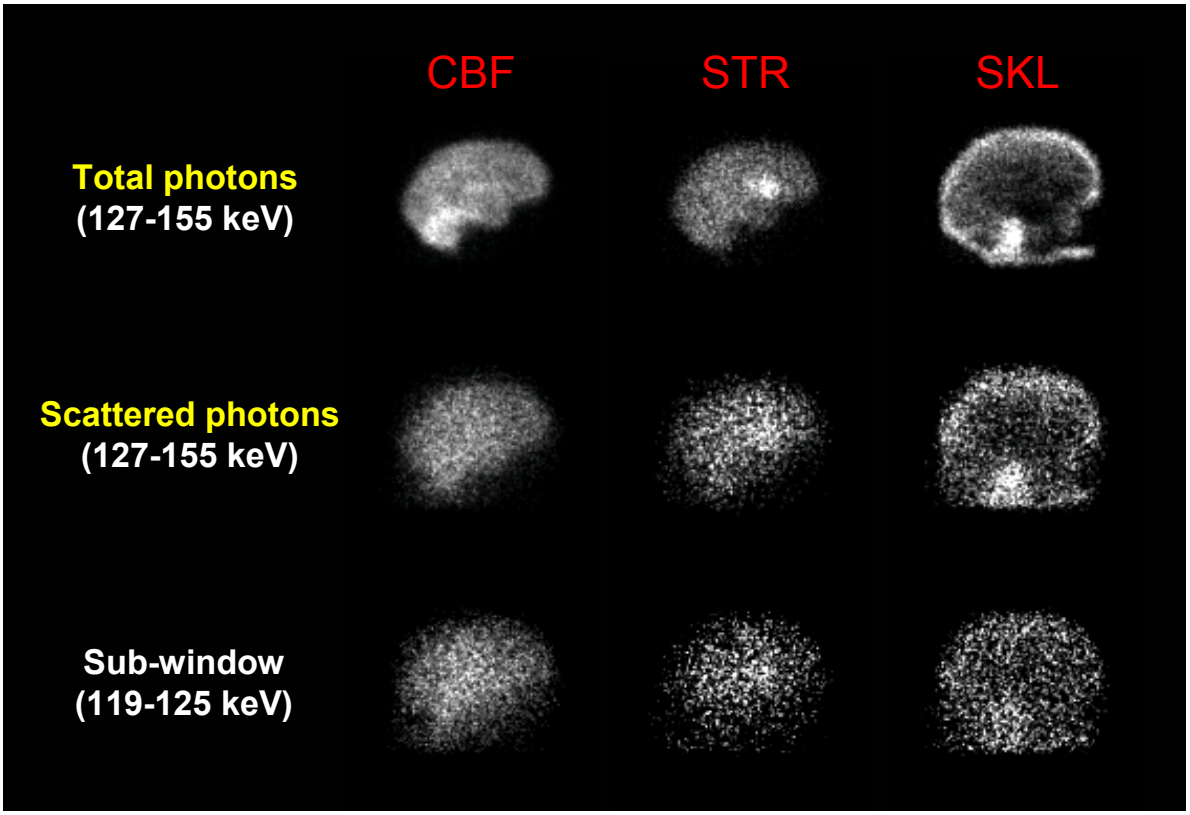

Fig 4 Projection data of total photons (primary +scatter), scattered photons and sub-window photons for the CBF, STR and SKL pattern using the HR collimator.

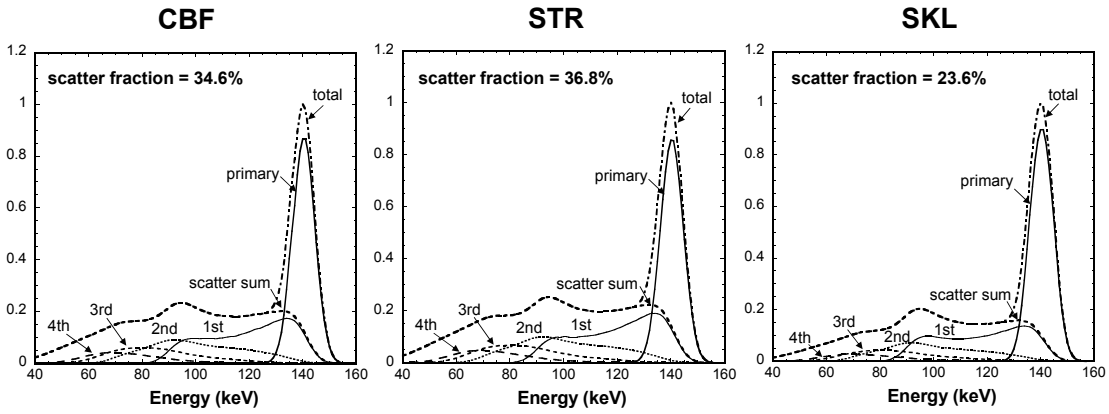

Fig 5 Energy spectrum for the CBF, STR and SKL radioactivity patterns using the HR collimator.

Table 2. Scatter fraction (%) for each radioactivity pattern and collimator

	CBF	STR	SKL
UHR	34.5	36.8	23.8
HR	34.6	36.8	23.6
GAP	34.6	36.9	23.7

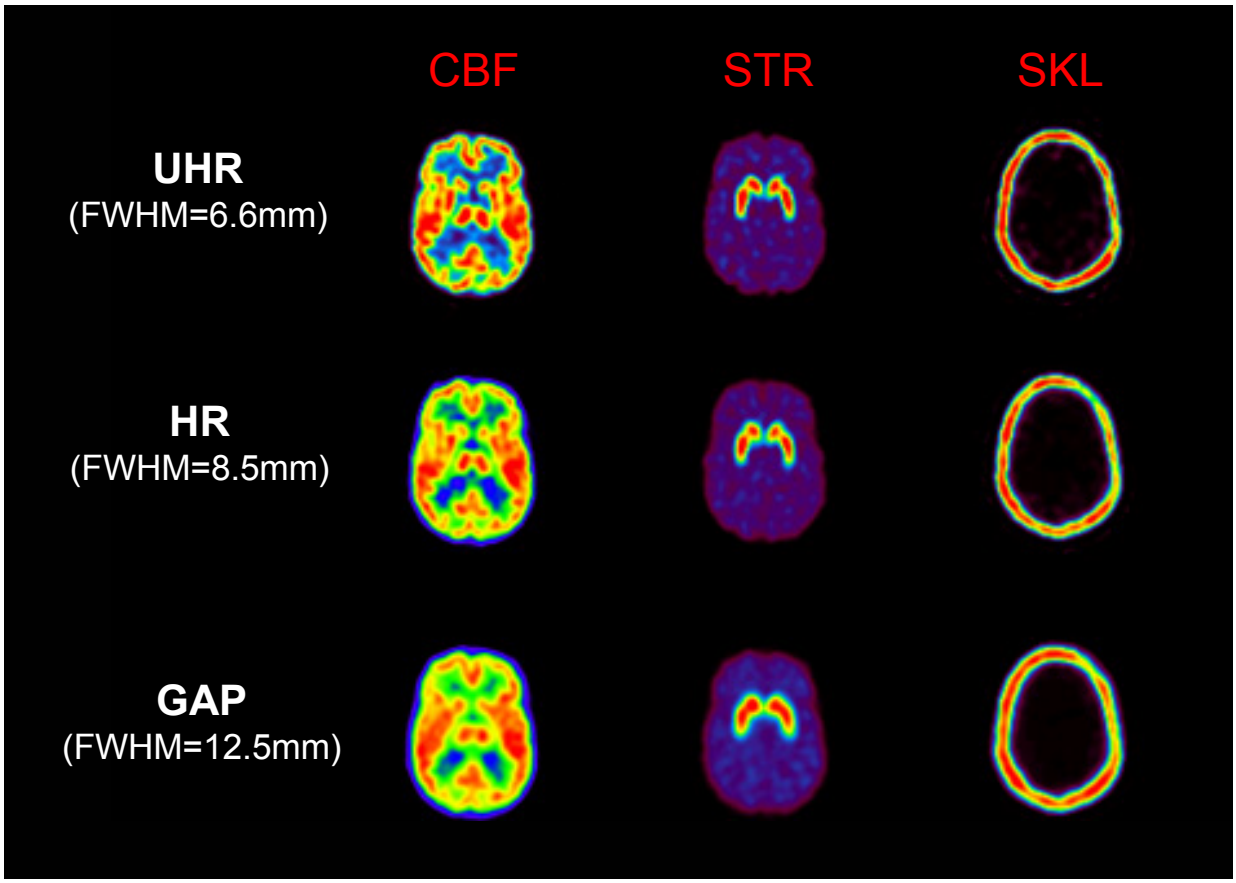

Fig 6 Reconstructed images for the CBF, STR and SKL patterns measured by three different collimators

IMPLEMENTATION AND PERFORMANCE EVALUATION OF DEPTH-DEPENDENT CORRECTION IN SPECT FOR MYOCARDIAL NUMERICAL PHANTOM: A SIMULATION SSTUDYUSING EGS4

Takeyuki Hashimoto 1), Toshikazu Imae 2), Daisuke Usuba 2), Toshihiro Momose 3), Hiroyuki Shinohara 2), Takashi Yokoi 4)

1) Dept. of Information Science, Yokohama Soei College, Yokohama, Japan
2) Dept. of Radiological Science, Tokyo Metropolitan University of Health Scinece, Tokyo, Japan
3) Dept. of Radiology, JR Tokyo Hospital, Tokyo, Japan
4) Bioimaging Laboratory, Inc, Kyoto, Japan

Abstract

A single-photon emission computed tomography (SPECT) system detects gamma rays emitted by a radioactive source. This SPECT reconstruction has three famous problems which are the attenuation , scatter and depth-dependent detector response. We are able to obtain the projection data of myocardial numerical phantom for SPECT which have three above‐mentioned problems using EGS4. Especially, EGS4 is able to generate the projection data without scattor. The iterative maximum likelihood expectation maximization (ML-EM) image reconstruction method and frequency-distance relation (FDR) are using to correct the depth-dependent detector response. ML-EM algorithm has become available as an alternative to filtered back projection in SPECT. This algorithm is able to include both attenuation correction and depth-dependent correction. On the other hand, FDR algorithm is for depth-dependent correction. In this study, we demonstrate three methods of the depth-dependent correction of SPECT myocardial numerical phantom. The projection data of this phantom with non-uniform attenuation and depth-dependent detector response was generated from EGS4. The simulated radioisotope was Tl-201. First method is using ML-EM algorithm for reconsturction, attenuation correction and depth-dependent correciton. Second method is using FDR algorithm for depth-dependent correction and using ML-EM algorithm for reconstruction and attenuation correction. FDR is non-iterative algorithm that it is able to combine with the other reconstruction methods. Third method is using FDR algorithm for depth-dependent correction and using the analytical reconstruction of SPECT for attenuation correction. We observed that first method is the best performance. Iterative ML-EM reconstruction algorithm is effective in compensating for non-uniform attenuation distribution and depth-dependent detector response, simultaneously.

1 Introduction

In SPECT, Radio Isotope (RI) is injected into the inside of the body, and an outside detection system detects the gamma ray which came out from there. RI distributions image of a cross section is reconstructed from the detected data. In numerical simulation of SPECT, it is reported that EGS4 is powerful tool for creating

the detected data [1]. This detected data includes the attenuation, scatter and depth-dependent detector response. One of the most important issues in SPECT is quantitative accuracy of RI distributions. In order to raise quantitative accuracy, it is necessary to correct the attenuation, scatter and depth-dependent detector response.

In this study, we present three reconstuction method for the attenuation correction and the depth-dependent correction. In the first method, we implemented the maximum likelihood expectation maximization algorithm [2,3]. In the second method, we implemented the depth-dependent correction algorithm which uses the frequency distance relation [4]. In the last method, we implemented the analytical method [5,6] for the uniform attenuation correction. We compared the images reconstructed by three methods using the projection data from the myocardial numerical phantom created by EGS4.

2 Theory

2.1 ML-EM algorithm

ML-EM algorithm is the iterative reconstruction method, as shown in Figure.1. Iterative reconstruction algorithm consists of projection, back-projection, and comparison. This algorithm is made to approach original image, comparing measurement data to projection data created from the assumed image.

Projection, back-projection and comparison of ML-EM algorithm is described as

$$\lambda_j^{(k+1)} = \frac{\lambda_j^{(k)}}{\sum_{i=1}^{n} C_{ij}} \sum_{i=1}^{n} \frac{y_i C_{ij}}{\sum_{j'=1}^{m} C_{ij} \lambda_{j'}^{(k)}},$$

where k is the iterative number. Explanation of this formula is shown in Figure 2. $\lambda_j^{(k)}$ is the value of reconstructed image at the pixel j for the k-th iteration, $\lambda_j^{(k+1)}$ is the value of next reconstructed image at the pixel j, y_i is the measured projection data at i-th bin, and C_{ij} is the detection probability that give the fraction of photons from pixel j to projection bin i.

2.2 Frequency Distance Relation (FDR)

FDR express the relation between a frequency image and a distance from a source to the detector. The frequency image is obtained by Fourier transformed a projection data in the lateral direction and Fourier series expanded in the angle direction. A projection image and this frequency image are shown in Figure 3.

Frequency distance relation is shown in Figure 4. The relation is given by

$$l \approx -\frac{n}{\omega},$$

where l is a distance between source and detector, ω and n is the coordinates of the lateral direction and the angle direction in a frequency image space respectively. Using this relation, depth-dependent correction is carried out in a frequency image.

2.3 Analytical method

When it is assumed that an object's attenuation is uniform, the analytical method is obtained. The flow of this method is shown in Figure 5. This method is carried out the attenuation correction in Fourier region which is one-dimensional Fourier transform for the lateral direction of the projection data. If it explains in detail, the Fourier series of the Fourier region data in the angle direction will be carried out, and it will correct using the formulas which is

$$F_n(\omega) = G_n(\gamma)\left[\frac{\gamma-\mu}{\gamma+\mu}\right]^{\frac{n}{2}},$$

where $G_n(\gamma)$ is the data which carried out one-dimensional Fourier transform of the projection data in the lateral direction, and carried out the Fourier series deployment in the angle direction. And γ is the coefficient of Fourier transform, n is the order of the Fourier series, and μ is the uniform attenuation coefficient. If Fourier composition is carried out from $F_n(\omega)$ which corrected the attenuation and two-dimensional inverse Fourier transform is performed, an original image will be reconstructed.

3 Simulation

3.1 Generation of a projection data

To evaluate the three methods of the depth-dependent correction of SPECT, we performed the simulation study using the myocardial numerical phantom. The distribution of attenuation coefficient and source activity of the phantom is shown in Figure 6. In this study, the simulated radioisotope was Tl-201. The phantom was a 128 x 128 matrix. A projection data as shown in Figure 6 was generated using EGS4 [7] and user extended program for a SPECT system coded by Narita et al [8,9]. The codes were implemented into the Windows based computer (Pentium IV, 3GHz, 2GB) by cygwin. The parameters of the data acquisition is summarized in Table 1.

3.2 Image reconstruction

We reconstructed the images from the projection data using the three reconstruction methods. First method was ML-EM algorithm with the attenuation correction and the depth-dependent correction. The algorithm was performed Until 100th Iterations. Second method was using FDR algorithm for the depth-dependent correction and ML-EM algorithm for the attenuation correction. ML-EM algorithm was performed Until 100th Iterations. The last method was using FDR algorithm for the depth-dependent correction and using analytical method for the attenuation correction. Since we assumed the uniform attenuation coefficient of the object for using analytical method, the correction was approximation. But it was non-iterative method.

4 Results and Discussion

Reconstructed images of first method which uses ML-EM algorithm for the attenuation and the depth-dependent correction are shown in Figure 7. Right iteration images are 1, 2, 3, 5, 10, 20, 50 and 100 iterations respectively. A image is so clear that the number of iterations increases. But a large number of iterations image is so noisy. In this case, the suitable iteration number could be about 20 iterations. This 20 iterations image is expanded and shown in the left-hand side of Figure 7. The region of myocardium is reconstructed almost uniformly.

Reconstructed images of second method which uses FDR algorithm for the depth-dependent correction and ML-EM algorithm for the attenuation correction are shown in Figure 8. Right iteration images are 1, 2, 3, 5, 10, 20, 50 and 100 iterations respectively. In this case, the suitable iteration number could be also about 20 iterations. This 20 iterations image is expanded and shown in the left-hand side of Figure 8. The value of the region at the upper left of myocardium is small a little.

A reconstructed image of the last method which uses FDR algorithm for the depth-dependent correction and analytical method for the attenuation correction are shown in Figure 9. Since this method is not the method of a iteration, only one reconstruction image is shown. The region of myocardium is reconstructed almost uniformly, but the image is noisy.

The first method will be the best if three methods are compared. This ML-EM method is very convenient since it is able to correct the attenuation and the depth-dependent blurring simultaneously.

5 Conclusion

In order to investigate the attenuation correction and the depth-dependent correction, the simulation of Myocardial SPECT is carried out. We observed that ML-EM method is the best performance of the three methods for the uniformity of myocardial region. Iterative ML-EM reconstruction algorithm is effective in compensating for non-uniform attenuation distribution and depth-dependent detector response, simultaneously. EGS4 is powerful tool for investigating the SPECT reconstrcution methods using the numerical phantoms.

Acknowledgment

We thank to Dr. Yuichiro Narita of Chiba Cancer Center for providing the projection program for EGS4.

References

[1] Y. Yokoi, H. Shinohara, T. Hashimoto, T. Yamamoto, Y. Niio, “Implementation and performance evaluation of iterative reconstruction algorithms in SPECT: A simulation study using EGS4”. Proceedings of the Second International Workshop on EGS, *KEK Proceedings 200-20* (2000) 224-234.

[2] L. Shepp and Y. Vardi, “Maximum likelihood reconstruction for emission tomography”, *IEEE Trans. Med. Imaging* **MI-1** (1982) 113-122.

[3] K. Lange and R. Carson, “EM reconstruction algorithms for emission and transmission tomography”, J.

Comput Assist Tomogr **8** (1984) 306-316.

[4] P.R. Edholm, R.N. Lewitt and B. Lindholm, "Novel properties of the Fourier decomposition of the sinogram", *Workshop on Physics and Engineering of Computerized Multidimensional Imaging and Processing, Proc, of the SPIE*, **671** (1986) 8-18.

[5] S. Bellini, M. Piacentini, C. Cafforio et al "Compensation of tissue absorption in emission tomography." *IEEE Trans Acoust Speech and Signal Process* **ASSP-27** (1979) 213-218.

[6] T. Inouye, K. Kose, A. Hasegawa "Image reconstruction algorithm for single-photon-emission computed tomography with uniform attenuation." *Phys Med Biol* **34** (1989) 299-304.

[7] W. R. Nelson, H. Hirayama, D. W. O. Rogers, "The EGS4 code system", Stanford Linear Accelerator Center Report *SLAC-265*, 1985.

[8] H. Iida, Y. Narita, S. Eberl, "Simulation of Compton scatter in single photon-emission computed tomography", Fifth EGS4 User's Meeting in Japan, *KEK Proceedings 95-9*, 33-46, 1995.

[9] Y. Narita, H. Iida, S. Eberl, et al. "Monte Carlo evaluation of accuracy and noise properties of two scatter correction methods for ^{201}Tl cardiac SPECT", *IEEE Trans. on Nucl. Sci.* **44** (1997) 2465-2472.

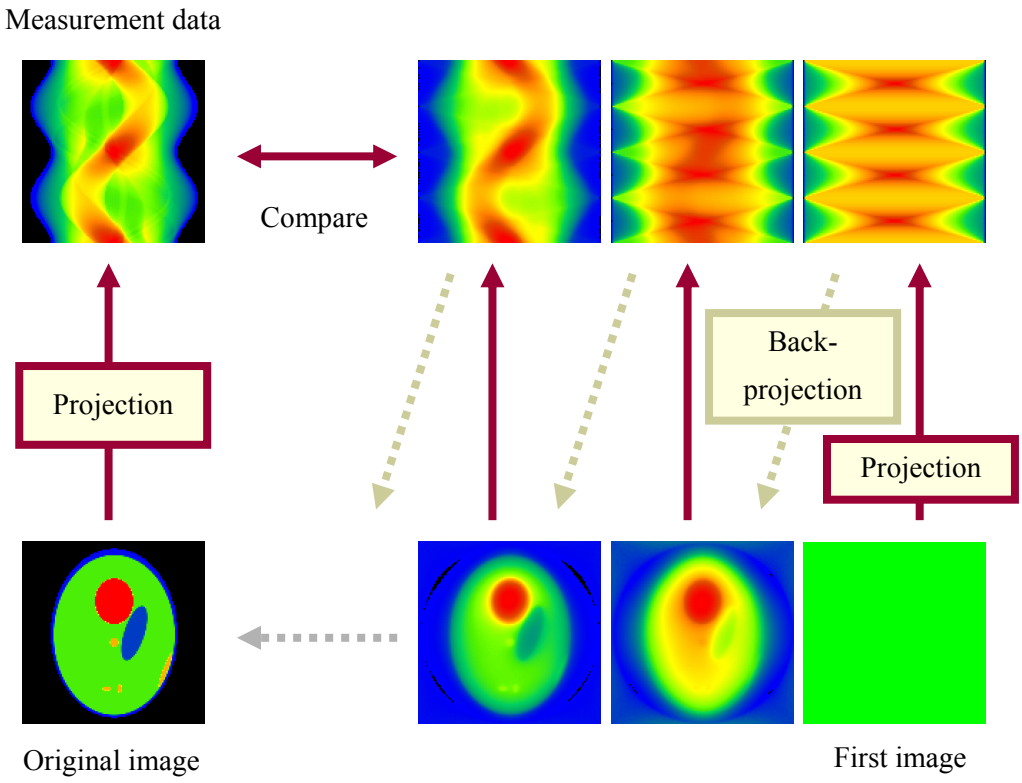

Figure 1 Iterative reconstruction algorithm.

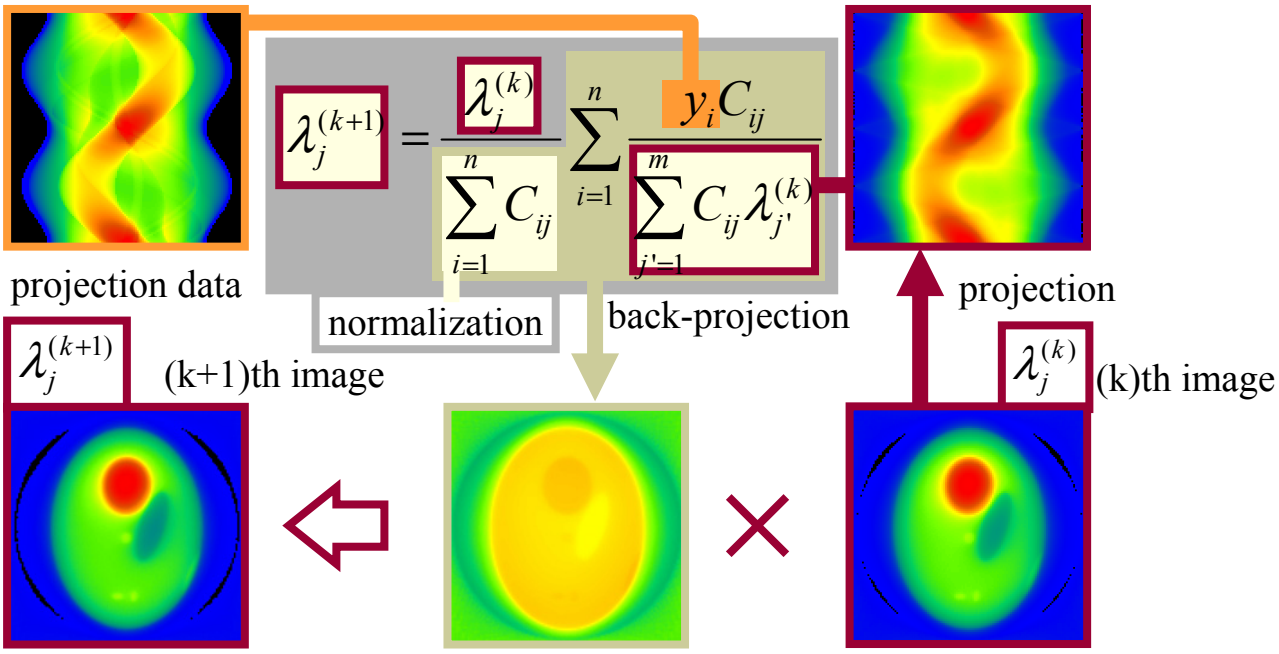

Figure 2 Iteration of ML-EM algorithm.

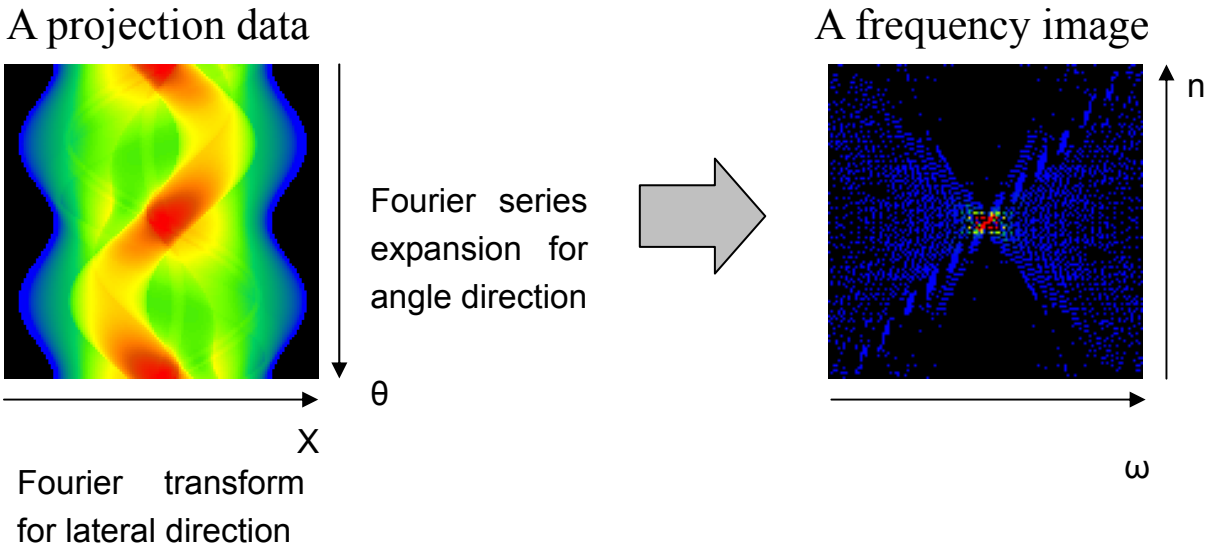

Figure 3 Fourier transform for lateral direction and Fourier series expansion for angle direction of a projection data.

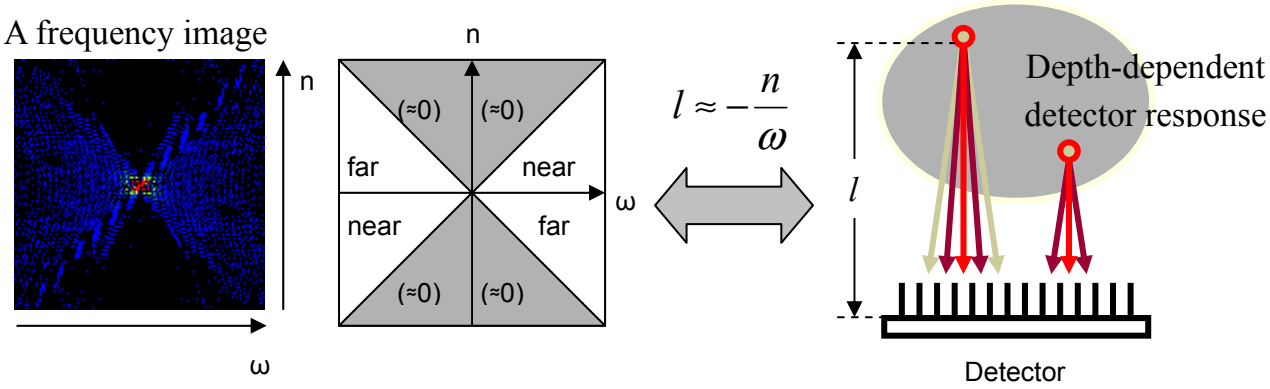

Figure 4 Frequency distance relation.

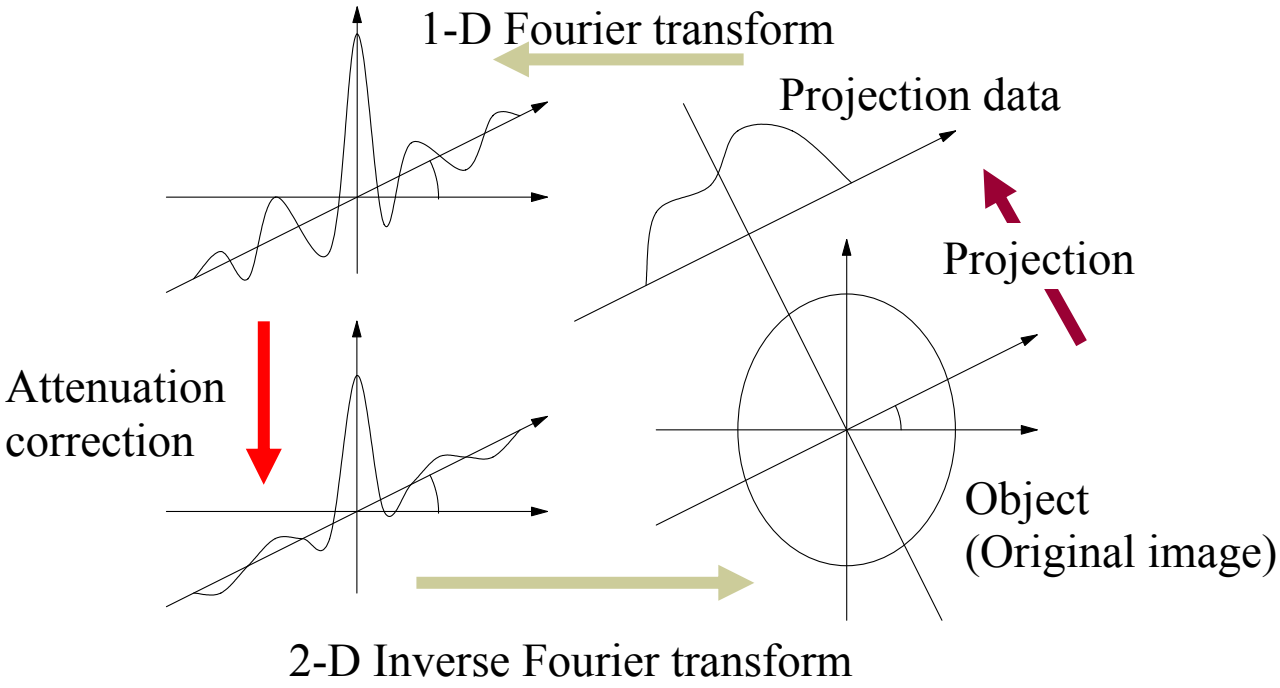

Figure 5 Reconstruction flow of the Analytical method.

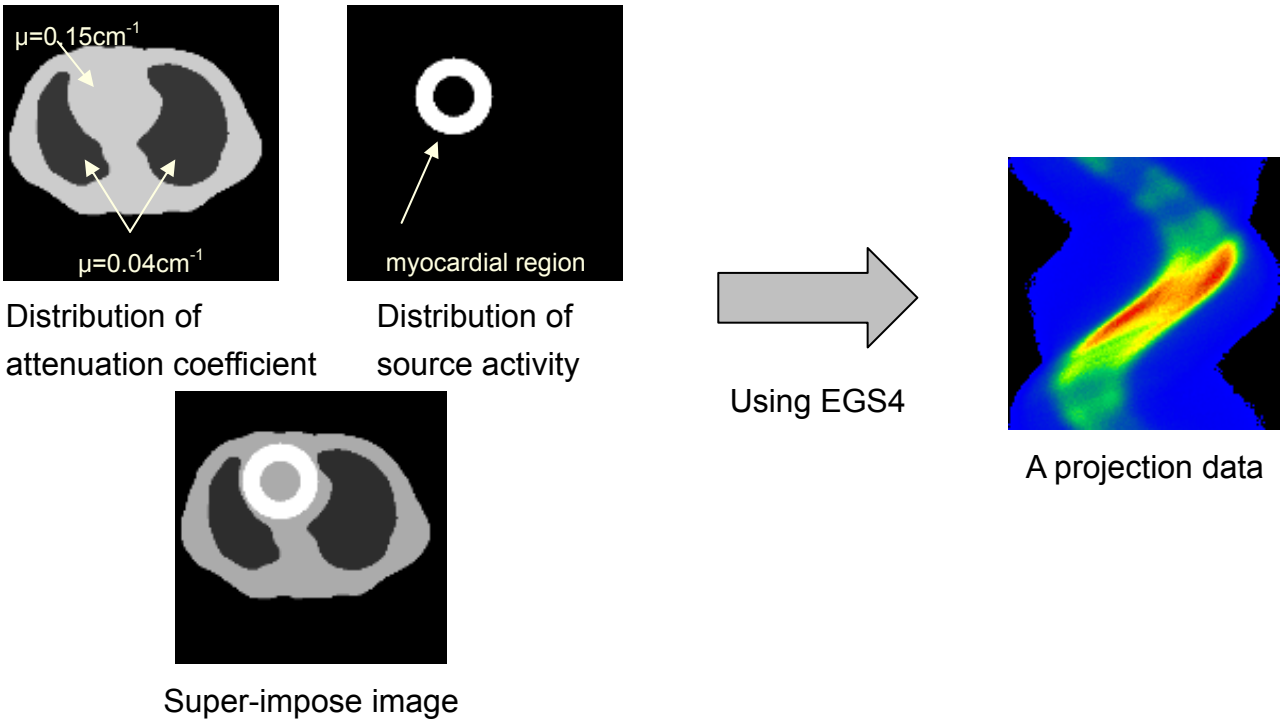

Figure 6 Distribution of attenuation coefficient and source activity, and a projection data.

Table 1　Conditions of the simulation.

Radioisotope	Tl-201
Collimator geometry	2.5 mm Φ x 41 mm
Energy window	47% on 74keV
Rotation radius	25.0 cm
Projection	128 bins x 128 views over 360 degree
Pixel size	0.3125 cm

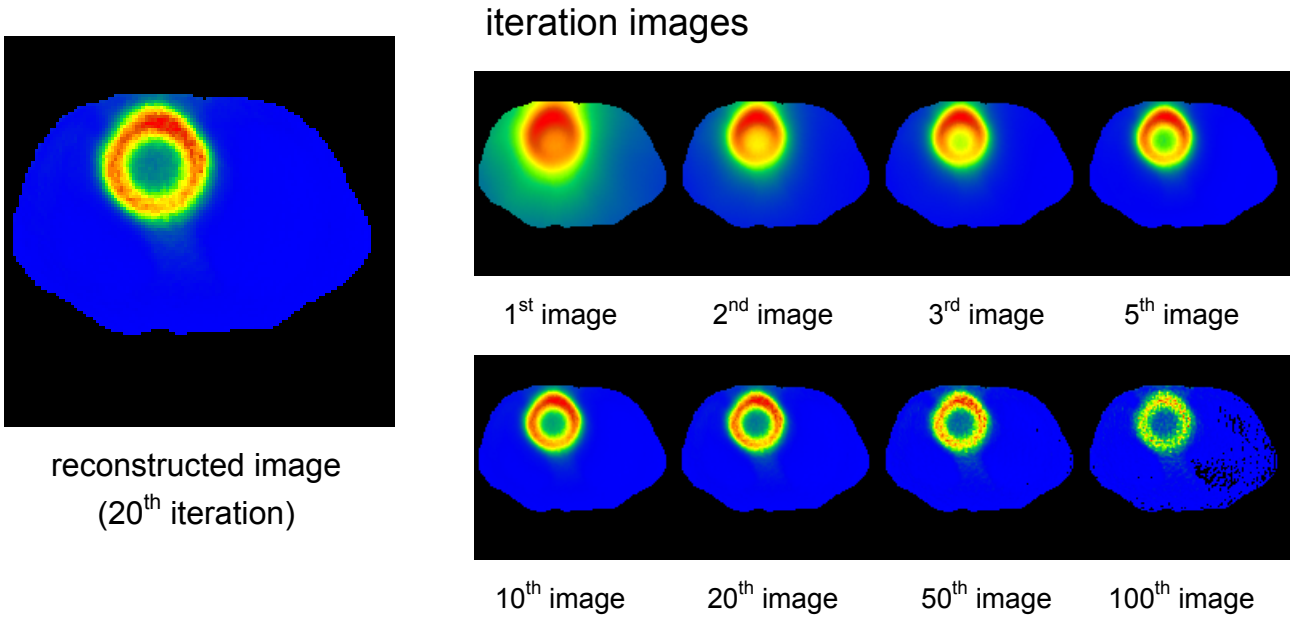

Figure 7　ML-EM reconstructed images with collimator correction.

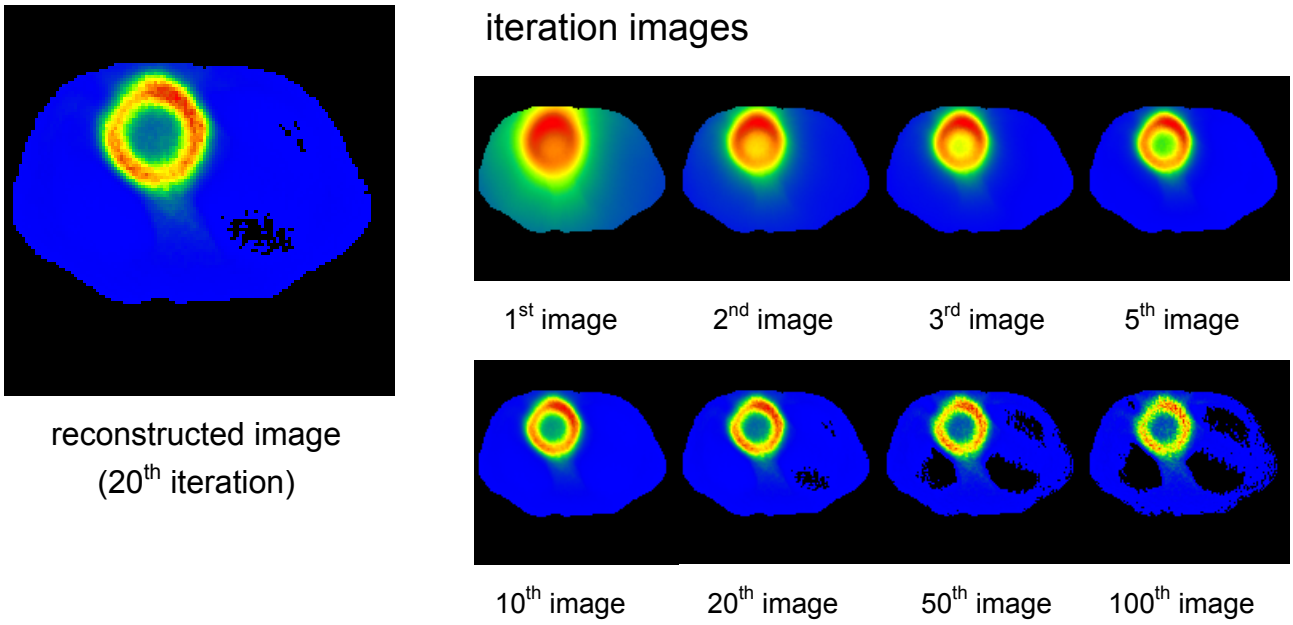

Figure 8 FDR collimator correction and ML-EM reconstruction.

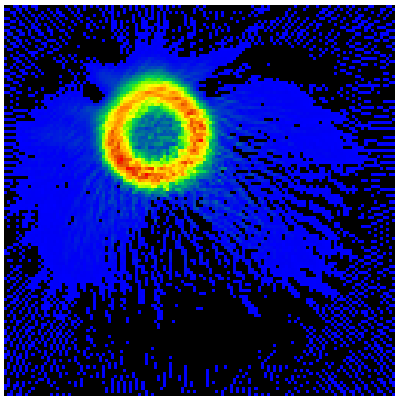

Figure 9 FDR collimator correction and Analytical reconstruction for uniform attenuation correction.

EXPOSURE DOSES TO MEDICAL WORKERS CONCERNING POSITRON EMISSION TOMOGRAPHY

I. Yamaguchi[a], H. Narita[b], Kobayashi[c]

[a]*Department of Environmental Health, National Institute of Public Health*
2-3-6 Minami, Wako, Saitama 351-0197 Japan
[b]*Department of Radiology, Jikei Univ. Hospital, Tokyo, 116-8551, Japan*
[c]*Department of Radiology, International Medical Center of Japan, Tokyo, 162-8655, Japan*
e-mail: drhyama@niph.go.jp

Abstract

The Radiation dose exposures to healthcare workers and the general public from patients having undergone FDG-PET imaging were estimated in various settings toward developing more effective protective measures against radionuclide exposure.
The radiation dose to medical worker who cares intensively much patients who administrated FDG and public transportation workers might exceed dose constrains recommended International Atomic Energy Agency in specific situation. However, appropriate protection method such as decay in waiting before leaving control area decreased their radiation doses.

1. Introduction

The applications of positron emission tomography (PET) in clinical medicine are expanding rapidly, posing greater risks for inadvertent radiation exposure. In PET examination, medical workers are exposed radiation during conveyance of radiopharmaceuticals, examination of patients, and after examination. Moreover, the patients and their excrements expose general public. The number of examination that could treat PET equipment was restricted until now. Therefore it was thought that special consideration was not required to the patient after examination[1),2)].

However, since the maximum number of examination cases per positron tomogram equipment and the number of positron tomogram equipment installed in a medical institution are increasing, it seems we have to more prudent about radiation protection concerning PET. Currently, the most widely used radiopharmaceutical in PET imaging is F-18 fluorodeoxyglucose (FDG). This study estimated radiation dose exposures to healthcare workers and the general public from patients having undergone FDG-PET imaging, to examine the necessity for specific radiation protection concerning clinical PET.

2. Materials and Method

Radiation exposure doses from FDG-PET were calculated using EGS4 (Electron Gamma Shower Version 4) to estimate Radiation doses to:

1) Healthcare workers caring for nonambulatory FDG-PET patients;
2) General hospital staff working at institutes employing FDG-PET;
3) Public transportation workers and the general public in contact with patients following PET imaging;
4) Healthcare workers from the radionuclide dispersed in air at PET imaging facilities.
5) Patient skin due to inadvertent intravenous injection of F-18.

2.1 Geometric conditions

For simplicity, it is assumed that a patient and a medical worker are rectangular parallelepiped and filled with water. It contained radioactive substances uniformly inside a patient. The size of a patient and worker was 30 by 30 by 20cm. The distance from a patient to a worker, the period a worker stays near a patient, prescribed dose were variables in this model. Concrete or iron was set around patients and workers and protective board was set to lead. Figure 1 shows the trajectory of 100 positrons emitted in a patient. The patient sits on a wheel chair with lead protective board in elevator. The thickness of board was 1cm. The distance from patient to a worker was 1m. It was assumed that the patient's arm was also rectangular parallelepiped. The thickness of radioactive substances extravasated layer was 200μm, and the deepness of extravasated layer was 1mm from skin surface.

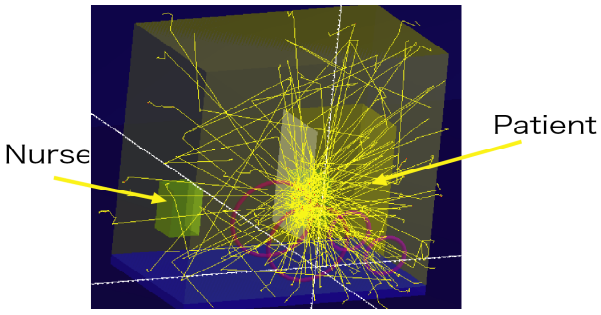

Fig.1The trajectory of radiation for 100 decays in the patient. The patient sits on a wheel chair with lead protective board (1cm) in elevater.

2.2 Clinical settings

1) The radioactivity of administration to a patient was 400MBq, number of patient was 20 persons per day, time to care was 5 minutes per a patient, examination days was 26 days per 3 months.
2) The radioactivity of administration to a patient was 400MBq, number of patient was 20 persons per day, length of passage was 10m, minimum distance to worker from a patient was 50cm, examination days was 26 days per 3 months.
3) Transported patient number was 4 persons per a day, service per week was 3 days, and radioactivity at the time of administration was 360MBq.
4) The radioactivity of administration to a patient was 400MBq, number of patient was 20 persons per day, working hour in examination room was 2 hours per a day, and the rate of drifted to the air was 0.001.
5) The radioactivity of administration to a patient was 400MBq; the rate of extravasations to subcutaneous was 10%. The effective half-life in subcutaneous and depth of lesion for dose calculation was variables in this model.

2.3 Other conditions

The personal dose equivalent, Hp (10) is called as 1cm dose equivalent in Japanese laws. There are several methods for evaluating the operational quantity. If both energy and angular distributions of photon fluencies are perfectly known, then Hp (10) can be calculated by using the conversion coefficients given by ICRP. In our case, however, it is difficult to apply this procedure because a time – consuming calculation is required for a sufficient statistical precision. The Hp (10) or the effective dose is approximated in this report by the absorbed dose averaged over the region with depths of 0.5 – 1.5 cm from the phantom surface.

The user codes for dose calculation were constructed based on the above assumptions, referring to "UCPHANTOM_REC1" (programmed by Dr. H. Hirayama (KEK) EGS4 USER CODE-- 26 JUL 2002/8030). Each positron with maximum kinetic energy 633 keV was emitted uniformly in a patient or each photon with 511keV energy was emitted uniformly from a patient. All radiation transports were pursued and the energy deposition in the slab phantom was finally summed up. The cut-off energies for the photons and the electrons were set to be 1keV and 5keV.

3. Results and discussions

3.1 Radiation doses to healthcare workers caring for nonambulatory FDG-PET patients

The radiation dose for healthcare workers continuously outside the controlled area exceeded the dose limit for general public, when patients were exposed to 400MBq, and when healthcare workers cared for 20 patients/day spending at least 5 minutes per patient. Therefore, the radiation doses for a nurse, for example, obliged to care for many FDG-PET patients may exceed safe exposure limits, unless suitably protected.

3.2 Radiation doses to general hospital staff working at institutes employing FDG-PET

Radiation dose in passageways did not exceed the standard dose limit for controlled areas, unless patients remained there for long periods. Therefore, radiation doses for general workers, e.g., a receptionist, would not exceed the dose limit for the general public.

3.3 Radiation doses to public transportation workers and the general public in contact with patients following PET imaging

The radiation dose for public transportation workers also exceeded the dose limit for the public, when nine patients are seated near a driver each week. For this reason, patient who leaves control areas should be instructed to follow restrictive actions of contact with others.

3.4 Radiation doses to healthcare workers from the radionuclide dispersed in air at PET imaging facilities

The contribution of internal and external exposure from air-dispersed FDG in PET imaging facilities was comparatively small. For this reason, if radionuclides are properly stored and managed, measures for monitoring air concentrations of FDG in PET facilities are largely unnecessary.

3.5 Radiation doses to patient skin due to inadvertent intravenous injection of F-18

The skin-absorbed dose due to extravasated FDG was not exceeded the threshold of critical functional effects if the effective half-life of FDG in subcutaneous tissue was short. However, the result indicated that extravasated FDG might cause mild skin injury at high specific radioactivity. There is a little possibility which radiopharmaceutical is infiltrated to the subcutaneous tissue at intravenous administration. The maximum energy of positron emitted from F-18 is 633keV. It thus appears that there are some risks for radiation dermatitis when F-18 was injected subcutaneously. Therefore it should be cautious not to leak from the blood vessel at the injection.

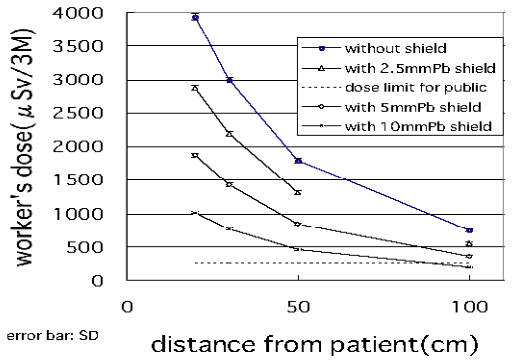

Fig.2 Radiation doses to healthcare workers caring for nonambulatory FDG-PET patients.
Radioactivity: 400MBq/patient, Patient number: 20 patients/hospital/day, Time to care: 5 minutes/patient, examination days: 26days/3months

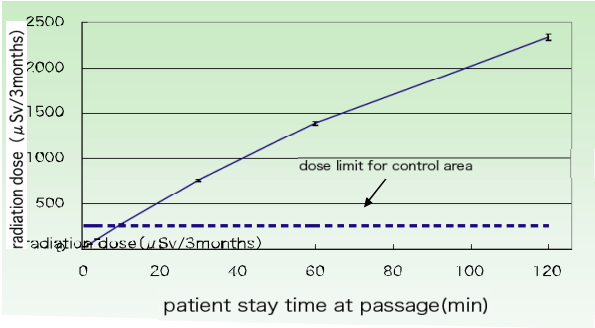

Fig.3 Radiation doses to general hospital staff working at institutes employing FDG-PET
The radioactivity: 400MBq/patient, Patient number: 20 patients/day, length of passage: 10m, Minimum distance to workers: 50cm, examination days: 26days/3months

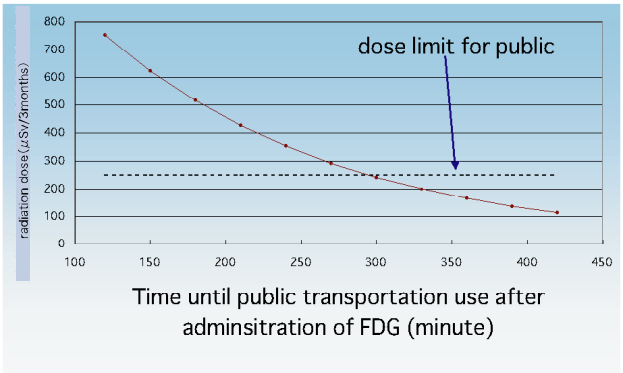

Fig.4 Radiation doses to public transportation workers and the general public in contact with patients following PET imaging.
Transported patient number: 4 persons/day, Service day per week: 3days, Radioactivity at the time of administration: 360MBq

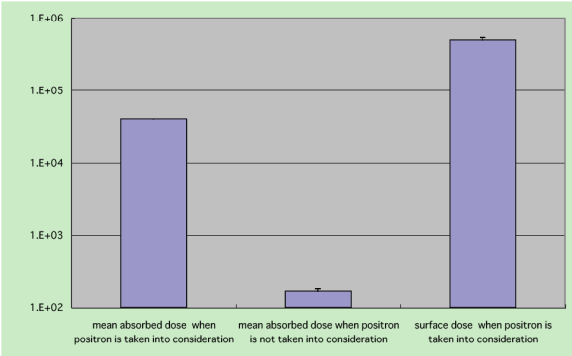

Fig.5 Radiation doses to general hospital staff working at institutes employing FDG-PET.
The radioactivity: 400MBq/patient, Patient number: 20 patients/day, Working hours: 2 hours, the rate of drifted to the air: 0.001

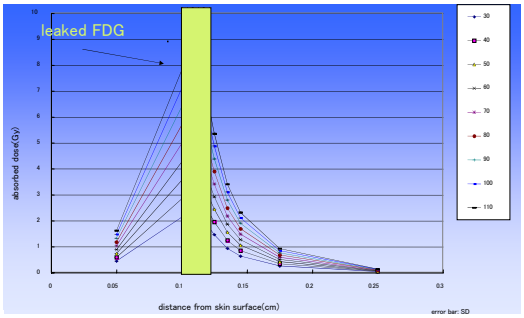

Fig.6 Radiation doses to dermis of patient when FDG was extravasated unintentionally.
Radioactivity at the time of administration: 400MBq, The rate of extravasations to subcutaneous: 10%, The depth of extravasations: 1mm from skin surface, thickness of extravasated FDG:200 μm

4. Conclusions

The Monte Carlo code EGS4 was employed to estimate the radiation dose to healthcare workers and the general public from patients having undergone FDG-PET imaging were estimated. The radiation dose to medical worker who cares intensively much patients who administrated FDG and public transportation workers might exceed dose constrains recommended International Atomic Energy Agency in specific situation. However, appropriate protection method such as decay in waiting before leaving control area decreased their radiation doses. The skin-absorbed dose due to extravasated FDG was not exceeded the threshold of critical functional effects if the effective half-life of FDG in subcutaneous tissue was short. However, the result indicated that extravasated FDG might cause mild skin injury at high specific radioactivity. Therefore it should be cautious not to leak from the blood vessel at the injection.

.

Acknowledgment

This work was supported in part by Grant-in-Aid for Scientific Research from Ministry of Health, Labour and Welfare of Japan.

References

1) ICRP. Release of Patients after Therapy with Unsealed Radionuclides (draft). 2003

2) Cronin B, Marsden PK and O'Doherty MJ. Are restrictions to behaviour of patients required following fluorine-18 fluorodeoxyglucose positron emission tomographic studies? Eur J Nucl Med. 1999 Feb; 26(2): 121-8.

EVALUATION OF EXTERNAL RADIATION EXPOSURE OF PERSONNEL INVOLVED IN VETERINARY NUCLEAR MEDICINE

N. Komatsubara[a], N. Ito[a], M. Natsuhori[a], T. Sano[a], T. Ishikawa[b], S. Hatakeyama[c], S .Futatsugawa [c], K . Terasaki[d], H. Hirayama[e]

[a]School of Veterinary Medicine, Kitasato University, Higashi,23-35-1,Towada, Aomori,034-8628,Japan
[b]Asahi Techno Glass Corporation, Gyouda 1-50-1 , Hunabashi, Chiba,273-0044,Japan
[c]Takizawa Laboratory, Japan Radioisotope Association,Azamegamori348-58,Takizawa,Iwate,020-0173,Japan
[d]Cyclotron Research Center, Iwate Medical University, Azamegamori348-58,Takizawa,Iwate,020-0173,Japan
[e] High Energy Accelerator Research Organization, Tsukuba, Ibaraki,305-0801,Japan

Abstract

Veterinary nuclear medicine has been widely applied in the US and Europe, especially for dogs, cats, and horses. The needs of the nuclear medicine in veterinary practice are also growing in Japan[1)]. This study was performed in order to make a safety guideline for veterinary nuclear medicine in Japan. Two sorts of well often medically used radionuclide, ^{18}F and ^{99m}Tc were chosen for evaluating the exposed doses of the veterinarian, the animal owner, and the general public. Air absorption doses around a physical phantom containing radioactive materials (^{18}F or ^{99m}Tc) were measured by glass dosimeters. (Asahi Techno Glass Ltd.)It was verified that the measurement values were corresponding to the calculation values using EGS4. Then, canine pectoral and abdominal mathematical phantom was designed, external radiation exposure of the veterinarian, the animal owner and the public from the phantom containing radioactive materials were calculated by using EGS4. Calculated exposure doses were compared with the dose limit or the dose constraint. (20mSv/yr for the veterinarian: ICRP, 5mSv/yr for the animal owner: IAEA, and 1mSv /yr for the general public: ICRP[2)]). The future integration exposed doses of the animal owner and the public didn't exceed the dose constraint or the dose limit at the release after 24 hours of the radiopharmaceutical administering. In this study, all the calculation conditions were set up on the safety side. Therefore, it is thought that actual exposed doses lower considerably. The safety guideline for the veterinary nuclear medicine in Japan will be established by further application of this type of research.

1. Introduction

The veterinary nuclear medicine is usually executed in the veterinary teaching hospitals and large veterinary hospitals in the United States and Europe. The *in vivo* veterinary nuclear medicine can not be performed in Japan, since regulatory rules are not established now. However, the veterinary nuclear medicine that obtains functional information in addition to morphological information on internal organs at the same time has been demanded. Prior to authorizing the use of radiopharmaceuticals for veterinary patients in Japan, it would be necessary to evaluate exposure doses of the general public and the animal owner, and to make guidelines for the safety use of radiopharmaceuticals in veterinary practice. The purpose of this study is to estimate the exposure doses of human from animal to which radiopharmaceutical was injected. The evaluation will be the important information for the guidelines of the safety usage of radioactive materials

in veterinary nuclear medicine. The computer simulation program was used to calculate exposure doses of human in order to avoid the animal experiment only for this purpose.

2. Materials and Method

2.1 Evaluation of air absorption doses from a physical phantom

In the first experiment, we evaluated air absorption doses from a simple physical phantom. Air absorption doses from a physical phantom were measured by glass dosimeters (Asahi Techno Glass Ltd.), and then measured values were compared with calculated values. Computer simulation calculations were performed by using Monte Carlo method (EGS4) and Point Kernel Method.

2.2 Estimation of exposure doses from a mathematical phantom

In the second experiment, we calculated the exposed doses from a mathematical phantom using EGS4. A canine pectoral and abdominal mathematical phantom containing some particular organs was designed based on veterinary anatomical data. And there were two kinds of the sizes of the phantom used to calculate, 1kg and 30kg. (Fig. 3) The selected organs were heart, muscle, bladder, kidney, lung, bone, liver, soft-tissue and the fat. Elementary composition of body tissue was quoted from ICRU Report 46[3]. The administered radiopharmaceutical was distributed in proportion to the weight of the organs of the heart, the liver, the kidney, and the bladder. Table 1 shows the amount of the activities of radioactive materials used. Radiopharmaceutical excretion to the outside of the body was not considered in this study. Exposure doses at the assigned distance from surface of mathematical phantom were calculated. The exposed dose estimation of the veterinarian, the animal owner, and the general public was performed under assumed working condition, distance from the sources, and the exposure time. Detailed conditions are shown in Table 2.

3. Results

3.1 Evaluation of air absorption dose from a physical phantom

Values calculated by EGS4 almost agreed with measured values. (Fig.1, 2) Values calculated by Point Kernel Method was different from both values calculated by EGS4 and measured values.

3.2 Estimation of exposure doses from a mathematical phantom

The absorbed dose on the surface of the phantom was not a homogeneous distribution. The exposed dose at the ventral in the cross-section that passed center of the liver was the maximum in the surface of the phantom. Therefore, the calculation values at the ventral in the cross-section that passed center of the liver were used for the evaluation. Calculated exposed doses were compared with the dose limit or the dose constraint. (20mSv/yr for the veterinarian: ICRP, 5mSv/yr for the animal owner: IAEA, and 1mSv /yr for the general public: ICRP[2]) The highest exposed dose of veterinarian was 140μSv/exam. (Fig.4) In the calculation, if the veterinarian performed 100 times/yr, their total exposed dose didn't exceed the dose limit. The future integration exposed doses of the animal owner and the public didn't exceed the dose constraint or the dose limit at the release after 24 hours of the radiopharmaceutical administering. (Fig.5, 6)

4. Discussion and Conclusions

It is thought that the simulation using Monte Carlo method should be applied to the estimation of human's exposed doses because values calculated by EGS4 correspond to measured values well. (Fig.1, 2) Because the energy of ^{18}F is higher than that of ^{99m}Tc, exposure doses from ^{18}F were higher than that of ^{99m}Tc. So, we must pay attention to exposure

when we handle ^{18}F. Exposure doses of the animal owner and the public didn't exceed the dose constraint or the dose limit in the release after 24 hours of the radiopharmaceutical administering. (Fig.5, 6) In this study, all the calculation conditions were set up on the safety side. Therefore, it is thought that actual exposed doses lower considerably. To make the safety guidelines for the veterinary nuclear medicine in Japan, the dose evaluation by the Monte Carlo method is useful.

5. Acknowledgement

This work was supported by Asahi Techno Glass Corporation, Takizawa Laboratory (Japan Radioisotope Association), Cyclotron Research Center and High Energy Accelerator Research Organization. Numerous advices with Dr. Hirayama (KEK) are gratefully acknowledged.

References

1) N. Ito, A. Hanawa, K. Suzuki, et al.: External dose estimation of the human associated with companion animals under veterinary nuclear medical diagnosis, Radioisotopes,53, 13-24(2004)

2) ICRP: 1990 Recommendations of the International Commission on Radiological Protection, Annals of the ICRP (1991)

3) ICRU: Photon, Electron, Proton and Neutron Interaction Data for body Tissues, ICRU Report 46.

Table1 Amount of activity of radioactive materials used.

Radionuclide	Weight	Used activity
F-18	B.W. 1kg	37MBq
	B.W. 30kg	185MBq
Tc-99m	B.W. 1kg	185MBq
	B.W. 30kg	740MBq

Table 2 Conditions used for calculation.

Evaluated Personnel	contact time*	distance from the source
1. Veterinarian	initial 10min	⇒10cm
at Nuc Med exam	10 – 50min	⇒100cm
	50 – 60min	⇒10cm
2. Animal Owner	6hrs - ∞	⇒0cm
after release	24hrs-∞	⇒0cm
3. General public	6hrs - ∞	⇒100cm
after release	24hrs-∞	⇒100cm

* The starting point is the time of a radiopharmaceutical administration.

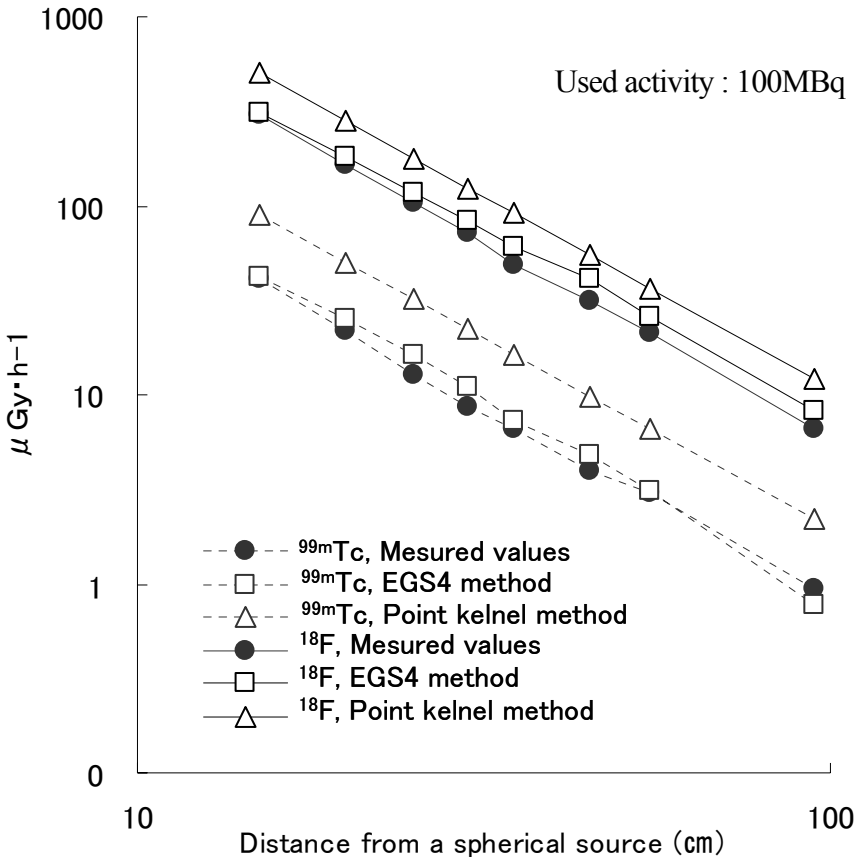

Fig.1 The relationship of calculate values and measurement values for ^{99m}Tc and ^{18}F.

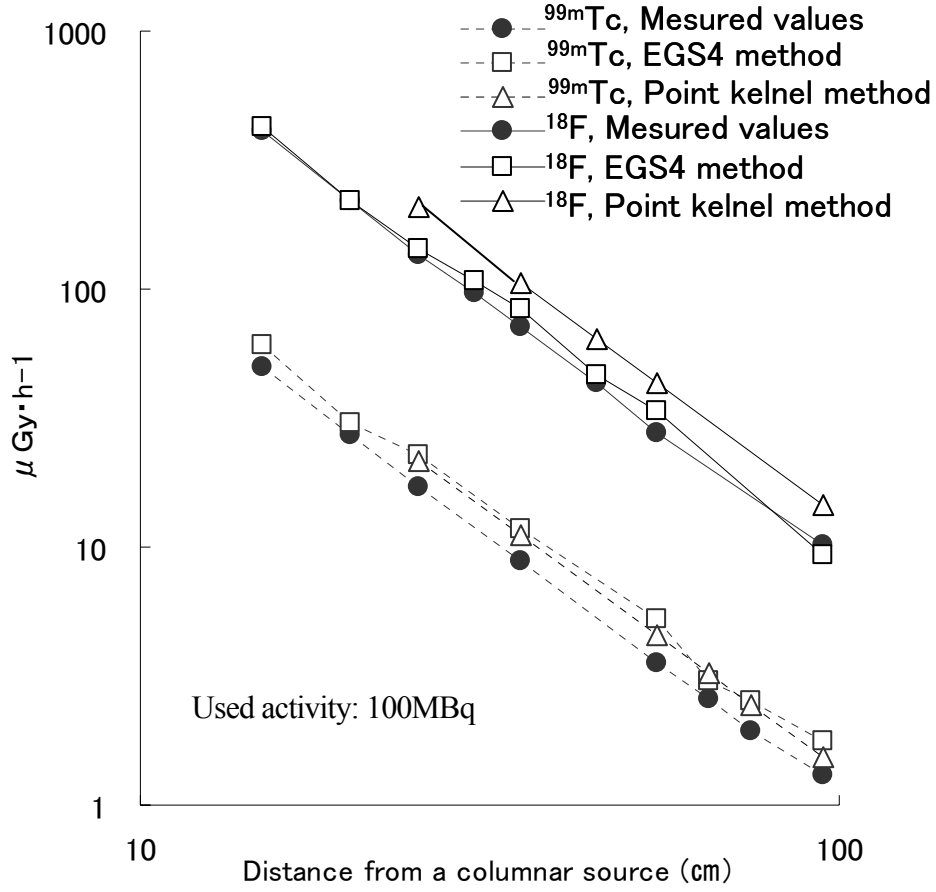

Fig. 2 The relationship of calculated values and measurement values on ^{99m}Tc and ^{18}F.

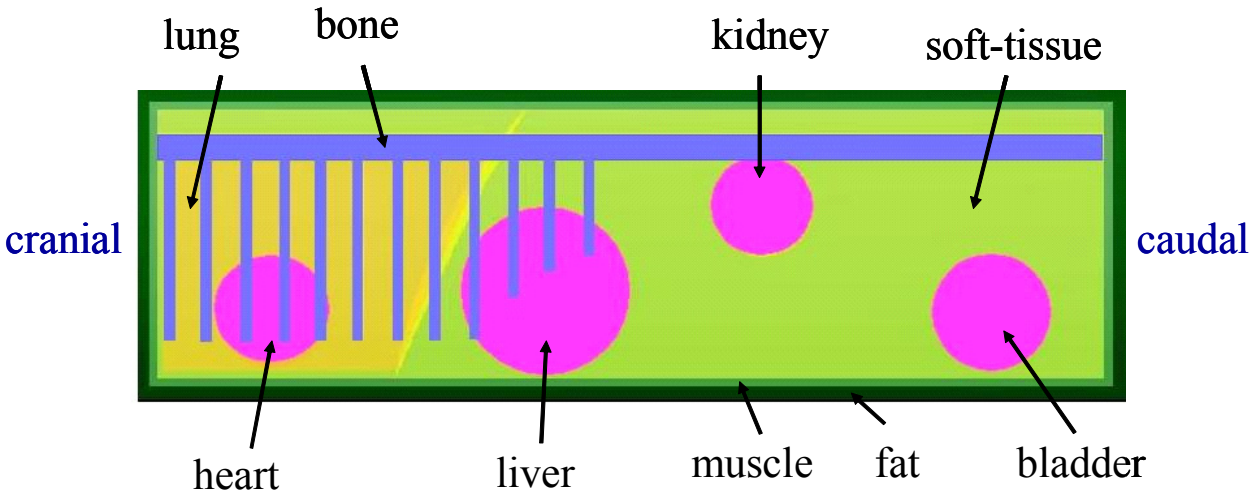

Fig.3 Canine pectoral and abdominal mathematical phantoms of dog (Small size; 1kg, Large size; 30kg) with some particular organs

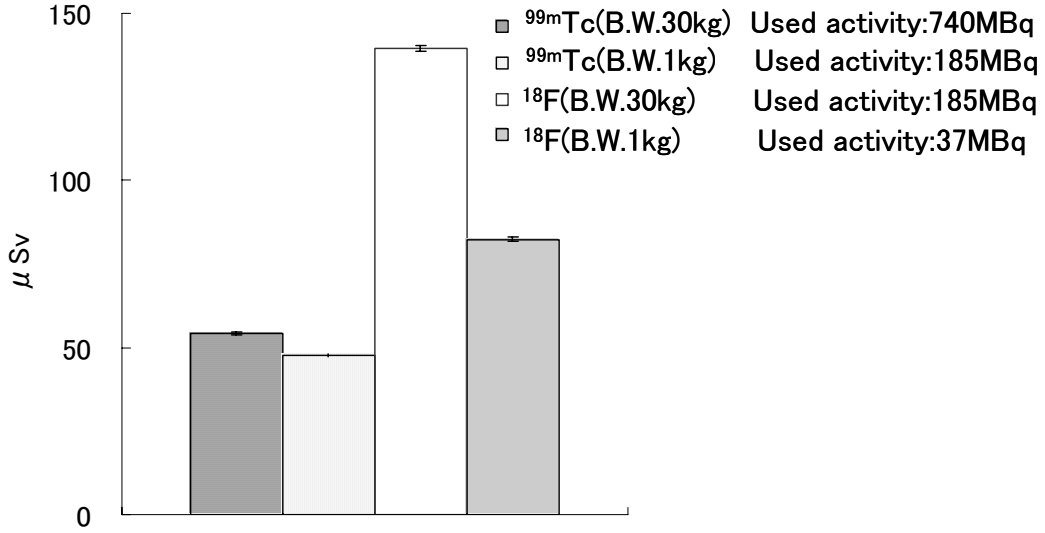

Fig.4 The estimated dose of external exposure to the veterinarian during a nuclear medicine examination.
Dose limit for veterinarian is 20mSv /yr.

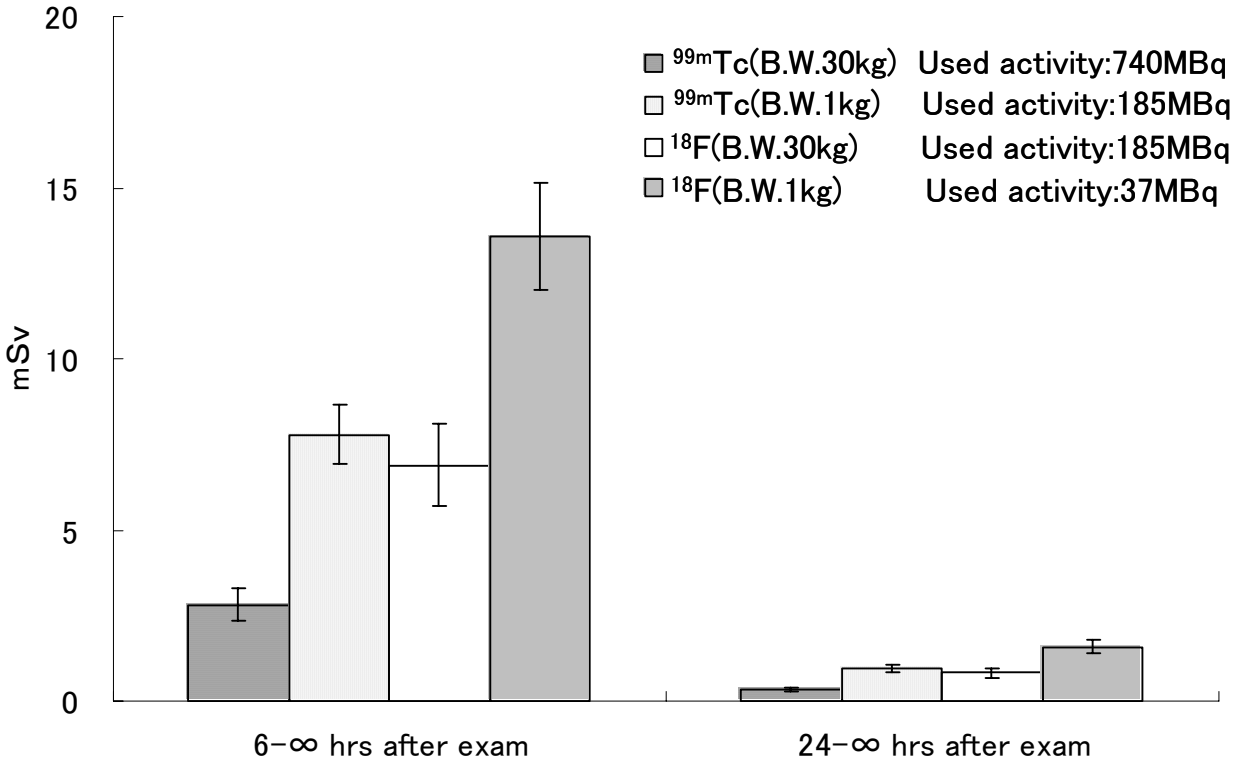

Fig.5 The estimated future integration exposed doses of the animal owner at the release after 6hrs and 24hrs of the radiopharmaceutical administering.
Dose constraint for animal owner is 5mSv/ exam

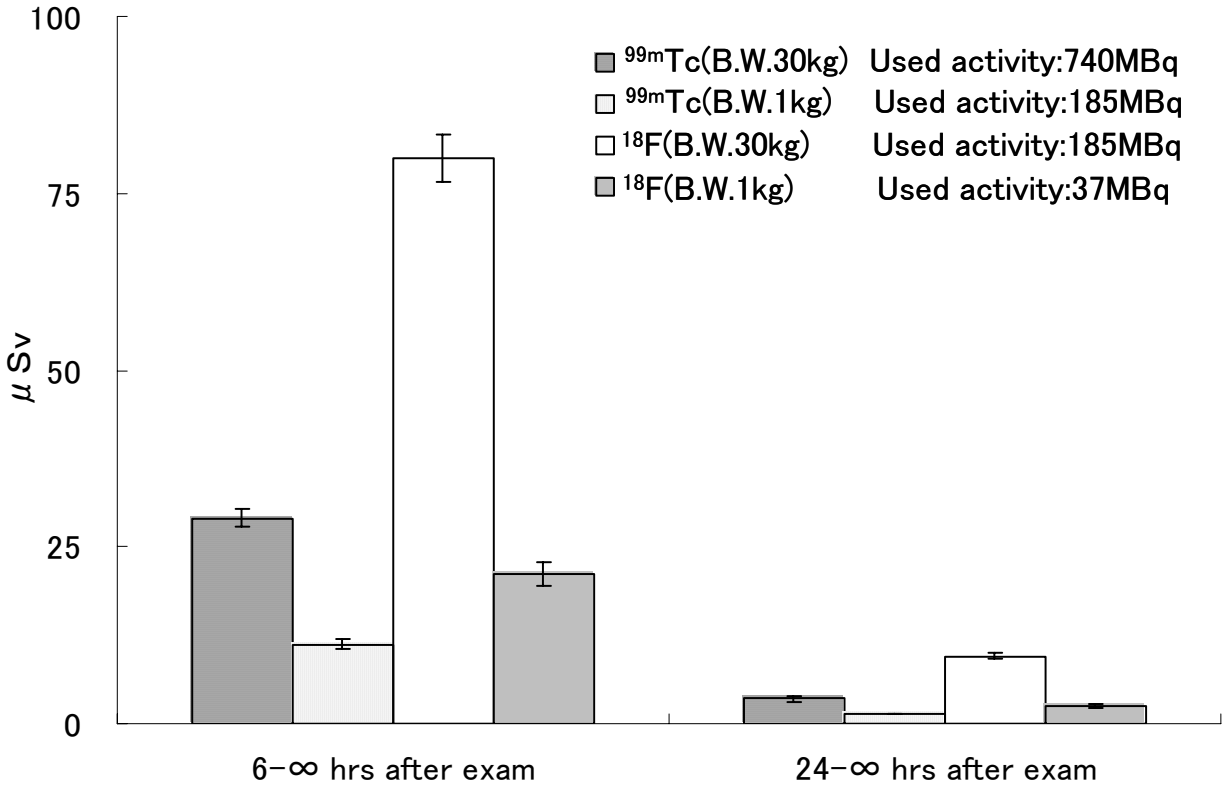

Fig.6 The estimated future integration exposure doses of the general public at the release after 6hrs and 24hrs of the radiopharmaceutical administering. Dose limit for general public is 1000μSv/yr.

APPLICATION OF EGS4 CODE TO EVALUATION OF SPECIFIC ABSORBED FRACTIONS AND S VALUES FOR INTERNAL DOSIMETRY

S. Kinase

Japan Atomic Energy Research Institute
Tokai-mura, Naka-gun, Ibaraki-ken 319-1195, Japan
e-mail: skinase@popsvr.tokai.jaeri.go.jp

Abstract

The EGS4 code was used for evaluating the fractions of energy emitted as specified radiation in a source organ that is absorbed in a unit target organ–specific absorbed fraction (SAF)– and the mean absorbed dose to the target organ per unit cumulated activity in the source organ (S value) for internal dosimetry. The SAFs and S values were evaluated on a voxel version of the MIRD 5 type phantom and Japanese adult voxel phantoms (Otoko and Onago phantoms) developed at the Japan Atomic Energy Research Institute (JAERI). The evaluated SAFs and S values were compared with several published data in order to demonstrate the use of the EGS4 code for the internal dosimetry and investigate the influence of certain parameters, such as the organ masses, on SAFs and S values. It was demonstrated that the EGS4 code is useful in the evaluation of the SAFs and S values for the internal dosimetry. It was also found that the SAFs and S values for organ self-absorption depend on the organ masses and would be affected by differences in the structure of the human body.

1. Introduction

The EGS4[1] Monte Carlo simulation has been the subject of many research papers and review articles on the internal dosimetry[2, 3]. However, to the author's knowledge, there have been a few efforts to evaluate the fractions of energy emitted as specified radiation in a source organ that is absorbed in a unit target organ–specific absorbed fraction (SAF)– and the mean absorbed dose to the target organ per unit cumulated activity in the source organ (S value) for sophisticated phantoms using the EGS4 code[4, 5]. At the Japan Atomic Energy Research Institute (JAERI), the UCSAF code[6, 7, 8] has been developed as an EGS4 user code with voxel phantoms[9, 10, 11] that were constructed from computed tomographic (CT) or magnetic resonance imaging (MRI) data of real persons. It is therefore necessary to examine usefulness of the UCSAF code in evaluating SAFs and S values for voxel phantoms. The purpose of this work is to demonstrate that the EGS4 code is useful in the evaluation of the SAFs and S values for voxel phantoms and to investigate the influence of certain parameters, such as the organ masses, on SAFs and S values.

2. Materials and Methods

2.1 Phantoms

In the present work three whole–body voxel phantoms were used: the MIRD 5 type hermaphrodite adult

phantom, the JAERI adult male "Otoko" and the JAERI adult female "Onago" phantoms. The voxel phantoms were made by the construction techniques in the previous development of the voxel phantoms at GSF[9]. The Otoko and Onago phantoms are constructed from CT data of real persons[10]. The CT data are 512 pixel×512 pixel resolution for the Otoko and Onago phantoms. The data of the MIRD 5 type voxel phantom are also 512 pixel×512 pixel resolution. The voxel size is 1.00×1.00×1.00 mm^3 for the MIRD 5 type voxel phantom and 0.98×0.98×10.0 mm^3 for the Otoko and Onago phantoms. Table 1 compares the tissue masses of the voxel phantoms (MIRD 5 type voxel, Otoko and Onago) with the adult MIRD 5 type phantom[12] and two other adult voxel phantoms [13, 14]. There are discrepancies between the tissue masses of the MIRD 5 type voxel phantom and those of the original MIRD 5 type phantom, and between the tissue masses of Otoko, Onago and the other phantoms.

2.2 Monte Carlo code

The UCSAF code was used for this work. The code was extended the UCPIXEL code[10] for internal dosimetry. In the UCSAF code, the radiation transport of electrons, positrons and photons in phantoms can be simulated, and correlations between primary and secondary particles are included. Beta-ray spectra for each radionuclide are taken as the relative number of beta-rays per MeV, $N(W)$, from the equation[15].

$$N(W) = p \cdot W \cdot (W_0\text{-}W)^2 \cdot \mathrm{F}(Z,W) \cdot a_n(Z,W)$$

where W is the total energy of the electron (kinetic energy + $m_e c^2$) in units of $m_e c^2$,

m_e is the electron mass and c is the velocity of light,

W_0 is the corresponding value at the maximum electron energy,

$p = (W^2\text{-}1)^{1/2}$ is the electron momentum in units of $m_e c$,

Z is the atomic number of the daughter nucleus,

$\mathrm{F}(Z,W)$ is the Fermi factor and

$a_n(Z,W)$ is a shape factor for a transition of order of forbiddenness n.

The beta-ray spectra can be generated for both allowed and first-forbidden transitions in the code. The Parameter Reduced Electron–Step Transport Algorithm (PRESTA)[16] to improve the electron transport in the low–energy region is used. The cross–section data for electrons are taken from ICRU report 37[17, 18] and the data for photons are taken from PHOTX[19, 20].

2.3 Calculation of SAF

SAFs for organ self-absorption in the MIRD 5 type voxel, Otoko and Onago phantoms were calculated using the UCSAF code in order to examine usefulness of the code. In addition, The SAFs were compared with published data[13, 14] to investigate the influence of organ masses on the SAFs. The kidneys were source/target organs. The kidneys are of importance since the kidneys represent frequent sources of radioactivity uptake as the major organs of the excretory pathway. The source of the photons was assumed to be monoenergetic in the energy range 10 keV to 4 MeV and uniformly distributed in the kidneys. A million or more histories were run in order to reduce statistical uncertainties below 5 %.

2.4 Calculation of S value

S values for the urinary bladder walls and the brains were evaluated from the viewpoint of developing a new beta-ray emitter dosimetry. The S values to the urinary bladder walls from uniformly distributed beta–ray emitters within the bladder contents were evaluated for the MIRD 5 type voxel, Otoko and Onago phantoms. To evaluate the S values, the total energies deposited in the urinary bladder walls per source particles were calculated using the UCSAF code. The results were converted into S values, through consideration of the masses of the urinary bladder walls and the decay

modes of the radionuclides. The energy contribution of beta-ray to the mucus in the bladder wall was taken to be unity. The beta-ray emitters were ^{14}C, ^{24}Na, ^{32}P, ^{60}Co, ^{89}Sr, ^{90}Sr, ^{90}Y, ^{91}Y, ^{137}Cs, ^{147}Pm and ^{204}Tl. The decay mode for each radionuclide was assumed to consist of a main branching since a few percentages branching for the decay mode would be insignificant for the S values evaluations. The S values for ^{24}Na and ^{60}Co were evaluated as pure beta-ray particles. In addition, self-dose S values for the brains were evaluated on the voxel phantoms. The brain was source/target organ. The beta-ray emitter -positron emitter such as ^{11}C, ^{15}O and ^{18}F- was uniformly distributed in the brain. To evaluate the S values, the total energies deposited in the brain per source particles were calculated using the UCSAF code. Positron annihilation processes were taken into account in the calculations. The results were converted into S values. The number of particle histories was determined to be a million..

3. Results and Discussion

3.1 Influence of individual anatomy on SAF

Figure 1 shows SAFs for the kidney self-absorption in the MIRD 5 type voxel, Otoko and Onago phantoms in the photon energy range 10 keV to 4 MeV. The SAFs in the MIRD 5 type phantom, Golem and Voxelman are also shown in the figure. A good agreement was found between the SAFs for all phantoms except for Voxelman, whose kidneys have a higher mass than those of all the other phantoms, and the SAFs are, consequently, lower. In particular, the SAFs for the MIRD 5 type voxel phantom agree with published data for the MIRD 5 type phantom. This calculation leads to the usefulness of the UCSAF code. The smaller discrepancies between the SAFs in the other phantoms are attributed mainly to differences in organs mass, the different anatomy of the phantom, different cross section data used in codes and the different transport calculations of secondary electrons in codes.

3.2 Influence of parameter on S value

S values for the urinary bladder walls in the MIRD 5 type voxel, Otoko and Onago phantoms are shown in Fig. 2. The S values show dependence on the phantoms. This fact indicates that the S values mainly depend on the urinary bladder wall masses. The S values, shown in the figure, increase with increasing beta-ray energy. Figure 3 shows the brain S values for ^{11}C, ^{15}O and ^{18}F; the contributions from positrons and the two annihilation photons are presented separately. The S values increase with an increase in mean energy of beta-ray. For nuclides with the large positron energies, positron interactions are large contributor to the brain S values.

4. Conclusions

The SAFs and S values for the voxel phantoms have been evaluated using the EGS4 code in conjunction with the UCSAF code. The main results obtained are shown below.

1. The codes are very useful in the evaluation of the SAFs and S values for the internal dosimetry.
2. The SAFs for the kidney self−absorption largely depend on the kidney masses and would also be affected by differences in the structure of the human body.
3. The S values for the brains and bladder walls are largely dependent upon the beta-ray energy and the mass of each organ. For nuclides with the large positron energies, the self-dose S values for the brains are largely contributed by the positron interactions.

References

1) W. R. Nelson, H. Hirayama and D. W. O. Rogers, The EGS4 Code System, SLAC-265 (1985).

2) J. W. Poston, Jr., K. A. Kodimer, W. E. Bolch and J. W. Poston, Sr, A Revised Model for the Calculation of Absorbed Energy in the Gastrointestinal Tract, *Health Phys*., 71, 307-314 (1996).

3) L. G. Bouchet, W. E. Bolch, D. A. Weber, H. L. Atkins and J. W. Poston, Sr, A revised Dosimetric Model of the Adult Head and Brain, *J. Nucl. Med*., 37, 1226-1236 (1996).

4) D. G. Jones, A Realistic Anthropomorphic Phantom for Calculating Specific Absorbed Fractions of Energy Deposited from Internal Gamma Emitters, *Radiat. Prot. Dosim*. 79, 411-414 (1998).

5) T. C. Chao and X. G. Xu, Specific Absorbed Fractions from the Image-based VIP-Man Body Model and EGS4-VLSI Monte Carlo Code: Internal Electron Emitters, *Phys. Med. Biol*. 46, 901-927 (2001).

6) S. Kinase, M. Zankl, J. Kuwabara, K. Sato, H. Noguchi, J. Funabiki and K. Saito, Evaluation of Specific Absorbed Fractions in Voxel Phantoms using Monte Carlo Simulation, *Radiat. Prot. Dosim*. 105 (1-4), 557-563 (2003).

7) S. Kinase, M. Zankl, J. Funabiki, H. Noguchi and K. Saito, Evaluation of S Values for Beta-ray Emitters within the Urinary Bladder. *J. Nucl. Sci. Technol*., Supplement 4, 136-139 (2004).

8) S. Kinase, M. Zankl, J. Funabiki, H. Noguchi and K. Saito, Evaluation of S Values for Beta-ray Emitters in Voxel Phantoms, KEK Proceedings 2003-15, 45-52 .

9) R. Veit, M. Zankl, N. Petoussi-Henß, E. Mannweiler, G. William, G. Drexler, Tomographic Anthropomorphic Models. Part Ⅰ. Construction Technique and Description of Models of an 8 Week Old baby and a 7 Year Old Child. GSF-Bericht 3/89 GSF−National Research Center for Environment and Health, Neuherberg, Germany (1989).

10) K. Saito, A. Wittmann, S. Koga, Y. Ida, T. Kamei, J. Funabiki and M. Zankl, Construction of a Computed Tomographic Phantom for a Japanese Male Adult and Dose Calculation System, *Radiat. Environ. Biophys*. 40, 69-76 (2001).

11) R. Kramer, J. W. Vieira, H. J. Khoury and F de Andrade Lima, MAX meets ADAM: A Dodimetric Comparison between A Voxel-based and A Mathematical Model for External Exposure to Photons, *Phys. Med. Biol*. 49, 887-910 (2004).

12) W. S. Snyder, M. R. Ford, G. G. Warner, MIRD Pamphlet No. 5 (Revised): Estimates of Specific Absorbed Fractions for Photon Sources Uniformly Distributed in Various Organs of Heterogeneous Phantom. The Society of Nuclear Medicine (1978).

13) N. Petoussi–Henß, M. Zankl, Voxel Anthropomorphic Models as a Tool for Internal Dosimetry, *Radiat. Prot. Dosim*. 79, 415-418 (1998).

14) H. Yoriyaz, A. Santos, M. G. Stabin, R. Cabezas, Absorbed Fractions in a Voxel-based Phantom Calculated with the MCNP-4B Code, *Med. Phys*. 27, 1555-1562 (2000).

15) ICRU. Dosimetry of External Beta Rays for Radiation Protection. ICRU Report 56 (1997).

16) A. F. Bielajew and I. Kawrakow, The EGS4/PRESTA-II electron transport algorithm: Tests of electron step-size stability, Proceedings of the XII'th Conference on the Use of Computers in Radiotherapy 153-154 Medical Physics Publishing (1997).

17) M. J. Berger and S. M. Seltzer, Stopping Power and Ranges of Electrons and Positrons (Second Edition), U. S. Department of Commerce Report NBSIR 82-2550-A (1983).

18) ICRU. Stopping Powers for Electrons and Positrons. ICRU Report 37 (1984).

19) RSIC. DLC-136/PHOTX Photon Interaction Cross Section Library (contributed by National Institute of Standards and Technology) (1989).

20) Y. Sakamoto, Photon Cross Section Data PHOTX for PEGS4, KEK Proceedings 93-15, 77-82 (in Japanese).

Table 1 Comparison of tissue masses for the phantoms

Phantoms	Kidneys (kg)	Total brain (kg)	Bladder wall (kg)
MIRD 5 type voxel	0.300	1.400	0.047
Otoko	0.266	1.472	0.012
Onago	0.257	1.148	0.024
MIRD 5 type	0.299	1.420	0.048
Golem	0.316	1.218	0.068
Voxelman	0.512	1.230	0.212

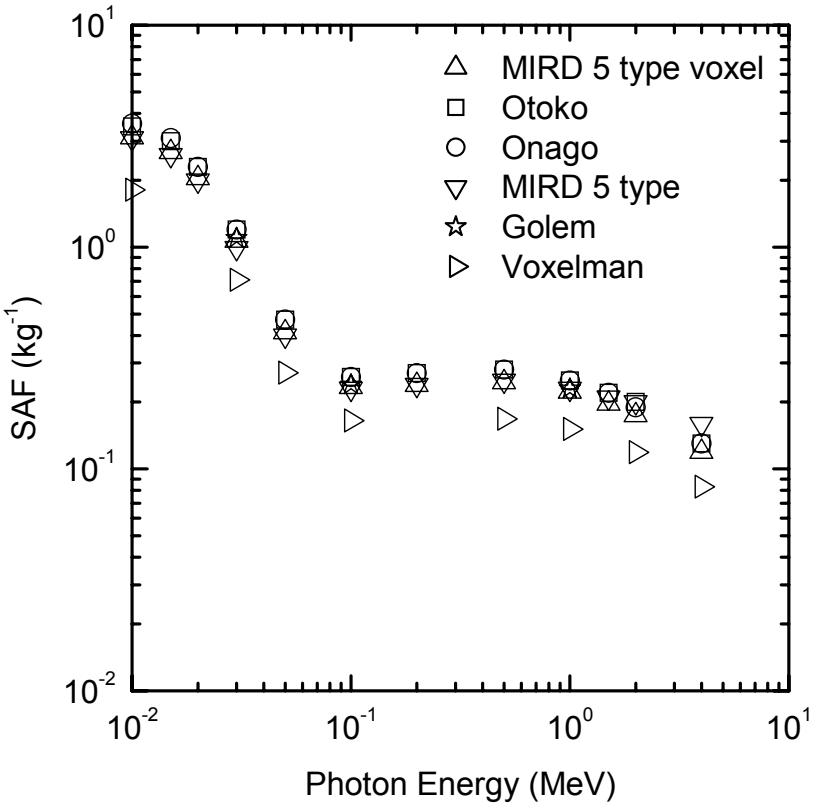

Figure 1 Specific absorbed fractions in the kidneys for MIRD 5 type voxel phantom, Otoko and Onago phantoms, MIRD 5 type phantom, Golem and Voxelman in the photon energy range of 10 keV to 4 MeV.

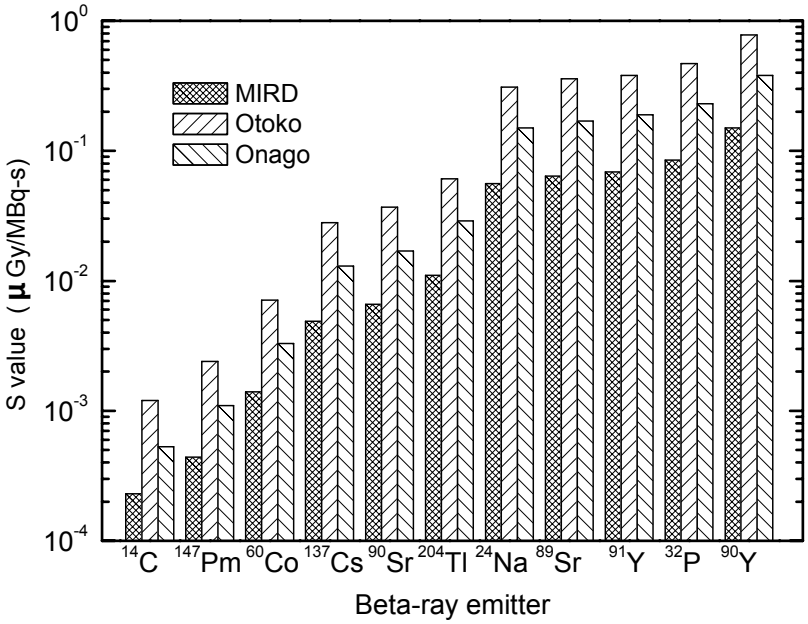

Figure 2 S values for the bladder walls in the MIRD 5 type voxel, Otoko and Onago phantoms.

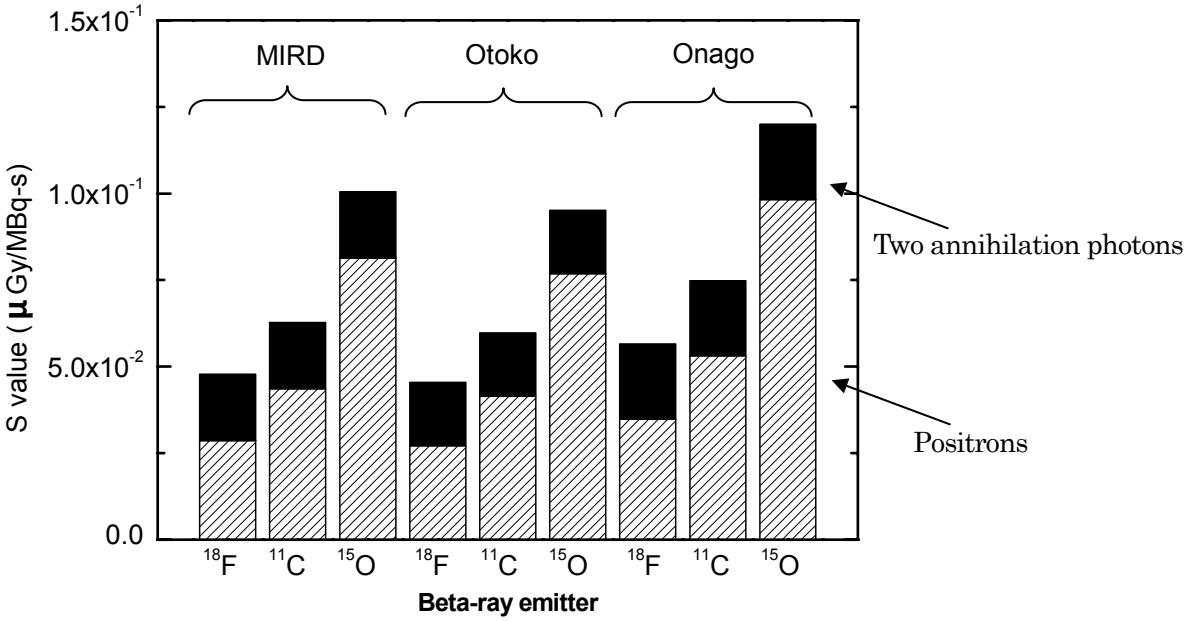

Figure 3 S values for beta-ray emitters distributed in the brains. Contributions from positrons and from two annihilation photons are illustrated for each S value.

MONTE CARLO CALCULATION OF NORMALIZED GLANDULAR DOSE IN MAMMOGRAPHY

Ju-Lin Hsu[1], Uei-Tyng Lin[2], Wei-Li Chen[1]

1. National Yang-Ming University, Taipei, TW; email: g39120004@ym.edu.tw

2. National Radiation Standard Laboratory, Institute of Nuclear Energy Research, Tao-Yuan, TW

1. Introduction

To get the dose evaluation in mammography be executed more easily, Monte Carlo simulation (EGS4-LSCAT) is utilized to calculate normalized glandular dose for mammographic x-ray spectra of wide ranges. Normalized glandular dose is just mean glandular dose, which is the most relevant indicator of risk in mammography, normalized to entrance surface dose. Clinically, entrance surface dose can be measured easily and mean glandular dose comes out after entrance surface dose being multiplied by normalized glandular dose. This study aims to establish a table of normalized glandular dose for different beam qualities (different half-value layers).

2. Material and Methods

We followed NIST to set 5 beam qualities with Mo anode and Mo filters of different thicknesses (half value layer: 0.282 mm Al, 0.302 mm Al, 0.342 mm Al, 0.358 mm Al, 0.389 mm Al) (table 1) and measured each spectrum at the National Radiation Standard Laboratory (NRSL) in the Institute of Nuclear Energy Research. These spectra were used in computation of normalized glandular dose(fig1~5).

The mean glandular dose and the entrance surface dose measured by an ion chamber could be simulated by the Monte Carlo method.

Computation of mean glandular dose (MGD): Several cylinders and plates were combined to become a breast and compression paddles (fig.6). The radius of inner annulus is 7.5 cm. The radius of middle annulus is 0.5 cm and that of the outer one is 13.64 cm. The thickness of slab3 in fig.6 could be changed from 2 to 5 cm to simulate 3~6cm thick breast. One piece of compression paddle is upon the breast and the other piece is under the breast. Both compression paddles were 0.3 cm thick. The breast had a central region which was composed of 50:50 mixture by weight adipose and glandular tissues and an outer shield region of adipose tissue 0.5 cm thick. The proportion of glandular and adipose tissue assumed to be 30:70, 70:30, or 100:0 in another trials. The elemental composition of gland tissue and adipose tissue came from ICRU.44 [1)]. The dose for x-ray spectra were calculated by appropriately weighting the monoenergetic results. Irradiation field was a 17.6cm × 17.6 cm square. Settings of altered field sizes were also simulated.

Computation of entrance surface dose (ESD): Several cylinders and plates were combined to become the upper piece of compression paddles and an flat cavity ion chamber (fig.7). The ion chamber had a thin window composed of polycarbonate and graphite. Thickness of graphite was only 0.01676 cm. The ion chamber was originally placed between the upper piece of compression and top surface of breast. Breast was omitted because we ignored the dose contributed from backscatter photons. The dose for x-ray spectra were calculated by appropriately weighting the monoenergetic results. Irradiation field was a 4.5 cm × 4.5 cm square. Settings of altered field sizes were also simulated.

3. Results

The outcome was compared with normalized glandular dose calculated by Dance[2)] in 5 situations (different breast thickness, fig 8~12). Normalized glandular dose increased with the beam half value layer (HVL) . Two sets of data had the same trend. But, there existed difference about 1.6 to 14% between them. The difference may be caused by simplified program settings: shape of entrance x-ray beam (fig.13). Spectrum were another reason which could produce difference. How sensitive spectrum affect conversion factor are in investigation. Table.2 was conversion factors of various thickness breasts. Fig. 14 showed relationship between conversion factors and breast thicknesses. Normalized glandular dose decreased with breast thickness. Table. 3 and Fig.15 were another trial, they displayed that fatty breast (less proportion of glandular tissue) had smaller conversion factor and dense breast (more proportion of glandular tissue) had larger conversion factor. Irradiation fields of different sizes made difference in calculation of dose. The larger the field was, the bigger the dose (fig .16).

4. Conclusion

Monte Carlo is a good method to evaluate the mean glandular dose that cannot be measured directly. Besides the breast thickness or beam half value layers, other factors also affect the glandular dose like breast composition and irradiation field size. By means of sensitivity study using EGS4 program we will understand how these factors affect normalized glandular dose and which factor has powerful effect . Tables of conversion factors of assumed breast were produced by this study. If statistic data of breast shape, thickness, composition are collected in our nation, the glandular dose caused by each mammography inspection will not be secret. And further, these information can be used to investigation of reducing glandular dose contributed by mammographic inspection.

References

1) ICRU. Tissue Substitutes in Radiation Dosimetry and Measurement. Report 44, Bethesda, MD:ICRU Publications, 1989.

2) Dance D R: Monte Carlo calculation of conversion factors for the estimation of mean glandular breast dose. Physics in Medicine and Biology 35(9), 1211-1219, 1990.

Table 1. Beam quality (beam code)

NIST Beam Code	Tube Voltage	Added Filter	Half-Value Layer
(Mo Anode)	(kVp)	(mm)	(mm Al)
Mo/Mo23	23	0.030Mo	0.282
Mo/Mo25	25	0.030Mo	0.302
Mo/Mo28	28	0.0325Mo	0.342
Mo/Mo30	30	0.0325Mo	0.358
Mo/Mo35	35	0.0325Mo	0.389

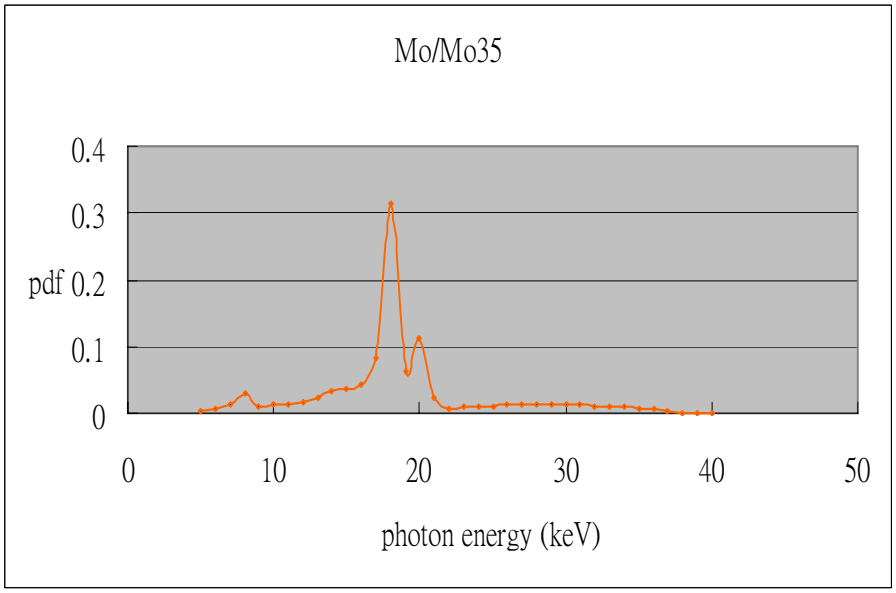

Figure 1. Spectrum of Mo/Mo35 beam code

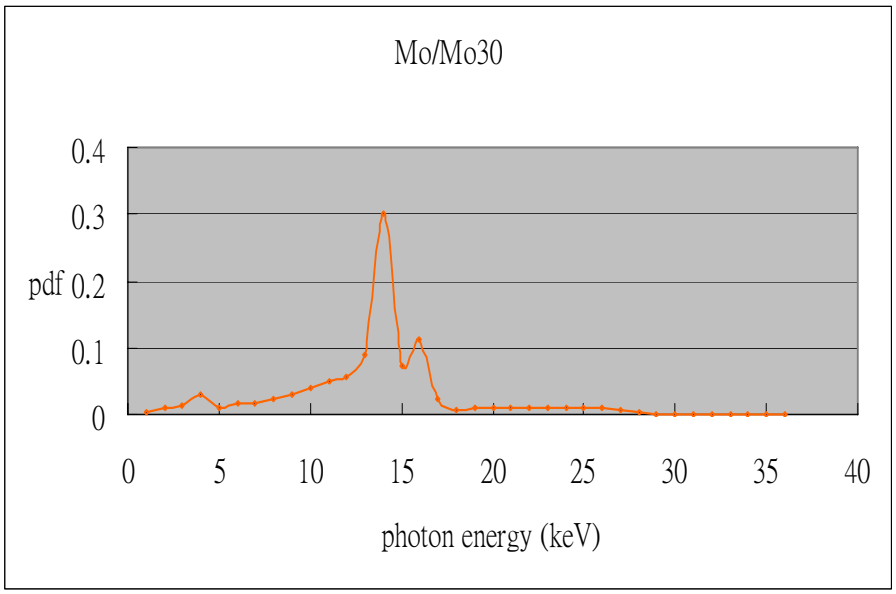

Figure 2. Fpectrum of Mo/Mo30 beam code

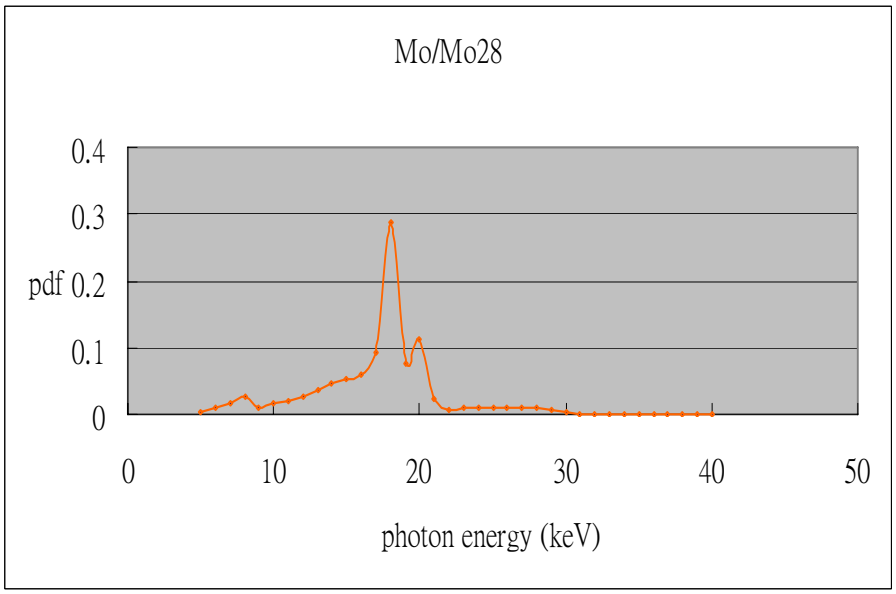

Figure 3. Spectrum of Mo/Mo28 beam code

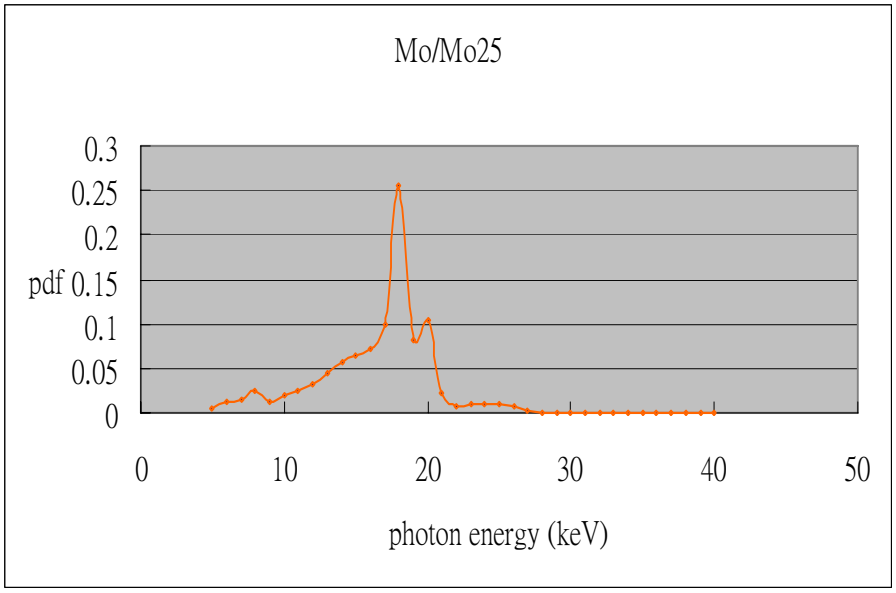

Figure 4. Spectrum of Mo/Mo25 beam code

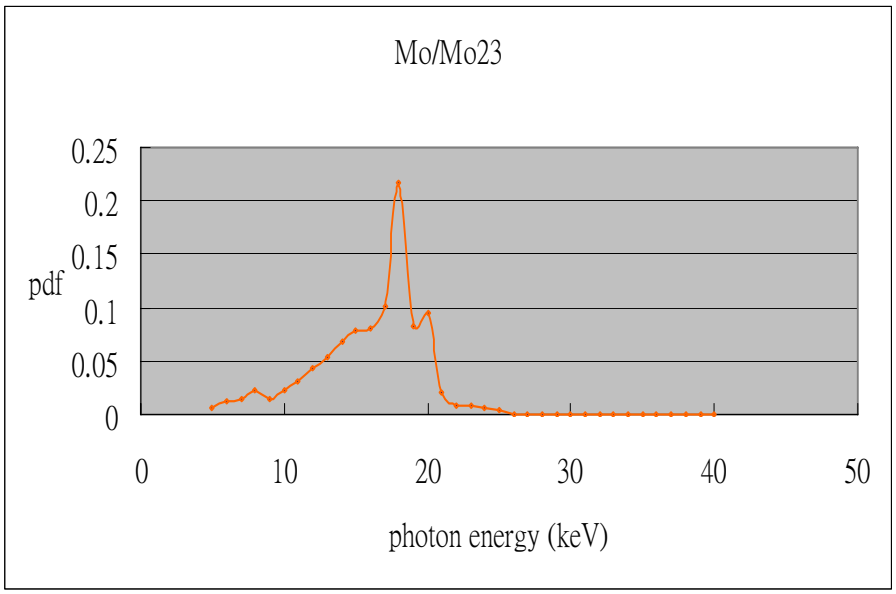

Figure 5. Spectrum of Mo/Mo23 beam code

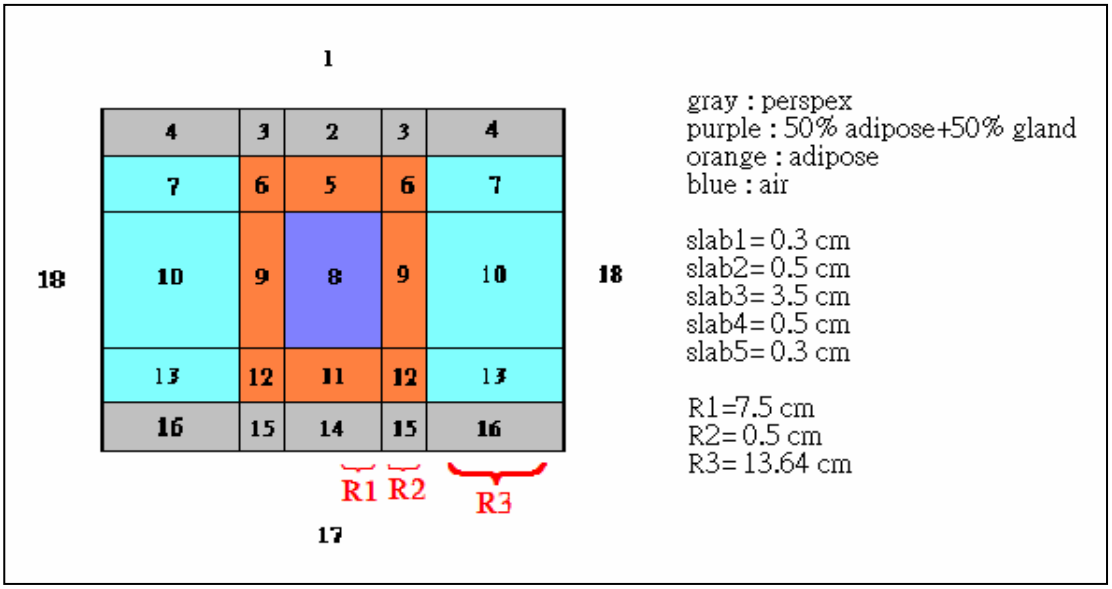

Figure 6. Geometry for computation of average glandular dose

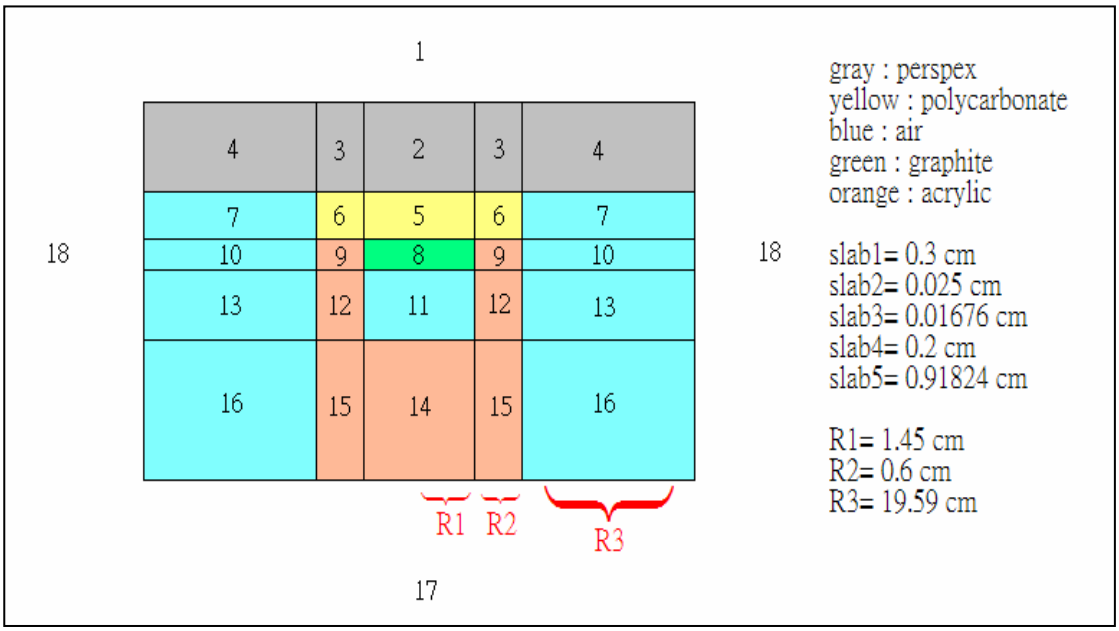

Figure 7. Geometry for computation of entrance surface dose

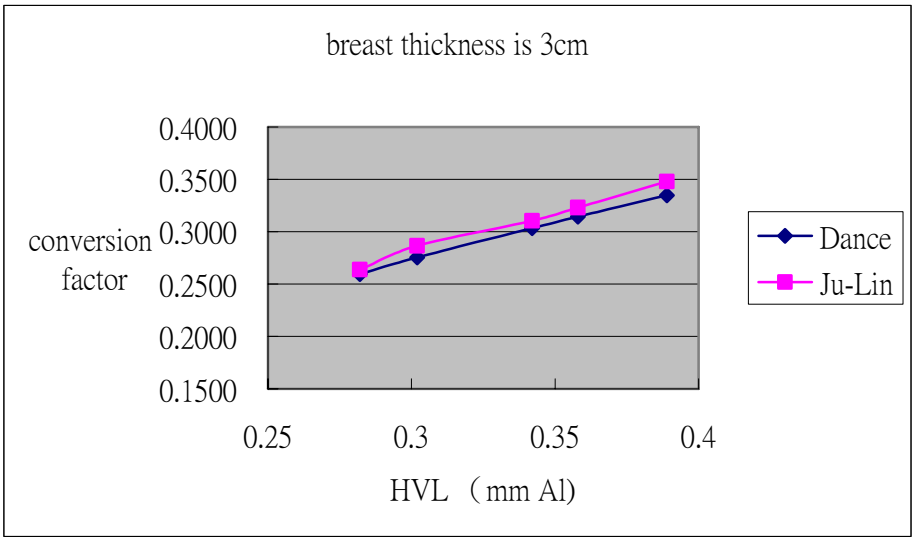

Figure 8.Cconversion factors for 3 cm thick breast

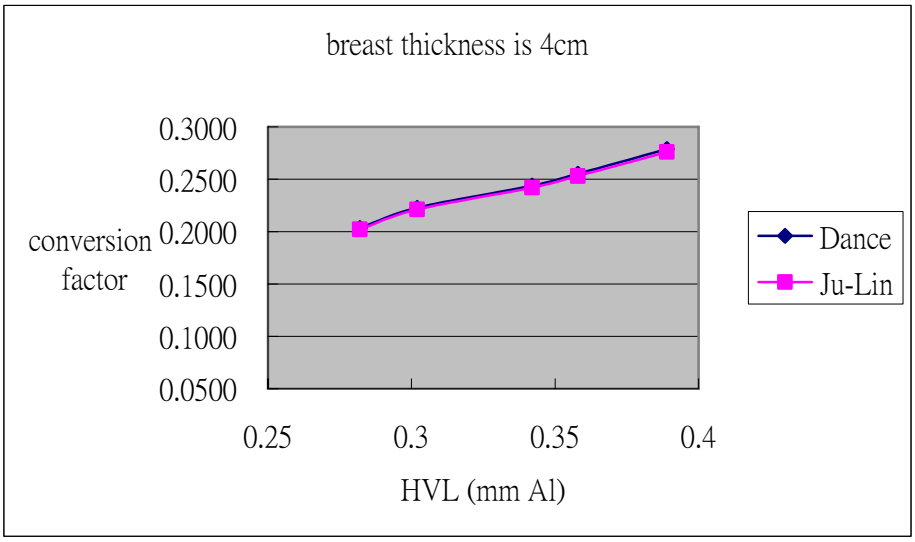

Figure 9.Cconversion factors for 4 cm thick breast

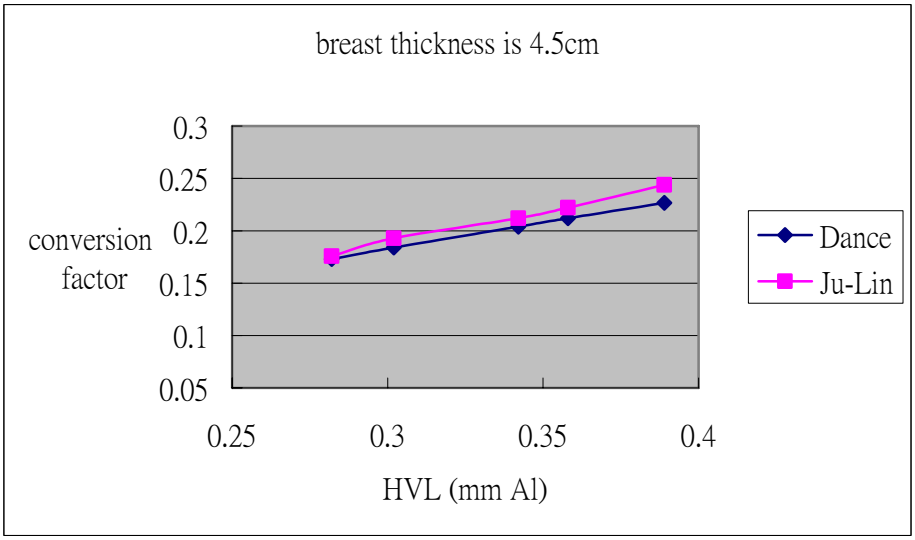

Figure 10. Conversion factors for 4.5 cm thick breast

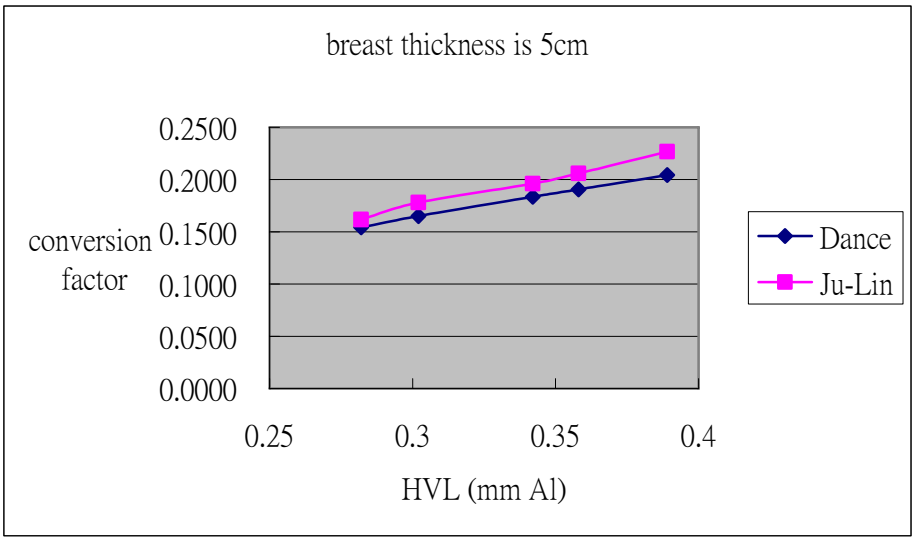

Figure 11. Conversion factors for 5 cm thick breast

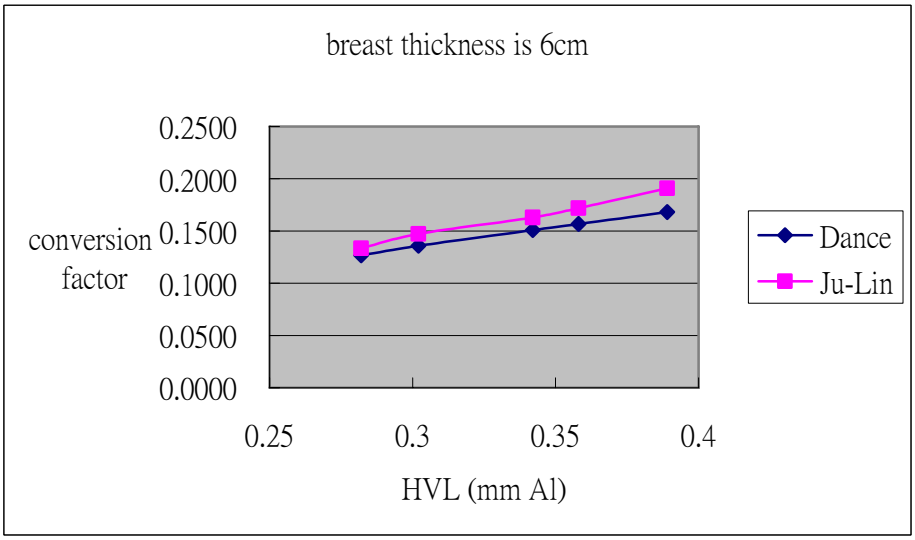

Figure 12. Conversion factors for 6 cm thick breast

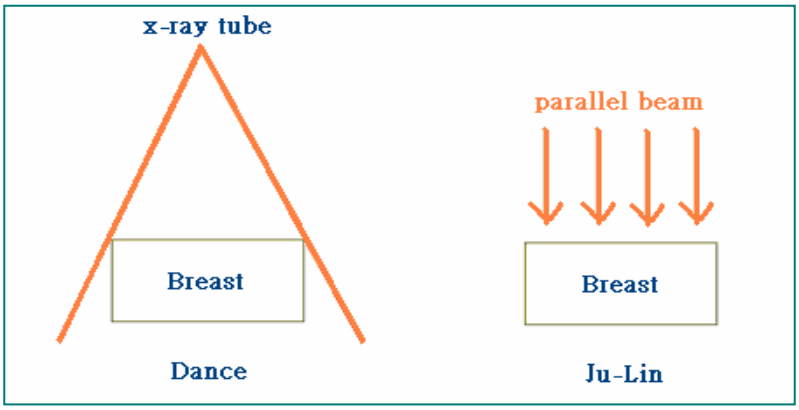

Figure 13. Different settings of x-ray beam shape

Table 2. Conversion factors of various thickness breast

breast thickness (cm)	conversion factor (50%adipose,50%gland)				
	Mo/Mo35	Mo/Mo30	Mo/Mo28	Mo/Mo25	Mo/Mo23
3	0.3478	0.3229	0.3105	0.2864	0.2639
4	0.2762	0.2532	0.2421	0.2212	0.2021
4.5	0.2438	0.2222	0.2120	0.1930	0.1758
5	0.2267	0.2057	0.1959	0.1778	0.1616
6	0.1909	0.1718	0.1630	0.1472	0.1333

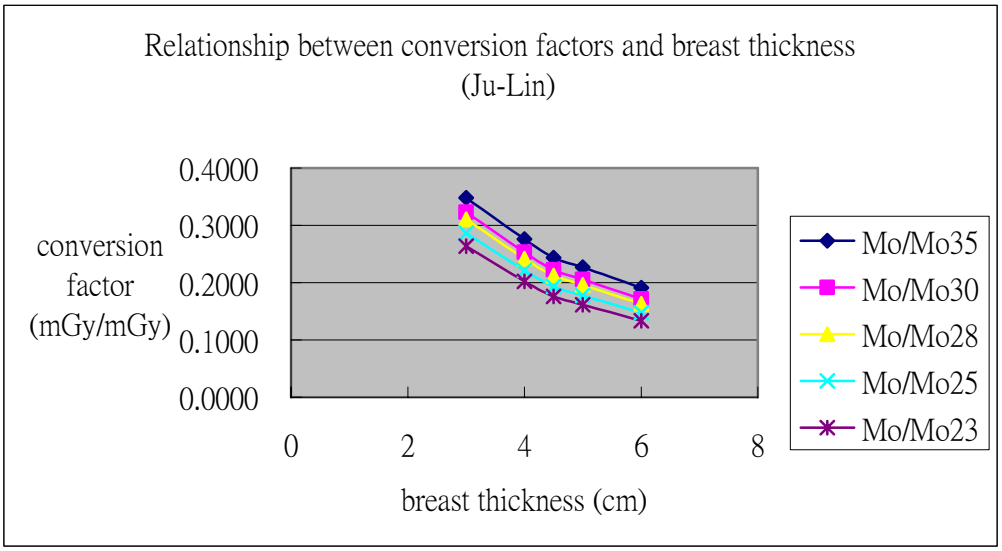

Figure 14. Effect of breast thickness on conversion factors. (Ju-Lin)

Table 3. Conversion factors for breast of different compositoin

Conversion factor (breast thickness=4cm)				
HVL (mm Al)	100% gland	70% gland	50% gland	30% gland
0.389	0.5016	0.3711	0.2762	0.1718
0.358	0.4550	0.3388	0.2532	0.1582
0.342	0.4332	0.3234	0.2421	0.1515
0.302	0.3931	0.2947	0.2212	0.1389
0.282	0.3573	0.2687	0.2021	0.1272

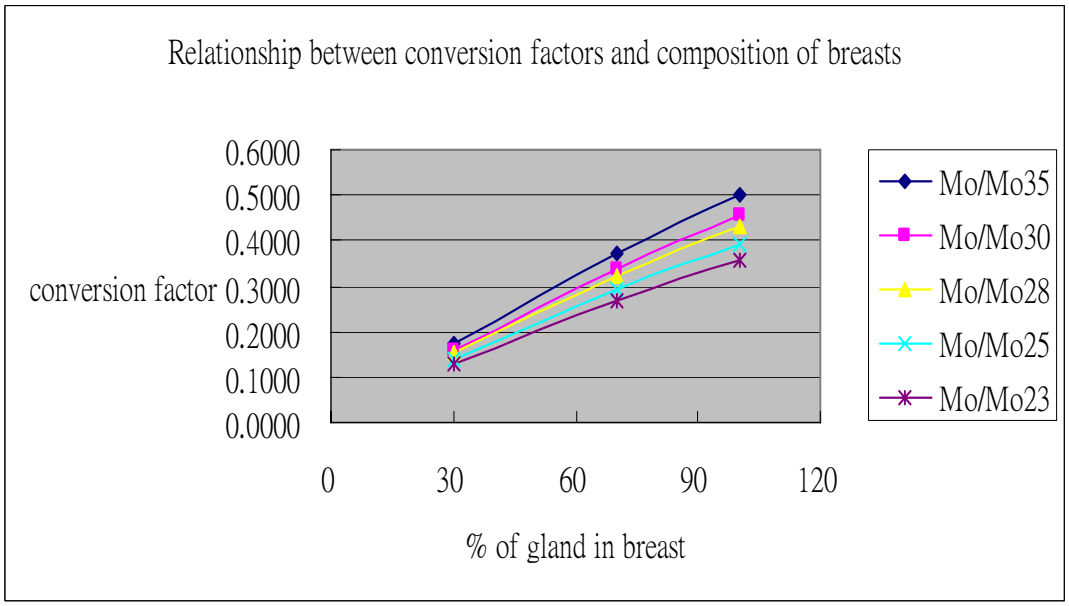

Figure 15. Effect of breast composition on conversion factors (Ju-Lin)

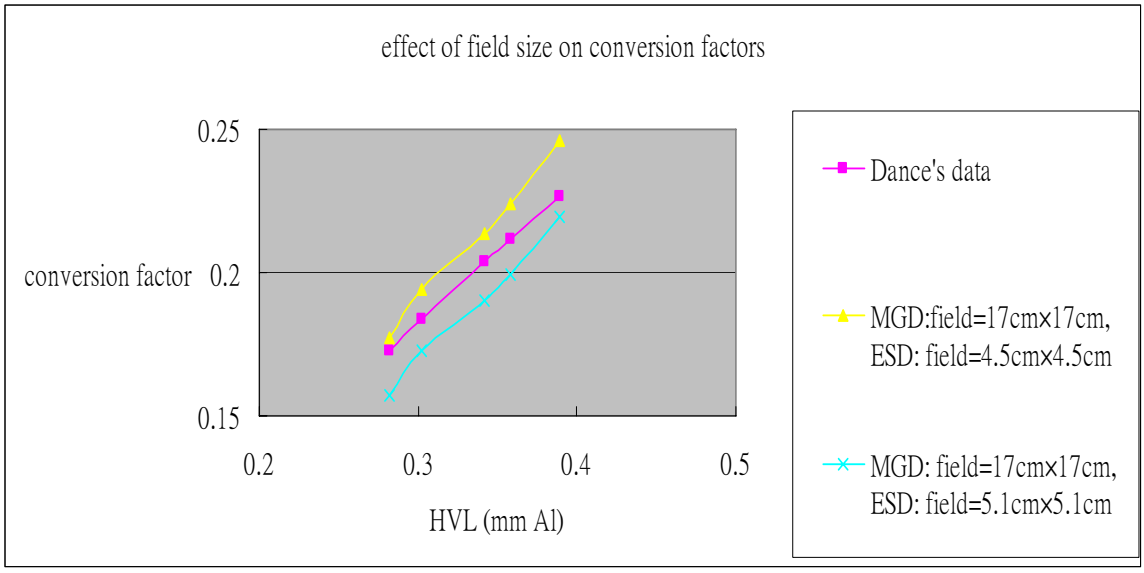

Figure 16. Effect of irradiation field size on conversion factors.

DOSE DISTRIBUTION IN THE HUMAN BODY IN GENERAL RADIOGRAPHY USING MONTE CARLO SIMULATION

M.Hayakawa, K.Koshida*,C.Kawabata, A.Chadani, H.Nakagawa and Keita Kuwamura*

Department of Radiological Technology, Graduate School of Medical Science, Kanazawa University 5-11-80, Kodatsuno, Kanazawa 920-0942, Japan

**Department of Radiological Technology, Kanazawa University 5-11-80, Kodatsuno, Kanazawa 920-0942, Japan*

Abstract

For the patient's absorbed dose, we evaluate the effective dose in the absorbed dose of each internal organ. Thus, the dose distribution in the human body phantom was analyzed using Monte Carlo simulation (EGS4), and the usefulness was studied. First, a Mix-DP phantom was used, and four points in the depth direction in the field center were measured using TLD. The same geometries were made, and the absorbed doses were calculated using EGS4. This was compared with the EGS4 simulation and the measurement. Next, the absorbed doses at three fields (in the Mix-DP phantom, the verge region and the external region of the exposure field) were calculated using EGS4. The difference between measurement by TLD and calculation by EGS4 was within the coefficient of variation.

1. Introduction

The exposure to the patient is evaluated using the patient's skin dose. On the other hand, the effective dose must be evaluated by the absorbed dose of each internal organ. Therefore, it is necessary to know a dose distribution with an internal absorbed dose. The human body phantom loaded with thermo luminescence dosimeter (TLD) was well used to obtain the internal organ dose.

For this paper, we examine the dose distribution by Monte Carlo simulation (EGS4), and compare with the simulation and the measurement by TLD.

2. Materials and Method

2.1. Attenuation on the axis of field center in each field size.

For the Mix-Dp phantom, four points (0 mm, 5 cm, 10 cm, and 15 cm) in the depth direction in the field center were measured using TLD. The model for the measurement is shown in Fig.1. The tube voltages were 80kV and 110kV added 0.2mmCu. The current was 200mA, and exposure time was 0.2sec. Focus-phantom distance was 100cm. Each radiation field size ($10\times10cm^2$, $20\times20cm^2$,and $30\times30cm^2$) was changed and measured.

The same geometries were made, and the field center absorbed doses in Mix-Dp were calculated using EGS4. The number of X-ray photons was 10^8. To confirm the geometries, the CG-View was used. By that software, it was compared with the EGS4 simulation and the measurement.

2.2. Absorbed doses at three places.

It was aimed at investigating the absorbed dose of the internal organs from a radiation field.

In the Mix-DP phantom, the absorbed doses in the depth direction at three places (center region, verge region, and external region of the exposure field) were calculated using EGS4.The model for the simulation is shown in Fig.2. The tube voltage was 80kV. Field size was 35.36×43.18 cm^2, and the distance from the x-ray tube focus to the phantom surface was 100cm.

3. Results and Discussion

3.1 Comparison with simulation and measurement at field center in each field size.

Fig.3 shows the attenuation of field center in each field size (10×10,20×20,$30\times30cm^2$).

In 80kV, the value of the calculated using EGS4 for a radiation field size $10\times10cm^2$ is greater than the value of measured value by 2.3%. The error was increasing as the depth become deep. For a radiation field $20\times20cm^2$, the calculated value is larger than the measured value in depth 5,10cm, but it is smaller than the measurement value in 15cm. For a radiation field $30\times30cm^2$, the error become the largest at a depth of 10cm, and become small after that.

In 110kV, for the each radiation field size the error of measured value and calculated value was similar in depth of 5cm and 10cm.

Table.1 shows the error of measured value and calculated value at each depth.

3.2 Absorbed doses at three places.

Fig.4 shows the internal absorbed dose of attenuated rate in three fields (center region, verge

region, and external region of the exposure field) calculated by EGS4.

The absorbed dose on the phantom surface was compared with the dose at two places (the verge region and external region). The dose in the verge region was attenuated from the exposure field center to 1/20, and the external region to 1/100. At 10 cm from the surface, the dose of the verge region was 1/3 of that in the center region, and the external region was 1/10.

The attenuation rates of the verge and external regions were flat with depth.

4. Conclusions

In the Mix-DP phantom, the difference between the value measured by TLD and that calculated by EGS4 showed an error of less than ±5% at a tube voltage of 80 kV, and ±7% at 110 kV. This was within the coefficient of variation in TLD.

In the internal absorbed dose calculation of the exposure field, the distribution of the verge region and the external region was flat.

The dose distribution calculation using Monte Carlo simulation is useful as to calculate the distribution of human body extensions, and the dose absorbed at each internal organ, and can be grasped visually.

Table.1 The error of measured value and calculated value at each depth.

	80kV			110kV		
	10×10	20×20	30×30	10×10	20×20	30×30
5cm	+2.3	+0.5	−4.3	+0.0	+0.9	+0.9
10cm	+5.2	+2.0	+5.0	−1.7	+0.7	+2.0
15cm	+7.1	−3.4	+2.5	−0.4	+5.0	−3.9

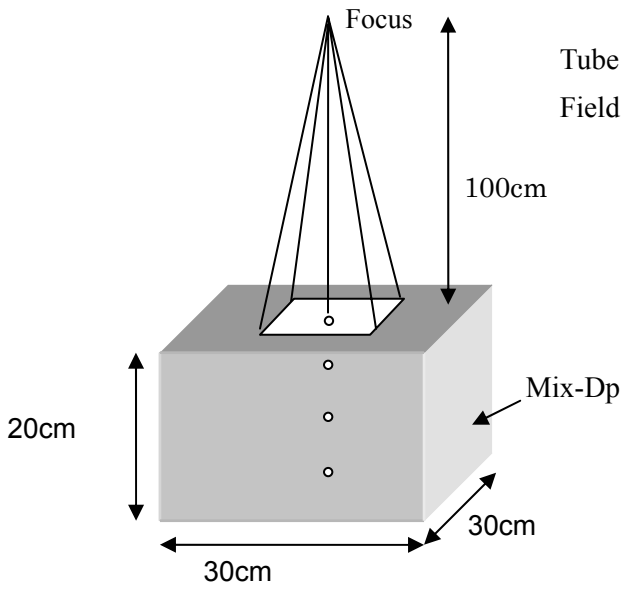

Tube voltage: 80,110kV

Field size: 10×10,20×20,30×30cm^2

∘ Measurement point

Fig.1 Geometrical place for measurement and simulation

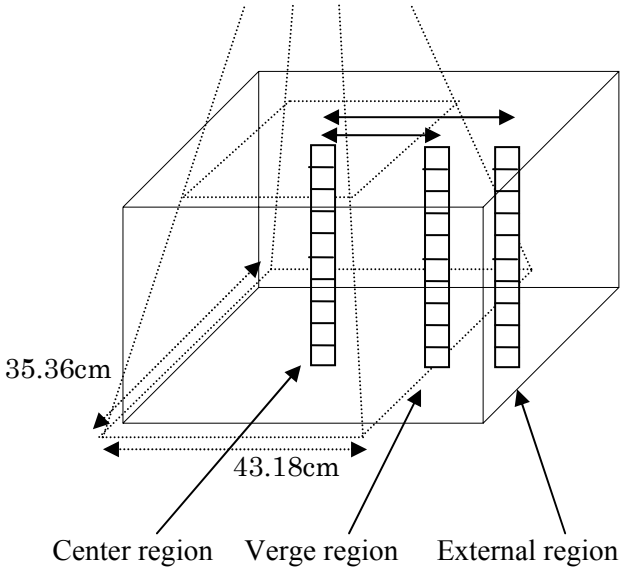

Tube voltage: 80kV

Center region: 0cm from field of center

Verge region: 20cm from field center

External region: 24cm from field center

Fig.2 Geometry of simulation

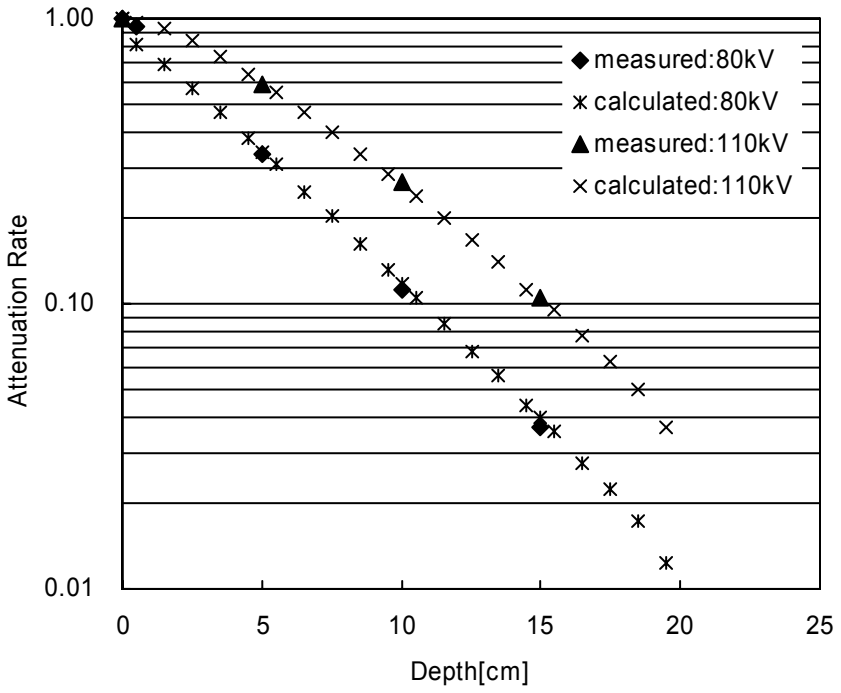

Fig.3-1 Attenuation of field center (Field size: 10×10cm^2)

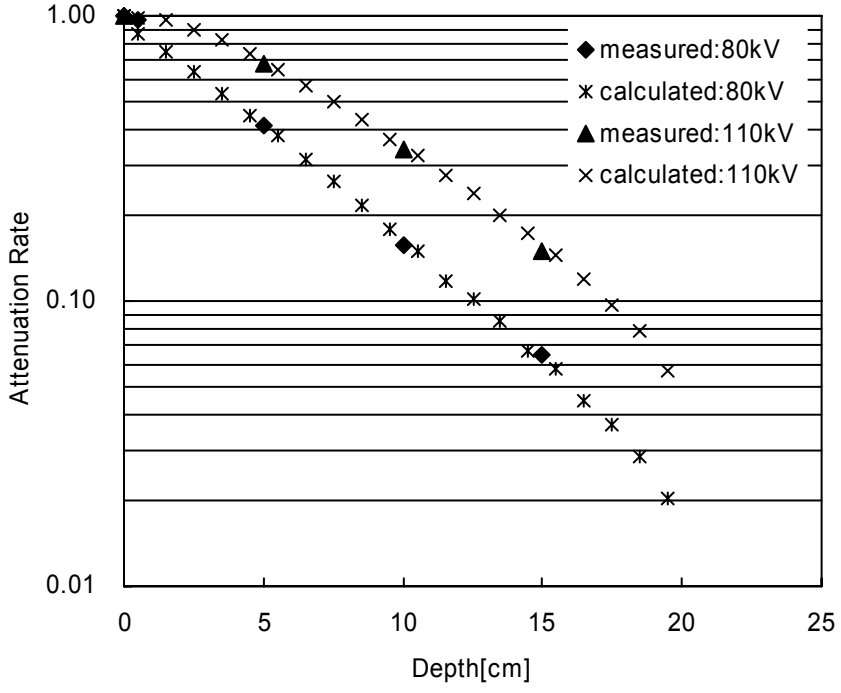

Fig3-2 Attenuation of field center (Field size: 20×20cm^2)

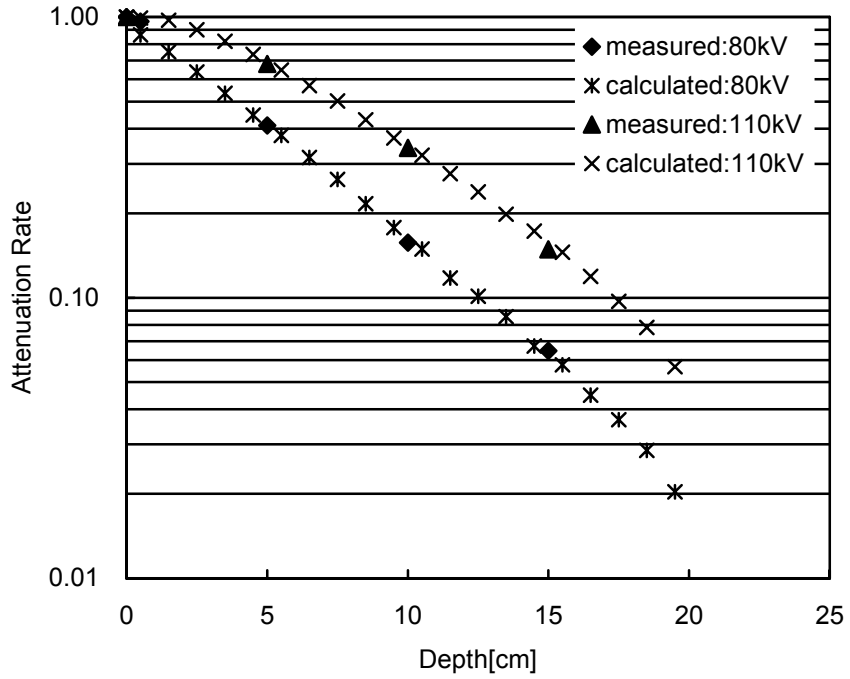

Fig.3-3 Attenuation of field center (Field size: 30×30cm^2)

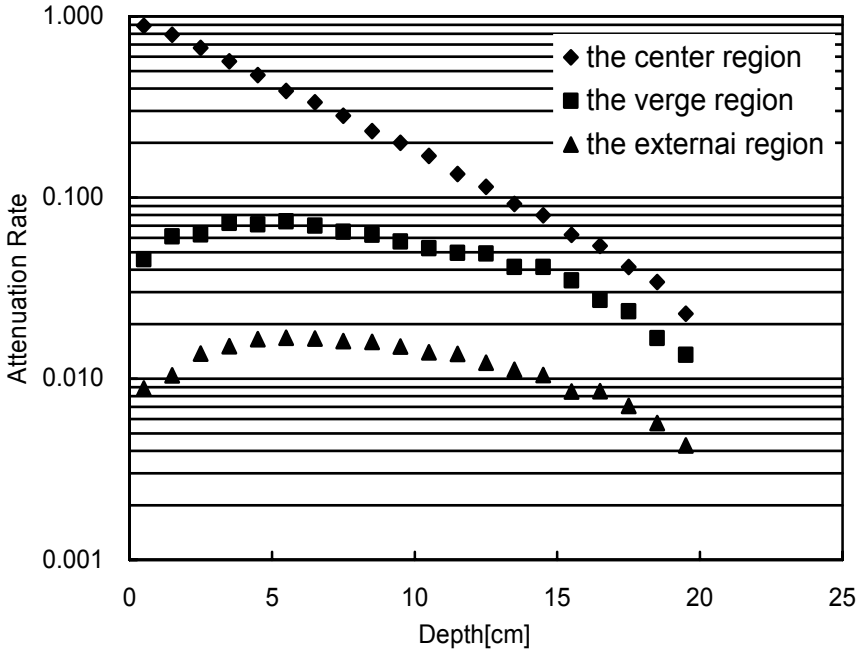

Fig.4 Absorbed dose at thee fields.

DOSE DISTRIBUTION OF STRAY RADIATION FOR INTERVENTIONAL RADIOLOGY

C. Kawabata, K.Koshida*, H.Nakagawa, M.Hayakawa

A.Chadani, A.Fukuda, K.Noto*** and T.Matsubara*****

Department of Radiological Technology, Graduate School of Medical Science, Kanazawa University
5-11-80, Kodatsuno, Kanazawa 920-0942, Japan
*Department of Radiological Technology, Kanazawa University
**Shiga Medical Center for Adults
***Department of Radiology, Kanazawa University Hospital

Abstract

The dose distributions of the stray (scattered) radiation at each applications of interventional radiology (head, chest and abdomen) were simulated using the EGS4 Monte Carlo Code. The doses were compared with the dosimetry to verify the suitability of each value. The results using the EGS4 Code were consequently similar to the results using the dosimetry. In each examination region, the positions from the floor, where the intensity of stray radiation is strongest, are different. We could determine the conditions of stray radiation by the EGS4 Monte Carlo simulation

1. Introduction

The applications of interventional radiology (IVR) are increasing in clinical examination, and tend to extend examination time. In addition, the risk of occupational exposure necessarily increases with this technique. The modalities of cardiac imaging system are also increasing. It is important to optimize radiation protection for medical staff in each IVR [1]. Radiation protection for medical staff is optimized by use of a suitable lead apron and a protection board etc. This protection needs consideration of the influence by stray radiation.

This study is performed to determine the distribution conditions of stray radiation using the EGS4 Code. In IVR examination of each part, the characteristics of stray radiation (spectra, relative intensity, and effective energy) were calculated. The dose calculated by EGS4 changed according to various factors, such as inspection tables, the form and the quality of material of the phantom, the beam limiting system and the additional filter. It is usually difficult to measure the spectrum of stray radiation but it can be determined correctly using EGS4.

2. Materials and Method

2.1 Simulations

The dose (air kerma) distributions of stray radiation at each IVR (head, chest, and abdomen) were simulated using the EGS4 Monte Carlo Code (LSCAT). The distribution of X-ray photons was calculated using the equation of Birch and Marshall.[2] Incidence x-ray spectra at a target angle of 12° and filtration 2.5 mm Al for each tube voltage were also examined. The history numbers were 10^6 per keV and the incident photon energy was changed from 10 keV to 110 keV in 1 keV steps. The X-ray tube voltage was adjusted between 70 and 110 kV. Moreover, the simulation was performed with and without a Pb attached to the surroundings of an X-ray tube. The values were compared with those obtained by dosimetry to verify the suitability of each value. An Optically Stimulated Luminescence (OSL) dose meter and a survey meter were used for dosimetry.

2.2 Geometry

The material of a phantom was shown in Table 1，and the geometry of each simulation was shown in Fig.1. The height from the tube focus was adjusted between 10 and 100cm, and it was calculated at each position. The detector was the air of $10 \times 10 \times 10$ cm^3 volume, and the radiation field was the area of 10×10 cm^2 on phantom surface in each simulation and dosimetry.

2.3 Calculation of the x-ray intensity

The emission energy of the calculated stray radiation was converted into kerma, K by

$$K = \int \left[\left(\mu_{en} / \rho \right)_E \times E \times \Phi_E \right] dE$$

The mass energy absorption coefficient, μ_{en}/ρ was calculated based on the photon attenuation coefficient data.

3. Results and discussion

3.1 HEAD MODEL

Figure 2 shows the intensity distribution of stray radiation in Head Phantom. The results obtained using the EGS4 Code were similar to those of dosimetry by survey meter. The highest point was 70 cm, and was normalized subsequently to 40 cm according to each result. The cover board (Pb) has a marked influence especially in a height of 10cm point. This is caused by a complicated construction of beam limiting device. In the simulation, the intensity calculated stray radiation was varied with the phantom material. Alderson phantom has a complicated structure，and the complicated geometry was required by the EGS4 Code.

3.2 ABDOMEN MODEL

Figure 3 shows the intensity which was normalized to 1.0 at the highest value of stray radiation. In the abdomen, the measurement results in OSL and the results of EGS4 were similar but the result of survey meter is different from others. This was because the sensitivity of the survey meter was not suited to the energy of stray radiation. The beam limiting device has a marked influence especially in the lower part as well as in the head model.

3.3 CHEST MODEL

The case that an additional filter (Cu) is inserted front of a focus was calculated by EGS4. Figure 4 shows the distributions changed by the additional filter. The intensity of stray radiation becomes low with an additional

filter on the tube voltage of 80kV, but it is a little high in 110kV. The Cu filter cuts the low energy photons in X-ray, but it is necessary to choose the most suitable filter as each tube voltage.

3.4 SPECTRA and EFFECTIVE ENERGY

In Figure5, the energy of stray radiation varied from the spectrum of EGS4. The spectra for each condition are showing the character of the stray radiation well. It is usually difficult to measure the spectrum of stray radiation but it can be determined correctly using EGS4. In spectra, the form or substances of the phantom, added filters and irradiation conditions have marked influences.

Table2 shows effective energy of stray radiation in each study. At a head model, there was a little change of the effective energy by height. In the model of a chest and an abdomen, there was the change of effective energy of about 5 keV by the difference in height. At the height position of 10cm, the number of photons is not sufficient for the statistic; therefore effective energy of stray radiation was a marked difference. Effective energy must be low at this point. In dosimetry, it is also important to determine the effective energy of stray radiation as the dose meter requires correcting by the effective energy.

4. Conclusions

The distribution using the EGS4 Code was similar to those obtained by dosimetry. We could determine the conditions of stray radiation by the EGS4 Monte Carlo simulation. It may be possible to determine an exact distribution using this method rather than a survey meter.

The dose calculated by EGS4 changed according to various factors, such as inspection tables, form and quality of material of the phantom, beam limiting system, and additional filters. EGS4 required geometry faithful to the actual conditions. Especially, it is necessary to measure the proper conditions corresponding to the X-ray tube assembly and the tube voltage.

References

[1] J. Valentin: Avoidance of radiation Injuries from Medical Interventional procedures. ICRP Publication85. (2000).

[2] R. Birch, Marshall: Computation of Bremsstrahlung X-ray Spectra and Comparison with Spectra Measured with a Ge(Li)Detector, PHYS. MED. BIOL. Vol.24, No.3, 505-517 (1978).

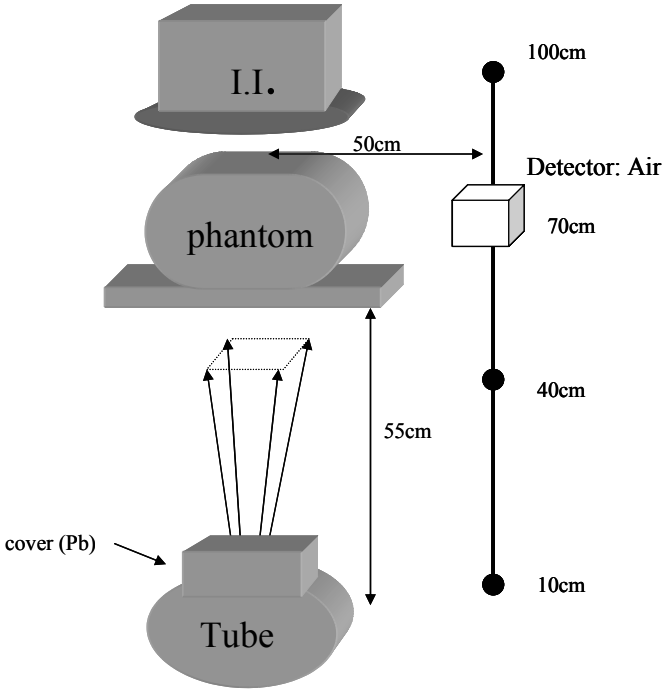

Figure1:Geometry of the elements to EGS4 and dosimetry

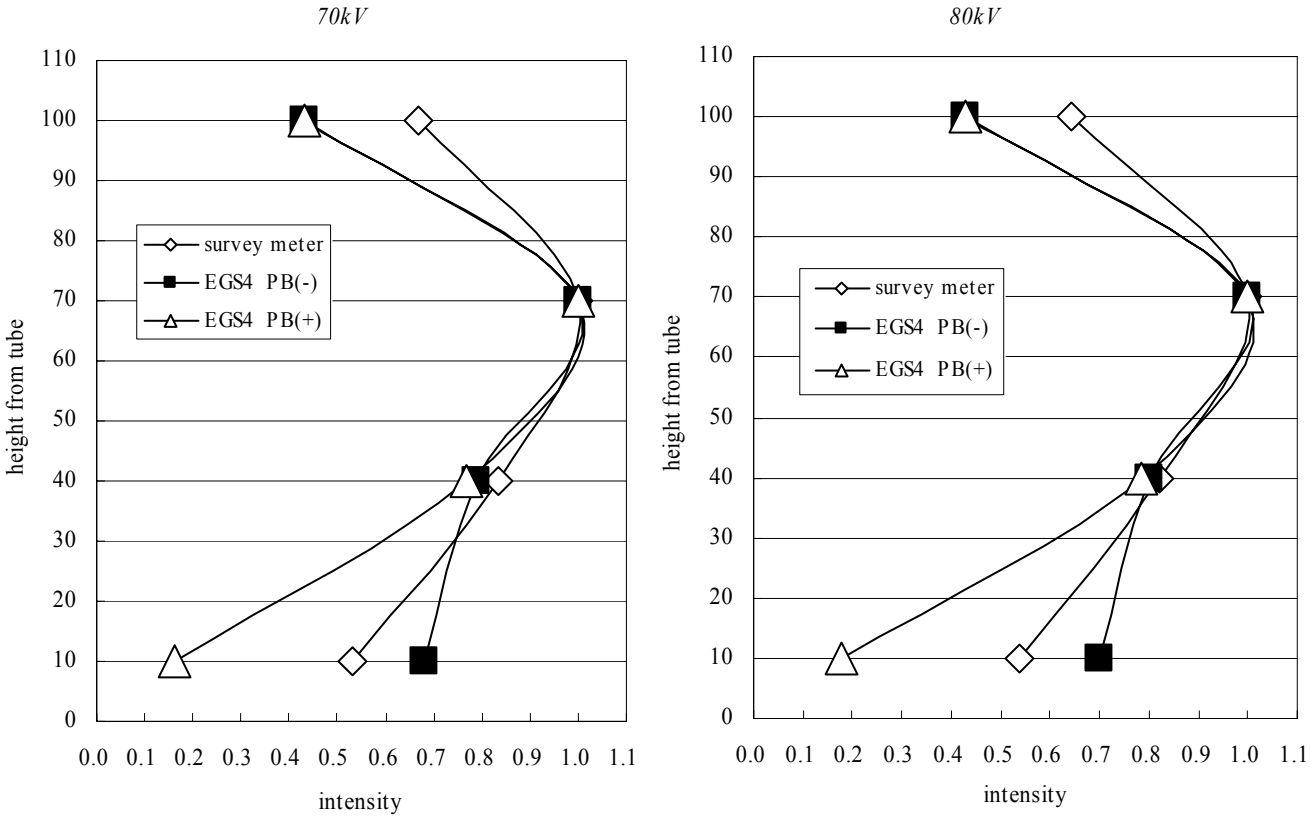

Figure2: Intensity Distribution of Stray Radiation in Head Phantom Model

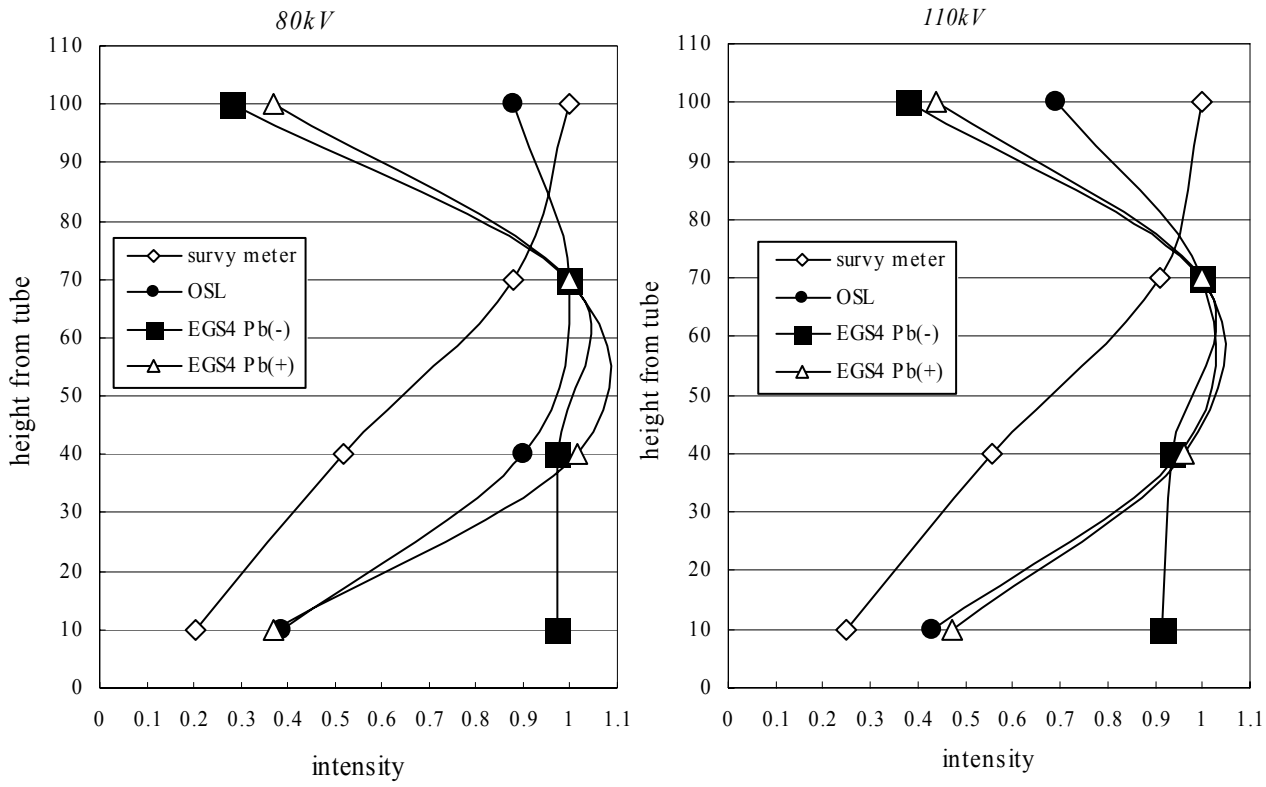

Figure3: Intensity Distribution of Stray Radiation in Abdomen Phantom Model

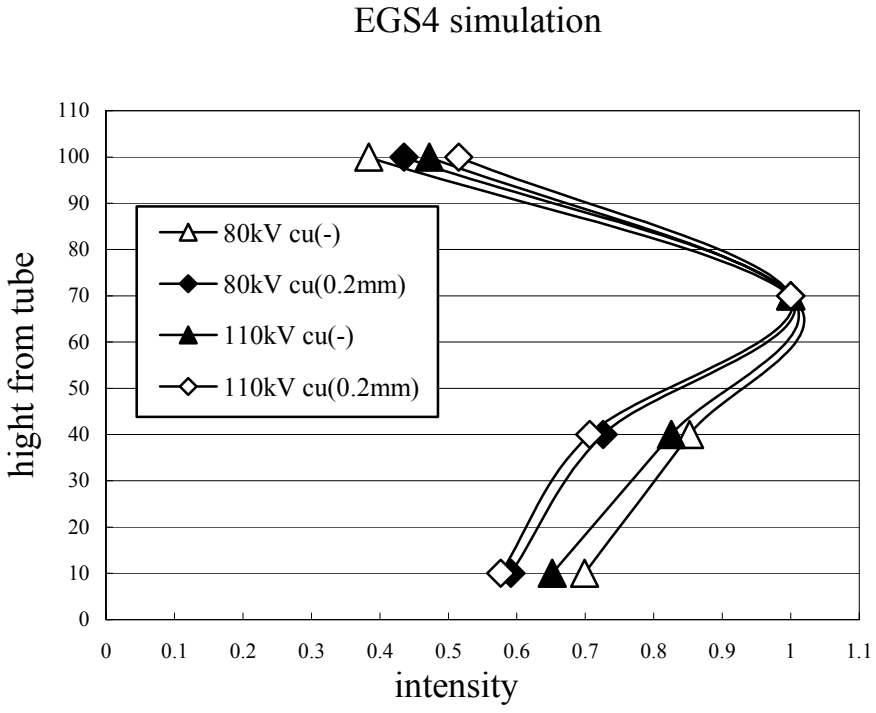

Figure4: Intensity Distribution of Stray Radiation in Chest Phantom Model

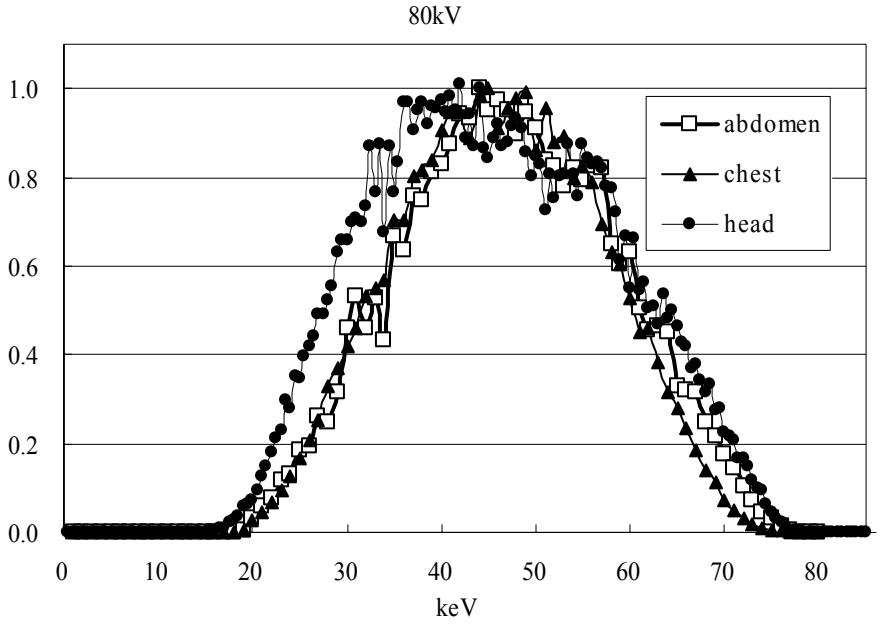

Figure5: A spectrum of stray radiation on a height from tube of 70 cm.

Table1 : the material of a phantom

Study	Phantom	Material of phantom	Phantom form
head	Alderson	Alderson bone	column
chest	Acryl Acid	Acryl Lung Bone	elliptical cylinder
abdomen	Water	Water	elliptical cylinder

Table2: Conditions and effective energy

Study	Pb cover	height from tube	effective energy
head	+	*100*	*43.2*
		70	*42.5*
		40	*42.1*
		10	*43.8*
abdomen	+	*100*	*41.4*
		70	*37.9*
		40	*36.7*
		10	*44.2*
chest	+	*100*	*43.7*
		70	*38.6*
		40	*37.3*
		10	*36.5*
		(cm)	*(keV)*

DEVELOPMENT OF THE USER CODE UCBEAM AND COMPARISON OF THE MEASURED DOSES USING A TORSO PHANTOM AND THE CALCULATED DOSES USING "OTOKO"

S.Ohnishi[a], N. Nariyama[b], K. Saito[c], N. Odano[a], K. Sawada[a], A. Konnai[a]

[a] National Maritime Research Institute, Maritime Safety Department, Tokyo, 181-0004, Japan
[b] Japan Synchrotron Radiation Research Institute, Beamline Division, Hyogo, 679-5198, Japan
[c] Japan Atomic Energy Research Institute, Department of Health Physics, Ibaraki, 319-1195, Japan
e-mail: sohnishi@nmri.go.jp

Abstract

A user code of EGS4, UCBEAM, was developed to analyze local exposures and to facilitate the data input preparation. This code can calculate both the organ doses and the absorbed dose distribution, using GSF formatted voxel phantom. An experiment was performed in SPring-8 using a resin phantom. The phantom shape is torso with a head simulating standard Japanese male person and was irradiated with a monoenergic narrow photon beam of which the energies were 40 keV and 80 keV. The doses were measured by thermoluminescent dosimeters (TLDs). A calculation was also performed by UCBEAM using Otoko phantom. The condition was the same as that of the experiment. Both Otoko numerical phantom and the physical phantom are based on average male Japanese person model. So those of the body size and the position of organs are similar. Most of the doses calculated using "Otoko" phantom and the measured doses using the torso phantom agreed within the factor of three. The construction of a numerical phantom based on the CT images of the torso phantom used in this experiment is planned.

1. Introduction

Many kinds of physical phantoms have been suggested to measure doses. They are classified according to their material compositions and shapes. The simplest one is an assembly of plastic slabs and the most complex one is human shape composed of various materials depending on its organs. These phantoms are distinguished depending on the purpose. Similarly, there are some kinds of numerical phantoms, for example, slab, sphere, and voxel type. Recently, a system to build phantoms based on the CT images of patients and to calculate doses of them is developing for aiding radiotherapy[1)].

In an application to radiation protection, a phantom which represents the group of interest is required and some physical and numerical phantom are suggested but individuality remains at some degrees. It is necessary to estimate how much the doses are influenced by the phantom individuality. Such effect is expected to be large especially in the case of local exposure. Monte Carlo method is useful to simulate local exposure but it requires tremendous amount of input data so that a user code of EGS4, UCBEAM, was developed to analyze local and whole body exposure and to facilitate input data preparation. In this work, measurement of doses using a physical phantom and TLDs, calculation of doses using Otoko phantom and UCBEAM code and comparison of the results have been done.

2. Code system

2.1 Structure

The calculation system is composed of a calculation code (EGS4), a numerical phantom (GSF formatted phantom), a user code (UCBEAM), and a postprocessor. This system can simulate photon and electron rectangle or circular cross section beam or whole body uniform irradiations.

EGS4 is a Monte Carlo code, originally developed at Stanford Linear Accelerator Center to calculate particle transportation in high energy region[2] and was modified to calculate keV-photon transportation including linear polarization, bound Compton scattering and Doppler broadening of the Compton scattered photon energy.[3]. The present system can simulate electromagnetic cascade shower in human body by EGS4. The GSF formatted phantom is a compressed voxel phantom. To reduce the phantom file size, the data of human body is described by the number of continuous voxels of which organ is the same. The UCBEAM user code interprets the input file described by a simple text and set the source conditions and geometry. The postprocessor outputs the organ doses, effective dose and distribution of energy deposition using an organ size or an arbitrary size of volume estimators.

2.2 Comparison with UCPIXEL

To verify the code system, UCBEAM was compared with the user code, UCPIXEL[4]. UCPIXEL is also a user code of EGS4 which can calculate personal doses using voxel phantom in case of whole body irradiation. Table 1 shows the equivalent doses of each organ calculated by UCBEAM and UCPIXEL[5]. The results show excellent agreement.

3. Experiment

3.1 Phantom

The shape of phantom employed in this experiment is torso with a head (hereafter refer this phantom as to "the torso phantom" simply) simulating standard Japanese male person. The torso phantom includes main organs such as lungs, heart, liver, kidneys, bladder, bone and so forth. The torso phantom is made of several kinds of resins. The lung and bone are made of "Toughbone" and "Toughlung" respectively, which are developed by KYOTO KAGAKU CO., LTD. and National Institute of Radiological Science[6]. The CT values of each resin are tabulated in Table 2[7] and the mass energy absorption coefficients of the main materials are shown in Figure 1. The phantom is sliced and has horizontal six cross sections at intervals of some cm, which is shown in Figure 2. Each section has small holes to set TLDs in. The positions of the holes are illustrated in Figure 3.

3.2 Source condition

The experiment was performed at a beamline BL38B1 in SPring-8. The beamline has a bending magnet light source of which magnetic field strength is 0.679 T and the photon energy range is 3.8 keV to 150 keV. The synchrotron radiation is highly polarized and the degree of polarization at the beamline was estimated to be more than 99.8 % in the energy region by SPECTRA[8] code. The torso phantom was irradiated with a horizontal monoenergic photon beam of 40 keV and 80 keV at the lower center of the breastbone: 3 cm below from the third phantom cross section, anterior to posterior. The beam cross section was rectangle, 1 cm in width and 0.2 cm in height, in both 40 keV and 80 keV irradiation cases. The photon flux was monitored by a free air ionization chamber[9].

3.3 Measurement

Considering the effective atomic numbers, GR-200 (LiF:Mg,Cu,P) and MSO (Mg_2SiO_4) TLDs were employed to measure the absorbed dose in the tissue and bone, respectively. The size of TLD holes on the phantom cross section is 5 mm in width, 1 mm in length and 5mm in depth. Two TLDs were set in a hole and the results were averaged. Because TLD case which modifies the response of dosimeter can not be used in such a small space, the measured value should be

corrected. In this experiment, the absorbed dose measured by TLD was corrected by the ratio of mass energy absorption coefficient of TLD and phantom material weighted by the organ-averaged photon spectrum calculated by UCBEAM. The energy dependence of luminescence efficiency of the TLD[10] was also considered. The absorbed dose D was estimated with this equation

$$D = D_{\mathrm{GR200}} \frac{\int (\mu_{\mathrm{en}}/\rho)_{\mathrm{organ}} \phi E \, \mathrm{d}E}{\int (\mu_{\mathrm{en}}/\rho)_{\mathrm{GR200}} \eta^{-1} \phi E \, \mathrm{d}E} \qquad (1)$$

in which D: absorbed dose at the position, D_{GR200}: absorbed dose of GR-200 TLD, $\eta(E)$: luminescence efficiency, $\varphi(E)$: photon flux and $(\mu_{\mathrm{en}}/\rho)_{\mathrm{i}}$: mass energy absorption coefficient of the TLD or organ "i".
D_{GR200} and $(\mu_{\mathrm{en}}/\rho)_{\mathrm{GR200}}$ were replaced by D_{MSO} and $(\mu\mathrm{en}/\rho)_{\mathrm{Mg2SiO}}$ respectively when calculating absorbed dose in bone.

4. Calculation

4.1 Otoko phantom

In this calculation, Otoko phantom was employed. Otoko phantom is a GSF formatted voxel phantom developed in Japan Atomic Energy Research Institute[5] based on the CT images of average Japanese male person. It simulates a human body in detail and is constructed by 182 parts, for example, skull, brain, bone of right hand, bone of left hand and so forth. To compare the doses, the same as the torso phantom, six horizontal cross sections were chosen and small volume estimators were set, considering the positions of organs. The positions of the estimators are illustrated in Figure 4. Both Otoko phantom and the torso phantom are based on the data of average Japanese male person, so that the distance between the cross sections differed slightly and the layout of organs are similar (see Figures 1 to 3.). It should be noticed that most of the spaces between TLDs in Figure 2 and estimators in Figure 3 are the same.

To compare with the torso phantom, Resin Body Otoko phantom has been developed. This numerical phantom has the same geometric properties such as size of voxel, number of voxels, positions of organs, height, width and so forth as Otoko phantom but the materials are different. All of the materials are replaced by several kinds of resin and the compositions and densities of organs are the same as that of the torso phantom. Likewise, six horizontal cross sections and the positions of the estimators were chosen.

4.2 Source condition

The source condition was that the beam was incident to the position 3 cm below from the third phantom cross section, the direction is anterior to posterior, the photon energy was 40 keV or 80 keV polarized horizontally and the beam cross section is 1 cm in width and 0.2 cm in height, simulating the experiments. These data were set in UCBEAM by simple text files.

5 Results and discussions

The figures 5 and 6 are the measured and calculated energy depositions at the spots illustrated in Figure 3 and 4 in each phantom section. Figure 5 is the results of 40 keV irradiation and Figure 6 is those of 80 keV irradiation. The tendencies of the measured and calculated absorbed doses were the same. Most of the results agreed within the factor of three except the doses calculated at the phantom section f. The statistical errors at section f in the case of 80 keV irradiation were too large or the tallies were zero because the number of particle history was not enough. This means few or no particles entered to the tally and the results are not reliable.

The calculated doses using Otoko Resin phantom tend to be larger or almost the same at the point above the

irradiated position (points belong to the phantom section (a, b, c)), and to be smaller at the point below the irradiated position (points belong to the phantom section (d, e, f)) than measured one using the torso phantom. This is because Otoko phantom has thinner abdominal muscle and adipose layer in front of the lungs so that the doses calculated with Otoko Resin become large. The smaller doses were caused by the difference of distance from the irradiated position. The section of Resin Otoko were chosen considering not distance from irradiation position but the position of organs, and the distances depends on phantom individuality.

6 Conclusions

Most of the calculated and measured absorbed doses have agreed within the factor of three. This means the torso phantom, which is not based on the data of a real person, appropriately simulate human body and the influence on doses caused by the individuality of these phantoms has proved to be in such extent. The distance between the irradiated point and the measured/calculated point is important and such distance characterizes a phantom.

In the case of local exposure, low energy scattering photon is important, and low energy photon flux attenuates in a short range. Variant reduction techniques are required in Monte Carlo calculation when tallying at the point apart from the irradiated position.

The construction of a numerical phantom based on the CT images of the torso phantom used in this experiment is planned. In the future works, we will evaluate the validity of UCBEAM in the case of local exposure and the differences caused by the individuality will be analyzed further.

Acknowledgment

This study was financially supported by the Budget for Nuclear Research of the Ministry of Education, Culture, Sports, Science and Technology, based on the screening and counseling by the Atomic Energy Commission.

References

1) K. Saito, E. Kunieda, Y. Narita et al : DEVELOPMENT OF THE ACCURATE DOSE CALCULATION SYSTEM IMAGINE FOR REMOTELY AIDING RADIOTHERAPY. Proceedings of the 11th EGS4 Users' Meeting in Japan. KEK Proceedings, pp. 81-87 (2003).

2) W. R. Nelson, H. Hirayama, D. W. O. Rogers : The EGS4 code System. SLAC-report-265 (1985)

3) Y. Namito, S. Ban and H. Hirayama : LSCAT: low energy photon-scattering expansion for the EGS4 Code. KEK Internal 95-10 (1995)

4) J. Funabiki, M. Terabe, M. Zankl et al : An EGS4 User Code with Voxel Geometry and a Voxel Phantom Generation System. Proceedings of the Second International Workshop on EGS, KEK Proceedings 200–20, pp. 48–55 (2000).

5) K. Saito, A. Wittmann, S. Koga et al : Construction of a computed tomographic phantom for a Japanese male adult and dose calculation system. Radiat. Environ. Biophys. 40, 69-76,(2001)

6) http://www.kyotokagaku.co.jp/english/products/phantom/Catalog/Therapy.htm

7) N. Nariyama, A. Konnai, S. Ohnishi et al : CALCULATION OF DOSIMETER RESPONSE FOR IN-HUMAN-PHANTOM MEASUREMENT TO LOW-ENERGY PHOTONS, Proceedings of the 11th EGS4 Users' Meeting in Japan. KEK Proceedings, pp. 55-64 (2003).

8) http://radiant.harima.riken.go.jp/spectra/index_e.html

9) N. Nariyama, N. Kishi, S. Ohnishi : Development of a portable free-air ionization chamber as an absolute intensity monitor for high-energy synchrotron radiation up to 150 keV. Nucl. Inst. & Meth. A524 324-331 (2004)

10) N. Nariyama, Y. Namito, S. Ban et al : Dose measurement in inhomogeneous bone/tissue and lung/tissue phantoms for angiography using synchrotron radiation. Phys. Med. Biol. 46, 717-728 (2001)

Table 1 Comparison of the equivalent dose per air kerma calculated by UCABEAM and UCPIXEL at AP irradiation.

	40 keV		100 keV	
	UCPIXEL	UCBEAM	UCPIXEL	UCBEAM
Bone marrow	3.25E-01	3.15E-01	1.02E+00	9.79E-01
Colon	8.06E-01	7.79E-01	1.46E+00	1.37E+00
Lungs	7.81E-01	7.24E-01	1.33E+00	1.29E+00
Stomach	5.45E-01	5.85E-01	1.28E+00	1.18E+00
Bladder	5.11E-01	5.08E-01	1.22E+00	1.31E+00
Liver	8.00E-01	7.92E-01	1.42E+00	1.40E+00
Oesophagus	5.02E-01	5.30E-01	1.22E+00	1.25E+00
Thyroid	1.29E+00	1.21E+00	1.75E+00	1.65E+00
Skin	8.22E-01	8.13E-01	1.14E+00	1.12E+00
Hard bone	2.10E+00	2.13E+00	2.48E+00	2.44E+00
Adrenals	2.97E-01	2.68E-01	7.99E-01	8.69E-01
Brain	2.23E-01	2.28E-01	8.10E-01	8.06E-01
Small intestine	9.50E-01	9.42E-01	1.63E+00	1.56E+00
Kidney	4.26E-01	4.28E-01	1.06E+00	1.04E+00
Muscle	5.93E-01	5.85E-01	1.08E+00	1.06E+00
Pancreas	6.54E-01	6.34E-01	1.37E+00	1.40E+00
Spleen	3.18E-01	3.43E-01	9.35E-01	9.20E-01
Thymus	8.45E-01	8.91E-01	1.67E+00	1.67E+00
Testes	1.42E+00	1.42E+00	1.89E+00	1.78E+00

Table 2. CT value of each organ[7] .

CT value	Organ
-7	soft tissue
10	bladder
30	pancreas, kidney
40	heart, bronchi, brain
50	spleen
70	liver
90	skeleton-cartilage

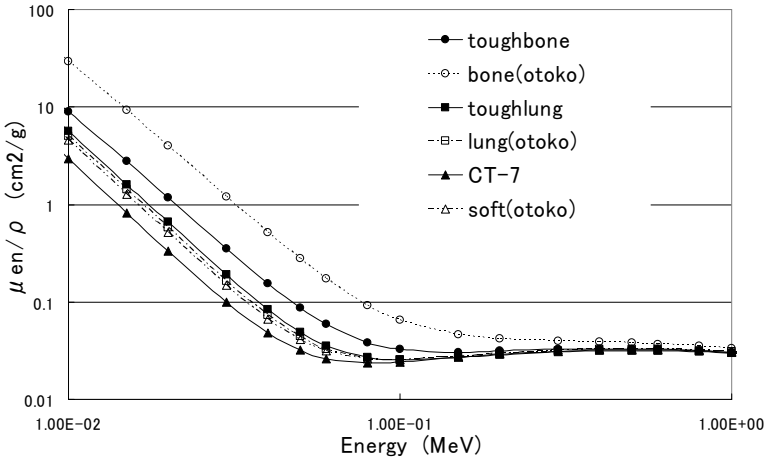

Figure 1. Mass energy absorption coefficients of main organs

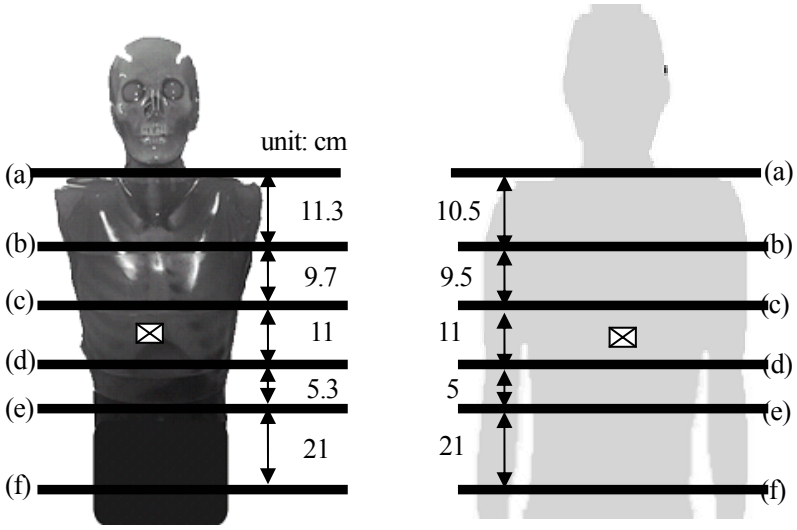

Figure 2. Cross sections in which doses were measured or calculated .
Left: The torso phantom. Right: Otoko phantom

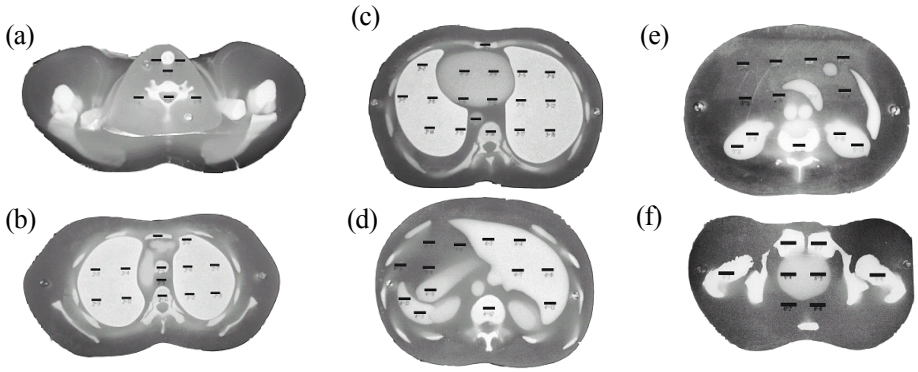

Figure 3. Cross sections of the resin body torso phantom. The solid rectangles are the positions of holes for TLDs.

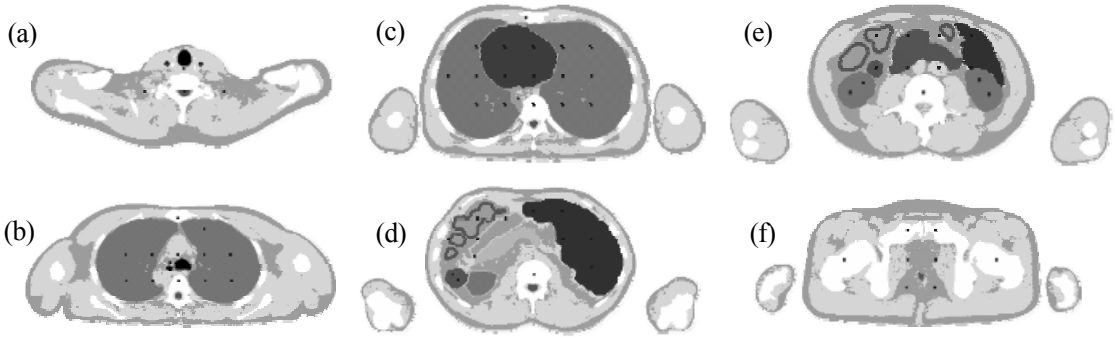

Figure 4. Cross sections of Otoko phantom. Solid circles are the positions of volume estimator

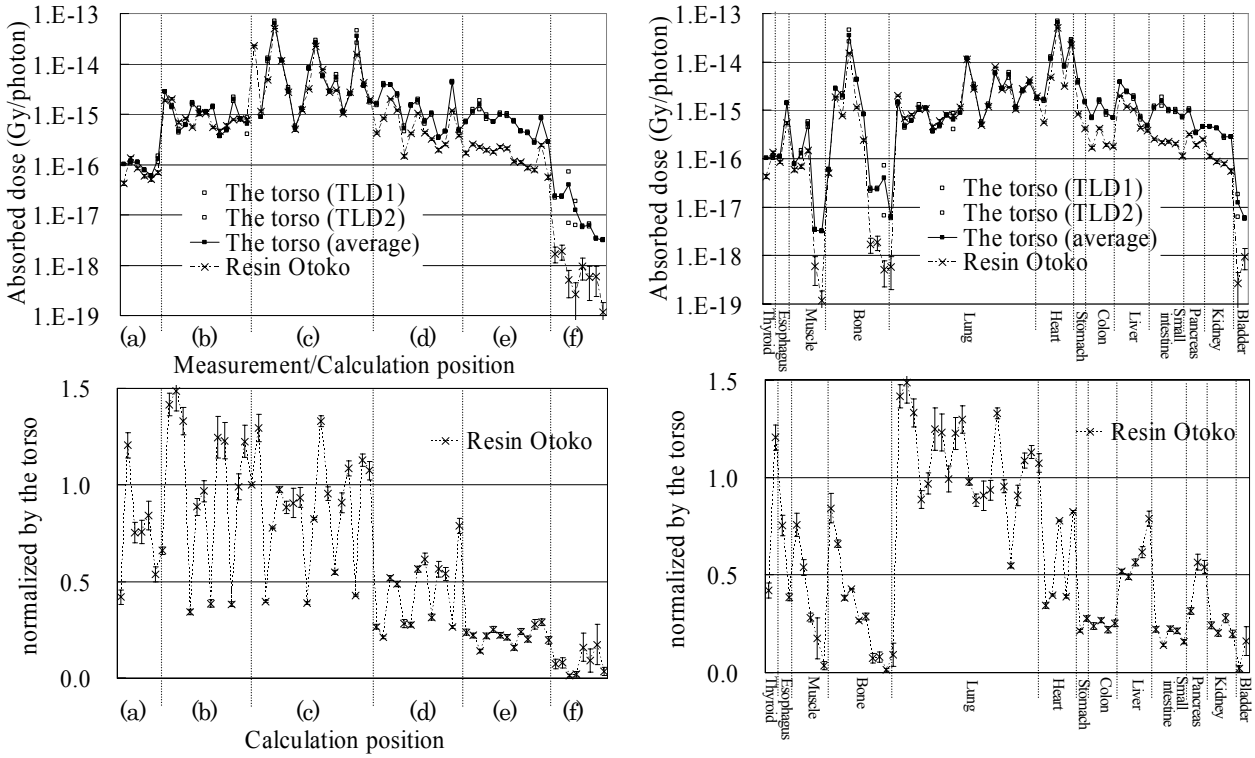

Figure 5. Absorption dose at 40 keV beam irradiation. Left: Sorted by phantom sections. The alphabets (a-d) correspond to the phantom sections in Fig. 2. Right: Sorted by organs.

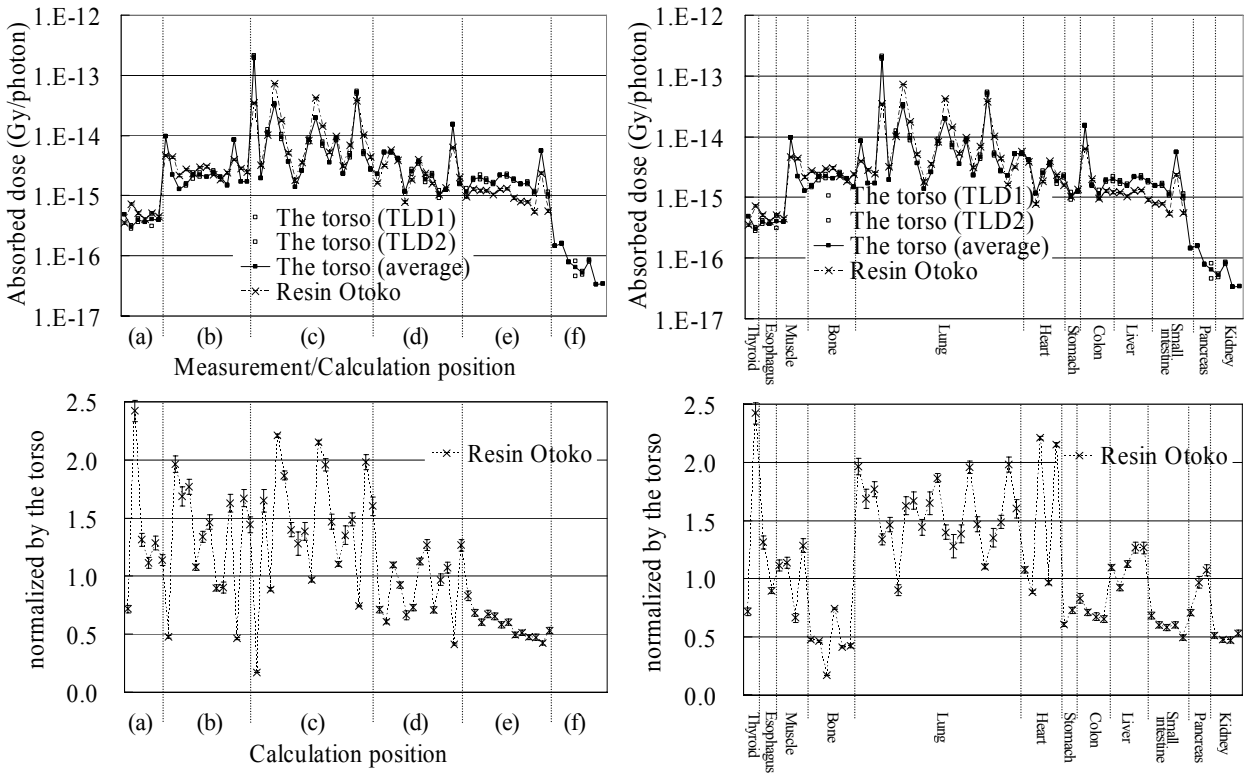

Figure 6. Absorption dose at 80 keV beam irradiation. Left: Sorted by phantom sections. The alphabets (a-d) correspond to the phantom sections in Fig. 2. Right: Sorted by organs.

ESTIMATION OF EFFECTIVE DOSE CAUSED BY STRAY RADIATION OF PHOTONS, ELECTRONS AND POSITRONS AROUND A SMALL STORAGE RING FOR A SYNCHROTRON RADIATION FACILITY

Y. Takashima and H. Kobayakawa

Department of Materials, Physics and Energy Engineering, Nagoya University, Nagoya, 464-8603 Japan
e-mail: takasima@numse.nagoya-u.ac.jp

Abstract

Spatial distribution of effective dose caused by loss electrons around a small electron storage ring for a synchrotron radiation source is calculated. In order to calculate the effective dose simply, we propose a simple formula which is applicable to calculate the effective dose of storage rings of which beam energies are from 200 MeV to 5 GeV. The formula is derived from Monte Calro simulation of radiation flux by using EGS4. We apply the formula to estimation of the effective dose distribution in a small synchrotron radiation facility planned by Nagoya University.

1. Introduction

In order to design radiation shieldings for accelerator facilities, we have to estimate the amount of radiations behind the shielding materials. There are many works to calculate the radiation doses around accelerators in consideration of shielding materials and thicknesses[1-8]. However, these works were done for large accelerator facilities which need to have thick bulk shieldings around the accelerators. But in small synchrotron radiation facilities, we have to construct simple and effective shields for radiation protection because of small areas of these facilities.

The precise information of radiation spectra in the facilities is necessary to design the effective shieldings. Most stray radiations around an accelerator are caused by beam loss. Some of electrons interact with the residual gases or other electrons in the same bunch and then leave their stable orbit and hit on the inner wall of the beam duct with small incident angles. As a result, cascade shower of particles are generated in the beam duct and spread over in the facility.

The Monte Carlo simulation code EGS4[9] was used to calculate radiation doses caused by the beam loss. We used a simple geometry for the calculation with the shielding materials lead and concrete for primary electron energy 0.2 GeV to 5 GeV. The materials of the beam duct were supposed to be iron and aluminum in the EGS4 calculation. The results were parameterized in simple formulas to calculate the radiation dose in the accelerator facilities.

As an example of the dose calculation using the simple formula, we present an estimation of radiation dose for the small synchrotron radiation facility which is planned to be constructed in Nagoya University.

2. Calculation of radiation dose

2.1 Monte Carlo calculation using EGS4 code

Monte Carlo calculation of radiation dose for the whole space in the experimental area of a synchrotron radiation facility using real geometry of the storage ring and shielding materials are very complicated.

Our strategy to calculate the radiation dose around a storage ring is the following: first, we calculate radiation flux of photons, electrons and positrons generated by loss electrons in a vacuum duct for a simple geometry shown in Figure 1 using EGS4 Monte Carlo code; second, we convert the radiation flux to the effective dose by using the conversion coefficients shown in Figure 2 and then we parameterize the results in a simple formula to calculate the effective dose around the beam duct; next, radiation dose at each point in the facility are derived by using the formula.

Figure 1 shows the geometry used in our EGS4 calculations. The shape of the beam duct was a cylinder and the thickness, the inner radius and the length of the duct were 2mm, 3cm, and 10m, respectively. The beam duct will be made from iron, which is a substitute for SUS, or aluminum. The beam duct was surrounded by spherical shielding materials.

Primary electron beam was incident on the inside of the duct of the cylinder with the incident angle of 1° on inner circumference "**c**" uniformly shown in Figure 1. The particles generated in the duct go into the shield. We used lead, iron and concrete for the shielding materials in our calculations. The composition of the concrete in our calculation was as follows, O_2 52 %, Si 32.5 %, Ca 6 %, Na 1.5 %, Fe 2 %, Al 4 %, and the density was 2.5 g/cm^3 [10]. The cut off energies of photons and electrons in materials were 50 keV and 1.5 MeV, respectively. The cut off energy of positrons was the same as it of electrons.

Radiations escaping from shielding materials were counted when they passed through the spherical surface "**S**" shown in Figure 1. We derive effective doses by using the conversion coefficients multiplied by radiation fluxes. The conversion coefficients are defined in ICRP Publication 74 [11] for the energy of photons and electrons below than 10 MeV which is much smaller than the electron beam energy circulating in storage rings. In order to calculate the effective dose for the particles of which energies are higher than 10 MeV, we use the conversion coefficients proposed in JAERI Report 1345 [12].

Photon and electron spectra generated from the vacuum duct are plotted in the Figure 3 (a) and Figure 3 (b), respectively, for the detection angles of 5 ° (circles), 30 ° (squares), 90 ° (triangles) and 150 ° (diamonds). The peaks of the photons by positron anihiration appear at about 0.5 MeV. We notice that, high energy particles reduce with increasing detection angle, so that radiation shieldings in the forward direction of long straight sections are significant. Otherwise, in the backward direction, we need shieldings for low energy stray photons.

The primary electron energy dependence of the radiation dose is shown in Figure 4. The radiation dose increase proportionally with primary electron energy between 200 MeV to 5 GeV.

The dependence of the effective dose on the thickness of the iron vacuum duct is shown in Figure 5. The calculations were done in the condition that the primary electron energy and incident angle to the inner wall of the beam duct were 1 GeV and 1 ° , respectively, with a lead shield of 5cm thick. Circles, squares, diamonds and crosses show the radiation dose of detection angles at 5 ° , 30 ° , 90 ° and 150 ° , respectively. The effective doses are almost the same value over 2 mm of the thickness except for small angle along with beam direction.

Figure 6 shows the dependence of the effective dose on the incident angle of a primary electron to the inner wall of the beam duct. The calculations were also done in the conditions that the primary electron energy was 1GeV with 5cm lead shield. The effective doses are nearly constant with the incident angle larger than 30 ° . In the case of small detection angle, the effective dose is increase with the incident angle. According to the beam tracking simulation, the incident angles of almost all the loss electrons are smaller than 1 ° , so that it is sufficient to use the effective dose at 1 ° for estimation of the radiation dose.

Figure 7 shows detection angle dependence of the effective dose calculated by EGS4 for primary electron energies of 1 GeV with incident angle on the inner wall of the beam duct of 1 ° . Circles and diamonds are calculated for iron duct of 2mm thick. Squares and crosses are for aluminum duct of 10.1 mm thick. Circles and squares are calculated without shielding materials, diamonds and crosses are calculated with lead shield of 5 cm thick. The radiation length of iron and aluminum are 17.6 mm and 89 mm, respectively. So that 2 mm thick iron and 10.1 mm thick aluminum have the same effective thickness in the unit of the radiation length. It is noticeable from the figure that, the effective doses for the different materials of the beam duct shows almost the same value if the thicknesses are the same in the unit of the

radiation length. The radiation dose is high in the forward direction and decreases exponentially with the detection angle over 0.1 rad.

2.2 Simple formula for calculation of effective dose

We propose the following formula in order to estimate the effective dose obtained by EGS4 calculations for one loss electron,

$$H(\mathrm{Sv/e\text{-}}) = \frac{H_0 \cdot E_{pr} \cdot e^{-a_1 \cdot t}}{\sqrt{\frac{1}{E} + \left(\frac{\theta}{\theta_c}\right)}^{3.0}} \cdot (y_1 + y_2 + 1.0) \cdot \frac{1}{r^2}, \quad (1)$$

$$y_1 = -\left(1 - \frac{1}{1 + e^{\frac{0.3-\theta}{0.09}}}\right) \cdot e^{-2 \cdot t}, \quad y_2 = \left(\frac{10}{1 + e^{\frac{0.3-\theta}{0.09}}}\right) \cdot e^{-a_2 \cdot t},$$

where H_0=1.2×10-11, E_{pr}(GeV) is the energy of the loss electron, t(cm) is the thickness of the thield, r is the distance from the radiation source to the detection point, θ is the detection angle and θc =0.08. The parameters of a_1 and a_2 are introduced for the effect of the absorption in the shielding materials. In the Table 1, a_1 and a_2 are given for some materials.

In Figure 8, Effective doses calculated by using equation (1) for primary electron energies of 1 GeV (a,d), 200 MeV (b,e), 5 GeV (c,f), with lead (a-c) and concrete (d-f) shields of several thicknesses. Dotted lines in the Figure 8 show the effective dose calculated by EGS4 and these are in good agreement with the results of equation (1).

3. Dose calculation for a small storage ring

As an example for the usage of the equation (1), we estimate the effective dose for Nagoya university small synchrotron radiation facility (NSSR) project. NSSR is planned to be a small synchrotron radiation facility for an x-ray source. The parameters of the accelerators of NSSR are shown in Table 2.

Figure 9 shows the sketch of NSSR storage ring. The lattice design is triple bend acrobat (TBA) and the number of super period is 2. In order to generate hard x-rays up to 20 keV, a super conducting wiggler with 7 T magnetic field will be inserted in one straight section.

As an example for our dose calculation, we supposed that NSSR storage ring is surrounded by lead wall. The thickness of the wall is 15cm and the height is 150 cm. We set the wall from 50 cm to 200 cm from the floor level.

The wall and the ceiling of the experimental hall are made in the concrete which composition is presented in the previous section. The area of the hall is 45 m × 45 m and the thickness of the concrete wall and ceiling is 30 cm.

We supposed for our dose calculation that the initial current in the NSSR storage ring is 300 mA and the all current is lost in 8 hours. We also supposed that the beam loss is occurred uniformly along the circumference of the storage ring. The beam loss in the injection time is ignored and we consider only the effective dose during the user time. The user time is 8 hours in one day and 5 days in a week. We evaluate the radiation dose in the facility as the effective dose in a week (Sv/week).

We divide the circumference of the storage ring into short parts in the length of 10 cm and the radiation dose from each part was derived by using the equation (1). The effective dose at each point in the facility is summed up the doses generated in all parts of the circumference. The photon beam lines which may scatter the radiations are ignored in our calculation.

Figure 10 shows results of our effective dose calculations in horizontal plane of the beam level. The effective dose is high in the forward direction of the straight sections but sufficiently be decreased by the shields.

4. Conclusion

We propose a simple formula to estimate the effective dose in a small synchrotron radiation facility. EGS4 is used to calculate the radiation flux generated from a beam duct, then the effective dose is derived by using the conversion coefficients proposed in ICRP Publication 74 and JAERI report 1345. The simple formula is used to estimate effective dose distribution in the facility of NSSR project and the effective doses are in the permissible range.

References

1) H. Dinter and K. Tesch, Nucl. Instrum. Methods in Phys. Res., **143**, (1977) 349.
2) H. Dinter, J. Pang and K. Tesch, Rad. Prot. Dosim., **25**, (1988) 107.
3) H. Dinter, J. Pang and K. Tesch, Rad. Prot. Dosim., **28**, (1989) 207.
4) H. Dinter, Nucl. Instrum. Methods in Phys. Res., A **276**, (1989) 1.
5) D.W.O. Rogers Health Phys., **46**, (1984) 891.
6) T. M. Jenkins, Nucl. Instrum. Methods in Phys. Res., **159**, (1979) 265.
7) W. P. Swanson, Technical Report Series No.188, IAEA (1979).
8) E. Braeuer, ESRF/SHIELD/88-04 Oct. (1988).
9) W. R. Nelson, H. Hirayama and D. W. O. Rogers, SLAC-Report-256, (1985).
10) Review of particle physics, Phys. Lett. B, (2004) 98.
11) ICRP Publication 74 (1996).
12) Y. Sakamoto, O. Sato, S. Tsuda, N. Yoshizawa, S. Iwai, S. Tanaka and Y. Yamaguchi, JAERI Report 1345, (2003).

	Pb	Fe	Concrete
a_1 (cm^{-1})	0.45	0.2	0.044
a_2 (cm^{-1})	2.0	1.2	0.4

Table 1　Parameters of attenuation coefficients in equation (1)

Lattice	TBA×2
Beam energy	1 (GeV)
Circumference	36 (m)
Current	300 (mA)
Straight section	6.4 (m)×2
Bending radius	2.38 (m)
Natural emittance	200 (nm rad)

Table 2　Parameters of NSSR storage ring.

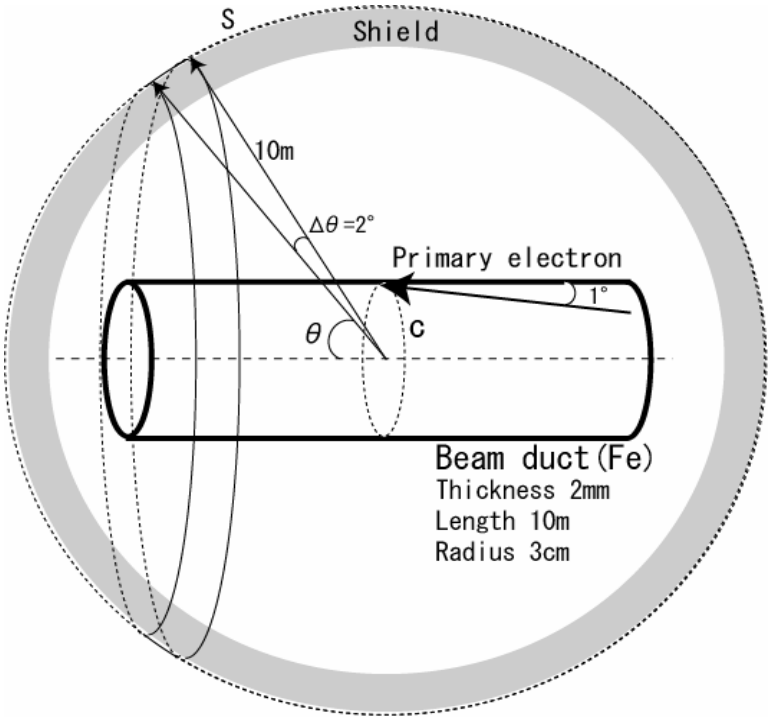

Figure 1　The geometry used in EGS4 calculations.

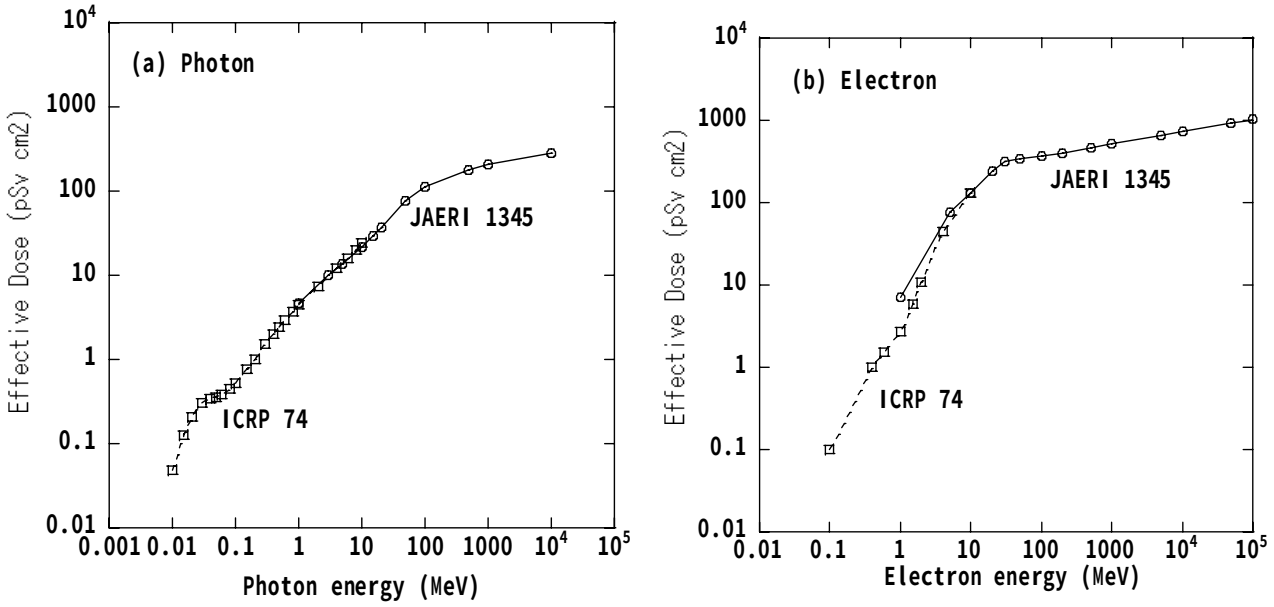

Figure 2 Conversion coefficients from radiation flux to effective dose. (a) is for photons and (b) is for electrons. We use the data of ICRP 74 for particle energies less than 10 MeV, JAERI 1345 for higher than 10 MeV.

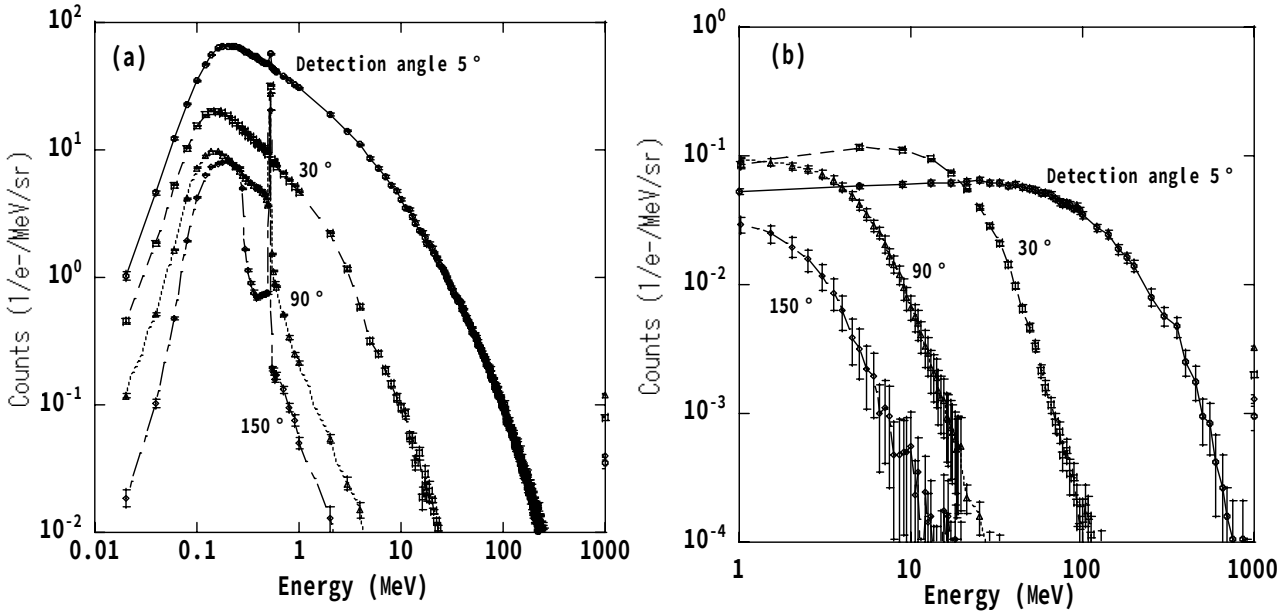

Figure 3 Photon (a) and electron (b) spectra calculated by EGS4 using the geometry of Figure 1 without shields. Solid, dashed, dotted and dashed-and-dotted lines show spectra at the detection angle of 5 ° , 30 ° , 90 ° and 150 ° , respectively.

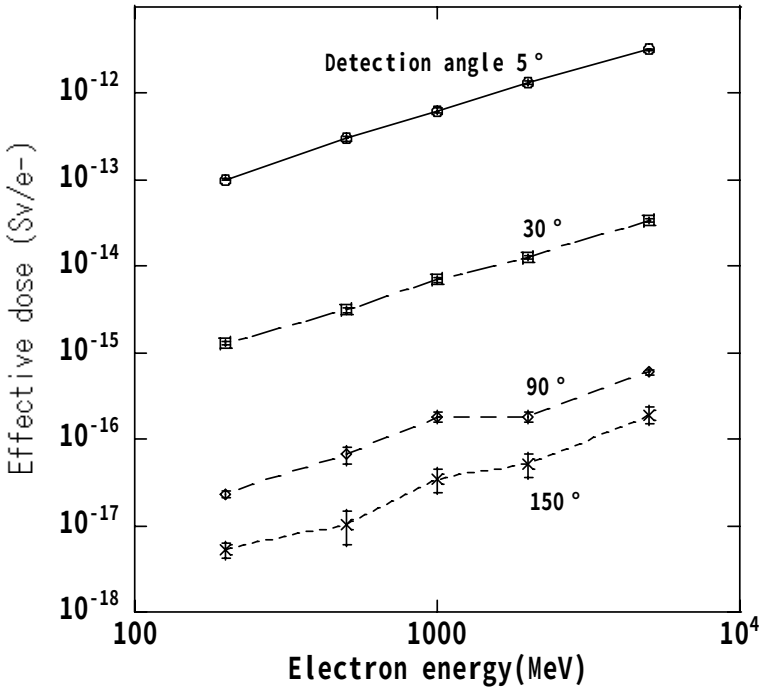

Figure 4　Primary electron energy dependence of the effective dose.

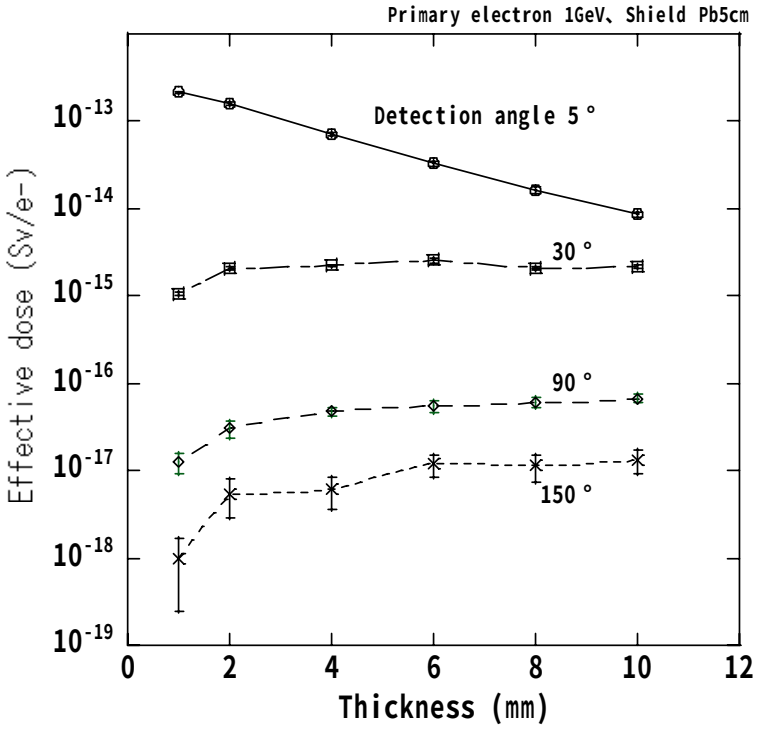

Figure 5　Duct thickness dependence of the effective dose. In this calculation, primary electron energy is 1GeV and we set 5cm thick lead shield.

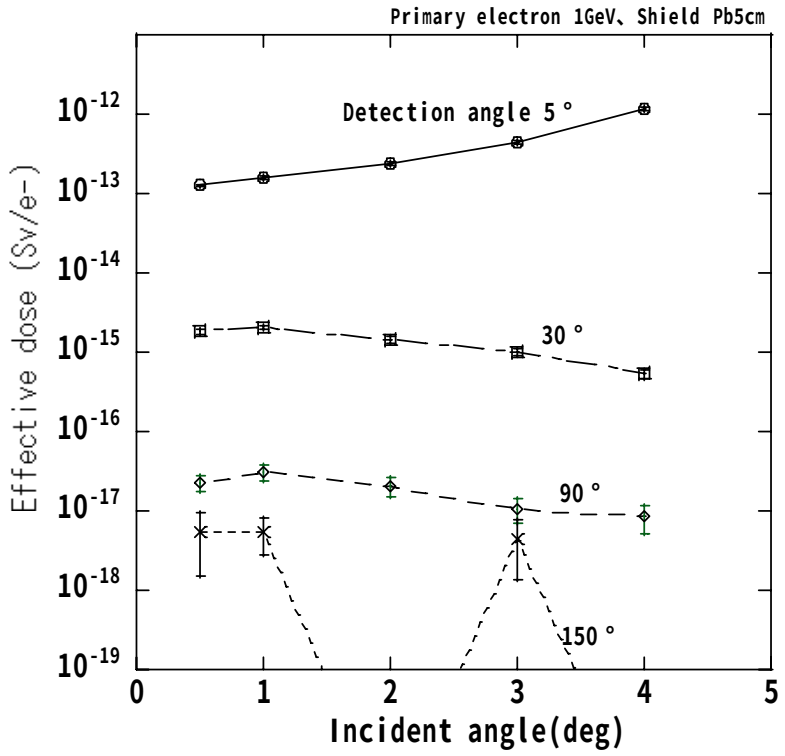

Figure 6　Dependence of the effective dose on the incident angle of a primary electron on the inner wall of the beam duct. Calculations were done in the condition that the primary electron energy was 1GeV with 5cm lead shield.

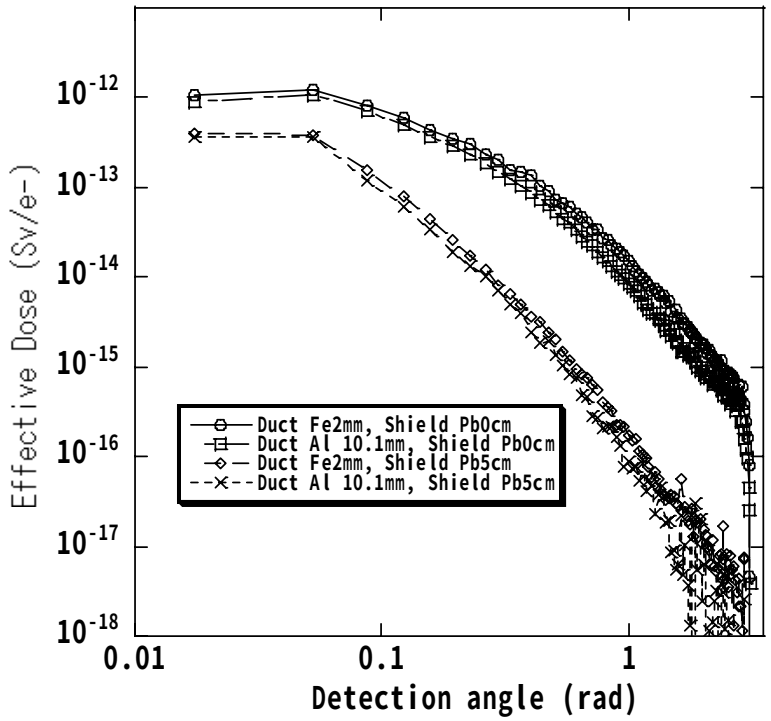

Figure 7　Detection angle dependence of effective dose calculated by EGS4 for the incident primary electron energy of 1 GeV with incident angle on the inner wall of the beam duct of 1 ° .

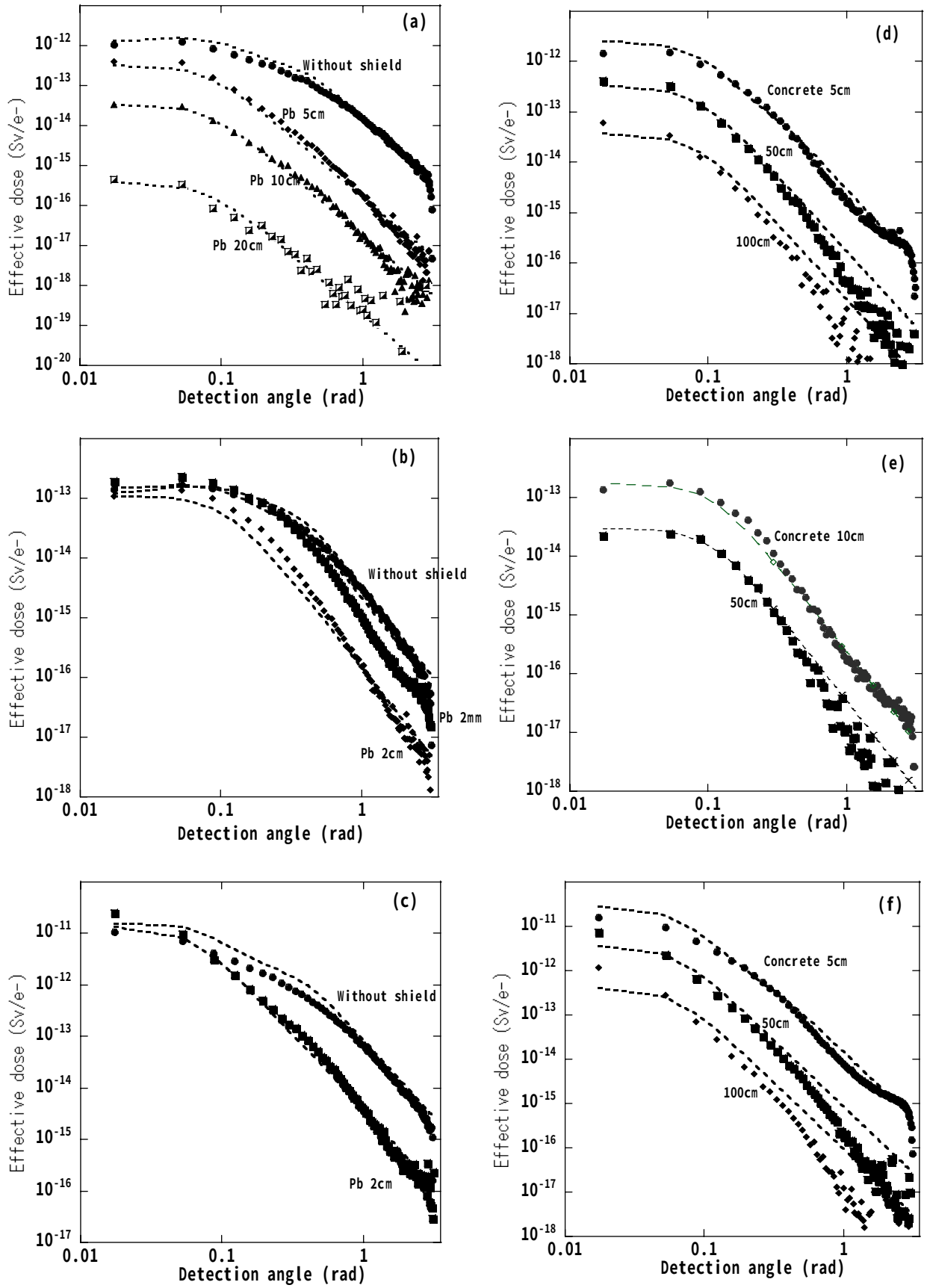

Figure 8 Effective doses calculated by using equation (1) for loss electron energies of 1 GeV (a,d), 200 MeV (b,e), 5 GeV (c,f), with lead (a-c) and concrete (d-f) shields of several thicknesses. Dotted lines in the Figure 8 show the effective doses calculated by EGS4 and these are in good agreement with equation (1).

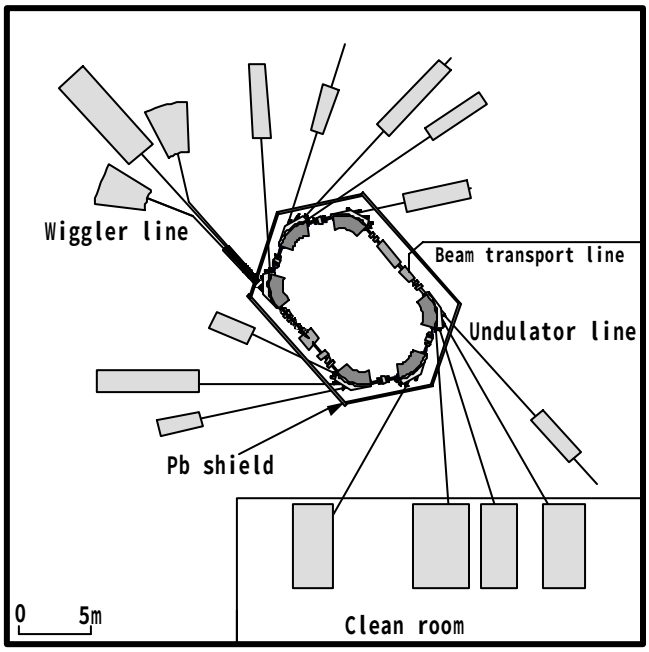

Figure 9 Sketch of NSSR storage ring.

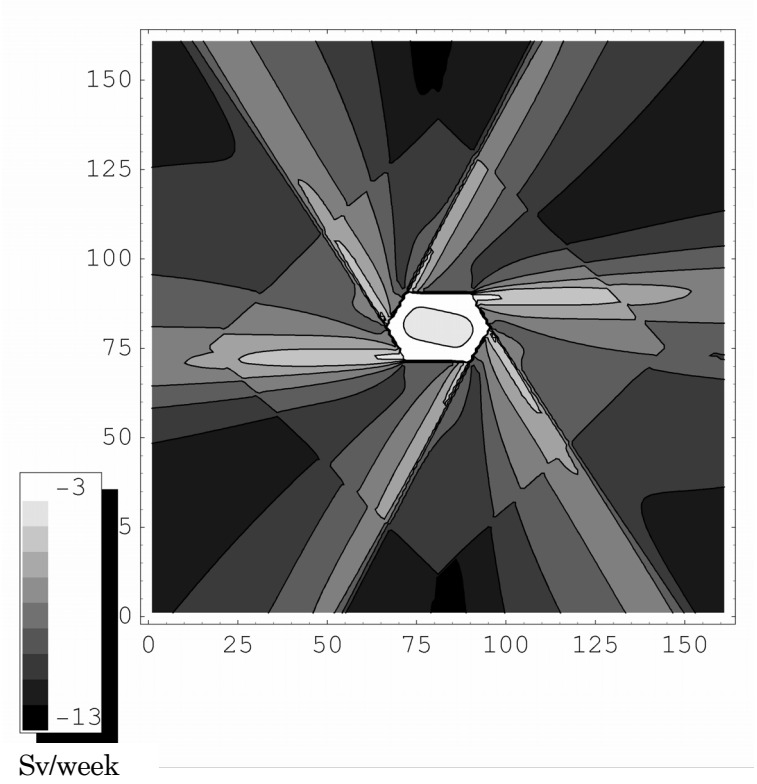

Figure 10 Effective dose distribution in NSSR facility calculated by using equation (1).